BIOMAT 2015

International Symposium on
Mathematical and Computational Biology

edited by

Rubem P Mondaini

BIOMAT 2015

International Symposium on
Mathematical and Computational Biology

This page intentionally left blank

BIOMAT 2015

International Symposium on
Mathematical and Computational Biology

Roorkee, Uttarakhand, India 2 – 6 November 2015

edited by

Rubem P Mondaini
Federal University of Rio de Janeiro, Brazil

World Scientific

NEW JERSEY • LONDON • SINGAPORE • BEIJING • SHANGHAI • HONG KONG • TAIPEI • CHENNAI • TOKYO

Published by

World Scientific Publishing Co. Pte. Ltd.
5 Toh Tuck Link, Singapore 596224
USA office: 27 Warren Street, Suite 401-402, Hackensack, NJ 07601
UK office: 57 Shelton Street, Covent Garden, London WC2H 9HE

British Library Cataloguing-in-Publication Data
A catalogue record for this book is available from the British Library.

BIOMAT 2015
Proceedings of the International Symposium on Mathematical and Computational Biology

ISBN 978-981-3141-90-2

Printed in Singapore

Preface

The BIOMAT 2015 International Symposium has been held in the Department of Mathematics of the Indian Institute of Technology Roorkee at Roorkee, Uttarakhand, India, on November 02–06, 2015. Senior representatives of the Indian Scientific Community have been in charge of the Local Organizing Committee. We thank the collaboration of Dr. Sandip Banerjee, Prof. Vinod Kumar Katiyar, Prof. Somdatta Sinha, Dr. Saugata Hazra, Prof. Govindan Rangaranjan.

The participants came from fourteen countries. From Europe (France, Germany, Hungary, Italy), from Americas (Brazil, Canada, Mexico, United States), from Africa (Morocco, South Africa, Nigeria), from Asia (India, Japan). In an informal atmosphere of continuous sessions, during five days, Plenary Speakers, authors of contributed papers and research students had the opportunity of discussing many research themes and to make commitments for future collaboration. The fine tradition of the BIOMAT Consortium has succeed once more at enhancing the scientific interdisciplinary activities of Mathematical and Biological Sciences of practitioners from developing countries.

Financial support has been given by the Indian Institute of Technology Roorkee in terms of sixty fellowships to cover the expenses of full pension accommodation of selected participants and we thank our Indian colleagues for their hospitality in Roorkee. Special thanks are due to Dr. Sandip Banerjee for all his efforts on the local organization of the conference and his kindness on the organization of social activities. On behalf of the BIOMAT Consortium, we thank very much all the representatives of the host institution.

On behalf of the BIOMAT Consortium-International Institute of Interdisciplinary Sciences (http:www.biomat.org), a non-profit international association of scientists and research students, which is responsible by the organization of the BIOMAT Symposium series and the BIOMAT series of indexed books, we would like to acknowledge the collaboration of Carmem Lucia Suprino Costa in the editorial work of the BIOMAT 2015 book and her help to the BIOMAT Consortium Secretariat during the analysis of reports from reviewers and the submission of corrected versions by successful authors.

The members of the BIOMAT Consortium Director Board for the period 2016-2019, have been nominated during the BIOMAT Consortium General Assembly of the BIOMAT 2015 International Symposium. The present

Director Board has representatives from Western Europe, Eastern Europe, North America, South America, Middle East and Asia. The representatives from Africa and Oceania will be announced soon.

Rubem P. Mondaini
President of the BIOMAT Consortium
Chairman of the BIOMAT 2015 Scientific Advisory Committee

Roorkee, Uttarakhand, India, November 2015

Editorial Board of the BIOMAT Consortium

Contents

This page intentionally left blank

NETWORK STRUCTURE AND ENZYMATIC EVOLUTION IN *LEISHMANIA* METABOLISM: A COMPUTATIONAL STUDY*

A. SUBRAMANIAN AND R. R. SARKAR†

Chemical Engineering and Process Development,
CSIR-National Chemical Laboratory, Pune, India
and
Academy of Scientific & Innovative Research (AcSIR),
CSIR-NCL Campus, Pune, India
†*E-mail: rr.sarkar@ncl.res.in*

Leishmaniasis is a widespread neglected tropical disease caused by *Leishmania* protozoan parasites that are transmitted to mammalian hosts through bites of infected female sandfly vectors. The human and sandfly hosts provide a harsh ecological niche for *Leishmania* parasites to survive and proliferate. Due to its adaptation to the host environment, *Leishmania* parasites optimize their metabolism to utilize the available inadequate resources for maximum growth and energy generation. This adaptation is developed through a long-standing evolutionary relationship of the parasite phenotype with the host. Understanding the role of metabolic function on evolution of enzymes requires a systems-wide perspective. In our study, we attempt to bridge the molecular evolution of the genotype with the phenotype thereby understanding the influence of metabolic network structure and its function on enzyme evolution in the *Leishmania* parasite. To explore this phenomenon, using an available reconstruction of *Leishmania major* metabolism, we attempt to understand the relationship of *in-silico* predicted flux profiles of the *L. major* metabolic network and its topological properties with the evolutionary rates of metabolic enzymes. Our results suggest that the central, highly connected metabolic enzymes evolve at a faster rate as compared to less connected enzymes. On the contrary, enzymes bearing a higher flux under a minimal environment with rich carbon sources presented by the host, experience higher evolutionary constraints. Performing a genome-wide flux coupling analysis, we also explain the trend of evolutionary rate within enzymes belonging to flux-coupled pathways. Also, we explain the relationship of codon usage with network flux to understand the influence of the genome on metabolic function. Our study highlights the importance of systems-based approaches to understand the role of enzymatic evolution in *L. major* thereby leading to an adaptive description of metabolic function.

*This work is supported by a grant from 12th FYP project HOPE (BSC0114) of Council of Scientific and Industrial Research (CSIR), India to RRS. AS acknowledges the Senior Research Fellowship from DBT-BINC.

1. Introduction

Leishmaniasis is a neglected tropical disease caused by *Leishmania* protozoan parasites and is transmitted to mammalian hosts (both human and animal) through bites of infected female sandfly vectors. Around 310 million people are at a risk of the leishmaniasis infection globally, with 1.3 million reported leishmaniasis cases worldwide [1]; this problem being intensified by the unavailability of a vaccine [2, 3, 4] and very few effective drugs [5, 6]. The reason for this incapability to eliminate the parasite is due to the incomplete understanding of parasite metabolism and its ability to adapt to different stress conditions. This problem is further intensified by the fact that the role of the genotype in establishing an adaptive phenotypic landscape is still not appropriately studied. These diverse problems can be addressed only by unraveling evolutionary events within the *Leishmania* genomes that lead to evolution of enzymes under environmental pressure. With the advent of evolutionary systems biology approaches [7, 8], the effect of enzyme evolution on the metabolic phenotype of organisms can further help to understand the coordinated functioning of metabolism so as to adapt to the environmental pressure.

Previously, a large number of topology-based studies have been used to infer evolution of enzymes in metabolic networks of bacteria and yeast [9, 10, 11]. Also, from the function or behavioral point of view, few studies have also attempted to understand the role of flux carried by an enzyme and its role in enzyme evolution [12, 13, 14, 15]. But, specifically for *Leishmania*, the genotype and phenotype has largely been analyzed independently without considering an explicit evolutionary linkage between them [16, 17, 18, 19]. Also, there is no available study on the phenotypic perspective of metabolic enzyme evolution in *Leishmania*. The aforementioned studies have been largely carried out in free-living species that experience different types of environmental stresses as compared to parasites which live in a constrained and less variable, nutrient-deprived stress environment.

In the present study, we attempt to explore the effect of phenotypic adaptation on enzyme evolution in *Leishmania major* metabolism by considering the different structural and behavioral network properties of the *L. major* metabolic network and identifying their associations with rates of enzyme evolution. By finding associations between genomic features like codon usage, GC content and the evolutionary rates, we hypothesize the nascent role of codon usage in modulating enzyme abundance and thereby producing an effective regulation of metabolic flux. Further, representing

the metabolic network as an enzyme graph, we calculate the connectivity and centrality of enzymes with other enzymes that produce or utilize their reactants or products and identify their associations with rates of enzyme evolution. With known systems biology approaches like Flux Balance Analysis (FBA) [20] and Flux Coupling Analysis (FCA) [21], we explore the flux distribution of the enzymes within the metabolic network to predict their associations with evolutionary rates and also to identify conserved physiological modules that tend to demonstrate similar evolutionary relationships. Further, we also asked the question whether the enzymes conserved during evolution display similar topological properties or not. Analyzing these properties, we shortlisted a set of enzymes that are highly conserved during evolution and also have an important position within the metabolic network. Together our results suggest the importance of a phenotype-based evolutionary study on evolution of enzymes in *L. major* metabolism — to delineate the effect of network structure and behavior on evolution of metabolic enzymes and to identify the degree to which the evolutionary conservation of enzymes within the genotype exerts a control over the phenotype.

2. Methods

2.1. *Dataset curation*

For calculation of K_a/K_s ratios of genes in *L. major*, coding set of sequences (CDS) datasets for 5 *Leishmania* genomes namely *Leishmania major* Friedlin, *Leishmania donovani* BPK282A1, *Leishmania infantum* JPCM5, *Leishmania braziliensis* MHOM BR75 M2904, and *Leishmania mexicana* MHOM GT 2001 U1103, and the whole proteome mass spectra data for each gene in *L. major* were downloaded from TriTrypDB release 25 [22] (updated as of 23rd July 2015). The *L. major* Friedlin dataset was further processed for extraction of CDS of genes belonging to the previously curated *L. major* iAC560 metabolic network [16]. Orthologous groups were downloaded for each gene considered in the iAC560 study from the TriTrypDB database [22], and their corresponding sequences were extracted from the genomes of *L. braziliensis*, *L. donovani*, *L. infantum* and *L. mexicana* using an in-house PERL code.

2.2. *Calculation of evolutionary rates*

The K_a/K_s ratio [ratio of number of non-synonymous substitutions per synonymous site (K_a) to number of synonymous substitutions per syn-

onymous site (K_s)] was calculated for each gene (enzyme) considered in the *L. major* iAC560 metabolic network [16]. K_a/K_s ratios for each gene were calculated by performing a multiple sequence alignment of the gene of interest with its orthologous sequences from the evolutionarily related *L. infantum*, *L. donovani*, *L. mexicana* and *L. braziliensis* species. The multiple sequence alignment file was further processed using a standalone version of the PAL2NAL [23] program to remove sequence positions with gaps and to extract corresponding codon alignments. The processed file was then provided to the PAML program version 4.8a [24] to calculate the K_a/K_s ratios for each metabolic gene using the Goldman and Yang codon substitution model [25]. The K_a/K_s ratio is a measure that quantifies the degree of natural selection acting on a protein. $K_a/K_s > 1$ indicates negative purifying selection, $K_a/K_s = 1$ indicates neutral evolution and a $K_a/K_s > 1$ denotes positive selection acting on a protein.

2.3. *Flux balance analysis*

The *L. major* iAC560 constraint-based metabolic model [16] was used to study the behavior of *L. major* metabolism. The model reactions with the corresponding metabolites can be represented as a stoichiometric matrix S, a mathematical representation of the metabolic network. The S matrix consists of m reactions and n metabolites. Each element in S_{ij} represents the stoichiometric coefficient of metabolite i in reaction j. The coefficients are positive if metabolite i is produced in reaction j and negative if it is consumed. The iAC560 model comprises of 1112 reactions and 1101 metabolites. Each reaction in the model is constrained with respect to some previously available information. For example, there are 63 exchange reactions within the model which can be selectively constrained as per the preference of the cell to mimic a specific metabolic behavior. After applying the required constraints to the iAC560 model, FBA [20] was performed.

The rate of change of concentration of every metabolite considered in the iAC560 model can be represented as a function of individual reaction fluxes

$$\frac{dC}{dt} = S.v \tag{1}$$

Where, C = vector of metabolite concentrations; S = stoichiometric matrix of m rows of metabolites and n columns of reactions; v = reaction flux vector for n reactions.

Assuming the system to function at steady state, from Eq. (1),

$$\frac{dC}{dt} = 0 \text{ and } S.v = 0 \quad (2)$$

As the nature of this system is underdetermined, FBA uses linear programming (LP) techniques to solve the above system of equations and identify a solution vector (flux distribution) in a particular constrained situation that would optimize a specific cellular objective.

Note that each reaction flux v_i in the flux vector is constrained between bounds a_i and b_i such that, the LP optimization problem is formulated as,

Maximize O,
subject to constraints S.v = 0 and $a_i \leq v_i \leq b_i$,
where O = Objective function to be maximized, a_i is the lower bound and b_i is the upper bound of flux through every reaction i in the model.

To perform FBA, all reversible reactions were bounded between a = -1000 and b = 1000 and irreversible reactions between a = 0 and b = 1000. Exchanges specifically considering release of a particular metabolite from the cell were bounded between a = 0 and b = 1000 whereas exchanges considering uptake of a metabolite were bounded between a = -1000 and b = 0. The *L. major* biomass reaction (Biomass_LM3) in the iAC560 model was used as the objective function for linear optimization. Minimal medium used in the analysis was previously predicted in the *L. major* iAC560 study [16]. The exchanges of metabolites that composed the minimal medium (arginine, cysteine, histidine, hypoxanthine, isoleucine, leucine, lysine, methionine, oxygen, phenyalanine, inorganic phosphate, threonine, tryptophan, and valine) were kept unconstrained (a = -1000, b = 0) due to their essential requirement. The metabolic flux magnitude for reactions, calculated in different conditions, is expressed in mmol/gDw/hr.

2.4. *Codon usage and GC content*

To understand the relationship between the genotype and the phenotype, both codon usage and GC content were studied and compared with metabolic behavior of *L. major*. Codon adaptation index (CAI) is a widely used measure of codon usage that assesses the degree of translation selection acting upon a gene [26]. CAI is calculated for every gene relative to a known reference set of highly expressing genes as a geometric mean of

relative synonymous codon usage (RSCU) values.

$$CAI = exp\frac{1}{L}\sum_{i=1}^{18}\sum_{j=1}^{k_i} x_{ij} ln(w_{ij}), \text{ where } w_{ij} = \frac{RSCU_{ij}}{RSCU_{imax}} \quad (3)$$

$RSCU_{imax}$ is the relative synonymous codon usage of the most frequently used codon for the i^{th} amino acid and L is the length of the gene. The weight w_{ij} is calculated from a reference set of highly expressing genes. The values of CAI are scaled between 0 and 1. CAI value for each gene in *L. major* used in the main analysis was taken from our previous study [18, 19].

The frequency of G and C in different codon positions (GC1s, GC2s, and GC3s) can be computed as the sum of counts of G and C nucleotides divided by the sum total of frequencies of A, T, G and C at the respective positions in the codons.

$$GCns = \frac{\sum G_n + \sum C_n}{\sum A_n + \sum T_n + \sum G_n + \sum C_n} \quad (4)$$

where *GCns* is the frequency of G and C at the n^{th} synonymous position of the codon (n = 1, 2, 3) in a particular gene. Average GC content for a gene and average GC content at the 3^{rd} position of a codon in each gene of the *L. major* genome were taken from our previous study [18, 19].

2.5. *Flux coupling analysis*

To identify functional modules within the *L. major* genome-scale metabolic network, the flux coupling analysis method was used [21]. Flux coupling analysis identifies directionally coupled, partially coupled, and fully coupled reaction pairs within the metabolic network under specific exchange constraints. Reaction pairs are directionally coupled when a non-zero flux in one reaction leads to a non-zero flux in the other reaction but the reversible is not possible, partially coupled when a non-zero flux in one reaction leads to a non-zero variable flux in the other reaction, and fully coupled when a non-zero flux in one reaction leads to a non-zero fixed flux through other reaction. The analysis was performed using the F2C2 tool [27] that computes a flux coupling table (fctable) for the iAC560 model that identifies a 714 x 714 flux coupled matrix that contains information about the coupled reaction pairs. For the purpose of identifying functional modules, an undirected flux coupled reaction graph was generated by modifying the fctable, considering the reaction pairs to be either coupled (1) or uncoupled (0).

The uncoupled reaction pairs were removed from the graph to generate a 614 x 614 adjacency matrix.

2.6. *Topological analysis of enzyme graphs*

To understand the topological properties of *L. major* metabolism, the iAC560 metabolic network was converted into an undirected reaction (enzyme) graph where the nodes are the enzymes and each edge is a connection between two enzymes through the substrate and product metabolites. The enzyme graph was generated using the TNA4OptFlux plugin [28] in OptFlux 3.2.8 [29]. Similarly, for the flux coupled reaction graph, the flux coupling table was modified to consider only coupled and uncoupled reaction pairs thereby generating an undirected flux coupled enzyme graph. The graph diagram for the flux-coupled reaction graph was generated in Gephi 0.8.2 using the Fruchterman-Reingold algorithm [30]. The aforementioned generated enzyme networks were then analyzed for its topological properties [31]. The following topological properties were calculated from the enzyme graphs:

(1) Degree centrality: This graph measure gives the information about the total number of enzymes connected to a particular enzyme within the enzyme graph. A node having a higher number of connections can imply the considered node to be a hub and random disruption of such nodes might lead to network failure.

(2) Closeness centrality: This graph measure gives information about enzymes that can communicate quickly with other enzymes in the network. Let $G = (N, E)$ be an undirected graph where N = nodes and E = edges, then the closeness centrality is defined as,

$$C_{closeness}(i) = \frac{1}{\sum_{x \in N}^{N} d(i,x)} \tag{5}$$

where $C_{closeness}$ indicates the closeness centrality of a particular enzyme and $d(i,x)$ denotes the distance or shortest path of enzyme i with another enzyme x in the network. This centrality measure has been previously used in metabolic networks to identify central nodes [32].

(3) Betweenness centrality: This graph measure gives information of the number of shortest paths between a pair of enzymes that passes through a given enzyme in the network. The enzymes thus identified

would act as bottlenecks (rate-limiting reactions) for functioning of a pathway. The betweenness centrality can be defined for a graph $G = (N,E)$ as,

$$C_{betweenness}(i) = \sum_{x,y \in N} \frac{\sigma_{x,y}(i)}{\sigma_{x,y}} \quad (6)$$

where $\sigma_{x,y}$(i) indicates the number of shortest paths passing through node i and $\sigma_{x,y}$ indicates the total number of shortest paths between x and y.

(4) Eigenvector centrality: This graph measure terms an enzyme within the network to be more important and powerful if it is a connected to a large number of important neighboring enzymes. In mathematical terms, the eigenvector centrality is the eigenvector (C_{ev}) of the largest absolute eigenvalue (λ_{max}) such that $C_{ev} = AC_{ev}$ where A is the adjacency matrix of graph G.

The degree, closeness and betweenness centralities were calculated using Cytoscape version 3.2.1 [33]. The eigenvector centrality was calculated using the CytoNCA 2.1.6 plugin within the Cytoscape environment [34]. Also, the completely connected components within the flux-coupled reaction graph were extracted using Cytoscape version 3.2.1 [33].

2.7. *Statistical analyses*

For finding associations between the genomic and pathway features, the non-parametric Spearman correlation was used. Spearman correlation coefficient is indicated by ρ in the following sections. Correlations were calculated using the Statistical toolbox within the MATLAB R2012, Mathworks. Throughout the study, correlation measures with p-values < 0.01 were considered to be significant.

3. Results

3.1. *Influence of network connectivity on enzyme evolution*

The connectivity of an enzyme with other enzymes in a metabolic network is an important factor that decides the utilization of metabolites and its distribution within a network. Further, enzymes belonging to central parts of metabolism tend to be more connected than the periphery [12]. Also, connectivity of proteins in a network provides information about functional modules that work in synchrony [13, 35]. To analyze this, the *L. major*

metabolic network was considered as an enzyme graph. Further, to understand the relationship between connectivity (total degree) of an enzyme within the *L. major* enzyme graph and its evolutionary rate, the relationship between calculated K_a/K_s ratios and connectivity of the enzymes was analyzed (Fig. 1(A)). The K_a/K_s ratios demonstrate a weak positive association with enzyme connectivity. Although the variance is low over large connectivity ranges, the positive association of median evolutionary constraints with connectivity can be observed for enzymes whose total degree ranges between 0 - 400 (Fig. 1(B)). Around 96% of the enzymes within the network have a degree between 0 - 400, suggesting that the positive association though weak, holds over a broad range of enzyme connectivities. In a previous study, the association of K_a/K_s ratios with closeness and betweenness centralities of the metabolic network was also computed [15] to understand the association of topological properties with evolutionary rates. Hence, we also calculated closeness and betweenness centralities for the network and analyzed its association with evolutionary rates. The closeness centrality is a topological measure that identifies nodes (enzymes) that can communicate spontaneously with other nodes in a network [31]. Closeness centrality of enzymes also, demonstrates a positive association with evolutionary rates. On the contrary, betweenness centrality that identifies bottleneck nodes in a network [31] did not display any significant correlation with evolutionary rates. These results collectively emphasize that highly connected and central enzymes are least constrained during evolution. The *L. major* metabolic network is thus, highly adaptive in nature and confers the ability for enzymes to acquire new connections. To understand the reason for this association the relationship of enzyme connectivity with protein abundance was analyzed and was found to display no significant correlation.

3.2. *Metabolic flux and enzyme evolutionary rates*

Metabolic networks of *Leishmania* parasites utilize various combinations of substrates from the cellular environment so as to optimize cellular growth under different environmental constraints [16, 17]. The activity of enzymes within the network is highly defined by the metabolite flux experienced by an enzymatic reaction. As parasites relatively experience a less variable but constrained host environment through evolution, the parasite metabolic network is highly adapted to its constrained environment. Hence, to understand the relationship between enzymatic flux and the rate of enzyme

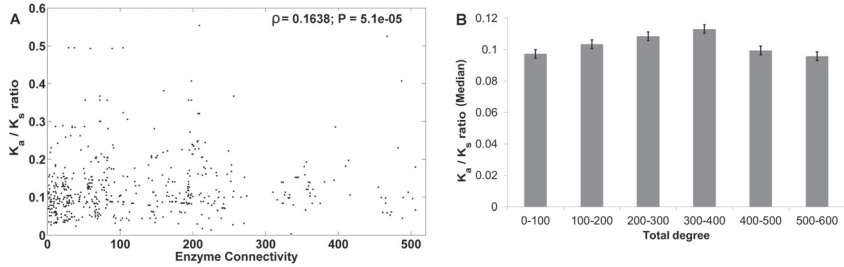

C

Property	Correlation with K_a / K_s (Spearman correlation)
Enzyme connectivity (Degree)	0.1638*
Betweenness centrality	0.0227
Closeness centrality	0.1422*

* p-values significant

Figure 1. Relationship of enzyme connectivity with evolutionary rates. (A) Scatter plot demonstrating the relationship of enzyme connectivity with evolutionary rates. (B) Histogram demonstrating the trend of median evolutionary constraints with enzyme connectivity (binned). The standard errors in each bin are also shown. (C) Associations of different topological properties with K_a/K_s ratios.

evolution, flux through each enzyme within the network was calculated using flux balance analysis [20] while considering various combinations of metabolite exchanges. As *Leishmania* parasites utilize a plethora of carbon sources from the environment [36, 37], metabolite exchanges of glucose, glycerol, and D-ribose were selectively constrained, along with exchanges that are known to be essential (representative of a minimal medium reported in [16]) and the relationship of reaction flux with evolutionary rates was studied. In each environmental condition, flux carried by the enzymes display a significant negative correlation with K_a/K_s ratios (Fig. 2(A)); with enzymatic flux in presence of glucose, glycerol and D-ribose displaying the strongest correlation. These results suggest that enzymes with a higher flux evolve slowly, over a broad range of environmental variations. Further, enzyme flux maintains an exponential relationship with evolutionary constraints (Fig. 2(B)). Enzymes carrying higher flux also demonstrate a significant positive association ($\rho = 0.2494$, $P < 0.01$) with enzyme abundance, suggestive of a likely increase in enzyme concentration towards optimal utilization of environmental sources. But, on the contrary, enzyme abundance did not significantly correlate with evolutionary rates, suggesting that abundance of a particular enzyme is used as a tool in maintaining optimal flux, although it is not evolutionarily constrained. Further, the flux as opposed to enzyme expression is significantly constrained during

evolution, indicative of the relative metabolic adaptation of the *L. major* metabolic network to environmental fluctuations.

A

Medium	Correlation of enzyme flux with K_a/K_s (Spearman correlation)
Minimal medium	-0.1274*
Minimal medium + glucose only	-0.1277*
Minimal medium + glycerol	-0.1296*
Minimal medium + D-ribose	-0.1343*
Minimal medium + above carbon sources	-0.1485*

* p-values significant

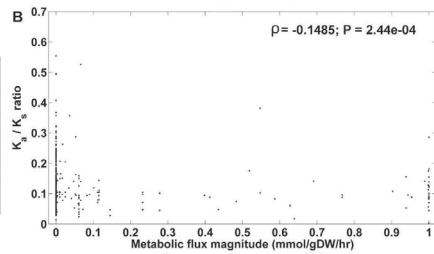

Figure 2. Metabolic flux carried by an enzyme and its relationship with rate of evolution. (A) Association of enzymatic flux with K_a/K_s ratios under different environmental constraints. (B) Relationship of K_a/K_s ratios with metabolic flux magnitude expressed in mmol/gDw/hr.

3.3. *Relationship of codon usage and GC content with evolutionary constraints*

Leishmania genomes are extensively GC-biased and demonstrate distinct codon usage bias [18, 19]. Further, the role of codon usage in governing translational selection of genes and GC mutational bias at the 3rd position in generating codon usage bias has been previously implicated in our work [18]. With this primary information, we asked the question whether codon usage and GC bias of proteins in *L. major*, the metabolic enzymes in particular, are associated with evolutionary rates or not. A significant negative correlation (ρ = -0.5407, P $<$ 0.01) between codon adaptation index (CAI) values of proteins in *L. major* and K_a/K_s ratios was observed (Fig. 3(A)). Thus, proteins in *L. major* with a high codon usage bias tend to be highly constrained during evolution. The negative association also holds for metabolic enzymes in particular within L. major (ρ = -0.4891, P $<$ 0.01). As observed previously [18], the GC content at 3rd position also negatively correlates with K_a/K_s ratio (Fig. 3(B)), suggestive of purifying selection at the wobble position leading to codon usage bias. The role of these genomic features in regulating the phenotype of the *L. major* is still unexplored. Hence, we also probed further to understand the relationship between codon usage and the metabolic flux phenotype of *L. major* metabolism. This flux profile was generated using FBA while constraining for glucose, glycerol and D-ribose exchanges, along with exchanges com-

prising the minimal medium. No significant association was obtained for CAI values of metabolic enzymes and flux. Previously in our work, we have implicated that codon usage bias is positively associated and might regulate protein expression/abundance [18]. As biased codon usage is an outcome of mutations and subsequent negative selection, genes of metabolic enzymes with high CAI are highly constrained for efficient translation. Hence, genes of enzymes with high CAI, demonstrate higher expression; thereby regulating enzymatic flux through the metabolic network. These results collectively suggest that the relationship between the genotype and phenotype is rather complicated and requires a similar in-depth analysis to identify the links.

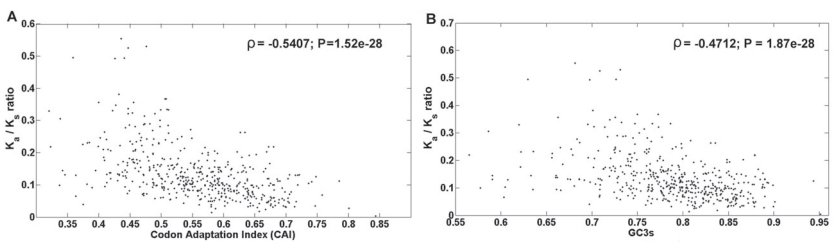

Figure 3. Relationship of genomic features with evolutionary rates. (A) Scatter plot showing relationship of CAI with K_a/K_s ratios for all genes (having greater than 200 codons) in *L. major*. (B) Scatter plot showing relationship of GC content at the 3rd (wobble) position of a codon with K_a/K_s ratios for all genes within the *L. major* genome.

3.4. *Metabolic modules and enzyme evolutionary rates*

Physiological modules in metabolic network have been reported to be evolutionarily conserved in *E. coli* [38]. Physiological modules can be discovered within metabolic networks through flux coupling analysis in genome-scale models [39]. The dependence of reactions for metabolites and cofactors on other reactions leads to flux coupling that enables a group of enzymes to be conserved during evolution.

3.4.1. *Flux coupling analysis of the metabolic network*

Flux coupling analysis in the *L. major* iAC560 metabolic model identified 1393 fully coupled, 718 partially coupled, and 11946 directionally coupled reaction pairs when constrained for essential metabolites (minimal medium)

along with carbon sources like glucose, glycerol, and D-ribose. Using this information, a flux-coupled reaction graph where each node corresponds to an enzymatic reaction and the edge representing a flux-coupled interaction was generated (See Methods section for details). Each node in this network represents an enzymatic reaction. The flux coupled reaction graph can be observed in Fig. 4(A), where the densely coupled enzymes (indicated by their degree) are in the center and loosely coupled enzymes arranged in the periphery. The generated flux-coupled reaction graph was further processed to extract completely connected components or subgraphs. It is to be noted that these subgraphs do not represent a complete graph or clique. Around 59 distinctly connected components were identified from the flux-coupled reaction graph (Fig. 4(B)). The largest subgraph consisted of 465 reactions belonging to various pathways. We term this subgraph as the core subnetwork as it uniquely contains core metabolic enzymatic reactions belonging to glycolysis, citrate cycle, oxidative phosphorylation, purine metabolism, pentose-phosphate pathway, and fatty acid biosynthesis. The other subgraphs represented small pathway modules, where each connected subgraph contains metabolic reactions uniquely representing a pathway. The modules thus identified comprised of enzymes related to limonene and pinene degradation, cysteine metabolism, glycerolipid metabolism, tyrosine metabolism, methionine metabolism, phenylalanine metabolism, glutamate metabolism, and arginine-proline metabolism (these modules have been presented in a row-wise order in Fig. 4(B)).

3.4.2. *Completely connected subgraphs and enzyme evolution*

Enzymes of subgraphs having more than two nodes were further scrutinized to study their evolutionary properties. Enzymes of the tyrosine, methionine, phenylalanine and arginine-proline pathway modules demonstrate same K_a/K_s ratios. Enzymes of the limonene and pinene degradation, cysteine metabolism, glycerolipid metabolism, and glutamate metabolism pathway modules display a minor variation in K_a/K_s ratios (Standard deviation ranging between 0.03–0.24). Thus, small pathway modules are evolutionarily conserved in *L. major* metabolism. Further, the core subnetwork was analyzed for its evolutionary properties. The enzymes of the core subnetwork displayed a large variation in K_a/K_s ratios with around 51% reactions displaying a strong negative selection [K_a/K_s ratios between 0–0.1] (Fig. 5(A)). We further investigated the functional significance of these evolutionarily conserved enzymatic reactions due to which they remain un-

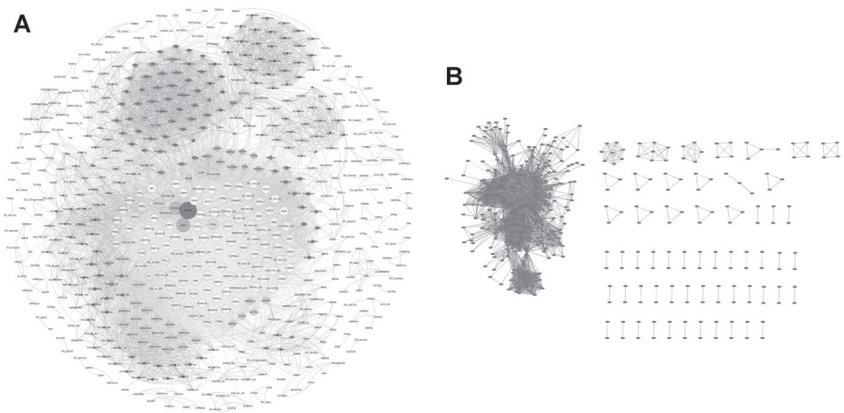

Figure 4. Flux coupling analysis of the *L. major* iAC560 constraint-based model. (A) Flux coupled reaction graph in a degree-sorted layout fashion. (B) Completely connected subgraphs extracted from the Flux-coupled reaction subgraph.

changed throughout evolution. For understanding their functional roles, topological properties of the core subnetwork enzymes was calculated for each of the enzymes demonstrating evolutionary rates between 0–0.1. The mean topological properties for enzymes in the core subnetwork have been reported in Table 1.

Table 1. Mean topological properties of the core subnetwork enzymes.

Property	**Value**
Closeness Centrality	0.4018
Degree centrality	55.0314
Betweenness centrality	0.0035
Eigenvector centrality	0.0298

Considering mean eigenvector and degree centralities as the cut-off (Table 1), it was observed that most of the conserved enzymatic reactions are less central (centralities less than average) in the core subnetwork representing the periphery and are coupled to a small set of enzymes (Figs. 5(B) and 5(C)). Peripheral nodes have been observed to support eukaryotes in adapting to different environments [40]. Whereas, enzymes having a centrality value greater than the mean centrality of enzymes within the core subnetwork represent the central innermost core (Figs. 5(B) and 5(C)). This hier-

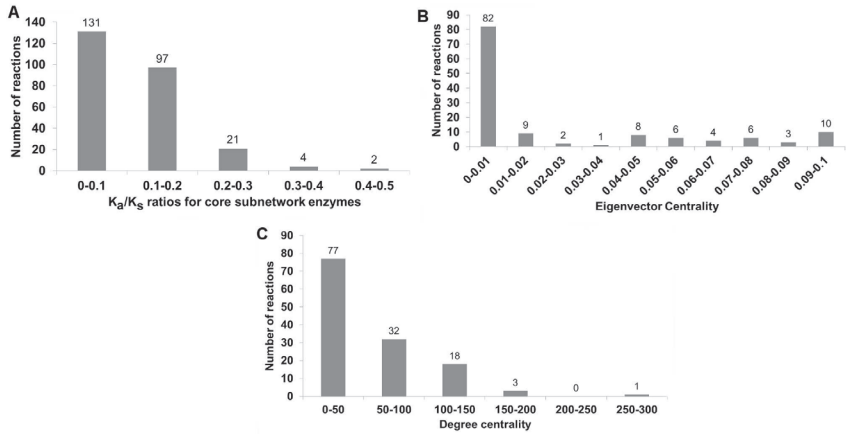

Figure 5. Evolutionary and topological modules within the core subnetwork. (A) Variation in the evolutionary rates of enzymes within the core subnetwork. (B) Number of core subnetwork enzymes (with K_a/K_s ratios between 0–0.1) for different bins of eigenvector centrality observed within subnetwork. (C) Number of core subnetwork enzymes (with K_a/K_s ratios between 0–0.1) for different bins of degree centrality observed within subnetwork.

archy probably allows the *L. major* metabolism to adapt to different carbon sources. These central enzymes are least sensitive to amino acid changes, whereas topologically the most sensitive as they are largely coupled to other metabolic reactions within the core subnetwork. These enzymes belong to a variety of pathways (Table 2) with purine metabolism representing 25–34% and pyrimidine metabolism representing 11–15% of total conserved core of enzymatic reactions. Some noteworthy mentions include mitochondrial ATP synthase that demonstrated the highest eigenvector centrality (0.0962) and degree (251), guanosine kinase (eigenvector centrality 0.0951; degree - 141), phosphomannomutase (eigenvector centrality 0.0942; degree - 137) and trypanothione reductase (eigenvector centrality 0.0936; degree - 132) within the core subnetwork.

4. Discussion

Leishmania major, causative organism of cutaneous leishmaniasis demonstrates a complex lifecycle within two distinct host environments the human macrophage and the midgut of the sandfly, where it is exposed to variable sets of environmental stresses. Even then, a long-standing evolutionary relationship of the *L. major* parasite with its hosts [41] has endured

Table 2. Number of core enzymatic reactions in each pathway with eigenvector and degree centrality greater than average.

Pathway Name	Enzymes having greater than average eigenvector centrality	Enzymes having greater than average degree centrality
Citrate cycle	1	2
Fatty acid biosynthesis	4	4
Fatty Acid Degradation	6	6
Fructose and mannose metabolism	1	1
Glutamate metabolism	1	1
Methionine metabolism	2	3
Trypanothione metabolism	1	1
Oxidative phosphorylation	1	1
Pentose phosphate pathway	1	1
Phenylalanine, tyrosine and tryptophan biosynthesis	1	0
Purine metabolism	13	13

the parasite metabolism with the ability to adapt and sustain the experienced stresses. The genome of the *L. major* parasite contains the historical account of the probable evolutionary events that must have led to the adaptive functioning of metabolism to the exposed environments. In our study, we analyze the blueprint of the *L. major* genome that is its genotype, and attempt to find associations with its phenotype thereby predicting a linkage between the evolutionary and functional features of *L. major* metabolism. For this, we attempt to understand the behavioral features of the previously curated *L. major* metabolic network [16] and its effect on the evolution of the corresponding enzymes within the *L. major* genome.

Our results reveal that the enzyme network of *L. major* is highly adaptive in nature as densely connected, central enzymes demonstrate faster evolutionary rates as compared to less connected enzymes [42]. This further indicates the possibility for the development of new functional associations within the metabolic network of *L. major*. A similar positive trend of enzyme connectivity and evolutionary constraints was observed in 96% of enzymes further substantiating our claim. Further, the distribution of the fluxes within the metabolic network tends to be negatively associated with evolutionary constraints, where enzymes with a higher flux tend to be relatively more constrained during evolution. A probable reason as specu-

lated in studies on yeast metabolism [12], enzymes carrying higher fluxes produce reaction products that would be utilized by a number of pathways and hence, they experience a high rate of purifying selection. It was further observed that this behavior holds true for environments with variable carbon sources establishing the evolutionary conservation of enzymes carrying higher fluxes, even under varying environmental conditions. This also revealed the possibility that the parasite might possess an evolutionarily conserved core catabolic pathway/route that has the ability to utilize different carbon sources.

Further, a positive association of enzymatic flux with enzyme expression/abundance also suggested that a higher flux is probably maintained through specific enzymes by regulation of their expression in response to environment. To further understand the possibility of regulation, we further probed into the role of genome in regulating metabolic flux. Previously, codon usage was shown to positively correlate with protein abundance [18]. Also, it could be observed that codon usage is negatively associated with evolutionary constraints. This result suggests the role of biased codon usage in influencing selection towards efficient translation and hence, regulation of protein expression. This was also supported by the fact that the 3^{rd} synonymous wobble position of the codon in *L. major* experiences a strong purifying selection. This further substantiates codon usage to be one of the most important mechanisms selected during evolution to store information regarding the adaptation of the metabolic network to its environment via regulation of enzyme expression.

From our study one can observe that the predicted associations between the genotype and phenotype properties are weak in magnitude; but on the other hand, it is obvious considering the fact that a number of factors other than flux, like gene regulation and structural constraints affect the evolution of enzymes. Apart from all this, an important point to be noted here is that, there is still a degree of significant association that exists between network function and enzyme evolution.

The negative association of flux with evolutionary constraints under different conditions further raised the possibility of a core metabolic route within the parasite. To verify this, we performed flux-coupling analysis where the flux-coupled reaction graph was extracted from the actual metabolic network. From the flux-coupled reaction graph, physiological functional modules or independently functioning groups were extracted and analyzed for their evolutionary rates. It was identified that enzymes in each physiological module tend to possess similar evolutionary rates. A similar

result was reported for different eukaryotes [40]. Also, a hierarchy can be further seen within the core subnetwork, where there are a large number of less connected peripheral nodes and less number of highly connected innermost core enzymes suggesting the probable role of this hierarchy in the maintaining the adaptability of the *L. major* metabolic network to absorb different nutrients from the environment and provide it to the core for its utilization. Further, it was also observed that enzymes belonging to the core subnetwork tend to demonstrate a significant variation in evolutionary rates. The topological properties of the enzymes with high evolutionary constraints (K_a/K_s between 0–0.01) were further investigated to get a functional perspective for evolutionary conservation. Topological analysis of the core subnetwork of the flux-coupled reaction graph revealed that there were a large number of peripheral nodes as compared to highly connected central nodes that demonstrate higher evolutionary constraints. Further, the densely connected central nodes belonged to important pathways for utilization of different carbon sources like glycolysis, fatty acid biosynthesis and degradation, glutamate metabolism, etc. each connected with pathways for energy generation, DNA/RNA synthesis and combat of oxidative stress. Enzymes of these pathways represent both, sensitivity to amino acid changes and to functional perturbations deeming them to be evolutionarily and topologically central and important modules for parasite survival under different conditions.

All these results indicate the existence of a complex relationship between the genotype and the phenotype of the *Leishmania major* parasite and the necessity of an in-depth analysis to reveal genomic features associated with the metabolic behavior. Most importantly, this study strongly emphasizes on the influence of metabolic network structure and function on rate of enzyme evolution. Also, by bridging the links between the genotype and phenotype, we highlight that the *L. major* genomes contain imprints of physiological adaptations to variable environmental conditions thereby exerting a slight but effective control over regulation of metabolism.

References

1. http://www.who.int/leishmaniasis/en/
2. M. Zand and M. L. Narasu, *Annals Biological Res.* **4**, 170 (2013).
3. J. Schroeder and T. Aebischer, *Hum. Vaccine* **7**, 10 (2014).
4. R. Kumar and C. Engwerda, *Clin. Transl. Immunol.* **3**, e13 (2014).
5. S. L. Croft, K. Seifert and V. Yardley, *Indian J. Med. Res.* **123(3)**, 399 (2006).

6. L. Monzote, *Open. Antimicrob. Agents. J.* **1**, 9 (2009).
7. E. V. Koonin and Y. I. Wolf, *Curr. Opinion. Biotech.* **17(5)**, 481 (2006).
8. B. Papp, R. A. Notebaart and C. Pál, *Nat. Rev. Genetics* **12(9)**, 591 (2011).
9. W-C. Liu, W-H. Lin, A. J. Davis, F. Jordn, H. Yang and M-J. Hwang, *BMC Bioinformatics* **8**, 121 (2007).
10. W. Zhou, C. Qi and L. Lei, *Chinese Science Bulletin* **54(5)**, 776 (2009).
11. S. D. Copley, *J. Biol. Chem.* **287(1)**, 3 (2012).
12. D. Vitkup, P. Kharchenko and A. Wagner, *Genome Biol.* **7**, R39 (2006).
13. C. Lu, Z. Zhang, L. Leach, M. J. Kearsey and Z. W. Luo, *Genome Biol.* **8**, 407 (2007).
14. C. F. Olson-Manning, C-R. Lee, M. D. Rausher and T. Mitchell-Olds, *Mol. Biol. Evol.* **30(1)**, 14 (2012).
15. M. Colombo, H. Laayouni, B. M. Invergo, J. Bertranpetit and L. Montanucci, *Evolution* **68(2)**, 605 (2013).
16. A. K. Chavali, J. D. Whittemore, J. A. Eddy, K. T. Williams and J. A. Papin, *Molecular Systems Biology* **4**, 177 (2008).
17. A. Subramanian, J. Jhawar and R. R. Sarkar, *PLoS One* **10(9)**, e0137976 (2015).
18. A. Subramanian, R. R. Sarkar, *Genomics* **106**, 232 (2015).
19. A. Subramanian, R. R. Sarkar, *Data in Brief* **4**, 269 (2015).
20. J. D. Orth, I. Thiele and B. Ø. Palsson, *Nat. Biotech.* **28(3)**, 245 (2015).
21. A. P. Burgard, E. V. Nikolaev, C. H. Schilling and C. D. Maranas, *Genome Res.* **14**, 301 (2004).
22. M. Aslett, C. Aurrecoechea, M. Berriman, J. Brestelli, P. B. Brunk, *et al.*, *Nucleic Acid Res.* **38(Database Issue)**, D457 (2010).
23. M. Suyama, D. Torrents and P. Bork, *Nucleic Acid Res.* **34(Web Server Issue)**, W609 (2006).
24. Z. Yang, *Mol. Biol. Evol.* **24(8)**, 1586 (2007).
25. N. Goldman and Z. Yang, *Mol. Biol. Evol.* **11(5)**, 725 (1994).
26. P. Sharp and W. Li, *Nucleic Acid Res.* **15(3)**, 1281 (1987).
27. A. Larhilmi, L. David, J. Selbig and A. Bockmayr, *BMC Bioinformatics* **13**, 57 (2012).
28. J. P. Pinto, R. Pereira, J. Cardoso, I. Rocha and M. Rocha, *BMC Res. Notes.* **6**, 175 (2013).
29. I. Rocha, P. Maia, P. Evangelista, P. Vilaca, S. Soares, J. P. Pinto, J. Nielsen, K. R. Patil, E. C. Ferreira and M. Rocha, *BMC Systems Biol.* **4**, 45 (2010).
30. M. Bastian, S. Heymann and M. Jacomy, *International AAAI Conference on Weblogs and Social Media.* (2009).
31. G. A. Pavlopoulos, M. Secrier, C. N. Moschopoulos, T. G. Soldatos, S. Kossida, J. Aerts, R. Schneider and P. G. Bagos, *BioData Mining* **4**, 10 (2011).
32. H-W. Ma and A-P. Zeng, *Bioinformatics* **19(11)**, 1423 (2003).
33. P. Shannon, A. Markiel, O. Ozier, N. S. Baliga, J. T. Wang, D. Ramage, N. Amin, B. Schwickowski and T. Ideker, *Genome Res.* **13(11)**, 2498 (2003).
34. Y. Tang, M. Li, J. Wang, Y. Pan and F-X. Wu, *BioSystems* **127**, 67 (2014).
35. J. Yoon, Y. Si, R. Nolan and K. Lee, *Bioinformatics* **23(18)**, 2433 (2007).
36. F. Bringaud, L. Rivire, V. Coustou, *Mol. Biochem. Parasitol.* **149**, 1 (2006).

37. T. Merlen, D. Sereno, N. Brajon, F. Rostand, J. L. Lemesre, *Am. J. Trop. Med. Hyg.* **60**, 41 (1999).
38. C. Pal, B. Papp and M. J. Lercher, *Nat. Rev. Genetics.* **37(12)**, 1372 (2005).
39. R. A. Notebaart, B. Teusink, R. J. Siezen and B. Papp, *PLoS Comput. Biol.* **4(1)**, e26 (2007).
40. J. W. Whitaker, G. A. McConkey and D. R. Westhead, *Genome Biology* **10**, R36 (2009).
41. J. Lukes, I. L. Mauricio, G. Schonian, J-C. Dujardin, K. Soteriadou, J-P. Dedet, K. Kuhls, K. W. Q. Tintaya, M. Jirku, E. Chocholova, C. Haralambous, F. Pratlong, M. Obornik, Ales Horak, F. J. Ayala and M. A. Miles, *Proc. Natl. Acad. Sci.* **104(22)**, 9375 (2007).
42. J. M. Flowers, E. Sezgin, S. Kumagai, D. D. Duvernell, L. M. Matzkin, P. S. Schmidt and W. F. Eanes, *Mol. Biol. Evol.* **24(6)**, 1347 (2007).

LONG-TERM POTENTIAL OF IMPERFECT SEASONAL FLU VACCINE IN PRESENCE OF NATURAL IMMUNITY*

S. GHOSH

Department of Mathematics
School of Natural Sciences
Shiv Nadar University, NH91, Gautam Buddha Nagar
Uttar Pradesh, 201314, India
E-mail: suma.ghosh@snu.edu.in

J. M. HEFFERNAN

Modelling Infection and Immunity Lab
Centre for Disease Modelling
Department of Mathematics & Statistics
York University, 4700 Keele St.
Toronto, Ontario M3J 1P3, Canada
E-mail: jmheffer@yorku.ca

Influenza causes many deaths and affects millions of individuals worldwide every year. Immunity against influenza can be acquired through natural infection or vaccination. Immunity, however, will wane over time as immune system cells die and the ciruclating influenza strains evolve. We have developed a model to study the effects of waning immunity over two years of infection and vaccination history. Results show that natural infection in the previous year and immunization in the current year provide the best protection against seasonal influenza, depending on the transmissibility of the circulating strain. Using our results, targets for reduction in influenza incidence can be determined. These results are relevant to public health, allowing updates of vaccination coverage targets are the relative fitness between the current circulating strain to the vaccine and previous year's circulating strain change.

1. Introduction

Influenza is a globally important respiratory pathogen that causes a high degree of morbidity and mortality from nearly annual epidemics and occasional pandemics. Influenza epidemics generally occur in the winter months:

*This work is supported by NSERC and MITACS.

November–April in the Northern hemisphere and in May–September in the Southern hemisphere. Worldwide, these annual epidemics result in about three to five million cases of severe illness, and about 250 000 to 500 000 deaths[1]. Despite preventive measures annual epidemics of influenza continue to cause a large economic burden and societal disruption.

The influenza virus continuously undergoes antigenic change by two mechanisms: antigenic drift and antigenic shift. Annual seasonal outbreaks of influenza are considered to rely on the process of antigenic drift, where gradual accumulation of amino acids (mutations) occur in all influenza gene segments, but particularly in the two surface glycoproteins HA and NA which are constantly subjected to selection pressure by the host's defense mechanism[2]. This continuous evolutionary process gives rise to viral strains which are sufficiently antigenically distinct from strains recognizable by host antibodies (acquired immunity), to other forms less recognizable and thus, more successful at infecting hosts.

For many viral and bacterial infections, the probability of reinfection of a recovered host increases as time following infection elapses. In other words, host immunity wanes with time. Recent studies suggest that acquired immunity to influenza decays rapidly over the first few months after infection and then gradally for a few years[3,4]. Since immunity wanes with time, the influenza virus need not mutate to a completely new antigenic form. Rather, the influenza virus benefits from each additional amino acid replacement in its surface proteins by becoming slightly less recognizable to the hosts on whom it previously conferred immunity. The combination of waning immunity and antigenic drift thus gives rise to immune-escape variants in a very short time period, 1–2 years[3]. Furthermore, herd immunity, where individuals that have not been infected by a particular strain are still protected from infection i.e. achieving a level of immunity in recovered individuals sufficiently high to measurably reduce attack rates in the community[5,6,7,8], is deemed ineffective, and human populations are exposed to new but related influenza strains on an annual basis.

Vaccination is used to combat the effects of antigenic drift and the waning of immunity, to induce immunity in individuals such that, if they are exposed to viral strains related to those included in the vaccine, they have a high probability of resisting infection. Vaccines can give a high degree of protection in healthy immunocompetent individuals[9,10]. However, the efficacy of the annual influenza vaccine varies from year to year due to changes in the identity of the circulating influenza strains. Also, immunity gained from vaccination also wanes with time[11,12]. Vaccination can benefit

a population by inducing short term herd immunity (for 1–2 seasons), but, if the allotted vaccine provides less than 70% protection, the vaccine will not be effective in halting an epidemic[9]. A vaccine providing a high level of protection in some individuals, also, may not be effective in producing herd immunity since the induction of immunity is specific to the individual and may depend on the individual's immune system characteristics and vaccination history[13,14,15,16,17,18,19,20,21]. Finally, through antigenic drift, the circulating influenza strains may also evolve such that the vaccinating strains becomes less effective over each seasonal epidemic[22,23].

Since 1968, antigenic drift and the waning of immunity have forced regular vaccine updates[8,24]. Typically, three strains are included in the annual vaccine, with these three strains chosen to be as similar as possible to those projected to be the most prominent circulating strains in the upcoming influenza season. Influenza strains are reviewed in February (for the northern hemisphere) and September (for the southern hemisphere), and during the epidemic season, to detect new immune-escape variants and determine if an update to the vaccine composition is necessary[9,25,26]. Vaccination for influenza epidemics takes place annually in March-April for southern hemisphere and in September-October for northern hemisphere populations. In tropical and sub-tropical areas influenza activity tends to have less distinct peak seasons and may occur throughout much of the year, but often with two periods in which increased activity occurs.

The short-term evolution of influenza virus, annual flu vaccination and the wanning immunity of individual whether it is acquired from prior infection or vaccination are interrelated in the evolution and progression of influenza. We are interested in studying the dynamics of seasonal influenza A infections including the effects of antigenic drift, vaccination and waning immunity in-host. The goal is to determine the impact of imperfect vaccines on the influenza season for various rates of influenza evolution. We have developed a mathematical model of influenza capturing consecutive epidemic (infection seasons) and inter-epidemic (between seasons) periods, with and without vaccination. We compare the cumulative infection following two vaccination strategies — either throughout the entire epidemic season or the first few days of each epidemic. In both cases, the vaccine is assumed to be imperfect (70%–90% degree of protection), and covers 10%–30% of the population each epidemic season.

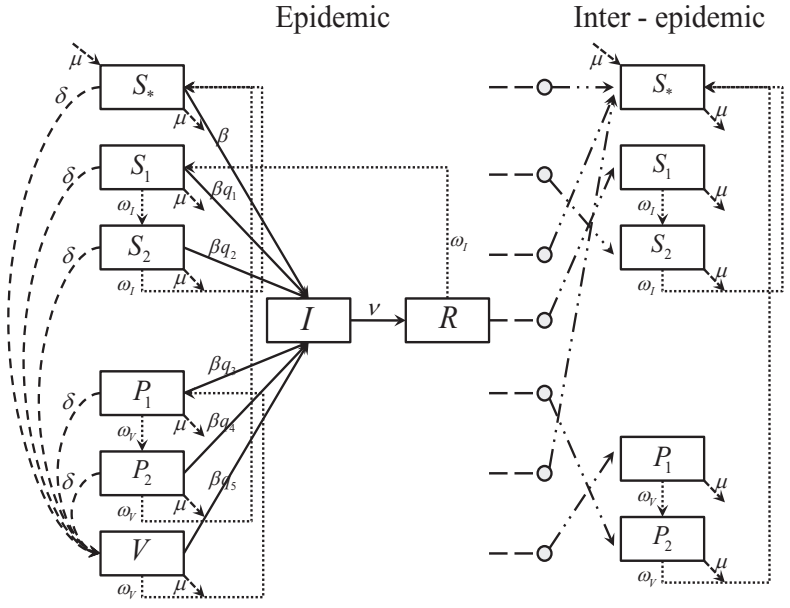

Figure 1. Schematic diagram of epidemic and inter-epidemic model.

2. Model

The mathematical model is composed of two parts describing the epidemic phase and the inter-epidemic phase respectively. A shematic of both models can be seen in Figure 1.

2.1. *Epidemic phase*

The epidemic model consists of a system of ordinary differential equations describing the interactions and dynamics of susceptible (S), infected (I), recovered (R), and vaccinated (V) hosts. Susceptible and vaccinated hosts are further delineated by infection and/or vaccination history, where the most recent infection or vaccination is used to denote a host's level of susceptibility. Two years of infection and/or vaccination history are tracked where S_i and V_i, $i = *, 1, 2$, denote susceptible and vaccinated individuals that are fully susceptible in the current year (S_*), vaccinated in the current year (V), were most recently infected by influenza i years ago where $i = 1, 2$, or were most recently vaccinated i years ago where $i = 1, 2$. It is assumed that vaccine uptake (δ) is constant over all susceptible and vaccinated classes,

and that the infection/vaccination status decreases susceptibility (q_i) to the circulating influenza strain during the epidemic season. It is also assumed that acquired immunity from the current or previous influenza seasons or vaccinations will wane over time, and that the waning rate depends on the current host class (ω_j, j = S, V). Note that the waning rate pertains only to the effective immunity towards the current circulating strain. Acquired immunity gained from previous infections that is not effective against the current circulating strain is not included in this model. Since it is assumed that only the most recent infection determines the future immune status, once infected (β), all S and V hosts move into the same infected class (I), and then progress (ν) to the same recovered class (R). Natural birth and death are also included in the model (μ). The model is as follows:

$$\frac{dS_*}{dt} = \mu(1 - S_*) - \beta S_* I + \omega_S S_2 + \omega_V V_2 - \delta S_* \tag{1}$$

$$\frac{dS_1}{dt} = -\beta q_1 S_1 I - \mu S_1 + \omega_S R - \omega_S S_1 - \delta S_1 \tag{2}$$

$$\frac{dS_2}{dt} = -\beta q_2 S_2 I - \mu S_2 + \omega_S S_1 - \omega_S S_2 - \delta S_2 \tag{3}$$

$$\frac{dV_1}{dt} = -\beta q_3 V_1 I - \mu V_1 + \omega_V V - \omega_V V_1 - \delta V_1 \tag{4}$$

$$\frac{dV_2}{dt} = -\beta q_4 V_2 I - \mu V_2 + \omega_V V_1 - \omega_V V_2 - \delta V_2 \tag{5}$$

$$\frac{dV}{dt} = -\beta q_5 V I - \mu V - \omega_V V + \delta(S_* + S_1 + S_2 + V_1 + V_2) \tag{6}$$

$$\frac{dI}{dt} = \beta I(S_* + q_1 S_1 + q_2 S_2 + q_3 V_1 + q_4 V_2 + q_5 V - \nu I - \mu I) \tag{7}$$

$$\frac{dR}{dt} = \nu I - \mu R - \omega_S R \tag{8}$$

where, $\beta = \beta_0(1 + \beta_1 cos 2\pi t/365)$, the parameters q_i's for $i = 1, .., 5$ represent the relative susceptibility of S_1, S_2, V_1, V_2 and V respectively. It is assumed that the relation

$$q_5 < q_1 < q_3 < q_2 < q_4 \tag{9}$$

is satisfied, and reflects the relationship of the current ciruclating strain to the circulating and vaccine strains of previous seasons i.e. the current ciruclating strain is most closely related to the current vaccine followed by last year's circulating strain and then the vaccine given previous to that influenza season, and then the cirulating strain two years previous and then the vaccine strain given previous to that influenza season.

Note that the epidemic model (8) can be classifed as an evolutionaly epidemic model[27] since it accounts for changes in the influenza strain through differences in host susceptibility and through waning immunity.

2.2. *Inter-epidemic phase*

During the inter-epidemic phase, the time elapsed between two consecutive epidemics, it is assumed that the immune status of hosts changes to reflect the waning of acquired immunity and the evolution of the virus via antigenic drift. At the commencement of the inter-epidemic phase recovered hosts from the epidemic model (R) are moved to the S_1 class, individuals in S_1 class are moved to the S_2 class, and vaccinated individuals V_1 are moved to the V_2 class. Hosts in the S_2 class or V_2 class lose immunological memory from prior infection or vaccination completely and move to the naive class S_*. Effective immunity against new infections also wanes with rate (ω_j, j = I, V) similar to the epidemic model (8). In the inter-epidemic phase natural birth and death (μ) also occur. The model stands as follows:

$$\frac{dS_*}{dt} = \mu(1 - S_*) + \omega_S S_2 + \omega_V V_2 \tag{10}$$

$$\frac{dS_1}{dt} = -\mu S_1 - \omega_S S_1 \tag{11}$$

$$\frac{dS_2}{dt} = -\mu S_2 + \omega_S S_1 - \omega_S S_2 \tag{12}$$

$$\frac{dV_1}{dt} = -\mu V_1 - \omega_V V_1 \tag{13}$$

$$\frac{dV_2}{dt} = -\mu V_2 + \omega_V V_1 - \omega_V V_2 \tag{14}$$

2.3. *Uncertainty and sensitivity analysis*

Numerical analysis is used to predict the impact of seasonal influenza vaccines over a 10-year, 20-year and 30-year period. Flu vaccine is assumed to be 70%–90% effective (updated every year intending the dominant flu strain) to that year's strain and cover 10%–30% population in the first 40 days of each epidemic season. To account for uncertainty in parameter values, we sample parameter ranges using latin hypercube sampling[28,29]. Each parameter is assigned a probability distribution function. Table 1 indicates the parameter ranges used for the uncertainty analysis. Simulations are run 1000 times (with a unique parameter set for each simulation) for epidemics with low, moderate or high initial transmissibility. Population-level effects

Table 1. Parameter values.

Parameter	Definition	Minimum	Maximum
q_1	Reduced susceptibility of S_1	0.1	0.5
q_2	Reduced susceptibility of S_2	0.5	0.9
q_3	Reduced susceptibility of P_1	0.35	0.75
q_4	Reduced susceptibility of P_2	0.5	1
q_5	Reduced susceptibility of V	0.1	0.3
δ	Proportion of population daily vaccinated	0.001	0.009
		Values	
R_0	Basic reproductive ratio	$1.4, 1.8, 2.2$	
β	Transmissibility	$\beta_0(1+\beta_1\cos(2\pi t/365))$	
β_0	Baseline transmission	$R_0/(\nu+\mu)$	
β_1	Seasonality	0.2	
ν	Recovery rate	1/3	
μ	Natural death rate	0.00038706	
ω_S	Waning immunity due to previous infection	1/(3*365)	
ω_V	Waning immunity due to vaccination	1/(3*365)	

of acquired and waning immunity are determined when infection and vaccination are included in the model. Results from these studies are compared to the results when vaccination is not included. To determine key model parameters, time-dependent sensitivity analysis is conducted through the calculation of partial rank correlation coefficients (PRCCs)[28]. PRCCs are determined using 1000 values for each parameter, from the latin hypercube sampling table, and the 1000 outcome values for the population-level effect. Coefficients with the greatest magnitude (greater than 0.5 or less than -0.5) indicate parameters with the largest effects on the outcome variables. Parameters used in the uncertainty analysis are assumed to be uniformly distributed.

2.4. *Parameter values and model assumptions*

Parameter values used for 8 and 14 are provided in 1. Vaccination is introduced into the population when the susceptible populations (S_*, S_1 and S_2)(in absence of vaccine) are at a consistent periodic orbit (a seasonal epidemic). Each influenza season is initiated with one infected individual and ends when the infected population is approximately zero ($\approx 10^{-8}$). The model is analyzed to anticipate the population-level impact of the seasonal flu vaccine when the virus has low ($R_0 = 1.4$) moderate ($R_0 = 1.8$) and high ($R_0 = 2.2$) levels of transmissibility.

Model assumptions are as follows:

(1) It is assumed that one influenza strain is responsible for producing the majority of infections in an influenza seasons. New strains of influenza A are continuously arising due to genetic drift. However, less than 1% of strains that successfully become globally established account for 90% of all disease incidence globally[3].
(2) It is also assumed that acquired immunity from vaccinations or previous infections is only effective in fighting influenza infection for the next two influenza seasons. Influenza strains only survive in circulation for 2–3 years[3]. Also, influenza can escape a significant amount of herd immunity after only 2-3 years of mutation[6,7,8].
(3) It is assumed that the influenza vaccine must be updated yearly, and that the vaccine will be imperfect i.e. will not match the current circulating strain with 100% probability. Short-term influenza evolution gives rise to immune-escape variants that force updates in vaccine composition. Regional and local epidemics, last between 3 and 6 months harbor the majority of viral reproduction and are most likely to be the source of novel immunity-evading strains[22].
(4) It is assumed that the current ciruclating strain is most closely related to the current vaccine followed by last year's circulating strain, then last year's vaccine, then the cirulating strain two years previous, and then the vaccine strain given previous to that influenza season. Influenza vaccine production begins as early as 6–9 months before the beginning of vaccine distribution, before the onset of the influenza season. The strains included in the vaccine are selected depending on which strains are currently in circulation, how each strain is spreading, and how well the current vaccine protects against newly identified strains. It is therefore reasonable to assume that immunity acquired from a vaccine preceding an influenza season will have a higher affinity to the current circulating strain than immunity acquired from infection in the previous season.
(5) It is assumed that the immunity acquired from the most recent infection or vaccination dominates the immune response against the current circulating strain. This is assumed because the most recent infection or vaccination will develop immunity (and boost cross-reactive immunity) that is most closely related to the current ciruculating strain than previous infections or vaccinations.

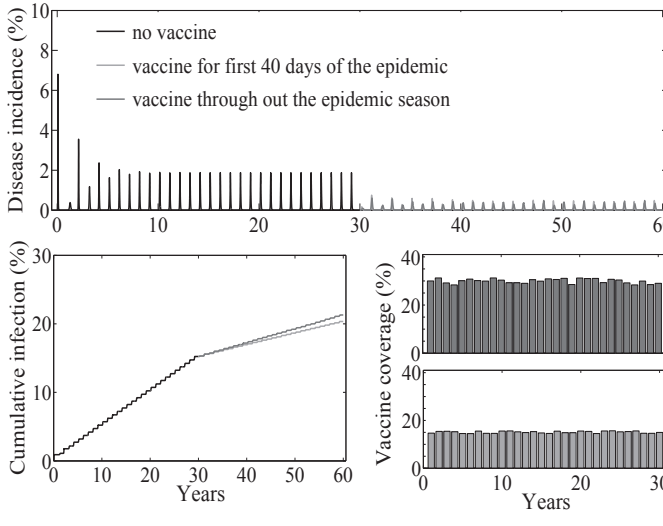

Figure 2. Epidemics with or without vaccine. (a) Daily new infection for first 25 years without vaccine (blue), next 25 years with vaccine by two different strategies — for first 40 days in each epidemic (light gray) and throughout the entire epidemic (dark gray). (b) Cumulative infection for first 25 years without vaccine and next 25 years with vaccine. (c) Vaccination coverage for 25 years in two different strategies, light green (for first 40 days), dark green (throughout the entire epidemic season). Yearly total vaccine coverage is 30% in average for both the strategies, where daily uptake rate for first 40 days strategy is 0.0087, and the daily uptake rate for continuous vaccine throughout the epidemic is 0.0027. Here $R_0 = 1.8$.

3. Results

3.1. *Epidemic dynamics without vaccine*

Seasonal outbreaks of influenza are produced by the epidemic and inter-epidemic models (8) and (14). Fig. 2(top, black line) shows that after approximately twelve epidemics, the model produces periodic infections representing influenza seasons where the basic reproduction ratio R_0 is 1.8. Cumulative infection over these epidemics is also shown in Fig. 2(bottom left, black line).

3.2. *Epidemic dynamics with vaccine*

Vaccination against influenza can be given early in an epidemic season or throughout it. The epidemic and inter-epidemic models (8) and (14) are shown in Fig. 2(a) when vaccination is given throughout an epidemic period

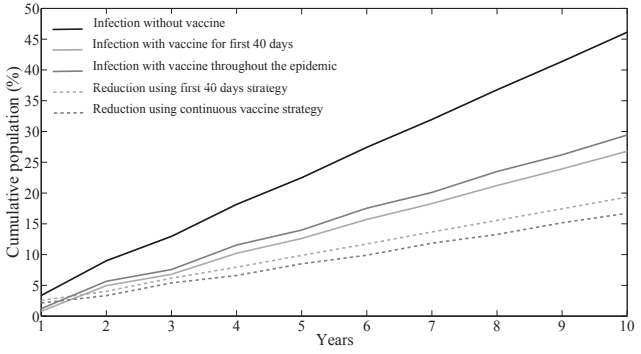

Figure 3. Cumulative reduction in new infections after 10 years of vaccination using two strategies. Cumulative reduction after 10 years using first 40 days strategy is higher than the cumulative reduction using continuous vaccination throughout the epidemic.

(dark gray) or in the first 40 days (light gray). When vaccine is available throughout the entire epidemic season, the proportion of the population vaccinated daily is 0.0027, where as if vaccine is only available during the first 40 days of the epidemic season, the proportion of the population vaccinated daily is 0.0087. In both cases it is assumed that the same proportion of the population has been successfully vaccinated with 30% annual coverage and that the vaccine is 80% effective in producing a reduced susceptibility of $q_5 = 0.2$ to the current circulating strain. It is evident that seasonal epidemics are produced under both vaccination strategies, seasonal epidemics of almost equal magnitude from year to year are realized.

Vaccination campaigns carried out in the beginning of an influenza season are more effective in reducing infections (Fig. 2, light gray) versus vaccination campaigns that continue throughout a season (Fig. 2, dark gray). For example, Fig. 2 shows that, with the same level of vaccination coverage over an epidemic season (30%, Fig. 2(c)), the cumulative number of infections is lower when the vaccine is given early in the epidemic (Fig. 2(b)). This is further demonstrated in Fig. 3. Here within, we study only the vaccination program completed at the beginning of an epidemic.

3.3. *Effect of acquired immunity with no vaccination*

Acquired immunity from previous influenza infections results in partial protection against the current circulating influenza strain, but effective immunity providing partial protection will wane as immune system cells die and

the influenza strain evolves. Uncertainty analysis with respect to q_1 and q_2, the two key parameters responsible for the degree of protection from earlier infection, shows that the total number of infecteds over an epidemic season increases more steadily as immunity wanes. Figure 4 shows the results of the uncertainty analysis for q_1 (left column) and q_2 (right column) for low (a), moderate (b) and high (c) rates of transmission (corresponding to $R_0 = 1.4, 1.8, 2.2$). In each case the median (gray line), inter-quartile values (25% and 75%) and minimum and maximum values of the range increase as q_1 and q_2 increase. This increase is almost linear in some cases (b and c, with greater slope for q_1 vs q_2), but non-linear in others (a). Figure 4 also shows that the variability in the total number of infecteds over an epidemic season is greater as susceptibility increases when the transmissibility is low (top row).

3.4. *Effect of acquired immunity with vaccination*

Acquired immunity from vaccination will provide some protection against the circulating strain, but this immunity will also wane over time as immune system cells die and the influenza strain evolves.

Figure 5 shows the cumulative reduction in new infections compared to the case when no vaccine is used (assuming a vaccine efficacy of 70–90%). The effects of acquired immunity from earlier infection or yearly vaccination coverage are assumed to lie within the range 10%–30% (with $q_5 < q_1 < q_3 < q_2 < q_4$) in each epidemic. The effect of vaccination can vary greatly, between 2%–18% reduction in cases (minimum and maximum values, dashed lines), depending on the parameter values used (determined through Latin Hypbercube Sampling). In a population with a low infection rate ($R_0 = 1.4$) and 10%–30% vaccination coverage each year, it takes almost 30 years before the incidence is reduced by one-tenth (Fig. 5(a), gray line). When the transmission rate is moderate ($R_0 = 1.8$), a median of 2.8% (interquartile range [IQR], 2%–3.4%) of new infections is prevented after 10 years of vaccination, reaching a median of 8.5% (IQR, 6.5%–10.3%) by year 30 (Fig. 5(b)). In a population with a high initial prevalence, the population-level effect increases slowly and reaches a median of 6.1% (IQR, 4.3%–7.7%) by year 30 (Fig. 5(c)). In all cases, the median percent reduction in new cases increases almost linearly (gray line).

We are interested in determining what characteristics of waning immunity, vaccine efficacy, and vaccine uptake most affect the cumulative reduction in infections. Table 2 lists the partial rank correlation coefficients for

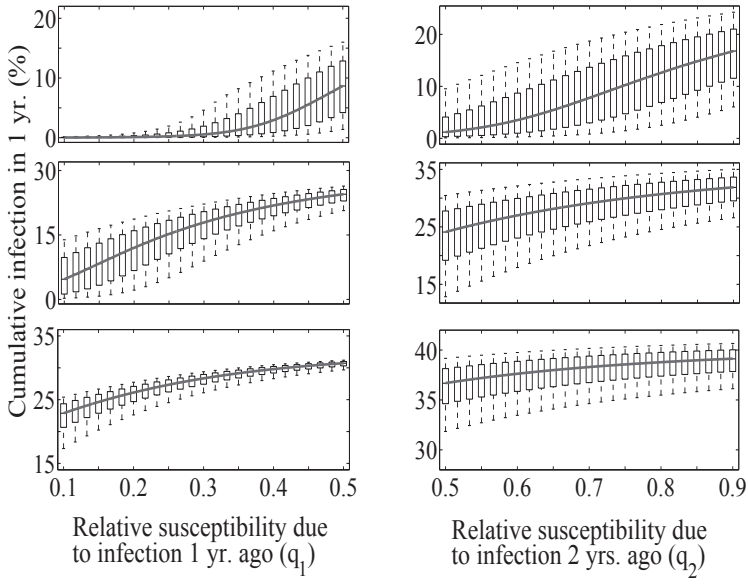

Figure 4. Effect of immunity from previous years' infection when no vaccine is introduced in the epidemic season (y-axis in different scale). As the immunity from infection 1 year ago wanes making the chance of susceptibility in the current year 10%–50% (left panel) and immunity from infection 2 years ago wanes making the chance of susceptibility in the current year 50–90% (right panel), cumulative infection increases. (top row) Low initial transmissibility ($R_0 = 1.4$), (middle row) Moderate initial transmissibility ($R_0 = 1.8$), (bottom row) High initial transmissibility ($R_0 = 2.2$). Increase in relative susceptibility increases the infection burden.

q_i, $i = 1 - 5$ and δ. Parameters of reduced susceptibility due to acquired immunity from natural infection 1 or 2 years ago (q_1, q_2) and vaccination in the current epidemic season (q_5) have significant PRCC values ($> |0.5|$), however, the proportion of the population vaccinated δ has the greatest effect overall. Note that, when the transmissibility of the infection increases (low to high) the PRCC values for these parameters increase or remain relatively constant. PRCC values show that the parameters q_3 and q_4 related to immunity through vaccination 1 and 2 years ago are most effective when there is a moderate transmission rate (middle column). Similary, our results show that as the transmissibility of the infection increases (low to high, left to right), the ranking of the parameters representing reductions in susceptibility q_i, $i = 1 - 5$ change. For example the PRCC value for the reduction in susceptibility due to vaccination in the current year q_5,

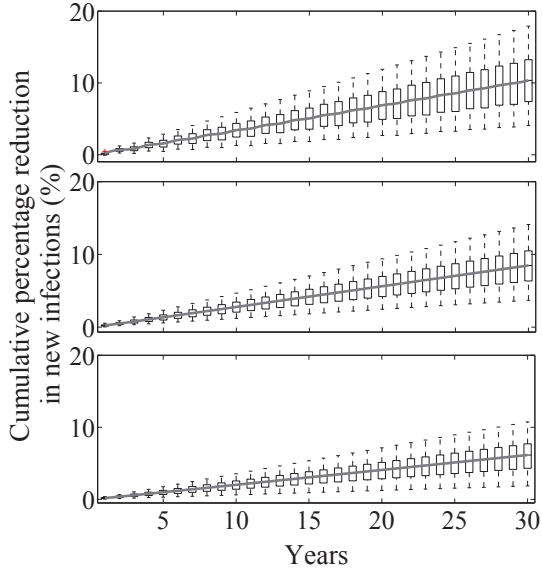

Figure 5. Impact of vaccination at the population-level: cumulative percentage reduction in new infections in a population which is pre-exposed. In presence of seasonal flu vaccine with first 40 days immunization strategy, cumulative new infections would be prevented (a) by a median of 10% (interquartile range [IQR], 7.4%–13.2%) for low initial transmission ($R_0 = 1.4$), (b) by a median of 8.5% (IQR, 6.3%–10.5%) for moderate initial transmission ($R_0 = 1.8$) and (c) by a median of 6.1% (IQR, 4.3%–7.7%) for high initial transmission ($R_0 = 2.2$) after 30 years of vaccination in a population partially immuned from prior infection. The vaccine coverage in each epidemic season varies between 10%–30%. Gray lines, median values (of 1000 simulations); boxes, IQRs; vertical lines, minimum and maximum values.

which ranges from 0.64 for low transmissibility to 0.89 for moderate transmissibility, changes from the third highest rank to the second highest rank in PRCC magnitude and again changes to third highest rank in case of high transmissibility. This implies that the chosen value of q_5 is highly significant for moderate transmissibility ($R_0 = 1.8$). Figure 6 shows the correlation of each of the parameters responsible for cumulative reduction at the population-level after 10 years, 20 years and 30 years.

The parameters q_1 and q_5, that represent the reduction in susceptibility from infection 1 year ago and vaccination in the current year, respectively, are both ranked second by PRCC magnitude in our sensitivity analysis (Table 2), Fig. 6. We now study the effect of increasing the proportion of

Table 2. Partial rank correlation coefficients with and without vaccine. Absolute value is shown. For $R_0 = 1.4$, vaccine coverage is 10%–30% which is equivalent to daily uptake rate 0.0027–0.0087, for $R_0 = 1.8$, vaccine coverage is 20%–40% which is equivalent to daily uptake rate 0.0067–0.0125, for $R_0 = 2.2$, vaccine coverage varies from 30%–50% which is equivalent to daily uptake rate 0.0087–0.017.

Parameter		Initial transmissibility								
		Low ($R_0 = 1.4$)			Moderate ($R_0 = 1.8$)			High ($R_0 = 2.2$)		
(a) *No vaccine*		1y.	5y.	10y.	1y.	5y.	10y.	1y.	5y.	10y.
Reduced susceptibility due to:										
Infection 1 yr. ago	q_1	0.98	0.94	0.95	0.98	0.99	0.99	0.97	0.99	0.99
Infection 2 yrs. ago	q_2	0.98	0.92	0.96	0.97	0.97	0.97	0.96	0.97	0.97
(b) *With vaccine*		10y.	20y.	30y.	10y.	20y.	30y.	10y.	20y.	30y.
Reduced susceptibility due to:										
Infection 1 yr. ago	q_1	0.85	0.81	0.85	0.83	0.83	0.84	0.92	0.93	0.94
Infection 2 yrs. ago	q_2	0.83	0.80	0.83	0.82	0.83	0.82	0.86	0.88	0.89
Vaccination 1 yr. ago	q_3	0.20	0.18	0.18	0.50	0.47	0.54	0.20	0.23	0.25
Vaccination 2 yrs. ago	q_4	0.05	0.01	0.08	0.10	0.08	0.08	0.07	0.01	0.01
Vaccination current yr.	q_5	0.64	0.70	0.66	0.89	0.87	0.89	0.73	0.70	0.71
Proportion vaccinated	δ	0.99	0.99	0.99	0.99	0.99	0.99	0.99	0.99	0.99

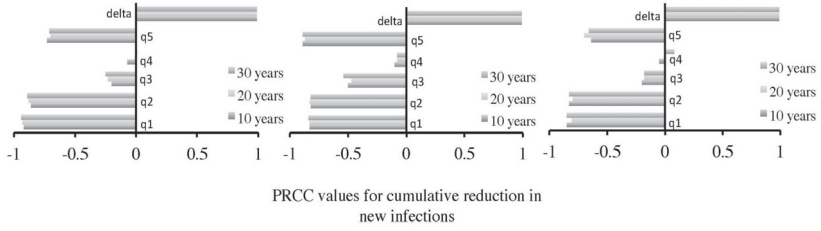

Figure 6. Tornado plots of partial rank correlation coefficients of the parameters related to the relative susceptibility due to prior exposure to infection or vaccination and daily vaccine take. Left, middle and right columns represent for low, moderate and high R_0. These parameters are responsible for cumulative reduction in new infections at the population level.

the population daily vaccinated δ against an increase in susceptibility q_1 and q_5, so as to determine a range of daily vaccination targets that are needed to achieve the same level of population protection (represented here as the cumulative percentage reduction in new infections over 10 years of vaccination). Again, we study the effects at low, moderate and high levels of transmissibility.

Figure 7(a) shows that for the same level of vaccination coverage, the cumulative percentage reduction in the total number of new infections increases as the relative susceptibility due to infection in the previous year increases. In other words, the degree of protection from natural infection does matter if the current vaccine strain is a good match to the current circulating strain. This relationship is constant for low (top row, left panel) but increases linearly for medium and high influenza transmissibility (middle and right panel of top row). As the rate of daily vaccine uptake increases, the reduction in cumulative infection also increases for low moderate or high transmissibility. But this reduction does not change as the relative susceptibility due to earlier infection increases for lower transmissibility ($R_0 = 1.4$)

Figure 7(b) shows that vaccines that induce a high degree of protection (low relative susceptibility) cause a greater reduction in infection for low and moderate transmissibility. The reduction in cumulative infection decreases linearly as the relative susceptibility due to vaccination increases for moderate and high transmissibility ($R_0 = 1.8, 2.2$ respectively). Here, the relationship is linear for low, moderate and high levels of influenza transmissibility (left to right) — constant for low transmissibility, but decreases linearly as the vaccine-induced immunity or immunity from previous infection decreases (i.e. relative susceptibility due to vaccination (q_5) or previous infection (q_1) steps-up). The slope for cumulative reduction in new infections are higher for low and moderate transmissibility as the vaccine induced immunity decreases (i.e. q_5 increases). Comparing the results for moderate (middle) and high (right) transmissibility, it can be seen that the reduction in infection is higher in case of moderate transmission rate for the same daily vaccination uptake δ. For example, in a population with moderate transmission (middle), a daily vaccine uptake rate of 0.012% of the population and a relative susceptibility due to previous year infection or vaccination ($q_1 = 0.1, q_5 = 0.1$) provides a reduction in the cumulative number of new infections in the range of 15%–20% (star (light gray)), but if transmissibility is high (left) the reduction lies in the range of 10%–15%. Thus, vaccination coverage needs to be increased to achieve the same level of reduction in influenza incidence if the strain transmissibility is high.

4. Discussion

Vaccination is the primary control strategy used against influenza. Vaccines are used to reduce disease incidence by reducing the size of the susceptible

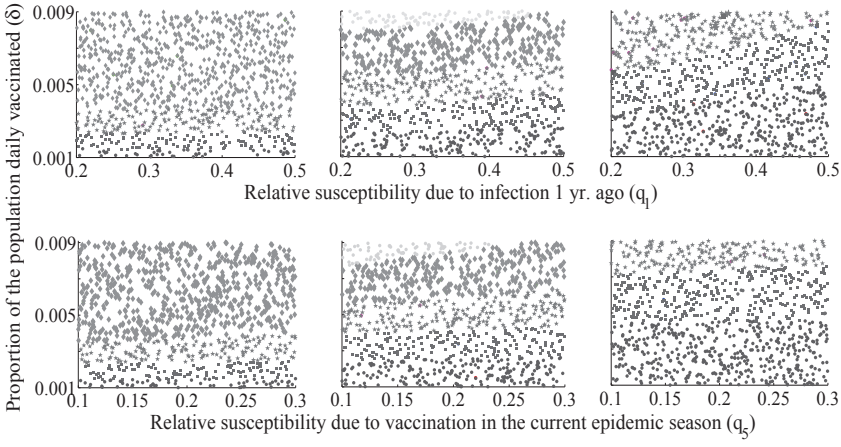

Figure 7. Sensitivity of the parameters related to reduced susceptibility and daily vaccine uptake on the population-level impact of vaccination. (a) Population-level impact as the proportion of daily vaccine take increases but degree of disease-induced immune protection against infection decreases. Results show the cumulative percentage reduction in new infections (filled circle (dark gray): <10%; filled square (gray): 10%–15%; star (light gray): 15%–20%, filled diamond (lighter gray): 20%–25%, filled circle (lightest gray): 25%–30%.) 10 years after vaccine introduction, for epidemic with low (left panel), moderate (middle panel) and high R_0 (right panel) under first 40 days vaccination strategy in each epidemic season. The y-axis (left panel) gives the daily vaccine uptake ranges from 0.0012–0.012 which corresponds to the yearly vaccine coverage of 5%–40% for $R_0 = 1.4$ and that (middle and right panels) ranges from 0.0012–0.017 which corresponds to yearly vaccine coverage 5%–50%. The x-axis gives the reduced susceptibility (q_1) due to previous year infection. (b) Population-level impact as the proportion of daily vaccine take increases but degree of vaccine-induced immune protection against infection decreases (i.e relative susceptibility due to vaccine in the current epidemic increases). Results show the cumulative percentage reduction in new infections (filled circle (dark gray): ¡10%; filled square (gray): 10%–15%; star (light gray): 15%–20%, filled diamond (lighter gray): 20%–25%, filled circle (lightest gray): 25%–30%.) 10 years after vaccine introduction in epidemics with low (left panel) moderate (left panel) and high R_0 (right panel). The y-axis gives the ranges of daily vaccine uptake (corresponds to annual vaccine coverage same as in (a) and the x-axis gives reduced susceptibility (q_5) due to immunization in the current epidemic season. For other parameters median values are used in both sets of figures.

population. Seasonal influenza epidemics are caused by new influenza virus variants that emerge because of antigenic drift (frequent antigenic changes resulting from point mutations that occur during viral replication). The evolution of influenza requires a vaccine assessment each year. However, the vaccine strains chosen from this assessment may not be optimal —

prediction of the dominant influenza strain is imperfect. This, in turn, affects the vaccine uptake rate that is needed to effectively protect the population.

In addition to the evolution of influenza strains through antigenic drift, the efficacy of a vaccination program also depends on the immune status of the population. Immunity can be gained through vaccination and natural infection, however, immunity can also wane over time. Effective immunity that provides some protection against infection, thus, will decrease over time with the waning of immune system cells and virus evolution. Thus, as effective immunity wanes, vaccines that can induce cross-protective and prophylactic immune responses are needed in each epidemic season for naive individuals with no immunity, but also to develop and boost immunity in individuals with varying degrees of effective immunity.

We have studied the effects of infection and vaccination induced immunity against seasonal influenza using two models representing the epidemic and inter-epidemic periods each year. In the epidemic model we considered the relative reduction in susceptibility due to prior infection or vaccination over two years of history. A constant proportion of the susceptible population, whether it is previously infected or vaccinated are assumed to be revaccinated in each season, where vaccines are assumed to have 70%–90% efficacy each season. The model was used to assess the impact of waning immunity from previous infection and annual vaccination during each epidemic season.

Our model replicates the qualitative dynamics of seasonal influenza with and without vaccination. Periodic epidemics are observed annually with similar magnitude in infection, and similar vaccination coverage each year (Fig. 2). In agreement with current knowledge, we also found that vaccine coverage at the beginning of an epidemic provides more protection to a population than continuous vaccination throughout the entire epidemic period (Fig. 2)

A study of routine vaccination coverage at the beginning of the epidemic showed that, depending on the transmissibility of the influenza strain (low to high), a vaccination program that covers 10%–30% of the population annually can reduce the cumulative number of infections by a median of 6%–10% (2% minimum to 18% maximum) over 30 years (Fig. 5).

A sensitivity analysis on all parameters representing susceptbility (q_i, $i = 1, ..., 5$) and vaccination coverage (δ) showed that changes in the proportion of the population vaccined (δ) has the greatest effect on the total number of infections over all influenza seasons (Table 2, Fig. 6). Rankings

of the parameters representing reductions in susceptibility (q_i, $i = 1, ..., 5$) varied by the number of years studied and the strain transmissibility (low to high) (Table 2). Reduction in susceptibility due to infection one year ago (q_1) and due to vaccination in the current year (q_5) both ranked second in the sensitivity analysis for different combinations of transmissibility and years studied. This means that the infection history of the previous year, and the current vaccination program characteristics most define the outcome of the current influenza season. A further analysis of q_1, q_5 and δ determined the conditions needed to obtain target ranges for reduction in the influenza incidence over 10 years of vaccination (Fig. 7). These results are relevant to current public health vaccination programs, whereby vaccination coverage targets can be updated if the relative fitness between the current circulating strain to the vaccine strain and the previous year's circulating strain can be determined.

We have studied the effects of waning immunity and vaccination coverage using a compartmental model that includes a two year history of vaccination and influenza infection. Model results show that parameters that represent the vaccination coverage in the current year (δ) and reduced susceptibility due to current vaccination (q_5) or infeciton in the previous year (q_1) most determine infection outcomes over 10, 20 and 30 years of vaccination programs. The reduction in susceptibility due to natural infection two years ago q_2, however, also ranked high in our sensitivity and uncertainty analysis. Future work will include a study of this result.

A goal of a vaccination program to provide some level of population protection. However, to achieve this goal, individuals in the population must decide to be immunized. Thus, vaccination programs efficacy must also be analyzed with respect to the benefits on individuals in a population i.e. total number of infections prevented due to vaccination. The current model can be employed to study these effects. This is a course for future work.

References

1. World Health Organization http://www.who.int/mediacentre/factsheets/fs211/en/ (2003).
2. R. B. Couch and J. A. Kasel, *Annu. Rev. Microbiol.* **37**, 529–49 (1983).
3. N. M. Ferguson, A. P. Galvani and R. M. Bush, *Nature* **422**, 1749–53 (2003).
4. Y. Xia, J. R. Gog, B. T. Grenfell, *Jour. Roy. Stat. Soc. C.* **54**, 659–72 (2005).
5. S. C. Schoenbaum, *Am. J. Med.* **82(6A)**, 26–30 (1987).
6. J. C. de Jong, G. F. Rimmelzwaan, R. A. M. Fouchier and A. D. M. E. Osterhaus, *J. Infect.* **40**, 218–28 (2000).

7. M. Coiras, J. Aguilar, M. Galiano, *et al.*, *Arch. Virol.* **146**, 2133–47 (2001).
8. A. J. Hay, V. Gregory, A. R. Douglas and Y. P. Lin, *Phil. Trans. R. Soc. Lond. B.* **356**, 1861–70 (2001).
9. M. E. Kitler, P. Gavinio and D. Lavanchy, *Vaccine* **20 (Suppl. 2)**, S5–14 (2002).
10. M. T. Osterholm, N. S. Kelley, A. Sommer and E. A. Belongia, *Lancet. Inf. Dis.* **12**, 36–44 (2012).
11. J. Castilla, I. Martinez-Baz, V. Martinez-Artola, *et al.*, *Eurosurveillance* **18**, Article 3 (2013).
12. R. B. Belshe, W. C. Gruber, P. M. Mendelman, *et al.*, *Jour. Inf. Dis.* **181**, 1133–37 (2000).
13. P. A. Gross, D. Herrington, H. S. Sachs, *et al.*, *Ann. Intern. Med.* **123**, 518–27 (1995).
14. F. Carrat, A. Lavenu, S. Cauchemez and S. Deleger, *Epidemiol. Infect.* **134**, 63–70 (2006).
15. W. E. P. Beyer, I. A. DeBruijn, A. M. Palache, *et al.*, *Arch. Intern. Med.* **159**, 182–8 (1999).
16. T. W. Hoskins, J. R. Davis, A. J. Smith, *et al.*, *Lancet.* **1**, 33–5 (1979).
17. W. A. Keitel, T. R. Cate, R. B. Couch, *et al.*, *Vaccine* **15**, 1114–22 (1997).
18. W. E. P. Beyer, I. A. DeBruijn, R. G. J. Westendorp and A. D. M. E. Osterhaus, *Vaccine* **16**, 1929–32 (1998).
19. D. J. Smith, S. Forrest, D. H. Ackley and A. S. Perelson, *PNAS.* **96**, 14001–6 (1999).
20. V. Gupta, D. J. Earl and M. W. Deem, *Vaccine* **24**, 3881–8 (2006).
21. J. T. Wu, L. M. Wein and A. S. Perelson, *Operations Research* **53**, 456–76 (2005).
22. M. F. Boni, J. R. Gog, V. Andreasen and M. W. Feldman, *Proc. R. Soc. B.* **273**, 1307–16 (2006).
23. X. Li, H. Jankowski, S. Wang and J. M. Heffernan, *BIOMAT 2014 Conference Proceedings* (2015).
24. D. J. Smith, A. S. Lapedes, J. C. de Jong, *et al.*, *Science* **305**, 371–6 (2004).
25. C. Gerdil, *Vaccine* **21**, 1776–9 (2003).
26. D. J. Fleming, J. van derWelden and W. J. Paget, *Vaccine* **21**, 1749–53 (2003).
27. C. M. Pease, *Theor. Popul. Biol.* **31**, 422–52 (1987).
28. S. M. Blower and H. Dowlatabadi, *Int. Stat. Rev.* **2**, 229–43 (1994).
29. M. D. McKay, R. J. Beckman, W. J. Conover, *Technometrics* **21**, 239–45 (1979).

IMPACT OF NON-MARKOVIAN RECOVERY ON NETWORK EPIDEMICS

GERGELY RÖST AND ZSOLT VIZI

Bolyai Institute,
University of Szeged,
Aradi vértanúk tere 1, Szeged 6720, Hungary
E-mail: rost@math.u-szeged.hu, zsvizi@math.u-szeged.hu

ISTVAN Z. KISS

School of Mathematical and Physical Sciences,
Department of Mathematics,
University of Sussex,
Falmer, Brighton BN1 9QH, UK
E-mail: i.z.kiss@sussex.ac.uk

We study how the distribution of infectious periods influences the dynamics of epidemics on networks. In our recently developed framework, we use pairwise models for network epidemics with non-Markovian recovery times. It is shown for typical families of distributions (such as gamma, uniform and lognormal) that higher variance in the recovery times generates lower reproduction numbers and different epidemic curves within each distribution family. We also show that knowing the expected value and the variance of the recovery times is not sufficient to determine the key characteristics of the epidemics such as initial growth rate, peak size, peak time and final epidemic size. For accurate predictions, more detailed information on the distribution of the infectious period is required, thus carefully estimating this distribution in the case of real epidemics has paramount public health importance.

1. Introduction

Networks (or graphs) offer a flexible framework to explicitly incorporate various heterogeneities in how individuals within a population interact[2,7,13,22,23]. This framework has led to a number of models where the strong assumptions of random mixing of the classical compartmental models can be relaxed. Because of the flexibility of the network approach, nodes can represent not only single individuals but also groups of individuals or locations. Similarly, links can represent contacts between individuals

along which diseases can spread, or interactions between groups such as flight routes between different locations.

In standard epidemiological models, the population is divided into classes depending on the status of individuals. In the simplest SIR (susceptible-infected-recovered) model, S, I and R denote the number (or proportion) of susceptible, infected and recovered individuals, respectively. The most important quantity associated with most epidemic models is the basic reproduction number (denoted by $\mathcal{R}_0$), which expresses the expected number of secondary infections generated by a 'typical' individual introduced into a susceptible population[8]. Naturally, if $\mathcal{R}_0 < 1$ the epidemic will die out, while if $\mathcal{R}_0 > 1$ the disease will spread. The other useful measure of epidemic severity is the final epidemic size, which is the total number of individuals who become infected during an epidemic, and often these two quantities can be related implicitly to capture factors such the network properties, and even properties of the transmission or recovery process (e.g. Poisson processes with exponentially distributed waiting time between events or general stochastic processes).

The transmission of epidemics on networks has been widely studied[23]. Most SIR models on networks assume that both the disease transmission and recovery process are Markovian. In other words, time to next infection along a link, where one node is susceptible and the other is infectious, is exponentially distributed and so is the time spent by an infectious node in the I state. Pairwise models have been very successful in capturing the average behaviour of a stochastic epidemics on networks[14]. These are formulated in terms of the expected values for the number of susceptible ($[S]$), infected ($[I]$) and recovered ($[R]$) nodes, which in turn depend on the expected values of (SS) pairs ($[SS]$) and (SI) pairs ($[SI]$) pairs. Introducing the following general notations

(1) $[X](t)$ is the expected number of nodes in state X at time t,
(2) $[XY](t)$ is the expected number of links which have a node in state X at one end and a node in state Y at the other, and
(3) $[XYZ](t)$ is the expected number of triplets in state $X - Y - Z$,

where, $X, Y, Z \in \{S, I, R\}$, and by accounting for all possible transitions,

the pairwise model is

$$\begin{aligned}
[\dot{S}](t) &= -\tau[SI](t),\\
[\dot{I}](t) &= \tau[SI](t) - \gamma[I](t),\\
[\dot{SS}](t) &= -2\tau[SSI](t),\\
[\dot{SI}](t) &= \tau[SSI](t) - \tau[ISI](t) - \tau[SI](t) - \gamma[SI](t),
\end{aligned} \tag{1}$$

where τ is the per contact infection rate and γ is the rate of recovery. Furthermore, $[S]+[I]+[R]=N$ and above we only listed equations which are necessary to derive a full self-consistent system. It can be seen, that the system is not closed, because the equations for links contain triplets, thus we have to break the dependence on higher order terms. The closure approximation formula $[XSY] = \frac{n-1}{n}\frac{[XS][SY]}{[S]}$, where n is the average number of links per node and N is the number of nodes in the network, leads to the self-consistent system

$$\begin{aligned}
[\dot{S}](t) &= -\tau[SI](t),\\
[\dot{I}](t) &= \tau[SI](t) - \gamma[I](t),\\
[\dot{SS}](t) &= -2\tau\frac{n-1}{n}\frac{[SS](t)[SI](t)}{[S](t)},\\
[\dot{SI}](t) &= \tau\frac{n-1}{n}\left(\frac{[SS](t)[SI](t)}{[S](t)} - \frac{[SI](t)[SI](t)}{[S](t)}\right) - (\tau+\gamma)[SI](t).
\end{aligned} \tag{2}$$

Closing at the level of pairs with the approximation $[XY] = n[X]\frac{[Y]}{N}$, leads to the so called mean-field model

$$\begin{aligned}
\dot{S}(t) &= -\tau\frac{n}{N}S(t)I(t),\\
\dot{I}(t) &= \tau\frac{n}{N}S(t)I(t) - \gamma I(t),
\end{aligned} \tag{3}$$

and the network structure is less important at this point. For this model the basic reproduction number is

$$\mathcal{R}_0 = \frac{n}{N}\tau\mathbb{E}(\mathcal{I})S_0, \tag{4}$$

where, $\mathbb{E}(\mathcal{I}) = 1/\gamma$ is the expected infectious period. Various results for the Markovian case exist[14]. For the pairwise model, the final epidemic size is given by the following implicit relation

$$\frac{s_\infty^{\frac{1}{n}} - 1}{\frac{1}{n-1}} = \frac{n-1}{N}\frac{\tau}{\tau+\gamma}[S]_0\left(s_\infty^{\frac{n-1}{n}} - 1\right), \tag{5}$$

where $[S]_0$ is the number of susceptible individuals at time $t = 0$ and $s_\infty = [S]_\infty/[S]_0$, where $[S](\infty) = [S]_\infty$. The assumption of Markovianity in both infection and recovery is a strong simplifying assumption, as especially in the context of epidemiology, the period of infectiousness has paramount importance[15,18], and often this is approximated from the empirical distribution of observed infectious periods of various diseases by log-normal and gamma (smallpox[9,20]), fixed-length (measles[1]) or Weibull distributions (ebola[4]). Newman[21], with his results later made more precise by Kenah and Robins[16], gives a relation between the average transmission rate and final epidemic size, using a bond percolation approach, and his result is applicable for more general infection and recovery processes. Recently, however there is renewed interest in modelling non-Markovian processes, such as epidemics on networks[3,5,6,12,16,17,19,24,25], and random walks[11]. Kiss et al.[17] considered an SIR epidemic with deterministic infectious period (i.e. the recovery time is constant) and derived the mean-field and pairwise models for this case. The mean-field model is given by, see[17],

$$\begin{aligned} S'(t) &= -\tau \frac{n}{N} S(t) I(t), \\ I'(t) &= \tau \frac{n}{N} S(t) I(t) - \tau \frac{n}{N} S(t-\sigma) I(t-\sigma). \end{aligned} \tag{6}$$

The pairwise model for fixed infectious period was derived[17] as

$$\begin{aligned} [\dot{S}](t) &= -\tau [SI](t), \\ [\dot{SS}](t) &= -2\tau \frac{n-1}{n} \frac{[SS](t)[SI](t)}{[S](t)}, \\ [\dot{I}](t) &= \tau [SI](t) - \tau [SI](t-\sigma), \\ [\dot{SI}](t) &= \tau \frac{n-1}{n} \frac{[SS](t)[SI](t)}{[S](t)} - \tau \frac{n-1}{n} \frac{[SI](t)[SI](t)}{[S](t)} - \tau [SI](t) \\ &\quad - \tau \frac{n-1}{n} \frac{[SS](t-\sigma)[SI](t-\sigma)}{[S](t-\sigma)} e^{-\int_{t-\sigma}^{t} \tau \frac{n-1}{n} \frac{[SI](u)}{[S](u)} + \tau du}. \end{aligned} \tag{7}$$

We note that both models are now delay differential equations rather than ordinary differential equations (ODEs), as is the case for Markovian epidemics. In the same paper Kiss et al. have shown that the for the final size the following relation

$$\frac{s_\infty^{\frac{1}{n}} - 1}{\frac{1}{n-1}} = \frac{n-1}{N} \left(1 - e^{-\tau\sigma}\right) [S]_0 \left(s_\infty^{\frac{n-1}{n}} - 1\right) \tag{8}$$

holds, where a newly introduced basic reproduction-like number is defined as $\mathcal{R}_0^p = \frac{n-1}{N} \left(1 - e^{-\tau\sigma}\right) [S]_0$. Furthermore, in Ref. 17 it has been pre-

sented that for arbitrary infectious periods, the basic reproduction number associated to the pairwise model is

$$\mathcal{R}_0^p = \frac{n-1}{N}\left(1 - \mathcal{L}[f_{\mathcal{I}}](\tau)\right)[S]_0, \tag{9}$$

where $\mathcal{L}[\cdot]$ is the Laplace transform and $f_{\mathcal{I}}$ is the probability density function of the recovery process. With this new definition, numerical tests (and in special cases analytical results) have confirmed, see Ref. 17, that the following implicit relation for the final epidemic size holds

$$\begin{aligned}\frac{s_\infty^{\frac{1}{n}} - 1}{\frac{1}{n-1}} &= \mathcal{R}_0^p\left(s_\infty^{\frac{n-1}{n}} - 1\right)\\ &= \frac{n-1}{N}\left(1 - \mathcal{L}[f_{\mathcal{I}}](\tau)\right)[S]_0\left(s_\infty^{\frac{n-1}{n}} - 1\right),\end{aligned} \tag{10}$$

and this can be applied for any general recovery time distributions.

Notice, while $\mathcal{R}_0$ depends on the expected value only, see (4), the pairwise reproduction number (9), uses the complete density function, thus the average length of infectious period does not determine exactly the reproduction number. This remark implies, that for an epidemic we have to know as precisely as possible the shape of the distribution. In the sequel we denote by $\mathcal{I}$ the random variable that describes the recovery time, which is, in the SIR-setting, the same as the distribution of the infectious period.

In this paper we exploit the generalised basic reproduction number (9) and the general implicit relation for the final epidemic size (10) to determine how these depend on the precise shape of recovery time distribution. We give some analytic results, as well as results based on simulations to shed light on the time evolution of the epidemics. The paper is structured as follows. Sections 2, 3, and 4 concern with recovery times of gamma, uniform and lognormal distributions, respectively. The dependence of the reproduction number, as well as the shape of the epidemic curve, on the distribution parameters is analysed in details in each case. In Section 5, by comparing epidemics generated by different types of the recovery time distributions, we illustrate that estimating the expected value and the variance of the recovery time is not sufficient to give a realistic description of the epidemics and more detailed knowledge of the shape of the empirical distribution is needed to give a reasonable approximation of a real epidemics.

2. Gamma Distributed Recovery Time

The gamma distribution is one of the most commonly used distributions in the epidemiology literature to approximate empirically observed latent

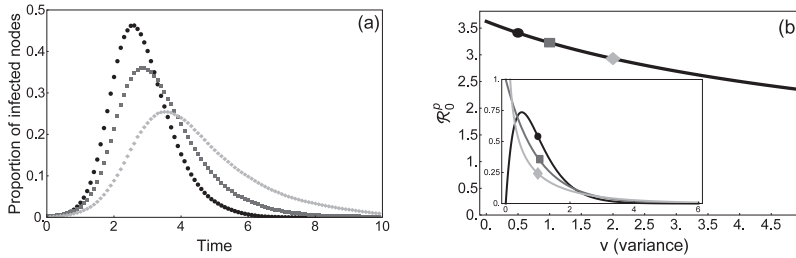

Figure 1. **(a)** Epidemic curves as averages of explicit stochastic simulations for non-Markovian epidemics, where the transmission rate is $\tau = 0.3$ and the initial number of susceptibles is $S_0 = 999$ on a homogeneous network with $N = 1000$ nodes and degree $n = 15$. The circles/squares/diamonds correspond to simulations for gamma distributed recovery time with parameters $(a, b) = (2, 0.5)/(1, 1)/(0.5, 2)$, respectively. **(b)** The solid curve shows the reproduction number $\mathcal{R}_0^p$ as a function of variance v for fixed $m = 1$, and the circle/square/diamond represent the cases simulated in Fig. (a). In the inset figure, the shapes of the three corresponding probability density functions are presented.

periods and infectious periods, because of its flexibility and the possibility of incorporating it into ordinary differential equation models by the method of stages (also called linear chain)[18] . For example, it has been fitted to the incubation period and infectious period of smallpox[9], bluetongue disease[10] and so on.

The usual notation of gamma distribution is $\text{Gamma}(a, b)$, where a is called the shape parameter and b is called the scale parameter. The probability density function and its Laplace transform are

$$f_{\mathcal{I}}(x) = \frac{x^{a-1}e^{-\frac{x}{b}}}{\Gamma(a)b^a}, \quad \mathcal{L}[f_{\mathcal{I}}](s) = \left(\frac{1}{1+sb}\right)^a,$$

where $\Gamma(a)$ is the gamma function evaluated at a. If the infectious period $\mathcal{I}$ is gamma distributed with shape parameter a and scale parameter b, that is $\mathcal{I} \sim \text{Gamma}(a, b)$, then the expected value is $m := \mathbb{E}(\mathcal{I}) = ab$, and the variance is $v := \text{Var}(\mathcal{I}) = ab^2$, and for simplicity later we shall use the notation m and v to denote the mean (expected value) and the variance of distributions.

Proposition 2.1. *Consider two random variables* $\mathcal{I}_1 \sim \text{Gamma}(a_1, b_1)$ *and* $\mathcal{I}_2 \sim \text{Gamma}(a_2, b_2)$ *such that* $\mathbb{E}(\mathcal{I}_1) = \mathbb{E}(\mathcal{I}_2)$ *and* $\text{Var}(\mathcal{I}_1) \leq \text{Var}(\mathcal{I}_2)$. *If* $\mathcal{I}_1$ *and* $\mathcal{I}_2$ *represent the recovery time distribution, then for the corresponding reproduction numbers the relation* $\mathcal{R}^p_{0,\mathcal{I}_1} \geq \mathcal{R}^p_{0,\mathcal{I}_2}$ *holds (i.e. for gamma distributions with a given mean, the pairwise reproduction number is monotonically decreasing in variance).*

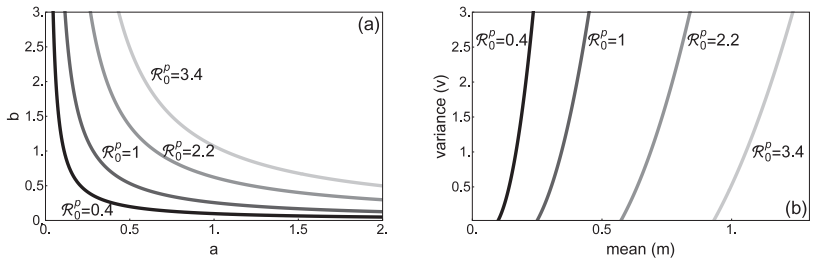

Figure 2. Contour lines of $\mathcal{R}_0^p$ as a two-variable function of the parameters of the gamma distribution. The transmission rate is $\tau = 0.3$, the network has $N = 1000$ nodes and degree $n = 15$ and initial number of susceptibles is $S_0 = 999$. In **(a)**, the contour lines are given as the function of the shape and scale parameter, while in **(b)** they are depicted as the function of the mean and the variance of the gamma distribution.

Proof. Fix m as the same mean of $\mathcal{I}_1$ and $\mathcal{I}_2$, then the scale parameter can be expressed as $b = \frac{m}{a}$. Using that $v = \mathrm{Var}(\mathcal{I}) = ab^2$ and

$$\mathcal{L}[f_{\mathcal{I}}](\tau) = \left(\frac{1}{1+\tau b}\right)^a,$$

we can express the parameters in terms of the mean m and variance v, and thus the Laplace transform can be written as

$$\lambda_m(\tau; v) := \mathcal{L}[f_{\mathcal{I}}](\tau) = \left(\frac{1}{1+\frac{\tau}{m}v}\right)^{\frac{m^2}{v}},$$

where the notation $\lambda_m(\tau; v)$ for the Laplace transform is meant to emphasize that the Laplace transform evaluated at τ for a fixed m is a function of v. For arbitrary $0 < x < y < 1$ and $0 < a < b$, the inequalities

$$x^{\frac{m^2}{a}} < x^{\frac{m^2}{b}}, \quad x^{\frac{m^2}{b}} < y^{\frac{m^2}{b}}$$

hold. For $v_1 \le v_2$ and for $\tau > 0$ we have $\frac{1}{1+\frac{\tau}{m}v_2} \le \frac{1}{1+\frac{\tau}{m}v_1}$, and using the relations above we obtain

$$\left(\frac{1}{1+\frac{\tau}{m}v_1}\right)^{\frac{m^2}{v_1}} \le \left(\frac{1}{1+\frac{\tau}{m}v_1}\right)^{\frac{m^2}{v_2}} \le \left(\frac{1}{1+\frac{\tau}{m}v_2}\right)^{\frac{m^2}{v_2}},$$

which means that $\lambda_m(\tau; v)$ is monotone increasing in v. Therefore, the pairwise reproduction number

$$R^p_{0,\mathcal{I}} = \frac{n-1}{N}[S]_0(1 - \lambda_m(\tau; v))$$

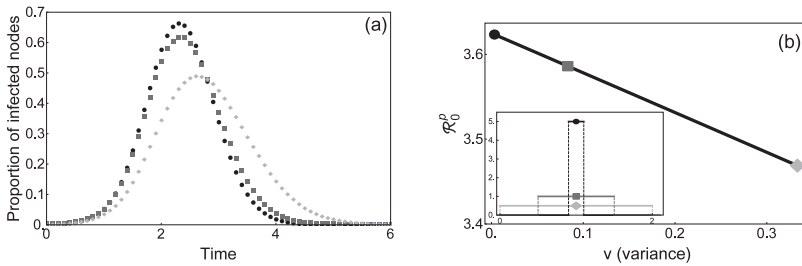

Figure 3. **(a)** Epidemic curves as averages of explicit stochastic simulations for non-Markovian epidemics, where transmission rate is $\tau = 0.3$ and initial number of susceptibles is $S_0 = 999$, on homogeneous network with $N = 1000$ nodes and degree $n = 15$. The circles/squares/diamonds correspond to simulations for uniformly distributed recovery time with parameters $(a, b) = (0.9, 1.1)/(0.5, 1.5)/(0, 2)$, respectively. **(b)** The solid curve shows the reproduction number $\mathcal{R}_0^p$ as the function of variance v for fixed $m = 1$, and the circle/square/diamond represent the cases simulated in Fig. (a). In the inset figure, the three uniform density functions are depicted.

is monotone decreasing in v. □

The monotonicity of the reproduction number in the variance is depicted in Fig. 1(b). For a fixed mean but different variances of the gamma distribution, we can observe different epidemic curves in Fig. 1(a), and correspondingly different reproduction numbers (see Fig. 1(b)). The dependence of $R^p_{0,\mathcal{I}}$ on the distribution parameters is detailed in Fig. 2.

3. Uniformly Distributed Recovery Time

Since its simplicity allows us to make explicit calculations, in this Section we outline how the reproduction number and the disease dynamics behave when the recovery time follows uniform distribution. Uniformly distributed incubation and infectious periods have been used in the modeling of avian influenza[26]. Let Uniform(a, b) denote a uniform distribution corresponding to the interval $[a, b]$, where $a \geq 0, b > a$. If $\mathcal{I} \sim$ Uniform(a, b), then the expected value is $m = \mathbb{E}(\mathcal{I}) = \frac{a+b}{2}$, and the variance is $v = \mathrm{Var}(\mathcal{I}) = \frac{(b-a)^2}{12}$. The probability density function and its Laplace transform are given as

$$f_{\mathcal{I}}(x) = \begin{cases} \frac{1}{b-a} & \text{for } a \leq x \leq b \\ 0 & \text{otherwise} \end{cases}, \quad \mathcal{L}[f_{\mathcal{I}}](s) = \frac{e^{-sa} - e^{-sb}}{s(b-a)}.$$

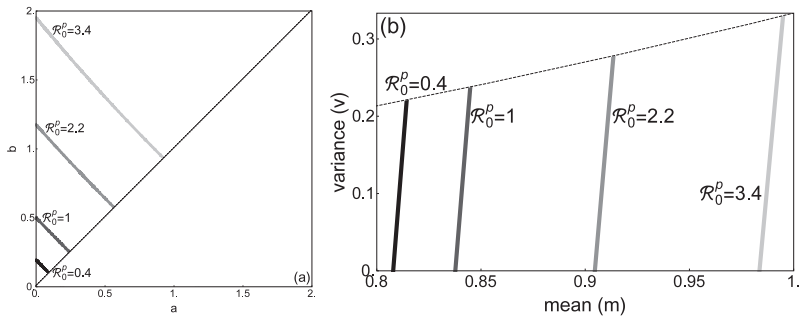

Figure 4. **(a)** Contour lines of $\mathcal{R}_0^p$ as a two-variable function of the parameters of the uniform distribution. **(b)** Contour lines of $\mathcal{R}_0^p$ as a two-variable function of m and v for uniform distribution. For both (a) and (b), the transmission rate is $\tau = 0.3$, the network has $N = 1000$ nodes and degree $n = 15$ with an initial number of susceptibles $S_0 = 999$.

Proposition 3.1. *Consider two random variables* $\mathcal{I}_1 \sim \text{Uniform}(a_1, b_1)$ *and* $\mathcal{I}_2 \sim \text{Uniform}(a_2, b_2)$ *such that* $\mathbb{E}(\mathcal{I}_1) = \mathbb{E}(\mathcal{I}_2)$ *and* $\text{Var}(\mathcal{I}_1) \leq \text{Var}(\mathcal{I}_2)$. *If* $\mathcal{I}_1$ *and* $\mathcal{I}_2$ *represent the recovery time distribution, then for the corresponding reproduction numbers the relation* $\mathcal{R}^p_{0,\mathcal{I}_1} \geq \mathcal{R}^p_{0,\mathcal{I}_2}$ *holds (i.e. for uniform distributions with a given mean, the pairwise reproduction number is monotonically decreasing in variance).*

Proof. Fixing the mean m, the right endpoint of the interval is $b = 2m - a$. Using that $v = \text{Var}(\mathcal{I}) = \frac{(b-a)^2}{12}$ and $\mathcal{L}[f_{\mathcal{I}}](\tau) = \frac{e^{-\tau a} - e^{-\tau b}}{\tau(b-a)}$, by simple algebra we can express the parameters by m and the variance v, and consequently the Laplace transform can be written as the function of v:

$$\lambda_m(\tau; v) = \frac{e^{-\tau m}}{2m} \frac{e^{\tau\sqrt{3v}} - e^{-\tau\sqrt{3v}}}{\tau\sqrt{3v}},$$

where $v \in \left(0, \frac{m^2}{3}\right]$ from our assumptions on a and b. Expanding the exponentials in $\lambda_m(\tau; v)$ into Taylor series, we can notice that the negative terms cancel out, and we obtain

$$\begin{aligned}
\lambda_m(\tau; v) &= \frac{e^{-\tau m}}{2m} \frac{\left(1 + (\tau\sqrt{3v}) + \dots\right) - \left(1 - (\tau\sqrt{3v}) + \dots\right)}{\tau\sqrt{3v}} \\
&= \frac{e^{-\tau m}}{2m} \frac{2\tau\sqrt{3v} + 2\frac{(\tau\sqrt{3v})^3}{3!} + \dots}{\tau\sqrt{3v}} \\
&= \frac{e^{-\tau m}}{m} \sum_{n=0}^{\infty} \frac{(\tau\sqrt{3v})^{2n}}{(2n+1)!}, \qquad (11)
\end{aligned}$$

which is monotone increasing in v for $m > 0$ and $\tau > 0$. Therefore, the pairwise reproduction number $R^p_{0,\mathcal{I}} = \frac{n-1}{N}[S]_0(1 - \lambda_m(\tau; v))$ is monotone decreasing in v. □

The monotonicity of the reproduction number in the variance is depicted in Fig. 3(b). Similarly to the gamma distribution, for a fixed mean but different variances of the uniform distribution we can observe different epidemic curves in Fig. 3(a), and correspondingly different reproduction numbers (see Fig. 3(b)). The dependence of $R^p_{0,\mathcal{I}}$ on the distribution parameters is detailed in Fig. 4.

4. Lognormal Distributed Recovery Time

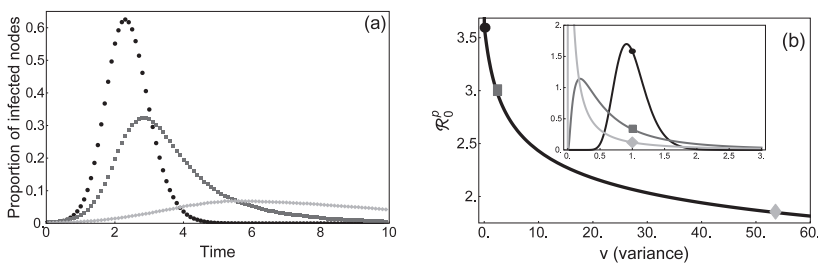

Figure 5. **(a)** Epidemic curves as averages of explicit stochastic simulations for non-Markovian epidemics, where transmission rate is $\tau = 0.3$ and initial number of susceptibles is $S_0 = 999$, on homogeneous network with $N = 1000$ nodes and degree $n = 15$. The circles/squares/diamonds correspond to simulations for lognormally distributed recovery time with parameters $(\mu, \sigma) = (-0.03125, 0.25)/(-\frac{\ln(3)}{2}, \sqrt{\ln 3})/(0, 2)$, respectively. **(b)** The solid curve shows the reproduction number $\mathcal{R}_0^p$ as the function of variance v for fixed $m = 1$, and the circle/square/diamond represent the cases simulated in Fig. (a). Inset figure shows the shape of these three distributions.

The lognormal distribution is also widely used in epidemiology. They have been fitted, among others, to the incubation and infectious periods of smallpox[20]. Let $\ln\mathcal{N}(\mu, \sigma^2)$ denote a lognormal distribution, i.e. its logarithm is a normal distribution with expected value μ and variance σ. Then for the lognormal distribution $m = \mathbb{E}(\mathcal{I}) = e^{\mu+\frac{\sigma^2}{2}}$, $v = \mathrm{Var}(\mathcal{I}) = e^{2\mu+2\sigma^2} - e^{2\mu+\sigma^2}$, and the probability density function is, for $x > 0$,

$$f(x) = \frac{1}{x\sqrt{2\pi}\sigma} e^{-\frac{(-\mu+\ln(x))^2}{2\sigma^2}}.$$

Unfortunately a closed form formula does not exist for its Laplace transform, thus we can not repeat the analysis of the previous two sections.

However, we can still investigate numerically the impact of m and v on the reproduction number and the time course of the epidemic. The density function can again be expressed in terms of m and v by the formula

$$f_m(x;v) = \frac{1}{x\sqrt{2\pi}\sqrt{\ln\left(\frac{v}{m^2}+1\right)}} e^{-\frac{\left(\ln(x)-\ln(m)+\frac{1}{2}\ln\left(\frac{v}{m^2}+1\right)\right)^2}{2\ln\left(\frac{v}{m^2}+1\right)}}, \text{ for } x>0. \quad (12)$$

By straightforward calculation, we can find $\mu = \ln(m) - \frac{1}{2}\ln\left(1+\frac{v}{m^2}\right)$ and $\sigma^2 = \ln\left(1+\frac{v}{m^2}\right)$, and then the formula above can be derived. Using this formula for the density, we can plot the numerically determined pairwise reproduction number as a function of the variance for any given m, see Fig. 5(b). The epidemic curves corresponding to these distributions can be seen in Fig. 5(a), and the dependence of $\mathcal{R}_0^p$ on the distribution parameters is detailed in Fig. 6.

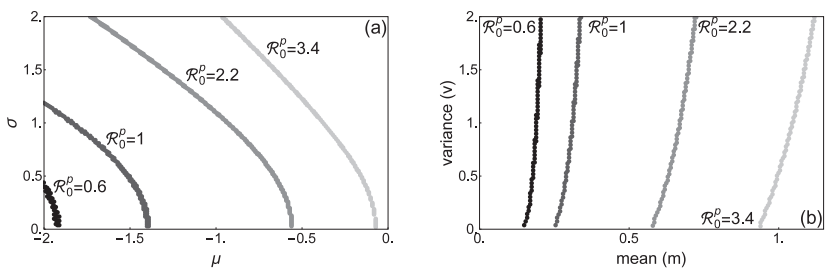

Figure 6. **(a)** Contour lines of $\mathcal{R}_0^p$ as a two-variable function of the parameters of the lognormal distribution. **(b)** Contour lines of $\mathcal{R}_0^p$ as a two-variable function of the mean and variance for lognormal distribution. For both (a) and (b), the transmission rate is $\tau = 0.3$, the network has $N = 1000$ nodes and degree $n = 15$ with an initial number of susceptibles is $S_0 = 999$.

5. Discussion

We used our recently developed non-Markovian pairwise model[17] for network epidemics to investigate the impact of the shape of the distribution of the recovery times on SIR epidemics. In particular, we utilized our formula for the reproduction number which includes the Laplace transform of the probability density distribution of the infectious period[17]. We chose three families of common distributions (gamma, uniform and lognormal), and in each case we showed that (for the first two analytically, for the third one only numerically) if the mean recovery time is given, then smaller variance

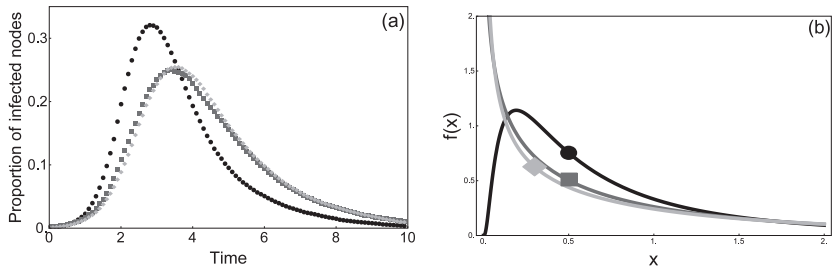

Figure 7. **(a)** Comparison of three epidemic curves after averaging explicit stochastic simulations with three different distributions of recovery times. The diamond/circle/square corresponds to Gamma$(0.5, 2)$, $\ln\mathcal{N}\left(\frac{\ln(3)}{2}, \sqrt{\ln(3)}\right)$ and Weibull$(0.72, 0.81)$ distributions, respectively. All three distributions have mean $m = 1$ and variance $v = 2$. **(b)** Probability density functions corresponding to the three distributions.

leads to higher reproduction number, and consequently the epidemic curve is characterised by faster initial growth rate and higher prevalence peak, see Figs. 1, 3 and 5. We note that our simulations were done only for homogeneous graphs, where the pairwise approximation works well[5]. The possible interplay of degree heterogeneity, or the clustering of the network, and the distribution of recovery times is an interesting future question.

For two-parameter distribution families, it is possible to regard $\mathcal{R}_0^p$ as a function depending on two variables, e.g. the mean m and variance v, see Figs. 2, 4, 6. Since our general final size relation (10) is monotone in $\mathcal{R}_0^p$, we conclude that smaller variance generates more infections.

It is important to observe that this statement, i.e. that smaller variance implies higher $\mathcal{R}_0^p$ is true only if we compare distributions from the same family. In Fig. 7, we compared three distributions from different families, each having $m = 1$ and $v = 2$. Besides the gamma and the lognormal distributions, for the sake of comparison we selected a third type of continuous distribution, namely Weibull distribution, which has been fitted to the infectious period for the recent ebola outbreak[4]. Figure 7 illustrates that the mean and the variance of the recovery times alone are not able to determine the key characteristics of the epidemic curves, and a large variety of outbreaks can be generated from having the same mean and variance. This is especially the case in Fig. 7, where the gamma distributed infectious period leads to a very different epidemic, compared to that corresponding to the lognormally distributed infectious period, despite the mean and the variance are being identical. Therefore, in a real life situation, it is crucial

to estimate the empirical distribution of the infectious period as accurately as possible, since the mean and the variance alone do not provide enough information for accurate predictions.

Acknowledgements. GR was supported by ERC StG 259559 and OTKA K109782. ZsV was supported by TÁMOP-4.2.2.B-15/1/KONV-2015-0006.

References

1. N. T. J. Bailey. On estimating of latent and infectious periods of measles. i. families with two susceptibles only. *Biometrika*, 43: 15–22, 1956.
2. S. Boccaletti, V. Latora, Y. Moreno, M. Chavez and D.-U. Hwang. Complex networks: Structure and dynamics. *Physics reports*, 424(4): 175–308, 2006.
3. M. Boguná, L. F. Lafuerza, R. Toral and M. A. Serrano. Simulating non-markovian stochastic processes. *Phys. Rev. E*, 90(4): 042108, 2014.
4. G. Chowell and H. Nishiura. Transmission dynamics and control of Ebola Virus Disease (EVD): A review. *BMC Medicine*, 196, 2014.
5. F. Cooper. Non-Markovian network epidemics, MA Thesis, 2013. *www.dtc.ox.ac.uk/people/13/cooperf/files/MA469ThesisFergusCooper.pdf*
6. E. Cator, R. Van de Bovenkamp and P. Van Mieghem. Susceptible-infected-susceptible epidemics on networks with general infection and cure times. *Phys. Rev. E*, 87(6): 062816, 2013.
7. L. Danon, A. P. Ford, T. House, C. P. Jewell, M. J. Keeling, G. O. Roberts, J. V. Ross and M. C. Vernon. Networks and the epidemiology of infectious disease. *Interdisciplinary perspectives on infectious diseases*, 2011.
8. O. Diekmann, J. A. P. Heesterbeek and J. A. J. Metz. On the definition and the computation of the basic reproduction ratio R 0 in models for infectious diseases in heterogeneous populations. *J. Math. Biol.* 28(4): 365–382, 1990.
9. M. Eichner and K. Dietz. Transmission potential of smallpox: estimates based on detailed data from an outbreak. *Am. J. Epidemiol.*, 158: 110–117, 2003.
10. S. Gubbins, S. Carpenter, M. Baylis, J. L. Wood and P. S. Mellor. Assessing the risk of bluetongue to UK livestock: uncertainty and sensitivity analyses of a temperature-dependent model for the basic reproduction number. *Journal of the Royal Society Interface,* 5(20): 363–371, 2008.
11. T. Hoffmann, M. A. Porter and R. Lambiotte. Generalized master equations for non-Poisson dynamics on networks. *Phys. Rev. E*, 86(4): 046102, 2012.
12. H.-H. Jo, J. I. Perotti, K. Kaski and J. Kertész. Analytically solvable model of spreading dynamics with non-Poissonian processes. *Phys. Rev. X*, 4(1): 011041, 2014.
13. M. J. Keeling and K. T. D. Eames. Networks and epidemic models. *Journal of the Royal Society Interface*, 2(4): 295–307, 2005.
14. M. J. Keeling. The effects of local spatial structure on epidemiological invasions. *Proc. R. Soc. B*, 266(1421): 859–867, 1999.
15. M. J. Keeling and B. T. Grenfell. Understanding the persistence of measles:

reconciling theory, simulation and observation. *Proc. R. Soc. B*, 269(1489): 335–343, 2002.
16. E. Kenah and J. M. Robins. Second look at the spread of epidemics on networks. *Physical Review E*, 76(3): 036113, 2007.
17. I. Z. Kiss, G. Röst and Zs. Vizi. Pairwise-like models for non-Markovian epidemics on networks. *Phys. Rev. Letters, in press, arXiv preprint arXiv:1504.04639*, 2015.
18. A. L. Lloyd. Realistic distributions of infectious periods in epidemic models: changing patterns of persistence and dynamics. *Theor. Pop. Biol.*, 60(1): 59–71, 2001.
19. B. Min, K. I. Goh and I. M. Kim. Suppression of epidemic outbreaks with heavy-tailed contact dynamics. *EPL (Europhysics Letters)*, 103(5): 50002, 2013.
20. H. Nishiura and M. Eichner. Infectiousness of smallpox relative to disease age: estimates based on transmission network and incubation period. *Epidemiol. Infect.*, 135: 1145–1150, 2007.
21. M. E. J. Newman. Spread of epidemic disease on networks. *Physical review E*, 66(1): 016128, 2002.
22. M. E. J. Newman. The structure and function of complex networks. *SIAM Review*, 45(2): 167–256, 2003.
23. R. Pastor-Satorras, C. Castellano, P. Van Mieghem and A. Vespignani. Epidemic processes in complex networks. *arXiv preprint arXiv:1408.2701*, 2014.
24. P. Van Mieghem and R. Van de Bovenkamp. Non-Markovian infection spread dramatically alters the susceptible-infected-susceptible epidemic threshold in networks. *Phys. Rev. Lett.*, 110(10): 108701, 2013.
25. R. R. Wilkinson and K. J. Sharkey. Message passing and moment closure for susceptible-infected-recovered epidemics on finite networks. *Physical Review E*, 89(2): 022808, 2014.
26. Y. Yang, M. E. Halloran, J. D. Sugimoto and I. M. Longini Jr. Detecting human-to-human transmission of avian influenza A (H5N1). *Emerging Infectious Diseases*, 13(9), 1348, 2007.

A MODELLING FRAMEWORK FOR SEROTYPE REPLACEMENT IN VACCINE-PREVENTABLE DISEASES*

MINGSONG KANG

Department of Immunology
University of Toronto
Toronto, Ontario, Canada M5S 1A8
E-mail: Mingsong.kang@utoronto.ca

AQUINO L. ESPINDOLA

Departamento de Física
Instituto de Ciências Exatas - ICEx
Universidade Federal Fluminense
Volta Redonda, RJ, Brazil, 27.213-145
E-mail: aquinoespindola@id.uff.br

MAREK LASKOWSKI, SEYED M. MOGHADAS

Agent-Based Modelling Laboratory
York University, 4700 Keele St.
Toronto, Ontario M3J 1P3, Canada
E-mail: mareklaskowski@gmail.com, moghadas@yorku.ca

The discovery of glycoconjugate vaccines has had a significant impact on reducing the health burden of several infectious diseases, including *Haemophilus influenzae* serotype b. However, the use of such vaccines against a single or several serotypes of some pathogens has been a concern for serotype replacement. Previous studies have demonstrated this replacement phenomenon with limited evidence. However, the possible mechanisms of serotype replacement in the context of vaccination are not well understood. Here, we propose a modelling framework, which integrates the two scales of in-host and between-host infection dynamics to investigate the pathogen-host characteristics that are essential for serotype replacement. We integrate a stochastic model of pathogen dynamics in-host with an agent-based model of disease transmission between-hosts, which provides a novel approach for our investigation. We apply this multi-scale modelling framework to better understand the factors involved in serotype replacement of as a result of vaccination.

*This work was supported in part by NSERC and Mitacs (Canada).

1. Introduction

Glycoconjuate vaccines have proven as one of the most advanced strategy in prevention of several encapsulated bacteria, especially for the two members of the normal bacterial flora of the human nasopharynx, *Streptococcus pneumoniae* and *Haemophilus influenzae*. Prior to the extensive use of glycoconjuate vaccines, *Streptococcus pneumoniae* and *Haemophilus influenzae*, serotype b (Hib) were major contributors to the morbidity and mortality worldwide.[1,2,3,4] Following the introduction of the glycoconjugate vaccine in the late 1980s, the incidence of these diseases reduced by more than 90% in developed countries.[5,6,7]

The dramatic decline in disease incidence is largely attributed to the effect of herd immunity generated by vaccination.[8,9] However, the preceding decade has witnessed the emergence of different serotypes of Streptococcus pneumoniae and Haemophilus influenzae, raising the concern about serotype replacement as a result of vaccination. Both Streptococcus pneumoniae and Haemophilus influenzae have different serotypes, which are diverse depending on their polysaccharide capsules. Haemophilus influenzae has six capsular types (serotypes a-f) and unencapsulated (non-typeable), while Streptococcus pneumoniae is characterized with 90 serotypes, many of which are pathogenic in humans. Due to the weak cross-protection among different serotypes, it has been suggested that the reduction of incidence for vaccine-preventable serotypes may have led to an ecological niche filled by other serotypes for which no vaccine is available.[10]

The comprehensive studies on serotype replacement initiated for pneumococcal population after a seven-valent pneumococcal conjugate vaccine (PCV7) was introduced and widely used in many countries.[1,11] This vaccine contains antigens that trigger immune protection against seven pneumococcal serotypes. The PCV7 has demonstrated 95% efficacy against invasive disease caused by these serotypes, but no evidence of decrease in the prevalence of other serotypes.[12,13] In fact, different serotypes have emerged as the dominant serotypes after the introduction of PCV7.[14] Moreover, in several clinical data collected from other pneumococcal conjugate vaccine clinical trials, serotype replacements were observed.[10,15] In contrast, serotype replacement has not been widely detected since the introduction of Hib conjugate vaccine. However, recent studies indicate that the increase in the incidence rates of Haemophilus influenzae serotype a (Hia) in several parts of the world could be a explained by the serotype replacement.[5,16,17,18,19] The evidence presented in these studies suggest that the serotype replacement

has occurred after the introduction of conjugate vaccine for Hib; however, the causes of this phenomenon are poorly understood.

Due to the limitation of biological approaches, mathematical and computational models are essential to elucidate the underlying mechanisms of serotype replacement.[23,24,25,26] In this paper, we propose a computational modelling framework that combines the dynamics of infection processes at the individual level with disease spread at the population level. Using this framework, we investigate the possible reasons of serotype replacement in the presence of vaccination.

2. Modelling Framework

To investigate the competitive interference between pathogen serotypes, we developed a square lattice agent-based model (ABM) for the transmission dynamics of a multi-strain disease in an in-silico population. The basic structure of the ABM includes three main compartments,[20] referred to as disease states in this study: susceptible; infected; and recovered or immune. We further considered two sub-states of disease associated with infection caused by each pathogen serotype. Our main assumption is that immunity conferred through natural infection or vaccination against one serotype does not provide any cross-protection against infection with the other serotype. The model includes both natural and disease-induced deaths as demographic variables. All deaths were replaced by newborns into the susceptible state, maintaining a constant population size. Increased yearly probability of natural death was calculated from its associated distribution with the median life expectancy of 60 years.

At the population level, there are two basic entities in this model:[21,22] (i) agents that represent individuals living in the simulated population; and (ii) the environment that represents the place in which individuals are situated and interact. The interaction of agents is determined by modular behavioural components, each containing state information relative to that behaviour. For example, each agent's disease component maintains the state of disease specific to that agent. It also maintains a list of contacts by virtue of being co-located with another agent at a particular position and at a particular time step in the environment. Disease may spread from infected to susceptible agents that are located at the same position on a particular time step according to the disease state component. We excluded simultaneous infection with both serotypes of the pathogen in a single agent.

For the dynamics of infection at the individual level, we implemented a logistic growth for each serotype of the pathogen in infected individuals. Following exposure to the disease (if infection occurs), the pathogen can replicate and grow to reach a carrying capacity (K) defined as the characteristic of the host environment. The equation governing the pathogen growth is

$$B_i'(t) = \gamma_i B_i(t) \left(1 - \frac{B_i(t)}{K}\right), \quad i = 1, 2 \tag{1}$$

where B_i is the population size of the serotype i at time t, γ_i is the growth rate of the serotype i, and K is the maximum amount of pathogen replicating in the host environment. The time-dependent transmission rate β_i of infection with serotype i is defined by

$$\beta_i = b_i \frac{B_i(t)}{K}, \tag{2}$$

where b_i is the baseline transmission rate when the serotype i is at its carrying capacity. The infection will trigger the development of the serotype-specific immune responses, which leads to the control of infection over time. The immune response will develop with some delay following exposure to the pathogen (due to the ensuing processes of antigen presentation, cell activation and proliferation, and antibody production). The growth of immune response and its effect (in terms of eliminating bacteria from the host environment) are proportional to the amount of replicating pathogen serotypes.

For disease spread between each susceptible-infected pair of agents, we considered the serotype-specific transmission probability:

$$P_i = 1 - \left(1 - \prod_{N_i} (1 - \sigma_i)\beta_i\right) \tag{3}$$

where N_i is the number of contacts infectious with serotype i, β_i is the transmissibility of the infectious contact with serotype i, and σ_i is the immune protection level conferred by natural infection or vaccination against serotype i. In our model, the simplified assumption of full or no protection for individuals means that either $\sigma_i = 0$ or $\sigma_i = 1$. Disease transmission was implemented as independent Bernoulli trials to select the infecting serotype. When the sampling suggested the possibility of infection with both serotypes, the serotype with larger $P_i N_i$ was selected for transmission.

After recovery from infection with one serotype, individuals are fully protected against re-infection with the same serotype for a certain period

of time. We assumed that, with decline of immunity, this protection period elapses and individuals become fully susceptible again to the infection with that serotype.

Vaccination against only one serotype was implemented in the model with the same protection period as natural infection. We investigated the dynamics of infection spread by both serotypes in the population in the presence and absence of vaccination. Individuals were randomly selected to be vaccinated with a daily probability of vaccination.

3. Model Implementation

We computationally implemented the model to investigate the effect of vaccination on serotype replacement. The model was initialized with a constant population size of 100489 agents. The parameter values used for the simulations are provided in Table 1. These parameters are chosen only for the purpose of illustration in this study, and they may not correspond to any biological setting.

Table 1. Description of parameters and their values (ranges) used in model simulations.

Parameters	Description	Value/Range
K	pathogen carrying capacity	10^8 bacteria
b_1	baseline transmissibility of serotype B_1	0.00172
b_2	baseline transmissibility of serotype B_2	0.00164
B_0	initial pathogen load at the time of exposure	500 – 5000 bacteria
γ	serotype-specific reproduction rate	0.08 hr^{-1}
η	immune response reproduction rate	1.01–1.03 hr^{-1}
T	activation of immune response following exposure	24–48 hr
θ_f	period of full protection	varied in years
p_v	daily probability of vaccination	4.4×10^{-3}
δ_v	proportion of the target age group vaccinated	0.8
d	probability of death due to infection	8.3×10^{-5}

With baseline transmissibilities of $b_1 = 0.00172$ and $b_2 = 0.00164$, we obtained the reproduction numbers $R_0^{(1)} = 1.73$ and $R_0^{(2)} = 1.69$ for the corresponding serotypes. When transmission occurred, the initial amount of pathogen serotype was sampled from uniform distribution in the range 500–5000. We considered two scenarios for the start of vaccination at the onset of simulations and two years into epidemic after the start of simulations. For each scenario, we simulated the model when the period of full protection after natural infection or vaccination was 2–4 years and 4–8

years. This protection period was randomly selected for each individual from the simulated range in each scenario. In our simulations, we considered a maximum age for vaccination, as indicated by epicurves in Figures 1–4.

4. Results

With parameter values given in Table 1, model simulations were seeded with a single initial infectious case for each pathogen serotype. Time profiles of infection for each serotype were obtained by averaging 1000 independent realizations. Figure 1 shows the fraction of population infected with different serotypes for 10 years after the onset of epidemic. In the absence of vaccination (thick black curves), serotype 1 dominates due to its initial higher reproduction number (Figure 1(A)). As infection spread through the population, herd immunity increases and therefore epicurves of both pathogen serotypes decline after reaching their maximum. When vaccination against serotype 1 starts at the onset of epidemic, the spread of infection is dramatically reduced compared to the scenario with no vaccination. We observed that when only individuals with 0–5 years of age are vaccinated, a second infection curve (thick gray curve) appears about 6 years after the start of epidemic. This is explained by the fact that the vaccine-induced protection has a short duration of 2–4 years (randomly sampled for each vaccinated individual), which leads to an increase in the pool of susceptible population once the vaccine protection has waned. We did not observe this second infection curve for serotype 1 within the first 10 years of simulations when a larger fraction of population is vaccinated (thin black and gray curves). Interestingly, infection curves of serotype 2 in the presence of vaccination for serotype 1 increase above the corresponding infection curve in the absence of vaccination (Figure 1(B)). This illustrates an improved competitive advantage for serotype 2 in the presence of vaccination for serotype 1, and may explain the phenomenon of serotype replacement observed in the epidemiological contexts of some multi-serotype pathogens. However, the effect of increasing the size of population vaccinated against serotype 1 on enhancing the competitive advantage of serotype 2 remains unclear.

We further simulated the model for the scenarios in which vaccination starts 2 years after the onset of epidemic (Figure 2). Similar results were observed for curtailing the serotype 1 infection through vaccination (Figure 2(A)). We also observed an increase in the spread of infection by serotype 2 that occurs with some delay following the start of vaccination (Figure 2(B)).

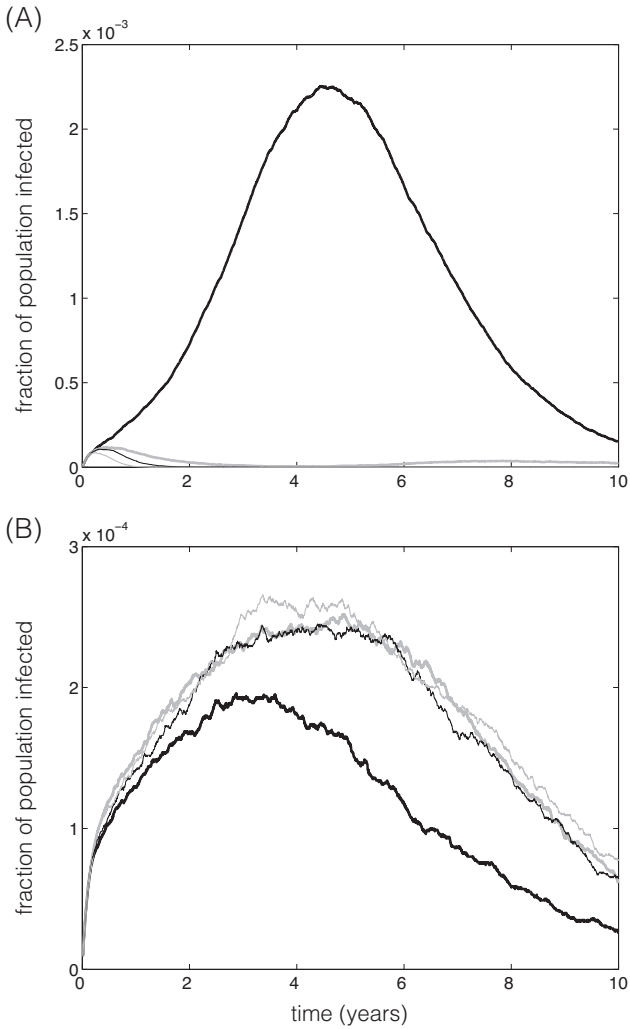

Figure 1. Fraction of the population infected with serotype 1 (A) and serotype 2 (B) of the pathogen. Thick black, thick gray, thin black, and thin gray curves correspond to epicurves without vaccination, vaccination for the 0–5 years individuals, vaccination for the 0–10 years individuals, and vaccination for the 0–20 years individuals, respectively. Vaccination starts at the onset of epidemic, and the duration of immunity following recovery from natural infection or vaccination is 2–4 years.

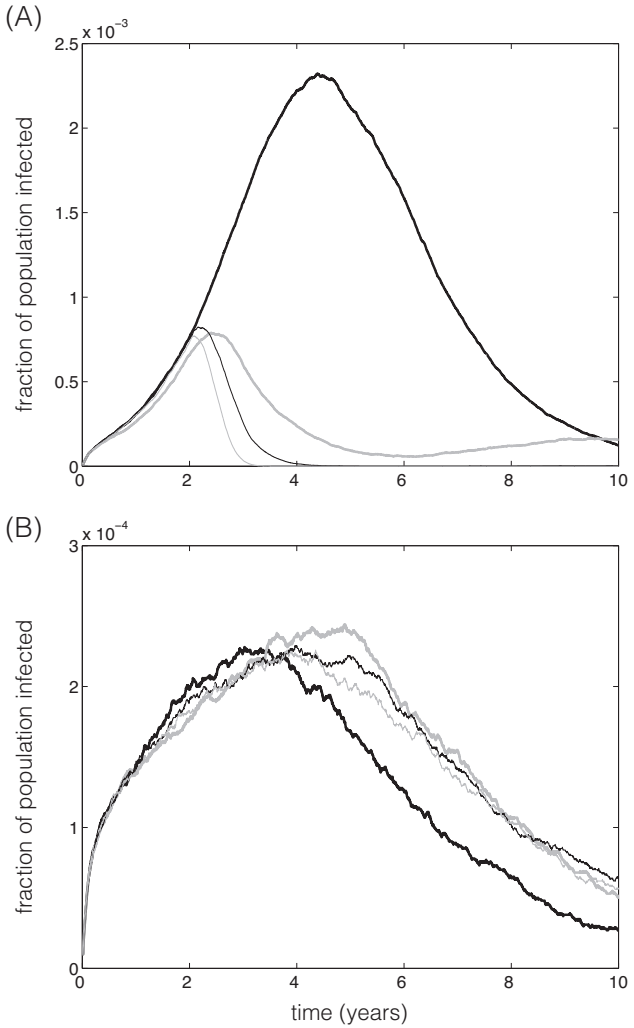

Figure 2. Fraction of the population infected with serotype 1 (A) and serotype 2 (B) of the pathogen. Thick black, thick gray, thin black, and thin gray curves correspond to epicurves without vaccination, vaccination for the 0–5 years individuals, vaccination for the 0–10 years individuals, and vaccination for the 0–20 years individuals, respectively. Vaccination starts 2 years after the onset of epidemic, and the duration of immunity following recovery from natural infection or vaccination is 2–4 years.

These results remain qualitatively intact when the duration of vaccine-induced protection is in the range 4–8 years (Figures 3 and 4). With a longer duration of vaccine-induced protection, a second infection curve of serotype 1 is also prevented within the first 10 years. These findings suggest that vaccination can play a significant role in the infection dynamics of competing serotypes of a pathogen in the population.

5. Concluding Remarks

In this study, we developed a general framework linking the infection dynamics within host to the spread of disease between hosts. We explored several scenarios for the competitive interference between two serotypes of a pathogen without any cross-protection between these serotypes due to natural infection or vaccination. Expectedly, in the absence of vaccination, we observed that the serotype with a higher reproduction number dominates. However, vaccination can overturn this transmissibility advantage, and encourage the serotype with the lower reproduction number to spread in a larger magnitude compared to the scenario without vaccination. This is often referred to as the serotype replacement, where the suppression of one serotype leads to the growth of another serotype in terms of the magnitude of its spread.

While the framework developed here can be used to explore the mechanisms underlying serotype replacement, it has several limitations. We considered a period of full protection following vaccination or recovery from natural infection. Once this period has elapsed, the individuals become fully susceptible again. This approach overlooks the gradual decline of immune response, and therefore the model does not include the possibility of partial protection with reduced susceptibility to infection. We also used a simplifying assumption to exclude the possibility of co-infection with both serotypes in a single host. Realistically, different serotypes may compete for available resources in the host environment to enhance their fitness and growth. In this context, vaccination may play a significant role in the dynamics of such competition. Finally, we modelled the immune response in a basic way, omitting the complexity of adaptive immune response development. These considerations merit further investigation.

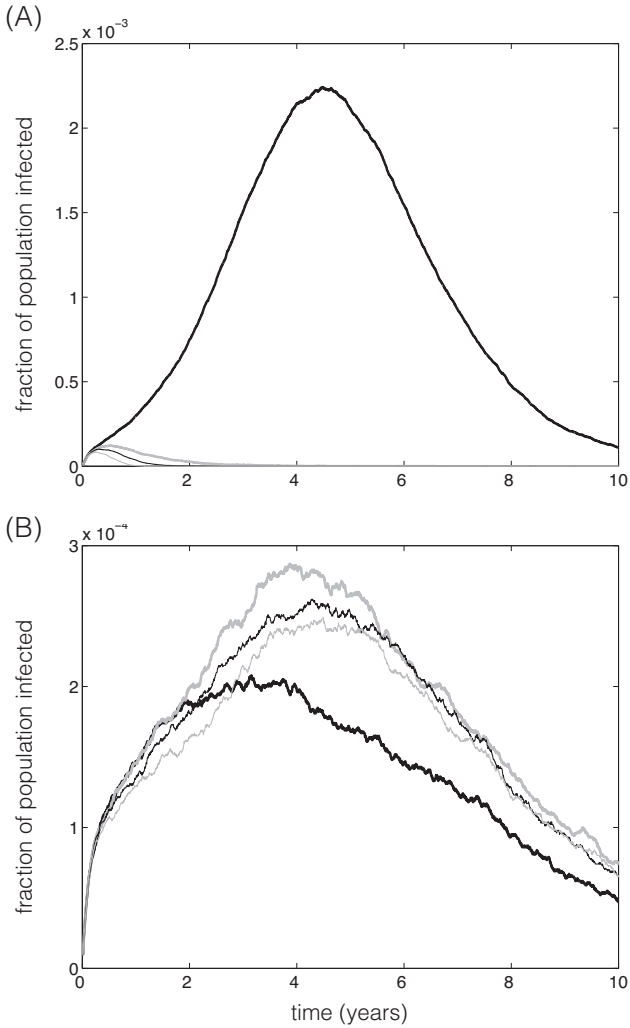

Figure 3. Fraction of the population infected with serotype 1 (A) and serotype 2 (B) of the pathogen. Thick black, thick gray, thin black, and thin gray curves correspond to epicurves without vaccination, vaccination for the 0–5 years individuals, vaccination for the 0–10 years individuals, and vaccination for the 0–20 years individuals, respectively. Vaccination starts at the onset of epidemic, and the duration of immunity following recovery from natural infection or vaccination is 4–8 years.

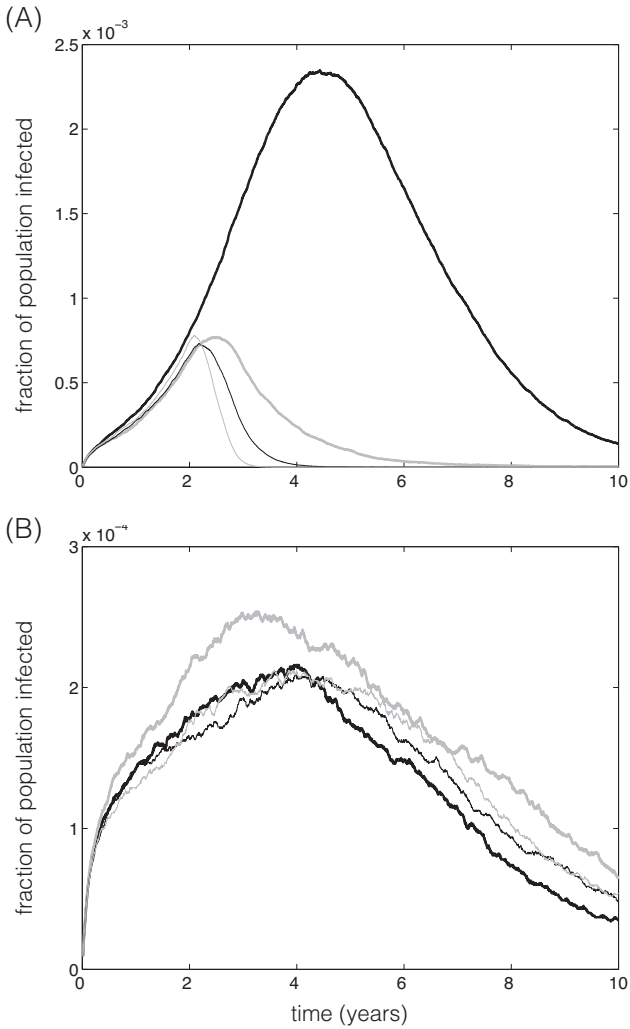

Figure 4. Fraction of the population infected with serotype 1 (A) and serotype 2 (B) of the pathogen. Thick black, thick gray, thin black, and thin gray curves correspond to epicurves without vaccination, vaccination for the 0–5 years individuals, vaccination for the 0–10 years individuals, and vaccination for the 0–20 years individuals, respectively. Vaccination starts 2 years after the onset of epidemic, and the duration of immunity following recovery from natural infection or vaccination is 4–8 years.

References

1. M. R. Griffin, Y. Zhu, M. R. Moore, C. G. Whitney and C. G. Grijalva, *New Engl. J. Med.* **369**(2), 155–163 (2013).
2. R. S. Tsang, M. G. Bruce, M. Lem, L. Barreto and M. Ulanova, *Epidemiol. Infect.* **142**(7), 1344–1354 (2014).
3. J. Oikawa, N. Ishiwada, Y. Takahashi, H. Hishiki, K. Nagasawa, S. Takahashi, M. Watanabe, B. Chang and Y. Kohno, *J. Infect. Chemother.* **20**(2), 146–149 (2014).
4. S. Davis, D. Feikin and H. L. Johnson, *BMC Public Health* **13**(Suppl 3), S21 (2013).
5. M. Ulanova and R. S. Tsang, *Lancet Infect. Dis.* **14**(1), 70–82 (2014).
6. S. F. Hale, L. Camaione and B. M. Lomaestro, *Ann. Pharmacother.* **48**(3), 404–411 (2014).
7. M. C. Pirez, G. Algorta, F. Chamorro, C. Romero, A. Varela, A. Cedres, G. Giachetto and A. Montano, *Pediatr. Infect. Dis. J.* **33**(7), 753–759 (2014).
8. P. O. Lang and R. Aspinall, *Expert Rev. Vaccines* **11**(2), 167–176 (2012).
9. P. A. Kristiansen, F. Diomandé, A. K. Ba, I. Sanou, A. S. Ouédraogo, R. Ouédraogo, L. Sangaré, D. Kandolo, F. Aké, I. M. Saga, T. A. Clark, L. Misegades, S. W. Martin, J. D. Thomas, S. R. Tiendrebeogo, M. Hassan-King, M. H. Djingarey, N. E. Messonnier, M. P. Préziosi, F. M. Laforce, D. A. Caugant, *Clin. Infect. Dis.* **56**(3), 354–363 (2013).
10. D. M. Weinberger, R. Malley and M. Lipsitch, *Lancet* **378**(9807), 1962–1973 (2011).
11. E. Koshy, J. Murray, A. Bottle, M. Sharland and S. Saxena, *Thorax* **65**(9), 770–774 (2010).
12. N. J. Croucher, J. A. Finkelstein, S. I. Pelton, P. K. Mitchell, G. M. Lee, J. Parkhill, S. D. Bentley, W. P. Hanage and M. Lipsitch, *Nat. Genet.* **45**(6), 656–663 (2013).
13. B. Pichon, S. N. Ladhani, M. P. Slack, A. Segonds-Pichon, N. J. Andrews, P. A. Waight, E. Miller and R. George, *J. Clin. Microbiol.* **51**(3), 820–827 (3013).
14. E. Chacon-Cruz, Y. Velazco-Mendez, S. Navarro-Alvarez, R. M. Rivas-Landeros, M. L. Volker and G. Lopez-Espinoza, *J. Infect. Dev. Ctries.* **6**(6), 516-520 (2012).
15. W. P. Hanage, *J. Infect. Dis.* **196**(9), 1282–1284 (2007).
16. G. S. Ribeiro, J. B. Lima, J. N. Reis, E. L. Gouveia, S. M. Cordeiro, T. S. Lobo, R. M. Pinheiro, C. T. Ribeiro, A. B. Neves, K. Salgado, H. R. Silva, M. G. Reis and A. I. Ko, *Vaccine* **25**(22), 4420–4428 (2007).
17. Z. Jin, S. Romero-Steiner, G. M. Carlone, J. B. Robbins and R. Schneerson, *Infect. Immun.* **75**(6), 2650–2654 (2007).
18. M. Ulanova and R. S. Tsang, *MEEGID* **9**(4), 594–605 (2009).
19. A. McConnell, B. Tan, D. Scheifele, S. Halperin, W. Vaudry, B. Law and J. Embree, *Pediatr. Infect. Dis. J.* **26**(11), 1025–1031 (2007).
20. A. L. Espindola, A. Souto Martinez and S. M. Moghadas, *BIOMAT Proc.* 374–388 (2014).

21. L. C. MostacoGuidolin, N. J. Pizzi, A. B. Demko and S. M. Moghadas, *Biomedical Engineering, Trends, Researches and Technologies*, InTech, Chapter 33, 641–664 (2011).
22. M. Laskowski M and S. M. Moghadas, *BIOMAT Proc.* 318–339 (2014).
23. C. Bottomley, A. Roca, P. C. Hill, B. Greenwood and V. Isham, *J R Soc Interface* **10**, 20130786 (2013).
24. M. Lipsitch, *Emerg Infect Dis.* **5**, 336–345 (1999).
25. Y. H. Choi, M. Jit, S. Flasche, N. Gay and E. Miller, *PLoS ONE* **7**, e39927 (2012).
26. M. Lipsitch, *Proc. Natl. Acad. Sci. USA* **94**, 6571–6576 (1997).

AN INTEGRATIVE APPROACH FOR MODEL DRIVEN COMPUTATION OF TREATMENTS IN REPRODUCTIVE MEDICINE

R. EHRIG, T. DIERKES, S. SCHÄFER, S. RÖBLITZ

Zuse Institute Berlin,
Takustrasse 7, 14195 Berlin, Germany
E-mail: ehrig@zib.de

E. TRONCI, T. MANCINI, I. SALVO, V. ALIMGUZHIN, F. MARI, I. MELATTI, A. MASSINI

Computer Science Department Sapienza University of Rome

T.H.C. KRÜGER

Dpt. of Psychiatry, Social Psychiatry and Psychotherapy Hannover Medical School

M. EGLI, F. ILLE

CC Aerospace Biomedical Science & Tech. Luzern Univ. of Appl. Sciences & Arts

B. LEENERS

Division of Reproductive Endocrinology University Hospital Zurich

We present an overview of the current status of the European collaborative project PAEON. The challenge of PAEON is to provide specialists in reproductive medicine with a computerised model of the menstrual cycle under normal and various pathological conditions, which will allow them to get further insight in fertility dynamics. This model also enables the simulation of treatment protocols, which were used within in vitro fertilization. By the definition of virtual patients through biologically admissible parametrizations our approach allows not only the evaluation of a given treatment strategy *in silico*, but also the design and optimization of such protocols. Once a protocol is formalized in the virtual hospital, the success can be controlled by a treatment execution monitor, which works then as a clinical decision support system. All these tools will be combined in a virtual hospital environment, enabling the access to the PAEON services through the web.

1. Introduction

For many couples, having children is one of the major life aims. Failure is associated with guilt, inadequacy and loss of the sense of life, bearing an increased risk for negative psycho-social functioning, such as depression and anxiety disorders[11,8,9]. Furthermore, changes in population demographics, greater focus on education and careers among women have resulted in great numbers of women attempting pregnancy at older ages when they are inherently less biologically fertile. In Europe, for example, infertility affects 10% to 15% of couples of reproductive age, and experts assume that these figures will double in a decade[13,5].

Investigation and treatment of infertility is directly and indirectly (by time consuming medical consultations, expensive medical techniques, limited success rates leading to repetitive treatment attempts, time-off from work, etc.) associated with high expenses for the individual as well as for the society. Indeed, costs for individual couples in Europe are around 10% of annual household expenditures[3]. Overall, infertility in Europe costs approximately 1 billion Euros per year.

In about 50% of the cases, infertility is caused by female health problems, more than 40% of which are related to endocrinologcal diseases. Human fertility is based on physiological events like adequate follicle maturation, ovulation, ovum fertilisation, corpus luteum formation as well as endometrial implantation, proceeding in a chronological order. Diseases such as endometriosis, Prolactin (PRL) associated disorders or Polycystic Ovary Syndrome (PCOS) seriously disturb menstrual cycle patterns, oocyte maturation and consequently fertility; pelvic endometriosis, occurring in up to 40% of infertile women, is a hormone dependent disease characterised by ectopic proliferation of endometrial cells, which occurs nearly exclusively during the reproductive phase.

Beside endocrine diseases, several environmental and lifestyle factors have a negative impact on fertility: up to 13% of female infertility may relate to smoking. Obesity, which increases not only in European countries, is associated with menstrual dysfunction, decreased fertility, as well as increased risks of miscarriage.

Modern Assisted Reproductive Techniques (ART), like In Vitro Fertilisation (IVF) or Intracytoplasmatic Sperm Injection (ICSI), have nowadays dramatically increased the chances for successful reproduction. Nevertheless, current success rates reach only 35% even in leading clinical centers. Many of the pathophysiological effects of endocrine diseases and environ-

mental/lifestyle factors on fertility as well as dynamics in fertility treatment still remain unclear. Thus, a better understanding of the endocrinological concert orchestrating the physiology of fertility would open new opportunities for therapeutic options for improved natural fertility as well as success rates in ART.

We address this problem by using a systems biology approach that aims at integrating clinical data collection with mathematical modeling of the complex biological system. Although the relevant components and feedback mechanisms have been identified from experiments and have been described qualitatively for many years, dynamic (time-dependent) mathematical models, i.e. models that permit medically sound *quantitative predictions* for the periodic changes in hormone levels and follicular function have started to be developed only a few years ago. In fact, even though half of the world's population is female, the female menstrual cycle has so far received comparably little attention in systems biology.

For these reasons, since 2013 the European Commission has been funded the collaborative research project PAEON-"Model Driven Computation of Treatments for Infertility Related Endocrinological Diseases" within the EU VPH (Virtual Physiological Human) initative. The project consortium consists of the Sapienza University of Rome, the Lucerne University of Applied Sciences and Art, the Hannover Medical School, the University Hospital Zurich, and the Zuse Institute Berlin.

The PAEON project rests on three main components, whose objectives may be summarised as follows.

(1) *Define a mathematical model of the human menstrual cycle which is able to simulate the healthy cycle as well as infertility-related endocrine disorders. This model should also enable individualized, patient specific models.*
Existing models of the human menstrual cycle were usually constructed for very specific purposes, e.g. GynCycle[10] for simulating GnRH analogue treatment, models for analysing prolactin patterns[4] or the follicular development[2]. None of these models is able to simulate whole cycles in which pathological hormone concentrations go along with insufficient follicular development. Our goal is to enrich and combine these models with components and mechanisms involved in endocrine disorders like PCOS or endometriosis, also taking into account external factors (e.g. drugs) as well as environmental factors. Furthermore, the models should allow also the re-

alistic simulation of individualised treatment strategies (protocols).

(2) *Develop a Virtual Hospital (VH) combining mathematical models of the treatment and the individual patient.*
The availability of a mathematical model of both the individual patient and the medical treatment allows an innovative perspective based on a system control engineering approach, if one regards the system composed of the treatment and the patient as a feedback-loop control system, where the physician acts as a feedback-loop controller for the patient. This view enables us to use powerful control engineering and computer science methods for its analysis. A medical treatment protocol generally asks to take certain measurements on the patient and, depending on their outcome, suggests certain actions. Actions consist of, e.g., taking further measurements or administering specific amounts of certain drugs. We regard a medical treatment as a computer procedure that, observing patient measurements, strives to steer them towards optimal values for the number and size of mature follicles at the end of the treatment.

(3) *Perform measurements or collect data from available databases to permit validation and refinement of currently available models.*
The presently available models are based on small study samples and include only a part of the parameters relevant for the regulation of the human menstrual cycle. Therefore they need validation with larger samples not only from normally cycling women but also hormonal secretion patterns from patients suffering from endocrinological diseases such as endrometriosis, PRL-associated disorders, or PCOS. Even though this is a tedious and expensive part of our project we will focus here only on the first two main parts of PAEON.

2. Models of the Hormonal Cycle and Treatment Protocols

2.1. *Models of the healthy female hormonal cycle*

In order to construct a physiological model, species or components (e.g. hormones, follicular properties) and mechanisms (inhibition, stimulation, chemical reactions) that are essential for the regulation of the menstrual cycle have to be determined. Within the hormonal cycle, the most important compartments are the hypothalamus, the pituitary gland, and the ovaries, connected by the bloodstream. They are generally referred to as the Hypothalamic-Pituitary-Ovarian (HPO) axis. During the reproductive

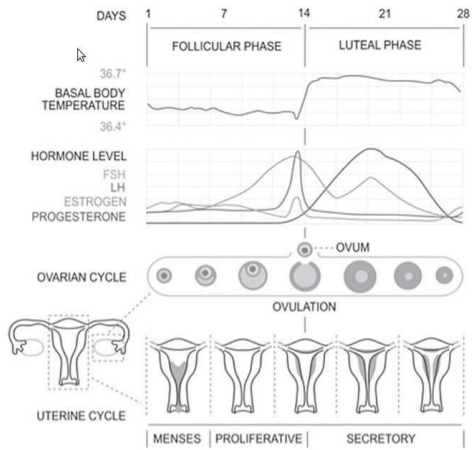

Figure 1. Schematic sketch of the female hormonal cycle.

cycle, hormones of the HPO-axis fluctuate periodically, leading to the formation of cycles with a period of typically 28 days (Figure 1).

A model of the hormonal cycle has to deliver a qualitative description of the following regulatory circuits. In the hypothalamus, the hormone GnRH (gonadotropin-releasing hormone) is formed, which reaches the pituitary gland through a portal system in pulses and stimulates the release of the gonadotropins luteinising hormone (LH) and follicle stimulation hormone (FSH) into the bloodstream. The gonadotropins regulate the multi-stage maturation process of follicles in the ovaries (follicular phase). The number of follicles that mature is dependent on the amount of FSH available to the gonad and the sensitivity of the follicles to the gonadotropins. During that phase, the maturing follicles secrete mainly estradiol (E2) and inhibin B. If gonadotropin stimulation is adequate, one of the several follicle units will advance to ovulation. Any disequilibrium in the amount and timing of involved hormones may result in reduced oocyte quality unsuitable for fertilisation. During the following luteal phase the corpus luteum secrets mainly progesterone but also E2 and inhibin A. Through the blood, these hormones reach the hypothalamus and pituitary gland, where they again influence the formation of GnRH, LH, and FSH. The cycle starts anew with the menstrual bleeding initiated by the decreased progesterone secretion from the corpus luteum.

Once the medical and biological mechanisms have been formulated in

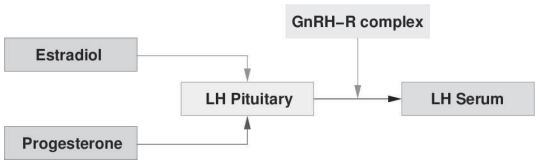

$$\mathrm{Syn}_{\mathrm{LH}}(t) = (b_{\mathrm{Syn}_{\mathrm{LH}}} + m_{\mathrm{E2}} \cdot H^{+}(\mathrm{E2}, T_{\mathrm{E2}}, n_{\mathrm{E2}})) \cdot H^{-}(\mathrm{P4}, T_{\mathrm{P4}}, n_{\mathrm{P4}})$$

$$\mathrm{Rel}_{\mathrm{LH}}(t) = (b_{\mathrm{Rel}_{\mathrm{LH}}} + m_{\mathrm{GnRH\text{-}R}} \cdot H^{+}(\mathrm{GnRH\text{-}R}, T_{\mathrm{GnRH\text{-}R}}, n_{\mathrm{GnRH\text{-}R}})) \cdot \mathrm{LH}_{\mathrm{Pit}}(t)$$

$$\frac{d}{dt}\mathrm{LH}_{\mathrm{Pit}}(t) = \mathrm{Syn}_{\mathrm{LH}}(t) - \mathrm{Rel}_{\mathrm{LH}}(t)$$

$$\frac{d}{dt}\mathrm{LH}_{\mathrm{blood}}(t) = \frac{1}{V_{\mathrm{blood}}}\mathrm{Rel}_{\mathrm{LH}}(t) - k_{\mathrm{on}} \cdot \mathrm{LH}_{\mathrm{blood}} \cdot R_{\mathrm{LH}} - c \cdot \mathrm{LH}_{\mathrm{blood}}$$

Figure 2. LH model and the corresponding ODEs. H^{+} and H^{-} are stimulating and inhibitory Hill functions with thresholds T and exponents n. LH production in the pituitary is stimulated by E2 and inhibited by Progesterone (P4). The release of LH into the blood is stimulated by the GnRH-receptor complex, if its concentration is higher than some threshold.

a qualitative manner, the next step is to translate them into quantitative mathematical equations. Since we are mainly interested in the answer of a given system (the human menstrual cycle) to disturbances (e.g. treatments), this can only be modelled by time-dependent equations, e.g. ordinary differential equations (ODEs) or differential-algebraic equations. To formulate the differential equations of a quantitative mathematical model, the physiological and biological processes that occur must be known very accurately. However, the exact chemical reaction mechanisms are often not understood in sufficient detail; often one only knows whether certain hormones have a stimulating or inhibiting effect on other hormones. In semi-quantitative modelling of such switch behaviour, Hill functions are used. If the reaction mechanisms are known more specifically, for example from data bases, more detailed equations can be formulated. Figure 2 illustrates this approach for the LH submodel and the corresponding ODEs. If all processes are included, one obtains a usually "large" system of differential equations. The qualitative dependencies of our model are visualised in Figure 3.

Hence, an initial value problem (IVP) can be formulated, where the change in the species y depends both on the species themselves and on a parameter vector p. Such autonomous (i.e. not explicitly time dependent) equations are usually used to describe closed systems, whereas non-autonomous (i.e. explicitly time dependent) equations will be used, for example, to model environmental factors or drug administrations that change

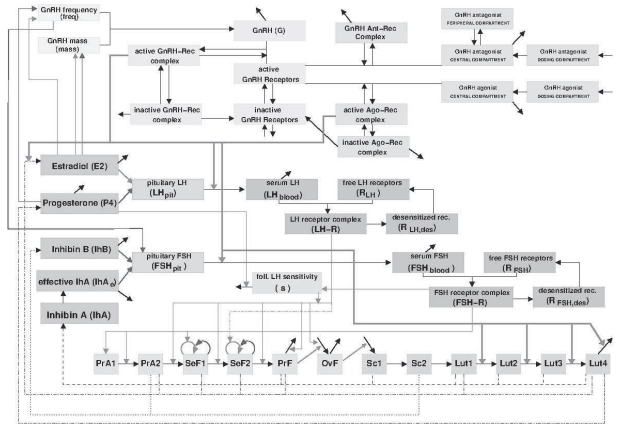

Figure 3. Flowchart of the GynCycle model for the human menstrual cycle with 33(+8) ODEs, 114 parameters.

with time. Moreover, it is assumed that some discrete experimental data (in form of species concentrations versus time) are available. Usually, only a certain amount of the species concentrations are measurable observables. The task at hand now is to quantify the unknown parameters and initial values by comparing model values with the measured data. A complete data set, of course, must also include statistical tolerances for each measurement. This task may be computationally solved by appropriate Newton algorithms (local search) or stochastic approaches (global search). As an example, Figure 4 depicts the results of parameter fitting to a set of experimental data from 12 normally cycling women for LH, FSH, P4, and E2.

2.2. *Treatment modelling*

Even if there exists a number of newer approaches (e.g. the antagonist protocol), there are two methodologies which, depending on the age and other conditions, are the most commonly used treatments. They consist of two phases, he suppression of FSH and LH by GnRH (downregulation, long protocol) or by P4 (preparation, short protocol), followed by a usually two weeks long stimulation phase with the combined administration of GnRH agonists, FSH, and LH. Within the second phase one tries to stimulate follicle growth in order to induce growth of a cohort between 5 and 15 follicles aiming to have as many ripe oocytes in one cycle as possible. The

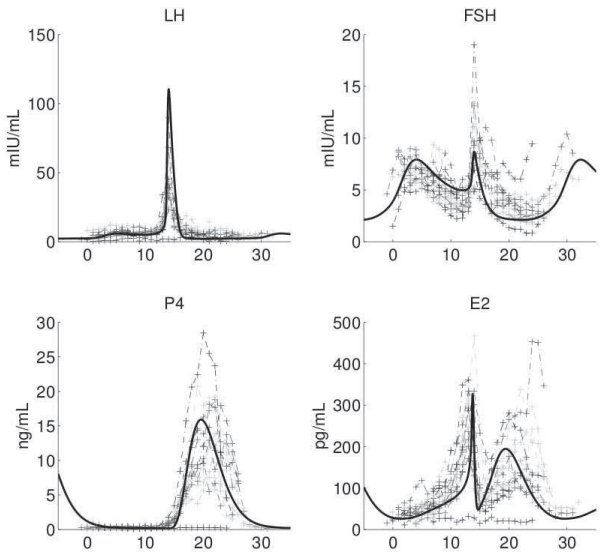

Figure 4. Results of parameter estimation for the GynCycle model to 12 normally cyling women.

actual follicle maturation is monitored by transvaginal ultrasound and E2 blood levels. Future follicle growth can be estimated from biological age, anti-Müllerian hormone (AMH) levels, FSH and the antral follicle count (AFC). Hormone doses for the stimulation treatment are based on this estimation. Too modest dosages of hormones are associated with the risk of an insufficient number of oocytes, too aggressive treatments, especially in patients with PCOS, are associated with a high risk of overstimulation syndrome and a reduced quality of obtained oocytes. If the result with respect to AFC and E2 levels are satisfactory, ovulation will be induced by one additional higher dose of LH.

In many cases, the drugs administered differ considerably from their natural counterpart in their chemical structure, metabolism, and activity. It is therefore more reasonable to construct a separate differential equation for the concentration $c(t)$ of each administered substance,

$$\frac{dc\,(t)}{dt} = \Phi\,(t) - c_L c\,(t)\,, \tag{1}$$

with a time dependent source term $\Phi(t)$ and a clearance term c_L. The solution of this equation may then be used in other equations where the drug and/or its natural counterpart has an effect.

In most cases, drug administration leads to plasma concentration profiles with a left-skewed peak. These time courses are usually described by some pharmacokinetic parameters. A commonly accepted approach is, e.g., to measure the peak plasma concentration $c_{\max}$, the time point $t_{\max}$ of this maximum, and the integral over the concentration-time curve, $AUC_{0-\infty}$ (area under the curve).

Within our model of the hormonal cycle we have successfully modelled such profiles based on the probability density function of the gamma distribution with fixed parameter $\alpha = 2$. This approach leads to the following differential equation for the drug concentration,

$$\frac{dc\,(t)}{dt} = D\beta^2 t \exp\left(-\beta t\right) - c_L c\,(t)\ , \tag{2}$$

where the parameter D represents the amount of the drug administered. The parameters β and c_L can easily be determined numerically on the basis of measured values $c_{\max}$, $t_{\max}$, and $AUC_{0-\infty}$. A similar approach is

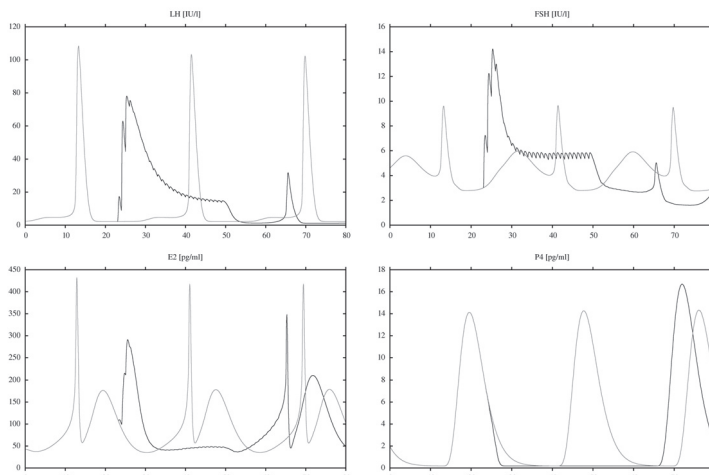

Figure 5. Results of a simulation of a whole long protocol for LH, FSH, E2, and P4 (black) compared with the normal hormonal cycle (gray). The downregulation with the GnRH agonist Triptoreline lasts 27 days (cycle days 23 until 50), the stimulation then lasts 14 days. The rise of E2 during stimulation indicates a successful treatment.

also possible in terms of other pharmacokinetic parameterizations, e.g. the volume of distribution, the clearance rate or half-life times[a]. With this methodology, we are able to use all different pharmacological data available in the literature[1], and to store them in a common data base for all drugs relevant in clinical practice. Figure 5 presents preliminary results for a simulation of the long protocol. In addition, our model enables not only the simulation of normal healthy cycles with and without treatments, but also the simulation of other limit cycles as they are typical for, e.g., PCOS.

2.3. *Patient-specific models*

Unfortunately, a fully automatic procedure that just computes values for the model parameters that fit the (few) available measurements (*parameter identification*) typically leads to species behaviours that, while being mathematically correct solutions to the ODE model, are meaningless from a biological point of view. Moreover, we have to take into account that the parameter value space is huge.

We overcome the above mentioned obstacles by splitting our computation into two phases: an *off-line* phase that narrows our search space, and an *on-line* phase that computes patient-specific predictions. The first phase produces an almost *complete* set of biologically sound parameter values, whereas the second phase selects the parameter value that minimises the mismatch between model predictions and patient measurements.

The overall architecture of our approach is depicted in Figure 6. Starting from a default parameter value λ_0 that results from our accepted standard model, the off-line procedure extracts from the parameter value space a complete set S of biologically sound parameter values. *Biological soundness* asks for S to contain *only* parameter values leading to biologically meaningful time evolutions for the species in the model. *Completeness* asks for S to include *all* parameter values leading to biologically meaningful behavior for the model. The on-line phase selects the parameter value in S that best fits with patient measurements, searching in the set of biologically sound parameters computed in the off-line phase.

Intuitively, we search for parameter values λ that lead to trajectories $x(\lambda, t, u)$, with u an external time-dependent input function, e.g. a treatment, that are both quantitatively and qualitatively similar to the trajec-

[a]Since GnRH is active only in the brain, the GnRH agonists blood levels are not responsible for the effects of the administration. We have, therefore, implemented a simple compartment model for GnRH.

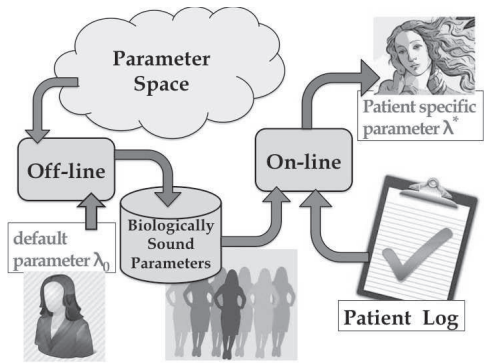

Figure 6. Architecture of the patient-specific parameter identification procedure.

tory $x(\lambda_0, t, u)$. We capture the fact that two trajectories are similar (i.e. they differ because of a "shift" and/or a "stretch") by introducing three measures of similarity. The *cross-correlation* $\rho_{\lambda_0,\lambda,i}$ measures qualitative aspects of the trajectories $x_i(\lambda_0, t, u)$ and $x_i(\lambda, t, u)$ (for example, if they have the same peaks) whereas the *average normalised differences* $\mu_{\lambda_0,\lambda,i}$ and the *normalised differences of autocorrelations* $\chi_{\lambda_0,\lambda,i}$ are two measures of the average distance between $x_i(\lambda_0, t, u)$ and $x_i(\lambda, t, u)$. Biological soundness of the parameter λ with respect to λ_0 requires that differences between $x_i(\lambda_0, t, u)$ and $x_i(\lambda, t, u)$ in terms of these three measures are below given thresholds. Our goal is to identify a set of biologically sound model parameter values that describes as many biologically meaningful behaviours as possible but, at the same time, is not too large in order to speed up our on-line computation. The first phase of our procedure finds (with high confidence) the set S of all *biologically sound* parameter values with respect to a default parameter λ_0. The set S is computed by checking parameter values in a finite subset $\hat{\Lambda}$ of Λ (*discretised parameter space*).

Since the number of parameters to be identified is quite large (75 in our case study) the discretised parameter space is huge (10^{75} if we consider 10 possible values for each parameter), thus making an exhaustive search in the discretised parameter space $\hat{\Lambda}$ unfeasible. To overcome such an obstruction, we followed an approach inspired by statistical model checking[7,6]. At the end, the set S contains *only* and (with arbitrarily high confidence) *all* biologically sound values for the patient-specific parameters. Note that such an algorithm does not depend on patient-specific data. Thus it must be run *off-line* once and for all, and its output (the set S) can be stored for

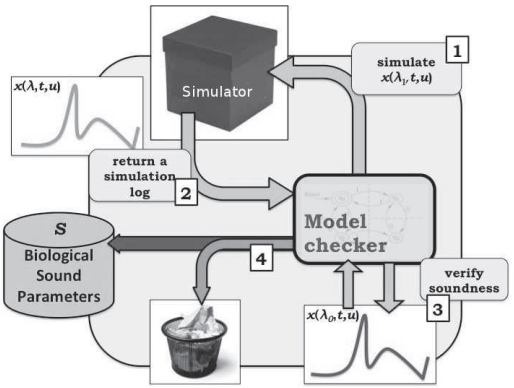

Figure 7. Architecture of *off-line* computation of biologically sound parameters.

further processing. The computation of an appropriately large set of biologically admissible (BA) parameters may need several days even on a cluster with many CPUs. Details of the approach can be found elsewhere[12]. The biologically admissible parametrizations may be interpreted also as *virtual patients*.

The architecture of our algorithm is depicted in Figure 7. A model checker randomly generates parameter values λ in the discretised parameter space $\hat{\Lambda}$ (point 1 in the picture). The simulator is called for a simulation of $x(\lambda, t, u)$ and returns a file containing a set of points of the trajectory $x(\lambda, t, u)$ (point 2). At this point, this trajectory is compared with the trajectory $x(\lambda_0, t, u)$ obtained by considering the default parameter λ_0 (point 3). If $x(\lambda, t, u)$ passes the biological soundness test, λ is added to the set S of biologically sound parameters, otherwise it is discarded (point 4).

The algorithm stops when N attemps fail to find a biologically sound parameter. Given two positive real numbers δ and ε, N is chosen in such a way that with confidence $1-\delta$ the probability of finding other biologically sound parameter values not in S is less than ε. The results in Figure 8 demonstrate the variability of the individual time courses. In this computation, the algorithm has found more than 7000 different BA parametrizations.

3. PAEON Virtual Hospital (VH)

One of the main goals of the PAEON project is to provide effective computational tools as Web-based services through a Web portal named Virtual Hospital (VH), in order to aid medical researchers and doctors in their

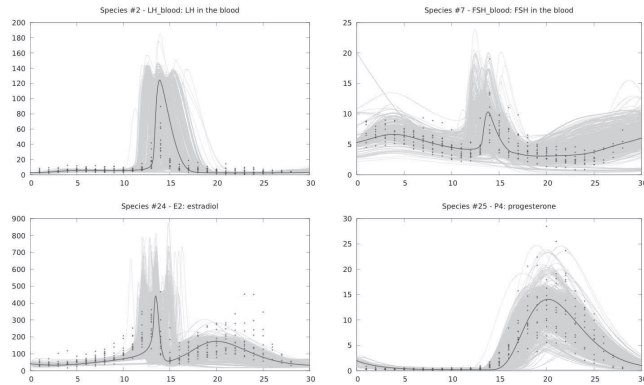

Figure 8. Results of the *off-line* computation of all biologically parametrizations for LH, FSH, E2, and P4 compared with 12 normal hormonal cycles.

everyday work. The PAEON VH Web-application will enable researchers, within and outside the PAEON project, to exploit results by providing services to: 1) upload/download models and results from clinical trials or from computations, 2) use the computational tools developed in the project. Furthermore, VH will support the iterative refinement approach of our project by acting as a coordination tool between the modelling activities, the computational tool development and the clinical trials.

VH will provide access and data security services compliant with clinical data and security policies along with a graphical user interface to seamlessly fit into hospital environments and thus clinicians needs. This in turn will allow the hospitals in our consortium to insert (anonymised) experimental data that, via the VH, are immediately available to the research partners working on modelling or model analysis tools. This guarantees constant alignment between the modelling/computation activities and the clinical trial activities. The VH Data Repository will provide a knowledge base for storing (generic) models, patient-specific models (digital patients), treatment protocol models (digital physicians), anonymised experimental results from the clinical trials, and experimental results from running PAEON computational tools on given clinical data. The overall PAEON VH software architecture is sketched in Figure 9.

Here, we will describe only some of the computational services, namely the Treatment Execution Monitor (TEM), the Model-Based Verification of Treatment Protocols (MBV-TP), and the Model-Based Design of Individ-

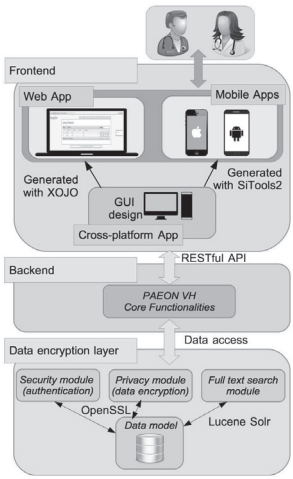

Figure 9. PAEON VH Software Architecture.

ualised Treatment Protocols (MBD-ITP).

3.1. *Treatment Execution Monitor*

Within TEM, protocol models keep track of the status of a *treatment protocol* for each patient under treatment, and suggest *actions* to clinicians. In a treatment protocol, typical actions are: when to administer a drug, the dose, and when to take next measurements. A clinical treatment protocol is a description of a complex activity that involves decisions during the treatment execution. In Figure 10 the overall structure of a treatment protocol is sketched.

The TEM is a tool designed to support clinicians during treatment protocols. It behaves as a Clinical Decision Support System (CDSS) that, on the basis of the modelled treatment protocol and the recorded treatment data (patient data, patient measurements), suggests actions (e.g., timing and amount of drug to be administered) to clinicians. TEM takes as input a formalised treatment model and provides as output what the protocol prescribes in a given situation. Physicians can follow the suggestions of TEM or override them. In any case, all decisions are recorded by TEM and possibly used during future treatments.

In order to model fertility treatments currently in use, we have designed and implemented the Vanilla Automata Language (VAL) language. After a

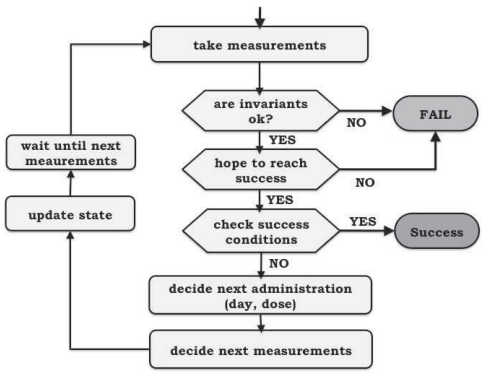

Figure 10. General structure of a treatment protocol.

careful analysis, carried out by computer scientists together with clinicians, the protocols currently in use at the University Hospital Zurich (UZH) were implemented in VAL. Instead of explaining the details of VAL, Figures 11 and 12 show a small section of the protocol as used at the UZH and the formalized counterpart.

The TEM GUI we have designed can already be used for training or educational purposes in reproductive medicine departments. Furthermore, other clinics could compare their own protocols with those of the UZH, one of the leading clinics in reproductive medicine in Europe. We are planning also to include the administration strategies of other European reproductive medicine centers with high success rates into TEM.

3.2. *Model-Based Verification of Treatment Protocols (MBV-TP)*

The MBV-TP computational service aims at evaluating, *in silico*, the effectiveness of a treatment protocol by executing treatment simulations. Simulations will be performed on a model that consists of a VPH model and a treatment model for (subsets of) all biologically admissible (BA) parameters.

Since treatment protocols are designed to work on all patients (or at least a class of patients), they adapt dosages and duration of drug administration to patient measurements. In this scenario, it is reasonable to address the problem of verifying that a given treatment protocol reaches its goal *for each* possible patient, or, more realistically, evaluating its suc-

4.5. **Mid-time measurement step**:

4.5.1. On day "End preparation day" + 3 or day "End preparation day" + 4 (no medical reason, just logistic reasons), measure E2 and P4 (lab requires 3 hours to provide values):

4.5.1.1. if $E2 \geq 250$ pmol/l and $P \geq 6$ nmol/l, then Halt the protocol.

4.5.2. Wait till the end of the day defined in Req. 4.5.1.

4.6. **Stimulation phase**:

4.6.1. We call the current day "Day 1 (of the stimulation phase)". "Day 1" is "End preparation day" + 4 or "End preparation day" + 5 (depending on the choice taken in Req. 4.5.1.). This day is always a Friday, given Req. 4.4.5.

4.6.2. The last day of the stimulation phase is the day when we induce ovulation. This day will be called "ovulation induction day" in the following. It will be a day between Day 8 and Day 13 (of the simulation phase).

4.6.3. From "day 1 of the stimulation phase" until the "ovulation induction day", administer D 0.1mg/day

4.6.4. From "stimulation drug administration start day" (as chosen as in Req. 4.3.) until the "ovulation induction day" (as defined as Req. 4.6.2.), administer the chosen stimulation drugs (as decided in Req. 4.2.3.) each day

4.6.5. On day 6 (of the stimulation phase), measure E2 and P4:

4.6.5.1. If $E2 < 500$, then change the doses for days 6 and 7 of the drug(s) (as chosen in Req. 4.2.3. and Req. 4.2.5.) into:

Figure 11. Part of a treatment protocol currently in use at UZH.

```
Trans
        s'= if (dayStim==0 & (e2Input > 250 | p4Input > 6)) then FAIL
            else if (dayStim == 5 & p4Input >= 40) then FAIL
            else if (dayStim > 8 & follicleCount(fpCurrent)<3) then FAIL
            else if (day == 0) then DOWNREGULATION
            else if (day == downLength) then STIMULATION
            else s;
        day'= day+1;
        dayStim'= if (day >= downLength) then (dayStim + 1) else dayStim;
        e2'= if (dayStim == 0 | dayStim == 5 | dayStim == 8)
            then e2Input else e2;
        p4'= if (needP4 & (dayStim == 0 | dayStim == 5 | dayStim == 8))
            then p4Input else p4;
        needP4'= if (dayStim == 5 & p4Input < 4) then false;
        doseStim'= if (dayStim == 0)
                then computeDoseStim(age,amh,afc)
                else if (dayStim == 5)
                    then changeDoseStim(age,amh,afc,e2Input,doseStim)
                    else doseStim;
        fpLast'= if (dayStim == 8 | dayStim == 11 | dayStim == 13)
            then fpCurrent
            else fpLast;
        fpCurrent'= if (dayStim == 8 | dayStim == 11 | dayStim == 13)
                then FollicleProfile
                    .fs9 = fs9Input, .fs10_11 = fs10_11Input,
                    .fs12_13 = fs12_13Input, .fs14_15 = fs14_15Input,
                    .fs16_17 = fs16_17Input, .fs18_19 = fs18_19Input,
                    .fs20 = fs20Input
                else fpCurrent;
```

Figure 12. Part of the protocol strategy used at UZH in formalized description.

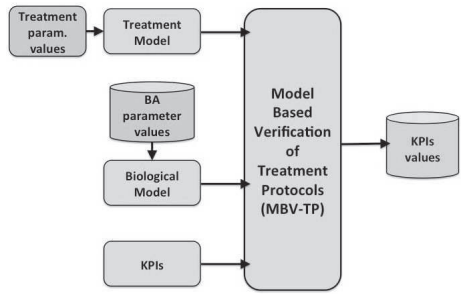

Figure 13. MBV-TP inputs and outputs.

cess rate. In our model based approach this means that, since treatment models adapt their behaviour to the biological model behaviour, treatment protocol verification consists of checking if the treatment reaches its goals *for a large number* of BA parameter values.

Treatment goals have been generalised using the notion of *Key Performance Indicators* (KPIs). A KPI provides a measure of the effectiveness of a treatment. This allows to evaluate treatments from different points of view, each of which is formalised as a KPI. In the context of fertility treatments considered in the PAEON project, the treatment model is an executable description of a fertility treatment currently in use in clinical practice. The biological model is a model of the menstrual cycle together with a pharmacokinetic model for drug administration, and the KPIs are related to, e.g. E2 levels, number and size of follicles, and the total amount of administered drugs.

MBV-TP takes the following inputs:

- a parametrised treatment protocol
- values for all treatment parameters, so that one obtains a specific treatment
- the set of BA parameters on which the treatment will be verified
- a set of KPIs associated to the treatment

and yields the following output:

- values for all the KPIs given as input, for each given BA VPH model parameter.

In Figure 13 the overall structure of MBV-TP is sektched. As an example, we can evaluate if the treatment under consideration ensures *safety*

conditions (in our context they are evaluated mainly by checking E2 levels, to check the risk of overstimulation), and the percentage of BA parameter values for which the treatment is successful.

In Figure 14. the right column shows the VPH model evolution under a sample BA model parameter (virtual patient) for which the treatment succeeds, achieving a full success condition (FSC). It can be observed that the E2 and P4 levels are always below their safety thresholds, and that the follicles gradually grow during stimulation (letting the treatment achieve FSC). The left column of Figure 14 shows another treatment success case, but in this case only a minimum success condition (MSC) is achieved (and, in fact, only three follicles reach maturation stage).

To see an example where the treatment fails, consider the right column in Figure 15, showing the VPH model evolution under a sample BA model parameter (virtual patient) for which the treatment does not achieve MSC. It can be seen that follicles do not grow satisfactorily, and that the treatment correctly reacts to such a slow follicle growth by increasing the daily dose of the stimulation drug (from 300 IU to 450 IU), as safety thresholds for E2 and P4 are far from being reached. Notwithstanding treatment adaptations, only two follicles reach maturation. The first two columns show two interrupted treatments due to unsuccessful down-regulation (left) and P4 safety threshold reached during stimulation (centre). In the first case, the follicle profile is not shown at all (as stimulation is not started), while in the second, stimulation is interrupted due to an too early P4 peak.

3.3. *Model-Based Design of Individualised Treatment Protocols (MBD-ITP)*

MBD-ITP aims at supporting medical doctors and researchers in the design of individualised treatments in a clinical setting, by automatically evaluating the effectiveness of a treatment protocol over a set of possible values for the treatment parameters. Compared to the verification task, the individualised treatment design activity deals with more complex treatments. The main ingredient of our treatment synthesis approach is the definition of *parametrised treatment* models. Instead of synthesising a treatment from scratch, we take a template treatment with parameters and find suitable values for these parameters.

Parametrised treatments have essentially the same structure of treatments currently in use in clinical practice, but their execution depends on some parameters. Having the same structure of the template treatment,

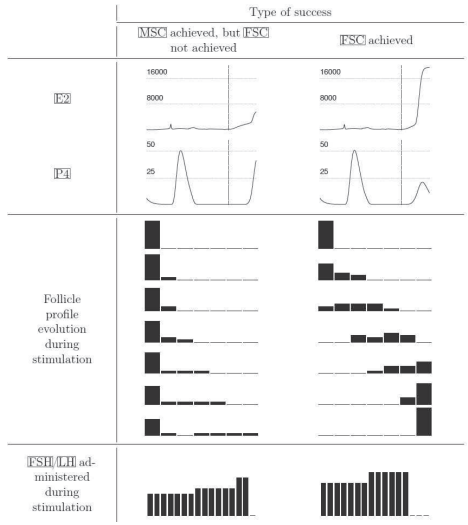

Figure 14. VPH model evolutions computed by MBV-TP, showing treatment successes.

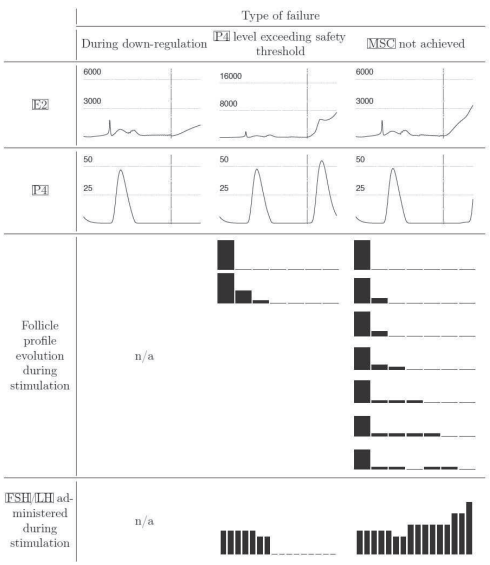

Figure 15. VPH model evolutions computed by MBV-TP, showing treatment failures.

they are more likely to be accepted in the clinical practice. Example of treatment parameters are thresholds that influence treatment decisions, or doses of administered drugs. Moreover, as in the treatment verification task (MBV-TP), we consider a set of KPIs to evaluate treatment effectiveness.

Therefore, our approach to the treatment synthesis problem consists of solving a search problem over the set of possible treatment parameter values, looking for the treatment parameter values that optimise the KPIs. Since the optimisation of a set of KPIs is a multi-objective optimisation problem, we select all those treatment parameter values that lead to a tuple of KPIs values that are not *Pareto dominated* by other treatment parameter values.

The input for MBD-ITP ist the same for MBV-TP except that it needs additionally a parameterized treatment. The output is correspondingly a set of parameter vectors, each treatment parameter vector defines an individualised treatment which is considered optimal with respect to the set of given KPIs and for the set of BA VPH models, see Figure 16.

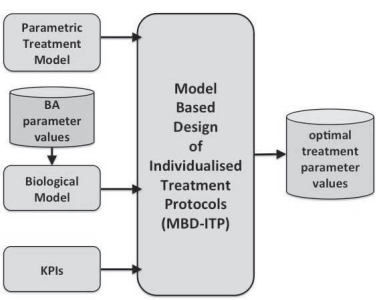

Figure 16. MBD-ITP inputs and outputs.

This approach is computationally demanding. We ran MDB-ITP on 15 Xenon-based machines with an overall number of 121 cores. To present an example, we changed in the reference protocol of UZH the age classification with a parameter $\delta_{age} \in [-4, 4]$, similarly also the classification with respect to the AMH levels and AFC, and, as a treatment parameter, the administered doses of the stimulation drug.

Figure 17 shows the outcome of an execition of the MBD-ITP service, where 14 Pareto-optimal treatments were returned. Obviously, the reference treatment from UZH (black) balances quite well its performance over all KPIs.

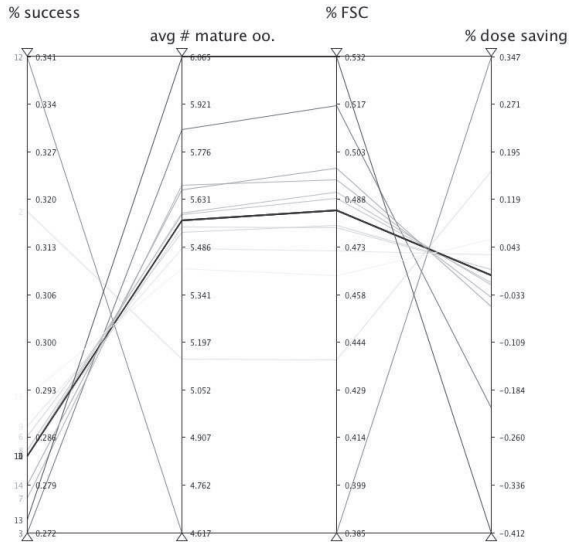

Figure 17. Pareto-optimal treatments computed by MBD-ITP. The reference treatment is in black.

Also the other candidate treatments show interesting properties. For example, one treatment at the same time minimises the overall amount of drug used (saving, on average, 34.7% of stimulation drug with respect to the reference treatment) and maximises the number of cases in which it succeeds (34.1%, vs. 28% of the reference treatment), at the cost of allowing the retrieval of (on average) fewer mature oocytes (4.617 vs. 5.571 of the reference treatment) and to approach FSC less frequently (38.5% on average vs. 48.5% for the reference treatment).

This work is supported by the European Commission's Seventh Framework Programme.

References

1. Fachinformation des Arzneimittel-Kompendiums der Schweiz, http://www.kompendium.ch/home/de.
2. A. Chávez-Ross, S. Franks, H. D. Mason, K. Hardy and J. Stark. Modelling the control of ovulation and polycystic ovary syndrome. *J. Math. Biol.*, 36(1):95–118, 1997.
3. J. Collins. An international survey of the health economics of IVF and ICSI. *Hum. Reprod. Update*, 8(3):265–277, 2002.

4. M. Egli, B. Leeners and T. H. C. Krüger. Prolactin secretion patterns: basic mechanisms and clinical implications for reproduction. *Reproduction*, 140(5):643–654, 2010.
5. C. Gnoth, D. Godehardt, E. Godehardt, P. Frank-Herrmann and G. Freundl. Time to pregnancy: results of the German prospective study and impact on the management of infertility. *Human reproduction*, 18(9):1959–1966, 2003.
6. R. Grosu and S. A. Smolka. Quantitative model checking. In *Preliminary Proc. of ISoLA*, pages 165–174, 2004.
7. R. Grosu and S. A. Smolka. Monte Carlo model checking. In *Proc. of TACAS*, pages 271–286, 2005.
8. D. L. Herbert, J. C. Lucke and A. J. Dobson. Depression: an emotional obstacle to seeking medical advice for infertility. *Fertility and Sterility*, 94(5):1817–1821, 2010.
9. M. Ogawa, K. Takamatsu and F. Horiguchi. Evaluation of factors associated with the anxiety and depression of female infertility patients. *Biopsychosoc. Med.*, 5(1):15, 2011.
10. S. Röblitz, C. Stötzel, P. Deuflhard, H. Jones, D.-O. Azulay, P. van der Graaf and S. Martin. A mathematical model of the human menstrual cycle for the administration of gnrh analogues. *J. Theor. Biol.*, 321:8–27, 2011.
11. M. B. Sexton, M. R. Byrd, W. T. O'Donohue and N. N. Jacobs. Web-based treatment for infertility-related psychological distress. *Arch. Womens Ment. Health*, 13(4):347–358, 2010.
12. E. Tronci, T. Mancini, I. Salvo, S. Sinisi, F. Mari, I. Melatti, A. Massini, F. Davì, T. Dierkes, R. Ehrig, S. Röblitz, B. Leeners, T. H. C. Krüger, M. Egli and F. Ille. Patient-specific models from inter-patient biological models and clinical records. In *Proc. of FMCAD*, pages 207–214, 2014.
13. X. Wang, C. Chen, L. Wang, D. Chen, W. Guang and J. French. Conception, early pregnancy loss, and time to clinical pregnancy: a population-based prospective study. *Fertility and Sterility*, 79(3):577–584, 2003.

THE NETWORK ROUTE TO BIOLOGICAL COMPLEXITY*

SOUMYA JYOTI BANERJEE, RAJDEEP KAUR GREWAL,
SAPTARSHI SINHA AND SOUMEN ROY

Bose Institute,
93/1 Acharya PC Roy Road,
Kolkata 700 009 India
E-mail: soumen@jcbose.ac.in

Networks are known to effectively represent the architecture of many complex biological systems. We propose a new network metric, edge proximity, $\mathcal{P}_e$, which identifies proteins with essential cellular functions in protein-protein interaction networks. It pinpoints regulatory neural connections and important portions of the neural and brain networks, respectively. Energy flow interactions identified by $\mathcal{P}_e$ form the backbone of long food web chains. We briefly discuss the potential that networks possess in diagnostics and how this can be utilised to build suitable biomedical devices. We introduce the technique of differential networks (DN). DN lend us valuable information about the light-dark transition observed in an entire class of light-sensitive proteins having wide applications in synthetic protein designing, especially with regard to optogenetics. It provides a suitable alternative and simultaneously introduces a framework to guide extensive mutagenesis studies.

1. Introduction

Complex systems are composed of components which interact among themselves and often with their environment in a non-trivial manner. Many a time, these interactions are non-linear. Complex systems are known to exhibit collective behaviour. Ranging from subatomic realms to ecosystems and human societies, complexity exists at different levels of organization[5]. In biology it is ubiquitous at all levels, from molecules and cells to tissues and entire organisms. In the last decade and half, the field of network science has been rather successful in mapping a number of such complex systems, *especially in biology*[1,2,3,4]. Not so long back, scientists adopted reductionist approaches towards understanding the essential functioning of complex biological systems. That is, these systems were analyzed by scru-

*SJB is financially supported by CSIR, India and RKG & SS by UGC, INDIA.

tinising their individual components separately, rather than studying the system as a whole. Such an approach has served to be very successful in understanding many basic biological processes. But with the deluge of information from recent "omic" sciences, gathered from large scale studies of genome, proteome or transcriptome, the drawbacks of such an approach are now increasingly prominent[5].

As aforementioned, the interactions among individual components of a given system function in synchrony, giving rise to holistic characteristics of the system (emergent properties). Thus, to have a better understanding of a system one needs to look for approaches which require the study of all constituent elements with possibly complicated interactions, all together. Network science or the theory of complex networks, presents itself as a rather promising candidate in this respect. It tries to understand complex systems by modeling the smallest components of a system as nodes and the interactions between them as edges. Network theory has proved to be an effectual and successful tool in unraveling details of systems with topologies that are neither fully regular nor purely random in nature. For example, the neural network of *C.elegans* is known to have small world topology, i.e, it posseses small characteristic path length but is highly clustered unlike random networks. Network theory sheds useful insights into understanding the unifying principles and underlying mechanisms that govern a vast variety of biological systems, at different scales of length and time.

In biological networks, nodes are entities like metabolites or macromolecules like proteins, RNA and genes, while the edges are physical, biochemical and other structural or functional interactions among them. There are various network metrics which have been useful in understanding these networks and which help in determining local properties of nodes and edges, as well as global properties to gain deeper knowledge of the system. We present a number of such examples from various biological systems in the present chapter. We begin this chapter by discussing a new edge-based metric, which we refer to as *edge proximity*.

2. Biological Networks and Edge Based Metrics

2.1. *Edge based metrics*

In a given connected network, $\mathcal{G}$; let $\mathcal{V}$ and $\mathcal{E}$ denote the set of nodes and edges respectively. $\mathcal{N} = |\mathcal{V}|$ and $\mathcal{S} = |\mathcal{E}|$ are the total number of nodes and edges in $\mathcal{G}$, respectively. The most well-known edge-based measure, *edge betweenness*[7,8], $\mathcal{B}_e$ is defined as:

$$\mathcal{B}_e = \sum_{s \neq t} \frac{\sigma(s,t|e)}{\sigma(s,t)}, e \in \mathcal{E} \tag{1}$$

$\mathcal{B}_e$ is the ratio of the number of shortest paths, $\sigma(s,t|e)$, between node, s, and node, t, which pass through edge, e; to the total number of directed shortest paths, $\sigma(s,t)$, between node, s, and node, t, in the network. It attempts to capture the frequency of an edge lying on the shortest paths between all pairs of vertices in a network. Edges with the highest $\mathcal{B}_e$ are most likely to lie between subgraphs, rather than inside them. Thus, targeting by node or edge betweenness ensures rapid disconnection of networks by a small number of deletions[6,9]. Betweenness has been found to be very useful in an array of applications ranging from controllability in networks[10] to diagnostics[11] and scalable devices for successful feature extraction in image processing[12].

We introduce an edge-based network metric, edge proximity, $\mathcal{P}_e$, which successfully identifies the hitherto unknown importance of many interactions[13]. The $\mathcal{P}_e$ of an edge, $e \in \mathcal{E}$, is the inverse of the sum of its shortest distance $d(e,f)$, with every other edge, $f \in \mathcal{E}$, in $\mathcal{G}(V,E)$. $\mathcal{P}_e$ lends clues as to how close each edge is to every other edge in $\mathcal{G}$ through the shortest paths between them. Thus,

$$\mathcal{P}_e = \frac{\mathcal{S}-1}{\sum_{f \in \mathcal{E}} d(e,f)}, e \in \mathcal{E} \tag{2}$$

The effects of removing edges with high $\mathcal{P}_e$ might initially not be displayed clearly. However, these removals eventually cause great harm to the network. Compared to existing strategies, the removal of edges by $\mathcal{P}_e$ leads to a remarkable increase in average shortest path length and diameter in undirected networks. $\mathcal{P}_e$ can be consistently used to divide the network into two nearly equal components. Therefore, removal of edges by $\mathcal{P}_e$ presents a slow but powerful strategy to greatly harm a network[13]. It has also been observed that edges with higher edge proximity value are the starting edges of the driver nodes for edge controllability under switchboard dynamics[14]. Edges with high edge proximity value have good potential to control many edges under switchboard dynamics dynamics whereas edges with very small edge proximity value fail to do so.

2.2. *Importance of edge based metrics in biological networks*

The analysis of $\mathcal{P}_e$ and $\mathcal{B}_e$ for the edges of PPI, food web, neural and brain networks are conducted in the following sections and their biological significance discussed at length. For this purpose, the $\mathcal{Z}-$score has been calculated as,

$$\mathcal{Z}(\mathcal{Q}) = \frac{\mathcal{Q} - \mu(\mathcal{Q})}{\sigma(Q)}, Q \in \{\mathcal{P}_e, \mathcal{B}_e\}. \tag{3}$$

$\mu(\mathcal{Q})$ is the mean and, $\sigma(\mathcal{Q})$, the standard deviation of the $\mathcal{Q}$ distribution. For consistency, we restrict ourselves to the top 2% of edges, with $\mathcal{Z}(\mathcal{Q}) \geq 1$ for all networks.

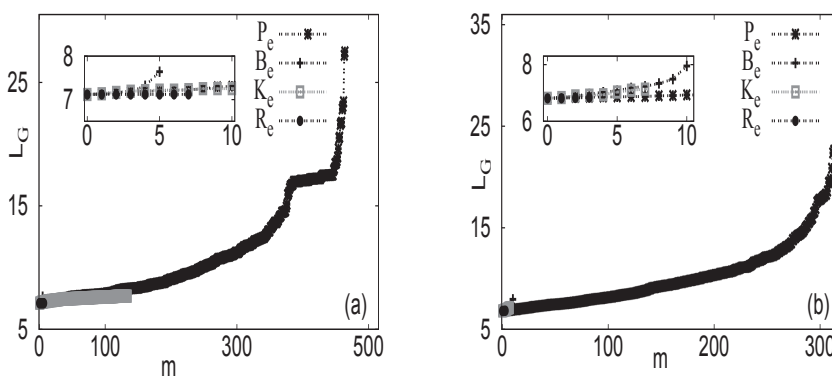

Figure 1. Average path length, $\mathcal{L}_G$ of the (a) *E. coli* and (b) *S. cerevisiae* protein-protein interaction networks. when edges are progressively removed by highest edge proximity, $\mathcal{P}_e$, edge betweenness, $\mathcal{B}_e$, edges with highest degree at any end, $\mathcal{K}_e$ and purely at random, $\mathcal{R}_e$. (Inset) Initially, $\mathcal{B}_e$ might seem to cause more harm in the network as in (a) or might even rapidly rupture it as in (b). However, in the long run, $\mathcal{P}_e$ is clearly shown to cause the maximum increase in $\mathcal{L}_G$.

2.3. *Protein-protein interaction networks*

Protein-protein interaction networks play an important role in maintaining inter-cellular coordination and in performing various types of cellular functions. Systemic study of protein-protein interactions should reveal many unknown facets of inter-cellular mechanisms. Experimental backbone of

these studies use high throughput yeast-two-hybrid screening, affinity purification, mass spectroscopy etc.[15,16]. Topological structure analysis of protein-protein interaction networks uncovers many hidden properties of biological networks and their working strategies[17].

In protein-protein interactions networks, nodes are the proteins and edges represent a physical interaction between two proteins. The edges are undirected. Therefore, it is not immediately apparent from the network, as to which protein functionally influences the other.

It is known that protein-protein interaction networks (PPINs) of *S. cerevisiae* exhibits distinct scale-free behavior[18,19]. Scale-free networks are known to be vulnerable upon targeted attacks, on their highly connected nodes. Therefore, mutations of highly interacting proteins are expected to be lethal for the cell. Importance of interactions between proteins have also been investigated[13,20]. What would happen if two such proteins bound together, ceased to interact due to some unfavorable conditions in cells? Therefore, there should exist some crucial interactions (edges) without which the entire protein-protein interaction system might collapse[13]. Effect of edge deletion is observed in terms of increase of average shortest path length and diameter of *S. cerevisiae* and *E. coli* PPINs, till the first disconnection.

The *Average shortest path length,* L_G*,* is the average of all the shortest path lengths between any pair of nodes in $\mathcal{G}$ and is defined as,

$$\mathcal{L}_G = \frac{1}{\mathcal{N}(\mathcal{N}-1)} \sum_{s,t \in \mathcal{V};\ s \neq t} d(s,t) \tag{4}$$

The *Diameter* of $\mathcal{G}$ is defined as,

$$\mathcal{D} = max(d(s,t)),\ \forall\ s,t \in \mathcal{V};\ s \neq t; \tag{5}$$

$d(s,t)$ being the shortest path from s to t. From the definition of $\mathcal{L}_G$ and $\mathcal{D}$ it is clear that $\mathcal{L}_G$ and $\mathcal{D}$ become infinite when $\mathcal{G}$ becomes disconnected.

Removal of interactions by $\mathcal{P}_e$ increases $\mathcal{L}_G$ and $\mathcal{D}$ of PPINs the most. Important reactions in protein-protein interaction networks have been mapped by using edge betweenness and edge proximity[13] metrics. By using edge betweenness metrics many significant types of functional clustering can be conducted[20]. On the other hand edge proximity metric could identify some crucial protein-protein interactions, which are important to overcome "stress". One of such protein is *E. coli* $60kDa$ chaperonin protein. Remarkably, edges denoting interaction of $60kDa$ chaperonin protein in *E. coli* protein-protein interaction network exhibit the highest edge proximity

value. Interactions of these proteins resembles the interactions of date hubs which are important for global organization of the entire protein-protein interaction network[21].

2.4. *Food web networks*

Two of the most basic components of our ecosystem are autotrophs and heterotrophs. Autotrophs can produce their own food from their surroundings, where as heterotrophs depend on autotrophs for their energy. Thus, there is a directed network of energy flow between them, which is also called the food web. Food webs has generally more complex than other biological networks in terms of their connectedness[22]. A good number of studies on food web, shows conflict among a number of network characteristics. Degree distribution, clustering coefficient, characteristic path length and centrality measure can vary widely among food webs[23,24]. There also exist studies on identifying important interactions inside food webs by edge based metrics. Directed edges between species indicates who feeds upon whom or denotes the energy flow direction in the ecosystem. Analyzing three coral reef food webs[25] network (Cayman Island, Cuba and Jamaica) and four trophic food web from South Florida Ecosystem[26,27], it can be clearly shown that the removal of interactions having high edge betweenness value could block many tropic interactions. On the other hand, interactions identified by high edge proximity value, are basically the root interactions of dominator tree of that ecosystem. These interactions are thus important in maintaining the energy flow in food webs. If these interactions were removed, it could lead to many secondary extinctions. These are basically the starting interactions of food pyramids where autotrophs make foods from the basic components.

2.5. *Neural network*

Emergent behavior from complex neural networks is a subject of great attention in the field of neural networks. These networks are composed of interconnected neurons where neurons are the nodes and synaptic connections constitute the edges. One of great challenges of neural networks is the wide unavailability of experimental datasets. *C. elegans* neural network dataset is the only available completely mapped neural network dataset. This network was constructed via connectivity reconstruction through electron microscopy[28]. The connectivity data includes 6393 chemical synapses, 1410 neuromuscular junctions and 890 electrical junctions[29]. A total number of 394 neurons and 7 neurotransmitters are reported. Identification of

synapses by edge based network analysis shows that synapses with the highest edge proximity value are responsible for backward movement, where as synapses with highest edge betweenness are associated with both thermotaxis and backward movement. Thus, it seems that edge proximity analyses can group synaptic junctions better, according to functionality.

2.6. *Brain network*

A number of studies have also been conducted in brain networks. These network are comprised of different parts of the brain connected via neural fibers. The experimental basis of these type of network constructions, depends on modern non-invasive medical imaging techniques. These techniques include high resolution magnetic resonance imaging (MRI). Not only that, advanced computer hardware and simulation software enable us to conduct simulations of thousands of spiking neurons. Combined pictures of these technique enable us to resolve brain network in great detail[30,31]. Structural analyses of brain networks by network based metrics enable us to understand such networks properly. Edge based analyses could group the neural fibers into distinct functional categories, merely from the connectivity data. Neural fibers of the Macaque brain network (CoCoMac)[32] with high edge betweenness values indicate neural connections, which are localized in prefrontal cortex. On the other hand, fibers with high edge proximity value identify various starting connections of long information processing pathways like the cortex to thalamus, temporal lobe and frontal lobe.

3. Application of Network Theory to Diagnostics and Biomedical Science

Thermal imaging has only been recently introduced to diagnostics. The main reason for this is that previously, thermal imaging was restricted for military use only. As such its diagnostic potential is still relatively unexplored. Variability of steady state thermal behaviour due to environmental thermal fluctuations are responsible for the restrictive use of this powerful non-invasive technique. Aqueous deficient dry eye disease (ADDE) is a common, painful disease of the eye. Current techniques which are widely in use are mostly non-invasive. Non-invasive thermal imaging of the patients eyes can be converted to a time series. These time-series can then be converted into networks[33]. Edge betweenness, $\mathcal{B}_e$, discussed above serves as a powerful discriminator and helps in diagnosis of healthy and patients

suffering from ADDE[11]. Such methods can be utilised to build scaleable biomedical devices[12].

4. Networks and Photoreceptors

4.1. *Optogenetics and LOV-photoreceptors*

The recently discovered field of optogenetics has drawn tremendous attention of the entire scientific community. In 2010, optogenetics was named by the journal *Science*[34] among "The insights of the decade" and by the journal *Nature Methods* as "Method of the Year"[35]. Optogenetics has its roots in neuroscience and the initial aim was to control the neuronal activity in organisms using light-sensitive proteins with unprecedented precision[36]. This field has now developed in its own right and has grown beyond the use of naturally existing proteins to control specific events within living cells. This is a crucial step towards the understanding of multifarious biological events and more importantly to control them with a high level of precision. For clever design of artificial photosensors, an in-depth knowledge of their underlying signaling mechanisms is of utmost importance.

Photoreceptors are light-sensitive proteins consisting of two parts: a sensor domain, which absorbs light, and, an effector domain which carries out the desired physiological activities. Photoreceptors usually absorb light from visible spectra to carry out the required biological activities within an organism. Light-Oxygen-Voltage (LOV) domains are a class of photoreceptors that absorb blue light from the visible spectra[37]. They consist of a chromophore, namely flavin chromophore (FMN or FAD), an organic, non-protein part which absorbs photons initiating a series of signaling events throughout the domain. LOV domains have shown a promising role in designing effective artificial light-sensitive proteins[38,39]. Upon absorption of photon, a cysteine-flavin adduct[40] formation takes place, which is a well known phenomenon, marking the beginning of signaling events within the domain. A domain may remain in its exited state, called the light state, for a duration ranging from a few seconds to a few hours; after which it returns to its initial state known as dark state. This transition from light to dark state or vice-versa is a reversible process. Although, the events initiating the signal propagation are well studied and known, the detailed understanding of the underlying signaling mechanism is still lacking. While photoreceptors have been studied in some detail, the light-dark transition in such systems are not clearly understood. A thorough and insightful knowledge of signal mechanism within the LOV domains will not only pro-

vide us with a clear understanding of functioning of these domains but will definitely also help in rational designing of synthetic photoreceptors.

4.2. *Network theory on LOV domains*

4.2.1. *Network construction*

Network theory can be used to model proteins as residue interaction networks[41]. We introduce techniques from complex networks to analyze and understand the light-dark transition in photoreceptors. All LOV domains with available crystal structures in both light and dark were analyzed. There are six available sets of light-dark structures of LOV domains, each from different species, namely - YtvA from *B. subtilis*[43,44] (PDB ids: 2pr6, 2pr5), Vivid (VVD) from the fungus *N. crassa*[45] (PDB id: 2pdr, 2pd7), LOV2 domain from *A. sativa* (Oat)[46] (PDB id: 2v1b, 2v1a), Aureochrome1 (Aureo1) from the photosynthetic marine alga, *V. frigida*[47] (PDB ids: 3ulf, 3ue6), LOV1 domain of Phot1 from the green alga *C. reinhardtii*[48] (PDB id: 1n9o, 1n9l) and LOV2 domain from the phototropin of chimeric fern photoreceptor (Phy3-LOV)[40] (PDB id: 1jnu, 1g28) for light and dark states respectively[42]. Remarkably, both light and dark state structures all of these crystals belong to the same space group.

To construct a network from a given LOV domain crystal structure, each amino acid is consider as a node. Any two residues i and j, with, $|i-j| > 2$ [49], are said to be interacting if the interaction strength, given by

$$I = \frac{n_{ij}}{\sqrt{N_i N_j}}, \tag{6}$$

is greater than the critical cut-off, I_C[50]. n_{ij} represents total number of side chain atom interactions between i^{th} and j^{th} residue within 4.5 Å[51]. The normalization factors, N_i and N_j, denote the total number of heavy atoms in i^{th} and j^{th} residue, respectively[52]. The interaction strength at which the size of largest connected component of the network sharply decreases from its initial value at $I = 0$ is termed as I_C.

While comparing the light and dark state networks of each LOV domains, we analyze distribution profiles for network metrics, namely eccentricity (a local network property) and edge betweenness (global network metric)[42]. Eccentricity of a node is defined as the maximum of shortest distance of all nodes connected to it. Thus,

$$e_i = max(d_{ij}) \tag{7}$$

Here, d_{ij} is the shortest distance from node, i, to any other node, j, connected to it in the network $\mathcal{G}$.

We observe a characteristic consistency for the distribution profiles among all LOV domains consider, from dark to light state[42]. As shown in Fig. 1 for the case of VVD, the residues in dark state network acquire high eccentricity values when compared to the corresponding light state network. This indicates a rearrangement among residues during the light-dark transition which brings other residues in close proximity with each other. On the other hand, edge betweenness distribution profiles for dark state of all six LOV domains possess long tails in comparison to their respective light state distribution profiles from which we can infer that the information/signal flow in dark state is much more channelized via few edges having higher edge betweenness values. In contrast, for the light state, the near absence of "bottlenecks" represents a homogeneous flow of information throughout the domain. Hence, we conclude that the transition brings about crucial characteristic changes within the domain for proper functioning and sustenance of signalling mechanisms. Based on the above observations, we conclude that the gain or loss of interactions during transition bears significant information about the structural changes and their effects during the light-dark transition of LOV domains.

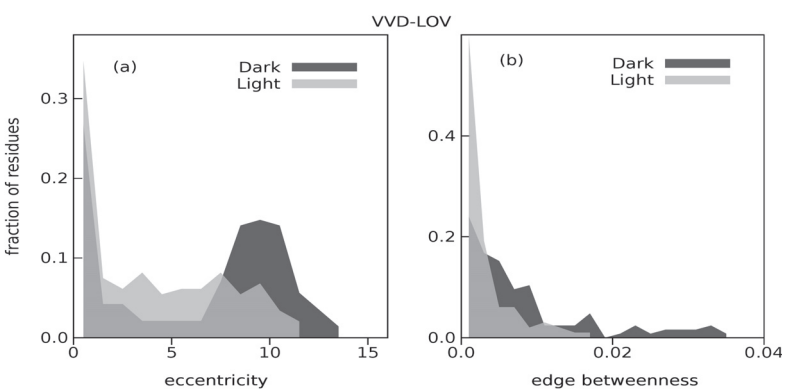

Figure 2. Distribution profiles of (a) Eccentricity and (b) Edge betweenness for VVD. (a) There is leftward shift of eccentricity distribution profile showing decrease in eccentricity of residues in light state as compared to dark state. (b) The shorter tail in the light state indicates minimal presence role of "bottlenecks" in the light state which is quite different from the behaviour observed in dark state. Bioinformatics (OUP) (2015).

4.2.2. *Differential Networks to understand light-dark transition*

The Differential Network (DN) approach centers on the set of interactions that are lost or gained during the transition. The Light Differential Network (LDN) consists of edges that are present only in light state but are absent in the dark state. Similarly, the set of edges that are unique to the dark state form the Dark Differential Network (DDN). Upon deletion of these edges, newly formed or lost edges during transition, from parent light and dark state structures we identified biologically crucial key-residues and interactions[42]. The structural changes in light and dark states are known to be subtle[53], although the DN technique effectively captures these changes and provides new insights into biological behavior of LOV domains.

We analyze the change in network metrics upon deletion of edges, that belong to LDN or DDN, from parent light and parent dark state networks respectively[42]. We analyze both node and edge based metrics to measure the resultant change of node and edge centralities upon the deletion of "unique" edges given by,

$$\triangle \mathcal{M}_k^i = \frac{|\mathcal{M}^{parent,i} - \mathcal{M}^{remaining,i}|}{\langle \mathcal{M} \rangle} \tag{8}$$

Here, $\mathcal{M}$ represents metric under consideration, i.e, node betweenness, node closeness, edge proximity[13] or edge betweenness. The node closeness is given as the inverse of the average shortest distance of node i to every other node j connected to it and is given by,

$$\mathcal{C}_i = \frac{\mathcal{N} - 1}{\sum_j d_{ij}}, \tag{9}$$

We consider the global node and edge based centralities to measure the effect of edge removal on the remaining other distant nodes and edges throughout the network. $\mathcal{M}^{parent,i}$ and $\mathcal{M}^{remaining,i}$ represents value of $\mathcal{M}$ for i^{th} node (or edge) before and after removal of the k^{th} edge respectively, where, $k \in LDN(DDN)$. $\langle \mathcal{M} \rangle$ is the mean value of $\mathcal{M}$ in the parent light or dark state averaged over all residues or edges. We observe that only few edges belonging to LDN or DDN, upon their removal from their respective parent states, significantly affect not only the incident node but also the distant nodes/edges in the network. Thus, the cumulative effect of $\mathcal{M}$ in the entire network due to the removal of an individual edge is obtained as,

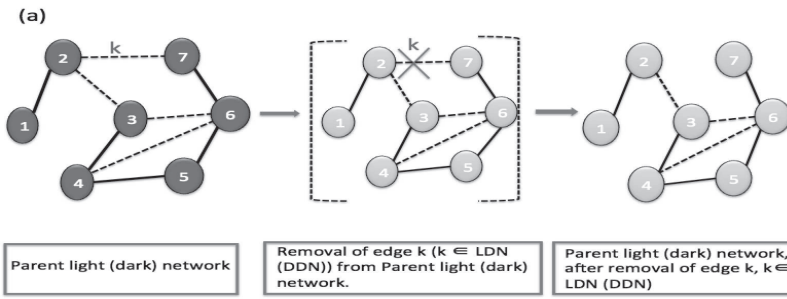

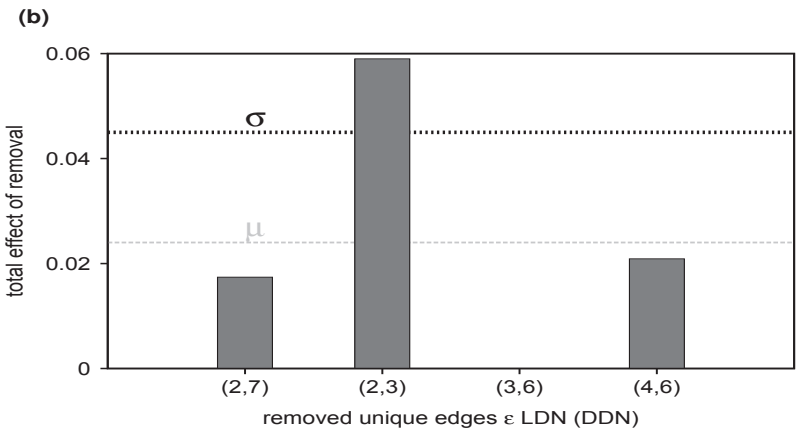

Figure 3. Edge removal strategy using dark differential networks (DDN) or light differential networks (LDN) and identification of key interactions/residues. (a) A toy network featuring a light (dark) state network. The solid lines represents common edges while dashed lines are unique edges belonging to LDN (DDN) (b) The plot shows the total effect as calculated from Eq. 10, due to the removal of the k^{th} edge of LDN (DDN) or equivalently the q^{th} edge of the parent light (dark) network (a). μ (gray colored line) denotes the mean and σ (black colored line) is the corresponding standard deviation. Edges with overall effect lying above the black line are considered as key interactions. Bioinformatics (OUP) (2015).

$$\triangle \mathcal{M}_k = \frac{1}{(\mathcal{N}'-a)} \sum_{i'} \triangle \mathcal{M}_k^{i'} \tag{10}$$

Here, the summation runs over all the nodes or edges in the network

after removal except the incident nodes, to ignore the obvious effect over the incident nodes. Thus, $\mathcal{N}' = \mathcal{N}$ and $a = 2$ for node closeness or node betweenness. For edge proximity or edge betweenness, $\mathcal{N}' = \mathcal{S}$ and $a = 0$.

To determine the significance of affect caused by each edge removal we calculate $\mathcal{Z}_k$ score, which is given by

$$\mathcal{Z}_k = \frac{\triangle\mathcal{M}_k - \langle\triangle\mathcal{M}_k\rangle}{\sigma_{\Delta\mathcal{M}_k}}, \tag{11}$$

where, $\langle\triangle\mathcal{M}_k\rangle$ is the mean effect of the deletion of every individual edge (one at a time), in LDN or DDN calculated from Eq. 10. $\sigma_{\Delta\mathcal{M}_k}$ is the associated standard deviation. Edges in LDN and DDN with $\mathcal{Z}_k \geq 1$ are termed as key interactions and the corresponding incident nodes as key residues.

For each of the six LOV domains we identify only a few important edges or the key interactions[42]. We find that most of the key-residues identified either belong to the FMN/FAD binding site or N-terminal and C-terminal signaling helixes. Most of them have been experimentally validated to be biological significant through mutational analysis. The success rate being $> 85\%$ for the case of well studied YtvA-LOV and VVD, and, 70% and 66% respectively for the lesser studied Aureo-LOV and Oat-LOV[42]. Since, the remaining two LOVs (Phy3 and Phot1) lack detailed studies with crystal structure of Cr-LOV lacking both its N-terminal and C-terminal signaling helixes, the success rate is expectedly lower. We also performed structure-sequence alignment analysis to predict biological significance of key residues that are not yet experimentally verified yet are found to be significant through network analysis. Such residues are amenable for experimental verification. Thus, Differential Network approach provides us with a framework to guide further experimental mutational analysis and understand structure as well as function of LOV-domains.

Due to crystallographic constraints, there are obvious limitations of this approach. Nevertheless, we are able to successfully capture functionally relevant residues which in turn provide insights on photo-adaptation. The detailed knowledge of signaling mechanism is a definite step for rational designing of artificial photoreceptors in optogenetics.

References

1. R. Albert and A.-L. Barabsi, *Rev. Mod. Phys.* 74, 47 (2002).
2. M. E. J. Newman, Networks: An Introduction (Oxford University Press, Oxford, UK, 2010).

3. V. Filkov *et al.*, *Europhys. Lett.* 86, 28003 (2009).
4. S. Roy and V. Filkov, *Phys. Rev. E* 80, 040902(R) (2009).
5. F. Mazzocchi, *EMBO Rep.* **9**, 10 (2008).
6. D. R. Wuellner, S. Roy and R. M. D'Souza, *Phys. Rev. E* **82**, 056101 (2010).
7. M. E. J. Newman and M. Girvan, *Phys. Rev. E* **69**, 026113 (2004).
8. M. Girvan and M. E. J. Newman, *PNAS USA* **99**, 7821 (2002).
9. S. Roy, *Syst. Synth. Biol.* **6**, 31 (2012).
10. S. J. Banerjee and S. Roy, arXiv:1209.3737.
11. S. J. Banerjee *et al.*, arXiv:1506.02602 (2015).
12. S. Roy *et al.*, A system and method for analyzing videos of application or function for feature identification of the videos and related application or function. Indian Patent 628/KOL/2015 (2015).
13. S. J. Banerjee, S. Sinha and S. Roy, *Phys. Rev. E* **91**, 022807 (2015).
14. T. Nepusz and T. Vicsek, *Nat. Phys.* **8**, 568 (2012).
15. P. Uetz *et al.*, *Nature* **403**, 6770 (2000).
16. Y. Ho *et al.*, *Nature* **415**, 6868 (2002).
17. D. Bu *et al.*, *Nucleic acids research* **31**, 9 (2003)
18. H. Jeong, S. P. Mason, A. L. Barabási and Z. N. Oltvai, *Nature* **411**, 6833 (2001).
19. A. Wagner, *Molecular biology and evolution* **18**, 7 (2001).
20. R. Dunn, F. Dudbridge and C. M. Sanderson, *BMC bioinformatics* **6.1**, 39 (2005).
21. J. D. J. Han *et al.*, *Nature* **430**, 6995 (2004).
22. J. A. Dunne, R. J. Williams and N. D. Martinez, *PNAS USA* **99**, 12917 (2002).
23. T. W. Schoener, the Robert H. MacArthur Award Lecture *Ecology* **70**, 1559 (1989).
24. J. M. Montoya and R. V. Solé, *Journal of theoretical biology* **214**, 405 (2002).
25. P. D. Roopnarine and R. Hertog, *Dataset Papers in Ecology* **2013** 857470 (2013).
26. R. E. Ulanowicz, J. J. Heymans and M. S. Egnotovich, *Annual Report of the Biological Resources Division of the U.S. Geological Service* (U.S. Geological Service, Austin, TX, 2000).
27. V. Batagelj and A. Mrvar, *Pajek datasets.* Available at: http://vlado.fmf.uni-lj.si/pub/networks/data/ (2006).
28. J. G. White, E. Southgate, J. N. Thomson and S. Brenner, *Phil.Trans. Roy. Soc. London B* **314**, 1 (1986).
29. B. L. Chen, D. H. Hall and D. B. Chklovskii, *Nat. Phys.* **8**, 568 (2012).
30. O. Sporns, *Dialogues in clinical neuroscience* **15**, 247 (2013).
31. R. Bakker, T. C. Potjans, T. Wachtler and M. Diesmann, *BMC Neuroscience* **12**, P72 (2011).
32. K. E. Stephan *et al.*, *Phil. Trans. Roy. Soc. London B* **356**, 1159 (2001).
33. A. S. L. O Campanharo, *et al.*, PLoS ONE 6, e23378 (2011).
34. Science **330**, 1612–3 (2010)
35. Nature Methods **8**, 1 (2011)
36. K. Deisseroth *et al.*, *J. Neurosci.* **26**, 10380–6 (2006).

37. E. Huala *et al.*, *Science* **278**, 2120–2123 (1997).
38. A. Möglich *et al.*, *J. Mol. Biol.* **385**, 1433–1444 (2009).
39. D. Strickland, K. Moffat and T. R. Sosnick, *Proc. Natl. Acad. Sci. USA* **105**, 10709–10714 (2008).
40. S. Crosson and K. Moffat, *Proc. Natl. Acad. Sci. USA* **98**, 2995–3000 (2001).
41. R. K. Grewal and S. Roy, *Protein & peptide letters*, **22**, 923–933 (2015)
42. R. K. Grewal, D. Mitra and S. Roy, *Bioinformatics* (2015). DOI: 10.1093/bioinformatics/btv429
43. A. Losi *et al.*, *Photochem. Photobiol.* **81**, 1145–52 (2005).
44. A. Möglich and K. Moffat, *J. Mol. Biol.* **373**, 112–126 (2007).
45. B. D. Zoltowski *et al.*, *Science* **316**, 1054–1057 (2007).
46. A. S. Halavaty and K. Moffat, *Biochemistry* **46**, 14001–14009 (2007).
47. F. Takahashi *et. al.*, *Proc. Natl. Acad. Sci. USA* **104**, 19625–19630 (2007).
48. R. Fedorov *et al.*, *Biophys. J.* **84**, 2474–2482 (2003).
49. M. Bhattacharyya, C. R. Bhat and S. Vishveshwara, *Protein Sci.* **22**, 1399–416 (2013).
50. K. V. Brinda and S. Vishveshwara, *Biophys. J.* **89**, 4159–4170 (2005).
51. J. Heringa and P. Argos, *J. Mol. Bio.* **220**, 151–171(1991).
52. C. Chennubhotla and I. Bahar, *Mol. Syst. Biol.* **2**, 36 (2006).
53. P. L. Freddolino, K. H. Gardner and K. Schulten, *Photochem. Photobiol. Sci.* **12**, 1158–1170 (2013).

A SYSTEMS BIOLOGY APPROACH TO BOVINE FERTILITY AND METABOLISM: INTRODUCTION OF A GLUCOSE INSULIN MODEL*

JULIA PLÖNTZKE, MASCHA BERG, CLAUDIA STÖTZEL, SUSANNA RÖBLITZ

Computational Systems Biology Group,
Zuse Institute Berlin (ZIB),
Takustraße 7,
14195 Berlin, Germany,
E-mail: ploentzke@zib.de

To counteract the antagonistic relationship between milk yield and fertility in dairy cow, a deeper understanding of the underlying biological mechanisms is required. For this purpose, we study physiological networks related to reproduction and metabolism of dairy cows. We interactively develop dynamic, mechanistic models by fitting the models to experimental data and mechanistic knowledge.

We have already developed models for potassium balance and hormonal regulation of fertility in the dairy cow, which will briefly be reviewed here. The main focus of this article is on a currently developed glucose-insulin model. This model links the bovine hormonal cycle and the potassium balance to glucose and thus to energy metabolism. The models can be applied in scientific research, education, experimental planning, drug development and production on farms.

Introduction

In dairy cows, concurrent with increasing milk yield, decreasing fertility and increasing metabolic problems have been reported in the last decades[9]. To achieve a deeper understanding of the interactions between nutrition, fertility and the development of diseases we apply a holistic systems biology approach to hormonal regulation, energy and mineral metabolism in the dairy cow. In order to explore and analyze the underlying biological interactions, we integrate experimental data into predictive, mechanistic, dynamic models.

*This work is supported by the BMBF, the Federal Ministry for Education and Research, e:Bio project BovSys.

In an interdisciplinary team with mathematicians and veterinarians, we develop these models on the basis of ordinary differential equations (ODEs), which describe the dynamic feedback mechanisms and alterations of the most relevant involved substances over time. Dynamic, mechanistic ODE models are developed iteratively by fitting parameters to field data and refining modeled processes with mechanistic knowledge according to the interest of application. By using SBML (Systems Biology Markup Language[21]) we make models accessible for a growing community and an increasing variety of software tools.

Currently, we are working with three mechanistic ODE models of physiological networks in dairy cows: a model for the bovine estrous cycle, named BovCycle[1], a model for potassium balance[6], and a recently developed model for glucose metabolism. The latter will be introduced in this article. With the BovCycle model the inter-individual variability in the number of follicular waves per estrous cycle has been analyzed, such that parameter sets for individuals under varying conditions could be found using Fourier analysis[7] and an empirical approach[5]. In the potassium balance model we identified parameters for low potassium cows with an empirical approach[6], exploring the phenomenon that individuals show intracellular potassium concentrations of around either 20 mmol/l or 50 mmol/l[18]. In our work, parameter identification is performed with a Gauss-Newton algorithm called NLSCON[19], which is implemented in the freely available software package BioPARKIN[8] suitable for SBML models. The potassium model was partly developed and experiments were performed with the freely available software CellDesigner[20].

Prospectively, these models can be adapted for versatile applications in research, education, experimental planning, drug development and production on farms.

1. The BovCycle Model

The BovCycle model has been built to describe the bovine estrous cycle with its key mechanisms and their regulation[1,2]. The complete model description, parameters and initial values can be found in Stoetzel et al. 2012[2]. With the BovCycle model, periodic estrous cycles lasting 21 days can be simulated, describing the growth and the decay of follicles and the corpus luteum (CL) and the key reproductive hormones regulating the system. The BovCycle model consists of 15 ODEs and 60 parameters and

is available in SBML at the BioModels database[a]. The mechanisms are depicted in Figure 1[2].

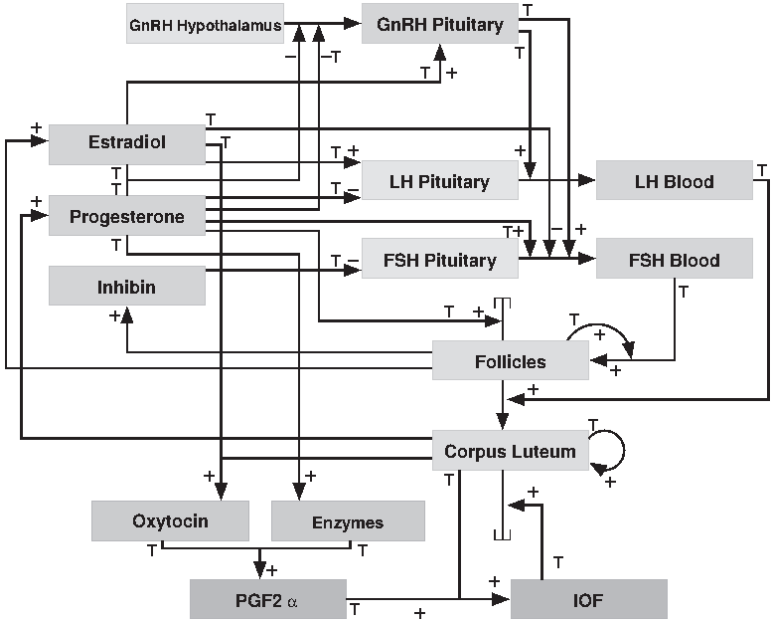

Figure 1. Graphical description of the estrous cycle model BovCycle in the dairy cow.

The hormone GnRH is synthesized in the hypothalamus and released into the pituitary. There, it stimulates the release of the hormones FSH and LH into the blood. They are affecting the development of the follicles and the CL on the ovaries. The follicles produce estradiol (E2) and inhibin (Inh) and the CL produces progesterone (P4), which are released into the blood and act locally at the ovaries. They influence GnRH, FSH and LH, and stimulate oxytocin and different enzymes that control the action of PGF2α. This, together with several intra-ovarian factors initiate the decay of the CL. These mechanisms are modeled in the BovCycle model as a closed system. No external stimuli are needed for the periodic behavior, which results only from the developed dynamics and the parametrization of the model. In one application performed with this model, drug administration of prostaglandin F2α (PGF2α) has successfully been simulated[2].

[a] https://www.ebi.ac.uk/biomodels-main/BIOMD0000000481

2. The Potassium Model

The model of potassium balance in dairy cows is the basis for computer simulations of potassium intake, distribution in the organism, and excretion. The model has been developed and validated with experimental data from the Clinic for Ruminants at Freie Universität Berlin. The mechanisms are depicted in Figure 2. With *DMI* (dry matter intake) food is taken up. K_{FEED} is the potassium fraction in the food. Potassium passes to the digestive tract K_{GIT} and is then resorbed to the extracellular space of the blood K_{ECF}. Physiological extracellular potassium concentrations range between 3.5 and 5.8 mmol/l[22], outside this range life-threatening conditions occur. In the model, potassium distributes between extracellular space K_{ECF}, intracellular space K_{ICF}, and the tissues K_{TISS}, in which it is stored. Potassium is excreted via urin K_{URIN}, saliva K_{SAL}, sudor, feces and milk K_{MILK}. Insulin, pH, the hormone Aldosterone, and the potassium amount in the food regulate the system.

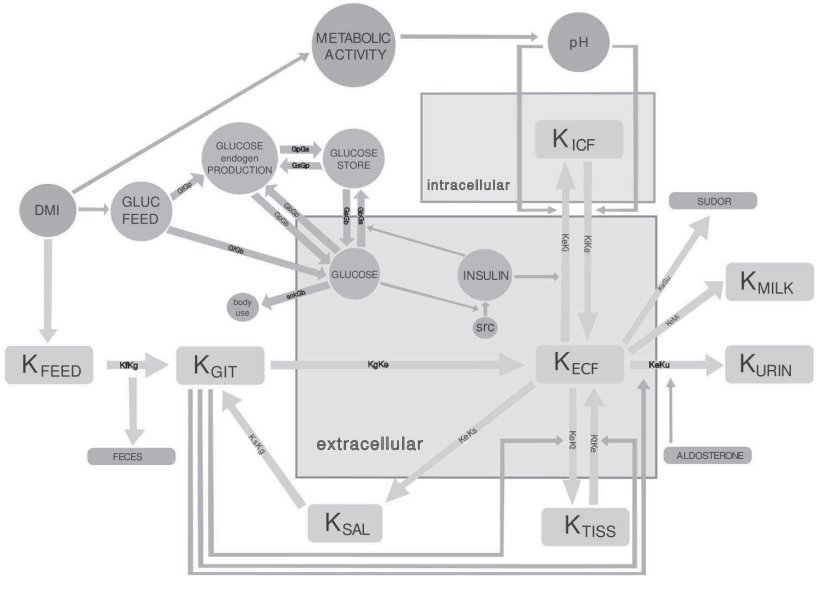

Figure 2. Graphical description of the model for potassium balance in the dairy cow.

3. The Glucose Insulin Model

The motivation to build a glucose insulin model was to study the influence of this metabolic network on potassium balance and on hormonal regulation of fertility. Glucose metabolism and homeostasis are of special concern in any mammal because glucose is a very important and, for some tissues, essential substrate[10]. For the potassium balance model the glucose-insulin metabolism is of special interest due to the interaction of insulin with the shift of potassium from extracellular to intracellular space. The interaction of the glucose-insulin system with the hormonal regulation of fertility is characterized by long term effects, where long term food reduction may lead to reversible functional disturbances in follicular development up to anestrus[12]. There are common pharmaceutical interventions in the glucose metabolism, as application of glucocorticoids, whose effects on potassium balance and the hormonal reproductive system have not yet been studied in detail.

Due to the fermentative character of their digestion, glucose metabolism in ruminants is different compared to monogastical species. Carbohydrates ingested with the *DMI* are processed by microbes to the intermediary product pyruvate and then to short chain fatty acids[11], which are resorbed and serve, amongst others, as precursor substances for endogen glucose production via gluconeogenesis. High amounts of starch in *DMI* cannot be metabolized in the rumen. So called bypass starch is split enzymatically in the small intestine and is then resorbed as glucose. The mechanisms of the glucose–insulin model are depicted in Figure 3. In the model, the fraction of substances in *DMI* that are glucose or can be transformed to glucose are pooled in the component $Gluc_{FEED}$. These glucoplastic substances are transported to the component $Gluc_{PROD}$ with a rate $GfGp$. In this component we pool the endogenous production of glucose. The dairy cow needs to cover up to 90% of her glucose demand by gluconeogenesis[13].

The remaining part of $Gluc_{FEED}$ is directly transported to blood glucose, $Gluc_B$. The corresponding rate $GfGb$ represents direct glucose resorption from the intestine, including bypass starch. Glucose production is also fed by the storage component $Gluc_{STOR}$ with the rate $GsGp$.

Glucose produced in $Gluc_{PROD}$ is shifted to $Gluc_B$ with the rate $GpGb$.

The excess is shifted back to $Gluc_{STOR}$ with the rate $GpGs$.

Glucose is cleared from the blood at a rate $SnkGb$, representing the metabolic use of glucose.

Storage of glucose is represented by the component $Gluc_{STOR}$. In vivo,

glucose is stored as glycogen, with muscle, liver, and kidney being the main tissues storing glucose. In the default condition, storage capacity for a cow with 600 kg body weight is calculated with 280 kg storable tissue weight[14].

We assume that there is a maximum storage capacity, that cannot even be exceeded with increasing carbohydrate uptake. The dimension of this storage is calculated with 2% glycogen weight in the muscle tissue and 10% in liver[23]. Hence, in 9 kg liver an amount of 900 g glycogen can be stored, and in 265 kg muscle an amount of about 5300 g can be stored. Finally, a maximum storage capacity of 6200 g is obtained.

Glucose is transported from the storage to the blood with a rate $GsGb$, which increases for low levels of $Gluc_B$ and diminishes for high levels of $Gluc_B$.

Glucose and insulin influence each other. *Insulin* in the blood increases in response to rising $Gluc_B$, thus promoting the transport of glucose from $Gluc_B$ to $Gluc_{STOR}$ with the rate $GbGs$.

If the storage $Gluc_{STOR}$ is already full or if the levels of $Gluc_{FEED}$ are low, this rate decreases.

In vivo, insulin is secreted from pancreatic beta cells in response to elevated blood levels of nutrients such as glucose or amino acids. It causes uptake of glucose as glycogen into cells of liver, muscle, and storage. Furthermore, insulin causes uptake of potassium in insulin sensitive cells by enhancing the activity of Na/K-ATPase[15]. Optional, the model is able to simulate glucose in milk by varying p_{55}, which represents the liter of milk produced per hour (see Appendix). In the herein presented simulations no milk production has been included.

4. Results and Discussion

The glucose-insulin model gives insight into dynamics of the glucose metabolism. In the following we present simulation outcomes with the glucose-insulin model for various amounts of food, modeled by varying the variable *DMI*. The first simulation shows results with 100% *DMI*, which is the default condition. In the second experiment we decreased the food to 10% of *DMI*, and in the third experiment we increased the food to 250% of *DMI*. The fraction of glucose and substances available for glucose production $Gluc_{FEED}$ was chosen as 8.54% of *DMI* and is the same in all presented experiments.

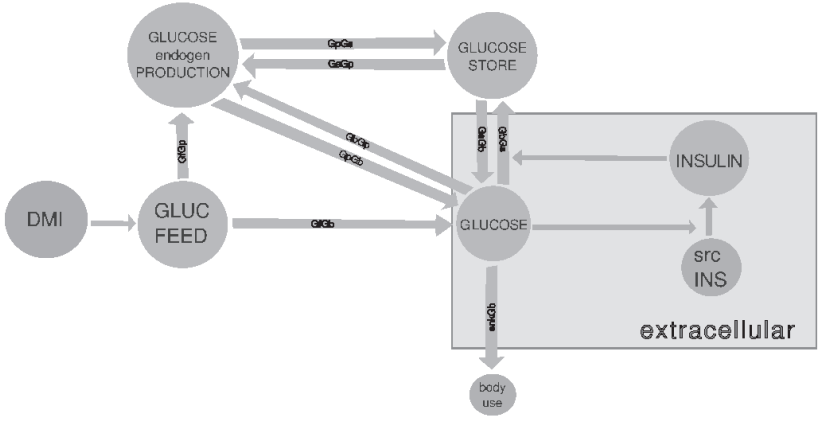

Figure 3. Graphical description of the model for glucose insulin metabolism in the dairy cow.

4.1. *Default condition*

In the default condition the cow ingests 11700 g of food. This amount was given from the study data we used to develop the potassium model (see Section 2). The simulation outcome for the default condition can be seen in Figure 4. The glucose production (a) is dependent on DMI and $Gluc_{FEED}$ (e). The amount of glucose produced by the cow per day is 927 g, and 8.54% of $Gluc_{FEED}$ are resorbed directly from the gastro-intestinal tract as hexose sugar and by-pass starch, here 80 g. Thus, the cow has 1007 g glucose per day available. The use of glucose in the model is 1000 g per day. This is in the expected range of the glucose production and demand per day[17] for a 600 kg non-lactating dairy cow. The storage (b) is filled up to about one half of its filling capacity and the oscillation is very low, as we expect when glucose demand is in the range of production. Glucose in blood (c) is in its physiological range of 0.39 - 0.59 g/l[16]. Insulin in the blood (d) is also in the qualitative range given from the study data (f).

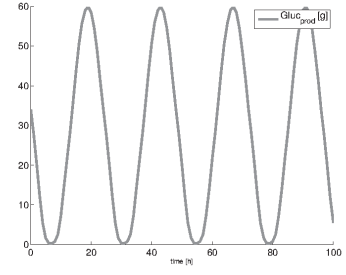

(a) Glucose production

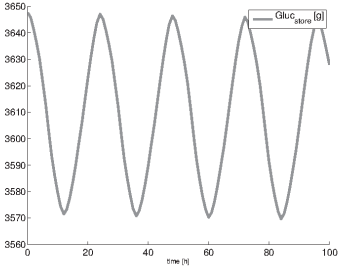

(b) Glucose stored in tissues

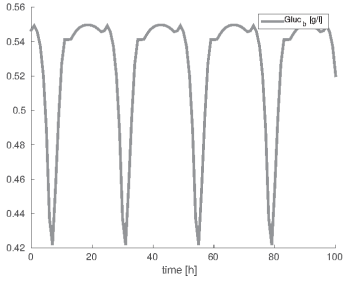

(c) Glucose

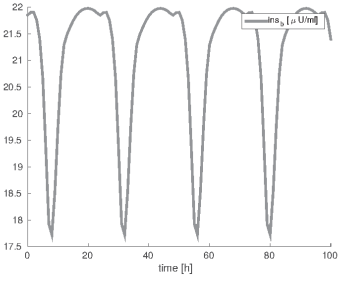

(d) Insulin

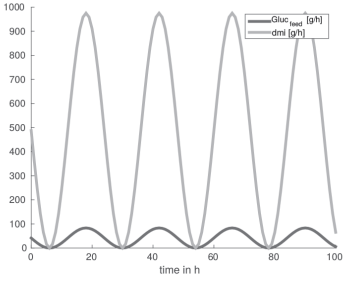

(e) DMI and $Gluc_{FEED}$

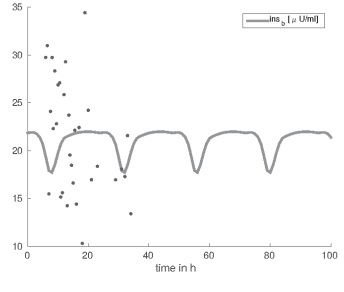

(f) Simulated insulin with data from one cow of the clinical study

Figure 4. Simulation outcome for the components of the glucose-insulin model with 100 % DMI.

4.2. *Decreasing food*

In the following experiment we decreased the *DMI* to 10% of the default condition. Within this, the cow ingests 1170 g of *DMI* per day, which is very little. In Figure 5 we observe that glucose production (a) also decreases, and now only 120 g of glucose are produced per day by the cow. Together with the directly resorbed glucose from the digestive system, the cow has 129 g glucose available per day, while she is using 335 g per day. The storage (b) is filled up to over one half of its maximum capacity at the beginning of the experiment and decreases constantly by the amount the cow is using and which is not available from other sources. After 410 h (around 17 days) of simulation, the glucose stores are nearly empty and no more glucose is available from there. Glucose in blood (c) is in its physiological range of 0.39 - 0.59 g/l[16] as long as there is glucose available from the store, and it drops to very low and clinically critical values when the stores are empty. Insulin in the blood (d) follows the dynamic of glucose and also drops when stores are empty.

4.3. *Increasing food*

In the following experiment we increased the *DMI* to 250% of the default condition. The modelled cow now ingests 29250 g of *DMI* per day. In vivo, this amount of food would suit to a high producing cow. Since our model cow is not producing milk, we suppose that she is doing much exercise, e.g. walking long distances, pregnant. In Figure 6 we can observe the simulation outcome for the components. The glucose production (a) is very high with 2303 g per day. Totally available glucose is 2503 g per day, and the daily use is 2244 g per day. This production and demand are in the expected range for a highly metabolic active cow[17]. The storage (b) is filling up over the simulated period but not reaching the maximum storage capacity, yet. Glucose in blood (c) is in its physiological range of 0.39 - 0.59 g/l[16]. Insulin in the blood (d) follows the dynamics of glucose.

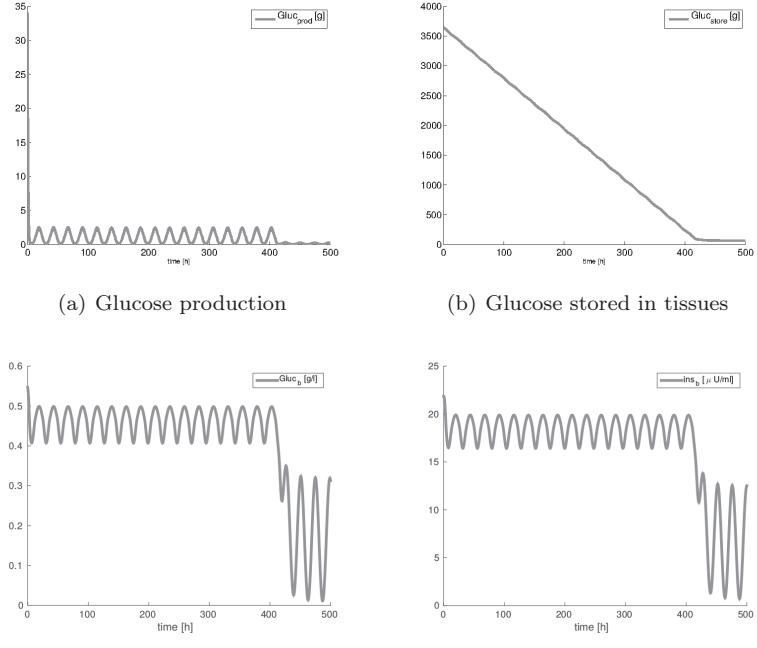

(a) Glucose production

(b) Glucose stored in tissues

(c) Glucose

(d) Insulin

Figure 5. Simulation outcome for the components of the glucose-insulin model with 10 % *DMI*.

5. Conclusion

The herein presented glucose-insulin model is linking the previously developed physiological network models for the bovine estrous cycle and potassium balance to the glucose metabolism in the dairy cow. The model simulates the basic components on a level of organs and functional units. Simulation results qualitatively reproduce literature knowledge, particularly if environmental conditions are varied. Prospectively, we aim to couple the glucose-insulin model with the existing models to explore the interaction of these system.

Especially, we are interested in conducting experiments with interventions frequently performed in veterinary practice, as application of glucocorticoides. Studying the systems behaviour will give new insights on short and long term effects and interactions, without the need for new animal experiments.

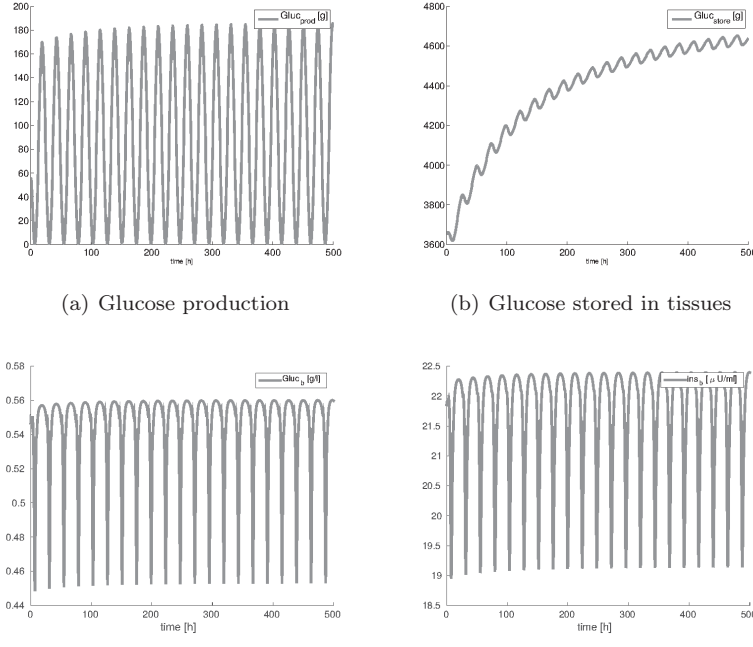

(a) Glucose production

(b) Glucose stored in tissues

(c) Glucose

(d) Insulin

Figure 6. Simulation outcome for the components of the glucose-insulin model with 250 % *DMI*.

Appendix A. Equations

		Unit
DMI	$y_{DMI} = p_{54} \cdot 487.5 \cdot \left((1 - \sin(\frac{\pi \cdot t}{12})\right)$	g/h
$Gluc_{FEED}$	$y_{Gluc_{FEED}} = p_{46} \cdot y_{dmi}$	g/h
$Gluc_{PROD}$	$\frac{d}{dt} y_{Gluc_{PROD}} = GfGp - GpGb - GpGs + GsGp$	g
$Gluc_B$	$\frac{d}{dt}(y_{Gluc_B} \cdot V_{extra}) = GfGb - GbGs + GsGb - SnkGb + GpGb$	g/l
$Gluc_{STOR}$	$\frac{d}{dt} y_{Gluc_{STOR}} = GbGs - GsGb + GpGs - GsGp$	g
$Insulin$	$\frac{d}{dt}(y_{Ins} \cdot V_{extra}) = p_{49} \cdot y_{Gluc_B} - p_{41} \cdot y_{Ins}$	μU/ml

Appendix B. Initial Values for ODEs

$$\begin{aligned} \mathrm{y}_{Gluc_{PROD}}(0) &= 34.0337 \\ \mathrm{y}_{Gluc_B}(0) &= 0.5466 \\ \mathrm{y}_{Gluc_{STOR}}(0) &= 3647.747 \\ \mathrm{y}_{Ins}(0) &= 21.853 \end{aligned}$$

Appendix C. Rates

$GfGp = (1 - p_{48}) \cdot y_{Gluc_{FEED}}$

$GfGb = p_{48} \cdot y_{Gluc_{FEED}}$

$GsGp = p_{60} \cdot H^-(y_{Gluc_{FEED}}, p_{61}, 5) \cdot H^+(y_{Gluc_{STOR}}, p_{35}, 10)$

$GpGb = (p_{39} \cdot y_{Gluc_{PROD}}) \cdot H^-(y_{Gluc_B}, p_{50}, 10)$

$GpGs = p_{51} \cdot y_{Gluc_{PROD}} \cdot H^-(y_{Gluc_{STOR}}, p_{57}, 10) \cdot H^-(p_{55}, p_{62}, 10)$

$SnkGb = H^+(y_{Gluc_B}, p_{58}, 10) \cdot (p_{28} \cdot y_{Gluc_B} + p_{59} \cdot y_{Gluc_{PROD}} \cdot e^{-p_{66} \cdot p_{55}} + p_{55} \cdot p_{47})$

$GsGb = H^+(y_{Gluc_{STOR}}, p_{35}, 10) \cdot (H^-(y_{Gluc_{FEED}}, p_1, 10) \cdot p_{17} \cdot (p_7 - y_{Gluc_B}) + H^+(p_{55}, p_{64}, 10) \cdot p_{63} \cdot H^-(y_{Gluc_B}, p_{65}, 10))$

$GbGs = H^+(y_{Gluc_{FEED}}, p_1, 10) \cdot p_{12} \cdot y_{Gluc_{PROD}} \cdot H^-(y_{Gluc_{STOR}}, p_{57}, 10) \cdot y_{Gluc_B} \cdot y_{Ins} \cdot H^-(p_{55}, p_{36}, 10)$

Appendix D. List of Parameters

Num	Value	Unit	Explanation
p_1	40.4	$\frac{g}{h}$	Threshold for $Gluc_{FEED}$
p_7	0.925	$\frac{g}{l}$	Glucose threshold
p_{12}	0.0105	$\frac{ml \cdot l}{\mu U \cdot h \cdot g}$	Factor for $Gluc_{PROD}$ influencing GsGb rate
p_{17}	16	$\frac{g}{h}$	$Gluc_B$ dependant glucose in GsGb rate
p_{28}	25	$\frac{l}{h}$	Glucose available for metabolic use from $Gluc_B$
p_{35}	100	g	Threshold for $Gluc_{STOR}$
p_{36}	1	$\frac{l}{h}$	Threshold for milk production
p_{39}	30	$\frac{1}{h}$	Fraction of $Gluc_{PROD}$ transported to $Gluc_B$
p_{41}	20	$\frac{l}{hl}$	Factor for insulin clearence
p_{46}	0.0854	-	Fraction of glucose and glucoplastic substances in DMI
p_{47}	72	$\frac{g}{l}$	Glucose in milk
p_{48}	0.08	-	Fraction directly resorbed from $Gluc_{FEED}$
p_{49}	800	$\frac{\mu U \cdot l}{mg \cdot h}$	Scaling factor for $Gluc_B$ influencing insulin production
p_{50}	0.4	$\frac{g}{l}$	Threshold for $Gluc_B$
p_{51}	0.1	$\frac{1}{h}$	Fraction of $Gluc_{PROD}$ transported to $Gluc_{STOR}$
p_{54}	1	$\frac{g}{h}$	Feeding amount as fraction of DMI
p_{55}	0	$\frac{l}{h}$	Milk produced
p_{57}	3800	g	Threshold for $Gluc_{STOR}$
p_{58}	0.01	$\frac{g}{l}$	Threshold for $Gluc_B$
p_{59}	1	$\frac{1}{h}$	Fraction of $Gluc_{PROD}$ for metabolic use
p_{60}	2	$\frac{g}{h}$	Basic glucose rate from $Gluc_{STOR}$ to $Gluc_{PROD}$
p_{61}	5	$\frac{g}{h}$	Threshold for $Gluc_{FEED}$
p_{62}	1	$\frac{l}{h}$	Threshold for milk production
p_{63}	800	$\frac{g}{h}$	Scaling factor for glucose in milk production
p_{64}	0.2	$\frac{l}{h}$	Threshold for milk production
p_{65}	0.3	$\frac{g}{l}$	Threshold for $Gluc_B$ in milk production
p_{66}	1.4	$\frac{h}{l}$	Exponent for milk production

References

1. H. M. T. Boer, C. Stötzel, S. Röblitz, P. Deuflhard, R. F. Veerkamp and H. Woelders, *J. Theor. Biol.* **278**, 20–31 (2011).
2. C. Stötzel, J. Plöntzke, W. Heuwieser and S. Röblitz, *Theriogenology* **78(7)**, 1415–1428 (2012).

3. H. M. T. Boer, S. Röblitz, C. Stötzel, R. F. Veerkamp, B. Kemp and H. Woelders, *Journal of Dairy Science* **94(12)**, 5987–6000 (2011).
4. BovCycle in SBML *http://www.ebi.ac.uk/biomodels-main/BIOMD0000000481.*
5. H. M. T. Boer, S. Röblitz, C. Stötzel, R. F. Veerkamp, B. Kemp and H. Woelders, *J. Dairy Sci.* **94(12)**, 5987–6000 (2011).
6. J. Plöntzke, M. Berg, A. Olany, S. Leonhard-Marek, K. Müller and S. Röblitz, *ZIB-Report* **13–09** (2013).
7. C. Stötzel, R. Ehrig, H. M. T. Boer, J. Plöntzke and S. Röblitz, *BIOMAT - Proceedings of the 14th International Symposium on Mathematical and Computational Biology* (2015).
8. T. Dierkes, S. Röblitz, M. Wade and P. Deuflhard, *CoRR - Computing Research Repository* **abs/1303.4928**, (2013).
9. L. M. Chagas, J. J. Bass, D. Blache, C. R. Burke, J. K. Kay, D. R. Lindsay, M. C. Lucy, G. B. Martin, S. Meier, F. M. Rhodes, *et al.*, *Journal of Dairy Science* **90(9)**, (2007).
10. M. Stangassinger, *G. Physiologie der Haustiere, Enke in Hippokrates Verlag*, 453–466 (2005).
11. G. Breves and S. Leonhard-Marek, *Physiologie der Haustiere, Enke in Hippokrates Verlag*, 357–366 (2005).
12. M. G. Diskin, D. R. Mackey, J. F. Roche, J. M. Sreenan, *Animal Reproduction Science* **78**, (2003).
13. R. P. Brockman, *Quantitative aspects of ruminant digestion and metabolism*, 249–265 (1993).
14. R. Pfuhl, O. Bellmann, C. Kuhn, F. Teuscher, K. Ender, J. Wegner, *Archiv für Tierzucht* **50(1)**, (2007).
15. J. H. Youn, A. A. McDonough, *Annual review of physiology* **71**, (2009).
16. *http://www.vetmed.uni-leipzig.de/ik/wmedizin/labor/diagnostik/referenzwerte/rind.htm* (retrieved 10.07.2015).
17. C. K. Reynolds, *Florida ruminant nutrition symposium*, 143–154 (2005).
18. P. Christinaz, H. J. Schatzmann, *The Journal of Physiology* **224(2)**, (1972).
19. U. Nowak, L. Weimann, *http://www.zib.de/weimann/CodeLib/de/nonlin.html* (retrieved 15.07.2015).
20. *http://www.celldesigner.org* (retrieved 15.07.2015).
21. M. Hucka, A. Finney, H. M. Sauro, H. Bolouri, J. C. Doyle, H. Kitano, *et al.*, *Bioinformatics* **19**, (2003).
22. O. Sejersted, G. Sjøgaard, *Physiological Reviews* **80(4)**, (2000).
23. J. M. Berg, J. L. Tymoczko, L. Stryer, *Biochemistry, WH Freeman*, **5th edition** Chapter 21, Glycogen Metabolism, (2002).

BIOGRAPHER: VISUALIZATION OF GRAPH THEORETICAL PATTERNS, MEASUREMENTS, AND ANALYSIS IN MATHEMATICAL BIOLOGY

RAMA VISWANATHAN*

(Emeritus) Departments of Chemistry, and Mathematics and Computer Science
Beloit College, 700 College Street,
Beloit, WI 53511, U.S.A.

SIJIA LIANG, YANG YANG

Department of Statistics, University of Minnesota Twin Cities
224 Church Street SE, Room 313
Minneapolis, MN 55455, U.S.A.

JOHN R. JUNGCK

Departments of Biological Sciences and Mathematical Sciences
University of Delaware
221 Academy Street ISE Lab 402,
Newark, DE 19716, U.S.A.

*Work partially supported by NSF CCLI Grant DUE-0633651.

Graph theory provides mathematical insight into many areas of contemporary biology such as genomics, metabolonomics, ecology, evolution, biochemistry, etc. because it provides a highly visual and easily comprehensible representation of patterns, processes, and products for testing causal hypotheses. Thus, there is an enormous need for graph theoretic visualization tools that make it easy for biologists to enter data, interact with existing data bases, and generate a variety of different layouts of graphs. BioGrapher is a versatile Excel front-end for the Graphviz graphical visualization library and software package that we have contributed to the Biological Excel Simulations and Tools for Exploratory, Experiential Mathematics (ESTEEM) collection, available online at www.bioquest.org/ESTEEM. While a number of excellent stand-alone applications that incorporate Graphviz for different platforms and operating systems are available, BioGrapher is unique in that, in keeping with the best practices standards of the ESTEEM suite of which it is a part, it uses the standard and ubiquitous Excel environment as the front-end and graphical user interface. It implements the visualization of graphs (nodes and edges) that are specified as standard adjacency matrices using the Excel spreadsheet paradigm of rows and columns, with connections between nodes represented by a non-zero (non-empty) cell value for the appropriate row and column. A complete Visual Basic for Applications (VBA) Excel interface has been programmed and implemented as an additional custom menu bar menu, with enough functionality for the user to invoke many graphical drawing and manipulation routines. Herein we present details of the Excel app (available for both MacOS X and MS Windows 7/8) and its applications in problem solving in mathematical biology. Specifically, we present details for food webs as canonical examples of biological networks that may display the properties and features associated with small world networks. An algorithmic approach using graph theory, BioGrapher, and the complementary JavaBENZER app for generation of interval graphs is demonstrated.

1. Introduction

Graph theory has been used as a powerful mathematical tool to represent, characterize the structure, and study the dynamics of many systems of interest to biologists. In particular, over the past thirty years, the techniques developed to model, simulate, and visualize networks in computer science and information theory have become important and ubiquitous mathematical tools for research in systems biology [1, 2]. Other areas of biology, including environmental biology [3–5], genomics and bioinformatics [6], and epidemiology [7], have also witnessed the successful application of these techniques. Thus, the nature and applications of graph theory in biology are well documented in books [8] and reviews [9]. A relatively recent and very important development in the application of network theory in biology is the formulation and analysis of biological systems from the standpoint of small world networks, first formulated by Watts and Strogatz [10] in 1998. This was later popularized by Watts [11] and others, e.g., Hayes [12], using the colloquial term "six degrees of separation" to describe such networks,

which demonstrate remarkable scale-free properties and have been shown to be an essential signature of many biological systems. The theoretical framework for studying small world biological networks was first developed in a landmark paper by Barbasi and Albert [13] in 1999. Since then small world network theory has become a key technique used by the mathematical and theoretical biologist to explore the structure (clustering, neighborhoods) and dynamics of biological networks, including connectivity, feedback, oscillations, as well as the interplay between structure and dynamics. A large number of groundbreaking and elegant studies have been reported, including studies of the brain as a complex network [14], and numerous studies of cellular networks [15].

The authors of this work constitute an inter-disciplinary team of faculty (RVchemical physics and computational science, JRJmathematical biology and computational science) and students (most recently SL and YY, math and biology majors) at Beloit College, who have been researching the properties of biological and other networks and visualizing them over the past decade [16, 17], in particular in an effort to enhance the pedagogy and curriculum of computational science and mathematical biology courses and programs at the undergraduate level. One of the problems that we encountered early on was the lack of inexpensive, ubiquitous and easy to use tools that were specifically designed to study the properties (described in a separate section below) and visualize small world networks. Sophisticated graph theoretical functions and macros available in the standard mathematical software packages such as Mathematica [18] and MATLAB [19] as well as dedicated commercially available packages like Tom Sawyer [20] can be used, but data organization, input and customization requires computational software expertise, which often is not easily available or accessible to biologists, who may be more interested in quickly and easily extracting key parameters of the systems being studied to understand their scaling and small world properties.

Therefore, in this paper, we describe our use of an Excel app, BioGrapher [16], as a front-end for the sophisticated and powerful open access software libraries for network visualization available in the Graphviz [21] software suite. Graphviz was developed by experts at AT&T Bell Labs, a pioneering R&D organization with deep research interests in networks because they have had to work with and understand the structure and dynamics of one of the largest man-made networks, namely the phone network. We have combined the visualization capabilities of Graphviz with the powerful built-in analytical capabilities of Excel and further customized and

modified these capabilities specifically for small world network analysis. This combination was achieved through the use of custom Visual Basic for Applications (VBA) code embedded as macros and which can be invoked by users via a set of menus and menu items added to the standard Excel menu bar, thus providing a convenient and easy to use app-like Graphical User Interface (GUI) for the user. BioGrapher has been successfully used in teaching and research for almost a decade now. In the sections that follow, we describe the basic features of small world networks and the approach that we used in developing the software to characterize those features as well as to visualize the results. We also present details and results of research on biological networks, specifically food webs, carried out using two of our in-house software tools, BioGrapher and JavaBENZER, both of which are freely available for download in the public domain as part of the ESTEEM [22] set of Excel tools.

2. Overview of Small World Networks

Standard abstract graph theoretical representations of networks use the terms *vertices* and *edges* to refer to the corresponding physical entities in computer and biological networks, namely nodes and links respectively. We use the standard mathematical terminology through the remainder of our paper, but will refer to nodes and links where appropriate to highlight the properties of real-world networks.

We first summarize the unique properties that help us identify small world networks in terms of the formulation by Watts [23]. The key properties of small world networks, namely clustering coefficient k and diameter d, are in between those of perfectly ordered networks (clustering coefficient $k \rightarrow 1$) and completely random networks($k \rightarrow 0$). The diameter d is relatively small and representative of a sparse network. In general, small world networks exhibit $d \approx logN$, where N is the number of vertices. Finally, small world networks are scale-free and exhibit an interesting power-law degree dependence [13] that accounts for their ubiquity in nature, presumably because of efficient information retrieval and transfer through an optimum number of nodes and edges.

Some of the interesting biological systems that have been identified as small world networks include: (1) brain circuitry of *C. elegans* [24]; (2) metabolic pathways [25, 26]; (3) food webs [27]; and (4) genomic circuits [28]. A beautiful recent summary [29] discusses these small worlds of diverse biological systems as examples of evolutionary morphospaces. Given the

diversity and importance of small world networks in biology, we believe that their input, analysis, and visualization in BioGrapher and JavaBENZER provides an easily workable approach for many biologists to explore their properties.

3. The Biographer App

We use the screen shot below (Figure 1) to describe a few of the properties of the Excel app, compatible with both Macintosh and Windows PC Desktop Operating Systems.

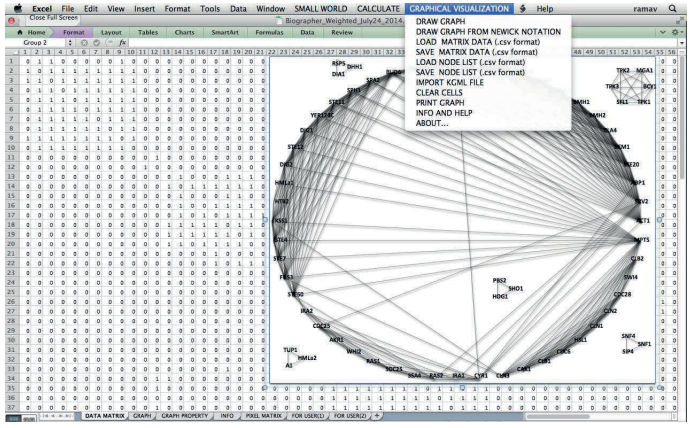

Figure 1. A screen shot of BioGrapher circular graph layout format output for yeast gene expression data [30].

The data representation for a network of interest with N edges corresponds to a $N \times N$ adjacency matrix with ones and zeroes (if unweighted) or appropriate weights for vertices with weights. Both directed and undirected graphs can be represented. Such data matrices can be conveniently entered or imported into Excel since the representation corresponds to the Excel paradigm of a 'spreadsheet' with rows and columns. The screen capture above shows representative data and the results of the visualization of portions of the yeast cellular network, based on data reported in a beautiful study by Rives and Galitsky [30]. Note that all computations of properties, manipulations, and visualizations of the adjacency matrix/graph are accomplished through custom pull down menus added to the standard Excel menu bar (Figure 2).

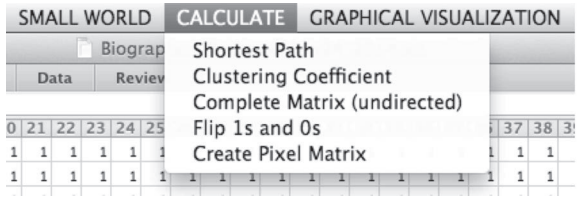

Figure 2. Several features of the BioGrapher suite of tools include the ability to find the shortest paths between nodes in a graph, the clustering coefficient, and the ability to produce a complementary graph by flipping the ones and zeros. These are available from the drop down menu shown above.

The CALCULATE menu computes small world properties, including shortest paths (from which the diameter is also computed and displayed with the results) and the clustering coefficient. Log-Log plots of the degree vs. nearest neighbor count are also displayed when the 'Clustering Coefficient' menu item is selected.

The SMALL WORLD menu permits simulations of 'model' graphs, including Watt's beta graphs [23] and the Barbasi-Albert Preferential Attachment Model [13], to generate comparable graphs with the same number of vertices and edges. The GRAPHICAL VISUALIZATION menu includes a DRAW GRAPH menu item, which, when selected, displays a dialog box with a variety of graphical layout options (Figure 3) that invoke the appropriate Graphviz layout libraries [21]. Other display properties of the graph can also be conveniently specified via the dialog box.

A final feature to be noted in the options available for visualizing networks (Figure 3) is the choice of producing a weighted graph. An especially nice example of visualization using the various options is the network graph that we generated from quantitative data on a quorum-sensing biological circuit [31]. We re-represent their microarray data as a weighted adjacency matrix in Table 2 to show that the expression of several genes involved in chemotaxis and motility are altered in the luxO mutant as a network visualization in Figure 4.

Thus, the Excel BioGrapher app [16] provides a versatile and convenient way of using the powerful GraphViz suite of visualization libraries [21], combining the visualizations with analytical results based on Excel computations. It should be emphasized again that the data input for both of these operations is the adjacency matrix representation of the graph.

We now proceed to discuss some specifics for the use and application of BioGrapher and JavaBENZER in researching the properties of biological

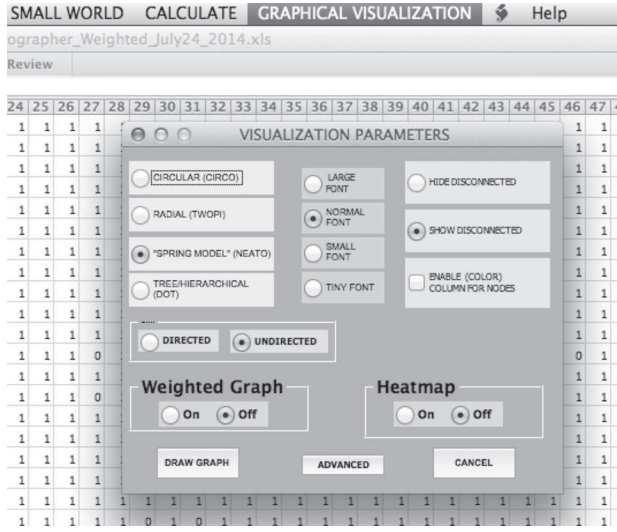

Figure 3. We note that there are flexible visualization options available in BioGrapher. We can display output graphs in any one of four layouts, based on Graphviz circular, radial, spring, and (where applicable) tree algorithms [21], by simply selecting the appropriate button.

Table 1. Data matrix for quorum-sensing biological circuit [31]. The matrix elements in the 10×10 matrix refer to a scaled quantitative expression amount.

Gene#	1	2	3	4	5	6	7	8	9	10
1	0	1	2	3	4	5	9	7	8	2
2	1	0	6	7	8	1	10	8	4	1
3	2	6	0	9	10	2	3	5	2	4
4	3	7	9	0	3	3	8	7	2	10
5	4	8	10	3	0	4	6	4	1	6
6	5	1	2	3	4	0	5	7	6	7
7	9	10	3	8	6	5	0	5	8	9
8	7	8	5	7	4	7	5	0	10	3
9	8	4	2	2	1	6	8	10	0	2
10	2	1	4	10	6	7	9	3	2	0

networks, using data readily available in the literature.

4. Food Webs

Food webs can be thought of as many food chains all linked together. A web contains a set of organisms in a single habitat or a composite of several

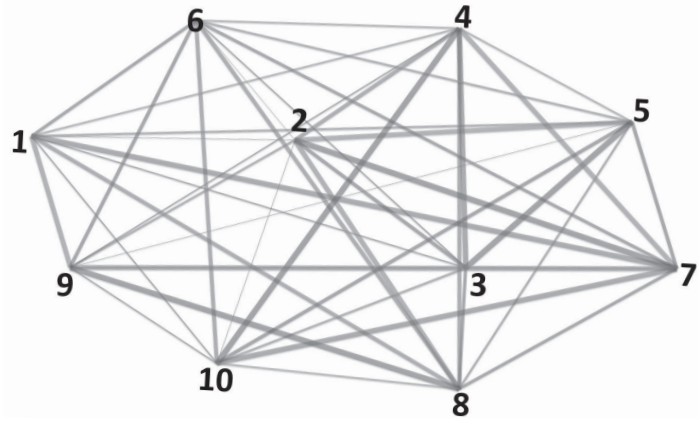

Figure 4. A weighted network graph representation of the quorum-sensing biological circuit in Vibrio cholera, based on raw data [31] in Table 1. The weights show that "the expression of several genes involved in chemotaxis and motility are altered in the luxO mutant." [31] The weights range from 1 (e.g., for 1–2, 4–9) to 10 (e.g., 3–5, 2–7). Note that highly expressed genes maximal clique size is only two and these cliques are not always contiguous. However, these cliques are always within one edge of one another.

habitats, and describes their eating relationships within the set. A community food web is obtained by picking within a habitat or set of habitats, a set of organisms on the basis of taxonomy, size, location, or other criteria, without prior regard to the eating relations among the organisms [32]. In a food web, many producers and consumers (herbivores, carnivores, and omnivores) interact and are interrelated. Even a simplified food web can show a complicated network of trophic relationships. Diets vary significantly between ecological communities, and this influences their organization. The minimum number of variables required to represent the overlaps among consumers' diets is called the dimension of the trophic niche space. For dimensions greater than one, a single variable like food size alone is not sufficient to describe the overlap [33].

A community food web can be represented as a directed graph (Figure 5) or as an adjacency matrix (Table 2). The vertices of the directed graph represent species in the web. There exists a directed edge from vertex a to vertex b if and only if species b feeds on species a. For example, for the eight-species food web shown in Figure 5, by examining the directed edge from mice to snakes we can determine that snakes feed on mice. In general, if N is the total number of predators and M is the total number of prey species., then the adjacency matrix A of the food web, an $N \times M$ matrix,

is a predator-prey matrix. If the element in A_{ij} in row i and column j equals 1 then the species in row i is eaten by the species in column j. If the element is 0, then the species in the row is not eaten by the species in the column. Since the food web directed graph and the food web predator-prey (adjacency) matrix describe the same eating relation, we use the term 'food web' to refer to the relation regardless of whether the web is represented by a directed graph or a matrix of 1's and 0's.

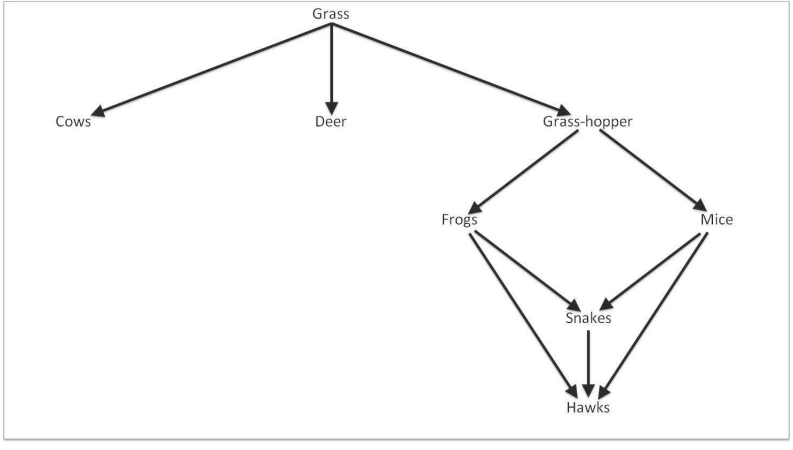

Figure 5. A food web represented as a directed graph and visualized using BioGrapher. This food web contains 8 species.

Table 2. An adjacency Matrix displaying Predators vs. Prey. Columns represent predators and rows represent prey. This is the same food web represented in Figure 5. The eating relationship of a predator eating prey can be found by looking a predator column. If the predator eats the prey in a specific row then that matrix element is 1.

	Cows	Deer	Grass-hopper	Frogs	Mice	Snakes	Hawks
Grass	1	1	1	0	0	0	0
Grass-hopper	0	0	0	1	1	0	0
Frogs	0	0	0	0	0	1	1
Mice	0	0	0	0	0	1	1
Snakes	0	0	0	0	0	0	1

Food webs include information about the number of trophic dimensions in the niches of species in a community. If two species eat a common food species, then their niches must overlap along the trophic dimensions.

Thus, a symmetric $N \times N$ niche overlap matrix (Table 3) can describe the overlaps among the trophic niches, with predator overlap for a common prey represented by a matrix element 1. If there is no overlap, then the element is a 0. The overlap matrix is symmetric with respect to its main diagonal (all 1's) and the number of niche overlaps is equal to the number of matrix elements that are 1's above the main diagonal.

Table 3. A Niche Overlap Matrix (Predators vs. Predators) displaying the niche overlaps of the food web example from Table 2 and Figure 5. This matrix is symmetric along the main diagonal. The matrix element is a 1 in the matrix if two predators have some kind of prey in common.

	Cows	Deer	Grass-hoppers	Frogs	Mice	Snakes	Hawks
Cows	1	1	1	0	0	0	0
Deer	1	1	1	0	0	0	0
Grass-hoppers	1	1	1	0	0	0	0
Frogs	0	0	0	1	1	0	0
Mice	0	0	0	1	1	0	0
Snakes	0	0	0	0	0	1	1
Hawks	0	0	0	0	0	1	1

If two kinds of predators both eat the same prey species, then the niches of these two predators must overlap along some trophic dimension. When these dietary overlaps among consumers in a community can be described by the overlaps among intervals of a single variable, the community web is an interval web. If intervals of more than one variable are required to describe the dietary overlaps among consumers in a community, the web is non-interval. A food web is interval, and its trophic niche overlaps can be represented in a one-dimensional niche space, when the web's overlap matrix is the adjacency matrix corresponding to an interval graph. An interval graph is the intersection graph of a set of intervals of the real line. It must be noted that not every conceivable food web is interval or has niche overlaps that can be represented in one dimension. The graph theoretical properties of food webs outlined above are based on the detailed definitions and descriptions in the definitive works by Cohen and collaborators [32,33].

Based on the application of these definitions to real data, it has been found that, within similar physical and temporal habitats, the overlaps among niches in terms of their trophic feeding dimensions can be represented in a one-dimensional space far more often than expected by chance alone. If a one-dimensional niche space can represent trophic niche overlaps in a single habitat, the single dimension identified in one community may

not be the same as in another [33]. Thus, it is important to understand interval graphs and the different techniques for using food webs to gain information about the dimensionality of a niche space.

5. Interval Graphs

Interval graphs have been intensively studied, due to their central role in many applications. They arise in many practical problems [17] that require the construction of a time line where each particular event or phenomenon corresponds to an interval representing its duration. Among the applications are planning, scheduling, archaeology, time-based sequencing and reasoning, medical diagnosis, and circuit design. There are also applications in genetics and behavioral psychology that do not involve time sequences [34].

Interval graphs arose in connection with a problem in genetics called Benzer's problem. Classically, geneticists have treated the chromosomes as a linear arrangement of genes. Benzer was interested in whether the same was true for the fine structure inside the gene [34]. The Benzer model deals with the conditions under which two subsets of the fine structure inside a gene overlap, on the basis of mutation data. The overlap information is consistent with the hypothesis that the fine structure inside the gene is linear and can be defined by an interval graph [35, 36].

A graph G is called an interval graph if there is a one-to-one correspondence between the vertices of G and a collection of intervals on the line so that two vertices of G are adjacent when the corresponding intervals overlap. Figure 6 displays a simple graph G and its interval representation.

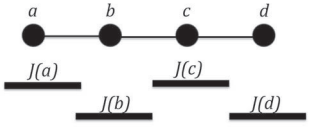

Figure 6. A simple graph G, and its representation as an interval graph.

However, not every graph is an interval graph. Consider the circuit of length 4, Z_4, with $V(Z_4) = \{u, v, w, x\}$ and $E(Z_4) = \{uv, ux, vw, wx\}$ (Figure 7(a)). Z_4 is not an interval graph, but can be represented (Figure 7(b)) as a circular arc graph [37, 38].

We now discuss the concepts of transitivity and complementary graphs. Given that the orientation of a graph G refers to the assignment of direc-

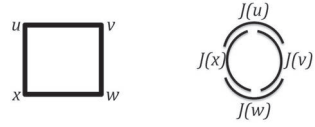

Figure 7. (a) Graph Z_4; (b) Z_4, represented as a circular arc graph.

tion to each and every edge in G^c, an orientation of G^c converts G into a directed graph. A transitive graph is a graph whose corresponding relation is transitive, i.e., if there is an edge from vertex x to vertex y and an edge from vertex y to vertex z, then there is also an edge from vertex x to vertex z. This is illustrated in Figure 8 below.

Figure 8. A graph G represented without and with transitive orientation.

The complementary graph of the graph $G^c = (V, E^c)$, is defined to be $G = (V, E)$ with the same set of vertices, but now with edges between exactly those pairs of vertices not linked in G. In general, if a graph has more pairs of vertices joined by edges than pairs not joined by edges, then its complement will have fewer edges and thus will probably be simpler to analyze. Adding graph G and graph G^c results in joining every pair of vertices with an edge, resulting in a complete graph. Figures 9(a–c) show a graph G, its complementary graph G^c, and the corresponding complete graph $G + G^c$, respectively.

Figure 9. Figure 9a. A graph G; Figure9b. G's complementary graph G^c; Figure 9c. Complete graph $G + G^c$.

Using the background information and definitions above, it is possible to determine whether a given graph is an interval graph or not based on the theorem [37, 38] that a graph G is an interval graph if and only if it

satisfies the conditions (a) Z_4 is not a generated subgraph of G, and (b) G^c is transitively orientable.

We illustrate the theorem using an example, a graph G with six nodes labeled a through f, as shown in Figure 10(a) below. Note that a is a source with outgoing degree 3 and f is a sink with incoming degree 3. We already know that Z_4 is not an interval graph and consequently, any graph with an induced Z_4 subgraph cannot be an interval graph either. By examining the graph, one can see that G does not contain any Z_4's. To satisfy the next part of the theorem, G^c (Figure 10(b) below) must be transitively oriented so that an ordering of the intervals can be found. One can determine that G^c is transitive by starting at any vertex edge directed away from a. The next thing we do is look at the other vertices of the graph. The edge from e to b must be directed from b to e because there is no edge that connects a to b, the principal of transitivity. Similarly the edge that connects f to b must be directed from b to f for the same reason, there is no edge from e to f. The last edge to give orientation to is the edge connecting f to d. a is not connected to d and b is not connected to d. Therefore the edge in question must be directed from d to f. This results in the transitive orientation of G^c (Figure 10(c)) and tells us that G can be represented as an interval graph.

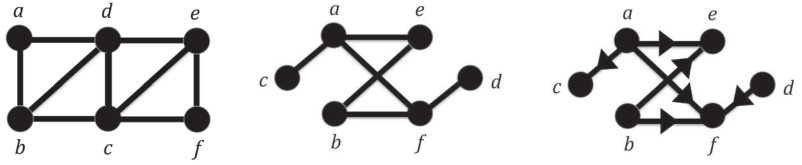

(a) Graph G (b) Graph G^c (c) Transitive orientation of G^c

Figure 10. Three forms of G.

6. Generation of Interval Graphs: A Graph Theoretical Algorithm

Several algorithms exist for solving interval graph problems. Here we use the robust algorithm described by Jungck *et al.* [39] and dependent on the theorems of Gilmore and Hoffman [37], and Fulkerson and Gross [38], as implemented using our software. Two other algorithms that readers may

want to consider were developed by Booth and Leuker [40] and Habib *et al.* [41].

The easiest way to prove that a graph is an interval graph is to express an interval assignment. When a food web describes the biological system of interest, he first step is to convert the food web into the competition graph G, which is undirected. Again, species are represented as vertices and edges represent a feeding relation. We then construct the complement graph G^c to the competition graph. Next, we attempt to determine if the interval graph theorem stated in the previous section is valid. If graph G does not contain any Z_4's then we need to determine if G^c can be made transitive.

If we assume the interval theorem described in the previous section holds true for graph G above (Figure 10(a)), we can enumerate and examine the set of maximal cliques of G and introduce a linear ordering on it. A clique is defined as a subset S of vertices V where every pair of vertices in S is joined by at least one edge. Thus, a clique of a graph G is a maximal subset of adjacent vertices in G. A clique itself is maximal if it is not contained in a larger clique.

There are 19 cliques for graph G, specifically 1:$\{a\}$; 2:$\{b\}$; 3:$\{c\}$; 4:$\{d\}$; 5:$\{e\}$; 6:$\{f\}$; 7:$\{a, b\}$; 8:$\{a, d\}$; 9:$\{b, c\}$; 10:$\{b, d\}$; 11:$\{c, d\}$; 12:$\{c, e\}$; 13:$\{c, f\}$; 14:$\{d, e\}$; 15:$\{e, f\}$; 16:$A\{a, b, d\}$; 17:$B\{b, c, d\}$; 18:$C\{c, d, e\}$; and 19:$D\{c, e, f\}$, with A, B, C, and D being maximal. The subgraph generated by the vertex a is a clique. It is not maximal, because it is contained in the larger clique generated by vertices a and b. This in turn is also not maximal because it is contained in the clique $\{a, b, d\}$, which is the maximal clique A.

Suppose the graph G does not contain any Z_4's and suppose that G^c has transitive orientation. Let C denote the collection of maximal cliques in G. One can build a new graph G^q, where $V(Gq) = C$ and there is an edge between vertices if the maximal cliques are distinct from each other. This makes Gq a complete graph. Next, the orientation of Gq is found by applying the transitive orientation of G^c. The order of the intervals can be found by finding a Hamiltonian path through the vertices of Gq. A Hamiltonian path is a path through every vertex of a graph, with the constraint that a vertex may only appear once in the path, i.e., there cannot be any circuits. The Hamiltonian path indicates the order of the intervals. We are now able to construct the interval graph equivalent to the competition graph G. One simply constructs a line with the maximal cliques ordered in the same sequence as their Hamiltonian path. Then each

vertex will overlap those maximal cliques of which it is a vertex. This procedure is now illustrated for graph G and also visualized in Figure 11.

The maximal cliques for the food web represented by graph G contain the following species: $C_A(G) = \{a, b, d\}$, $C_B(G) = \{b, c, d\}$, $C_C(G) = \{c, d, e\}$, and $C_D(G) = \{c, e, f\}$. The cliques are represented in the clique graph G (Figure 10(a)) and the transitive orientation of G^c (Figure 10(b)) has been applied, resulting in the graph shown in Figure 10(c). The Hamiltonian path through the four maximal clique vertices is A, B, C, D. All one has left to do is construct the intervals. The result is shown visually by the interval graph of Figure 11. This interval graph indicates that the feeding relationship between species is sufficient to describe the corresponding biological system, namely the food web. Clearly, we can also gain insights on the niche overlaps by looking at the intervals in the graph. For instance, we can see that not only does species c overlap with species d and species e from clique C but it also overlaps with species f from clique D.

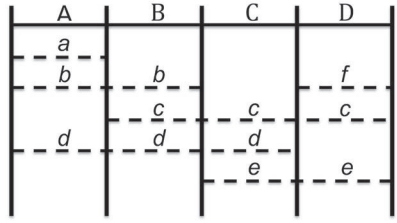

Figure 11. Interval graph of Graph G in Figure 10(a). The upper case letters refer to the four maximal cliques, which are ordered along the Hamiltonian path $A \to B \to C \to D$.

Food webs have been traditionally illustrated as hand-drawn diagrams such that species at various trophic levels have meaningful and readable names, without much attention being paid to the mathematical characteristics of the web per se. However, as we have outlined above, Cohen and his collaborators [32, 33] have demonstrated that many food webs can be analyzed and understood as one-dimensional groups of their community structure, i.e., as interval graphssee [17, 39] and references therein. Below we demonstrate how one such food web [42] that apparently has not been analyzed in this fashion can be illustrated with BioGrapher. Visualizations such as this can be of tremendous help to biologists in seeing patterns in their data in a variety of rich fashions that highlight both qualitative and quantitative relationships. We start by representing the complex food web system for which data are available in the literature [42] by a predator/prey

matrix that scores whether a predator species consumes a prey species or not (Figure 12).

Predator/Prey Matrix

	1	2	3	4	5	6	7	8	9	10	11	12	13	14	15	16	17	18	19	20	21
1. Primary Production																1					
2. Pike				1	1										1						
3. Wels					1										1						
4. Eal		1				1	1	1						1				1	1	1	
5.Crucian carp		1	1			1	1	1											1	1	
6. Detritus				1	1		1		1	1	1	1	1		1						
7. Molluscs				1	1	1			1	1	1	1	1		1						
8. Chironomids				1	1				1	1	1	1	1	1	1	1					
9. Goby						1	1	1								1		1	1	1	1
10. Roach						1	1	1								1			1	1	1
11. White bream						1	1	1								1			1	1	1
12. Rudd						1	1	1								1			1	1	1
13. Bream I						1	1	1								1			1	1	1
14. Bleak				1				1								1	1	1	1	1	1
15. Bream II		1	1			1	1	1												1	1
16. Zooplankton	1							1	1	1	1	1	1	1	1		1				
17. Razor fish														1		1					1
18. Mysids				1					1					1					1		
19. Periphyton				1	1				1	1	1	1	1	1				1		1	
20. Amphipods				1	1				1	1	1	1	1	1	1				1		
21. Pikeperch									1	1	1	1	1	1	1		1				

Figure 12. A predator/prey matrix based on data published by Biro [42].

In order to understand competition of predators for a common prey, we convert the asymmetric predator/prey matrix to a square symmetrical predator/predator matrix, as shown in Figure 13 below:

The predator/predator matrix of Figure 13 is visualized below using BioGrapher (Figure 14(a)) and the complementary software package JavaBENZER [22, 43]. The spring model-based graphical visualization using BioGrapher clearly shows the five maximal cliques, but they are nested since edge-crossing avoidance is not complete. This may be compared to the JavaBENZER representations (Figures 14(b) and (c)). In Figure 14(b), the predator/predator matrix (Figure 13) has been symmetrically rearranged to achieve Shkurba form [35] and the five maximal cliques are easier to distinguish as blocks. Figure 14(c) is the interval graph produced using JavaBENZER of the niches in the food web described by the predator/predator adjacency matrix in Figure 13. The predators are represented in rows in the same vertical order that produces the Shkurba form in the symmetrical predator/predator matrix, shown in Figure 14(b). The columns are the corresponding maximal cliques that appear along the diagonal in Figure 14(b).

In ecology, three of the common diagrams used to represent community

Predator/Predator Matrix

	2	3	4	5	7	8	9	10	11	12	13	14	15	16	17	18	20	21
2. Pike	1	1																1
3. Wels	1	1																1
4. Eel			1	1	1	1	1	1	1	1	1	1	1		1	1	1	1
5.Crucian carp			1	1	1	1	1	1	1	1	1	1	1		1	1	1	
7. Molluscs			1	1	1	1							1				1	
8. Chironomids			1	1	1	1							1				1	
9. Goby			1	1			1	1	1	1	1	1	1		1	1	1	
10. Roach			1	1			1	1	1	1	1	1	1		1	1	1	
11. White bream			1	1			1	1	1	1	1	1	1		1	1	1	
12. Rudd			1	1			1	1	1	1	1	1	1		1	1	1	
13. Bream I			1	1			1	1	1	1	1	1	1		1	1	1	
14. Bleak			1	1			1	1	1	1	1	1	1		1	1	1	
15. Bream II			1	1	1	1	1	1	1	1	1	1	1		1	1	1	
16. Zooplankton														1				
17. Razor fish			1	1			1	1	1	1	1	1	1		1	1	1	1
18. Mysids			1	1			1	1	1	1	1	1	1		1	1	1	
20. Amphipods			1	1	1	1	1	1	1	1	1	1	1		1	1	1	
21. Pikeperch	1	1	1												1			1

Figure 13. Symmetrical predator/predator matrix from Figure 12. "1" represents competition between the two (appropriate row and column) species. Data source: Biro [42].

structure are: (1) food webs, (2) trophic levels, and (3) energy pyramids. Each of these captures some element of biomass productivity or energy flux between trophic levels. However, it is challenging to precisely and scientifically display the complexity of relationships among species and attempt to find answers to questions such as: What is the niche space of each species? How much do predators compete for particular prey? What is the impact of the removal of a species in a food web or energy pyramid? Mathematically, visualizing the relationship of predators and prey by using graph theory-based BioGrapher software has provided us with additional insights that may help answer some of these questions about ecological communities. By utilizing JavaBENZER, the predator-prey matrix is transformed into a symmetrical predator-predator matrix and then by applying the theory of partially ordered sets, the predator-predator matrix is transformed into Shkurba format [35] in order to produce an interval graph wherein each interval is a maximal clique that identifies a niche space. In a forthcoming paper, we plan to describe how we imported quantitative biomass data following the structure of the niche space and trophic levels of a specific community into Mathematica [18] to re-represent the food web as a three-dimensional bar chart. By adding biomass and energy analysis, we have constructed a three dimensional graph where we can plot niche space,

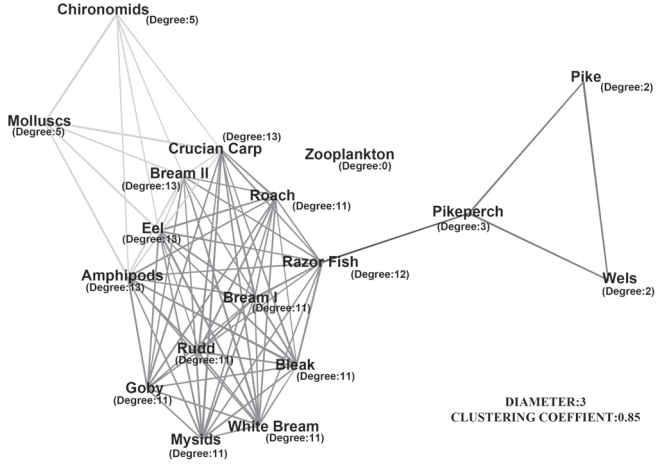

(a) "Spring model" visualization of the predator/predator matrix of Figure 13 using BioGrapher software.

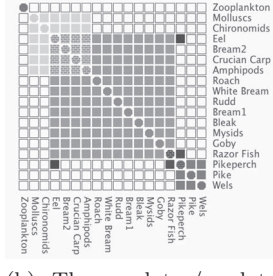

(b) The predator/predator matrix (Figure 13) has been symmetrically rearranged using JavaBENZER [22, 43] to achieve Shkurba form [35].

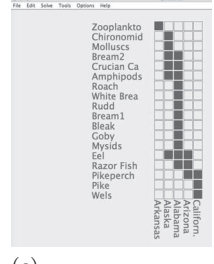

(c) Interval graph produced in JavaBENZER of the niches in the food web described by the predator/predator adjacency matrix in Figure 14a. Note that the Arkansas maximal clique could be on either the left side or the right side in this interval graph because it does not overlap any of the other four maximal cliques.

Figure 14. Different graphical representations of the same adjacency matrix.

trophic level, and either biomass or energy in order to follow the flux of biomass or energy within this ecological community. We can also compute the eigenvectors of these matrices to measure various components of symmetry in these communities related to their robustness, complexity, and fragility. We believe that by applying fundamental graph theoretic algorithms, data visualization, and measurement of graph properties, these three-dimensional food web histograms enable a fuller comprehension of complex ecological communities.

Another avenue we are pursuing with these multidimensional visualizations is to follow up on the recent work of Allesina *et al.* [44] who have pointed out that food webs, in addition to being largely interval, also have broad degree distributions, and contain few trophic cycles. They believe these properties are strongly correlated to the stability of food webs. Their fundamental work tries to compare assumptions of cascade and niche models for the construction of food webs. Allesina *et al.* [44] challenge much of the prior literature "on the relationship between mean interaction strength and stability." Furthermore, they argue that their matrix algebraic approach will allow them "to study the influence on stability of other important food web properties, such as modularity, the presence of trophic groups, and the division of trophic levels." We believe that our tools for visualizing the graph theoretical patterns in traditional predator/prey graphs, predator/predator graphs, predator/predator complementary graphs, Shkurba forms, and multidimensional niche space-trophic level-energy or biomass flux, etc., in multiple configurations gives us the ability to develop alternative visualizations and quantitative measures of these networks to address these claims separately and in combination.

7. Conclusions

Graphical visualization of incidence matrices and adjacency matrices based upon actual biological data allows users to perceive underlying patterns in their data that are not easily observed in canonical biological visualizations. Above we have taken food webs and gene expression patterns as two such cases. Traditional diagrams used to represent community structure-food webs, trophic levels, and energy pyramidsdo not let biologists infer niches in community ecology or easily see flux in food chains or the modularity of sub-networks within complex biological networks. The simplicity of one-dimensional ordering of interval graphs is a strong counterpoint to the physiological ecologists' perspective of n-dimensional niche space with

the various dimensions usually focusing more on abiotic parameters such as temperature, humidity, turbulence of an aqueous environment or acidity of a terrestrial soil, etc.

Graphical visualization software tools like BioGrapher [16] and JavaBENZER [22,43] can be of value to biologists by facilitating their focus on simple dyadic interactions: Who eats whom? Who eats some other species in common? Which substrates go to which products? What turns genes on and off? Who is the parent and who is the progeny? Who is the ancestor and who is the descendent? Most biologists do not think of their food webs, metabolic pathways, pedigrees, and phylogenies as mathematical objects. However, by enabling them to easily convert their associative data into formal graphs with alternative visualizations, quantitative measures of their properties, and simplifications by topological reduction of data, we have the potential for addressing many interesting questions about the complexity, stability, and structure of biological systems.

Acknowledgement

JRJ appreciates the help and advice of Joel Cohen at Rockefeller University and Midge Cozzens at Rutgers University for generating our group's interest in the use of interval graphs for food webs. Two students, Wendy Black and Donald Rohr, did early work on checking out the interval graph properties of 113 published food webs using our software. Their work served as the foundation for significantly improving our tools while we were producing them as they enabled us to test our algorithms and code using actual biological data.

RV acknowledges the contributions of a student, Min Aung, in debugging and enhancing the features of the latest version of BioGrapher, and for his help in documenting code dependencies.

References

1. A. L. Barábasi and Z. N. Oltvai, "Network biology: Understanding the cell's functional organization," *Nat. Rev. Genet.*, vol. 5, pp. 101–13, 2004.
2. O. Mason and M. Verwoerd, "Graph theory and networks in biology," *IET Syst. Biol.*, vol. 1, pp. 89–119, 2007.
3. J. Bascompte, "Networks in ecology," *Basic Appl. Ecol.*, vol. 8, pp. 485–90, 2007.
4. C. P. Brooks, "Quantifying population substructure: Extending the graph-theoretic approach," *Ecology*, vol. 87, pp. 864–72, 2006.
5. R. J. Dyer and J. D. Nason, "Population graphs: the graph theoretic shape of genetic structure," *Mol. Ecol.*, vol. 13, pp. 171–327, 2004.

6. M. Kanehisa, *Post-Genome Informatics*. Oxford University Press, 2000.
7. X. Jiang and R. E. Neapolitan, "Leap: Biomarker inference through learning and evaluating association patterns," *Genetic Epidemiology*, vol. 39, pp. 173–184, 2015.
8. R. Robeva, ed., *Algebraic and Discrete Mathematical Methods for Modern Biology*. New York: Academic Press, 2015.
9. See, for example, review by G. Pavlopoulos, M. Secrier, C. N. Moschopoulos, T. G. Soldatos, S. Kossida, J. Aerts, R. Schneider and P. G. Bagos. Using Graph Theory to Analyze Biological Networks. BioData Mining 4:10, 2011. http://www.biodatamining.org/content/4/1/10.
10. D. J. Watts and S. H. Strogatz, "The collective dynamics of 'small-world' networks," *Nature*, vol. 393, pp. 440–442, 1998.
11. D. J. Watts, *Six Degrees: The Science of a Connected Age*. New York: Norton Press, 2003.
12. B. Hayes. Graph Theory in Practice: Part I: Amer. Sci. 88:9–13. Part II: Amer. Sci. 88:104–9, 2001.
13. A. L. Barbasi and R. Albert, "Emergence of scaling in random networks," *Science*, vol. 286, pp. 509–512, 1999.
14. O. Sporns, *Networks of the Brain*. Cambridge, Massachusetts: The MIT Press, 2011.
15. M. Walhout, M. Vidal and J. Dekker, *Handbook of Systems Biology-Section II: Network Properties of Biological Systems*, pp. 45–193. New York: Academic Press, 2012.
16. R. Viswanathan, "Biographer and wdisplay: Excel modules for data visualization," *BioQuest Notes*, vol. 15, pp. 6–7, 2006.
17. J. R. Jungck and R. Viswanathan, "Graph theory in systems biology: Interval graphs, motifs, and pattern recognition," in *Algebraic and Discrete Mathematical Methods for Modern Biology* (R. Robeva, ed.), New York: Academic Press, 2015.
18. Wolfram Research, Champaign, Illinois, U.S.A. http://www.wolfram.com/mathematica/.
19. The MathWorks Inc, Natick, Massachusetts, U.S.A. http://www.mathworks.com/products/matlab/.
20. Tom Sawyer Software, Berkeley, California, U.S.A. https://www.tomsawyer.com/industries/networking.php.
21. J. Ellson, E. Gansner, L. Koutsofios, S. C. North and G. Woodhull, "Graphviz–open source graph drawing tools," *Lecture Notes in Computer Science*, vol. 2265, pp. 483–484, 2002.
22. Biological ESTEEM: Excel Simulations and Tools for Exploratory, Experiential Mathematics. http://www.bioquest.org/ESTEEM.
23. D. J. Watts, *Small Worlds: The Dynamics of Networks Between Order and Randomness*. Princeton University Press, 1999.
24. L. A. N. Amaral, A. Scala, M. Barthlmy and H. E. Stanley, "Classes of small-world networks," *PNAS*, vol. 97, pp. 11149–11152, 2000.
25. D. A. Fell and A. Wagner, "The small world of metabolism," *Nature Biotechnology*, vol. 18, pp. 1121–1122, 2000.

26. D. A. Fell and A. Wagner, "The small world inside large metabolic networks," *Proc. R. Soc. Lond. Ser. B*, vol. 268, pp. 1803–1810, 2001.
27. J. M. Montoya and R. V. Sol, "Small world patterns in food webs," *Journal of Theoretical Biology*, vol. 214, pp. 405–412, 2002.
28. P. Brazhnik, A. de la Fuente and P. Mendes, "Gene networks: How to put the function in genomics," *Trends in Biotechnology*, vol. 20, pp. 467–472, 2002.
29. A. Avena-Koenigsberger, J. Goi, R. V. Sol and O. Sporns, "Network morphospace," *J. R. Soc. Interface*, vol. 12, p. 20140881, 2015.
30. A. W. Rives and T. Galitsky, "Modular organization of cellular networks," *PNAS*, vol. 100, pp. 1128–33, 2003.
31. J. Zhu, M. B. Miller, R. E. Vance, M. Dziejman, B. L. Bassler and J. J. Mekalanos, "Quorum-sensing regulators control virulence gene expression in vibrio cholerae," *PNAS*, vol. 99, pp. 3129–3134, 2002.
32. J. E. Cohen, *Food Webs and Niche Space*, pp. 20–21. Princeton University Press: (MPB-11) (Monographs in Population Biology), 1978.
33. J. E. Cohen, F. Briand and C. M. Newman, *Community Food Webs: Data and Theory (Biomathematics Volume 20)*. Berlin: Springer-Verlag, 1990.
34. F. Roberts, *Discrete Mathematical Models, with Applications to Social, Biological, and Environmental Problems*. Englewood Cliffs, NJ: Prentice-Hall, 1976.
35. J. R. Jungck and V. Streif, "Deletion mapping of genetic 'fine structure': Supplementing ad hoc problem solving approaches with algorithms and heuristics," *Bioscene*, vol. 12, pp. 13–27, 1986.
36. R. Balakrishnan and K. Ranganathan, *A Text Book of Graph Theory*. New York: Springer, 2012.
37. P. C. Gilmore and A. J. Hoffman, "A characterization of comparability graphs and of interval graphs," *Canadian Journal of Mathematics*, vol. 16, pp. 539–548, 1964.
38. D. R. Fulkerson and O. A. Gross, "Incidence matrices and interval graphs," *Pacific J. Math.*, vol. 15, pp. 835–855, 1965.
39. J. R. Jungck, G. Dick and G. A. Dick, "Computer-assisted sequencing, interval graphs and molecular evolution," *BioSystems*, vol. 15, pp. 259–273, 1982.
40. K. S. Booth and G. S. Lueker, "Testing for the consecutive ones property, interval graphs, and graph planarity using pq-tree algorithms," *J.Computer System Sci.*, vol. 13, pp. 335–379, 1976.
41. M. Habib, R. McConnell, C. Paul and L. Viennot, "Llex–bfs and partition refinement, with applications to transitive orientation, interval graph recognition and consecutive ones testing," *Theoretical Computer Science Archive*, vol. 234, pp. 59–84, 2000.
42. P. Biro, "Biodiversity of freshwater food-webs: What can they teach us?," in *Frontiers in Biology: The Challenges of Biodiversity, Biotechnology and Sustainable Agriculture* (C. H. Chou and K. T. Shao, eds.), Tihany, Hungary: Academia Sinica, 1998.

43. J.R. Jungck, V. Streif, P. Jungck and S. Everse. 2005. JavaBENZER. http://bioquest.org/ESTEEM.
44. S. Allesina, J. Grilli, G. Barabas, S. Tang, J. Aljadeff and A. Maritan, "Predicting the stability of large structured food webs," *Nature Communications*, vol. 6, p. 7842, 2015.

MODELLING THE EARLY GROWTH OF STEM CELL TISSUES*

R. A. BARRIO, S. OROZCO-FUENTES, R. ROMERO-ARIAS
Instituto de Física Universidad Nacional Autónoma de México
Mexico 01000, D.F., Mexico
E-mail: barrio@fisica.unam.mx

In developmental biology, molecular genetic components have been considered as key in regulating the developmental mechanisms of plants and animals. Stem cells divide at a different rate depending on their position in the tissue, and eventually differentiate to form a recognisable anatomic entity. How this process happen if stem cells are identical sharing the same composition, DNA, genes and genetic networks? We propose that cells collect positional information on their environment by sensing mechanical and chemical fields. We propose a dynamical model to describe the early development of stem cells in a tissue. We choose the root meristem of Arabidopsis thaliana to explore the emergence of cellular patterns through a cooperative dynamics, as this system is well studied at the molecular, genetic and cellular levels and presents the key features of multicellular stem-cell niches. We successfully predict the variations of cell life cycle seen in the actual root meristem. Our model could be applied to other systems of interest, as the emergence of colorectal cancer. We also give a brief description of the dynamics of stem cells in the colonic crypts.

1. Introduction

A central question in developmental biology is to unravel the mechanisms by which stem cells develop and eventually differentiate to form tissues with specific functions. Ideal models to investigate this issue are the meristems of plants, which are groups of undifferentiated stem cells that are present throughout the whole life of the plant. During the early stages of cell reproduction, the domain in which they are confined, either in the floral meristem, or the root meristem, acquires a particular shape, being almost spherical in the case of the flower, and in a form of a tube in the case of the root.

*This work is supported by Conacyt, México, through project 179616.

It is seen that all 250000 species of angiosperms presents a unique configuration of the organelles consisting of a series of concentric circles where sepals are on the outside layer, followed by petals, stamens and finally carpels in the central layer of the domain. In a former paper[1] we were able to explain this universal disposition by assuming that stem cells acquire positional information within the domain from a physical field that senses the local curvature of the domain, which in turn couples to the regulatory genetic networks involved in flower development. The local curvature was introduced by an energy density functional defining a phase field model that was coupled to a field u acting directly on the genes. Numerical calculations with this model were able not only to recover the geometrical disposition of the organelles in wild type flowers, but to predict the geometry of flowers with mutated genes.

The central point of this work is that cells obtain positional information from chemical and physical fields that allow them to choose their final fate when genes act during differentiation. This hypothesis can be applied and tested in various scenarios concerning stem cells, namely the root meristem in plants and the groups of stem cells in colonic crypts in the intestine of animals, with little modifications[2]. In what follows we shall describe the modelling of these systems based on this key hypothesis. Our aim is to develop a dynamical model in which the known experimental facts are taken into account.

2. The Root Meristem

The root meristem is an ideal model to test our hypothesis. Here the situation is more complicated that in the flowers, because the regulatory genetic networks involved in the early development of the root are not known completely. However, the root meristem in the early stages of development presents distinguishable zones along the apical basal axis of the root. At the tip of the root there is the stem cell niche (SCN), consisting of stem cells surrounding the quiescent centre cells or the organiser cells (QC). Towards the base of the plant, one encounters a cell proliferation domain (CPD) where cells have high rates of cell division, then they enter a transition domain (TD), where cells have low division rates, but they preserve their length. The SCN, the CPD and the TD comprise the root apical meristem (RAM). More distally from the organiser centre, cells cease to proliferate and start to grow in the elongation domain (EZ). This situation suggest that the geometry of the tip of the root produces a physical field that is

able to distinguish between the different zones of the domain and consequently translate this positional information to the mechanisms responsible of regulating cell division.

2.1. *Dynamical model*

Taking advantage of the cylindrical symmetry of the domain we can reduce our study to two dimensions, that is a cylinder with a parabolic cap simulating the tip, in which stem cells are defined by points r_i that produce a Voronoi tessellation of the inner space. The outer layer consists of a row of epithelial cells. These cells produce an elastic field due to the fact that the tend to have a uniform size in adulthood, and a similar spherical shape. A key process that has been tested experimentally is the important role that auxins play in regulating the concentration of cyclins that ultimately dictate the period of the life cycle of stem cells. Therefore, we propose that a complex coupled dynamics takes place between the three key processes, namely: 1) The physical elastic field dictated by the geometry, 2) The sensitivity of auxins to this field, which allows them to be transported actively along the root, producing a concentration gradient that is able to define the sections of the root along the axis, and 3) The direct dependence of the period of the cell cycle on the local concentration of auxins. A detailed description of the model that integrates the three key dynamical processes considered to explore the emergence of cellular patterns during *A. thaliana* root development can be found in Ref. 3.

Elastic fields

The elastic field regulates the form and shape of every root cell and has the form

$$V(x_i, y_i, t) = \frac{K_v}{2}(A_i(t) - \bar{A}_0(t))^2 + \frac{K_c}{2}(\vec{r}_i(t) - \vec{r}_{0_i}(t))^2, \qquad (1)$$

where A_i is the volume of cell i and A_0 represents the volume of an adult cell. The instantaneous position of the cell i is $\vec{r}_i(t)$ and the centre of mass position is $\vec{r}_{0_i}(t)$. The first term helps cells to grow to the adult cell size, and the second term favours an isotropic cell shape. K_v and K_c are elastic constants that can be associated to the elastic moduli of the cell wall. The elastic potential of the outer cells (labeled e) is different, but should be analogous to the original potential for the internal cells, with the condition that outer cells have different elastic response and their displacement should

be along the outer surface. Therefore, the potential for cells in the outer surface is

$$V(x_e, y_e, t) = \frac{K_e}{2}(A_e(t) - \bar{A}_0(t))^2 + \frac{K_c}{2}(\vec{r}_e(t) - \vec{r}_{0_e}(t))^2, \tag{2}$$

where K_e is an elastic constant, in principle different from K_v, and A_e differs from A_i. Thus, the dynamics of any cell (i, e) is

$$\frac{d\vec{v}_{(i,e)}}{dt} = -\nabla V(x_{(i,e)}, y_{(i,e)}, t) - k\vec{v}_{(i,e)}, \tag{3}$$

where k is a friction coefficient. This equation can be solved with the boundary condition $\nabla V \cdot \hat{n} = 0$ for the outer cells, where $\hat{n}$ is a unit vector normal to the surface at each point.

Auxin transport dynamics

The mechanism by which the mechanical forces participate in the transport of auxins can be modelled by proposing an active transport of auxins through the membrane that follows D'Arcy's law, in which the permeability (P) of the membrane is modified by the PIN polarisation. Let us examine the general transport equations. Conservation of mass implies the continuity equation $\partial c/\partial t = -\nabla \cdot \vec{J}$, where $\vec{J} = \vec{v}c$ is the the flux. Normal diffusion means that the flux is proportional to the gradient of c, with the diffusion coefficient D_0 being the proportionality term. Therefore, the exchange of auxins per unit are per unit time for cell i can be written as,

$$\frac{\partial c_i}{\partial t} = \alpha \left[\sum_m A_{i,m} P_{im} (V_m - V_i)(c_m - c_i) \right] + D_0 \nabla^2 c_i, \tag{4}$$

where α is a constant with proper physical units and the summation is over all m neighbours of cell i. The term is square brackets represents the active hydrodynamic transport given by D'Arcy's law and the second term on the right is diffusion through the intercellular medium. Active transport should be proportional to the contact area between cells $A_{i,m}$, the permeability of the membrane $P_{i,m}$, the "pressure drop", proportional to the the local potential difference, and the auxin concentration difference between adjacent cells.

PIN polarization dynamics

The term in square brackets in Eq. 4 could enhance or deplete normal diffusion depending if it is positive or negative, respectively. If P_{im} is constant, this term is proportional to $\nabla V_i \cdot \nabla c_i$. Thus, the key quantity that regulates the active transport against the concentration gradient is precisely the elastic potential difference between cells and PIN polarisation, which could make the permeability zero or negative. In order to model PIN polarisation we have constructed a boolean network that takes into account the experimental information of the process, which involve the elastic potential, auxin interactions with proteins that regulate the kinases which produce the polarisation states. Once the attractors that define the two PIN polarisation states we can translate the boolean network into a set of ordinary differential equations which allows us to represent the permeability of the membrane as,

$$P_{i,m} = \Theta[(V_m - V_i)(c_m - c_i)]\text{sign}(V_m - \bar{V}), \tag{5}$$

where $\Theta[...]$ is the Heaviside function, being zero when the argument is negative, and $\bar{V} = \sum_i V_i/N$ is the average value of the potential over the N cells in the meristem.

The way in which epidermal cells divide is exactly the same as the meristematic cells, except that division always occurs horizontally, that is, the mother cell lies exactly below the daughter, and the parameter β, that regulates the period of the cell cycle[3] could, in principle, be different. In order to clarify the way in which the different dynamics occur and interact in our model, we show in Fig. 1 a flow diagram of the computational platform to integrate the model.

2.2. *Results*

In Fig. 2 we show typical results of our calculations. In (A) we show the profile of the auxin's concentration along the longitudinal axis of the root (dashed line). We also show the normalised potential (continuous grey line), and the number of cell divisions (black continuous line). These profiles are very similar to our published results[3] and follow the experimental data very closely. In (B) we show three snapshots taken at different times of the growth process. In the upper part the auxin concentration and in the lower part the elastic potential values.

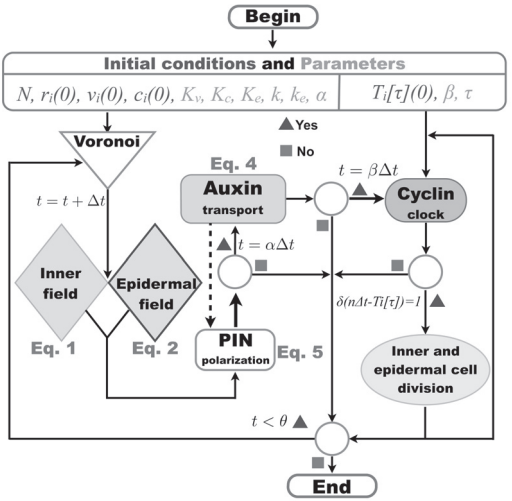

Figure 1. Flow diagram of the platform built for numerical calculations of the root growth.

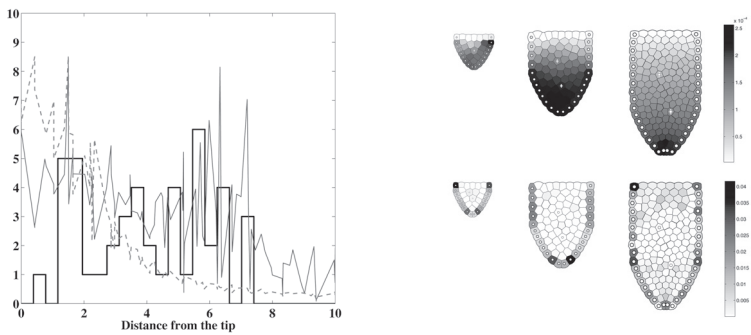

Figure 2. (A) Profile of the auxin's concentration along the longitudinal axis of the root (dashed line). We also show the normalised potential (continuous grey line), and the number of cell divisions (black continuous line). (B) Three snapshots taken at different times of the growth process. In the upper part the auxin concentration and in the lower part the elastic potential values.

3. Modelling Colonic Crypts

3.1. *The problem*

Morphogenesis is a process that takes place during embryonic development where it controls the spatial distribution of cells, and inside a mature organ-

ism with cell renewal or regeneration[16]. This process is driven by substances present in the tissue, known as morphogens, which diffuse through the tissue and specifies *via* concentration gradients, positioning and differentiation of stem cells. Recent discoveries have pointed out that this biological process plays a significant role during many pathological processes, such as the formation of tumour cell masses and carcinogenesis[17].

Therefore, the study of how stem cells can maintain their ability to divide (multipotency) and give rise to daughter cells that differentiate into tissues and organs is fundamental to understanding the development of multicellular organisms and the formation of tumours and cancer. Particularly, it has been shown that carcinogenesis occurs due to modifications of gene expression, related to changes in the environment which trigger cellular response, signalling and chemotaxis[4,8]. A model system to study carcinogenesis is the structure of the lining of the intestine.

The epithelial layer of the human intestine tract is the body's largest mucosal surface, divided into two segments, the small and the large intestine or colon. The small intestine mucosa is composed with a single layer of cells organised into finger-like protrusions, also known as *villi*, and invaginations or crypts of Lieberkün. The large intestine, on the other side, is only composed with a single layer of cells organised in crypts and lacks of villi. Cells lining the intestinal epithelium are replaced every 2-3 days in the mice and every 3-5 days in humans[24], making it the most rapidly renewing tissue in the mammalian body and a suitable model for studying adult mammalian stem cells. Since, this tissue is formed by about 2×10^7 crypts, which are "test-tube" shaped invaginations in the epithelium of the colon, they provide a huge surface area for the absorption of water and nutrients while forming a protective barrier from harmful substances entering the lamina propia[23].

Colonic crypts are tightly packed cylindrical tubes which are evenly distributed with a central hole down the length of crypt, also known as the crypt lumen, see Fig. 3(A). A human colonic crypt contains approximately 2000 cells, with about 75-110 cells long and an average crypt circumference of 23 cells[20]. Experimental studies indicate an ordering along the crypt where proliferative cells are located at the base of the crypt and mature cells at the crypt orifice (lumen). Observations of cell proliferation markers suggest a sharp boundary between the proliferative and mature regions, where the proliferative cells occupy the lower third of the crypt[25].

A healthy human colonic crypt contains a population of 5 to 6 stem-cells that reside at or near the base of the crypt[20]. These stem cells divide to

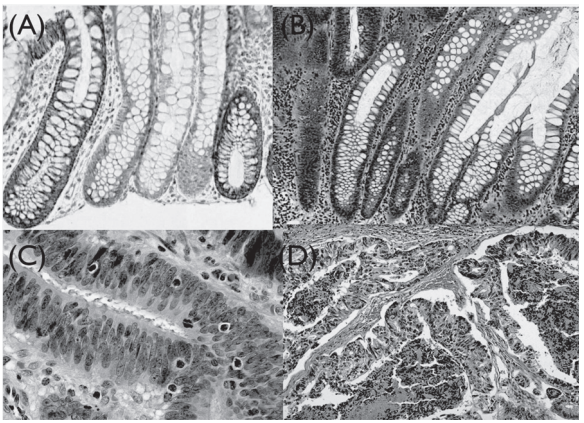

Figure 3. Neoplasia in a colonic crypt: (A) normal tissue, (B) early adenoma, (C) late adenoma and (D) adenocarcinoma. (Taken from Wikipedia)

produce transit amplifying (TA) cells which proliferate rapidly and mature as they migrate up the crypt. These TA cells perform several symmetric divisions before terminally differentiating. Since only the cells located at the base of the crypt proliferate (due to mitotic activity), this process creates a cell migration up the crypt, resulting in a pressure driven cell flow. When differentiated epithelial cells reach the crypt collar, they undergo apoptosis and/or are shed into the lumen. In addition to this, a process of programmed cell death, known as *anoikis*, is triggered when there is inadequate adhesion of the epithelial cells to the extracellular matrix[18]. This detachment induce apoptosis (cell death) and under healthy circumstances all these processes combined maintain tissue homeostasis by restricting proliferation to a monolayer and by preventing cells from reattaching and resuming growth in another location. The establishment of an upward migration and removal of cells inside the crypt gives a defence mechanism against mutated cells, via renewing the epithelial layer every few days. The balance disruption in these regulatory processes is linked to the formation of adenomas and carcinomas, see Fig. 3. Transit from the crypt base to the surface takes 5-6 days in humans. In the rat's small intestine, experiments have showed that cell velocity increases linearly with the crypt height and exhibits circadian variation[19]: Cells move at 13μm/hr at the upper crypt and 34μm/hr in the base of the *villus*, with this velocity increasing to 51.8μm/hr in the upper villus (where cells are continuously enlarged)[21].

Colorectal Cancer (CRC) is one of the most frequent cancer disease in

the population with one million of new cases every year (worldwide) and with 33% of mortality rate. CRC is thought to originate due to genetic and epigenetic alterations that affect the cellular dynamics of the crypts lining the large intestine. When these genetic mutations occur, cells can accumulate and this alter the cell migration flow velocity, then such cells acquire the ability to persist and multiply inside the crypts[5,9]. It is generally believed that formation of tumours in the colon start as disease connected with mutations in stem cells, that continuously produce (*via* proliferation) more progenitor tumor cells[22]. Experimental studies and computational models have been developed to study the clonal conversion of the colonic crypt due to the competition between wild-type (healthy cells) and mutant cells at the base of the crypt[6,10,7,11].

Therefore, understanding how cells organise inside the crypts is important to gain insight into the origins of adenomas (see Fig. 3(B) and (C)). Disorganisation of crypt dynamics increase stress on the walls of the crypts and if some stem cell acquire a mutation that increases proliferation, inhibits apoptosis or alter cell-cell adhesion in its progeny, this mutant clone can colonise the entire crypt and replace the non-mutant cell population.

There are many biochemical pathways, whose dysfunction leads to genetic mutations in the crypt and their study are of particular importance to assess the origin of colorectal cancer[7,12]. The Wnt signalling pathways have an important role in many biological processes in animals, regulating embryonic development, cell fate determination (canonical), cell movement and tissue polarity (non-canonical) and carcinogenesis (see Fig. 3(D)). In the normal intestinal epithelium Wnt signalling pathways maintains self-renewal of intestinal stem cells and progenitor cells via proliferation and differentiation. Wnt's are a large family of secreted proteins that acts as morphogens and activate receptors on the cell surface which triggers a myriad of events inside the cell *via* modulating the expression of target genes[14]. In particular, the canonical Wnt signalling has been implicated in the regulation of intestinal stem cells and crypt dynamics. Mutations and aberrant regulation of the Wnt/β-catenin pathway and APC (adenomatous polyposis coli) gene leads to the onset and progression of CRC[13].

3.2. *Numerical calculations*

The geometry of the colonic crypts allows us to simplify the problem domain by using a quasi-one dimensional model. Following Ref. 3, we construct a crypt as a regular shape with points lying along the boundaries of two semi-

circles patched at both open ends with two parallel walls. These boundary points are fixed in space, the interior ones define the crypt lumen, while the exterior ones represent the basement membrane which maintains the integrity and structure of the epithelial layer, gives mechanical support and acts as a physical barrier between the epithelial cells and the connective tissue.

We propose that the cells in the crypt obtain positional information from a physical elastic field obtained from a potential function exactly the same as in the case of the root. We assume that the transcription of this information to the mechanisms regulating the life cycle period is performed by the Wnt signalling pathway, similar to the role of auxins in plants, that is, the period of the life cycle regulated by cyclins is inversely proportional to the square root of the concentration of Wnt, which in turn depends linearly on the value of the potential energy in each cell.

Numerical calculations were performed in several domains with different geometrical proportions. In Fig. 4 we show a snapshot of the calculation in which only the cells at the bottom of the crypt reproduce. The cells at the extremes of the quasi one dimensional domain migrate out of it as the space in the crypt is occupied by the newly born cells.

Figure 4. Numerical calculation representing a healthy crypt. The gray scale code represents the value of the potential in each cell and the white cells at the bottom of the crypt are the ones that divide.

The parameters used in Fig. 4 were $k_V = k_c = 120$, $k = 5$, $\beta = 8$, $D_o = 0$ and $\alpha = 1$. The region of parameters where homeostasis is achieved is quite reduced, and also depends very much on the geometric proportions of the domain.

In Fig. 5 we show calculations made in domains with several shapes, with the same set of parameters $k_V = 1$, $k_c = 4$, $k = 3$, $\beta = 25$, $D_o = 0$

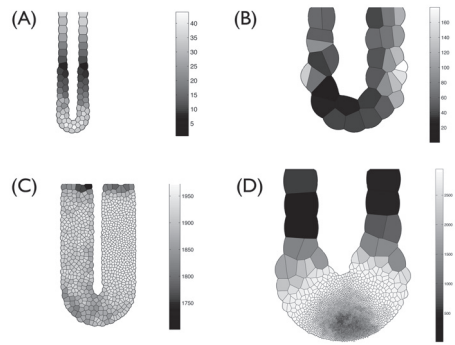

Figure 5. Effect of the geometry of the domain. (A) Healthy crypt. (B) Stem cells migrate in a wide crypt. (C) MIgrated stem cells reproduce rapidly before mature cells migrate. Observe that mature cells are situated in the vicinity of the lumen only, this allows cancer cells to abandon the crypt and presumably this represents metastasis of a cancerous tumour. (D) anomalies in a wider cell in which uncontrolled reproduction takes place only at the bottom of the crypt, resulting in a localised tumour. The gray scale code represents the value of the potential in each cell and the white cells at the bottom of the crypt are the ones that divide.

and $\alpha = 1$. We notice that anomalies on morphology are seen.

4. Conclusions

We have presented a model involving coupled dynamics of three different processes, that combined result in a functional dynamical development of a set of stem cells that allow the subsequent differentiation promoted by genes. This model is simple, from the point of view of Biology, but shows some universal mechanisms that should be present in many biological systems. The key idea is that functional differentiation takes place because stems cells interact with their environment through physical and chemical fields that provide them with spacial and temporal information. The universality of this approach is demonstrated by recovering the developmental dynamics seen in three rather different stem cell systems, namely, the flower meristem, the root meristem and the renewal of cells in colonic crypts.

References

1. R. A. Barrio, A. Hernández-Machado, C. Varea, J. R. Romero-rias and E. R. Álvarez-Buylla, *PLoS One*, **5**, 10, (2010).
2. R. Heidstra and S. Sabatini. *Nature Reviews / Molecular Cell Biology*, **15**, 301 (2014).

3. R. A. Barrio, J. R. Romero-Arias, M. A. Noguez, E. Azpeitia, E. Ortiz-Gutiérrez, V. Hernández-Hernández, Y. Cortes-Poza and E. R. Álvarez-Buylla, *PLOS: Computational Biology*, **9(5)**, (2013).
4. A. d'Onofrio and I. P. M. Tomlinson, *Journal of Theoretical Biology*, **244**, 367 (2007).
5. D. Cunningham, W. Atkin, H. J. Lenz, H. T. Lynch, B. Minsky, B. Nordlinger and N. Starling, *The Lancet*, **375**, 1030 (2010).
6. A. Humphries and N. A. Wright, *Nature Reviews: Cancer*, **8**, 415 (2008).
7. S. K. Kershaw, H. M. Byrne, D. J. Gavaghan and J. M. Osborne, *IET Syst. Biol.*, **7(3)**, 57 (2013).
8. I. P. M. Tomlinson and W. F. Bodmer, *PNAS*, **92**, 11130 (1995).
9. X. Liu, M. Jakubowski and J. L. Hunt, *Am. J. Clin. Pathol.*, **135(2)**, 245 (2011).
10. G. R. Mirams, A. G. Fletcher, P. K. Maini and H. M. Byrne, *Journal of Theoretical Biology*, **312**, 143 (2012).
11. Y. Kagawa, N. Horita, H. Taniguchi and S. Tsuneda, *J. Gastroentero.*, **49**, 263 (2014).
12. A. G. Fletcher, P. J. Murray and P. K. Maini, *arXiv:1506.05019v1 [q-bio.TO]*, 26 (2015).
13. P. Polakis, *Genes & Dev.*, **14**, 1837 (2000).
14. O. Voloshanenko, G. Erdmann, T. D. Dubash, I. Augustin, M. Metzig, G. Moffa, C. Hundsrucker, G. Kerr, T. Sandmann, B. Anchang, K. Demir, C. Boehm, S. Leible, C. R. Ball, H. Glimm, R. Spang and M. Boutros, *Nature Communications*, **4**, 13 (2013).
15. C. H. F. Chan, P. Camacho-Leal and C. P. Stanners, *PLOS One*, **2**, e1353 (2007).
16. E. F. Rossomando and S. Alexander, *Morphogenesis: An Analysis of the Development of Biological Form, CRC Press*, (1992).
17. N. Barker, R. A. Ridgway, J. H. van Es, M. van Wetering, H. Begthel, M. van den Born, E. Danenberg, A. R. Clarke, O. J. Sansom and H. Clevers, *Nature*, **457**, 608 (2009).
18. S. Frisch and H. Francis, *J. Cell. Biol.*, **124**(4), 619 (1994).
19. P. Kaur and C. S. Potten, *Cell Tissue Kinet.*, **19**(6), 591 (1986).
20. A. M. Baker, B. Cereser, S. Meltonand, A. G. Fletcher, M. Rodriguez-Justo, P. J. Tadrousand, A. Humphries, G. Elia, S. A. McDonald, N. A. Wright, B. D. Simons, M. Jansen and T. A. Graham, *Cell Rep.*, **8**(4), 940 (2014).
21. S. Tsubouchi, *Cell Tissue Kinet.*, **1**6(5), 441 (1983).
22. P. A. Beachy, S. S. Karhadkar and D. M. Berman, *Nature*, **432**, 324 (2004).
23. L. W. Peterson and D. Artis, *Nature Reviews: Immunology*, **14**, 141 (2014).
24. B. Creamer, R. G. Shorter and J. Bamforth, *Gut*, **2**, 110 (1961).
25. S. J. Leedham, P. Rodenas-Cuadrado, K. Howarth, A. Lewis, S. Mallappa, S. Segditsas, H. Davis, R. Jeffery, M. Rodriguez-Justo, S. Keshav, S. P. L. Travis, T. A. Graham, J. East, S. Clark and I. P. M. Tomlinson, *Gut*, **62**, 83 (2013).

NON-LOCAL HYDRODYNAMICS OF SWIMMING BACTERIA AND SELF-ACTIVATED PROCESS

SISIR ROY

National Institute of Advanced Studies,
IISC Campus, Bangalore 560012, India
E-mail:sisir.sisirroy@gmail.com

RODOLFO LLINÁS

Department of Neuroscience and Physiology,
New York University School of Medicine, NY, USA
E-mail: llinar01@endeavor.med.nyu.edu

Water fluidity is modified, in a nontrivial manner, by the presence of bacteria above a threshold number density. Under such threshold conditions swimming bacterial suspensions impose a coordinated water movement on a length scale of the order (10–100) micrometers compared with a bacterial size of the order of 3 micrometers. This observation leads to fundamental questions concerning the cell-to-cell communication presently known as quorum sensing. The aim of this paper is to study the quorum state using non-local hydrodynamics. We emphasize that densely packed bacteria may be viewed as 'bacterial fluid' or 'living fluid' similar to that of dense granular systems. The behaviour of the fluid of granular mass is quite different from that of typical fluids. This granularity imposes a second source of fluctuations because grains cannot be treated as points at any length scale. This type of fluctuation is known as non-local noise in contrast to local noise in usual hydrodynamic flow. The non-local hydrodynamical framework is applied here to consider the effect of non-local noise. In this framework of non-local hydrodynamics viscosity is generated by self-induced noise. This viscosity leads the actively moving bacteria into the meta-stable states required to support quorum, given the non-local nature of stresses mediated by autoinducers. The shear stress created non-locally within this framework depending on the non-local noise of granularity and the viscosity associated to the this noise can be tested experimentally. The existence of this kind non-chemical self-induced process may be present not only in cell-to-cell bacteria communication but also in eukaryotic cell-to-cell interactions.

1. Introduction

Water fluidity is modified, in a nontrivial manner, by the presence of bacteria, above a threshold number density. At such threshold condition swim-

ming bacterial suspensions impose a coordinated water movement on a length scale of the order of $(10 - 100)\mu m$ compared with a bacterial size of the order of $3\mu m$[1]. This observation raises fundamental questions concerning the cell to cell communication mechanism among bacteria, presently known as quorum sensing.[2,3] Bassler and her groupwaters regard role of the chemicals released by bacteria (known as quorum sensing molecules) responsible for evoking behavioral modification on their neighbors. Their study utilizes the behavior of Vibrio Harvey bacteria as a possible approach to analyzing the mechanism of multisignal integration. Recently, Alberghini *et al.*[4] critically reviewed the current observations and have considered the various assumptions underlying the theoretical framework for quorum sensing.

The early observations of Vibrio fisheris behavior where bacterial growth within a host fish body lead to a concept of minimum cell density. In this hypothesis such density must attain critical threshold value before all subsequent activity can take place. This kind of interpretation is based usually on two assumptions:

- The presence of a homogenous system such that signal density is close to isotropic, allowing informational simultaneity along the entire population.
- Growth should be congruent with the density increase i.e. the environment of the suspended bacteria must be such that cells do not actively migrate or disperse.

However, the study of substrate geometry indicates that the above paradigm may not be optimal for addressing biofilm bacterial communication. And so, an alternative interpretation of diffusion sensing has been proposed. Alberghini *et al.*,[4] after studying the consequences of critical cellular distribution and calculating the gradient profiles (based on the mechanism of diffusion of autoinducer molecules) concluded that diffusion sensing is a viable hypothesis.

Hydrodynamic model of swimming bacteria or bacterial colonies[1–7], seems to be one of the most comprehensive alternative models defining the possible quorum sensing mechanism. Here densely packed bacteria may be viewed as a bacterial fluid or living fluid similar to that of dense granular systems. Lega and Passot[5] initially assumed that two-phase hydrodynamic equations taking the bacteria and water as two interpenetrating and interacting continua.

However, by considering the relatively high bacterial density, given the fact that no water motion is observed (under isothermal conditions and in the sense of displacement sheer viscosity, while rotational bulk viscosity may be present) in the absence of the bacteria, we assume the dynamics of the suspended bacteria is governed by bacterial dynamics. Under these conditions bacteria and water appear to move as a single fluid at hydrodynamic scale. Here, the bacterial fluid is considered as a granular medium where the bacteria has a definite size. The granularity imposed by the bacterial size gives rise to a noise called non-local noise which is different from thermal noise. So the two types of noise like usual thermal noise and the non-local noise are always present in the bacterial fluid and hence in non-local hydrodynamics.

In fluid mechanics,the basic state space is usually considered to be function of the density ρ and the velocity gradients of the density ρ in addition to the density ρ and the space is spanned by the variables

$$(\rho, \nabla\rho, \vec{v}, \nabla\vec{v}, ..)$$

Ginzburg-Landau equation can be considered as the first such non-local extension of a homogeneous relaxation equation of internal variables. It is worth mentioning that Quantum Mechanics is a non-local theory, while Bohmian quantum potential depends on the derivative of quantum probability density. This indicates that quantum mechanics is a type of weakly non-local fluid mechanics[8,9]. However, the concept of nonlocality in quantum mechnaics is different from that in non-local hydrodynamics. In non-local fluid mechanics the weakly non-local field is introduced to determine the origin of viscosity, or adhesive force, in the physically more realistic setting of large-scale structure formation at the cosmological scale. This was first introduced by Zeldovich[10] with soft initial assumptions to understand the large scale structure formation. In this approach viscosity is driven by stochastic force and the dynamics is governed by Burgers equation. It is well known that the noisy Burgers equation, in one dimension, may provide the simplest continuum description of an open driven nonlinear system exhibiting scaling and pattern formation aspects of the Noisy Burger Equation[11]. We propose that bacterial fluid is consistently described by weakly non-local hydrodynamics where kinematic viscosity is generated due to self- induced noise. This viscosity in turn leads to the formation of a metastable state of the actively moving bacteria. This meta-stable state is necessary for the simultaneous activation of the bacteria to support quorum, given the existence of non-local nature of stresses mediated

by autoinducers. Stress fluctuation-activated processes have been studied in understanding the dense granular flows[12,13]. Thermally activated processes have been considered to explain many physical phenomena. However, thermal fluctuations are seen to be negligible in case of granular medium. In case of dense granular material fluctuation of stress somewhere in the material produces rearrangement of the granules. This rearrangement produces shear somewhere else and hence non-local. This is a kind of self induced process. The shear stress created non-locally by autoinducers produces gene expression and hence the quorum. Initially we will briefly review the framework of weakly non-local hydrodynamics. Section 2 will address the collective behaviour of bacterial displacement (swimming) and the formation of the meta-stable/stable state based on non-local hydrodynamics. Then, the fluctuation of shear stress of the autoinducers and gene expression will be discussed in Section 3. In Section 4 quorum sensing of bacteria and cellular ensemble communication will be discussed. A comparative study of Non-local Hydrodynamic model is made in comparison to Quorum sensing and Diffusion sensing in Section 5. Finally we briefly discuss the possible implications in Section 6.

2. Weakly Non-local Hydrodynamics and Collective Behavior of Bacteria

Closed packed populations of suspended swimming bacteria develop a coordinated motion on length scales $(10-100)\mu m$ in comparison to the size of an individual bacterium of the order of 3 μm when the concentration of the bacteria reaches a sufficiently high value. Recently, Koch and Subramanian[1] discussed the collective hydrodynamics of such living organisms called living fluids and tried to understand the behavior based on numerical analysis and stability analysis. We emphasize that the behavior of the closed packed bacteria is similar to the behavior of dense granular systems. It is well known that the dense granular systems behave like a fluid which is fundamentally different from ordinary fluids. The existence of intermediate length scale, due to the fact that the grains cannot be considered as points at any length scale, lead us to introduce a second source of fluctuations in addition to thermodynamic fluctuations. This second type of fluctuation is known as non-local noise and has been discussed extensively in the context of flow of granular materials. Both type of noise are present in this type of system and the dominance of one over the other depends on the force, $F_g = \frac{f}{\rho g}$ applied to the system where f be the volume

density of the forcing and g the acceleration due to gravity. Hydrodynamical equations have been studied for the both the limits i.e. strong and weak forcing limits. In case of closely packed bacteria though the size of the bacterium is smaller than that of the system, it cannot be considered as a point. The existence of intermediate scale gives rise to non-local noise. Moreover, the swimming induced stresses on the bacteria that may change the local arrangement of bacteria and induce stress fluctuations. These stress fluctuations may lead to shear motion somewhere else and hence is also called non-local. The rearrangement occurring due to shear stress is considered to be a self-activated process. The shear due to this self- activated process makes gene expression possible. The above analysis lead us to formulate a non-local hydrodynamic framework to study the collective behaviour of bacteria in order to understand quorum sensing. The weakly non-local extension of hydrodynamics has been studied by several authors in the context of continuum mechanics with internal structures, coarse graining, or gradient of the density and its higher order derivatives[8].

2.1. *Weakly non-local hydrodynamics and viscosity*

The state space of one component fluid is described by the density ρ and $\vec{v}$ the velocity of fluid. The state space $(\rho, \vec{v})$ and velocity gradient span the domain of constitutive functions. The stress tensor or the pressure term is the only constitutive quantity in this framework. The weakly non-local extension of this framework is done by considering the higher order derivatives of the basic variables, such as density and velocity, in constitutive equations. In a fluid dynamical framework, the balance of mass and balance of momentum are usually expressed as

$$\dot{\rho} + \rho \nabla \dot{\vec{v}} = \sigma_m \tag{1}$$

and

$$\rho \dot{\vec{v}} + \nabla \dot{P} = \rho \vec{f} \tag{2}$$

respectively. Here P is the pressure and $\vec{f}$ be the force density. This is known as Cauchy momentum equation. Now we extend this framework by considering the state space spanned by the variables

$$(\rho, \nabla\rho, \vec{v}, \nabla\vec{v}, \nabla^2\rho).$$

Now the balance of mass and balance of momentum can be rewritten taking the time and space derivatives of the constitutive variables denoted by

$$(\dot{\rho}, \nabla\dot{\rho}, \dot{\vec{v}}, \nabla\dot{\vec{v}}, \nabla^2\vec{v}, \nabla^3\rho)$$

It has been proved by Van and Fulop[8] that there exists a scalar valued function ϕ_v or non-local potential such that

$$\nabla \cdot \sigma = -\nabla\phi_v \tag{3}$$

where ϕ_v is the course-grained potential or kinematic viscosity potential and σ_{ij} be shear tensor. This viscosity potential can be calculated from the entropy function as:

$$\phi_v = \nabla.(\rho\partial_{\nabla\rho}s) - \partial_\rho(\rho s) \tag{4}$$

where s is entropy. Choosing particular form of s we can study specific non-local fluids. We can choose the simplest potential function using the following entropy density function

$$s(\rho, \nabla\rho) = -\nu\frac{\nabla\rho^2}{4\rho} - \frac{\vec{v}^2}{2} \tag{5}$$

The non-local potential can be deduced from this entropy as

$$-\frac{\nu}{2}\nabla^2\rho \tag{6}$$

ν is a constant coefficient called kinematic viscosity. Let us define a *kinematic velocity* $\vec{u_k}$ as

$$\vec{u_k} = \nabla\rho$$

The kinematic velocity is introduced in order to relate to a kind of fluctuations due to the course grained nature of the fluid. After some algebraic calculations we can write a general expression

$$\nabla\vec{u} + (\vec{u}.\nabla)\vec{u} = \nu\nabla^2\vec{u} + \nabla\eta \tag{7}$$

where

$$\nabla\eta = -\nu\nabla^2(\Delta\vec{u_k}).$$

Here,

$$\Delta\vec{u_k} = \vec{u} - \vec{u_k}$$

The above equation is noisy Burgers equation. Now we discuss this framework to understand phenomena of quorum sensing among the bacteria.

3. Quorum Sensing and Metastable State

The bacteria confined in a particular volume can change their environment when they reach a particular density.Experimental observations[14] clearly indicate the existence of some cooperative activities of the cells when they reach a particular density. This cooperation can change the environment and produces coordinated action when sufficient density of cells is available. Here, the cell to cell communication is used for this coordinated action. Bacteria release some molecules known as signaling molecules or more precisely autoinducers. The term quorum sensing was coined by Fuqua *et al.*[14] to indicate the minimum behavioral unit of cells as a quorum of bacteria. There exists various *apparently* conflicting hypothesis regarding the function of this type of signaling. Quorum Sensing (QS) and Diffusion Sensing (DS) are generally considered as two competing hypotheses. Burkhard *et al.*[15] proposed a new explanation unifying these two "apparently conflicting hypotheses" knwon as Efficiency Sensing (ES). Moreover, West *et al.*[16] critically analyzed the three proposals i.e. QS, DS and ES and claimed that ES is not required to unite QS and DS.

We emphasize that the framework of non-local hydrodynamics can explain the phenomena from a more physical perspective in a consistent way. It is evident from our analysis in previous section that the rearrangement of the configuration of the coarse grained systems produce a noise which gives rise to kinematic viscosity. Zeldovich[10] used this kind of viscosity to understand disk like structure formation at galactic scale which is popularly known as adhesive approximation. The noise associated to viscosity is discussed by Saluena and other workers[17] in connection with the hydrodynamics of dense granular systems. This type of noise plays a crucial role in understanding quorum sensing of the cells in the following way.

Closely packed cells or bacteria in suspension interact through the hydrodynamic disturbance when the concentration becomes sufficiently high. The colony of bacteria seems to interact with the medium, say, water in which they are suspended and one needs to take care of this interaction in understanding their behaviour. Since no motion is observed in the medium in the absence of the bacteria or if the bacteria are dead and also due to the fact that the density of bacteria is high, it is reasonable to assume that the bacteria and the water moves as a single fluid. However, the behaviour of this fluid is very different from ideal fluid. It is similar to the behaviour of fluid associated to the dense granular systems since there exists a non-local (athermal) noise due to finite size of the bacterium and hence an inter-

mediate scale. In non-local hydrodynamics for dense granular materials the state space is considered as function of $(\rho, \nabla\rho, \vec{v})$ and other higher order derivatives of density and velocity. The nonlocality is mathematically expressed through these higher order derivatives.

3.1. *Position based sensing*

The discovery of autoinducer molecules[18] laid down the physical basis of cell to cell bacterial communication. The diffusion of these autoinducers have been studied by several groups where it is possible to calculate the gradient profiles either around a single cell or at the center of increasing densities of cell. Alberghini *et al.*[4] studied positional sensing of the cells vs quorum sensing and cell to cell communication. They emphasized that one should consider cell to cell communication in terms of positional sensing where instead of considering concentration of a mixed bulk solution it is necessary to take care of the topologically distinct values sensed by individual cell at different positions of the environment. We consider the gradient of density as another state variable for the fluid description of densely packed bacteria within the framework of non-local hydrodynamics. The concept of velocity (for the bacterial fluid) similar to kinematic velocity in the framework of non-local hydrodynamics is defined as

$$\vec{u_{kin}} = \nabla\rho$$

where ρ is the density of the fluid. Because of existence of non-local noise arising from the intermediate scale due to finite size of the bacterium $\vec{u_{kin}}$ velocity will vary and

$$\Delta\vec{u_{kin}} \equiv \vec{u} - \vec{u_{kin}}$$

where $\vec{u}$ is the mean velocity. This will give rise to a viscosity

$$\nabla\eta \equiv -\nu\nabla^2(\Delta\vec{u_{kin}}).$$

This viscosity forms a metastable state of the bacteria similar to adhesive approximation of Zeldovich giving rise to a disk at galactic scale. This noise term will add an extra term in Burgers equation (as mentioned in equation 7) and the stability of noisy Burgers equation has been studied with small viscosity.[19]

3.2. *Metastable state*

The multi-time scale behaviors of Burgers equation with small viscosity as studied by Beck *et al.*[19] indicates the possible existence of metastable states in physical system. The stationary or stable states of physical systems are well studied in applied mathematics. The metastable states are not fixed points of the equation of motion but a family of states which emerge relatively quickly and ultimately goes to asymptotic state. Here, multi time scales are important in the sense that at one time scale metastable state emerges and for another asymptotic states emerge. In two dimensional fluid flows, the metastable states play important role. In case of bacteria, the kinematic viscosity (as the ratio of dynamic viscosity and the density) will be small since the density is very high to form quorum. The emergence of metastable state is possible for this kind of physical system with high density (small viscosity) for short time scale. During this time period as the sates are metastable, the fluctuation of stress due to autoinducing molecules will produce a fluctuation in the configuration of the system which induce shear somewhere else. This process is a self activated process and occurs in non-local rheology.

3.3. *Self-activated process and ratio of bulk to shear viscosity*

The shear force exerted by the autoinducing molecules will produce fluctuation of the stress in the configuration of the densely packed bacteria. As soon as the concentration of the auntoinducers reach a threshold it leads to the change of the arrangement of the configuration and gives rise change in bulk viscosity. The bulk viscosity for dense fluid is related to irreversible resistance. This is different from thermal fluctuation since thermal fluctuation is negligible for dense granular fluid. This change in bulk viscosity will produce shear to some where else. In densely granular medium the fluctuation of the stress and consequent production of shear is considered to be a self-activated process. In the present scenario of densely packed bacteria the ratio of bulk viscosity and the shear viscosity is associated to this type of self-activated process which make the expression of genes possible and synchronization happens. Iberall and one of the present authors (RL)[20] postulated that the basic organizing force for the living system control dynamically the ratio of bulk to shear viscosity.

It is to be noted that gene regulation due to shear stress has become an active area of research[21]. More than 40 genes have been identified to

be modulated by the shear stress in endothelial cells. These genes are shown to be involved in cell prolification, differentialtion, thrombosis etc. In the context of quorum sensing the genes have been already identified which express as soon as density of the cells reach a threshold value. The expression of these genes in QS can be tested in laboratory experiments by changing shear stress.

4. Quorum Sensing in Bacteria and Cellular Ensemble Communication

The proposed non-local hydrodynamic model of quorum sensing of bacteria clearly indicates that communication among bacteria has an important physical component. Indeed, while autoinducing molecular interactions have been considered as responsible for communication among bacteria some are best assigned to physical parameters. We propose that hydrodynamic parameters are essential in the understanding of the quorum sensing as an ensemble event. Indeed, kinematic viscosity arising from noise associated to medium granularity is an essential parameter to be considered, as granularity is related to the finite length scale associated with bacterial size. This parameter generates a noise addressed as non-local noise. Moreover, as this length scale vanishes so thus such non-local noise. From the above analysis it is evident that the role of this noise, and hence the viscosity is a fundamental parameter in producing metastable states in bacterial ensembles and is. critically dependent on density, a critical value of the viscosity parameter. It is to be mentioned that Pollack and his collaborators[22−26] investigated the structure of water from molecular level to bulk scale and predicted the fourth phase of water as liquid crystalline one apart from solid, liquid and vapour. They have also studied the long range interaction in water. The detail investigations are needed to find a relation of our approach based on non-local hydrodynamics and the long range ordered water hypothesis as studied by Pollack *et al.*[22−26]. We emphasize that metastable states are an absolute pre-requisite for quorum behaviour. Indeed, autoinducing molecules alone are in themselves not sufficient to implement a metastable community. Beyond bacterial ensembles cellular organization, specially among eukaryotes and most particularly among neurons requires other essential parameters. Thus in nerve nets, the cells are intimately connected by either chemical junctions (synapses) or by direct membrane contact as in the case of the so called gap junctions. This later supports direct electrical communications amongst neurons. Another em-

bodiment is generated by the presence of tight junctions that support tissue organization in multi cellular animals. Thus it is difficult to equate a granular cell ensemble in contrast to the granular medium consisting of bacteria where bacteria are not physically connected.

5. Quorum Sensing, Diffusion Sensing and Non-local Hydrodynamic Model

Various approaches have been proposed to understand co-operative strategy and cell to cell communication among bacteria. There have been two main theories widely discussed among the community, namely Quorum Sensing (QS) and Diffusion Sensing (DS). A co-operative strategy known as Quorum Sensing as understood by the release of signaling substance (called autoinducing molecules) is used to determine the cell density. On the other hand Diffusion sensing strategy is basically non-co-operative where the autoinducers are used to determine the dimensions of the space surrounding the cell. Both the theories are considered as much more complex than what occur in laboratory condition. However, to consider evolutionary effect as well as to tackle heterogeneous enviornment in a more comprehensive way Efficiency Sensing (ES)[27] is proposed. The main idea behind "efficiency sensing" approach the autoinducer senses efficiently the diffusible extracellular effectors produced by a given cell, including proteins that are costly to produce. Both the above theories i.e. Quorum sensing and Diffusion sensing may be the secondary functions of efficiency sensing. Darch *et al.*[28] tested experimentally the fundamental assumption of quorum sensing and found that the secretion of of autoinducing molecules is more beneficial at high densities. This has not been tested before.

Recently, Koch *et al.*[1] indicated that experimental observations on the suspension of swimming bacteria and their coordianted movement at high density can be properly described by hydrodynamic interaction. However, they emphasized that it is necessary to conduct experiments so as to monitor the quantities like effective viscosity, velocity etc. Moreover, several authors[29,30] found from their analytical and numerical investigations related to the suspension of swimming bacteria that long range hydrodynamic interactions reduce viscosity dramatically at low concentration but increases at higher concentration. But in this type of framework, the bacteria is treated as point particle.

In the present paper the authors propose more realistic framework for swimming bacteria using general hydrodynamical framework called Non-

local hydrodynamics. In this framework the granularity i.e. the finite size of the bacteria instead of point like particle produces an internal noise. This internal noise gives rise to kinematic viscosity at large concentration. Again the above mentioned framework of Sokolov and others[28] clearly demonstrated the increase of viscosity at large concentration. We emphasize that at high concentration the rise of effective viscosity can be related to this kinematic viscosity in our framework. The effective viscosity can be measured experimentally and it is possible to compare the increase of viscosity due to local hydrodynamical model in comparison to non-local hydrodynamical as proposed by the present authors.

6. Discussion

It is evident from the above analysis that we need to consider two major steps in understanding quorum sensing of bacteria. As the density of the bacteria becomes high and reaches a threshold, a metastable state is formed for a particular time period and then the ratio of bulk to shear viscosity associated to a self regulatory process due to stress fluctuation by autoinducer molecules gives rise to shear making gene expression possible. The metastable state is produced for small viscosity arising out of the internal non-local noise. The water fluidity is modified here and the phase is similar to ordered water hypothesis as discussed by Pollack *et al.* It may be possible to estimate the viscosity produced by non-local noise by studying the quorum sensing of bacteria from the metastable state. This will be compared with the viscosity in local hydrodynamic model and will be discussed in future publication. Here we have a single framework where one need not to consider QS, DS or ES separately for the description of cell to cell bacteria communication. It is worth-mentioning that the adhesive approximation which is used in the context of disk formation at galactic scale is also useful in understanding the metastable state for cell to cell communication. It sheds new light on the issues of applicability of physical principles in biological systems.

References

1. Donald L. Koch and Ganesh Subramanian, (2011) Annu. Rev. Fluid Mech. **43**, 637–59.
2. C. M. Waters and B. I. Bassler, (2005) Annu Rev. Cell Div. Bio. **21**, 319–46.
3. T. Long, K. C. Tu, Y. Wang, P. Mehta P, N. P. Ong, *et al.*, (2009) PLoS Biol **7**(3): e1000068. doi:10.1371/journal .pbio.1000068
4. Sara Alberghini *et al.*, (2009) FEMS Microbiol Lett. **292**, 149–161.

5. J. Lega and T. Passot, (2003) Phys. Rev. E **67**, 031906–17.
6. J. Dunkel *et al.*, (2013) Phys. Rev. Lett. **110**, 228102–5.
7. M. C. Marchetti *et al.*, (2013) Rev. Mod. Phys. **85**, 1143–1189.
8. P. Van and T. Fulop, (2004) Weakly Nonlocal Fluid Mechanics — The Shrodinger Equation, arXiv:quant-ph/0304062v2
9. A. L. B. Ribeiro and J. G. Peixotode Faria, (2005) Weakly Non local Hydrodynamics and The origin of Viscosity in the Adhesion Model: arXiv:astro-ph/050258v1
10. Y. B. Zeldovich, (1970) A & A **5**, 84.
11. H. C. Fogedby, (1998) Phys. Rev. E **57**, 4943–68.
12. Olivier Pouliquen, Yoel Forterre and S. Ledizes, (2001) Advances in Complex Systems **4**, 441–450.
13. Olivier Pouliquen and Yoel Forterre, (2009) Phil. Trans. R. Soc. A **367**, 5091–5107.
14. W. C. Fuqua, S. C. Winans and E. P. Greenberg, (1994) J. Bacterol Vol. 176, 269–275.
15. A. Burkhard *et al.*, (2007) Nature Reviews /Microbiology **5**, 230–9.
16. Stuart A. West *et al.*, (2012) Trends in Microbiology **20**, 586–94.
17. Clara Saluena *et al.*, (1997) In P. P. Behringer, J. T. Jenkins (Eds) Powders and Grains '97, Balkama (Rotterdam) pp. 341–344.
18. M. B. Miller, B. L. Bassler, (2001) Annu. Rev. Microbiol. **55**, 165–199.
19. C. Margaret Beck, C. Eugene Wayne, (2009) SIAM J. Appl. Dyn. Syst. **8**, no. 3, 1043–1065.
20. Rodolfo R. Llinás and Arthus Iberall, (1977) Biosystems **8**, 233–5.
21. Susan M. McCormick *et al.*, PNAS u July 31, (2001) **98**, no. 16, 8955–8960.
22. G. H. Pollack, (2013) The fourth phase of water: beyond solid, liquid and vapour (Ebner and Sons Publishers)
23. J. Zheng *et al.*, (2006) Advances in Colloid and Interface Science **127**, 19–27.
24. G. H. Pollack, (2013) J. Phys. Chemistry B **117**, 7843–7846.
25. M. Rohani and G. H. Pollack, (2013) Langmuir **29**, 6556–61.
26. Hense A. Burkhard, Christina Kuttler, Johannes Mller, Michael Rothballer, Anton Hartmann & Jan-Ulrich Kreft, (2007) Nature Reviews Microbiology **5**, 230–239.
27. Sophie E. Darcha, Stuart A. Westb, Klaus Winzera and Stephen P. Digglea, (2012) PNAS **109**, 8259–8263.
28. A. Sokolov and I. S. Aranson, (2009) Phys. Rev. Lett. **103**, 148101–4.
29. Shawn D. Ryan *et al.*, (2011) Phys. Rev. E **83**, 050904–8.

GEOMETRIC ANALYSIS OF THE CONFORMATIONAL FEATURES OF PROTEIN STRUCTURES

MANISH DATT

Institute of Life Sciences, Ahmedabad University
Gujarat - 380009, India
E-mail: manish.datt@ahduni.edu.in

Proteins exhibit intriguing diversity in their three dimensional conformations that enables them to perform different functions. Detailed understanding of protein conformational landscape is imperative for application in structure based inhibitor design. In this study, protein structures have been analyzed for the pattern of convex hulls based on Cα atom coordinates. A convex hull is a polygon whose vertices are a subset of a given set of points such that all the points are enveloped within the polygon. Iterative calculations of convex hull for proteins have provided interesting insights into their conformational features. A detailed and comprehensive analysis of convex hull pattern for non-redundant dataset of proteins revealed that the number of layers per protein ranged from 5 to 20 with an average of 8 layers. Statistical analysis shows that there exist 70% correlation between number of convex hull layers and radius of gyration of a protein. Correlation between radius of gyration and number of convex hull layers for different structural classes of proteins has also been performed. These results provide a novel approach for convex hull based interpretation/ comparison of proteins structures.

1. Introduction

Proteins are biopolymers that mediate variety of essential physiological functions. Proteins fold into a precise three dimensional structure that dictates their function[1]. Therefore understanding the structure of proteins is indispensable for interpreting their physiological roles. X-ray crystallography and Nuclear Magnetic Resonance (NMR) are two main experimental techniques for protein structure determination[2]. Effective utilization of these techniques have resulted in deposition of more than one lac experimentally determined protein structures in the Protein Data Bank (www.pdb.org). Over the decades, these structures have provided invaluable insights into the conformational landscape of proteins[3]. The data from these experiments have shown that polypeptide adopts well-defined secondary structure conformation such as α-helix and β-strand which then

folds into a characteristic tertiary structure. Some proteins can further adopt quaternary structure by assembly of different subunits. The enormous diversity in the structural features of proteins requires innovative methods for their classification. Secondary and tertiary structure features of proteins have been used to structurally classify proteins. SCOP[4] and CATH[5] are two widely used protein structure classification systems. SCOP classifies proteins into classes, folds, superfamilies, and families whereas in CATH the different levels comprise of class, architecture, topology, and hierarchy. Analysis of different classes of protein structure has advanced our understanding of structure-function relationship[6]. Recent years have seen tremendous advancement in computational methods for analysis of protein structures[7]. These methods can be used to analyze wide range of conformational features of proteins such as multimer assembly, domain assignment, identification of ligand binding pockets, channels within protein structure, molecular surface analysis, protein- protein/ ligand interactions etc.[8,9,10,11,12]. One of the characteristic features of protein structures is the packing of amino acid within the structure. Solvent accessibility calculation provides quantitative estimation for the location of amino acids with the structural envelop[13]. Amino acid residues with high solvent accessibility are located on the periphery of the structure while lower solvent accessibility indicates that residues are buried. These calculations are based on rolling a sphere (size of water molecule) along the surface of protein. This binary classification for residues in protein i.e. exposed vs. buried is rather inadequate since the buried residue could be in the core or just below the exposed ones. Previous studies have shown that convex hull calculations can provide complimentary information to the solvent accessibility analysis for proteins[14]. In this study, geometric analysis of the protein structures has been done based on the convex hull pattern. A convex hull is a polygon whose vertices are a subset of a given set of points such that all the points are enveloped within the polygon. Cartesian coordinates of Cα atoms were used to calculate convex hull for protein structures. This convex hull thus represents the bounding surface of the Cα atoms within the protein. Further, layers of convex hull within the protein were calculated by iteratively computing the convex hull after removing the coordinates for Cα atoms in the preceding layer. Comparative analysis of convex hull layers with the radius of gyration of the protein has provided interesting insights into the geometric features of protein structures. The results presented here would prove useful in developing novel strategies for detailed analyses of proteins and their complexes.

2. Methods

2.1. *Convex hull calculations*

Coordinates of experimentally derived protein structures were retrieved from the protein data bank (PDB)[15]. Biopython module[16] within python programming language was used to read the protein structure files. Scipy implementation of Qhull library was used for fast and accurate calculations of convex hull. [X, Y, Z] coordinates of all the Cα atoms within the protein were used for calculations. Layer of convex hull for a given protein structure was computed by iteratively removing coordinates forming the vertices of preceding convex hull.

2.2. *Radius of gyration calculation*

Radius of gyration (Rg) provides quantitative estimates for the dimensions of the protein. Mathematically, Rg is average distance of a set of coordinates from the centroid. Centroid for the protein structure was calculated using the formula:

$$(X, Y, Z)_{(Centroid)} = \left(\frac{\sum_i^n (x_i)}{n}, \frac{\sum_i^n (y_i)}{n}, \frac{\sum_i^n (z_i)}{n} \right)$$

Where, X, Y, Z are the 3D coordinates for the centroid to be calculated for a given set of n atoms. x_i, y_i, and z_i are 3D coordinates for each Cα atom i within total number of Cα atoms n. The radius of gyration for protein was then calculated by finding the root mean squared distance of each Cα atom from the centroid of the protein.

2.3. *Dataset of protein structures*

Non-redundant set of protein structures with sequence similarity cut-off of 20% and structures having crystallographic resolution of better than 3.0Å was retrieved from the PISCES database[17]. These structures were used for iterative convex hull analysis. In addition, another dataset of protein structure were retrieved from the SCOP database[4]. This database provides classification of structures based on their secondary structure properties and was used for calculating correlation between convex hull layers and radius of gyration for different classes of proteins. PyMol (Schrdinger, LLC) was used for protein structure visualization. The open-source python program for convex hull analysis was developed in house.

3. Results

Proteins exhibits enormous diversity in their shapes and sizes that allows them to perform different physiological functions. Over the years, experimental and computational methods have provided valuable insights into the structural characteristic of proteins. Detailed understanding of conformational landscape of the proteins is essential for interpreting structure-function correlation. To this end, this study presents a geometric analysis of protein structures based on their convex hull patterns. An open-source python based program has been developed for calculation of convex hull using Cartesian coordinates of protein structures (see methods). By using scientific and numeric libraries the speed and accuracy has been well optimized for convex hull calculations. Iterative calculation of convex hull based on coordinates of Cα atoms from a non-redundant dataset of protein structures was also done. Based on the analysis of 2,756 structures, the results show that the number of hull layers varies from 5 to 20 depending upon the size and conformation of the protein. On an average, protein structures were observed to have 7 layers of convex hulls. Figure 1(A) shows cartoon representation of apolipoprotein (PDB ID 1AEP)[18] having 5 convex hull layers. The radius of gyration for this protein is 15.2Å. Crystal structure of Nck-associated protein (PDB ID 3P8C)[19] had maximum number of convex hull layers. The number of convex hull layers and radius of gyration for this protein was observed to be 20 and 47.4Å, respectively. In addition, the crystal structure of RNA polymerase I (PDB ID 4C2M)[20] was also observed to have 20 convex hull layers with Rg of 39Å. This analysis quantitatively highlights the diversity in protein structures based on the convex hull pattern. This remarkable geometric variation in proteins was further investigated and correlated with other quantitative structural features.

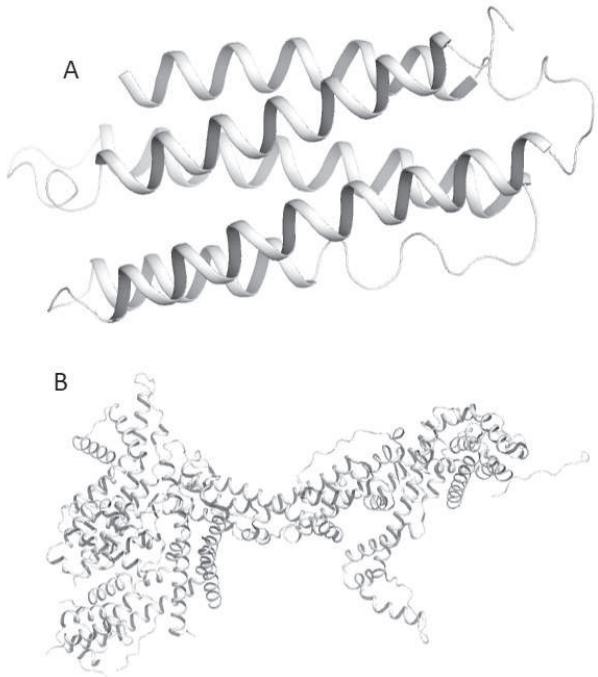

Figure 1.

Next, number of atoms constituting the vertices of convex hull in all the layers for all proteins was calculated. This analysis would provide insight into the packing of atoms with the protein core. Figure 1 shows the distribution for number of atoms in different convex hull layers. Overall, there was a continuous decrease is the number of atoms constituting the convex hull (Figure 2). This is expected since the total number of atoms would decrease after each iteration of convex hull calculation. The first convex hull layer had a median of 20% of the total Cα atoms of the protein. For different structures in the dataset there was huge variation in the number of atoms constituting the first convex hull layer. The minimum and maximum number of Cα atoms in first layer was 4.5% and 36.8%, respectively.

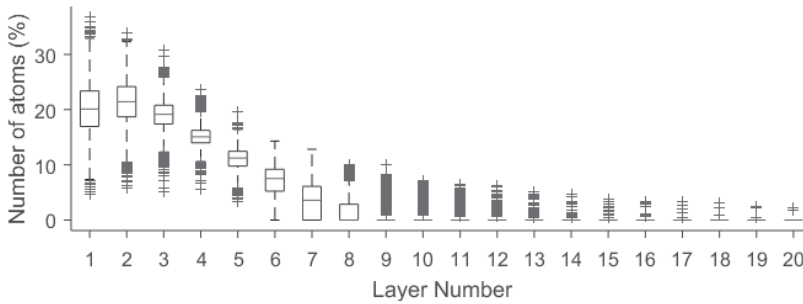

Figure 2. Box and whisker plot showing percentage of Cα atoms present in each convex hull layer in a dataset of non-redundant protein structures. The horizontal line within the box represents the median value for that distribution.

Intriguingly, the second convex hull layer was observed to have, on an average, higher number of atoms as compared to the first layer with median value of 21.4%. The minimum and maximum number of atoms in first layer was 5.8% and 33.9%, respectively. This observation suggests that there exist a higher density of atoms underneath the first layer of surface exposed atoms. This is indeed a remarkable finding from this analysis and it must be noted here this information is not available from the conventional surface analysis of proteins. From the third convex hull layer onwards there was a continuous decrease in the percentage of atoms constituting the convex hull (Figure 2). Radius of gyration (Rg) for all the protein structures in dataset were calculated and compared with number of hull layer in each structure. Rg provides a quantitative measure for the dimensions of the protein such that larger proteins would have higher Rg as compared to smaller ones. The correlation between number of convex hull layers and Rg was observed to be 72%. Figure 3 shows the correlation between convex hull layers and radius of gyration for each proteins structure. This rather low correlation indicates that the convex hull pattern of a protein is not directly related to the size of the protein. E.g. similar number of convex hull layers was observed for proteins with Rg range of more than 10Å (Figure 3). Therefore the convex hull layers provide complimentary geometric information to what is given by the radius of gyration of the proteins.

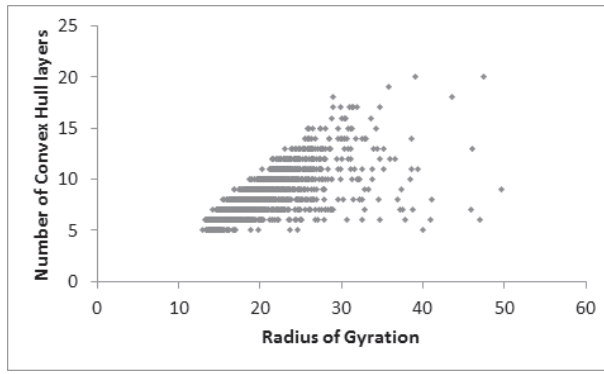

Figure 3. Scatter plot for the correlation between radius of gyration (Å) and number of convex hull layers in protein structures from a non-redundant dataset.

To evaluate whether the observed correlation between Rg and number of convex hull layers is present across all structural classes of proteins; the above analysis was performed on different structural classes of proteins. This is important because different class of proteins might have characteristic packing of the atoms within the core. Representative structures were downloaded from SCOP database having protein structures classified based on the secondary structure features. For all alpha and all beta proteins the correlation coefficient was observed to be 71% and 74%, respectively. This correlation is rather low as compared to what is observed for other class of proteins. Intriguingly, for alpha-beta (α/β) proteins the correlation was highest amongst all structural class of protein with a value of 87%. This class of proteins comprise mainly of parallel beta sheets with beta-alpha-beta units. Interestingly, for alpha and beta ($\alpha+\beta$) proteins (having mainly antiparallel beta sheets with segregated alpha and beta regions) the correlation was observed to be 74%. In case of multi-domain protein, high correlation of 85% was observed between Rg and number of hull layers. Table 1 presents the summary of the results for this analysis. Different values of correlation between number of convex hull layers and Rg evidently indicates that different classes of proteins have different packing characteristics.

Table 1: Correlation between radius of gyration and number of convex hull layers in protein structures from SCOP database.

SCOP class	Number of structures	Correlation between Rg and number of convex hull layers
(A) All alpha	685	0.71
(B) All beta	925	0.74
(C) Alpha and beta (α/β)	3135	0.87
(D) Alpha and beta ($\alpha+\beta$)	1276	0.74
(E) Multi domain	234	0.85

These results indicate that prior knowledge of secondary structure of the protein could be exploited to predict the correlation between radius of gyration and number of convex hull layers. E.g. for proteins having primarily alpha helices or beta sheets the correlation would be less as compared to / or multi-domain proteins. This information would be vital to predict packing characteristic of amino acid within the protein structure. Further, the results presented here suggest that packing characteristic could be predicted based on secondary structure features of protein. This would be an interesting area to pursue considering that there are methods which can predict secondary structure for a protein sequence at very high accuracy (95%)[21]. In addition, it is a lot easier to get secondary structure information from biophysical methods than to elucidate tertiary structure by experimental techniques. Overall, the study provides new insights into geometric features of proteins structures based on their convex hull pattern.

4. Conclusions

Detailed understanding of conformational features of proteins is essential to interpret their function. This study provides a comprehensive analysis of protein structure geometry based on the convex hull pattern. Iterative calculation of convex hull layers has quantitatively highlighted the diversity in conformation that different proteins adopt. Correlation between number of convex hull layers and radius of gyration of protein was observed to fluctuate for different structural classes of protein. These findings advance our understanding of the geometric topologies of protein structure and would pave the way for further development of methods aiming at geometric analysis of proteins.

References

1. L. C. James, D. S. Tawfik, "Conformational diversity and protein evolution a 60-year-old hypothesis revisited", Trends in Biochemical Sciences, vol. 28, no. 7, pp. 361–368, Jul. 2003, ISSN: 09680004. DOI: 10.1016/S0968-0004(03) 00135 - X [Online]. Available: http://linkinghub. elsevier. com/retrieve/pii/S096800040300135X.
2. A. A. Yee, A. Savchenko, A. Ignachenko, J. Lukin, X. Tu, T. Skarina, E. Evdokimova, C. S. Liu, A. Smesi, V. Guido, A. M. Edwards, C. Arrowsmith, "NMR and x-ray crystallography, complementary tools in structural proteomics of small proteins", Journal of the American Chemical society, Vol. 127, no. 47, pp. 16512-16517, Nov. 30, 2005, ISSN: 0002-7863, DOI: 10.1021/ja053565+.
3. F. Forouhar, A. Kuzin, J. Seetharaman, I. Lee, W. Zhou, M. Abashidze, Y. Chen, W. Yong, H. Janjua, Y. Fang, D. Wang, K. Cunningham, R. Xiao, T. B. Acton, E. Pichersky, D. F. Klessig, C. W. Porter, G. T. Montelione, L. Long, "Functional insights from structural genomics", Journal of Structural and Functional Genomics, Vol. 8, no. 2, pp. 37–44, Sep. 2007, ISSN: 1345-711X. DOI: 10.1007/s10969-007-9018-3.
4. N. K. Fox, S. E. Brenner, J.-M. Chandonia, "SCOPe: structural classification of proteins-extended, integrating SCOP and ASTRAL data and classification of new structures", Nucleic Acids Research, Vol. 42, pp. D304–D309, D1 Jan. 1, 2014, ISSN: 0305-1048, 1362-4962. DOI: 10.1093 / nar.oxfordjournals.org /lookup /doi/ 10.1093/nar /gkt1240.
5. I. Sillitoe, T. E. Lewis, A. Cuff, S. Das, P. Ashford, N. L. Dawson, N. Furnham, R. A. Laskowski, D. Lee, J. G. Lees, S. Lehtinen, R. A. Studer, J. Thornton, C. A. Orengo, "CATH: comprehensive structural and functional annotations for genome sequences", Nucleic Acids Research, Vol. 43, pp. D376–381, D1 Jan. 28, 2015, ISSN: 0305-1048, 1362-4962. DOI: 10.1093/ nar/ gku947. [Online]. Available: http//nar. oxfordjournals.org/ lookup/ doi/ 10. 1093/ nar/ gku947.
6. T. R. Hvidsten, A. Lgreid, A. Kryshtafovych, G. Anderson, K. Fidelis, J. Komorowski, "A comprehensive analysis of the structure-function relationship in proteins based on local structure similarity", PLoS One, Vol. 4, no. 7, J. L. Sussman, ed., e6266, Jul. 15, 2009, ISSN: 1932-6203, DOI: 10.1371/ journal.pone.0006266. [Online]. Available: http://dx . plos.org/10.1371 / journal . pone . 0006266.
7. S. Goldsmith-Fischmann, B. Honig, "Structural genomics: computational methods for structure analysis" Protein Science, Vol. 12, no. 9, pp. 1813–1821, Sep. 2003, ISSN: 09618368, 1469896X. DOI: 10.1110 / ps . 0242903.
8. J. G. Kiselar, M. Datt, M. R. Chance, M. A. Weiss, "Structural analysis proinsulin hexamer assembly by hydroxyl radical foot printing and computational modeling", The Journal of Biological Chemistry, Vol. 286, no. 51, pp. 43710–43716, Dec. 23, 2011, ISSN: 1083-351X. DOI: 10.1074/ jbc. M111. 297853.
9. M. Datt, A. Sharma, "Conformal landscapes for KMSKS loop in tyrosyl-

tRNA synthetases", Journal of Structural and Functional Genomics, Vol. 15, no. 2, pp. 45–61, Jun. 2014, ISSN: 1345-711X, 1570-0267. DOI: 10.1007/ s10969-014-9178-x. [Online]. Available: http: // link. springer. com/ 10.1007/s10969-014-9178-x.

10. H. Kaur, M. Datt, M. K. Ekka, M. Mittal, A. K. Singh, S. Kumaran, "Cysgly specific dipeptidase dug1p from s. cerevisiae binds promiscuously to di-, tri-, and tetra-peptides: peptide-protein interaction, homology modeling, and activity studies reveal a latent promiscuity in substrate recognition", Biochimie, Vol. 93, no. 2, pp. 175–186, Feb. 2011, ISSN: 1638-6183. DOI: 10.1016/ j. biochi. 2010.09.008
11. D. Kapoor, V. Kumar, S. K. Chandrayan, S. Ahmed, S. Sharma, M. Datt, B. Singh, S. Karthikeyan, P. Guptasarma, "Replacement of the active surface of a thermophile protein by that of a homologous mesophile protein through structure-guided 'protein surface grafting' ", Biochimica Et Biophysica Acta, Vol. 1784, no. 11, pp. 1771–1776, Nov. 2008, ISSN: 0006-3002. DOI: 10.1016/ j. bbapap. 2008.05.007.
12. P. Shahar, M. Kaushik, S. S. Gill, S. K. Gakhar, N. Gopalan, M. Datt, A. Sharma, R. Gill, "Genome-wide collation of the plasmodium falciparum WDR protein superfamily reveals malarial parasite-specific features", PLoS One, Vol. 10, no. 6, e0128507, 2015, ISSN: 1932-6203. DOI: 10.1371/ journal. pone. 0128507.
13. M. L. Connolly, "Solvent-accessible surfaces of proteins and nucleic acids", Science (New York, N.Y.), Vol. 221, no. 4612, pp. 709–713, Aug. 19, 1983, ISSN: 0036-8075.
14. M. Stout, J. Bacardit, J. D. Hirst, N. Krasnogor, "Prediction of recursive convex hull class assignments for protein residues", Bioinformatics, Vol. 24, no. 7, pp. 916–923, Apr. 1, 2008, ISSN: 1367-4803, 1460-2059. DOI: 10. 1093/ bioinformatics/ btn050. [Online]. Available: http:// bioinformatics. oxfordjournals. org/cgi/doi/ 10.1093 / bioinformatics / btn050.
15. F. C. Bernstein, T. F. Koetzle, G. J. Williams, E. F. Meyer, M. D. Brice, J. R. Rodgers, O. Kennard, T. Shimanouchi, M. Tasumi, "The Protein data bank: a computer file archival file for macromolecular structures", Journal of Molecular Biology, Vol. 112, no. 3, pp. 535–542, May 25, 1977, ISSN: 0022-2836.
16. P. J. A. Cock, T. Antao, J. T. Chang, B. A. Chapman, C. J. Cox, A. Dalke, I. Friedberg, T. Hamelryck, F. Kauff, B. Wilczynski, M. J. L. de Hoon, "Biopython: freely available python tools for computational molecular biology and bioinformatics", Bioinformatics, Vol. 25, no. 11, pp. 1422–1423, Jun. 1, 2009, ISSN: 1367-4803, 1460-2059, DOI: 10. 1093/ bioinformatics/btp163. [Online]. Available: http:// bioinformatics. oxfordjournals. org/cgi/doi/10.1093/ bioinformatics/btp163.
17. K. Wang, J. Gao, S. Chen, J. A. Tuszynski, J. Ruan, G. Hu, "An accurate method for prediction of protein-ligand binding site on protein surface using SVM and statistical depth function", BioMed Research International, Vol. 2013, e409658, Sep. 30, 2013, ISSN: 2314-6133. DOI: 10.1155/ 2013/ 409658. [Online]. Available: http://www.hindawi. com/ journals/ bmri/

2013/ 409658/ abs/.
18. D. R. Breiter, M. R. Kanost, M. M. Benning, G. Wesenberg, J. H. Law, M. A. Wells, I. Rayment, H. M. Holden, “Molecular structure of an apolipoprotein determined at 2.5-a resolution”, Biochemistry, Vol. 30, no. 3, pp. 603–608, Jan. 22, 1991, ISSN: 0006-2960.
19. Z. Chen, D. Borek, S. B. Padrick, T. S. Gomez, Z. Metlagel, A. M. Ismail, J. Umetani, D. D. Billadeau, Z. Otwinowski, M. K. Rosen, “Structure and control of the actin regulatory WAVE complex”, Nature, vol. 468, no. 7323, pp. 533–538, Nov. 25, 2010, ISSN: 1476-4687. DOI: 10.1038/ nature09623.
20. C. Engel, S. Sainsbury, A. C. Cheung, D. Kostrewa, P. Cramer, “RNA polymerase structure and transcription regulation”, Nature, Vol. 502, no. 7473, pp. 650–655, Oct. 31, 2013, ISSN: 1476-4687. DOI: 10.1038/nature12712.
21. A. Yaseen, Y. Li, “Context-based features enhance protein secondary structure prediction accuracy”, Journal of Chemical Information and Modeling, Vol. 54, no. 3, pp. 992–1002, Mar. 24, 2014, ISSN: 1549-9596, 1549-960X. DOI: 10.1021/ ci400647u. [Online]. Available: http://pubs.acs.org/doi/abs/10.1021/ci400647u.

PREDICTION OF SYSTEM STATES, ROBUSTNESS AND STABILITY OF THE HUMAN WNT SIGNAL TRANSDUCTION PATHWAY USING BOOLEAN LOGIC

LOSIANA NAYAK* AND RAJAT K. DE

Machine Intelligence Unit,
Indian Statistical Institute,
Kolkata 700108, India
E-mail: {losiana_t,rajat}@isical.ac.in

ABHIROOP DATTA

A.K. Choudhury School of Information Technology,
University of Calcutta,
Kolkata, India
E-mail: abhiroopdatta7@gmail.com

*Work supported by a postdoctoral fellowship f.15-1/2013-14/pdfwm-2013-14-ge-ori-19068(sa-ii) of the university grants commission.

Biological systems are complex, large and quasi-deterministic. Study and analysis of such large systems by holistic approaches are difficult in most cases due to lack of various resources. But if the system can be reduced to an abstract level without compromising the essential data, it can be handled and still significant results can be inferred from it. Boolean Networks provide one way of such abstract level analysis for dynamic biological systems. State transition matrices derived from dynamic behavior of these systems allow application of standard inference methods to discover dependencies among the elements present in such a system. Signal transduction pathways (by which cells detect, convert, and internally transmit information) can be modeled by ideas taken from such predictive methods. Wnt signal transduction pathway is an appropriate candidate for such kind of modeling due to its crucial presence in multiple types of cancers. Here we present a methodology pipeline for detecting i) stable system states, ii) robustness, and iii) stability of a whole system using Boolean logic based thumb rules. A unique thumb rule is designed for each biological interaction found in signal transduction pathways. A predicted system state is deemed as stable when it can be predicted without any clash of thumb rules. Robustness of a stable system state is measured by the number of permissible state transitions it can tolerate without loosing its stability. Stability of a whole system is studied by creating a state transition diagram, where stable system states are nodes and the transitions among them are edges. The methodology pipeline is tested on a 5-node (4 interactions) hypothetical network, a 14-node (15 interactions) example network and the human Wnt signal transduction pathway (59 nodes and 68 interactions). In the hypothetical network only two stable system states are found against the predicted 2^5 states. In the example network, system states 1 and 17 are found to be maximally robust. State transition diagram of the example network revealed it to be a bistable system with two distinct phases each containing one of the maximum robust system states. The human Wnt signal transduction pathway is found to exist in 8 distinct phases that can be supported by existing works.

1. Introduction

The exchange and processing of information between biomolecular entities within a cell give rise to many complex biological networks. Signal transduction pathways form one category of such complex biological networks. They mediate the sensing and processing of stimuli. These molecular circuits detect, amplify, and integrate diverse external signals to generate responses such as changes in enzyme activity, gene expression, or ion-channel activity. Their behavior needs to be understood in the context of how cellular events occur. A simple procedure, often followed to understand the behavior of signal transduction pathways, has been to depict interactions pictorially as a wiring diagram, and then construct a model to study its outcomes[1,2]. But, as the network grows, in terms of vertices, corresponding interactions, edge directions of the interactions, self loops, interaction weights, constructing a wiring diagram becomes time consuming and clumsy for interpretation.

On the other hand, these interactions can be represented as a Boolean network[3]. Boolean algebra (or Boolean logic) is a logical calculus of truth values, developed by George Boole in the 1840s. It resembles the algebra of real numbers, but with the numeric operations of multiplication $x \times y$, addition $x+y$, and negation $-x$ replaced by the respective logical operations of conjunction $x \wedge y$, disjunction $x \vee y$, and negation $-x$. The Boolean operations are these and all other operations that can be built from these, such as $x \wedge (y \vee z)$. These turn out to coincide with the set of all operations on the set {0,1} that take only finitely many arguments; there are 2^{2^n} such operations when there are n arguments. For a network (system) possessing n vertices, there are 2^n Explicitly Enumerated (EE) system states. EE vouches for a detail ordered listing of all of the elements of a set, a notion commonly used in Mathematics and Theoretical Computer Science.

Boolean network modeling of genetic regulatory networks has gained wide acceptance in the modeling community, based on pioneering works by Kauffman[4] and Thomas[5]. Several Boolean network simulators for biological systems have been developed, including NetBuilder, BooleanNet[6], SimBoolNet[7], BooleSim[8], BoolNetan R package[9], and The NetBuilder' project[10] among others.

Jack *et al.*[11] have developed an asynchronous threshold Boolean network simulation algorithm to model signal transduction in a single cell, and then used an ensemble of these models to estimate the aggregate response across a cell population. The authors have showed that populations of hepatocytes can be simulated to predict experimentally observed quantitative responses. Zou[12] has proposed a novel method to study intrinsically the relationship between experimental data and the possible Boolean networks, which can be used to model the underlying system. A Boolean model for the fruit fly *D. melanogaster* is used to explain the method. The authors have addressed the problem of completing the truth table starting from given incomplete truth table and partial information on the interactions among the genes considered. Cancer is a systems biology disease. It has remarkable complexity at the molecular level, with multiple genes, proteins, pathways and regulatory interconnections being affected. Nagraj and Reverter[13] have introduced a systems biology approach to study cancer that formally integrates the available genetic, transcriptomic, epigenetic and molecular knowledge on cancer biology and as a proof of concept applied it to colorectal cancer. In this respect, Eduatti *et al.*[14] have proposed a simple method that involves inference of Boolean tables from data to classify whether a particular combination of stimulus and inhibitor is affecting

the protein, reconstruction of a cause-effect network from Boolean tables and prediction of test data by linear combination of training data, using rules based on the reconstructed network.

A Boolean network describes a signal transduction pathway as a digital circuit in which logical elements (proteins or genes) are either ON or OFF with a value of 1 or 0 respectively. The temporal evolution of a signal transduction pathway can be calculated using a set of Boolean functions (AND, OR, NOT) to model regulatory interactions. The state of the pathway at any instant is the union of all the states of its regulating vertices. The regulatory connections (activation or inhibition) and inputs alter the state of the vertices. Over a period, the states reach a stable configuration called as singleton attractors, which correspond to a particular cellular event. Singleton attractors represent permanent changes in cellular behavior, unlike the non-singleton attractors. Non-singleton attractors represent periodic events and the transient states of a network[15,16]. Singleton attractors can also be used to determine underlying reasons for the cause of a disease[3]. Since they offer a biologically relevant and computationally efficient formalism for analyzing the relationship between molecular network topology and function, Boolean networks have been used extensively to simulate the behavior of cells based on their network activity[4,17,6,18].

In this article we present an idea of detecting system states and checking their robustness with possible state transitions for an example network as well as human Wnt signal transduction pathway. The human Wnt signal transduction pathway is an important machinery of cells associated with embryonic development[19], axis formation[20], cell fate specification[21], cell proliferation[21], cell migration[22], insulin sensitivity[23], various kinds of cancer[24], and type II diabetes[23] among others. By this study, behavior of this signal transduction pathway can be modeled. Here we have introduced the Boolean concept as it can define whether there exists any valid interaction among two components in a network in a very simplified form. In this study Boolean logic is introduced to reduce the complexity of an entire system so that Boolean networks can be used extensively to simulate the behavior of any biological entity based on their network activity.

2. Data and Methodology

Signaling pathways involve hierarchical assembly in space and time of multiprotein complexes that regulate the flow of information according to logical rules. They are embedded in networks having stimulatory (activa-

tion, phosphorylation, expression), inhibitory (inhibition, dephosphorylation), cooperative (binding/association), uncooperative (dissociation), destructive (ubiquitination) and other (compound, indirect effect) interactions to ensure appropriate interpretation of a signal *in vivo*. Each of these interactions can be governed by thumb rules inspired from Boolean logic.

Let A and B be substrate and product respectively; $X \uparrow$ be over-expression and $X \downarrow$ be under-expression of X. Then the possible thumb rules for various types of interactions are designed as given:

- activation(a) $[(A \uparrow, B \uparrow)$ and $(A \downarrow, B \downarrow)] \Rightarrow$ [(1,1) and (0,0)]
- inhibition(i) $[(A \uparrow, B \downarrow)$ and $(A \downarrow, B \uparrow)] \Rightarrow$ [(1,0) and (0,1)]
- binding(b) $[(A \uparrow, B \uparrow, AB \uparrow)$, $(A \uparrow, B \downarrow, AB \downarrow)$, $(A \downarrow, B \uparrow, AB \downarrow)$ and $(A \downarrow, B \downarrow, AB \downarrow)] \Rightarrow$ [(1,1,1), (1,0,0), (0,1,0) and (0,0,0)]
- dissociation(d) $[(AB \uparrow, A \uparrow, B \uparrow)$ and $(AB \downarrow, A \downarrow, B \downarrow)] \Rightarrow$ [(1,1,1) and (0,0,0)]
- ubiquitination(u) $(U \uparrow A \downarrow)$, U being Ubiquitin $\Rightarrow$ (1,1)

During 'activation', high concentration of A stimulates proportionate amount of B and vice versa, hence the states, (1,1) and (0,0). High concentration of A inhibits function of B during an 'inhibition' process. So a few of them will be active as in state (1,0). Alternatively, low concentration of A will facilitate function of high number of Bs as in state (0,1). High concentration of A and B indicate towards production of more number of ABs during 'binding' as in state (1,1,1). If anyone or both of A and B is present in low concentrations AB production will be less as in states (1,0,0), (0,1,0) and (0,0,0) respectively. During 'dissociation', formation of A and B is directly proportional to concentration AB. The phenomenon gets reflected in states (1,1,1) and (0,0,0). 'Ubiquitination' is a process by which unwanted and molecules in excess get purged from the intracellular environment. As only the unwanted/excess molecules get affected by ubiquitin, there is a steady maintenance of the required concentration of the molecule. Hence, that state is designed as (1,1). Some of the interactions are difficult to be represented by rules, *i.e.*, indirect effect. At this stage, we are not considering such interactions. We have done our initial study with a hypothetical network of 5 nodes and 4 interactions as given in Figure 1. Different types of interactions are presented with different kind of arrow marks [activation: $\rightarrow$, inhibition: $-|$, binding: $-$ and ubiquitination: $-\blacksquare$].

A single node can attain one of the two possible states, *i.e.*, ON (1) or OFF (0). So, theoretically a system of n nodes, can exist in 2^n system states. Each system state will be a string of n number of '1's and '0's.

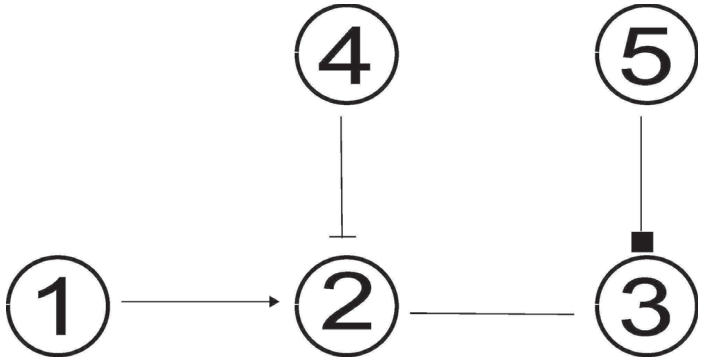

Figure 1. A hypothetical network.

But, often these interactions are linked among each other and the scenario becomes more complex. Hence, it is expected that the attainable number of states will be much less than the predicted 2^n system states.

Here we can represent Figure 1 as a set of following interactions: [w: (1,2,a); x: (2,3,b); y: (2,4,i); z: (3,5,u)]. The interactions are named as w, x, y and z respectively. The set of interactions present in a network define it as one system and their temporal variations create multiple system states. For the network of 5 nodes (Figure 1), we can expect the system to exist in 2^5 system states, each system state being a string of five '1's and '0's. But, after following the thumb rules and avoiding clash of rules we found only 2 stable system states (states 8 and 30) of the system (Table 1). When single or multiple thumb rules clashed while creating a system state, it was ignored. Once the stable system states are detected, a measure of their tolerance level towards change can define robustness of the system. Such a study was done with the example network (Figure 2).

3. Results and Discussion

In this Section, the Boolean logic based thumb rules are applied first to an example network (Figure 2) and then to the human Wnt signal transduction pathway (Figure 5).

3.1. *The example network*

The example network is a random simulated network that consists of 14 nodes and 15 interactions as given in Figure 2. Analyses of the network

Table 1. All Possible (2^5) States for a 5 node Hypothetical Network.

States	Node 1	Node 2	Node 3	Node 4	Node 5	Remarks
State 1	0	0	0	0	0	does not hold interactions y and z
State 2	0	0	0	0	1	does not hold interactions y and z
State 3	0	0	0	1	0	does not hold interactions y and z
State 4	0	0	0	1	1	does not hold interaction z
State 5	0	0	1	0	0	does not hold interactions y and z
State 6	0	0	1	0	1	does not hold interaction y
State 7	0	0	1	1	0	does not hold interaction z
State 8	**0**	**0**	**1**	**1**	**1**	**Valid**
State 9	0	1	0	0	0	does not hold interactions w and z
State 10	0	1	0	0	1	does not hold interactions w and z
State 11	0	1	0	1	0	does not hold interactions w, y and z
State 12	0	1	0	1	1	does not hold interactions w, y and z
State 13	0	1	1	0	0	does not hold interactions w and z
State 14	0	1	1	0	1	does not hold interaction w
State 15	0	1	1	1	0	does not hold interactions w, y and z
State 16	0	1	1	1	1	does not hold interactions w and y
State 17	1	0	0	0	0	does not hold interactions w, y and z
State 18	1	0	0	0	1	does not hold interactions w, y and z
State 19	1	0	0	1	0	does not hold interactions w, y and z
State 20	1	0	0	1	1	does not hold interactions w, y and z
State 21	1	0	1	0	0	does not hold interactions w, y and z
State 22	1	0	1	0	1	does not hold interactions w, y and z
State 23	1	0	1	1	0	does not hold interactions w, y and z
State 24	1	0	1	1	1	does not hold interaction w
State 25	1	1	0	0	0	does not hold interaction z
State 26	1	1	0	0	1	does not hold interaction z
State 27	1	1	0	1	0	does not hold interactions y and z
State 28	1	1	0	1	1	does not hold interactions y and z
State 29	1	1	1	0	0	does not hold interaction z
State 30	**1**	**1**	**1**	**0**	**1**	**Valid**
State 31	1	1	1	1	0	does not hold interactions y and z
State 32	1	1	1	1	1	does not hold interaction y

showcased interesting results. Theoretically the system can exist in 2^{14} system states, each system state being a string of fourteen '1's and '0's. But, after following the thumb rules and avoiding clash of rules only 64 stable states were found. When single or multiple thumb rules clashed while creating a system state, it was ignored.

Next, we introduced point mutations in the system states one-by-one. It was practically picking a string of fourteen '1's and '0's, and changing its value from 1 to 0 or 0 to 1 for each position one after another. With a change in positional value, a string has two options. Either it will resemble another system state out of the 64 possible system states or it will be a system state, where one/more thumb rules are clashing. The former

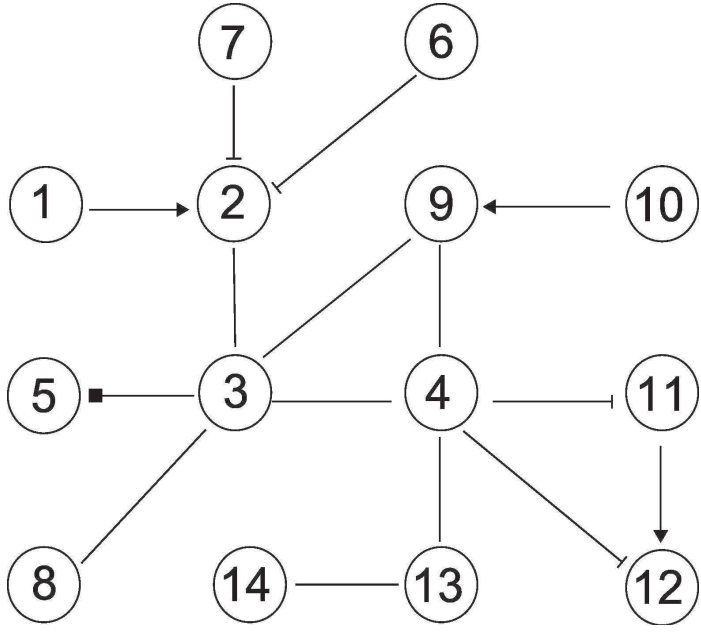

Figure 2. An example network.

phenomenon was noted down. A measure of the system states' tolerance level towards change of positional values ('1's and '0's) can define robustness of the network. The hypothesis is that the more number of times a string can tolerate a positional value change, the more robust is that system state. In addition a state transition diagram among multiple system states will throw light on modes of operation of the network. A diagram depicting the state transitions among multiple system states is known as the "state transition diagram". The hypothesis is that the state transition diagram may depict a whole network of system state transitions or exist in multiple distinct sub-networks. In the later case each of the distinct sub-networks represents possibly a distinct phase (mode of action) of the system. Based on that, stability pattern of the system can be guessed.

Figure 3 depicts the extent of robustness of the system states of the example network (Figure 2). Among them, system states 1 (0-0-1-0-1-1-0-0-0-1-1-0-0-1) and 17 (0-0-1-1-1-1-0-0-0-0-0-0-0-1) showed maximum extent of robustness by tolerating 7 positional value changes. When, the state transitions were viewed as a hierarchical layout network with help of

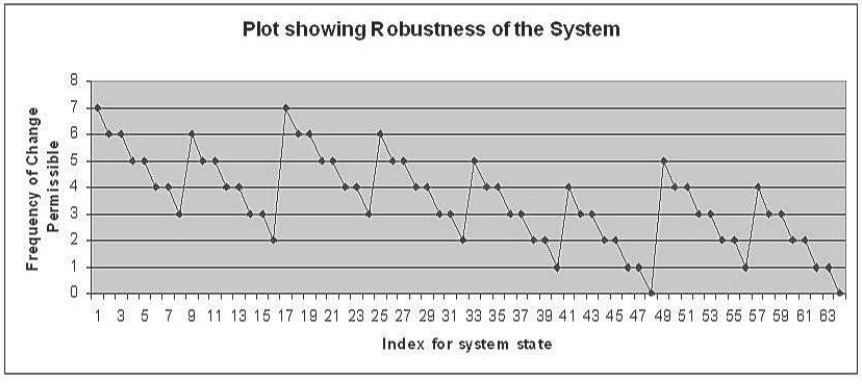

Figure 3. Robustness plot of the example network.

Cytoscape[25] two distinct networks were observed among the system states (Figure 4). Most interestingly, each of the most robust system states (1 and 17) were found to belong to the two different phases rather than to any one of the phases. Such a phenomenon might indicate towards bistability of the system.

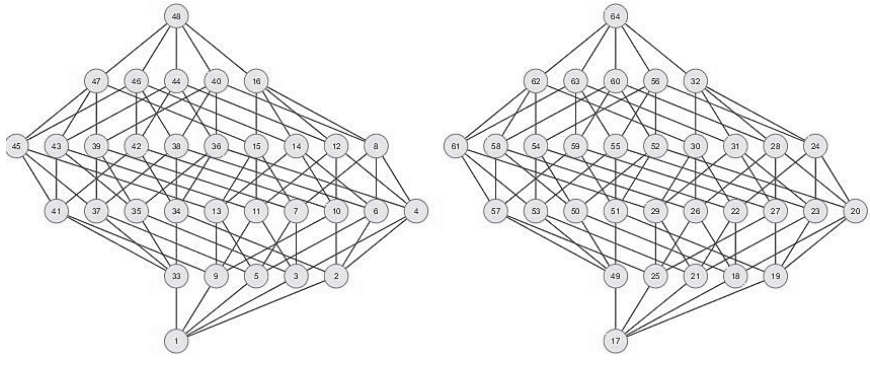

Figure 4. State transition diagram of the example network [each node represents a stable system state and an edge between a pair of nodes represents a state transition, multiple edges between same pair of nodes has not been plotted].

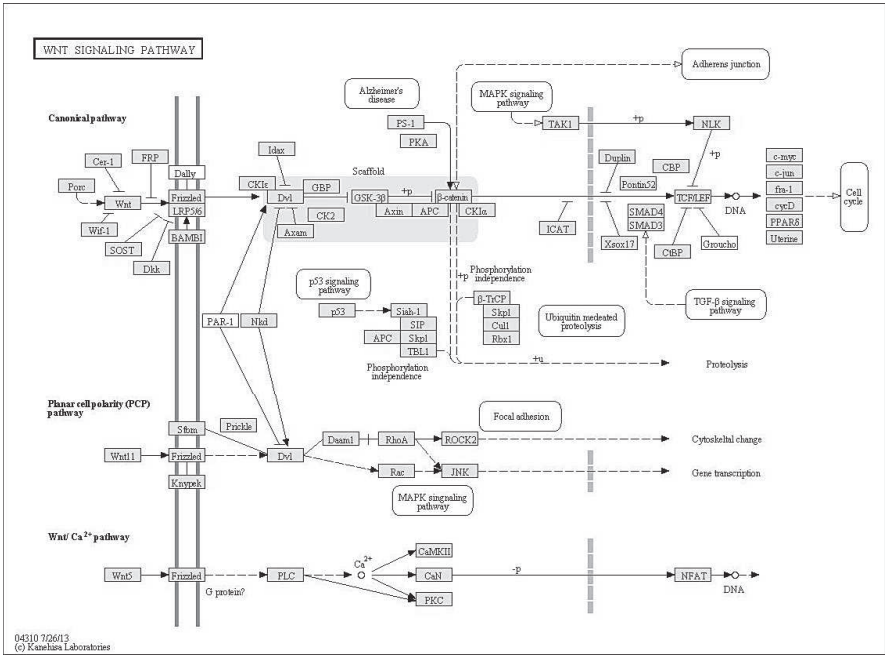

Figure 5. The human Wnt signal transduction pathway from KEGG/Pathway database.

3.2. *Human Wnt Signal Transduction Pathway*

The human Wnt Signal Transduction Pathway is taken from KEGG/Pathway database[26] as given in Figure 5. The Pathway has 59 nodes connected among themselves by 68 interactions.

After following the thumb rules and avoiding the clash of rules we found 2,62,144 stable system states for this pathway. After doing single point mutation on the these stable system states, we found 19,66,014 number of state transitions among the system states. We also calculated the number of transitions for which one valid system state gets mutated to another valid system state. The maximum number of transitions that happened for a system state is 15. As it is hard to analysis 19,66,014 number of transitions we adapted a minimum to maximum approach. We introduced a threshold to the data and took the system states with higher than 90% of the maximum number of transitions that happened for a system state, *i.e.*, 13. This step

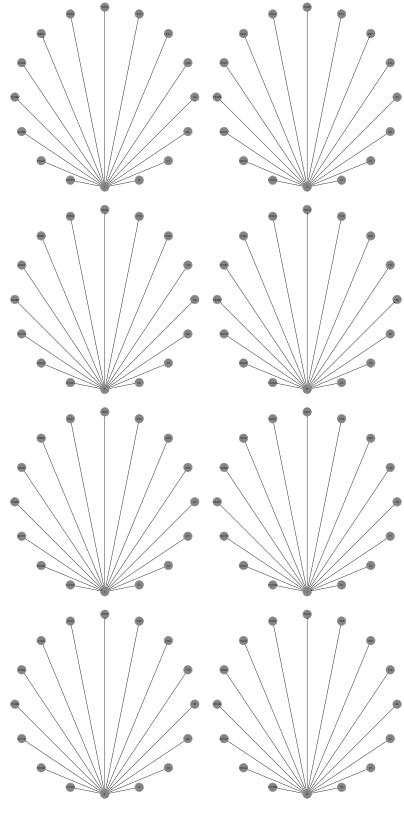

Figure 6. System state transitions among highly robust system states (threshold > 13) in the human Wnt signal transduction pathway [each node represents a stable system state and an edge between a pair of nodes represents a state transition, multiple edges between same pair of nodes has not been plotted].

truncated the number of state transitions to 120. These state transitions when plotted with Cytoscape (degree distribution layout)[25], separated into 8 different phases (Figure 6). We have labeled each phase with a number, *i.e.*, phases 1, 2, 3, 4, 5, 6, 7 and 8. Then we added neighbors of these system states, *i.e.*, we took all system state transitions where at least one system state can tolerate greater than 13 transitions irrespective of the other system state's robustness. Such an extension increased the number of state transitions to 1800 and their Cytoscape plotting still maintained the 8 different phases as shown in Figure 7. A closer look at the phases

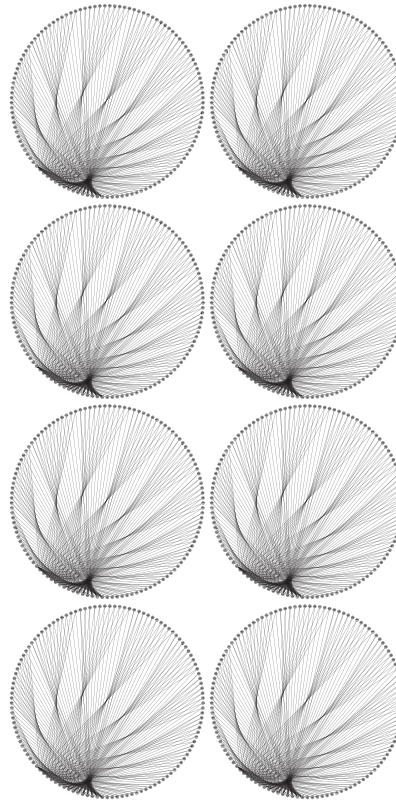

Figure 7. Different extended phases among highly robust system states in the human Wnt signal transduction pathway with at least one of the states belonging to the (threshold > 13) category [each node represents a stable system state and an edge between a pair of nodes represents a state transition, multiple edges between same pair of nodes has not been plotted].

revealed addition of state transitions to the existing system states as seen in Figure 8. It is interesting to note that the human Wnt signaling pathway (as given in KEGG) does exist in 8 modules[27,28]. This strengthens our methodology pipeline for prediction of system states, testing of their robustness and phase detection by state transition diagram.

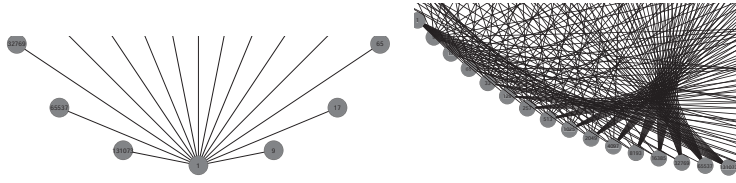

(a) Phase 1 of Figure 6 (magnified)

(b) Phase 1 of Figure 7 (magnified)

Figure 8. A closer look at state transition diagram (Phase 1) of the human Wnt signal transduction pathway [each node represents a stable system state and an edge between a pair of nodes represents a state transition, multiple edges between same pair of nodes has not been plotted].

4. Discussion

In this study, we defined Boolean logic based rules for different kinds of interactions found in biological networks, especially signal transduction networks. Based on these rules, we predicted possible attainable system states of a 14-node example network. Altogether 64 permissible system states were found for the system, against the predicted 2^{14} system states. Among them, system states 1 and 17 were found to be the most robust states in terms of their tolerance towards point mutations. A state transition diagram of the system states established two distinct phases among the state transitions, which might indicate towards bistability of the example network. We have done similar kind of study on a real life human Wnt signal transduction pathway (59 nodes). Altogether 2,62,144 stable system states were found for the system, against the predicted 2^{59} system states. We found 8 distinct phases among the system states, *i.e.*, phases 1, 2, 3, 4, 5, 6, 7, and 8 with introduction of 90% cut-off threshold (minimum to maximum approach). The methodology pipeline can be applied to any biological network with appropriate Boolean logic based rules.

5. Ongoing Work

We are following the same methodology pipeline for a network where the human Wnt signal transduction pathway is combined with its neighboring pathways mentioned and available in KEGG/Pathway database. The neighboring pathways are the pathways responsible for adherens junction,

Alzheimer's disease, cell cycle, focal adhesion, ubiquitin mediated proteolysis, MAPK signal transduction pathway, and TGF-β signal transduction pathway of *H. sapiens*. The complex network has a node size of 467. The number of possible system states is 2^{467}. We are trying to optimize our implementation by reducing time-complexity, designing distributed computing algorithms and reducing space complexity.

References

1. Hiroaki Kitano. Systems biology: a brief overview. *Science*, 295(5560):1662–1664, 2002.
2. Melody K Morris, Julio Saez-Rodriguez, Peter K Sorger and Douglas A Lauffenburger. Logic-based models for the analysis of cell signaling networks. *Biochemistry*, 49(15):3216–3224, 2010.
3. Suhas V Vasaikar, Bhyravabhotla Jayaram and James Gomes. Rapid computation and interpretation of Boolean attractors in biological networks. *Journal of Complex Networks*, page cnu011, 2014.
4. Stuart A Kauffman. Metabolic stability and epigenesis in randomly constructed genetic nets. *Journal of theoretical biology*, 22(3):437–467, 1969.
5. René Thomas. Boolean formalization of genetic control circuits. *Journal of theoretical biology*, 42(3):563–585, 1973.
6. István Albert, Juilee Thakar, Song Li, Ranran Zhang and Réka Albert. Boolean network simulations for life scientists. *Source code for biology and medicine*, 3(1):1–8, 2008.
7. Jie Zheng, David Zhang, Pawel F Przytycki, Rafal Zielinski, Jacek Capala and Teresa M Przytycka. SimBoolNeta Cytoscape plugin for dynamic simulation of signaling networks. *Bioinformatics*, 26(1):141–142, 2010.
8. Matthias Bock, Till Scharp, Chaitanya Talnikar and Edda Klipp. BooleSim: an interactive boolean network simulator. *Bioinformatics*, 30(1):131–132, 2014.
9. Christoph Müssel, Martin Hopfensitz and Hans A Kestler. BoolNetan R package for generation, reconstruction and analysis of boolean networks. *Bioinformatics*, 26(10):1378–1380, 2010.
10. Katja Wegner, Johannes Knabe, Mark Robinson, Attila Egri-Nagy, Maria Schilstra and Chrystopher Nehaniv. The netBuilder'project: development of a tool for constructing, simulating, evolving, and analysing complex regulatory networks. *BMC Systems Biology*, 1(1):1–2, 2007.
11. John Jack, John F Wambaugh and Imran Shah. Simulating quantitative cellular responses using asynchronous threshold Boolean network ensembles. *BMC systems biology*, 5(1):109, 2011.
12. Yi Ming Zou. Modeling and analyzing complex biological networks incooperating experimental information on both network topology and stable states. *Bioinformatics*, 26(16):2037–2041, 2010.
13. Shivashankar H Nagaraj and Antonio Reverter. A Boolean-based systems biology approach to predict novel genes associated with cancer: Application

to colorectal cancer. *BMC systems biology*, 5(1):35, 2011.
14. Federica Eduati, Alberto Corradin, Barbara Di Camillo and Gianna Toffolo. A Boolean approach to linear prediction for signaling network modeling. *PloS one*, 5(9):e12789, 2010.
15. Sui Huang and Donald E Ingber. Shape-dependent control of cell growth, differentiation, and apoptosis: switching between attractors in cell regulatory networks. *Experimental cell research*, 261(1):91–103, 2000.
16. Ranadip Pal, Ivan Ivanov, Aniruddha Datta, Michael L Bittner and Edward R Dougherty. Generating Boolean networks with a prescribed attractor structure. *Bioinformatics*, 21(21):4021–4025, 2005.
17. Jasmin Fisher and Thomas A Henzinger. Executable cell biology. *Nature biotechnology*, 25(11):1239–1249, 2007.
18. Rui-Sheng Wang, Assieh Saadatpour and Reka Albert. Boolean modeling in systems biology: an overview of methodology and applications. *Physical biology*, 9(5):055001, 2012.
19. Catriona Y Logan and Roel Nusse. The Wnt signaling pathway in development and disease. *Annu. Rev. Cell Dev. Biol.*, 20:781–810, 2004.
20. Qinghua Tao, Chika Yokota, Helbert Puck, Matt Kofron, Bilge Birsoy, Dong Yan, Makoto Asashima, Christopher C Wylie, Xinhua Lin and Janet Heasman. Maternal Wnt11 Activates the Canonical Wnt Signaling Pathway Required for Axis Formation in *Xenopus* Embryos. *Cell*, 120(6):857–871, 2005.
21. Karl Willert and Katherine A Jones. Wnt signaling: is the party in the nucleus? *Genes & development*, 20(11):1394–1404, 2006.
22. Alexandra Schambony and Doris Wedlich. Wnt Signaling and Cell Migration. *Wnt Signaling in Development*, page 240, 2003.
23. John C Yoon, Aylwin Ng, Brian H Kim, Antonio Bianco, Ramnik J Xavier and Stephen J Elledge. Wnt signaling regulates mitochondrial physiology and insulin sensitivity. *Genes & development*, 24(14):1507–1518, 2010.
24. Roel Nusse and Harold Varmus. Three decades of Wnts: a personal perspective on how a scientific field developed. *The EMBO journal*, 31(12):2670–2684, 2012.
25. Paul Shannon, Andrew Markiel, Owen Ozier, Nitin S Baliga, Jonathan T Wang, Daniel Ramage, Nada Amin, Benno Schwikowski and Trey Ideker. Cytoscape: a software environment for integrated models of biomolecular interaction networks. *Genome research*, 13(11):2498–2504, 2003.
26. Minoru Kanehisa and Susumu Goto. KEGG: kyoto encyclopedia of genes and genomes. *Nucleic acids research*, 28(1):27–30, 2000.
27. Losiana Nayak and Rajat K De. Developmental trend derived from modules of Wnt signaling pathways. In *Pattern Recognition and Machine Intelligence*, pages 400–405. Springer, 2011.
28. Losiana Nayak and Rajat K De. Finding better partitions and conserved modules in Wnt signaling pathways. In *Proceedings of the International Conference on Bioinformatics and Computational Biology BIOCOMP'12*, pages 89–95, 2012.

ENTROPY MEASURES AND THE STATISTICAL ANALYSIS OF PROTEIN FAMILY CLASSIFICATION

R. P. MONDAINI, S. C. DE ALBUQUERQUE NETO

Federal University of Rio de Janeiro,
UFRJ - Centre of Technology, COPPE
21.941-972 - P.O. Box 68.511,
Rio de Janeiro - RJ, Brazil
Corresponding author: rpmondaini@gmail.com

The expertise of senior biologists has been used to identify and classify Protein Domains. In despite of usual discordances among biological research groups, a good overlap of conclusions has been obtained on the task of assembling Protein Domains into families. A subsequent classification obtained from assembling families into "Clans" is tested on the present work with ANOVA Statistical Techniques. The available results do not seem to reject the "Clan" classification but some suggestions for deleting families and the possible partition of "Clans' are proposed from the present statistical analysis.

1. Introduction

In the present work we report the statistical analysis which has been done to test the classification of Protein domain families into "Clans"[1,2]. The techniques of ANOVA statistical analysis[3,4] have been chosen to test the confidence of the results available in the literature. This analysis has been motivated by the suspicion that the mathematical techniques which have supported the sequence alignments for family identification, have been implemented on the computers of senior biologists but an independent and robust statistical test to check their conclusions is still missing. In order to organize the sample space for hypothesis testing, we consider the protein domains[5] to be represented by blocks of amino acids. We adopt two basic procedures for the organization of these blocks: a) We select a protein family of m domains (rows). There are $n_1, n_2, \ldots, n_m$ amino acids on each domain, respectively. We then consider a block of (m x n) amino acids where n is given by

$$n = min(n_1, n_2, \ldots, n_m) \tag{1}$$

b) The size (m x n) of the blocks is specified a priori. We then delete all proteins such that $n_j < n$ and we also delete $(n_j - n)$ amino acids on the remaining proteins. We adopt this second procedure to organize the sample space of (m x n)blocks of amino acids, according to Fig. 1 below. We have made the restriction to families containing a block of $m = 100$ rows (protein domains) and $n = 200$ columns (amino acids)

Figure 1. A block of m rows (protein domains) and n columns (amino acids).

To each column of m rows, we associate a vector p_j of 20 rows[6]:

$$p_j^{\mathrm{T}} = (p_j(a_1), p_j(a_2), \ldots, p_j(a_{20})), \tag{2}$$

where

$j = 1, 2, \ldots, n$;

$a_1, a_2, \ldots, a_{20} = A, C, D, E, F, G, H, I, K, L, M, N, P, Q, R, S, T, V, W, Y$

and

$$p_j(a) = \frac{n_j(a)}{m} \tag{3}$$

where $n_j(a)$ is the number of occurrences of amino acid "a" in the jth column.

We have:

$$\sum_a p_j(a) = 1,\ j = 1, 2, \ldots, n. \tag{4}$$

The statistical analysis has been made by using the published work of the experts on the organization of the Pfam database[1,2]. The table below will present an evolution of the database content since the year 2005. We have chosen to work with the 27.0 release which contains 14,831 curated protein families and 4,563 of which are classified into 515 "Clans".

Table 1. Evolution of the Pfam database.

Pfam DATABASE				
version	year	n° families	n° families class into clans	"Clans"
18.0	2005	7983	1181	172
22.0	2007	9318	1808	283
23.0	2008	10340	2009	302
24.0	2009	11912	3131	422
25.0	2010	12273	-	-
26.0	2011	13672	4243	499
27.0	2013	14831	4563	515
28.0	2015	16230	-	541

This introduction leads to think about the kind of game that Nature could be playing for organizing protein families. Is She tossing **n** times consecutively **m** "icosahedron dice" simultaneously? Are all these dice fair? Probably not! Anyhow, which seems to be essential in the understanding of a future evolution dynamics of protein families is the non-independence of the columns associated to Fig. 1 above. This means that the joint probabilities of occurrence of amino acids on a set of columns is essentially different from the product of simple probabilities of each column of the set, or

$$P_{jkl}(a, b, c, \ldots) \neq p_j(a)p_k(b)p_l(c)\ldots \tag{5}$$

In the present work we have not introduced any treatment of joint probabilities and corresponding entropy measures. We then proceed to the intensive analysis of protein family classification into "Clans" of the Pfam database by using distributions of simple probability $p_j(a)$.

2. Entropy Measures

We now consider some entropy measures from the literature. There are many ways of introducing these entropy measures, and we choose those which lead to a simple interpretation of results in the statistical calculations to be done.

We start from the Sharma-Mittal group of entropy measures[7]:

$$S_j(x,y) = -\frac{1}{2}\sum_a \frac{p_j^{x+y}(a) - p_j^{-x+y}}{x}, \tag{6}$$

where x,y are real parameters.

We then have as special cases:

1. The Kaniadakis Entropy measures:

$$K_j(x) = S_j(x,1) = -\frac{1}{2}\sum_a \frac{p_j^{x+1}(a) - p_j^{-x+1}}{x} \tag{7}$$

2. The Abe Entropy measures:

$$A_j(\beta) = S_j(\frac{\beta+\frac{1}{\beta}}{2}, \frac{\beta-\frac{1}{\beta}}{2}) = -\sum_a \frac{p_j^{\beta}(a) - p_j^{\frac{1}{\beta}}(a)}{\beta - \frac{1}{\beta}} \tag{8}$$

3. The Havrda-Charvat Entropy measures:

$$H_j(q) = S_j(\frac{1+q}{2}, \frac{1-q}{2}) = -\frac{1 - \sum_a p_j^q(a)}{1-q} \tag{9}$$

The Renyi Entropy measures are a set of additive entropies given by:

$$R_j(q) = \frac{1}{1-q} \ln \left(\sum_a p_j^q(a) \right) \leq -\frac{\left(1 - \sum_a p_j^q(a)\right)}{1-q} = H_j(q) \tag{10}$$

The Havrda-Charvat entropy measures (Eq. 9), can be also obtained from the inequality $ln(x) \leq (x-1)$, with $x = \sum_a p_j^q(a)$.

4. The Landsberg-Vedral Entropy measures:

$$L_j(q) = -\frac{1}{1-q} \left(\frac{1}{\sum_a p_j^q(a)} - 1 \right) = \frac{H_j(q)}{\sum_a p_j^q(a)} \tag{11}$$

All these entropy measures contain the Shannon Entropy measure[8] s_j as a limit

$$\lim_{x \to 0} K_j(x) = \lim_{\alpha \to 1} A_j(\alpha) = \lim_{q \to 1} H_j(q) = \lim_{q \to 1} R_j(q) = \lim_{q \to 1} L_j(q) = s_j \tag{12}$$

where

$$s_j = -\sum_a p_j(a) \ln p_j(a) \tag{13}$$

is the Shannon Entropy measure.

3. ANOVA (Analysis of Variance) of Protein Families

Let us consider a set of protein family groups ("Clans") $CL_1, CL_2, \ldots, CL_N$ with $\Phi_1, \Phi_2, \ldots, \Phi_N$ as the number of protein families on each "Clan". Let $\varphi_1, \varphi_2, \ldots, \varphi_N$, be the number of protein families on each sample after the restriction to families containing (m x n) blocks of amino acids, respectively. Fig. 2 below will clarify the scheme:

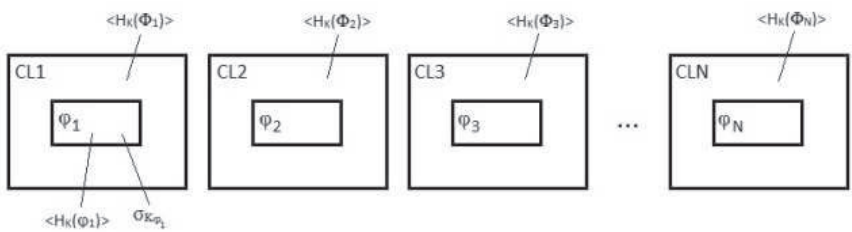

Figure 2. "Clans" and samples with restriction to (m x n) blocks of amino acids.

where $\langle H_k(\Phi_1)\rangle, \langle H_k(\Phi_2)\rangle, \ldots, \langle H_k(\Phi_N)\rangle$ are the generic means around the "Clans".

All the forthcoming calculations will be related to the $\varphi_1, \varphi_2, \ldots, \varphi_N$ variables and some useful functions of the entropy measure variables $H_k^p(\varphi_l)$, will be given by:

The overall mean per column of the (m x n) blocks of amino acids:

$$\langle H_k \rangle = \frac{1}{\sum_{l=1}^{N} \varphi_l} \sum_{l=1}^{N} \sum_{p=1}^{\varphi_l} H_k^p(\varphi_l) \tag{14}$$

The variability per column around this overall mean:

$$\Delta H_k^p(\varphi_l) = H_k^p(\varphi_l) - \langle H_k \rangle \tag{15}$$

The "Clan" means per column of the (m x n) blocks of amino acids:

$$\langle H_k(\varphi_l)\rangle = \frac{1}{\varphi_l} \sum_{p=1}^{\varphi_l} H_k^p(\varphi_l) \tag{16}$$

The variabilities per column around these "Clan" means :

$$DH_k^p(\varphi_l) = H_k^p(\varphi_l) - \langle H_k(\varphi_l)\rangle \tag{17}$$

$k = 1, \ldots, n \quad ; p = 1, \ldots, \varphi_l \quad ; l = 1, \ldots, N$

From Eqs. (14)–(17), we can write:

$$\sum_{p=1}^{\varphi_l} DH_k^p(\varphi_l) = 0 \tag{18}$$

$$\sum_{l=1}^{N} \varphi_l \big(\langle H_k(\varphi_l)\rangle - \langle H_k\rangle\big) = 0 \tag{19}$$

$$\sum_{l=1}^{N}\sum_{p=1}^{\varphi_l} \Delta H_k^p(\varphi_l) = 0 \tag{20}$$

and the left-hand sides of these equations have $(\varphi_l - 1)$, $(N-1)$ and $\left(\sum_{l=1}^{N} \varphi_l - 1\right)$ independent terms, respectively.

We now derive the corresponding Standard Deviations and these can be obtained from

$$\left(\sum_{l=1}^{N} \varphi_l - 1\right)\sigma_k^2 = \sum_{l=1}^{N}\sum_{p=1}^{\varphi_l} \Big(\Delta H_k^p(\Phi_l)\Big)^2 \tag{21}$$

$$(\varphi_l - 1)\sigma_{k_{\Phi_l}}^2 = \sum_{p=1}^{\varphi_l} \Big(DH_k^p(\Phi_l)\Big)^2 \tag{22}$$

We can write:

$$\underbrace{\left(\sum_{l=1}^{N} \varphi_l - 1\right)\sigma_k^2}_{\text{SST}} = \underbrace{\sum_{l=1}^{N}(\varphi_l - 1)\sigma_{k_{\Phi_l}}^2}_{\text{SSE}} + \underbrace{\sum_{l=1}^{N} \varphi_l \big(\langle H_k(\Phi_l)\rangle - \langle H_k\rangle\big)^2}_{\text{SSG}} \tag{23}$$

In order to check the number of independent terms on Eq. (23), we write:

$$\sum_{l=1}^{N} \varphi_l - 1 = \sum_{l=1}^{N} (\varphi_l - 1) + N - 1 \equiv \sum_{l=1}^{N} \varphi_l - N + N - 1 \tag{24}$$

All equations and definitions above are enough for introducing the Fisher's Correlation Coefficient of the One-way ANOVA statistics[4] per column:

$$F_k = \frac{\frac{SSG}{(N-1)}}{\frac{SSE}{\left(\sum_{l=1}^{N} \varphi_l - N\right)}} \tag{25}$$

We write:

$$F_k = \left(\frac{\sum_{l=1}^{N} \varphi_l - N}{N-1} \right) \left(\frac{\left(\sum_{l=1}^{N} \varphi_l - 1 \right) \sigma_k^2}{\sum_{l=1}^{N} (\varphi_l - 1) \sigma_{k_{\Phi_l}}^2} - 1 \right) \ , \ k = 1, \ldots, n \tag{26}$$

We have then to perform $\underline{\underline{n}}$ ANOVA tests on the m x n block samples

4. Some Mathematical Refinement

By defining vectors

$$\left(DH_k(\Phi_l)\right)_{\varphi_l \mathrm{x} 1}, \left(\Delta H_k(\Phi_l)\right)_{\varphi_l \mathrm{x} 1}$$

and matrices of several orders,

$$\left(DH_k(\Phi_l) D^{\mathrm{T}} H_k(\Phi_l)\right)_{\varphi_l \mathrm{x} \varphi_l} \ , \ \left(\Delta H_k(\Phi_l) \Delta^{\mathrm{T}} H_k(\Phi_l)\right)_{\varphi_l \mathrm{x} \varphi_l}$$

We also get a more symmetric formula for Eq. (26).

$$F_k = \left(\frac{\sum_{l=1}^{N} \varphi_l - N}{N-1} \right) \left(\frac{\sum_{l=1}^{N} \mathrm{Tr}\left(\Delta H_k(\Phi_l) \Delta^{\mathrm{T}} H_k(\Phi_l)\right)}{\sum_{l=1}^{N} \mathrm{Tr}\left(D H_k(\Phi_l) D^{\mathrm{T}} H_k(\Phi_l)\right)} - 1 \right), \; k = 1, 2, \ldots, n \tag{27}$$

5. Hypothesis Testing

The Null and Alternative Hypotheses of our problem are:

$H_0 : \langle H_k(\Phi_1)\rangle = \langle H_k(\Phi_2)\rangle = \ldots = \langle H_k(\Phi_N)\rangle \;\; \Rightarrow$ invalidation of the "Clan" concept.

$H_a : \langle H_k(\Phi_1)\rangle \neq \langle H_k(\Phi_2)\rangle \neq \ldots \neq \langle H_k(\Phi_N)\rangle$ (not all necessarily unequal) $\Rightarrow$ existence of "Clans".

On applying the $\underline{n}$ ANOVA tests to m x n block samples, we specify a significance level α and we compare the F-distribution critical values[4], $F_{a,b,\alpha}$, where a = numerator degrees of freedom = $(N-1)$, b = denominator degrees of freedom = $(\sum_{l-1}^{N} \varphi_l - N)$, as obtained from F-distribution tables[4], to the F_k values calculated from Eq. (26).

We then reject the Null Hypotheses H_0, if $F_k > F_{a,b,\alpha} \Rightarrow$ Validity of the "Clan" concept for the k_{th} column of the (m x n) block samples.

Or, if $F_k \leq F_{a,b,\alpha} \Rightarrow$ We cannot reject H_0 for the k_{th} column of the (m x n) block samples.

6. Some Technical Requirements for Data Validation

Assumptions for data to be used on ANOVA[3,4]:

1. The (m x n) blocks from the N populations ("Clans") are independent.

2. The (m x n) blocks should be normally distributed.

3. The (m x n) blocks should be selected from populations with equal variance $\sigma^2_{k_{\Phi_l}}$.

Some comments are now in order:

Assumptions 2, 3 can be more or less relaxed by trusting on the robustness of ANOVA statistics and F-test.

We consider that assumption 3 is not violated if the "spreads" (differences between the extremum values of entropy measures for the (m x n) blocks on each "Clan") are approximately the same.

We can also consider that the differences between the upper and lower quartiles (50% of the data) are approximately the same.

7. Checking the Data Validation on a Set of Eight Selected "Clans"

On Tables 2–7 below, we check the data corresponding to a set of eight "Clans". We also take the entropy measures of Section 2, Eqs. (7–11, 13) and we have chosen specific values of their parameters for data comparison.

Table 2. Kaniadakis entropy $\mathbf{x = 0}$ (Shannon entropy), ($\mathbf{m}$ x $\mathbf{n}$) = **100** x **200**.

clan	n° families	$\sigma_{k_{\Phi_l}}$ within families of each clan	mean	Range of Values Entropy Measures	Range of 50 % data
CL00023	119	0.515	2.292	2.903	0.562
CL00028	041	0.389	2.473	2.909	0.283
CL00063	092	0.438	2.407	2.938	0.386
CL00236	021	0.343	2.447	2.779	0.342
CL00020	038	0.319	2.478	2.809	0.282
CL00123	006	0.285	2.463	2.122	0.317
CL00186	029	0.280	2.540	2.749	0.242
CL00192	026	0.286	2.416	2.243	0.335

Table 3. Kaniadakis entropy $\mathbf{x = 0.5}$, $(\mathbf{m}$ x $\mathbf{n}) = \mathbf{100}$ x $\mathbf{200}$.

clan	n° families	$\sigma_{k_{\Phi_l}}$ within families of each clan	mean	Range of Values Entropy Measures	Range of 50 % data
CL00023	119	0.715	3.199	4.125	0.820
CL00028	041	0.550	3.460	4.135	0.438
CL00063	092	0.620	3.360	4.174	0.583
CL00236	021	0.485	3.414	3.894	0.516
CL00020	038	0.443	3.465	3.966	0.432
CL00123	006	0.406	3.424	2.906	0.475
CL00186	029	0.394	3.551	3.854	0.383
CL00192	026	0.414	3.366	3.165	0.533

Table 4. Abe entropy $\beta = \mathbf{0.5}$, $(\mathbf{m}$ x $\mathbf{n}) = \mathbf{100}$ x $\mathbf{200}$.

clan	n° families	$\sigma_{k_{\Phi_l}}$ within families of each clan	mean	Range of Values Entropy Measures	Range of 50 % data
CL00023	119	0.485	2.262	2.870	0.537
CL00028	041	0.371	2.437	2.876	0.284
CL00063	092	0.418	2.370	2.901	0.379
CL00236	021	0.324	2.408	2.709	0.336
CL00020	038	0.296	2.441	2.756	0.280
CL00123	006	0.269	2.416	1.992	0.308
CL00186	029	0.263	2.497	2.677	0.248
CL00192	026	0.274	2.378	2.170	0.348

Table 5. Havrda-Charvat entropy $\mathbf{q = 0.5}$, $(\mathbf{m}$ x $\mathbf{n}) = \mathbf{100}$ x $\mathbf{200}$.

clan	n° families	$\sigma_{k_{\Phi_l}}$ within families of each clan	mean	Range of Values Entropy Measures	Range of 50 % data
CL00023	119	1.182	5.121	6.728	1.403
CL00028	041	0.918	5.558	6.747	0.772
CL00063	092	1.037	5.388	6.815	1.019
CL00236	021	0.817	5.474	6.326	0.908
CL00020	038	0.742	5.564	6.462	0.761
CL00123	006	0.690	5.484	4.736	0.816
CL00186	029	0.665	5.708	6.266	0.678
CL00192	026	0.707	5.387	5.199	0.942

Table 6. Renyi entropy $\mathbf{q = 0.5}$, $(\mathbf{m}$ x $\mathbf{n}) = \mathbf{100}$ x $\mathbf{200}$.

clan	n° families	$\sigma_{k_{\Phi_l}}$ within families of each clan	mean	Range of Values Entropy Measures	Range of 50 % data
CL00023	119	0.399	2.505	2.947	0.386
CL00028	041	0.306	2.639	2.951	0.200
CL00063	092	0.345	2.588	2.966	0.270
CL00236	021	0.250	2.622	2.594	0.240
CL00020	038	0.222	2.649	2.699	0.198
CL00123	006	0.202	2.630	1.582	0.216
CL00186	029	0.197	2.689	2.537	0.174
CL00192	026	0.204	2.603	1.790	0.253

Table 7. Landsberg-Vedral entropy $\mathbf{q = 0.5}$, $(\mathbf{m}$ x $\mathbf{n}) = \mathbf{100}$ x $\mathbf{200}$.

clan	n° families	$\sigma_{k_{\Phi_l}}$ within families of each clan	mean	Range of Values Entropy Measures	Range of 50 % data
CL00023	119	0.149	1.415	1.542	0.107
CL00028	041	0.116	1.458	1.543	0.052
CL00063	092	0.128	1.442	1.546	0.071
CL00236	021	0.082	1.456	1.221	0.063
CL00020	038	0.071	1.464	1.309	0.052
CL00123	006	0.061	1.460	0.557	0.057
CL00186	029	0.062	1.476	1.172	0.045
CL00192	026	0.060	1.453	0.658	0.068

8. Spline Fitting of Sequences of Cumulative Entropy Measures

We associate another sequence of entropy measures, $[S_j]$ (cumulative entropy measures), to the original sequence S_j, through the relation:

$$S_j = j[S_j] - (j-1)[S_{j-1}] \ , \ j = 1, \ldots, n \tag{28}$$

We can then write,

$$[S_k] = \frac{1}{k} \sum_{j=1}^{k} S_j \ , \ k = 1, \ldots, n \tag{29}$$

Figures 3–8 correspond to the spline fitting of the sequences given by Eq. (29), for selected values of the parameters of Eqs. (7)–(13).

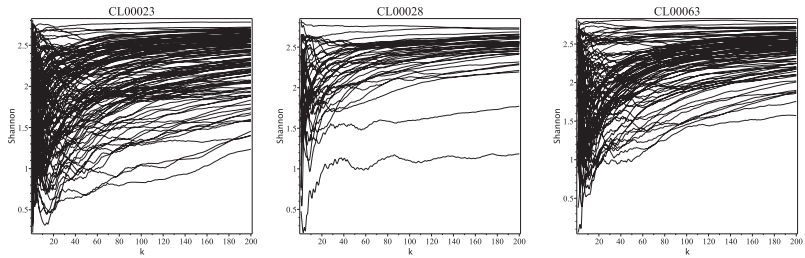

Figure 3. Kaniadakis cumulative entropies $\mathbf{x = 0}$ (Shannon cumulative entropies), $(\mathbf{m}$ x $\mathbf{n}) = \mathbf{100}$ x $\mathbf{200}$.

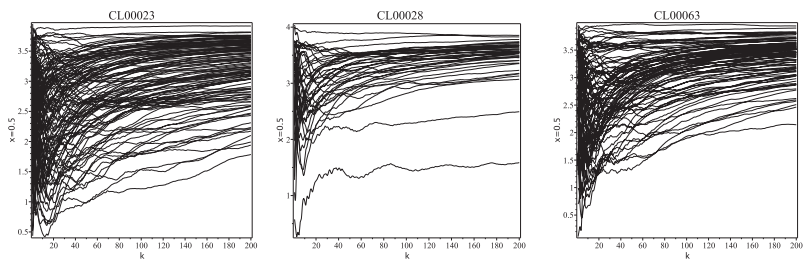

Figure 4. Kaniadakis cumulative entropies $\mathbf{x = 0.5}$, $(\mathbf{m}$ x $\mathbf{n}) = \mathbf{100}$ x $\mathbf{200}$.

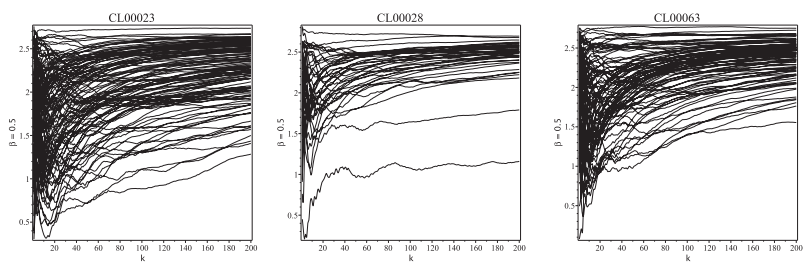

Figure 5. Abe cumulative entropies $\beta = \mathbf{0.5}$, $(\mathbf{m}$ x $\mathbf{n}) = \mathbf{100}$ x $\mathbf{200}$.

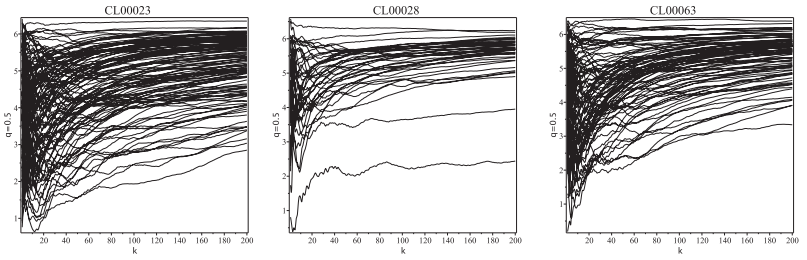

Figure 6. Havrda-Charvat cumulative entropies $\mathbf{q = 0.5}$, $(\mathbf{m}$ x $\mathbf{n}) = \mathbf{100}$ x $\mathbf{200}$.

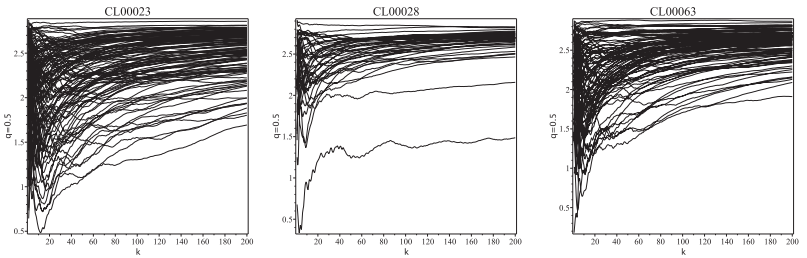

Figure 7. Renyi cumulative entropies $\mathbf{q = 0.5}$, $(\mathbf{m}$ x $\mathbf{n}) = \mathbf{100}$ x $\mathbf{200}$.

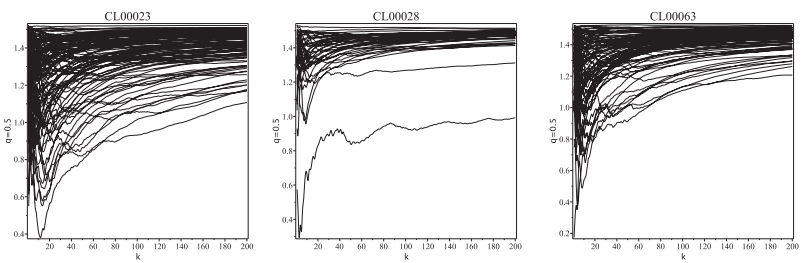

Figure 8. Landsberg-Vedral cumulative entropies $\mathbf{q = 0.5}$, $(\mathbf{m}$ x $\mathbf{n}) = \mathbf{100}$ x $\mathbf{200}$.

9. Hypothesis Testing

By assuming a Significance level $\alpha = 0.01$, (1%), we now present a summary of the calculations which have been done to perform the Hypothesis testing on ANOVA Statistics:

We have,

$$N = 8 \tag{30}$$

$$\sum_{l=1}^{N} \varphi_l = 119 + 41 + 92 + 21 + 38 + 6 + 29 + 26 = 372 \tag{31}$$

$$a = \sum_{l=1}^{N} \varphi_l - N = 372 - 8 = 364 \tag{32}$$

and

$$b = N - 1 = 8 - 1 = 7 \tag{33}$$

From the values above, we can then obtain from the F-distribution tables[4]

$$F_{a,b,\alpha} = F_{364,7,0.01} = 2.64 \ \ldots \ 2.79 \tag{34}$$

The exact calculation[3] leads to

$$F_{a,b,\alpha} = F_{364,7,0.01} = 2.68 \tag{35}$$

The Hypothesis testing will then lead to

$F_k > F_{364,7,0.01}$ — Reject $H_0 \Rightarrow$ "Clans" do exist.

$F_k \leq F_{364,7,0.01}$ — H_0 cannot be rejected $\Rightarrow$ we cannot say unequivocally that "Clans" do not exist.

These results can be seen on Figs. (9a,b), (10a,b) and (11a,b) below where we have plotted the original entropy S_k measures and the straight line corresponding to the value $F_{364,7,0.01} = 2.68$.

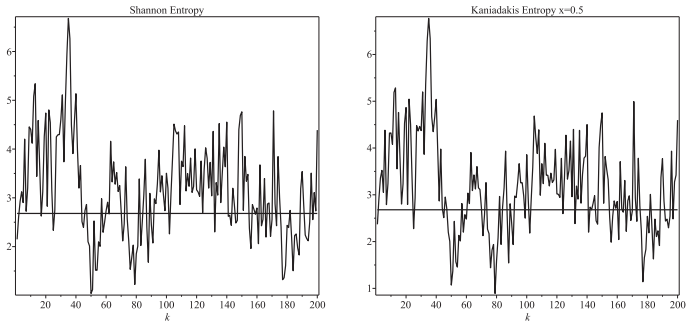

Figure 9. (a) F-tests for Shannon entropy measures, $\alpha = 0.01$, (b) F-tests for Kaniadakis entropy measures, $\alpha = 0.01$.

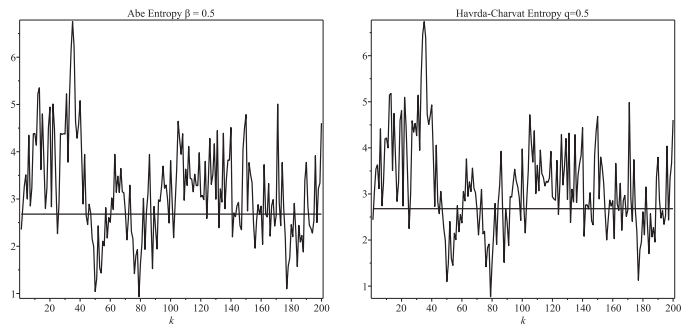

Figure 10. (a) F-tests for Abe entropy measures, $\alpha = 0.01$, (b) F-tests for Havrda-Charvat entropy measures, $\alpha = 0.01$.

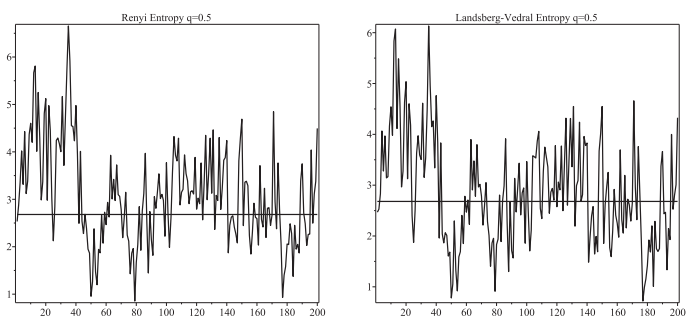

Figure 11. (a) F-tests for Renyi entropy measures, $\alpha = 0.01$, (b) F-tests for Landsberg-Vedral entropy measures, $\alpha = 0.01$.

10. Conclusions and Suggestions for Improvement

1. For blocks of (100x200) amino acids, we cannot say that protein families are not classified into clans. This also means that we are not able to declare the existence of "Clans".

2. The ANOVA Statistics is not robust enough to the non-normality of data distribution. Use of other statistics to improve the results obtained by using ANOVA like Levine's or Forsythe's statistics[9], could be advisable.

3. A more rigorous validation of data for the F-test. Maybe the exclusion of "Clans" with a greater spread of data, as can be seen on Tables 2–7.

4. Considering an equal number of families on each "Clan".

5. To work with greater number of "Clans" (N).

6. Greater number of families $\Rightarrow m < 100, n < 200$?

7. Use of Entropy Measures based on joint probabilities, $P_{jk}(a, b)$, $P_{jkl}(a, b, c)$, $P_{jklm}(a, b, c, d)$, ...

8. To delete the families with a "strange behaviour" of the sequence of cumulative entropies, as can be seen on Figs. 3–8, or the allocation of these families into different "Clans" — i.e. the partition of "Clans'. Anyhow, we will propose firstly to continue the present work by increasing the number of clans only in a forthcoming contribution.

11. Acknowledgements

Enlightening discussions with participants of the BIOMAT 2015 International Symposium at Indian Institute of Technology, Department of Mathematics, Roorkee, India, November 02–07, have been very useful to clarify the present statistical analysis.

References

1. R. D. Finn, A. Bateman, J. Clements, P. Coggill, R. Y. Eberhardt, S. R. Eddy, A. Heger, K. Hetherington, L. Holm, J. Mistry, E. L. L. Sonhammer, J. Tate, M. Punta - The Pfam protein families database - Nucleic Acids Research 42 (2014) D222 - D230.

2. R. D. Finn, P. Coggill, R. Y. Eberhardt, S. R. Eddy, J. Mistry, A. L. Mitchell, S. C. Potter, M. Punta, M. Qureshi, A. Sangrador-Vegas, G. A. Salazar, J. Tate, A. Bateman - The Pfam protein families database: towards a more sustainable future - Nucleic Acids Research 44 (2016) D279 - D285.
3. M. H. DeGroot, M. J. Schervish - Probability and Statistics, 4th edition, Addison-Wesley, 2012.
4. L. R. Jaisingh - Statistics for the Utterly Confused - 2nd edition, McGraw-Hill, 2006.
5. C. Branden, J. Tooze - Introduction to Protein Structure - 2nd edition - Garland Publ., Inc., 1999.
6. R. P. Mondaini - Entropy Measures based method for the classification of protein domains into families and clans - BIOMAT 2013 Int. Symp. 209-218, World Scientific Co. Pte. Ltd., 2014.
7. C. Beck - Generalised Information and Entropy Measures in Physics - Contemp. Phys, 50 (4) (2009) 495–510.
8. M. V. Volkenstein - Entropy and Information - Progress in Mathematical Physics, v. 57, Birkhäuser, 2009.
9. M. B. Brown, A. B. Forsythe - Robust Tests for the Equality of Variances - Journal of the American Statistical Association, 69, No. 346 (1974) 364–367.

CLUSTERING NEURAMINIDASE INFLUENZA PROTEIN SEQUENCES*

X. LI[1], H. JANKOWSKI[1], S. BOONPATCHARANON[1], V. TRAN[1], X. WANG[1], J. M. HEFFERNAN[1,2,3]

[1] *Department of Mathematics and Statistics*
[2] *Modelling Infection and Immunity Lab*
[3] *Centre for Disease Modelling*
York University, 4700 Keele St.
Toronto, Ontario M3J 1P3, Canada
E-mail: lixuan@mathstat.yorku.ca, hkj@yorku.ca, sawitree.boonpat@gmail.com, vickictran@gmail.com, stevenw@mathstat.yorku.ca, jmheffer@yorku.ca

We seek a better understanding of this evolution over influenza seasons. In a previous work, we studied the evolution (antigenic drift) of the highly variable influenza A H3N2 by focusing on the hemagglutinin (HA) viral glycoprotein. In this update, we include also the neuraminidase (NA) glycoprotein, another protein that contributes to the antigenic drift of influenza. Our method is based on a dimension reduction technique combined with a fully automatic Hamming distance statistical clustering method for categorical data (Zhang *et al.* JASA, 2006). The new NA results are compared with the previous HA results to provide a more complete picture of flu virus evolution.

1. Introduction

In the northern and southern parts of the world, influenza outbreaks occur mainly in the winter months while in areas around the equator outbreaks may occur at any time of the year[1]. The seasonal pattern of infection in the hemispheres has coined the name 'seasonal influenza'. Seasonal influenza is associated with significant human mortality and morbidity worldwide[1,3]. Much of the seasonal influenza burden is caused by influenza A[1].

Influenza A viruses are classified into subtypes based on antibody responses to their two surface glycoproteins, hemagglutinin (HA) and neuraminidase (NA). There are 16 HA and 9 NA subtypes known, but only HA 1, 2, and 3, and NA 1 and 2 are commonly found in humans[2,3]. Among

*This work is supported by NSERC.

the many subtypes of influenza A viruses, the influenza A H1N1 and H3N2 subtypes currently cause seasonal influenza epidemics, with H3N2 causing the vast majority of infections[3].

Influenza A viruses continuously undergo mutation in the HA and NA surface antigens. This is called antigenic drift. Through antigenic drift, an increasing variety of strains are created. The new strains can then cause seasonal epidemics, since the population can only gain partial immunity from previous infection(s). The HA protein has been identified to the be the major contributor to the antigenic drift seen in influenza A[3]. Changes in the NA protein, however, have also been shown to contribute[3].

Vaccination against influenza is recommended every year[1,4,5]. The continuous change in the circulating influenza strains requires the seasonal influenza vaccine formulation to be considered yearly. The vaccine, however, takes approximately six months to formulate and produce. Throughout this manufacturing period the influenza virus continues to evolve. This, in turn, affects the efficacy of the vaccine in the population. Between the years 1997 to 2007, vaccine efficacy ranged from 18%–90%[6]. Clearly, the methods employed to predict the circulating influenza strains from year to year are not optimal.

A second control strategy against influenza includes the use of antiviral drugs, which can reduce the severity of symptoms and pathogen transmission during influenza infection[7]. There are two classes of antiviral drugs currently in use, neuraminidase inhibitors (oseltamivir and zanamivir) and M2 protein inhibitors (adamantine derivatives). Currently, adamantine is not recommended for treatment of influenza[7]. When influenza is circulating in a community, either oseltamivir or zanamivir are recommended in the treatment of patients that have risk of severe complications from infection, but only if treatment can be initiated within 48 hours of the onset of symptoms[7]. NA mutations that confer resistance to oseltamivir and zanamivir have been identified in seasonal influenza epidemics[7]. Neuraminidase inhibitor efficacy, thus, is affected by changes in the NA glycoprotein[8].

We are interested in quantifying the evolution of the HA and NA glycoproteins. We have developed a formal cluster-based technique that can be used to study the evolution of influenza over time[9]. Previously, we employed our technique to determine families (or clusters) of the H3N2 HA glycoprotein genetic sequence[9]. Our results uncovered important new trends in HA evolution[9]. We now continue our study of seasonal influenza A H3N2 mutation focusing on the NA glycoprotein.

Table 1. Vaccine sequences in the dataset.

Stain Name	Number of sequences	Accession Number
A/Moscow/10/99	2	AY531035, DQ487341
A/Fujian/411/2002	2	CY088483, CY112933
A/California/7/2004	1	CY114373
A/Wisconsin/67/2005	4	CY033646, CY163936 CY114381, EU103823
A/Brisbane/10/2007	3	CY035022, CY039087 EU199366
A/Perth/16/2009	1	GQ293081
A/Victoria/361/2011	1	KC306165
A/Texas/50/2012	2	KC892248, KC892952

2. Data Description and Methodology

2.1. *Data acquisition*

The NA sequences considered in the study were obtained from the publicly available online repository known as the Influenza Research Database[10] (IRD), `www.fludb.org`. The specific sequences used were chosen based on the criteria given in Table 2. The calendar year, country and city of isolation for each sequence is provided in the IRD. We also wanted to make sure that strains used for vaccines (Table 1) were included in the data. Vaccine sequences containing the complete date (year, month, and day) are naturally selected by our search criteria. Some vaccine sequences did not have a complete date, and were added to the data set manually. The criteria yield a total of 2049 sequences with 550 amino acids each, and among these are 12 vaccine sequences.

Table 2. IRD criteria: All other settings kept default or blank.

Option	Criteria
"Data to return":	protein
"Virus type":	A
"Sub type":	H3N2
"Select segments":	NA
"Complete sequences":	Complete Segments Only
"Date range":	1998 to 2012
"Host":	Human
"Geographic grouping":	All
Advanced options	
"Month Range":	Sep 1998 to July 2012
"Remove Duplicate Sequences":	Yes

MEGA 5.2 software[11] was then used to translate the RNA sequences into protein sequences, while the software MUSCLE[12] was used to align the sequences. Perl script was written to order and combine the sequences for processing in Matlab. This procedure resulted in 2049 observations with 550 categorical variables, each containing 21 categorical states (20 for each kind of amino acid and one to represent a gap). The occurrence of gaps may be due to some deletion or transition of a nucleotide, which is highly related to random genetic drift and evolution. Another reason for gaps is the inappropriate alignment of the sequences. Since NA protein sequences are highly conservative and the alignment uses pairwise comparison, the probability of improper alignment should be quite small.

Files containing both the pre- and post-processed data are provided as supplementary material, and are also available online at `www.math.yorku.ca/~hkj/Research`.

2.2. *Clustering the sequences*

Our goal was to analyze the vaccine and observed strain sequences via clustering. Our methodology is the same as previously employed in Li *et al.*[9] and comprises two main steps: a dimension reduction step and a clustering step based on Hamming distance.

(1) **Dimension reduction step:** As the original data lives inside a space of dimension 21^{550}, a dimension reduction step is necessary. To do this, the entropy of the empirical distribution on proteins was calculated at each site for the 2049 observed sequences. The sites with no variability or only one varying location were removed from the data (these correspond to very small entropy or zero entropy). The remaining entropies were clustered using a Gaussian mixture model[14,16] implemented in the R software package[15]. The cluster with the highest entropy was then selected for further analysis. This allows us to consider only 75 sites with highest variability for the next step.

(2) **Clustering step:** In the second step we cluster the data, which now lives in a space of maximal size 21^{75}. The clustering method was that of Zhang *et al.* (JASA, 2006)[13], see also Li *et al.* (2015)[9] for additional details. We remark that the method is fully automatic, intuitive, and based on the Hamming distance between sequences.

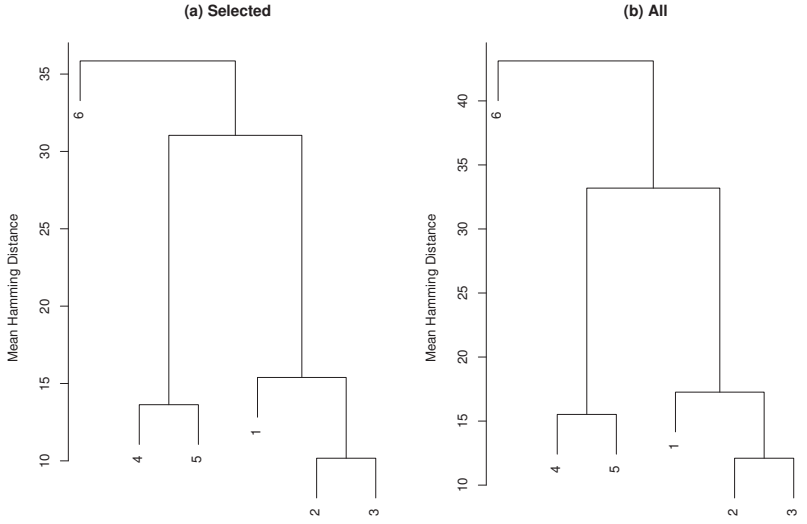

Figure 1. Dendrograms of clusters by mean Hamming distance. This plot is drawn using hierarchical cluster analysis with complete linkage. The left plot is based only on the 75 highest entropy sites, whereas the right plot uses all 550 sites to calculate the Hamming distance.

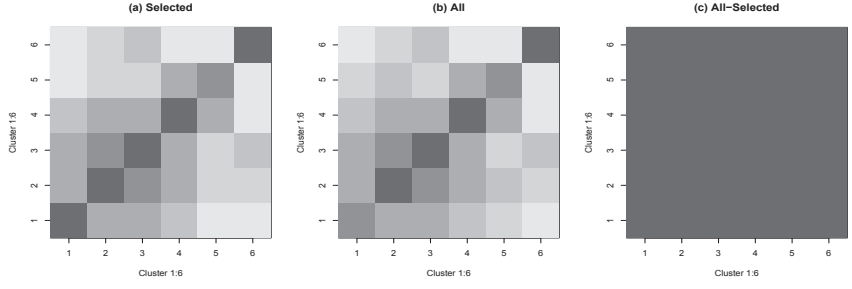

Figure 2. From left to right: mean Hamming distance matrix of 75 selected most varied sites by cluster, mean Hamming distance matrix of the whole sequence with 566 sites by cluster, absolute differences of the two matrices. Both matrices (left and centre) have been standardized by dividing by their corresponding maximum values.

3. Results

We first analyzed the sequence data as described above. The initial dimension reduction (step (1)) yielded 75 sites of "high variability." The clustering step (step (2)) yielded six clusters. Figure 1 shows the dendrograms of the

resulting clusters where the distance is based on the mean Hamming distance for (left panel) just the 75 sites of highest entropy/variability, and (right panel) all 550 sites. We can see that there is little difference between these two dendrograms, providing evidence that our dimension reduction step does not lose much (if any) important information. This is confirmed also in Figure 2, where the mean Hamming distances of the six clusters are compared when calculated for the 75 selected sites, and for all 550 sites.

Figure 3(a) shows histograms of the cluster size, where clusters containing vaccines are identified in black. Figure 3(b) shows the number of protein sequences within each cluster plotted against the calendar year of virus isolation. The dominant cluster, cluster five, overwhelms these results. For this reason, we added an additional analysis, whereby cluster five was again clustered (or sub-clustered) using the previously described two-step procedure. Details are given in the following section.

3.1. *Sub-clusters of cluster five*

To find sub-clusters of cluster five, we repeated steps (1) and (2) as above. Namely, selecting only the sequences of cluster five, we first performed the dimension reduction step on the entire length of the sequence. This yielded a reduction from 550 to 38 sites. Secondly, we performed the clustering step. This yielded 40 sub-clusters, which we denote as 5.1–5.40. Heatmaps confirming the validity of the dimension reduction step are given in Figure 4. Dendrograms of the clusters drawn by using the 38 sites and all 550 sites are given in Figure 5. Figure 5(a) shows all of the sub-clusters, which is difficult to read due to the large number of small sub-clusters. Figure 5(b) shows only those sub-clusters which contain at least 50 sequences. Here, the dendrograms are quite similar, again justifying the dimension reduction step.

Figure 6(a) shows histograms of the sub-cluster sizes, where sub-clusters containing vaccines are identified as black. Here, we identify five large (with at least 50 sequences) sub-clusters: 5.1, 5.2, 5.12, 5.19, and 5.38. We see a lot of "variability" here as well though - of the 40 sub-clusters, we only identify several dominant ones. Figure 6(b) shows the number of protein sequences within each cluster plotted against the calendar year of virus isolation. Here, we again clearly see the dominant sub-clusters. Notice that the largest of these sub-clusters, sub-cluster 5.1, does not include a vaccine strain.

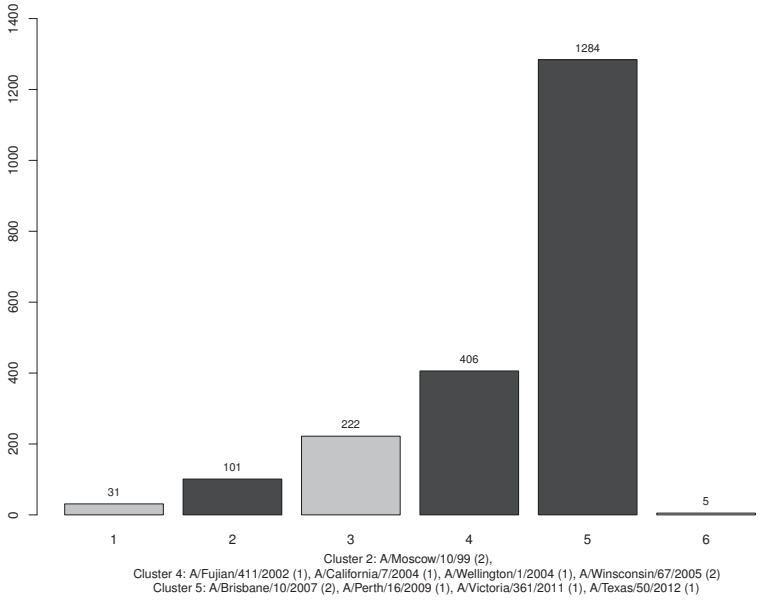

(a)

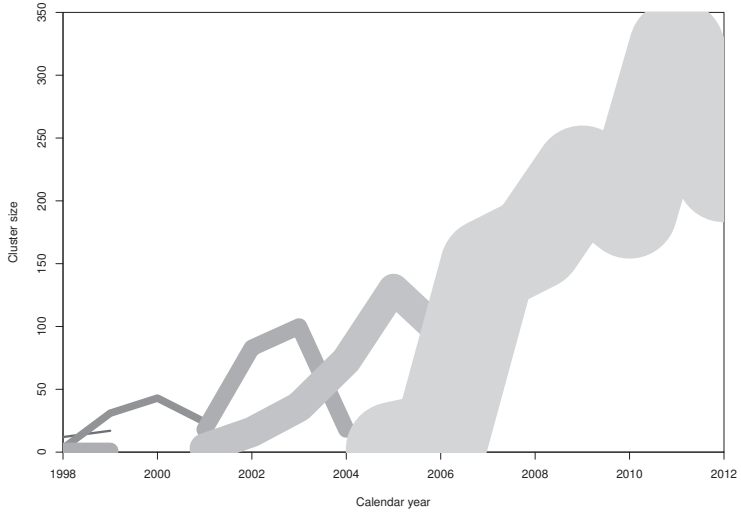

(b)

Figure 3. (a) Cluster sizes and vaccine locations. For convenience, the clusters have been re-ordered by earliest year of isolation. Clusters containing a vaccine strain are denoted in black. (b) The number of HA protein sequences within each cluster plotted versus calendar year of isolation.

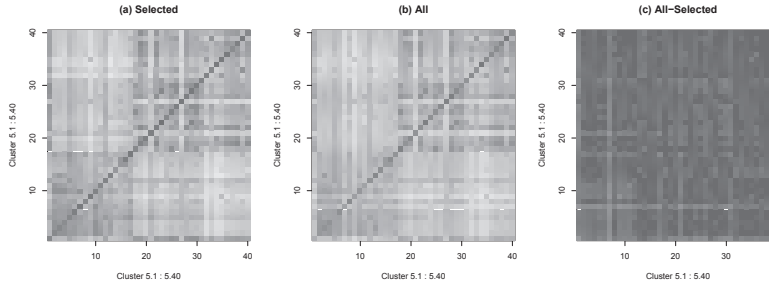

Figure 4. Mean hamming distance is shown for the (a) selected sites, (b) all sites, and (c) the difference between all and the selected sites.

4. Discussion

In this paper we have studied antigenic drift within the NA component of the influenza A H3N2 strain that causes seasonal influenza infections every year. We employed our previously reported method for clustering protein sequences to identify related NA glycoproteins across influenza A H3N2 strains. Analysis of the clusters found that the NA component of influenza A H3N2 is related by year (or 'flu season'), and that clusters appear to replace older clusters over time (Figure 3). In our results, cluster five contains almost half of the NA protein sequences in our data set. We therefore preformed further analysis of cluster five, which resulted in 40 sub-clusters. It is interesting to note that of the sub-clusters, the vaccine strains are mainly located in the "dominant" sub-clusters (largest sub-clusters). These dominant sub-clusters again appear to replace one another every few years. These results may point to a similar trend of genetic drift in the NA glycoprotein to that of the HA glycoprotein: cluster replacement every 2–5 years and evolution of the dominant seasonal strain[9].

The results reported above were observed from two subsequent implementations of our clustering method: once to identify clusters of the NA glycoprotein, and then again to identify sub-clusters of cluster five. Such recursive implementations of our methodology should be seen as an avenue for exploratory data analysis, but the methodology is not statistically rigorous. Additional work is required to develop of a formal statistical method that can extract both large scale (cluster-level) and small scale (sub-cluster level) evolutionary trends.

In both our previous and current studies of influenza A antigenic drift,

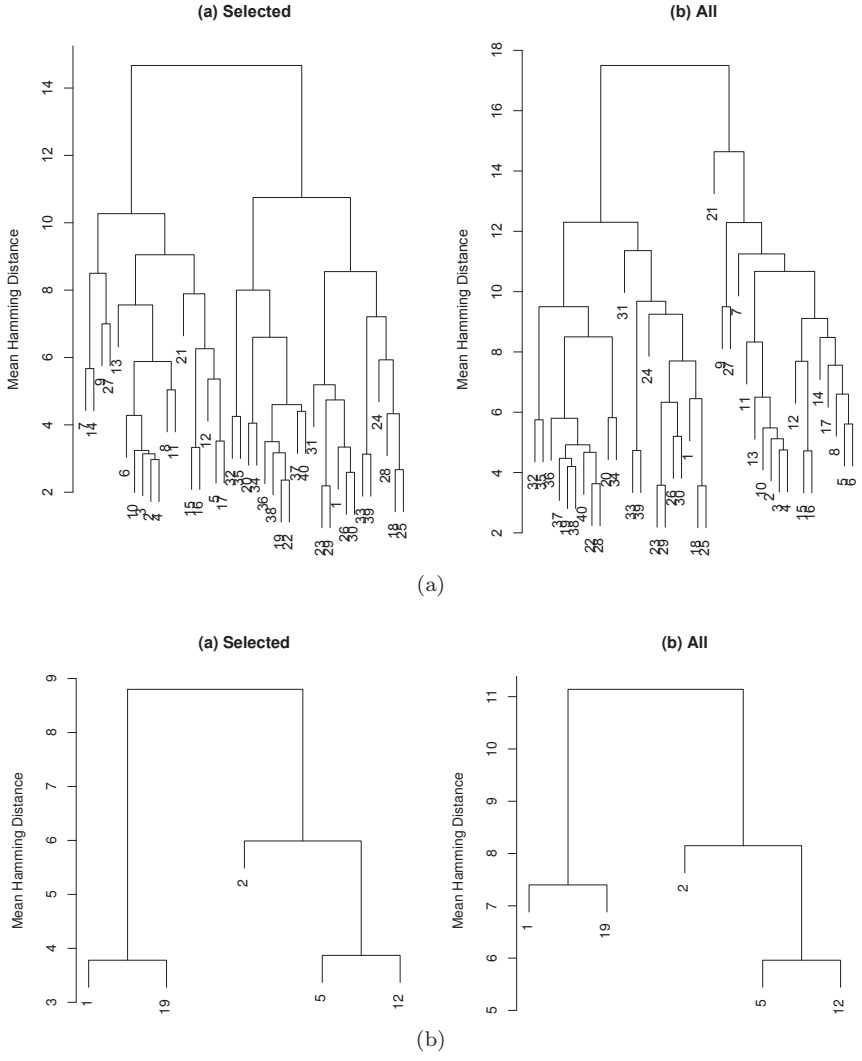

Figure 5. Dendrograms of clusters by mean Hamming distance. This plot is drawn using hierarchical cluster analysis with complete linkage. The left plot is based only on the 38 highest entropy sites, whereas the right plot uses all 550 sites to calculate the Hamming distance. (a) All sub-cluster are shown. (b) Only sub-clusters with at least 50 sequences are shown.

we have observed that dominant clusters of the HA and NA glycoproteins do not always include vaccine strains. For example, sub-cluster 5.1 in the current study does not house a vaccine strain, but sub-cluster 5.2,

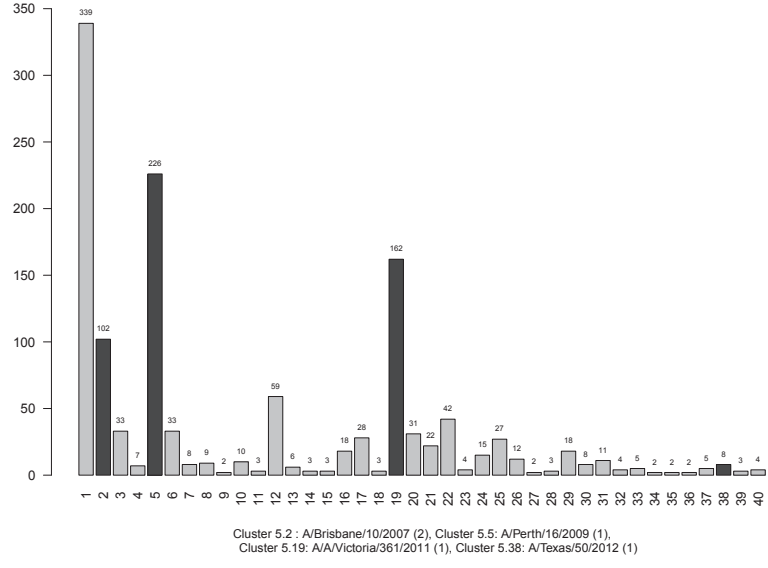

(a)

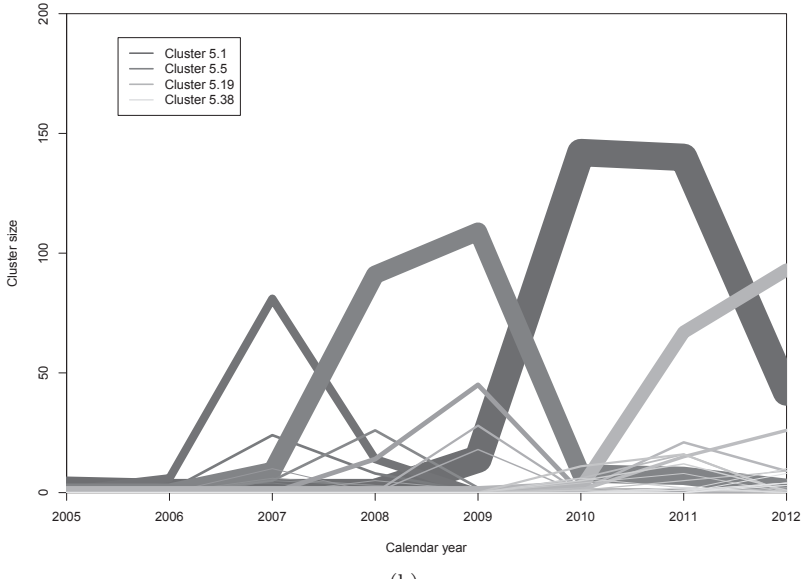

(b)

Figure 6. (a) Sub-cluster sizes and vaccine locations for the sub-clusters of the dominant cluster five. The subclusters have been re-ordered by earliest year of isolation. Clusters containing a vaccine strain are denoted in black. (b) The number of HA protein sequences within each sub-cluster of cluster five plotted versus calendar year of isolation.

which is smaller in size, does. Similar observations were made for the HA glycoprotein[9]. These results point to complications in the identification of the dominant strain from year to year.

Our methodology can be improved in several ways. First, as mentioned previously, future work is needed to address both large-scale and small-scale evolution. In addition, it is known that, in viruses, mutations related to immune-escape may occur in combination. The prevalence of epistasis in the evolution of Influenza A surface proteins has been previously studied[17]. We will expand our method to take epistatic mutations into account so that 'hot-spot' combinations of mutations can be identified.

References

1. World Health Organization http://www.who.int/influenza/en/.
2. E. G. Strauss and J. H. Strauss, *Academic Press* (2007).
3. D. M. Knipe and P. M. Howley, *Philadelphia: Lippincott Williams and Wilkins.* (2007).
4. Centres for Disease Control and Prevention http://www.cdc.gov/flu/professionals/vaccination/.
5. P. K. Tosh, R. M. Jacobsen and G. A. Poland, *Mayo Clin Proc.* **83**(3), 257–273 (2010).
6. F. Carrat and A. Flahault, *Vaccine* **25**(39–40), 6852–6862 (2007).
7. Centre for Disease Control, http://www.cdc.gov/flu/professionals/antivirals/antiviral-drug-resistance.htm .
8. M. Foll, Y.-P. Poh, N. Renzette, *et al.*, *PLOS Genetics* **10**(2): e1004185 (2014).
9. X. Li, H. Jankowski, S. Wang and J. M. Heffernan, *BIOMAT 2014 Conference Proceedings*, in press.
10. Influenza Research Database, www.fludb.org.
11. K. Tamura, D. Peterson, N. Peterson, G. Stecher, M. Nei and S. Kumar, *Mol. Bio. Evo.* **28**, 2731–2739 (2011).
12. Robert C. Edgar, *Nucleic Acids Res.* **32**(5), 1792–1797 (2004)
13. Peng Zhang, Xiaogang Wang and Peter X.-K. Song, *J. Amer. Statist. Assoc.* **101**(473), 355–367 (2006).
14. Chris Fraley and Adrian E Raftery, *J. Amer. Statist. Assoc.* **97**, 611-631 (2002).
15. R Development Core Team, *R Foundation for Statistical Computing*, Vienna, Austria, http://www.R-project.org. (2008).
16. Chris Fraley and Adrian E Raftery, *MCLUST Version 3 for R: Normal Mixture Modeling and Model-based Clustering*, Technical Report No. 504, Department of Statistics, University of Washington, (revised 2009).
17. S. Kryazhimskiy, J. Dushoff, G. A. Bazykin and J. B. Plotkin, *PLOS Genetics* **7**: e1001301 (2011).

OPTIMAL CONTROL FOR THERAPEUTIC DRUG TREATMENT ON A DELAYED MODEL INCORPORATING IMMUNE RESPONSE

P. DUBEY AND B. DUBEY*

Department of Mathematics
Birla Institute of Technology & Science Pilani-Pilani Campus
Pilani 333 031 Rajasthan, India
E-mail: preeti.dubey@pilani.bits-pilani.ac.in

UMA S. DUBEY

Department of Biological Sciences
Birla Institute of Technology & Science Pilani-Pilani Campus
Pilani 333031, Rajasthan, India
E-mail: uma@pilani.bits-pilani.ac.in

Millions of people get infected every year by viral pathogens. Newly emergent diseases such as Ebola, Swine-flu, HIV/AIDS, etc. are spreading worldwide at an alarming rate. We introduced a delayed mathematical model with immune response and therapeutic drug treatment to understand the dynamics of pathogen-immune interaction. Here, we are considering the innate immune response and the two major component of the acquired immune response, namely, cytotoxic T lymphocytes (CTLs) and humoral immunity. This model also incorporates the absorption of pathogens i.e. loss of pathogens and its related mechanisms. Further, an optimal control model is formulated with two optimal controls i.e. maximization of uninfected cells count and minimization of cost of treatments. This is done by using the Pontryagins' Maximum Principle. Existence of non-negative equilibria is established and their stability behavior is studied using theory of ordinary differential equations. Further, numerical simulations are carried out to exemplify the qualitative results.

1. Introduction

Viral pathogens infect the humans causing infectious diseases like Tuberculosis, Malaria, Ebola, Swine-flu, etc. The time delay in infected target cells

*Work partially supported by grant F.4-1/2006(BSR)/7-203/2009(BSR) of the University Grant Commission, India.

is emerging as a major concern which needs to be addressed. Effect of time delay at cellular level is very important to understand its impact on the prevention of infection. In the past decades, several delay differential equation models[1,2,3,4,5,6,7,8,9,10,11] have been developed to study the dynamics of the sub-populations. Researchers[3,4,5,6,7,8,9,10,11] have shown their interest in studying the dynamics of infectious diseases at cellular level considering the time delay. Cruz[3] has studied a mathematical model for HBV infection considering cure rate and intracellular delay for the maturation of virions to produce new infections. Xu[4] has investigated the global dynamics of HIV-1 infection with absorption of virions into uninfected cells. They considered saturated infection rate in place of mass action law. They have shown that the time delay between viral entry into a target cell and the production of new virus particle does not affect the global stability of the infected equilibrium point. Further, Tian and Xu[5] extended the previous model by introducing CTL mediated immune response. They have shown the global stability of CTL-inactivated infection equilibrium point and CTL-activated infection equilibrium point.

Zhu and Zou[6] investigated a mathematical model by introducing time delay between time the virus interacts to uninfected cell and the time when the cells becomes virus producing cell. Furthermore, they considered CTL immune response in their model and found that larger delay may help in eradication of infection. This model is further studied by Hattaf[11] et al. incorporating the optimal control. They introduced two optimal control functions to maximize the count of uninfected cells and minimize the cost of treatments. They have also derived a new scheme for numerical simulations of the model.

The time delay is a factor dependent on biological system under study and is specific as well as different for each pathogen-cell interaction. This time delay may be altered using appropriate therapeutic drug. In case of viral infections, absorption of pathogens into healthy cells, is also an important factor to be considered. During the infection mechanism, when pathogens enter into cells this reduces by one, which results into loss of pathogens. This mechanism is known as absorption of pathogens into uninfected cells. Very few authors[4,5] has been considered the effect of absorption.

Considering the above facts, a delayed mathematical model with immune response and therapeutic treatment is developed to understand the effect of intracellular time delay in infecting cells and thus inducing infection. Here, we consider the total immune response which comprises innate

immune response and acquired immune response (CTL immune response and Humoral immunity). Further, an optimal control model[11,12,13,14,15,16] has been formulated with two optimal controls namely maximization of uninfected cells count and minimization of cost of treatments.

In the next section, we formulate the mathematical model.

2. Mathematical Model

Let $x(t)$ be the density of uninfected target cells, $y(t)$ the density of infected cells, $p(t)$ the density of pathogens and $z(t)$ the density of immune response at any time $t \geq 0$. We assume that the infected cells are recruited at a rate λ and die at a rate δ_0. It is assumed that the interaction of uninfected cells with pathogens is governed by "mass-action" law (βxp). Keeping this in view, the dynamics of the system can be governed by the following system of delay differential equations:

$$\begin{cases} \dot{x} = \lambda - \delta_0 x(t) - \beta x(t)p(t) + \rho y(t), \\ \dot{y} = \beta e^{-\delta_1 \tau} x(t-\tau)p(t-\tau) - \delta_1 y(t) - \rho y(t) - k_1 y(t)z(t), \\ \dot{p} = r\delta_1 y(t) - \delta_2 p(t) - k_2 p(t)z(t) - a\beta x(t)p(t), \\ \dot{z} = \mu - \mu_0 z(t) + \mu_1 y(t)z(t) + \mu_2 p(t)z(t), \end{cases} \tag{1}$$

with initial conditions

$$(x(t), y(t), p(t), z(t)) = (x_0(t), y_0(t), p_0(t), z_0(t)), \quad -\tau \leq t \leq 0,$$

where $x_0(t)$, $y_0(t)$, $p_0(t)$, and $z_0(t)$ are non-negative continuous functions on [-τ, 0].

In model system (1), τ denotes the time delay between pathogen entry into an uninfected ells and the production of new pathogen particles. The infected cells die at a rate δ_1 and r is the total number of pathogens produced by an infected cell after its death. δ_2 is the natural death rate of pathogens. ρ is the cure rate of infected cells due to drug therapy. In the last equation of the model (1), μ denotes the innate immune response of the body. When the pathogen enters into the body and attacks the uninfected cells to get it infected, then the infected cell-specific lymphocytes proliferate with the rate $\mu_1 yz$. The pathogen specific lymphocytes proliferate with the rate $\mu_2 pz$. The corresponding decrease in the number of infected cells and pathogens are $k_1 yz$ and $k_2 pz$, respectively. μ_0 is the natural depletion

rate of the immune response. The term $a\beta xp$ in the third equation of model (1) represents the loss of pathogens due to absorption into uninfected cells, where $0 \leq a \leq 1$.

Further, we analyse the model system (1) using stability theory of delay differential equations[17]. First of all, we state the following lemma which is a region of attraction for the model (1). The proof of this lemma is easy and hence we omit it.

Lemma 2.1. $\Omega = \{(x, y, p, z) \in \Re^4_+ : x + y \leq \frac{\lambda}{\delta_m}, p \leq \frac{r\delta_1\lambda}{\delta_2\delta_m}, z \leq \frac{\mu}{\xi}\}$ *is positively invariant region of system* (1)*, where* $\xi = \mu_0 - \frac{u_1\lambda}{\delta_m} - \frac{\mu_2 r\delta_1\lambda}{\delta_2\delta_m}$.

3. Equilibrium and Stability Analysis

It is easy to found that the model system (1) has two non-negative equilibria: (i) Pathogen-free equilibrium $E_0(\frac{\lambda}{\delta_0}, 0, 0, \frac{\mu}{\mu_0})$, when there is no pathogen present in the body (i.e. $p = 0$). In this case there will not be any infected cell in the body. This equilibrium point exists trivially.
(ii) Pathogen-present equilibrium point is the one when infection is present in the body. Pathogen-present equilibrium point is represented by $E_1 = (\tilde{x}, \tilde{y}, \tilde{p}, \tilde{z})$.

Let us define basic reproduction number for the model (1) in absence of immune response as

$$R_0 = \frac{\beta\lambda r\delta_1 e^{-\delta_1\tau}}{(\delta_0\delta_2 + a\beta\lambda)(\delta_1 + \rho)}.$$

Basic reproduction number is the number of newly virus infected cells produced by a single infected cell when introduced into completely healthy cells. Basic reproduction number in presence of immune response is given by

$$\begin{aligned} R_I &= \frac{\beta\lambda r\delta_1 e^{-\delta_1\tau}}{(\delta_0(\delta_2 + k_2\frac{\mu}{\mu_0}) + a\beta\lambda)(\delta_1 + \rho + k_1\frac{\mu}{\mu_0})} \\ &= \frac{R_0}{1 + (\frac{k_1\mu}{(\delta_1+\rho)\mu_0}) + (\frac{k_2\mu\delta_0}{(\delta_0\delta_2+a\beta\lambda)}) + (\frac{k_1k_2\delta_0\mu^2}{(\delta_0\delta_2+a\beta\lambda)(\delta_1+\rho)})} \end{aligned}$$

For the given $R_I > 1$ i.e. $R_0 > 1 + \left(\frac{k_1\mu}{(\delta_1+\rho)\mu_0}\right) + \left(\frac{k_2\mu\delta_0}{(\delta_0\delta_2+a\beta\lambda)}\right) + \left(\frac{k_1k_2\delta_0\mu^2}{(\delta_0\delta_2+a\beta\lambda)(\delta_1+\rho)}\right)$, system has a pathogen-present equilibrium.

In next section we will see the existence of pathogen-present equilibrium.

3.1. *Existence of pathogen-present equilibrium* E_1

From second and third equation of model system (1) i.e. from $\dot{y}=0$, $\dot{p}=0$, we get

$$y=\left(\frac{\beta e^{-\delta_1\tau}(\delta_2+k_2z)}{\beta e^{-\delta_1\tau}r\delta_1-a\beta(\delta_1+\rho+k_1z)}\right)p,$$

here y is positive if $e^{-\delta_1\tau}r\delta_1>a\beta(\delta_1+\rho+k_1z)$.
From $\dot{x}=0$ and $\dot{p}=0$, after some algebraic manipulations, we get a quadratic polynomial in terms of z

$$[k_1k_2(\delta_0+\beta p)]z^2+[(k_1\delta_2+(\delta_1+\rho)k_2)(\delta_0+\beta p)+a\beta\lambda k_1-\rho\beta e^{-\delta_1\tau}k_2p]z$$
$$+(a\beta\lambda+(\delta_0+\beta p)\delta_2)(\delta_1+\rho)-\beta e^{-\delta_1\tau}(\lambda r\delta_1+\rho\delta_2p)=0.$$

Substituting the value of y in the equation $\dot{z}=0$ of the model system (1) and some algebraic calculation gives another quadratic equation in z

$$[\mu_0k_1a+e^{-\delta_1\tau}\mu_1k_2p-\mu_2ak_1p]z^2+[(\mu_2p-\mu_0)(e^{-\delta_1\tau}r\delta_1-a(\delta_1+\rho))$$
$$+e^{-\delta_1\tau}\mu_1\delta_2p-\mu k_1a]z+\mu(e^{-\delta_1\tau}r\delta_1-a(\delta_1+\rho))=0.$$

Let us assume

$$f_1(p,z)=[\mu_0k_1a+e^{-\delta_1\tau}\mu_1k_2p-\mu_2ak_1p]z^2+[e^{-\delta_1\tau}\mu_1\delta_2p+(\mu_2p-\mu_0)$$
$$(e^{-\delta_1\tau}r\delta_1-a(\delta_1+\rho))-\mu k_1a]z+\mu e^{-\delta_1\tau}r\delta_1-\mu a(\delta_1+\rho)=0. \tag{2}$$

$$f_2(p,z)=[k_1k_2(\delta_0+\beta p)]z^2+[(k_1\delta_2+(\delta_1+\rho)k_2)(\delta_0+\beta p)+a\beta\lambda k_1$$
$$-\rho\beta e^{-\delta_1\tau}k_2p]z+(a\beta\lambda+(\delta_0+\beta p)\delta_2)(\delta_1+\rho)$$
$$-\beta e^{-\delta_1\tau}(\lambda r\delta_1+\rho\delta_2p)=0. \tag{3}$$

For $p=0$, Eq. (2) gives

$$z=\frac{-B_1+\sqrt{{B_1}^2-4A_1C_1}}{2A_1}=z_1(say),$$

where $A_1=a\mu_0k_1$, $B_1=-(\mu ak_1+\mu_0(e^{-\delta_1\tau}r\delta_1-a(\delta_1+\rho)))$, $C_1=\mu(e^{-\delta_1\tau}r\delta_1-a(\delta_1+\rho))$. After simplification, we get

$$z_1=\frac{\mu}{\mu_0},$$

We also have

$$\frac{dz}{dp}=-\frac{\partial f_1/\partial p}{\partial f_1/\partial z}$$
$$=-\frac{P_1z^2+P_2z}{P_3z+P_4}$$

where $P_1 = e^{-\delta_1\tau}\mu_1 k_2 - \mu_2 a k_1$, $P_2 = \mu_2(e^{-\delta_1\tau} r\delta_1 - a(\delta_1+\rho)) + e^{-\delta_1\tau}\mu_1\delta_2$, $P_3 = 2(\mu_0 k_1 a + (e^{-\delta_1\tau}\mu_1 k_2 - \mu_2 a k_1)p)$, $P_4 = (\mu_2 p - \mu_0)(e^{-\delta_1\tau} r\delta_1 - a(\delta_1+\rho)) + e^{-\delta_1\tau}\mu_1\delta_2 p - \mu k_1 a$.
This implies that $\frac{dz}{dp} < 0$, if
$(\mu_1 e^{-\delta_1\tau} k_2) > \mu_2 a k_1$ and $p > \max\{\frac{\mu_0}{\mu_2}, \frac{\mu k_1 a}{e^{-\delta_1\tau}\mu_1\delta_2}\}$.
This shows that z is a decreasing function of p.
When $z = 0$, Eq. (3) gives

$$p = \frac{\lambda r\delta_1\beta e^{-\delta_1\tau} - (\delta_1+\rho)(\delta_0\delta_2 + a\beta\lambda)}{\beta(\delta_2\delta_1 + \rho\delta_2(1-e^{-\delta_1\tau}))}.$$

Here, p is positive for $R_0 > 1$. For $p = 0$, Eq. (3) reduces to

$$\begin{aligned}(k_1k_2\delta_0)z^2 + ((k_1\delta_2 + (\delta_1+\rho)k_2)\delta_0 + a\beta\lambda k_1)z \\ - (\lambda\beta e^{-\delta_1\tau} r\delta_1 - (a\beta\lambda + \delta_0\delta_2)(\delta_1+\rho)) = 0.\end{aligned}$$

From the above equation, we found two roots (one is positive and another one is negative) if $R_0 > 1$. For $R_0 < 1$ there is no positive real root.
Let us say $z = z_2 = \frac{-B_2 + \sqrt{B_2^2 - 4A_2C_2}}{2A_2}$, be the positive root of the above equation, where $A_2 = k_1k_2\delta_0$, $B_2 = ((k_1\delta_2 + (\delta_1+\rho)k_2)\delta_0 + a\beta\lambda k_1)$, and $C_2 = -(\lambda\beta e^{-\delta_1\tau} r\delta_1 - (a\beta + \delta_0\delta_2)(\delta_1+\rho))$.

$$\begin{aligned}\frac{dz}{dp} &= -\frac{\partial f_2/\partial p}{\partial f_2/\partial z} \\ &= -\frac{k_1k_2z^2 + P_5 z + P_6}{P_7 z + P_8}\end{aligned}$$

where $P_5 = ((k_1\delta_2 + k_2\delta_1) + \rho k_2(1-e^{-\delta_1\tau}))$, $P_6 = (\delta_2\delta_1 + \delta_2\rho(1-e^{-\delta_1\tau}))$, $P_7 = 2k_1k_2(\delta_0 + (\alpha\delta_0 + \beta)p)$, $P_8 = (k_1\delta_2 + (\delta_1+\rho)k_2)\delta_0 + (k_1\delta_2 + k_2\delta_1)\beta p + \rho k_2\beta(1-e^{-\delta_1\tau}) + a\beta\lambda k_1$.
We note that $\frac{dz}{dp} < 0$. Thus the two isoclines intersects at a pathogen-present equilibrium point if

$$z_2 > z_1,$$

i.e.

$$\frac{-B_2 + \sqrt{B_2^2 - 4A_2C_2}}{2A_2} > \frac{\mu}{\mu_0}$$

Simple manipulation leads to the condition

$$R_I = \frac{R_0}{1 + (\frac{k_1\mu}{(\delta_1+\rho)\mu_0}) + (\frac{k_2\mu\delta_0}{(\delta_0\delta_2+a\beta\lambda)}) + (\frac{k_1k_2\delta_0\mu^2}{(\delta_0\delta_2+a\beta\lambda)(\delta_1+\rho)})} > 1,$$

where R_I is the basic reproduction number of the model (1) in presence of immune response and when there is loss of pathogens into uninfected cells. This shows the existence of pathogen-present equilibrium.

3.2. *Stability of pathogen-free equilibrium* E_0

We linearize the model system (1) at E_0. At $E_0(\frac{\lambda}{\delta_0}, 0, 0, \frac{\mu}{\mu_0})$, the linearized model system (1) has two eigenvalues $-\delta_0$ and $-\mu_0$ and the other two eigenvalues are given by the following characteristic equation:

$$Q^2 + (q_1 + q_2)Q + q_1 q_2 - \frac{\beta\lambda r\delta_1 e^{-\delta_1\tau}}{\delta_0} e^{-Q\tau} = 0, \tag{4}$$

where $q_1 = \delta_1 + \rho + k_1\frac{\mu}{\mu_0}$, $q_2 = \delta_2 + k_2\frac{\mu}{\mu_0} + \frac{a\beta\lambda}{\delta_0}$.
For $\tau = 0$, the Eq. (4) takes the form

$$Q^2 + (q_1 + q_2)Q + q_1 q_2 - \frac{\beta\lambda r\delta_1}{\delta_0} = 0,$$

which gives eigenvalues with negative real part if $R_I < 1$ i.e. $R_0 < 1 + \left(\frac{k_1\mu}{(\delta_1+\rho)\mu_0}\right) + \left(\frac{k_2\mu\delta_0}{(\delta_0\delta_2+a\beta\lambda)}\right) + \left(\frac{k_1k_2\delta_0\mu^2}{(\delta_0\delta_2+a\beta\lambda)(\delta_1+\rho)}\right)$. This shows that in absence of time delay (i.e. $\tau = 0$) E_0 is locally asymptotically stable if $R_I < 1$ and unstable if $R_I > 1$.
Biologically this states that the pathogen-free equilibrium in presence of immune response is locally asymptotically stable if no newly infected cell is present.

Let $Q = i\omega(\omega > 0)$ is a solution of Eq. (4). Let us separate the real and imaginary parts and after squaring and adding these parts, it follows that

$$\omega^4 + (q_1^2 + q_1^2)\omega^2 + q_1^2q_2^2(1 - R_I^2) = 0. \tag{5}$$

Notice that Eq. (5) has roots only with negative real parts if $R_I < 1$ and Eq. (5) has at least one positive root if $R_I > 1$. One can summarize the above result as follows for $(\tau \neq 0)$:

Theorem 3.1. *The pathogen-free equilibrium is asymptotically stable if* $R_I < 1$ *and when* $R_I > 1$, *then the pathogen-free equilibrium is unstable and the pathogen-present equilibrium exists.*

Remark 3.1. It may be pointed out here that the stability behaviour of pathogen-free equilibrium E_0 is independent of τ.

3.3. *Stability of pathogen-present equilibrium* E_1

The Jacobian matrix of the model system (1) at $E_1(\tilde{x}, \tilde{y}, \tilde{p}, \tilde{z})$ is given by

$$M = \begin{bmatrix} -(\delta_0 + \beta\tilde{p}) & \rho & -\beta\tilde{x} & 0 \\ \beta\tilde{p}e^{-(\delta_1+\psi)\tau} & -(\delta_1 + \rho + k_1\tilde{z}) & \beta\tilde{x}e^{-(\delta_1+\psi)\tau} & -k_1\tilde{y} \\ -a\beta\tilde{p} & r\delta_1 & -(\delta_2 + k_2\tilde{z} + a\beta\tilde{x}) & -k_2\tilde{p} \\ 0 & \mu_1\tilde{z} & \mu_2\tilde{z} & -\frac{\mu}{\tilde{z}} \end{bmatrix}.$$

Characteristic polynomial of the Jacobian matrix M is given by

$$\psi^4 + A_1\psi^3 + A_2\psi^2 + A_3\psi + A_4 + [B_1\psi^2 + B_2\psi + B_3]e^{-\psi\tau} = 0, \qquad (6)$$

where

$$\begin{aligned}
A_1 &= \delta_0 + \beta\tilde{p} + {q_1}^* + {q_2}^* + \frac{\mu}{\tilde{z}}, \\
A_2 &= (\delta_0 + \beta\tilde{p})\left({q_1}^* + \delta_2 + k_2\tilde{z} + \frac{\mu}{\tilde{z}}\right) + \delta_0 a\beta\tilde{x} \\
&\quad + {q_1}^*\left({q_2}^* + \frac{\mu}{\tilde{z}}\right) + \mu_1 k_1\tilde{y}\tilde{z} + \mu_2 k_2\tilde{p}\tilde{z} + {q_2}^*\frac{\mu}{\tilde{z}}, \\
A_3 &= (\delta_0 + \beta\tilde{p})\left({q_1}^*(\delta_2 + k_2\tilde{z}) + (\delta_2 + k_2\tilde{z})\frac{\mu}{\tilde{z}} + \mu_2 k_2\tilde{p}\tilde{z}\right) \\
&\quad + (\delta_0 + \beta\tilde{p})\left({q_1}^*\frac{\mu}{\tilde{z}} + \mu_1 k_1\tilde{y}\tilde{z}\right) + \delta_0 a\beta\tilde{x}\left({q_1}^* + \frac{\mu}{\tilde{z}}\right) \\
&\quad + {q_1}^*\left({q_2}^*\frac{\mu}{\tilde{z}} + \mu_2 k_2\tilde{p}\tilde{z}\right) + k_1\tilde{y}(r\delta_1\mu_2\tilde{z} + {q_2}^*\mu_1\tilde{z}), \\
A_4 &= {q_1}^*(\delta_0 + \beta\tilde{p})\left((\delta_2 + k_2\tilde{z})\frac{\mu}{\tilde{z}} + \mu_2 k_2\tilde{p}\tilde{z}\right) + {q_1}^*\delta_0 a\beta\tilde{x}\frac{\mu}{\tilde{z}} \\
&\quad + (\delta_0 + \beta\tilde{p})k_1\tilde{y}(r\delta_1\mu_2\tilde{z} + (\delta_2 + k_2\tilde{z})\mu_1\tilde{z}) \\
&\quad + a\beta k_1\tilde{y}\tilde{z}(\delta_0\mu_1\tilde{x} - \rho\mu_2\tilde{p}), \\
B_1 &= -\beta e^{-\delta_1\tau}\left(\rho\tilde{p} + r\delta_1\tilde{x}\right), \\
B_2 &= -\beta e^{-\delta_1\tau}\left(\rho\tilde{p}\left(\delta_2 + k_2\tilde{z} + \frac{\mu}{\tilde{z}}\right) + r\delta_1\tilde{x}\left(\delta_0 + \frac{\mu}{\tilde{z}}\right) - \mu_1 k_2\tilde{x}\tilde{p}\tilde{z}\right), \\
B_3 &= \beta e^{-\delta_1\tau}\left(k_2\tilde{p}\tilde{z}(\delta_0\tilde{x}\mu_1 - \rho\tilde{p}\mu_2) - \frac{\mu}{\tilde{z}}(r\delta_1\delta_0\tilde{x} + \rho\tilde{p}(\delta_2 + k_2\tilde{z}))\right), \\
{q_1}^* &= \delta_1 + \rho + k_1\tilde{z}, \\
{q_1}^* &= \delta_2 + k_2\tilde{z} + a\beta\tilde{x}.
\end{aligned}$$

For $\tau = 0$, Eq. (6) reduces to

$$\psi^4 + A_1'\psi^3 + A_2'\psi^2 + A_3'\psi + A_4' = 0. \qquad (7)$$

where $A_1' = A_1$, $A_2' = (A_2 + B_1)$, $A_3' = (A_3 + B_2)$, $A_4' = (A_4 + B_3)$. Using Routh-Hurwitz criteria one can easily show that pathogen-present

equilibrium E_1 is locally asymptotically stable if the following conditions hold:

$$A_1' > 0, A_2' > 0, A_3' > 0, A_4' > 0, A_1'A_2'A_3' - {A_3'}^2 - {A_1'}^2 A_4' > 0. \quad (8)$$

It may be pointed out here that whenever condition in Eq. (8) is reversed, then change in stability is possible only when characteristic equation has purely imaginary roots for some values of τ. Hence, for $\tau > 0$, let $\psi = i\omega$ satisfies the characteristic Eq. (6), Then the equation becomes transcendental equation, separating real and imaginary parts of this equation we get

$$\omega^4 - A_2\omega^2 + A_4 = (B_1\omega^2 - B_3)cos\,\omega\tau - B_2\omega sin\,\omega\tau, \quad (9)$$

and

$$-A_1\omega^3 + A_3\omega = -(B_1\omega^2 - B_3)sin\,\omega\tau - B_2\omega cos\,\omega\tau. \quad (10)$$

Squaring and adding the above equations, we get

$$(\omega^4 - A_2\omega^2 + A_4)^2 + (A_3\omega - A_1\omega^3)^2 = ((B_1\omega^2 - B_3)cos\omega\tau - B_2\omega sin\omega\tau)^2 + ((B_1\omega^2 - B_3)sin\omega\tau + B_2\omega cos\omega\tau)^2.$$

A little simplification with $\omega^2 = \eta$, the above equation yields

$$f(\eta) = \eta^4 + C_1\eta^3 + C_2\eta^2 + C_3\eta + C_4 = 0, \quad (11)$$

where $C_1 = {A_1}^2 - 2A_2$, $C_2 = {A_2}^2 + 2A_4 - 2A_1A_3 - {B_1}^2$, $C_3 = {A_3}^2 - 2A_2A_4 + 2B_1B_3 - {B_2}^2$, $C_4 = {A_4}^2 - {B_3}^2$.
The Eq. (11) will not have any positive root if $C_1 > 0$, $C_2 > 0$, $C_3 > 0$ and $C_4 > 0$. We state the result of above computation as follows.

Theorem 3.2. *The pathogen-present equilibrium is locally asymptotically stable for all $\tau \geq 0$ if $R_I > 1$ and all the coefficients in Eq.* (11) *are positive i.e. $C_1 > 0$, $C_2 > 0$, $C_3 > 0$ and $C_4 > 0$.*

Remark 3.2. Theorem 3.2 shows that there is no change in the stability of E_1 if $C_i > 0$, $i = 1, 2, 3, 4$.

3.4. *Hopf bifurcation*

If $C_4 < 0$, then the Eq. (11) has an unique positive root ω_0, hence Eq. (6) has a pair of purely imaginary roots $(i\omega_0)$ and corresponding to this value of ω_0, from Eqs. (9)–(9), we have

$$cos\,\omega\tau = \frac{D_1}{D_2},$$

where $D_1 = ({\omega_0}^4 - A_2{\omega_0}^2 + A_4)(B_1{\omega_0}^2 - B_3) + (A_1{\omega_0}^3 - A_3\omega_0)B_2\omega_0$, $D_2 = (B_2\omega_0)^2 + (B_1{\omega_0}^2 - B_3)^2$,

$$\tau_n = \frac{2n\pi}{\omega_0} + \frac{1}{\omega_0} cos^{-1}\left(\frac{D_1}{D_2}\right). \tag{12}$$

Differentiating Eq. (6) w.r.t τ, we get

$$[L_1 - \tau L_2 e^{-\psi\tau}]\frac{d\psi}{d\tau} = \psi L_2 e^{-\psi\tau},$$

where $L_1 = 4\psi^3 + 3A_1\psi^2 + 2A_2\psi + A_3 + (2B_1\psi + B_2)e^{-\psi\tau}$, $L_2 = B_1\psi^2 + B_2\psi + B_3$. This gives

$$\left(\frac{d\psi}{d\tau}\right)^{-1} = \frac{L_1 - \tau L_2 e^{-\psi\tau}}{\psi L_2 e^{-\psi\tau}} = \frac{L_1}{\psi L_2 e^{-\psi\tau}} - \frac{\tau}{\psi},$$

and

$$e^{\psi\tau} = -\frac{L_2}{\psi^4 + A_1\psi^3 + A_2\psi^2 + A_3\psi + A_4}.$$

The transversality condition is

$$\begin{aligned} sign\left(\frac{d(Re\psi)}{d\tau}\right)_{\psi=i\omega_0} &= sign\left(Re\left(\frac{d\psi}{d\tau}\right)^{-1}\right)_{\psi=i\omega_0} \\ &= sign\left(\frac{4{\eta_0}^3 + 3C_1{\eta_0}^2 + 2C_2\eta_0 + C_3}{(\omega^4 - A_2\omega^2 + A_4)^2 + (A_3\omega - A_3\omega^3)^2}\right) \end{aligned}$$

We can summarize the above computation in the following theorem:

Theorem 3.3. *If $C_4 < 0$, the the pathogen-present equilibrium E_1 of the model (1) is locally asymptotically stable for $\tau < \tau_0$ and loses its stability for $\tau > \tau_0$. Hence the system (1) exhibits hopf bifurcation at $\omega = \omega_0$ and $\tau = \tau_0$.*

In the next section, we introduced optimal control to model (1).

4. Optimal Control Model Formulation

To maximize the density of uninfected cells and to minimize the cost of treatment, we introduced two controls u_1 and u_2 to the delay system model (1). The control function u_1 measures the efficiency of therapeutic drug which blocks new infection. The control function u_2 measures the efficiency

of therapeutic drug which inhibits pathogen proliferation. The model is given by the following system of differential equations:

$$\begin{cases} \dot{x} = \lambda - \delta_0 x(t) - (1 - u_1(t))\beta x(t)p(t) + \rho y(t), \\ \dot{y} = (1 - u_1(t))\beta e^{-\delta_1 \tau} x(t-\tau)p(t-\tau) - (\delta_1 + \rho + k_1 z(t))y(t), \\ \dot{p} = (1 - u_2(t))r\delta_1 y(t) - \delta_2 p(t) - k_2 p(t)z(t) - a\beta x(t)p(t), \\ \dot{z} = \mu - \mu_0 z(t) + \mu_1 y(t)z(t) + \mu_2 p(t)z(t). \end{cases} \tag{13}$$

The control functions $u_1(t)$ and $u_2(t)$ are bounded and Lebegue integrable functions. From the equations of model, it is clear that the inhibition is 100% when $u_2 = 1$ and there is no inhibition for $u_2 = 0$. Now our objective functional is given by

$$J(u_1, u_2) = \int_0^{t_f} \left\{ x(t) + z(t) - \left[\frac{a_1}{2} u_1^2(t) + \frac{a_2}{2} u_2^2(t) \right] \right\} dt, \tag{14}$$

where $a_1 \geq 0$ and $a_2 \geq 0$ are based on the benefits and costs of the treatment and t_f is the time period of the treatment. In this study, our main purpose is maximize the objective functional J by increasing number of uninfected cells, the immune response, minimizing the viral load and reducing the cost of treatment. In other words, we find the optimal control pair (u_1^*, u_2^*) s.t.

$$J(u_1^*, u_2^*) = \max\{J(u_1, u_2) : (u_1, u_2) \in \Gamma\} \tag{15}$$

where Γ is the control set defined by

$$\Gamma = \{u = (u_1, u_2) : u_i \quad measurable, 0 \leq u_i(t) \leq 1, t \in [0, t_f], i = 1, 2\}.$$

4.1. *Optimality system*

We use Pontryagin's Maximum Principle to get the necessary conditions for an optimal control problem, which converts the Eqs. (13)–(15) into a problem of maximizing an Hamiltonian, H, with respect to u_1 and u_2. The Hamiltonian function H is given by

$$H = x(t) + z(t) - \left[\frac{a_1}{2} u_1^2(t) + \frac{a_2}{2} u_2^2(t) \right] + \sum_{i=1}^{4} \Lambda_i f_i, \tag{16}$$

where f_i represents the right hand side of the i-th state variable of model system (13) and Λ_i are called adjoint variables.

$$\begin{aligned} H(t,x,y,p,z,x_\tau,p_\tau,u_1,u_2,\Lambda) = {} & x + z - \frac{a_1}{2}{u_1}^2 - \frac{a_2}{2}{u_2}^2 \\ & + \Lambda_1[\lambda - \delta_0 x - (1-u_1)\beta x p + \rho y] \\ & + \Lambda_2[(1-u_1)\beta e^{-\delta_1\tau} x_\tau p_\tau - \delta_1 y - \rho y - k_1 y z] \\ & + \Lambda_3[(1-u_2) r\delta_1 y - \delta_2 p - k_2 p z - a\beta x p] \\ & + \Lambda_4[\mu - \mu_0 z + \mu_1 y z + \mu_2 p z] \end{aligned}$$

After applying Pontryagin's Maximum Principle, we can state the following result.

Theorem 4.1. *Given optimal controls u_1^*, u_2^* and solutions x^*, y^*, p^* and z^* of the corresponding state system* (13)*, there exists adjoint variables, Λ_1, Λ_2, Λ_3 and Λ_4 satisfying the equations*

$$\begin{aligned} \Lambda_1'(t) &= -1 + \Lambda_1(t)(\delta_0 + (1-u_1^*(t))\beta p^*(t)) + \Lambda_3(t) a\beta p^*(t) \\ &\quad + \chi_{[0,t_f-\tau]}(t)\Lambda_2(t+\tau)((u_1^*(t+\tau)-1)\beta e^{-\delta_1\tau} p^*(t)), \\ \Lambda_2'(t) &= \Lambda_2(t)(\delta_1 + \rho + k_1 z^*) - \Lambda_1(t)\rho - \Lambda_3(t) r\delta_1(1-u_2^*(t)) - \Lambda_4(t)\mu_1 z^*, \\ \Lambda_3'(t) &= \Lambda_1(t)(1-u_1^*)\beta x^*(t) + \Lambda_3(t)(\delta_2 + k_2 z^*(t) + a\beta x^*(t)) - \Lambda_4(t)\mu_2 z^*(t) \\ &\quad + \chi_{[0,t_f-\tau]}(t)\Lambda_2(t+\tau)((u_1^*(t+\tau)-1)\beta e^{-\delta_1\tau} x^*(t)), \\ \Lambda_4'(t) &= -1 + \Lambda_2(t) k_1 y^*(t) + \Lambda_3(t) k_2 p^*(t) + \Lambda_4(t)(\mu_0 - \mu_1 y^*(t) - \mu_2 p^*(t)), \end{aligned}$$

and the transversality conditions $\Lambda_i(t_f) = 0$, $i = 1,\ldots,4$. Furthermore, optimal controls are

$$\begin{aligned} u_1^*(t) &= \max\left(0, \min\left(1, \tfrac{\beta}{a_1}\phi\right)\right), \\ \phi &= (\Lambda_1(t) x^*(t) p^*(t) - \Lambda_2(t) e^{-\delta_1\tau} x^*(t-\tau) p^*(t-\tau)), \\ u_2^*(t) &= \max\left(0, \min\left(1, -\tfrac{1}{a_2}\Lambda_3(t) r\delta_1 p^*(t)\right)\right). \end{aligned}$$

Proof. One can easily evaluate the adjoint equations and transversality conditions using the Pontryagins' Maximum Principle with delay as

$$\begin{aligned} \Lambda_1'(t) &= -\frac{\partial H}{\partial x}(t) - \chi_{[0,t_f-\tau]}(t)\frac{\partial H}{\partial x_\tau}(t+\tau), \quad \Lambda_1(t_f) = 0, \\ \Lambda_2'(t) &= -\frac{\partial H}{\partial y}(t), \quad \Lambda_2(t_f) = 0, \\ \Lambda_3'(t) &= -\frac{\partial H}{\partial p}(t) - \chi_{[0,t_f-\tau]}(t)\frac{\partial H}{\partial p_\tau}(t+\tau), \quad \Lambda_3(t_f) = 0, \\ \Lambda_4'(t) &= -\frac{\partial H}{\partial z}(t), \quad \Lambda_4(t_f) = 0. \end{aligned}$$

We can determine the optimal controls u_1^* and u_2^* from optimality conditions

$$\frac{\partial H}{\partial u_1}(t) = 0, \qquad \frac{\partial H}{\partial u_2}(t) = 0.$$

We have

$$\frac{\partial H}{\partial u_1}(t) = -a_1 u_1(t) + \Lambda_1(t)\beta x(t)p(t) - \Lambda_2(t)\beta e^{-\delta_1 \tau} x(t-\tau)p(t-\tau) = 0,$$
$$\frac{\partial H}{\partial u_2}(t) = -a_2 u_2(t) - \Lambda_3(t) r\delta_1 y(t) = 0.$$

Using the bounds in Γ of the controls, one can easily find the optimal control functions u_1^* and u_2^* as given in Theorem 4.1. □

Furthermore by substituting the values of $u_1^*(t)$ and $u_2^*(t)$ in model system (13) and the adjoint variables. We find following optimality system:

$$\frac{dx^*}{dt} = \lambda - \delta_0 x(t) - (1-u_1^*(t))\beta x^*(t)p^*(t) + \rho y^*(t), \tag{17}$$
$$\frac{dy^*}{dt} = (1-u_1^*(t))\beta e^{-\delta_1\tau} x^*(t-\tau)p^*(t-\tau) - (\delta_1+\rho)y^*(t) - k_1 y^*(t)z^*(t), \tag{18}$$
$$\frac{dp^*}{dt} = (1-u_2^*(t))r\delta_1 y^*(t) - \delta_2 p^*(t) - k_2 p^*(t)z^*(t) - a\beta x^*(t)p^*(t), \tag{19}$$
$$\frac{dz^*}{dt} = \mu - \mu_0 z^*(t) + \mu_1 y^*(t)z^*(t) + \mu_2 p^*(t)z^*(t), \tag{20}$$
$$\frac{d\Lambda_1}{dt} = -1 + \Lambda_1(t)[\delta_0 x^*(t) + (1-u_1^*(t))\beta p^*(t)] + \Lambda_3(t)[a\beta p^*(t)] - \Lambda_2(t+\tau)[(1-u_1^*(t+\tau)\beta e^{\delta_1\tau} p^*(t)], \tag{21}$$
$$\frac{d\Lambda_2}{dt} = -\Lambda_1(t)\rho + \Lambda_2(t)[\delta_1+\rho+k_1 z^*(t)] + \Lambda_3(t)[r\delta_1(u_2^*(t)-1)] - \Lambda_4(t)\mu_1 z^*(t), \tag{22}$$
$$\frac{d\Lambda_3}{dt} = \Lambda_1(t)[(1-u_1^*(t))\beta x^*(t)] + \Lambda_2(t+\tau)[(u_1^*(t+\tau)-1)\beta e^{-\delta_1\tau} x^*(t)] + \Lambda_3(t)[\delta_2 + k_2 z^*(t) + a\beta x^*(t)] - \Lambda_4(t)\mu_2 z^*(t), \tag{23}$$
$$\frac{d\Lambda_4}{dt} = -1 + \Lambda_2(t)k_1 y^*(t) + \Lambda_3(t)k_2 p^*(t) + \Lambda_4(t)[\mu_0 - \mu_1 y^*(t) - \mu_2 p^*(t)], \tag{24}$$

where

$$u_1^*(t) = \max\left(0, \min\left(1, \frac{\beta}{a_1}\phi\right)\right),$$
$$\phi = (\Lambda_1(t)x^*(t)p^*(t) - \Lambda_2(t)e^{-\delta_1\tau}x^*(t-\tau)p^*(t-\tau)),$$
$$u_2^*(t) = \max\left(0, \min\left(1, -\frac{1}{a_2}\Lambda_3(t)r\delta_1 p^*(t)\right)\right).$$

5. Numerical Simulations

In this section, we present the simulation results to validate analytical results using Matlab 7.10. We have considered here both the cases; (i) the one when $a = 0$ i.e. there is no loss of pathogens and (ii) when $a = 1$ i.e. full absorption of pathogens into uninfected cells. Let us consider the following set of parameters given in Table 1. In the first case, for $a = 0$

Table 1. List of parameters and values assigned.

Parameters	Values assigned (Unit)
λ	$5(mm^3d^{-1})$
δ_0	$0.03(mm^3d^{-1})$
δ_1	$0.035(mm^3d^{-1})$
δ_2	$0.04(mm^3d^{-1})$
β	$0.001(mm^3d^{-1})$
k_1	$0.001(d^{-1})$
k_2	$0.25(d^{-1})$
μ	$0.38(d^{-1})$
μ_0	$1.5(d^{-1})$
μ_1	$0.21(d^{-1})$
μ_2	$0.05(d^{-1})$
ρ	$0.06(d^{-1})$
r	$20(mm^3d^{-1})$

and $\tau = 0$, we found $R_I = 11.8529 > 1$ and in later case of full absorption of pathogens ($a = 1$), $R_I = 4.5363 > 1$ (all other parameters are same as in Table 1). The value of basic reproduction number in later case (with absorption) is lesser than that of first case (without absorption). This indicates that the consideration of absorption is important in prevention of infection. The full absorption of pathogens i.e. $a = 1$ has been considered for further simulations.

The pathogen-present equilibrium point exists in absence of delay $\tau = 0$ for the set of parameters given in Table 1. This is given by $x^* = 159.1815$,

$y^* = 5.7997$, $p^* = 3.5975$ and $z^* = 3.7182$. The eigenvalues of the characteristic Eq. (7) are -1.1749, -0.0302, -0.0791$\pm$0.3298i, these all are having negative real parts hence E_1 is locally asymptotically stable in the absence of delay and when full absorption is considered.

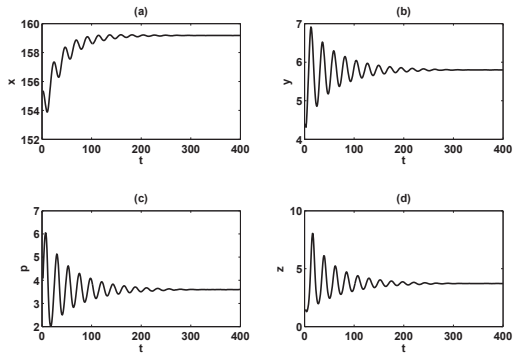

Figure 1. Solution trajectories of the model (1) for $\tau = 2$ ($\tau < \tau_0 = 3.0031$).

We computed the critical value of τ_0 for which E_1 changes its behavior from stable to unstable. For the above set of parameters, the condition for existence of purely imaginary roots is satisfied. The positive root of Eq. (11) is $\omega_0 = 0.2550$ and the corresponding value of $\tau_0 = 3.0031$.

We plotted the time series of all variables namely uninfected cells, infected cells, pathogens and immune response used in model (1) for $\tau = 2$ (Fig. 1). The trajectories initially show oscillations and at a later time they get settled to their equilibrium points. This shows the stability of pathogen-present equilibrium point as observed analytically in Theorem (3.3).

Similarly the solutions has been plotted for $\tau = 3.5$ in Fig. 2. Here the value of delay is more than the critical value, the trajectories show oscillatory behavior with equal period. The pathogen-present equilibrium point loses its stability as τ crosses its critical value ($\tau_0 = 3.0031$). This unstable behaviour of the system becomes difficult to manage therapeutically. The phase portrait in Fig. 3 has been plotted in $y - p - z$ plane for $\tau = 3.5$ and rest of the parameters are same as given in Table 1. The trajectories initiating from two different initial points ($IV1 \rightarrow [140, 3, 1.1, 2.1]$ $IV2 \rightarrow [170, 4.4, 2.5, 5]$) and approaches to the unique closed trajectory,

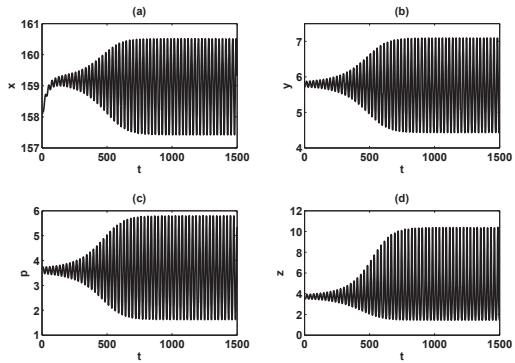

Figure 2. Solution trajectories of the model (1) for $\tau = 3.5$ ($\tau > \tau_0 = 3.0031$).

this figure represents a stable limit cycle.

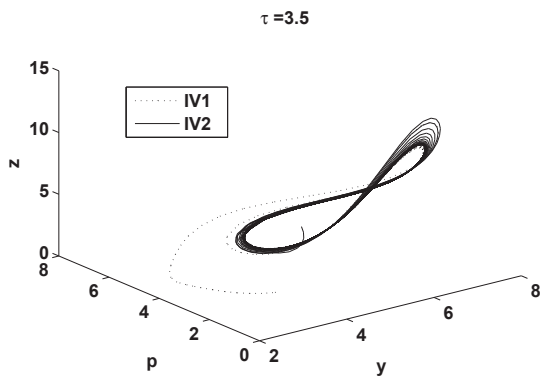

Figure 3. Phase portrait of the model (1) in $y - p - z$ plane for $\tau = 3.5$.

Figure 4 represents the variation of sub-populations (x and y) without delay and with delay considering different levels of therapeutic drug (keeping other parameters fix as in Table 1). Firstly, we kept $\tau = 0$ and observed the effect of drug on uninfected cells and infected cells (Figs. 4(a–b)). The trajectories in this case are first oscillating and then with increase in time, they approach to their equilibrium points. We observed the increase in uninfected cells and decrease in infected cells with increase in ρ. Further, we

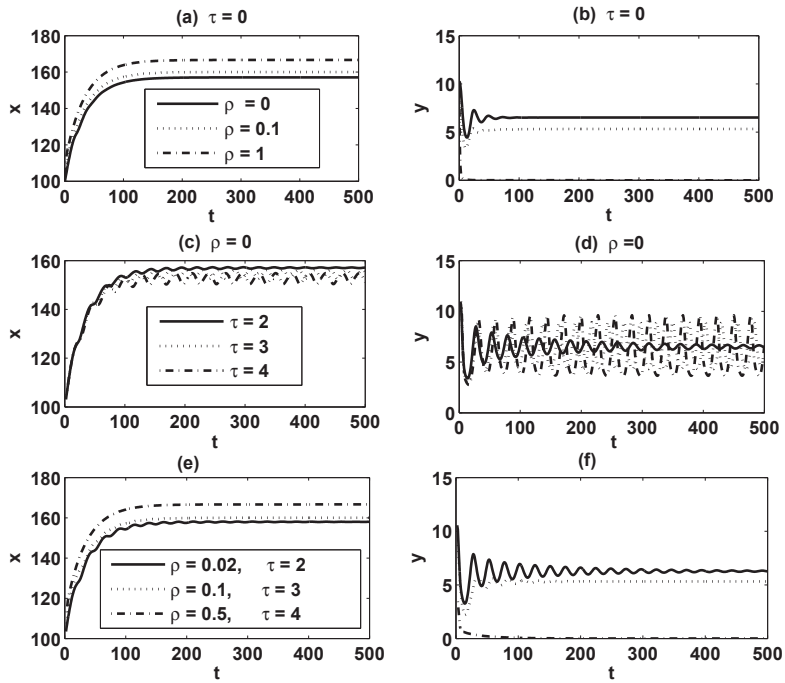

Figure 4. Variation of sub-populations for different values of ρ and τ.

fixed $\rho = 0$ and studied the effect of delay on uninfected cells and infected cells in absence of treatment (Figs. 4(c–d)). It is observed that in contrast to no delay, when the delay increases, the concentration of uninfected cells and that of the infected cells does not alter significantly. But the the trajectories of both sub-populations show oscillations initially with less period and then period of oscillations also increase with increase in delay. The effect of delay as well as therapeutic drug has been shown in Figs. 4(e–f). It is observed that in contrast to no treatment, when the treatment together with time delay increases the model system (1) converges to its equilibrium point lasting to a very low level of infected cells and a higher level of uninfected cells.

Further, we simulated the optimal control model 13 using the parameters of Table 1 with $\tau = 0.5$ (see Fig. 5). The solutions has been plotted without control and with control for final time period of 100 *days*. We notice that in Fig. 5(a), uninfected cells settle at high level in case of with control than that of without control. In Fig. 5(b), the density of infected

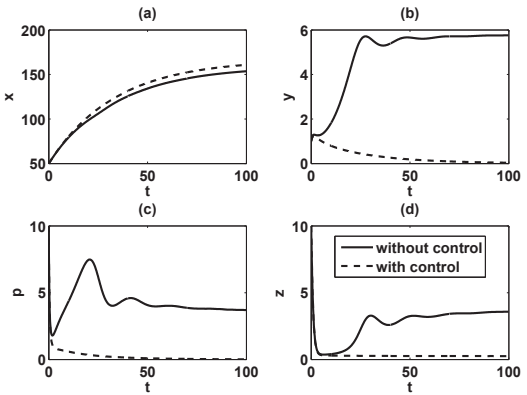

Figure 5. Variation of sub-populations without control and with control.

cells in first case (without control) is 5.7592 and that of in second case (with control) is 0.0360, total number of blocked infections is 5.7232. The efficacy of the control function in blocking infections is 99.37%. The density of pathogens in Fig. 5(c), in first case is 3.6989 and that of second case is 0.0163, total number of inhibited pathogens is 3.6826, which shows that the efficacy of control function in reducing pathogen or inhibiting pathogens is 99.55%. In Fig. 5(d), the density of immune response in second case (with control) is lesser than that of first case (without control) since infection is declining so the stimulation of acquired immune response due to infected cells and pathogens is also decreasing.

6. Conclusions

In this study, we investigated a mathematical model with therapeutic drug and time delay in vivo on uninfected cells, infected cells, pathogen and immune response. The absorption or loss of pathogens into uninfected cells has been considered. In order to understand the dynamics of pathogen-immune interaction, we have considered the total immune response. We computed the basic reproduction number for the model (1), which is dependent on τ. From the expression

$$R_I = \frac{\beta\lambda r\delta_1 e^{-\delta_1\tau}}{(\delta_0(\delta_2 + k_2\frac{\mu}{\mu_0}) + a\beta\lambda)(\delta_1 + \rho + k_1\frac{\mu}{\mu_0})},$$

it is clear that $R_I(\tau)$ is decreasing function of τ. As time delay between the infected cell and virus producing cell increases R_I decreases for

$\lim_{t\to\infty} R_I(\tau) = 0$.
Biologically this signifies that infection from the body can be reduced by increasing time delay. Therefore it can be suggested that increasing the time delay by therapeutic modalities is a significant approach to disease management.

The stability behaviour of pathogen-free equilibrium and pathogen-present equilibrium has been studied. We found that introduction of time delay will not affect the pathogen-free equilibrium. The pathogen-present equilibrium loses its stability as τ crosses its critical value $\tau_0 = 3.0031$ and the system exhibits hopf-bifurcation at this critical value. These analytical findings have shown graphically using simulations. It has been observed that in presence of pathogen, the trajectories for uninfected cells, infected cells, pathogens and immune response converges to their respective equilibrium points for a small delay in absence of any treatment. When the time delay crosses its critical value ($\tau_0 = 3.0031$) the system becomes unstable and this is difficult to predict. The enhancement of treatment leads to blocking of pathogens and declining the infected cells. From simulations of optimal control model (13), we observed that optimal control increases the count of uninfected cells and blocks the pathogen which leads in reduction of infected cells with 99.37% efficacy.

References

1. A. K. Misra and V. Singh, *J. Theor. Biol.* **301**, 49–56 (2012).
2. B. Dubey, *J. Biol. Syst.* **12(01)**, 35–43 (2004).
3. C. Vargas-De-Len, *Appl. Math. Comp.* **219(1)**, 389–398 (2012).
4. R. Xu, *Int. J. Biomath.* **5(03)**, 1260012 (2012).
5. X. Tian and R. Xu, *IMA J. Appl. Math.* **hxs** 069 (2012).
6. H. Zhu and X. Zou, *Discret. Contin. Dyn. S.*, **12(2)**, 511–524 (2009).
7. X. Jiang, X. Zhou, X. Shi and X. Song, *Chaos. Soliton. Fract.* **38(2)**, 447-460 (2008).
8. A. Elaiw, I. Hassanien and S. Azoz, *J. Korean Math. Soc.* **49(4)**, 779–794 (2012).
9. P. W. Nelson, J. D. Murray and A. S. Perelson, *Math. Biosci.* **163(2)**, 201-215 (2000).
10. H. Zhu, Y. Luo and M. Chen, *Comp. Math. Appl.* **62(8)**, 3091–3102 (2011).
11. K. Hattaf and N. Yousfi, *ISRN Biomathematics*, 2012 (2012).
12. K. Hattaf and N. Yousfi, *World J. Model. Simul.* **8**, 27–36, (2012).
13. D. Bichara, A. Caicedo-Casso, D. Toro-Zapata and S. Lee, *tech. rep., Arizona State University, http://mtbi. asu. edu/research/archive/paper/analysis-and-optimal-control-hiv-model-immuneresponse* (2011).
14. H. R. Joshi, *Optim. Control Appl. Meth.* **23(4)**, 199–213, (2002).

15. D. Kirschner, S. Lenhart and S. Serbin, *J. Math. Biol.*, **35(7)**, 775–792 (1997).
16. L. Gollmann, D. Kern and H. Maurer, *Optim. Control Appl. Meth.* **30(4)**, 341–365, (2009).
17. Y. Kuang, *Academic Press, San Diego* (1993).

BIFURCATIONS AND OSCILLATORY DYNAMICS IN A TUMOR IMMUNE INTERACTION MODEL

SUBHAS KHAJANCHI[1,2]

[1] *Department of Mathematics, Bankura University*
Bankura - 722146, India

[2] *Department of Mathematics, Indian Institute of Technology Roorkee*
Roorkee - 247667, Uttarakhand, India
E-mail: subhaskhajanchi@gmail.com

In this paper, we investigate a mathematical model depicting the dynamics between immune effector cells, healthy tissue cells or host cells and the tumor cells by using a system of nonlinear ordinary differential equations (ODEs). We characterize the dynamics of the ODE system by locating biologically meaningful equilibrium points and determine local stability analysis. We perform the Hopf-bifurcation analysis when the proliferation rate α of healthy tissue cells crosses the threshold value α_{cr}. Numerical simulations are carried out to illustrate the dynamical behavior of the model system for different values of α including the regular and irregular periodic oscillations, which indicates the long-term dynamics of tumor relapse.

1. Introduction

Cancer is a world-wide problem and the second most common cause of death in US alone. According to American Cancer report 2013, about 1, 660, 290 new cases diagnosed and 580, 350 Americans are projected to die in cancer and almost 1, 600 people per day[1]. Despite medical advances such as chemotherapy, radiation therapy, immunotherapy plays a pivotal role in the treatment of cancer but it still an enigma about its proliferation, destruction and the mechanisms of establishment. Clinician and oncologists believe that the dynamics of proliferation of tumor population is unpredictable. Mathematical modeling is a great tool to better understand the dynamics of such complex phenomena. Mathematical modeling of tumor growth provides a realistic and quantitative representations of biological phenomena and biological interpretation under different scenarios of the patients' condition.

The idea of mathematical modeling to the growth of tumor cells proposed by Thomlinson *et al.*[15]. After that, a large body of work has been developed to study the tumor-immune interaction system through mathematical modeling by numerous authors[3,4,8,10,11,13,14,16,17,18,19,20,21,24]. The dynamics of tumor growth and anti-tumor immune response *in vivo* are very complex and it is too difficult to understand the dynamics due to most of the states and measurements are impossible *in vivo*. Mathematical models not only provide the real phenomena observed *in vivo* but also explain good insight about the scenarios that are unexplored *in vivo*[4,14,16]. Kuznetsov *et al.*[13], developed a mathematical model of tumor and immune immune cells and their model able to explain the existence of 'tumor dormancy' which is a state of tumor evolution and where the tumor cells seem to be not growing or grow a very slowly especially in the early stages of the disease. They also illustrated that the cell population can converge to a 'dormant state' by decaying oscillations in the realistic rage of parameter values. Kirschner and Panetta[8], proposed and analyzed a mathematical model of tumor-immune system interactions by considering the role of interleukin-2 (IL-2). In their model the antigenicity of tumor cells play a vital role in the dynamics of tumor-immune interaction. The immune systems are unable to kill the tumor cells when the tumors are low antigenic, but for highly antigenic tumors the immune systems are able to reduce the tumor cells to a small dormant state. de Pillis and Radunskaya[3], studied a competitive mathematical model for tumor growth and their environments and drug therapy and obtained a new therapeutic protocol which shows that at the end of the treatment the tumor size being smaller. d'Onofrio[21], proposed and studied a mathematical model of tumor dynamics which exhibits the oscillatory dynamics of tumor-immune system interactions. Moreover, d'Onofrio established the conditions for the existence and uniqueness of stable limit cycle. U Fory's[24] studied a mathematical model of carcinogenesis based on Lotka-Volterra competitive system and define the conditions under which the tumor cells driven up to extinction. Letellier *et al.*[4], studied a mathematical model developed by de Pillis *et al.*[3], by considering the three populations, namely, tumor cells, immune effector cells and the host cells. In their model, they showed that a non-conventional analysis suggested a new trend to better understand the dynamics of tumor-immune system by computing observability coefficients and topological analysis. They also showed in their model that the killing of tumor cells by effector cells does not influence the system dynamics. Khajanchi and Banerjee[14], studied a modified mathematical model of Kuznetsov *et al.*[13], by considering the

role of discrete time delay. The novelty of their investigation is the single parameter bifurcation as well as the two parameter bifurcation region to better understand the treatment strategy. Their modified model demonstrate the regular and irregular periodic oscillations in the tumor-immune system which indicates the long-term phenomena of tumor relapse.

In this paper, we shall study the effects of tumor-immune interactive dynamics of the model originally developed by de Pillis and Radunskaya[3] and later the model studied by Letellier *et al.*[4]. Our model is different from the model de Pillis *et al.*[3], that we do not consider the constant influx of immune effector cells. The immune effector cells are Cytotoxic T-lymphocytes produces 'naive' cells which are unable to produce any response to tumor population unless they are activated via MHC-I and MHC-II (Major Histocompatibility Complex) pathways in the presence of tumor specific antigens. This was justified by Banerjee *et al.*[2], Itik and Bnaks[22], also Kronik *et al.*[23], Krischner and Panetta[8], neglect the constant influx of immune effector cells. We establish that our modified model exhibits the Hopf-bifurcation both analytically and numerically by using MATLAB and the software MATCONT. Also, we plotted the two parameter bifurcation diagram to better understand the dynamics of tumor-immune system interaction.

The subsequent part of this paper is organized as follows. In Section 2, we briefly discuss the tumor-immune interaction model and its non-dimensionalisation. In Section 3, we study the qualitative analysis of the model which includes the positivity and boundedness of the system, local stability analysis and the analysis of Hopf-bifurcation for the parameter α, the growth rate of healthy tissue cells. In Section 4, we perform the numerical simulations of our analytical findings with the selected range of parameter set. Finally, the conclusion and discussions are given in Section 5.

2. The Model

We consider a very simple mathematical model for the growth of tumor cells which is akin to a predator-prey system comprises of a system of three coupled of nonlinear ordinary differential equations, namely, the immune effector cells (E), healthy tissue cells (H) and the tumor cells (T). The single tumor - site compartment model originally developed by de Pillis and Radunskaya[3]. Our model system describing the proliferation, death and the interaction of this population is:

$$\begin{aligned}
\frac{dE}{dt} &= \frac{\rho ET}{g+T} - \beta_1 TE - \delta E \\
\frac{dH}{dt} &= \alpha H\left(1 - \frac{H}{k_1}\right) - \gamma_1 TH \\
\frac{dT}{dt} &= aT\left(1 - \frac{T}{k_2}\right) - \beta_2 TE - \gamma_2 TH
\end{aligned} \tag{1}$$

with initial conditions:

$$E(0) = E_0 > 0,\ H(0) = H_0 > 0,\ T(0) = T_0 > 0,$$

where $E(t)$, $H(t)$ and $T(t)$ represents the number of immune effector cells, healthy tissue cells or host cells and the number of tumor cells respectively. The first equation of the system (1), describe the rate of change for the immune effector cells. The first term represents the proliferation of immune effector cells is enhanced by tumor cells represented by the term $\frac{\rho TE}{g+T}$. This term is of Michaelis-Menten form to indicate the saturated effect of the immune effector cells, where ρ is the rate of proliferation and g is the half saturation constant. The second term represents the inhibition of immune effector cells by tumor cells at a rate β_1 and the immune effector cells naturally die at a rate δ. The second equation gives the rate of change of healthy tissue cells with time t. The first term represents the growth of healthy tissue cells which follow the logistic growth function where the intrinsic growth rate α and the maximum carrying capacity k_1. The second term represents the clearance of healthy tissue cells at the rate γ_1. The third equation corresponds to the rate of change of tumor cells at any time t. The first term represents the growth of tumor cells which follow the logistic fashion in absence of any immune intervention where a is the intrinsic growth rate and k_2 is the biotic capacity. We assume that the tumor cells proliferate more quickly than that of healthy tissue cells, that is, $\alpha < a$. The second term represents the degradation of tumor cells due to interaction with immune effector cells as presented by $\beta_2 TE$. The third term represents the clearance of tumor cells by healthy tissue cells at a rate γ_2. Further, we assume that the inactivation rate of healthy tissue cells by tumor cells is greater than that of tumor cells by heathy tissue cells, that is, $\gamma_1 > \gamma_2$.

We non-dimensionalize the model (1) by considering the following rescaling

$$x = \tfrac{E}{g}, \qquad y = \tfrac{H}{k_1}, \qquad z = \tfrac{T}{k_2}, \qquad \widetilde{t} = at,$$

we find the new set of parameters as

$$\widetilde{\rho} = \tfrac{\rho}{a}, \qquad \widetilde{g} = \tfrac{g}{k_2}, \qquad \widetilde{\beta_1} = \tfrac{\beta_1 k_2}{a}, \qquad \widetilde{\delta} = \tfrac{\delta}{a},$$
$$\widetilde{\alpha} = \tfrac{\alpha}{a}, \qquad \widetilde{\gamma_1} = \tfrac{\gamma_1 k_2}{a}, \qquad \widetilde{\beta_2} = \tfrac{\beta_2 g}{a}, \qquad \widetilde{\gamma_2} = \tfrac{\gamma_2 k_1}{a}.$$

After dropping the tilde notation (for notational clarity) the system of equation (1) takes the form $(E, H, T) \mapsto (x, y, z)$, that is, x represents the immune effector cells, y population for the healthy tissue cells and z population for tumor cells,

$$\begin{aligned} \frac{dx}{dt} &= \frac{\rho x z}{g+z} - \beta_1 x z - \delta x \\ \frac{dy}{dt} &= \alpha y(1-y) - \gamma_1 y z \\ \frac{dz}{dt} &= z(1-z) - \beta_2 x z - \gamma_2 y z \end{aligned} \tag{2}$$

with initial conditions:

$$x(0) = x_0 > 0, \quad y(0) = y_0 > 0, \quad z(0) = z_0 > 0. \tag{3}$$

3. Analysis of the Model

3.1. *Positive invariance*

The model system (2) can be written in the matrix form as

$$\dot{X}(t) = \mathcal{G}(X) \tag{4}$$

with $X = (x, y, z)^T \in \mathbb{R}^3_+$ and

$$\mathcal{G}(X) = \begin{pmatrix} \mathcal{G}_1(X) \\ \mathcal{G}_2(X) \\ \mathcal{G}_3(X) \end{pmatrix} = \begin{pmatrix} \frac{\rho x(t) z(t)}{g+z(t)} - \beta_1 x(t) z(t) - \delta x(t) \\ \alpha y(t)(1-y(t)) - \gamma_1 y(t) z(t) \\ z(t)(1-z(t)) - \beta_2 x(t) z(t) - \gamma_2 y(t) z(t) \end{pmatrix}.$$

It is easy to verify that $\mathcal{G}_i(X) \mid_{X_i(t)=0} \geq 0$ for $i = 1, 2, 3$. Due to the classical theorem by Nagumo (1942)[7], every solution of (4) with initial conditions (3) and the initial point $X_0 \in \mathbb{R}^3_+$, say, $X(t) = X(t; X_0)$, in such a way that $X(t) \in \mathbb{R}^3_+$ for all $t > 0$, that is, for all finite time if they start from an interior point of

$$\mathbb{R}^3_+ \;=\; \{(x, y, z) : x \geq 0, y \geq 0, z \geq 0\}.$$

Let us consider the first equation of (2) and by using the positivity of solutions yield the right hand side is bounded above by,

$$\frac{dx}{dt} \leq \frac{\rho xz}{g+z} - \delta x.$$

Hence, by using the differential inequalities it follows that

$$\frac{dx}{dt} \leq (\rho - \delta)x, \quad \Rightarrow \limsup_{t\to\infty} x(t) \leq 0 \quad if \quad \rho < \delta.$$

Using the positivity of state variables and from the second of (2) equation, we have

$$\frac{dy}{dt} \leq \alpha y(1-y) \Rightarrow \limsup_{t\to\infty} y(t) \leq 1.$$

In similar way, from the third equation, we have

$$\frac{dz}{dt} \leq z(1-z) \Rightarrow \limsup_{t\to\infty} z(t) \leq 1.$$

This prove the system of equations (2) are dissipative. We can summarize the results in the following proposition.

Proposition 3.1. *The solution of the model system (2) with non-negative initial conditions* (x_0, y_0, z_0) *are bounded in the region defined by*

$$\Theta = \{(x, y, z) : x \geq 0,\ 0 \leq y \leq 1,\ 0 \leq z \leq 1\}.$$

3.2. *Equilibria*

The model system (2) has six biologically feasible equilibria namely,
(i) the trivial equilibrium point $E_0(0, 0, 0)$,
(ii) the tumor-free equilibrium point $E_1(0, 1, 0)$,
(iii) the cancerous equilibrium point $E_2(0, 0, 1)$,
(iv) the boundary equilibrium point $E_3(\tilde{x}, 0, \tilde{z})$ where $\tilde{x} = \frac{1-\tilde{x}}{\beta_2}$ and $\tilde{z}$ is the positive root(s) of the quadratic equation $\beta_1\tilde{z}^2 + \tilde{z}(\delta + g\beta_1 - \rho) + g\delta = 0$ where, $\tilde{z} = \frac{(\rho-\delta-g\beta_1)+\sqrt{(\rho-\delta-g\beta_1)^2-4g\delta\beta_1}}{2\beta_1}$ which is positive for $\rho > \delta + g\beta_1$ and $\tilde{x} < 1$. In case, $\tilde{x} = 1$, the boundary equilibria E_3 reduce to cancerous equilibria E_2 that means the cancer will always persists.
(v) the effector cell free equilibrium point $E_4(0, \bar{y}, \bar{z})$ where $\bar{y} = \frac{\gamma_1-\alpha}{\gamma_1\gamma_2-\alpha}$ and $\bar{z} = \frac{\alpha(\gamma_2-1)}{\gamma_1\gamma_2-\alpha}$ provided $\gamma_1\gamma_2 \neq \alpha$.

In order to obtain the biologically feasible equilibria, the conditions $\gamma_2 > 1$, $\gamma_1 > \alpha$ and $\gamma_1\gamma_2 > \alpha$ must be satisfied. In the case of $\gamma_2 = 1$, the equilibrium point E_4 coincide with the cancer free equilibrium point

$E_1(0, y, 0)$.
(vi) the interior or coexistence equilibrium point $E^*(x^*, y^*, z^*)$ where $z^* = \frac{(\rho-\delta-g\beta_1)+\sqrt{(\rho-\delta-g\beta_1)^2-4g\delta\beta_1}}{2\beta_1}$, $y^* = \frac{\alpha-\gamma_1 z^*}{\alpha}$ and $x^* = \frac{\alpha(1-\gamma_2)+z^*(\gamma_1\gamma_2-\alpha)}{\alpha\beta_2}$.

For the existence of x^*, y^* and z^*, it is necessary that, $\rho > \delta + g\beta_1$, $\gamma_2 < 1$, $\gamma_1\gamma_2 > \alpha$ and $z^* < \frac{\alpha}{\gamma_1}$. From the existence condition of interior equilibrium E^*, it is clear that the effector free equilibrium $E_4(0, \bar{y}, \bar{z})$ will never exists as for the inactivation rate γ_2 of cancerous cells violate the existence of effector free equilibrium $E_4(0, \bar{y}, \bar{z})$.

3.3. *Local stability analysis*

To study the local stability of the system (2) around each of the equilibrium point, first we have to compute the variational matrix corresponding to each of the equilibrium point. The variational matrix of the model system (2) at any arbitrary point (x, y, z) is given by

$$J_E = \begin{pmatrix} \frac{\rho z}{g+z} - \delta - \beta_1 z & 0 & \frac{g\rho x}{(g+z)^2} - \beta_1 x \\ 0 & \alpha(1-2y) - \gamma_1 z & -\gamma_1 y \\ -\beta_2 z & -\gamma_2 z & 1 - 2z - \gamma_2 y - \beta_2 x \end{pmatrix}.$$

At the trivial equilibrium point $E_0(0, 0, 0)$, the eigenvalues of J_{E_0} are $\lambda_1^0 = -\delta(< 0)$, $\lambda_2^0 = \alpha(> 0)$ and $\lambda_3^0 = 1(> 0)$. Therefore, the trivial equilibrium point E_0 is unstable, it is saddle point with $y - z$ plane as its unstable manifold and in $x-$axis as its stable manifold. So, there is no path initiating in the positive octant can approach E_0.

At the cancerous free equilibrium point $E_1(0, 1, 0)$, the eigenvalues of J_{E_1} are $\lambda_1^1 = -\delta(< 0)$, $\lambda_2^1 = -\alpha(< 0)$ and $\lambda_3^1 = 1 - \gamma_2$. Therefore, the cancerous free equilibrium point E_1 will be locally asymptotically stable if $\lambda_3^1 < 0$, i.e. if $\gamma_2 > 1$. Otherwise, the system will be saddle type. If the cancerous free equilibrium point E_1 is stable then the existence of interior equilibrium E^* is violates.

At the cancerous equilibrium point $E_2(0, 0, 1)$, the eigenvalues of J_{E_2} are $\lambda_1^2 = \frac{\rho}{g+1} - \beta_1 - \delta$, $\lambda_2^2 = \alpha - \gamma_1$ and $\lambda_3^2 = -1$. Therefore, the cancerous equilibrium point E_2 will be locally asymptotically stable if $\rho < (\beta_1\delta)(g+1)$ and $\gamma_1 > \alpha$. Otherwise, the system will be unstable.

At $E_3(\tilde{x}, 0, \tilde{z})$, the eigenvalues of J_{E_3} are $\lambda_1^3 = \alpha - \gamma_1\tilde{z}$ and the other two eigenvalues $\lambda_{2,3}^3$ are the roots of the following characteristics equation $\lambda^2 + D_1\lambda + D_2 = 0$, where $D_1 = \delta + \beta_1\tilde{z} + \beta_2\tilde{x} + 2\tilde{z} - 1 - \frac{\rho\tilde{z}}{g+\tilde{z}}$ and $D_2 = \left(\frac{\rho\tilde{z}}{g+\tilde{z}} - \beta_1\tilde{z} - \delta\right)(1 - \beta_2\tilde{x} - 2\tilde{z}) + \beta_2\tilde{z}\left(\frac{g\rho\tilde{x}}{(g+\tilde{z})^2} - \beta_1\tilde{x}\right)$. The boundary equilibrium point E_3, will be locally asymptotically stable if $D_1 > 0, D_2 > 0$ and $\tilde{z} > \frac{\alpha}{\gamma_1}$, otherwise unstable.

At $E_4(0, \bar{y}, \bar{z})$, the eigenvalues of J_{E_4} are $\lambda_1^4 = \frac{\rho\bar{z}}{g+\bar{z}} - \beta_1\bar{z} - \delta$ and the other two eigenvalues $\lambda_{2,3}^4$ are the roots of the following characteristics equation $\lambda^2 + C_1\lambda + C_2 = 0$, where $C_1 = 2\bar{z} + \gamma_2\bar{y} - \alpha\bar{y} - 1$ and $C_2 = \alpha\bar{y}(2\bar{z} + \gamma_2\bar{y} - 1) - \gamma_1\gamma_2\bar{y}\bar{z}$. The effector cells free equilibrium point E_4 will be locally asymptotically stable if $C_1 > 0, C_2 > 0$ and $\lambda_1^4 < 0$. Now $\lambda_1^4 < 0$ implies that,
$\rho\alpha(\gamma_2 - 1)(\gamma_1\gamma_2 - \alpha) < \alpha(\beta_1 g + \delta)(\gamma_2 - 1)(\gamma_1\gamma_2 - \alpha) + \alpha^2\beta_1(\gamma_2 - 1)^1 + \delta g(\gamma_1\gamma_2 - \alpha)^2$ and $\lambda_{2,3}^4 < 0$ implies $\frac{\alpha+\gamma_2}{1+\gamma_1} > 1$ and $\gamma_2(\alpha + \gamma_1) > (\alpha + \gamma_1\gamma_2^2)$.

The characteristic equation of the model system (2) at $E^*(x^*, y^*, z^*)$ is given by

$$\lambda^3 + A_1\lambda^2 + A_2\lambda + A_3 = 0 \tag{5}$$

where,

$$A_1 = \delta + (\beta_1 + 1)z^* + \alpha y^* - \frac{\rho z^*}{g + z^*},$$

$$A_2 = (\alpha y^* + z^*)\left(\delta + \beta_1 z^* - \frac{\rho z^*}{g + z^*}\right) + \alpha y^* z^* - \gamma_1\gamma_2 y^* z^* + \beta_2 z^*\left(\frac{g\rho x^*}{(g + z^*)^2} - \beta_1 x^*\right),$$

$$A_3 = y^* z^*(\gamma_1\gamma_2 - \alpha)\left(\frac{\rho z^*}{g + z^*} - \beta_1 z^* - \delta\right) + \alpha\beta_2 y^* z^*\left(\frac{g\rho x^*}{(g + z^*)^2} - \beta_1 x^*\right).$$

According to classical Routh-Hurwitz criteria a set of necessary and sufficient conditions for the roots of the characteristic equation (5) to have

negative real parts if $A_1 > 0$, $A_3 > 0$ and $A_1A_2 - A_3 > 0$. Now,

$$A_1A_2 - A_3 = \left(\frac{\rho z^*}{g+z^*} - \beta_1 z^* - \delta\right)\left[(\alpha y^* + z^*)\left\{\delta + (\beta_1+1)z^* + \alpha y^* - \frac{\rho z^*}{g+z^*}\right\} + y^*z^*(\gamma_1\gamma_2 - \alpha)\right] + y^*z^*(\gamma_1\gamma_2 - \alpha)\left[\delta + \beta_1 z^* + z^* + \alpha y^* - \frac{\rho z^*}{g+z^*}\right] + \beta_2 z^*\left(\frac{g\rho x^*}{(g+z^*)^2} - \beta_1 x^*\right) \times \left[(\delta + (\beta_1+1)z^* + \alpha y^*) - \frac{\rho z^*}{g+z^*} - \alpha y^*\right].$$

Thus, we have the following theorem.

Theorem 3.1. *The necessary conditions for the model system (2) to be locally asymptotically stable around the interior steady state* $E^*(x^*, y^*, z^*)$ *is that, (i)* $\gamma_1\gamma_2 > \alpha$,
(ii) $\max\left\{\frac{(\delta+\beta_1 z^*)(g+z^*)}{z^*}, \frac{\beta_1(g+z^*)^2}{g}\right\} < \rho < (\delta + (\beta_1+1)z^* + \alpha y^*)\left(\frac{g+z^*}{z^*}\right)$.

3.4. *Analysis of Hopf-bifurcation*

In this section, the analysis of Hopf-bifurcation[5] will be investigated of the model system (2) around the interior steady state $E^*(x^*, y^*, z^*)$ with bifurcation parameter α (the growth rate of healthy tissue cells) varies over $\mathbb{R}$. The necessary and sufficient conditions for Hopf-bifurcation to happen if there exists a $\alpha = \alpha_{cr}$, such that,
(i) $A_1(\alpha_{cr}) > 0,\ A_2(\alpha_{cr}) > 0,\ A_3(\alpha_{cr}) > 0$,
(ii) $\psi(\alpha) \equiv A_1(\alpha_{cr})A_2(\alpha_{cr}) - A_3(\alpha_{cr}) = 0$,
(iii) $Re\left[\frac{d\lambda_j}{d\alpha}\right]_{\alpha=\alpha_{cr}} \neq 0 \quad \text{for} \quad j = 1, 2, 3.$

By the property of continuous function of all the root of $\psi(\alpha)$, there exists an open interval $(\alpha_{cr} - \epsilon, \alpha_{cr} + \epsilon)$ (say), for some positive ϵ. Thus for $\alpha \in (\alpha_{cr} - \epsilon, \alpha_{cr} + \epsilon)$, the characteristic polynomial (5) has no roots whose real parts are negative. Therefore, for $\alpha = \alpha_{cr}$, and using the second condition for Hopf-bifurcation the polynomial equation (5) becomes

$$\lambda^3 + A_1\lambda^2 + A_2\lambda + A_1A_2 = 0 \quad \Rightarrow (\lambda^2 + A_2)(\lambda + A_1) = 0 \tag{6}$$

From above equation it is obvious that, the equation (6) has two roots are purely imaginary, say $\lambda_1 = +i\sqrt{A_2}$, $\lambda_2 = -i\sqrt{A_2}$ and the another root is $\lambda_3 = -A_1$, at $\alpha = \alpha_{cr}$.

For, $\alpha \in (\alpha_{cr} - \epsilon, \alpha_{cr} + \epsilon)$, the roots are in general form:

$$\lambda_1(\alpha) = \xi_1(\alpha) + i\xi_2(\alpha),$$
$$\lambda_2(\alpha) = \xi_1(\alpha) - i\xi_2(\alpha),$$
$$\lambda_3(\alpha) = -A_1(\alpha).$$

Now, we need to verify the transversality condition,

$$Re\left[\frac{d\lambda_j}{d\alpha}\right]_{\alpha=\alpha_{cr}} \neq 0 \quad for \quad j = 1,\ 2. \tag{7}$$

Substitute $\lambda_1(\alpha) = \xi_1(\alpha) + i\xi_2(\alpha)$ into the equation (5) and computing the derivatives, then extracting the real and imaginary parts we have,

$$L(\alpha)\xi_1^{'}(\alpha) - M(\alpha)\xi_2^{'}(\alpha) + R(\alpha) = 0,$$
$$M(\alpha)\xi_1^{'}(\alpha) + L(\alpha)\xi_2^{'}(\alpha) + S(\alpha) = 0,$$

with

$$L(\alpha) = 3(\xi_1^2(\alpha) - \xi_2^2(\alpha)) + 2A_1(\alpha)\xi_1(\alpha) + A_2(\alpha),$$
$$M(\alpha) = 6\xi_1(\alpha)\xi_2(\alpha) + 2A_1(\alpha)\xi_2(\alpha),$$
$$R(\alpha) = A_1^{'}(\alpha)(\xi_1^2(\alpha) - \xi_2^2(\alpha)) + A_2^{'}(\alpha)\xi_1(\alpha) + A_3^{'}(\alpha),$$
$$S(\alpha) = 2\xi_1(\alpha)\xi_2(\alpha)A_1^{'}(\alpha) + A_2^{'}(\alpha)\xi_2(\alpha).$$

Since, $M(\alpha_{cr})S(\alpha_{cr}) + L(\alpha_{cr})R(\alpha_{cr}) \neq 0$ at $\alpha = \alpha_{cr}$, we have,

$$Re\left[\frac{d\lambda_j}{d\alpha}\right] |_{\alpha=\alpha_{cr}} = \frac{M(\alpha_{cr})S(\alpha_{cr}) + L(\alpha_{cr})R(\alpha_{cr})}{L^2 + M^2} |_{\alpha=\alpha_{cr}} \neq 0$$

and $\lambda_3(\alpha_{cr}) = -A_1(\alpha_{cr}) \neq 0$.

Thus the conditions for Hopf-bifurcation are verified. We have the following theorem.

Theorem 3.2. *If the interior equilibrium point $E^*(x^*, y^*, z^*)$ exists for the model system (2), then around the interior steady state E^* the model system (2) undergo Hopf-bifurcation when α crosses the threshold value α_{cr}.*

4. Numerical Results

In this section, we carry out extensive numerical simulations to investigate the feasibility of our analytical findings, regarding the existence of tumor free equilibrium point(s), interior steady state and the corresponding stability conditions as well as the Hopf-bifurcation analysis of the model system

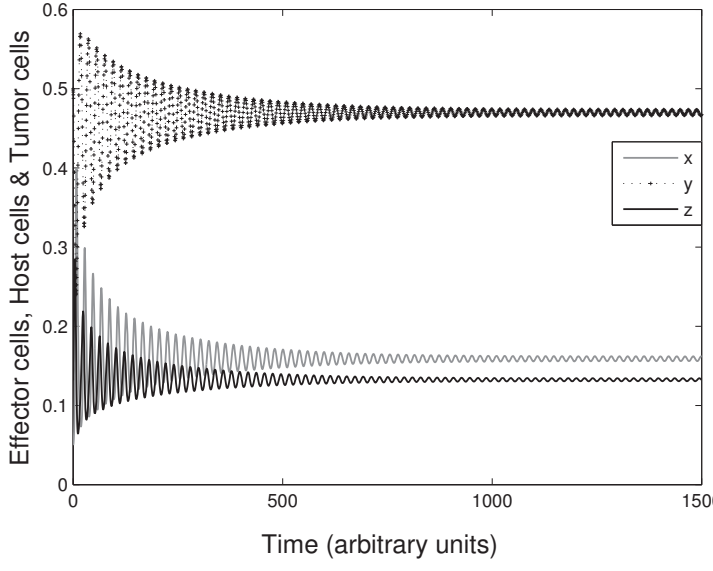

Figure 1. The figure shows the interior equilibrium point E^* is locally asymptotically stable for $\alpha = 0.375$ and other parameters are presented in Table 1.

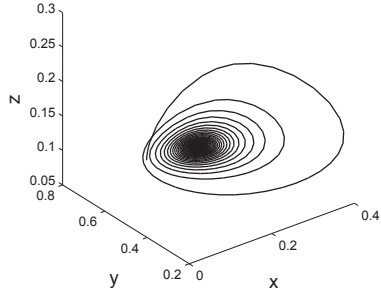

Figure 2. Stable limit cycle for $\alpha = 0.375$ and other parameters are presented in Table 1.

(2) around E^*. For the numerical computations, we use the set of parameter values are stated in Table 1 and the corresponding initial values $x(0)=$

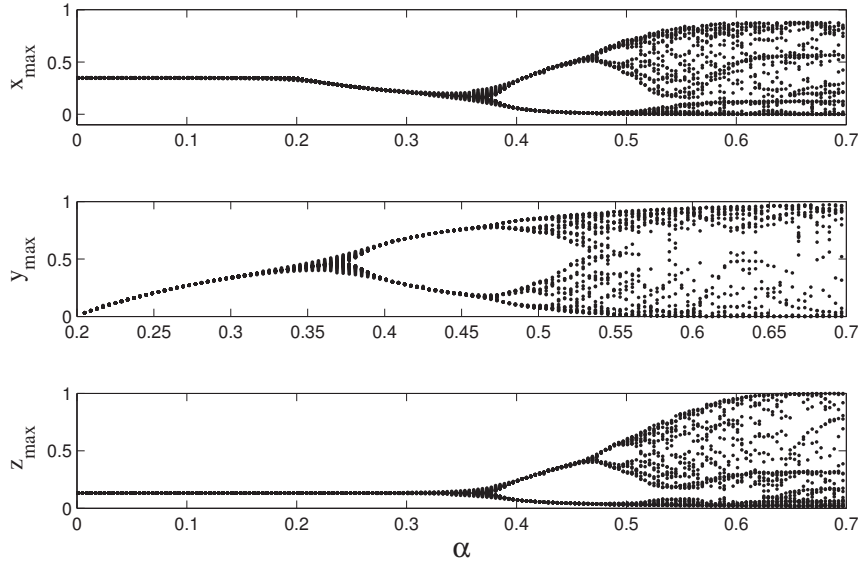

Figure 3. The figure shows the bifurcation diagram of the maximum number of effector cells (x), maximum number of healthy tissue cells (y) and the maximum number of tumor cells (z) by varying the parameter α and other parameters are presented in Table 1.

0.05, $y(0)$= 0.5 and $z(0)$= 0.132. We checked all the conditions for the existence of interior steady state E^* holds and the interior equilibrium point is $E^*(0.0795018, 0.668742, 0.132503)$ and the corresponding eigenvalues are -0.614352, $0.0403062 + 0.235126i$ and $0.0403062 - 0.235126i$. This clearly shows that E^* is 2-dimensional unstable manifold and 1-dimensional stable manifold, the point is thus define a saddle-focus.

Now, we investigate how the dynamics of the model system (2), influenced by the growth rate α of the heathy tissue cells. The qualitative behavior of the model system (2) has been changed at the threshold value $\alpha_{cr} = 0.382468$, which indicated as the bifurcation point. Now, the interior equilibrium point E^* is locally asymptotically stable for the lower value of α_{cr}, this scenario is presented in Figure 1, Figure 2, in terms of time series solutions (Figure 1) and the phase portrait diagram (Figure 2) when $0.375 < \alpha_{cr} = 0.382468$. At, $\alpha_{cr} = 0.382468$, the system experiences Hopf-bifurcation, which is presented in Figure 3. From the bifurcation diagram, it is clear that, in the range $0 < \alpha < 0.4740509$ the growth of tumor cells are well controlled by our immune system, in that range the tumor popu-

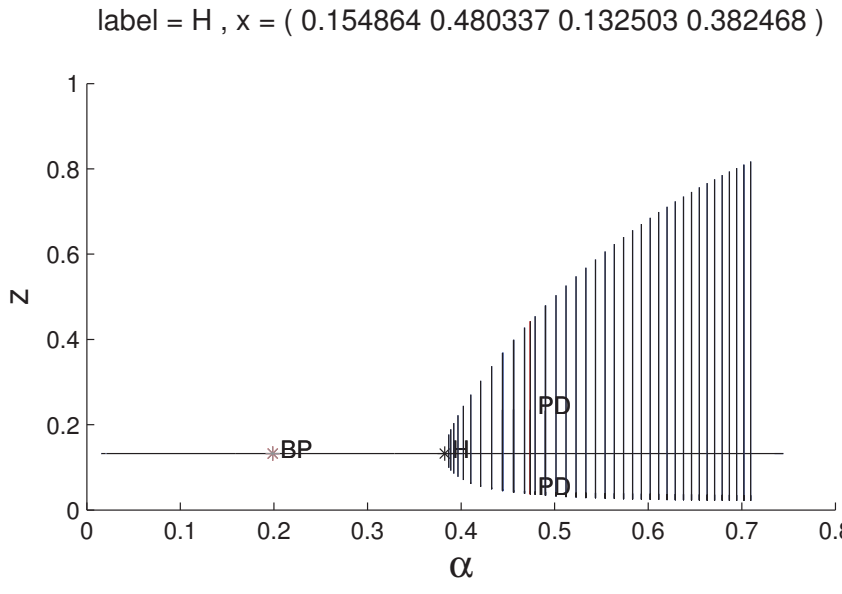

Figure 4. The figure shows the bifurcation diagram of the maximum number of tumor cells (z) by varying the parameter α and other parameters are presented in Table 1.

lation is non-invasive. For the range, $0 < \alpha < 0.382468$, the model system (2) spirals into a stable fixed point, that is, the model system reaching a stable fixed point which means that the growth of tumor cells are in avascular phase or in dormant state. For the range $0.382468 < \alpha < 0.4740509$, the interaction between tumor and immune system leads to the periodic behavior of the model system (2). Further increase the value of α, for the range $0.4740509 < \alpha < 0.7$ the period-doubling bifurcation leads to a high periodic or chaotic behavior, thus meaning that the growth rate of healthy tissue cells are highly dependent on tumor dynamics, that is, the tumor cells are invasive and the 'patient's conditions' are highly dependent on the growth rate of healthy tissue cells.

We also verified by using the software package MATCONT (MATLAB package for numerical bifurcation analysis)[25], the model system under consideration undergo Hopf-bifurcation at $\alpha_{cr} = 0.382468$, that is, $H = (0.154864,\ 0.480337,\ 0.132503,\ 0.382468)$ corresponding to the initial values $x(0) = 0.154864$, $y(0) = 0.480337$ and $z(0) = 0.132103$. Further, we studied the Hopf-bifurcation point and we obtained the period- bifurcation (PD) at $\alpha = 0.4740509$ and Limit point bifurcation cycle (LPC) at the

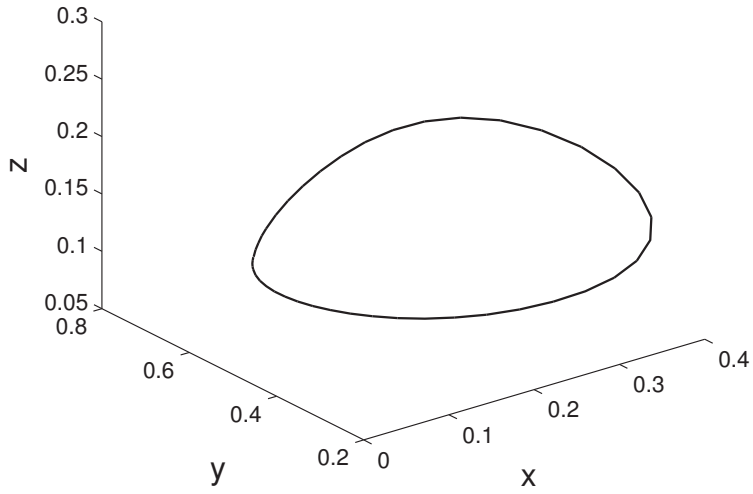

Figure 5. The figure shows the stable limit cycle occur at the Hopf-bifurcation point α = 0.382468 and other parameters are stated in in Table 1.

bifurcation point. The bifurcation diagram generated by MATCONT has been shown in Figure 4. Also, we plotted the limit cycle at the bifurcation point $\alpha = 0.382468$ has been shown in Figure 5.

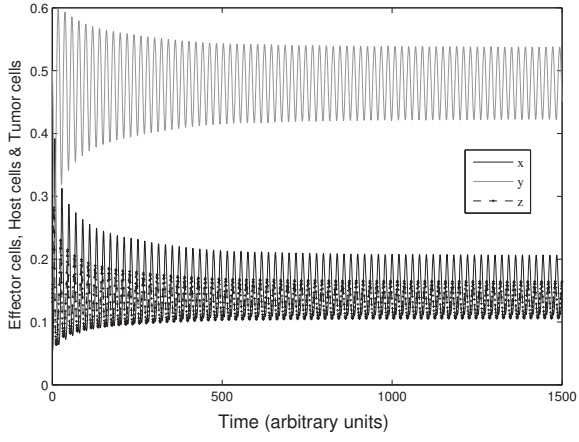

Figure 6. The figure shows the stable oscillations of all the populations around the interior equilibrium point E^* with $\alpha = 0.385$ and other parameters are presented in Table 1.

The significance of Hopf-bifurcation in this context is that at the bifurcating point a limit cycle is occurred around the rest point $E^*(0.0795018, 0.668742, 0.132503)$, thus a stable periodic oscillatory solution exists of the model system (2). The existence of periodic solutions has an impact in the tumor dynamics or tumor models as it implies that the level of tumor population may oscillate around the rest point E^* even in case of without treatment. In the therapeutic view point, such clinical observations is known as "Jeff's Phenomena"[26].

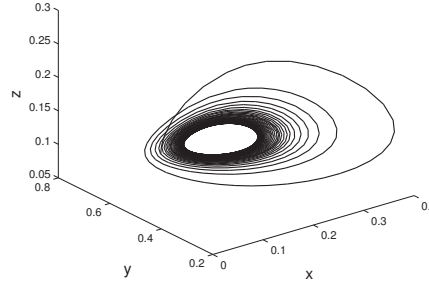

Figure 7. Stable limit cycles for $\alpha = 0.385$ and other parameters are presented in Table 1.

Figure 6 displays how the dynamics of tumor cells, host cells and tumor-specific immune effector cells are influenced by varying the growth rate α of host cells. When the growth rate α crosses the bifurcation value $\alpha_{cr} = 0.382468$, the system (2) shows the stable oscillation of all the three population around the interior equilibrium point E^* at $\alpha = 0.385$. From the figure (Fig. 6), it can be observed that the tumor cells (z) are very low immunogenic with respect to two other cells, which indicates that the tumor-specific immune effector cells (x) and host cells (y) are able to control the tumor cells (z). Figure 7 depicts that the model system (2) shows the stable limit cycle at $\alpha = 0.385$ around the interior steady state E^*.

In Fig. 8, we represent the time series evolution of the system (2) with respect to the growth rate (α) of host cells at $\alpha = 0.55$. We observe that the system changes stability to irregular periodic oscillations (and chaotic behavior). For the lower critical value of α, the system shows regular periodic oscillations. The cycle-to-cycle changeability of tumor cells (z) is reduced by increasing the growth rate (α) of host cells (y) in the sense that the cell count of host cells remain near its maximum value (near to 1) for a very short period of time but it is decreased very rapidly to zero (Fig. 8).

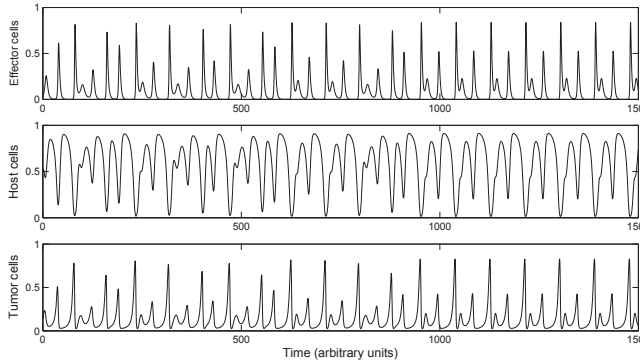

Figure 8. Time evolution of the effector cells, host cells and tumor cells for $\alpha = 0.55$ and other parameters are presented in Table 1.

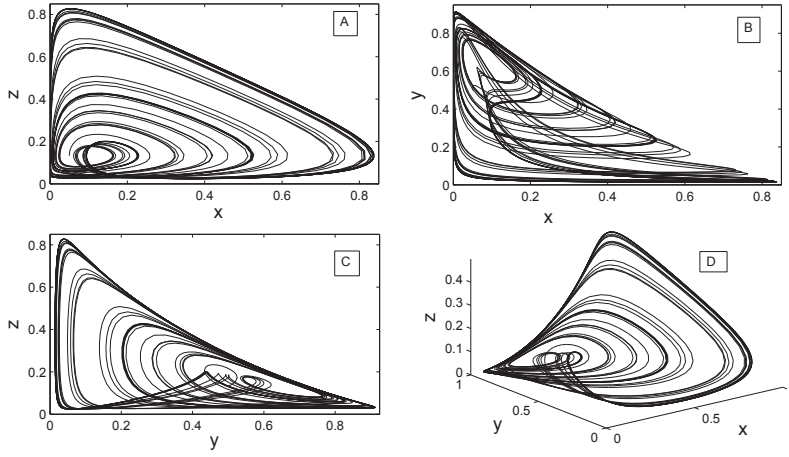

Figure 9. Phase portrait diagram A) Effector cells (x) vs. Tumor cells (z) B) Effector cells (x) vs. Host cells (y) C) Host cells (y) vs. Tumor cells (z) and D) Three dimensional phase portrait for $\alpha = 0.55$ and other parameters are presented in Table 1.

At the same time, the tumor cells remain near its minimum value (near to 0) and very quickly it is increased for a short period of time and then it is reduced. It can be observed that, for the lower value of α the oscillations are rare and irregular (tumor cells stay at their minimum value while the host cells stay at their maximum value). Figure 9, displays the phase-portrait diagram of the system (2) corresponding to the growth rate (α) of host cells at 0.55. From the phase-diagrams it is clear that the dynamics of

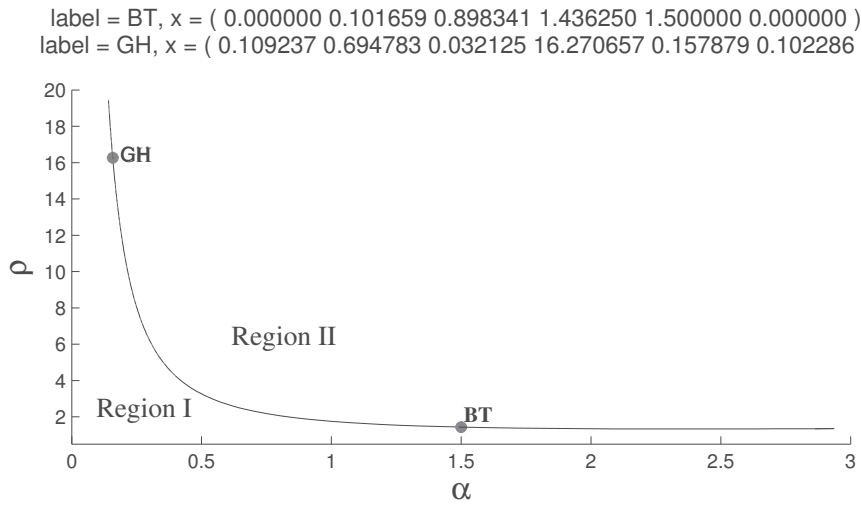

Figure 10. Two parameter bifurcation diagram (α, ρ) and the other parameters are described in Table 1.

tumor cells (z), host cells (y) and tumor-specific immune effector cells (x) are irregular.

With the given set of parameter values in Table 1, the stability region of (2) is given in Figure 10 in the $\alpha - \rho$ parameter space. It should be helpful in understanding the effect of the two parameters α and ρ on the stability of the interior steady state E^*. It is observed from the two parameter stability region (Fig. 10) that the Region I is stable and Region II is unstable.

Table 1. Interpretation of the parameters.

Name	Description	Values
ρ	proliferation enhancement effector cells	4.5
g	half saturation constant	1.0
β_1	inhibition rate of effector cells	0.2
δ	natural decay of effector cells	0.5
α	intrinsic growth rate of host cells	0.6
γ_1	host cells inactivation rate by tumor cells	1.5
β_2	tumor cells inactivation rate by effector cells	2.5
γ_2	rate of inactivation of tumor cells due to host cells	1.0

5. Discussion

We proposed a simple mathematical model envisioned by de Pillis and Radunskaya[3] is very interesting in the fact that it take into account interaction between two most commonly considered cells in cancer model namely, tumor and immune effector cells and another is rarely considered in cancer model known as host cells. To study the dynamics of tumor-immune system, a mathematical model comprising of three coupled nonlinear ordinary differential equations has been proposed and analyzed to understand the role of the growth rate α of healthy tissue cells or host cells. The positivity and boundedness of the model system (2) has been established. We studied the local stability analysis of the system with proper biological significance. We perform the analysis of Hopf-bifurcation with respect to the growth rate α of the host cells. In these dynamics a pivotal role is played by the growth rate α of host cells, above the threshold value of α_{cr}, the populations are highly angiogenic and below the threshold value of α_{cr}, all the populations are stable.

Numerical simulation of the model system (2) shows some rich dynamics, which mimic the dynamics of cancer patients, with very long oscillations and period-doubling oscillating solutions. We have verified our numerical simulations in MATLAB and a software package MATCONT (MATLAB package for numerical bifurcation analysis). The occurrence of regular and irregular periodic oscillations in the tumor-immune interaction model demonstrate the scenarios of long-term tumor relapse which has been investigated in some of existing literatures[4,6,13,14,22]. The regular periodic oscillations indicate the equilibrium process of cancer immuno-editing in the dual host-protective and tumor-promoting actions of immunity which has been observed in the experimental worked by Koebel *et al.*[9]. The occurrence of irregular periodic oscillations indicate that tumor may develop to a more invasive state. Although, our model does not take into account the complex biological scenarios, such as genomic instability, cell-structure, heterogeneity, but it focuses on generic interaction between different cell population. Also, the model was a single tumor-site compartmental model and therefore it was unable to reproduce relevant outcomes as the occurrence of metastasis. In order to overcome the limitations, a further investigation is needed. We leave these issues for our future endeavor.

Acknowledgments

I am thankful to my benevolent research advisor Dr. Sandip Banerjee, Department of Mathematics, IIT Roorkee for valuable suggestions, which helped in the better exposition of the manuscript.

References

1. A. C. Society, Atlanta: Cancer Facts & Figures (2013).
2. S. Banerjee, S. Khajanchi and S. Chaudhuri, *PLoS ONE* **10**, e0123611 (2015).
3. L. G. de Pillis and A. Radunskaya, *Math. Comput. Model.* **37**, 1221 (2003).
4. C. Letellier, F. Denis and L. A. Aguirre, *J. Theor. Biol.* **322**, 7 (2013).
5. S. Khajanchi, *Appl. Math. Comput.* **244**, 344 (2014).
6. S. Khajanchi, *Chaos Soliton. Fract.* **77**, 264 (2015).
7. N. Nagumo, *Proc. Phys. Math. Soc. Jpn.* **24**, 551 (1994).
8. D. Kirschner and J. C. Panetta, *J. Math. Biol.* **37**, 235 (1998).
9. C. M. Koebel *et al.*, *Nature* **450**, 903 (2007).
10. J. Arciero, T. Jackson and D. Kirschner, *Discrete Cont. Dyn-B* **4**, 39 (2004).
11. L. G. de Pillis, W. Gu and A. Radunskaya, *J. Theor. Biol.* **238**, 841 (2006).
12. R. R. Sarkar and S. Banerjee, *Math. Biosci.* **196**, 65 (2006).
13. V. A. Kuznetsov, I. A. Makalkin, M. A. Taylor and A. S. Perelson, *Bull. Math. Biol.* **56**, 295 (1994).
14. S. Khajanchi and S. Banerjee, *Appl. Math. Comput.* **248**, 652 (2014).
15. R. H. Thomlinson and L. J. Gray, *Br. J. Cancer* **9**, 539 (1955).
16. M. Moghtadaei *et al.*, *J. Theor. Biol.* **334**, 130 (2013).
17. R. P. Araujo and D. L. S. McElwaina, *Bull. Math. Biol.* **66**, 1039 (2004).
18. M. Bodnar and U. Fory's, *Appl. Math.* **27** 113 (2000).
19. F. Nani and H. I. Freedman, *Math. Biosci.* **163**, 159 (2000).
20. A. R. A. Anderson and M. A. J. Chaplain, *Bull. Math. Biol.* **60**, 857 (1998).
21. A. d'Onofrio, *Math. Comput. Model.* **47**, 614 (2008).
22. S. Khajanchi and D. Ghosh, *Appl. Math. Comput* **271**, 375 (2015).
23. N. Kronik *et al.*, *Cancer Immunol. Immunother.* **57** 425 (2008).
24. U. Fory's, *Math. Meth. Appl. Sci.* **33** 2287 (2009).
25. A. Dhooge *et al.*, *ACM Trans. Math. Software* **29**, 141 (2003).
26. R. Thomlinson, *Clin. Radiol.* **33**, 481 (1982).
27. M. Garcia-Barros, F. Paris, C. Cordon-Cardo, D. Lyden, S. Rafii, A. Haimovitz-Friedman, Z. Fuks and R. Kolesnick, *Science* **300**, 1155 (2003).
28. I. Malanchi, A. Santamaria-Martnez, E. Susanto, H. Peng, H.-A. Lehr, J.-F. Delaloye and J. Huelsken, *Nature* **481**, 85 (2012).

ON A NONLINEAR SYSTEM MODELING DARWINIAN DYNAMICS AND THE IMMUNE RESPONSE TO CANCER EVOLUTION*

ABDELGHANI BELLOUQUID AND MOHAMED CH-CHAOUI†

Cadi Ayyad University,
Ensa Marrakech,
Morocco
E-mail: mohamed.ch-chaoui@edu.uca.ma

ELENA DE ANGELIS

Department of Mathematical Sciences,
Politecnico, Torino, Italy
E-mail: elena.deangelis@polito.it

In this paper a mathematical model, at the cellular level, related to the onset and evolution of cancer cells contrasted by the immune system, is derived by tools of kinetic theory of active particles, for short KTAP's approach. The dynamics refers to an early stage of the competition, where cancer is viewed as sequence of phenotype mutations, which generate cells with the ability of suppressing the innate programmed death ability-apopthosis- on one side and on the other with the ability to escape recognition by immune cells. The subsequent dynamics of selection and competition for survivance determines the growth or depletion of tumor cells. The originated model introduced in Ref. 13, which has been further developed in Ref. 20 to include interactions with the outer environment, which can also be subject to mutation and selection[16,24]. More specifically, we develop an analytic study of the well-posdenes of the initial value problem, and we will investigate numerically how our model depict some interesting behaviors of the immune response, where some biological interpretations are discussed.

A recent paper[13] introduced a new approach, based on ideas from post-Darwinian theory of mutations, to model the onset and evolution of cancer cells contrasted by the immune system. This paper transferred into a dif-

*Mohamed CH-Chaoui and Elena De Angelis dedicate this work to the memory of Abdelghani Bellouquid, who prematurely passed away on August 31.
†Corresponding author.

ferential systems the conceptual biological framework delivered in Ref. 16. The basic idea is that cells are viewed as active particles, whose state evolves in time, while the dynamics includes the onset of new cell phenotypes generated by the same cell genotype. The subsequent dynamics of selection and competition for survivance determines the growth or depletion of tumor cells. The approach proposed in Ref. 13 has been further developed in Ref. 20 to include interaction with the outer environment, which can also be subject to mutation and selection.

The derivation of mathematical tools takes advantage of the so-called kinetic theory of active particles documented in many papers among others, see Refs. 1, 3, 9, 6, 7, 8, 10, 11, 14, 18, 19 and therein bibliography. Applications are not limited to developmental biology, but also include complex systems in which human behavior can play an important role in the dynamics, for instance crowd dynamics[15] and vehicular traffic[12]. Some recent papers have applied the general approach to networks[25], and social dynamics with applications that concern various aspects of behavioral sociology[2,5]. Interactions, in this specific approach, are modeled by means of theoretical game theory tools see, among others[4,23,26].

Paper[13] has shown that the model describes a number of consecutive selective mutations which can eventually generate cells with clonal proliferative competence[24,31]. This is a Darwinian type selection that is induced by the lower molecular scale of genes, that is the same cell genotype generates different cell phenotypes, which are apparently better fitted to the environment, but are characterized by a typical competence of degenerative diseases. Moreover, the qualitative analysis of the initial value problem related to the application of the model, which consists in a system of nonlinear integro-differential equations, shows that such a problem is well posed, while simulations reproduce the expected emerging behaviors, see also Ref. 27 for the qualitative analysis of a class of equations corresponding to Ref. 13. In general, progressive mutations of cancer cells are not contrasted (or the opposite "are contrasted") by the learning ability of the immune system. In some cases an equilibrium is reached, asymptotically in time, corresponding to the survivance of the two populations. This equilibrium can be either positively broken by therapeutical actions, or negatively by temporary states of immuno-depression.

This present paper develops the background ideas presented in Refs. 13 and 20 with the main aim investigate how mutation rates both for immune and cancer cells influence the outcome of the competition.

The interest in this type of investigation is motivated to the fact that

the onset of cancer and various degenerative diseases originate from mutations at the cellular level[22,28]. This onset generates challenging modeling, analytic, and computational problems, which motivate the contents of this paper. Additional hints on post-Darwinian viewpoints to model the system under consideration are given in Ref. 30, while the reader interested, from a biological standpoint, to the role of the immune system in detecting and depleting cancer cells is addressed to[16,17,21,29] and therein cited bibliography.

In detail, the content of this present paper is delivered by four more sections as follows: Section 2 presents the mathematical model of the immune competition which refers to the general structure proposed in Ref. 13, the model is simplified, with respect to that proposed in the same paper as it consider only one mutation for each population. This simplification allows to reduce the number parameters and allows a detailed parameters sensitivity analysis. Section 3 develops an analytic study of the well posedness of the initial value problem. Section 4 deals with a computational analysis of the initial value problem generated by the application of the system. Numerical simulations are related to the increase of mutation rate both for cancer and immune cells. Finally Section 5 provides a critical analysis of the work, and looks ahead to perspectives.

1. The Mathematical Model

1.1. *The mathematical structure*

Let us consider a large system of individuals called ***active particles*** with their individual state called ***activity***. This corresponds to genotype-phenotype expression, later, for brevity, also called ***expression***. The individuals corresponding to the same activities (expressions) are assembled into ***functional subsystems***, where the common tract is viewed as a functional expression that aims at survivance. The activity within the population is the micro-state, which is heterogeneously distributed, while the description of the overall state of the system is delivered by suitable distribution functions over the said micro-state. This variable is heterogeneously distributed and we assume that increasing values of the activity correspond to an increasing ability of the subsystem to express its biological function.

Pair interactions between active particles generate birth-death processes and, with relative small probability, modification of their expression, which amounts to generation of a new population. We consider the various stages of selective mutations of cancer cells based on their hallmarks, roughly

speaking the different levels of their ability to escape the immune defense[16].

The system is constituted by active particles and is decomposed into ***functional subsystems*** labeled by the subscripts $i = 1, 2, 3, 4$, each related to a different ***activity*** corresponding to different phenotype expressions. The state of each functional subsystem is represented, (in probability), by the distribution functions

$$f_i(t, u) : \mathbb{R}_0^+ \times [0, 1] \to \mathbb{R}_0^+, \tag{1}$$

where $R_0^+ = [0, +\infty)$, over the the ***activity variable*** $u \in [0, 1]$, collectively expressed by active particles of the subsystem. This distribution is linked to the so-called ***test particle***, which is representative of the subsystem, where the density $f_i(t, u)\, du$ denotes the number of cell per unit volume, whose state is, at time t, in the interval $[u,\ u + du]$.

The number of active particles in each subsystem at time t is obtained by integration of the distributions f_i over the activity variable u:

$$n_i(t) = \int_0^1 f_i(t, u)\, du, \quad \text{with} \quad n_i(0) := n_{i0} = \int_0^1 f_i(0, u)\, du. \tag{2}$$

Let us introduce the activation in each subsystem at time, defined as the mean of activity variable

$$A_i(t) = \int_0^1 u f_i(t, u)\, du, \text{with} \quad A_i(0) =: A_{i0} = \int_0^1 u f_i(0, u)\, du. \tag{3}$$

The following decomposition in subsystems is proposed:

1) $i = 1$: epithelial cells, whose selected function is the ability, supposed uniform for all cells, to feed proliferative phenomena. The cell cycle events can generate cells with the same phenotype, but also cells with different phenotype with the onset of cancer cells. It is supposed that the organism is a source of epithelial cells, so that their quantity can be regarded as constant in time;
2) $i = 2$: cells, generated by the first functional subsystem, that have acquired the ability of suppressing the immune reaction;
3) $i = 3$ cells of the innate immune system which have the ability to acquire, by a learning process, the capacity of contrasting the development of cancer cells;
4) $i = 4$ cells generated by the innate immune system, which have acquired the ability of contrasting the development of cancer cells.

Remark 1.1. The learning process of the immune system is modeled by considering one only functional subsystem and confining the learning process to a progression within it.

The evolution equation of each f_i reads, see Ref. 20:

$$\partial_t f_i(t,u) = C_i[\mathbf{f}](t,u) + P_i[\mathbf{f}](t,u) - \lambda_i[f_i](f_i - \widetilde{f}_i)(t,u), \tag{4}$$

for $i = 1,\dots,4$, where $\mathbf{f} = (f_1,\dots,f_4)$, so that the following formal mathematical structure for the right-hand-side terms of Eq. (4) is proposed:

I) C_i and P_i model the net flux of particles that, due to respectively conservative or proliferative/destructive interactions, fall into the elementary volume $[u, u+du]$ of each functional subsystem of active particles and they reads:

$$C_i[\mathbf{f}](t,u) = -f_i(t,u)\sum_{k=1}^{4}\int_0^1 \eta_{ik}[\mathbf{f}](u,u^*)\, f_k(t,u^*)\, du^* + \tag{5}$$

$$\sum_{k=1}^{4}\int_D \eta_{ik}\,[\mathbf{f}]\,(u_*,u^*)\,\mathcal{A}_{ik}[\mathbf{f}](u_* \to u|u_*,u^*)\, f_i(t,u_*)\, f_k(t,u^*)\, du_*\, du^*,$$

and

$$P_i[\mathbf{f}](t,u) = \sum_{h,k=1}^{4}\int_D \eta_{hk}[\mathbf{f}](u_*,u^*)\,\mathcal{P}^i_{hk}[\mathbf{f}](u_* \to u|u_*,u^*) \tag{6}$$
$$\times f_h(t,u_*)\, f_k(t,u^*)\, du_*\, du^*,$$

where $D = [0,1]\times[0,1]$ and the dynamics of interactions at the micro-scale (where, for short, particles belonging to the subsystem i are denoted by i-particles) is described by the following quantities:

- η_{hk} is the encounter rates of the interactions between h-particles with k-particles;
- $\mathcal{A}^i_{hk}$ models the probability density that a candidate h-particle, with state u_*, ends up into the state of a test i-particle with state u after an interaction with a field k-particle with state u^* and it is such that

$$\sum_{i=1}^{4}\int_0^1 \mathcal{A}^i_{hk}[\mathbf{f}](u_* \to u|u_*,u^*)\, du = 1, \tag{7}$$

for all for all $h,k \in \{1,\dots,4\}$, $u_*, u^* \in [0,1]$ and for all $\mathbf{f}$;

- test i-particles interact with field k-field particles and lose their state;
- $\mathcal{P}^i_{hk}$ models the birth-death rate for a candidate h-particle, with state u_*, into the state u of the i-th functional subsystem due to the interaction with a k-field particle with state u^*.

II) $\lambda_i[f_i]$ refers to the natural decay of each functional subsystem toward a level distribution $\widetilde{f_i}$ or to a death process of i-particles due to their natural extinction, where death occurs only within the same functional subsystem and state of the candidate particle.

1.2. *Derivation of the mathematical model for a closed system*

Let us now propose a model of the overall dynamics of the multicellular system based on the mathematical framework formally given by Eq. (4). With reference to the notation introduced in the previous Section, the non-zero interactions terms are summarized in the following Tables:

Table 1. Non-zero interactions between a h-candidate particle (represented by a square) with state u_* and a k-field particle (represented by a circle) with state u^*, $h, k \in \{1, \ldots, 4\}$, and $u_*, u^* \in [0, 1]$.

Interaction	**Encounters**	η_{ik}: the rate of interactions is assumed to be constant for all interactions but with different order of magnitude
$\boxed{1} \leftrightarrow ①$	between epithelial cells	$\eta_{11}[\mathbf{f}](u_*, u^*) = \eta_0$
$\boxed{2} \leftrightarrow ①$	epithelial cells-tumor cells	$\eta_{21}[\mathbf{f}](u_*, u^*) = \eta_0$
$\boxed{1} \leftrightarrow ②$	tumor cells-epithelial cells	$\eta_{12}[\mathbf{f}](u_*, u^*) = \eta_0$
$\boxed{3} \leftrightarrow ②$	innate immune system-tumor cells	$\eta_{32}[\mathbf{f}](u_*, u^*) = \sigma_0\,\eta_0$: $\sigma_0 << 1$
$\boxed{4} \leftrightarrow ②$	mutated immune system-tumor cells	$\eta_{42}[\mathbf{f}](u_*, u^*) = \sigma_0\,\eta_0$: $\sigma_0 << 1$
$\boxed{2} \leftrightarrow ④$	tumor cells-mutated immune system	$\eta_{24}[\mathbf{f}](u_*, u^*) = \sigma_0\,\eta_0$: $\sigma_0 << 1$

Table 2. Probability densities related to interactions between a h-candidate particle (represented by a square) with state u_* and a k-field particle (represented by a circle) with state u^*.

Interaction	$\mathcal{A}_{ik}^i = \mathcal{A}_{ik}$: probability density	**Description**
$\boxed{1} \leftrightarrow ①$	$\mathcal{A}_{11}(u_*, u^*) = \delta(u - u_* + \alpha_{11}(1 - u_*))$:	progression after interactions between epithelial cells
$\boxed{2} \leftrightarrow ①$	$\mathcal{A}_{21}(u_*, u^*) = \delta(u - u_* + \alpha_{21}(1 - u_*))$:	progression after interactions epithelial cells-tumor cells: $\alpha_{21} >> \alpha_{11}$
$\boxed{1} \leftrightarrow ②$	$\mathcal{A}_{12}(u_*, u^*) = 1$:	no change of their own state for epithelial cells in interactions tumor cells-epithelial cells
$\boxed{3} \leftrightarrow ②$	$\mathcal{A}_{32}(u_*, u^*) = \delta(u - u_* + \beta_{32}(1 - u_*))$:	progression after interactions innate immune system-tumor cells
$\boxed{4} \leftrightarrow ②$	$\mathcal{A}_{42}(u_*, u^*) = \delta(u - u_* + \beta_{42}(1 - u_*))$:	progression after interactions mutated immune system-tumor cells

Table 3. Mutation and proliferation net terms for interactions between a h-candidate particle (represented by a square) with state u_* and a k-field particle (represented by a circle) with state u^*.

Interaction	$\mathcal{P}_{hk}^i$: mutation and proliferation net terms	**Description**
$\boxed{1} \leftrightarrow ①$	$\mathcal{P}_{11}^2(u_*, u^*) = \gamma_{11}\, u_*\, \delta(u - u_*)$:	mutations from epithelial cells
$\boxed{2} \leftrightarrow ①$	$\mathcal{P}_{21}^2(u_*, u^*) = \gamma_{21}\, u_*\, \delta(u - u_*)$:	proliferation for tumor cells
$\boxed{3} \leftrightarrow ②$	$\mathcal{P}_{32}^4(u_*, u^*) = \gamma_{32}\, u_*\, \delta(u - u_*)$:	mutations from innate immune system
$\boxed{4} \leftrightarrow ②$	$\mathcal{P}_{42}^4(u_*, u^*) = \gamma_{42}\, \delta(u - u_*)$:	proliferation for immune cells
$\boxed{2} \leftrightarrow ④$	$\mathcal{P}_{24}^2(u_*, u^*) = -\gamma_{24}\, u^*\, \delta(u - u^*)$:	destructive term for tumor cells

Taking into account the terms defined in Tables 1–3, the corresponding evolution equations of the distribution functions $(f_1, ..., f_4)$, which arise from Eq. (4), read as follows:

$$\begin{aligned}\partial_t f_1(t,u) = \; & \eta_0 \, \frac{n_1(t)}{1 \, + \, \alpha_{11}} \, f_1 \left(t, \frac{u+\alpha_{11}}{1+\alpha_{11}} \right) \chi_{[-\alpha_{11},1]}(u) \; - \; \eta_0 \, n_1(t) \, f_1(t,u) \\ & + \eta_0 \, n_1(t) \, n_2(t) - \eta_0 \, f_1(t,u) \, n_2(t), \end{aligned} \tag{8}$$

$$\begin{aligned}\partial_t f_2(t,u) = \; & \eta_0 \, \frac{n_1(t)}{1 \, + \, \alpha_{21}} \, f_2 \left(t, \frac{u+\alpha_{21}}{1+\alpha_{21}} \right) \chi_{[-\alpha_{21},1]}(u) \; - \; \eta_0 \, n_1(t) \, f_2(t,u) \\ & + \eta_0 \, \gamma_{11} \, u \, f_1(t,u) \, n_1(t) + \eta_0 \, \gamma_{21} \, u \, f_2(t,u) \, n_1(t) \\ & - \sigma_0 \, \eta_0 \, \gamma_{24} \, u \, n_2(t) \, f_4(t,u), \end{aligned} \tag{9}$$

$$\begin{aligned}\partial_t f_3(t,u) = \; & \sigma_0 \, \eta_0 \, \frac{n_2(t)}{1 \, + \, \beta_{32}} \, f_3 \left(t, \frac{u+\beta_{32}}{1+\beta_{32}} \right) \chi_{[-\beta_{32},1]}(u) \\ & - \; \sigma_0 \, \eta_0 \, n_2(t) \, f_3(t,u) \\ & - \lambda_3 \big(f_3(t,u) - \widetilde{f_3}(t,u) \big), \end{aligned} \tag{10}$$

$$\begin{aligned}\partial_t f_4(t,u) = \; & \sigma_0 \; \eta_0 \frac{n_2(t)}{1 \, + \, \beta_{42}} \, f_4 \left(t, \frac{u+\beta_{42}}{1+\beta_{42}} \right) \chi_{[-\beta_{42},1]}(u) \\ & - \; \sigma_0 \, \eta_0 \, n_2(t) \, f_4(t,u) \\ & + \sigma_0 \, \eta_0 \, \gamma_{32} \, u \, f_3(t,u) \, n_2(t) + \sigma_0 \, \eta_0 \, \gamma_{42} \, f_4(t,u) \, n_2(t) \\ & - \lambda_4 \big(f_4(t,u) - \widetilde{f_4}(t,u) \big). \end{aligned} \tag{11}$$

Remark 1.2. The decay dynamics in (10) and (11) induces immune cells return to the sentinel level after suppression of the cells carrier of pathology, and we choose $\widetilde{f_3}(t,u) = f_{30}(u)$, and $\widetilde{f_4}(t,u) = f_{40}(u)$.

Remark 1.3. The biological meaning of the parameters introduced is here after summarized:

- σ_0 and η_0 refer to interaction rates;
- γ_{11}, and γ_{32} model the mutation rate for cancer and immune cells;
- α, β model the probability density in conservative progressions;
- γ_{21}, γ_{42} model the proliferation rate for cancer and immune cells;
- γ_{24} refers to suppression rate;

- $\lambda_3,\ \lambda_4$ refers to the relaxation of the innate immune system and the activated immune cells.

Remark 1.4. The above mathematical model derived, with the aim to investigate the role played by some pertinent parameters, especially those governing mutations both for cancer and immune cells. The dynamics refers to an early stage of competition which may end up either with the suppression of cancer cells or with their indefinite growth, which subsequently aggregate into condensed structures. Moreover, based on the idea that cancer is generated by Darwinian type mutations and selection[31], the immune system play an important role in this dynamics. In fact, immune cells gain new defense abilities by learning the presence of a pathological state, starting from the innate to acquired immunity[16,17]. The above model, simplified, with reference 13, as we consider only the last stage of selective mutations of cancer cells based on their hallmarks corresponding to their ability to escape the immune defense. As shown by simulations, the model shows a detailed sensitivity analysis, which has been focused on γ_{11} and γ_{32}.

2. Analytical Results

2.1. *Main results*

Let us consider the initial value problem for the model (8)–(11) corresponding to the mathematical structure (4) for a closed system, where the interaction terms C_i and P_i are defined in Eqs. (5)–(6). The statement of the initial value problem, endowed with suitable initial conditions, can be formally written as follows:

$$\begin{cases} \partial_t \mathbf{f}\,(t,u) = \mathcal{H}[\mathbf{f}](t,u), \quad (t,u) \in (0,\infty)\times[0,1], \\ f_{i0} = f_i(t=0,u), \quad i = 1,..,4, \end{cases} \tag{12}$$

where $\mathcal{H} = (\mathcal{H}_1, \mathcal{H}_2, \mathcal{H}_3, \mathcal{H}_4)$ is given by (8)–(11).

Let X^+ be the positive cone of the Banach space $X := \{L^1_u(0,1)\}^4$, endowed with the norm

$$\| \mathbf{f} \| = \sum_{i=1}^{4} \| f_i \|_1 .$$

Let Y be the Banach space $C([0,T],X_+)$ endowed with the norm

$$\| \mathbf{f} \|_Y = \sup_{t\in[0,T]} \| \mathbf{f}(t) \| .$$

First, problem (12) can be well-posed, as stated by the following:

Theorem 1. *For any initial data $f_0 \in X_+$, there exist two positive constants T and a_0 such that Problem (12) admits a unique, local in time, solution $\mathbf{f} \in C([0,T],X_+)$, which satisfies the following estimate:*

$$\| \mathbf{f}(t) \| \leq a_0 \| f_0 \|, \quad \forall t \in [0,T]. \tag{13}$$

The existence of solution $\mathbf{f}$ of Problem (12) can be extended over the whole real positive axis $\mathbb{R}^+$, by the following:

Theorem 2. *For any $T > 0$, there exists a unique solution $\mathbf{f}(t) \in C([0,T],X_+)$, of (12) with initial data $f_0 \in X_+$. Moreover the solution f satisfies*

$$\sup_{t\in[0,T]} \| \mathbf{f}(t) \| \leq C_T, \tag{14}$$

where C_T constant depending on T and on the initial data.

Proof of theorem 1 and 2.

First, some notations are useful to construct the proof of Theorem 1 and 2. In details, Problem (12) can be written as follow:

$$\mathbf{f} = \Lambda[\mathbf{f}] = \Big(\Lambda_1[\mathbf{f}], \Lambda_2[\mathbf{f}], \Lambda_3[\mathbf{f}], \Lambda_4[\mathbf{f}]\Big) \tag{15}$$

where $\Lambda[\mathbf{f}]$ is given by

$$\Lambda_i(\mathbf{f}) = f_{i0}(u) + \int_0^t \mathcal{H}_i^*[\mathbf{f}](s)ds, \quad i = 1,2, \tag{16}$$

$$\Lambda_i(\mathbf{f}) = f_{i0}(u) + \int_0^t \exp\Big(\lambda_i(s-t)\Big)\mathcal{H}_i^*[\mathbf{f}](s)ds, \quad i = 3,4, \tag{17}$$

where

$$\mathcal{H}^* = \Big(\mathcal{H}_1,\ \mathcal{H}_2,\ \mathcal{H}_3 + \lambda_3(f_3 - f_{30}),\ \mathcal{H}_4 + \lambda_4(f_4 - f_{40})\Big).$$

Briefly, the proof of the local existence and uniqueness is based on standard fixed point arguments. Let $\mathbf{f}$ and $\mathbf{g}$ in X, then $\mathcal{H}^*[\mathbf{f}] \in X$, and

$$\| \mathcal{H}^*[\mathbf{f}] \| \leq C \| \mathbf{f} \|^2, \tag{18}$$

$$\| \mathcal{H}^*[\mathbf{f}] - \mathcal{H}^*[\mathbf{g}] \| \leq C(\| \mathbf{f} \| + \| \mathbf{g} \|) \| \mathbf{f} - \mathbf{g} \| . \tag{19}$$

Exploiting (16)–(19), one has

$$\| \Lambda[\mathbf{f}] \|_Y \leq \| f_0 \| + CT \| \mathbf{f} \|_Y^2, \tag{20}$$

and

$$\| \Lambda[\mathbf{f}] - \Lambda[\mathbf{f}] \|_Y \leq CT(\| \mathbf{f} \|_Y + \| \mathbf{g} \|_Y) \| \mathbf{f} - \mathbf{g} \|_Y . \tag{21}$$

This implies, there exist two constant T and a_0 determinate only by C, and $\| f_0 \|$, such that

$$a_0 = \frac{1 - \sqrt{1 - 4CT \| f_0 \|}}{2CT \| f_0 \|}$$

and

$$1 - 4CT \| f_0 \| \geq 0.$$

which implies that Λ is a contraction on a ball in Y of radius $a_0 \| f_0 \|$ if $T < \dfrac{1}{4C \| f_0 \|}$. Thus, there exists a unique local solution $\mathbf{f}(t)$ of (12) on $[0, T]$.

Finally, due to non negativity of solution, its clear that Λ defined in (15) maps X_+ into itself if the initial condition is positive. This complete the proof of theorem 1. ∎

In view of theorem 1, global existence for Eq. (12) can be proved. It suffices to find a proper a priori estimates for the solution. First, integrating (8)–(11) over u, and using (2)–(3) yields the following equations for n_1, n_2, n_3, n_4:

$$\begin{cases} \partial_t n_1(t) = 0, & \text{(22a)} \\ \partial_t n_2(t) = \eta_0 \gamma_{11} n_1(t) A_1(t) + \eta_0 \gamma_{21} n_1(t) A_2(t) \\ \qquad\qquad -\sigma_0 \eta_0 \gamma_{24} n_2(t) A_4(t) & \text{(22b)} \\ \partial_t n_3(t) = -\lambda_3 n_3(t) + \lambda_3 n_{30}, & \text{(22c)} \\ \partial_t n_4(t) = \sigma_0 \eta_0 \gamma_{32} n_2(t) A_3(t) + \sigma_0 \eta_0 \gamma_{42} n_2(t) n_4(t) \\ \qquad\qquad -\lambda_4 n_4(t) + \lambda_4 n_{40}. & \text{(22d)} \end{cases}$$

Integrating Eq. (22a) over $(0, t)$ yields $n_1(t) = n_{10}$, then after integrating Eq. (22b) on check that

$$n_2(t) \leq n_{20} \exp(\eta_0\, \gamma_{21} n_{10} t) + n_{10} \frac{\gamma_{11}}{\gamma_{21}} \exp(\eta_0\, \gamma_{21} n_{10} t).$$

Hence the total number of cancer cells is bounded in each finite interval $[0\ T]$.
Integrating Eq. (22c) over $(0, t)$, it follows that

$$n_3(t) \leq 2\ n_{30},$$

which implies that n_3 is bounded in every finite interval $[0\ T]$. Now, from Eq. (22d), on can obtains

$$\partial_t n_4(t) \leq \sigma_0\, \eta_0\, \gamma_{42}\, n_2(t) n_4(t) + F(t), \tag{23}$$

with

$$F(t) = \lambda_4 n_{40} + \sigma_0\, \eta_0\, \gamma_{32} n_{30} n_2(t),$$

and after integrating (23) and using Gronwall's Lemma yields:

$$n_4(t) \leq n_{40} \exp(\Theta(t)) + \int_0^t F(s) \exp\Big(\Theta(t)\Big) ds := \Sigma(t), \tag{24}$$

where

$$\Theta(t) = \sigma_0\, \eta_0\, \gamma_{42} \int_0^t n_2(s) ds.$$

From Eq. (24) one check that, n_4 is bounded on each finite time interval $[0\ T]$, and C_T in (14) is given by

$$C_T = n_{10} + 2\ n_{30} + n_{20} \exp(\eta_0\, \gamma_{21} n_{10} T) + n_{10} \frac{\gamma_{11}}{\gamma_{21}} \exp(\eta_0\, \gamma_{21} n_{10} T) + \Sigma(T).$$

This concludes the proof of Theorem 2. ∎

3. Computational Analysis and Simulations

This section summarizes the results of numerical simulations of the initial value problem defined by endowing Eqs. (8)–(11) with suitable initial conditions. Simulations are addressed to show how some parameters of the model can affect the dynamics of the solution. These parameters are turned

case by case while the other ones are kept fixed, and their values are defined with an exploratory aim. The obtained results are discussed and justified under a biological perspectives.

The common parameters proposed for simulations are :

$$\alpha_{11} = 0.07, \quad \alpha_{21} = 0.3, \quad \beta_{32} = 0.9, \quad \beta_{42} = 0.9,$$

$$\eta_0 = 1, \quad \sigma = 0.01, \quad \gamma_{21} = 0.05, \quad \gamma_{42} = 0.15, \quad \gamma_{24} = 0.4,$$

$$\lambda_3 = 0.001, \quad \lambda_4 = 0.001,$$

and we choose

$$n_{10} = 0.086, \quad n_{30} = 0.026.$$

The aforementioned choice of parameters represents a consistent physiological state where epithelial cells are characterized by a low ability to reach a pathologic state, where the mutation can play a relevant role in the dynamics, whereas mutated immune cells proliferate with a not negligible rate, namely, a clonal expansion of activated cells occurs, through them, activated immune system become able to recognize and attacks mutated cancer cells.

Initial conditions are assumed to hold the following:

$$n_{20} = 0, \quad n_{40} = 0. \tag{25}$$

Conditions (25) model a biologically consistent scenario where cancer cells does not presenting inside the system, which would motivate the study on how their onset can stimulate the activation of naive immune cells. The immune response start at $t > 0$ after recognition and identification of cancer cells. The choice $n_{40} = 0$ corresponds to an immuno-suppressed state, whereas $n_4(t) > 0$ stands for an activated immune system.

In the present paper, we investigate the crucial role of mutated immune cells in controlling the evolution of cancer, depending on the aggressiveness of mutated cancer and the immune defense ability of mutated immune cells. In some cases, The immune system is able to contrast the aggressiveness of cancer cells, while in other cases, the action is sufficient to keep the

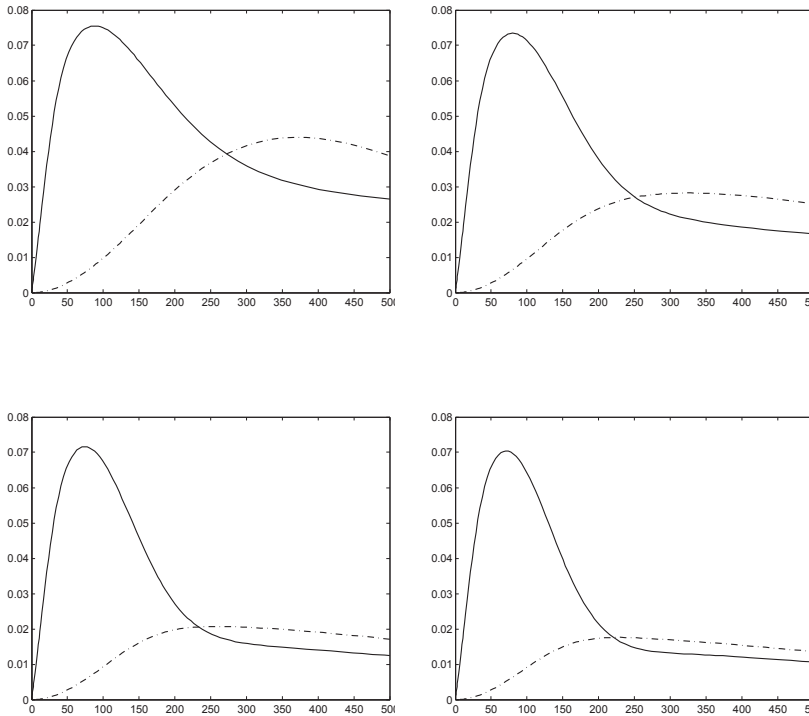

Figure 1. The evolution in time interval [0, 500] of the size of subsystems of mutated cancer cells (Continuous line), and mutated Immune cells (Dashed-dotted line) for fixed $\gamma_{11} = 0.15$, and different values of α_{32}: 0.15 (top left), 0.4 (top right), 0.7 (bottom left), 0.9 (bottom right).

pathology under control. More in details, we investigate, the behavior of n_2 and n_4, corresponding respectively to number densities of mutated cancer cells and mutated immune cells. These behaviors are well studied case by case in order to reproduce the main emerging phenomenon of the immune response against cancer evolution as well as to show the predictive ability of the model to prevent an eventual oncogenic state.

Now, we solve numerically the initial value problem (12) in the case where mutation phenomenons are are negligible within cancer cells. We set ($\gamma_{11} = 0.15$). The results drawn in Fig. 1 show n_2 versus time for fixed $\gamma_{11} = 0.15$. Increasing γ_{32} from $\gamma_{32} = 0.15$ on, simulations show an initial growth of tumor cells up to a maximum value, corresponding to an initial phase characterized by a rapid clonal expansion, able to suppress the immune

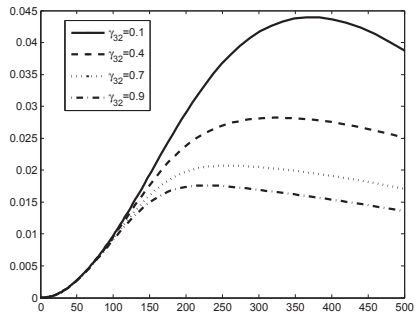

Figure 2. The evolution in time interval [0, 500] of the size of subsystems of mutated immune cells for different value for fixed $\gamma_{11} = 0.15$ and different value of γ_{32}.

reaction, and according to graphs of Fig. 1, this maximum value decreased for increasing γ_{32}. In the main time, mutated immune cells become able to contrast the development of the cancer cells and accordingly, n_2 start de decrease down to an asymptotic value. from now, the tumor cells can no longer return to grow and are kept under control by the immune system, which is relaxing to the healthy state. The graphs of Fig. 2 stands for the evolution of the number of mutated immune cells, such that increasing γ_{32} induce a relaxation ability of the immune system. While the results summarized in Fig. 3 show how the density n_2 of cancer cells reach an asymptotic value, where there exist an equilibrium between tumor cells to grow and the destructive ability of the immune system, which has a partial ability to contrast such growth.

Figure 4 represents a case with significant value of mutation rate $\gamma_{11} = 0.6$. The behavior is analogous to that shown in Fig. 1. However cancer cells grow to an threshold value less than the one obtained for a lower rate $\gamma_{11} = 0.15$. This trend changes significantly for increasing $\gamma_{32} = 0.8$, where mutated cancer cells show an aggressive trend until a critical time corresponding to $t_c = 70$ related to a situation considered as a switch of the immune system from the ability to prevent the growth of cancer cells to the opposite behaviors, and consequently a progressive depletion occurs within tumor cells, see the right panel of Fig. 4.

From a biological point of view, one comparing the panels of Fig. 1 and Fig. 4, this figures show how the mechanism of the immuno surveillance can induce a fast and strong reaction to the tumor growth depending to the mutation rate of cancer cells. More the tumor cells are characterized

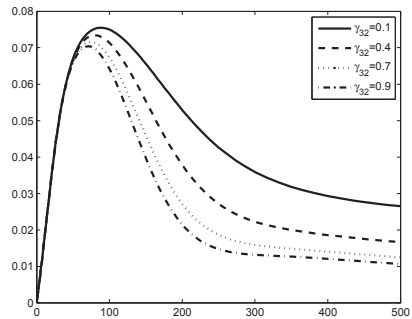

Figure 3. The partial destructive of the mutated cancer cells for increasing value of γ_{32} in the case of small $\gamma_{11} = 0.15$.

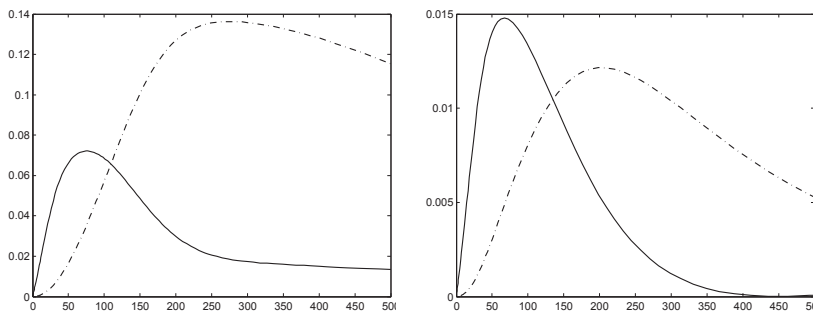

Figure 4. The evolution in time interval [0, 500] of the size of subsystems of mutated cancer cells (Continuous line), and mutated Immune cells (Dashed-dotted line) for fixed $\gamma_{11} = 0.6$, and different values of α_{32}: 0.1 (left), and 0.8 (right)

by fast trend to grow, more activated is the immune system, namely n_4 grows exponentially up to maximin value that suffices to make the tumor cells decrees to a lower values, whereby the immune system detects and eliminates tumor cells that have developed as a result of failed intrinsic tumor suppressor mechanisms. The elimination phase can be complete, where all mutated cancer cells are cleared, or incomplete when a portion of tumor cells are eliminated, see Fig. 4.

More specifically, a temporary state of equilibrium can be developed between immune system and mutated cancer cells, where both tumor cells and mutated immune cells coevolve. Thus, the immune system exerts a selective pressure by eliminating susceptible tumor clones where possible.

This pressure is sufficient to control tumor progression, but in some cases, activated immune cells cannot completely eliminate the tumor, and consequently a tumor cell variants are formed that are able to resist leading to the escape phase, where during it, the immune system can no longer achieve the elimination of the tumor.

4. Critical Analysis and Perspectives

A mathematical model has been proposed to describe the onset and the progression of cancer cells, viewed as a genetic disease where cells of the same genotype generate during the reproduction cycle, daughter cells characterized by a phenotype different from that of the mother cells. These new cells can be better or worse fitted to the environment so that a Darwinian evolution dynamics can be initiated. The dynamics refer to an early stage of competition may end up either with the suppression of cancer cells or with their indefinite growth, which subsequently aggregate into condensed structures. The model has shown the ability to depict some important emerging behaviors of the immune competition, including mutations and Darwinian selection, and simulations have investigated the relations between parameters governing the mutations both for cancer than immune system, and how increasing their value influence the behaviors of solutions. These behaviors are analyzed from the point view of what can be experimentally measured and increased with suitable therapeutical actions: the capacity of the immune system to recognize the specific hallmark of the tumor cells and consequently to mutate to keep the proliferating tumor cells at low numbers and with low levels of progression. The model of this paper have been analyzed from the point of view of the parameters related to the behavior of the immune response.

This specific model can be further improved. Empirical data and simulations can contribute to this objective. However, cancer cells are induced by DNA modifications related to the lower expression of genes. Additional interesting perspective consists in modeling the activation of the immune system[20,33].

Acknowledgments

Abdelghani Bellouquid and Mohamed CH-Chaoui were supported by Hassan II Academy of Sciences and Technology (Morocco), project “Méthodes mathématiques et outils de modélisation et simulation pour le cancer”.

References

1. L. Afraites, A. Atlas, A. Bellouquid and M. CH-Chaoui, Modelling the complex immune system response to cancer cells, *Mathematics in Engineering, Science and Aerospace*, **3**, 269–283, (2012).
2. G. Ajmone Marsan, N. Bellomo and M. Egidi, Towards a mathematical theory of complex socio-economical systems by functional subsystems representation, *Kinet. Relat. Models*, **1** 249–278, (2008).
3. L. Arlotti, E. De Angelis, L. Fermo, M. Lachowicz M., N. Bellomo, On a class of integro-differential equations modeling complex systems with nonlinear interactions, *Appl. Math. Letters*, **25**, 490–495, (2012).
4. B. Allen and M. Nowak, Games on Graphs, *Eur. Math. Soc. Surveys in Math. Sci.*, **1** (2014).
5. N. Bellomo, M. A. Herrero and A. Tosin, On the dynamics of social conflicts: looking for the Black Swan, *Kinet. Relat. Models*, **6** 459–479, (2013).
6. N. Bellomo, A. Elaiw, A. M. Althiabi, M. A. Alghamdi, On the interplay between mathematics and biology: Hallmarks toward a new systems biology, Physics of Life Reviews, **12**, 44–64, March (2015).
7. A. Bellouquid and M. Delitala, *Mathematical Modeling of Complex Biological Systems. A Kinetic Theory Approach*, Birkäuser, Boston, (2006).
8. A. Bellouquid and M. Delitala, *Mathematical models and tools of kinetic theory towards modelling complex biological systems*, *Math. Mod. Meth. Appl. Sci.*, **15**, 1639–1666, (2005).
9. A. Bellouquid and M. CH-Chaoui, Asymptotic analysis of a nonlinear integro-differential system modeling the immune response, *Comput Math Appl,* 68, 905–914, (2014).
10. A. Bellouquid and E. De Angelis, From Kinetic Models of Multicellular Growing Systems to Macroscopic Biological Tissue Models, *Nonlinear Analysis: Real World Applications*, 12, 1111–1122, (2011).
11. A. Bellouquid, From systems biology to analytic problems: Comment on the paper On the interplay between mathematics and biology, hallmarks toward a new systems biology by N. Bellomo *et al.*, *Physics of Life Reviews*, 12, 68-69, (March 2015).
12. A. Bellouquid, E. De Angelis and L. Fermo, Towards the modeling of vehicular traffic as a complex system: a kinetic theory approach, *Math. Models Methods Appl. Sci.*, **22** paper 1140003 (35 Pages), (2012).
13. A. Bellouquid, E. De Angelis and D. Knopoff, From the modeling of the immune hallmarks of cancer to a black swan in biology, *Math. Models Methods Appl. Sci.*, **23** 949–978, (2013).
14. N. Bellomo, On the interplay between mathematics and biology: Hallmarks toward a new systems biology, *Physics of Life Reviews*, 12, 44–64, (March 2015).
15. N. Bellomo, B. Piccoli and A. Tosin, Modeling crowd dynamics from a complex system viewpoint, *Math. Models Methods Appl. Sci.*, **22** paper 1230004 (29 pages), (2012).
16. F. Cavallo, C. De Giovanni, P. Nanni, G. Forni and P.-L. Lollini, 2011: the

immune hallmarks of cancer, *Cancer Immunol. Immunother.*, **60** 319–326, (2011).
17. E. L. Cooper, Evolution of immune system from self/not self to danger to artificial immune system, *Physics of Life Reviews*, **7** 55–78, (2010).
18. E. De Angelis and P. E. Jabin, Qualitative Analysis of a mean field model of tumor-immune system competition, *Mathematical Models and Methods in Applied Sciences*, **13**, 187–206, (2003).
19. E. De Angelis and P. E. Jabin, Mathematical models of therapeutical actions related to tumour and immune system competition, *Mathematical Models and Methods in Applied Sciences*, **28**, 2061–2083, (2005).
20. E. De Angelis, On the Mathematical Theory of Post-Darwinian Mutations, Selection, and Evolution *Mathematical Models and Methods in Applied Sciences*, 24, (2014).
21. J. Deguine, *et al.*, Intravital imaging reveals distinct dynamics for natural killer and $CD8^+$ T cells during tumor regression, *Immunity*, **33**, 632, (2010).
22. R. A. Gatenby, T. L. Vincent and R. J. Gillies, Evolutionary dynamics in carcinogenesis, *Math. Models Methods Appl. Sci.*, **15** 1619–1638, (2005).
23. H. Gintis, *Game Theory Evolving: A Problem-Centered Introduction to Modeling Strategic Interaction*, (Princeton University Press, 2009).
24. D. Hanahan and R. A. Weinberg, Hallmarks of cancer: the next generation, *Cell*, **144** 646–674, (2011).
25. D. Knopoff, On a mathematical theory of complex systems on networks with application to opinion formation, *Math. Models Methods Appl. Sci.*, **24** 405–426, (2014).
26. M. A. Nowak, *Evolutionary Dynamics - Exploring the Equations of Life*, (Harvard Univ. Press, 2006).
27. P. Pucci and M. C. Salvadori, On an initial value problem modeling evolution and selection in living systems, *Discrete Contin. Dyn. Sys. Ser. S*, **7** 807–821, (2014).
28. I. A. Rodriguez-Brenes, N. L. Komarova and D. Wodarz, Tumor growth dynamics: insights into evolutionary processes, *Trends in Ecology and Evolution*, **28** 597–604, (2013).
29. R. D. Schreiber, R. J. Old Lloyed and J. Smyth Mark, Cancer Immunoediting: Integrating Immunity's Roles in Cancer Suppression and Promotion, *Science*, **331**, 1565, (2011).
30. F. Thomas *et al.*, Applying ecological and evolutionary theory to cancer: a long and winding road, *Evolutionary Applications* **6**, 1–10, (2013).
31. R. A. Weinberg, *The Biology of Cancer*, (Garland Sciences - Taylor and Francis, 2007).
32. B. Jeremy Swann and Mark J. Smyth, Immune surveillance of tumors, J Clin Invest., 117 (5): 1137–1146, (May 1 2007).
33. P. L. Lollini, S. Motta and F. Pappalardo, Modeling tumor immunology, *Math. Models Methods Appl. Sci.*, **16** 10911125, (2006).

SEXUAL SELECTION IS NOT REQUIRED: A MATHEMATICAL MODEL OF SPECIES WITH SEXUALLY DIFFERENTIATED DEATH RATES

DOROTHY WALLACE, ERIN DAUSON, CASSIE PINION, KANOKA HAYASHI
Dartmouth College, Hanover, NH, USA

Under what circumstances is a higher death rate for males an acceptable trait? When, if ever, is a higher death rate for males an advantageous trait? These questions represent the null hypothesis for a variety of auxiliary reasons that have been proposed for the persistence from generation to generation of dichromatism and other forms of sexual dimorphism that appear to disadvantage the male.

Assume that two breeding species are in competition for the same resources. The only difference between the two species is that the death rate of the male of one species is higher than the death rate of the female of his species, which in turn is equal to the death rate of the competing species. Assume that the mating system of these species is efficient. That is, a relatively small number of males can impregnate females at a relatively high rate. We develop models demonstrating that the mathematics of mating (without sexual selection), birth, death, and competition are enough to guarantee a range of evolutionary patterns favoring sexual dimorphism that increases male death rates, without recourse to extra mechanisms or assumptions.

1. Introduction and Background

Darwin, while developing his theory of evolution, noted that the bright colors of the plumage of male birds in the species he was observing must be a detriment to survival. He was the first to wonder, in the context of evolution, how dichromatic species came to be (Darwin, 1871[2]). Since his writing many factors have been shown to be important to this question. The models we develop here illuminate one piece of the puzzle. Sexual dimorphism exists in many species, for quite possibly many reasons. As Darwin chose birds as his example, so shall we. But they are only one example of the question we ask here, which does not concern dichromatism so much as any sexual dimorphism that results in a higher death rate for males than for females.

It is not always true that predators of birds or other animals see what

we see. For the purposes of this paper it does not matter, because we are going to assume that the death rate is higher for the male of the species. For Darwin the question was how such a situation could arise. He suggested that the female preferred the brightly colored mate, thus giving him an evolutionary advantage over his duller brother. This behavior is a possibility and some studies attempt to document it, but both the development and disappearance of sexual ornamentation can precede changes in female preference (Wiens 2001[16]). More elaborate versions of Darwin's idea have been proposed, such as that the preference for bright males results in evolutionary compensation as the males get stronger or faster or improve in other ways.

When biologists refer to natural selection they use it to mean the increased survival and propagation of one particular individual's genes over another. But evolution ultimately works on entire populations, as entire populations or species can, as a group, exhibit different traits from each other. So, in this paper we also use "selection" to refer to the process by which one species prevails over another.

In any case, from a causal point of view the explanation of sexual selection is no explanation at all. It merely changes the focus of the question. We now have to ask why evolution would select for females with a preference for those males that have a higher death rate than themselves. We have simply moved the locus of the evolutionary force to another location, without answering the fundamental question of selection. Sexual selection is part of natural selection and must be explained according to the same principles.

Another hypothesis raises the question of ancestral forms. Perhaps the "original" form of the species is sexually dimorphic and it is in the process of evolving a male with more favorable (female) characteristics. Studies show that evolutionary transitions from dimorphic to monomorphic are more likely (Price and Birch 1996[11], Ormland 1997[8]). However, it goes both ways often enough that genetic drift has been proposed as the force behind dichromatism (Peterson 1996[10]). Similarly, it is possible that the ancestral state is bright (in birds for example, leading to a higher death rate) for both sexes, and the species has been evolving a less bright female (with lower death rate than the male).

A reduction of the death rate for either sex would seem to be adaptive. Even so, an unfavorable ancestral state cannot be a complete explanation, as relative fitness must also be taken into account. We will not explore this hypothesis here, although the models developed could certainly be used to

do so. Instead, we will focus on the seemingly more difficult question of increased death rates for the male.

Another difficulty with the question of ancestral forms is that evolution is such a long process that there is no "original" form of a species. Historical patterns of development create modern species, not merely the immediate ecology of their surroundings, as is pointed out by Badyaev and Hill (2003)[1].

One clue to the puzzle lies in a proposed, and sometimes documented, relationship between dichromatism and mating habits in birds. This short list of results gives the flavor of this relationship:

(1) Among "monogamous" species, those with more extra-pair paternity have more highly ornamented males (Moller and Birkhead 1993[7], Verner and Willson 1969[14]).
(2) Changes in mating system are correlated with changes in sexual dichromatism (Figuerolla and Green 2000[5]).
(3) Sexual dichromatism is greater in species with shorter pair bonds (Scott and Clutton-Brock 1989[12]).
(4) Dichromatism is greater among polygamous and lekking species than in monogamous species (Dunn *et al.* 2001[4]).

The literature presents a far more complicated picture than these few references suggest, and many factors are implicated in the loss or gain of brightness. However these studies suggest a relationship that can be explored through the mathematical models developed here. Simple genetic drift can explain how traits might arise, but natural selection should explain how they persist from generation to generation. One mechanism of species diversification, the process of isolation and reintroduction, allows multiple forms to meet. This process can be simulated with a pair of breeding populations to explore hypotheses about how evolution might allow for the phenomenon Darwin observed.

1.1. *The null hypothesis for all auxiliary reasons*

We are going to assume that two breeding species are in competition for the same resources. The only difference between the two species is that the death rate of the male of one species is higher than the death rate of the female of his species, which in turn is equal to the death rates of the competing species whose sexes are identical. We are going to assume that the mating system of these species is efficient. That is, a relatively small number of males can impregnate females at a relatively high rate, reflecting

the situation in the sources listed above. We will ask several questions:

(1) When is a higher death rate for males an acceptable trait?
(2) When, if ever, is a higher death rate for males an advantageous trait?

These questions represent the null hypothesis for a variety of auxiliary reasons that have been proposed for the persistence from generation to generation of dichromatism and other forms of sexual dimorphism that appear to disadvantage the male.

In the Section 2 we give a heuristic argument for the advantages of a higher male death rate. In Section 3 we develop models that capture the basic features of the hypothesis outlined here. Section 4 describes the basic results of these models: how dimorphic species fare, how success depends on efficiency of mating, and how competing populations fare upon reintroduction to each other. In Section 5 we discuss how the models of isolated and competing species fit together to tell a story about evolution, and in Section 6 we look at a slightly different version of that same story. Section 7 illustrates some interesting dynamics of the competition model, and Section 8 summarizes our results.

2. A Heuristic Argument

Darwin proposed that evolution improves the chances of survival of a species. More exactly, traits that improve the "fitness" of a species are those that tend to be propagated through successive generations. Darwin left it to those who followed him to define exactly what "fitness" might mean in each case. One possible way to measure the success of a population might be its numbers. In a state of equilibrium we might expect that species with greater population density would have an advantage against those with lesser density, especially if a random event could reduce populations greatly. But evolution is about successive generations, so we might equally well expect that a species with a higher production of offspring at the next generation would also have an advantage over those with lower production of offspring. These two advantages can be independent of each other, as the following argument shows.

Suppose the female of a species can produce a fixed number of offspring, N, in a season. Consider two populations of this species, both equipped with efficient mating strategies that allow many females to reproduce with a relatively small number of males. In population A there are 100 individuals,

50 female and 50 male. The number of offspring produced will be 50N. In population B there are only 80 individuals, but 60 are female and 20 are male. The number of offspring produced will be 60N. Although population A has the advantage of numbers, population B has the advantage of a higher absolute birth rate, even though the two relative birth rates, (N), remain the same.

Thus, depending upon what kind of stresses a population may experience, nature could favor a population that has evolved to keep its absolute birth rate relatively high. One way to do this is through unequal death rates for male and female. In a habitat with limited resources that are shared between males and females, a high death rate for males makes room for more females, effectively raising the absolute birth rate of the population.

In the sections that follow we pursue this argument computationally through a series of models.

3. Model Development

3.1. *Equations governing a single species*

$$x = x = a(1 - x - y)xy/(c + y) - bx \tag{1}$$

$$y' = a * (1 - x - y)xy/(c + y) - dy \tag{2}$$

Equations 1 & 2 are variants of the familiar logistic equation with relative growth rate a and carrying capacity 1 given by $T' = aT(1 - T)$. Here we have split the population into females (x) and males (y), replaced the factor of T by the functional response $f(x, y) = xy/(c + y)$, and separated death due to predation as given by its own linear term (bx or dy). The death rates b and d need not be the same for males and females. For the following discussion we will always assume $d > b$, that is, the males suffers greater loss due to predation than the female.

In the familiar logistic equation, growth is directly proportional to total population. In our adjusted equations, growth is directly proportional to the number of females. However the proportionality factor is adjusted to account for dependence on the male population as well. In perfectly efficient mating, all females would get pregnant. However, in nature a male is required, and a low population of males may mean that some females cannot find a mate. For example, if mating were completely probabilistic (as in the case of wind pollinated plants, for example), we might make the growth

term proportional to both x and y. For this study, we assume that the organism in question has behavioral or other strategies that improve on a system of chance encounters. The term given by $y/(c+y)$ is a nonlinear functional response that gives a value of zero when $y = 0$ and a limiting value of 1 as y approaches infinity. By reducing c one can obtain a value as close to 1 as desired when y is as small as desired. This choice of c amounts to choosing how efficient the mating process is at low values of y.

3.2. *Equations for two species in competition*

In the following equations, $T = x + y + u + v$.

$$x = a(k - T)xy/(c + y) - bx \tag{3}$$

$$y' = a * (k - T)xy/(c + y) - dy \tag{4}$$

$$u' = a * (k - T)uv/(c + v) - bu \tag{5}$$

$$v' = a * (k - T)uv/(c + v) - bv \tag{6}$$

The growth term $a * (k - T)xy/(c + y)$ is constructed in analogy with Equations 1 & 2 above. The limiting term of the logistic equation now includes the total of all four populations. The introduction of a carrying capacity, (k), allows us to investigate introduction of species into habitats of different sizes. All of the populations have the same death rate (b), except for the male of the first species (y), which has a larger death rate (d). Efficiency of mating, c, is assumed to be the same for both species. These equations represent two species sharing the same habitat which are identical in every way, except for a disadvantageous death rate for the male of one species.

4. Basic Results of the Model

4.1. *Behavior at extremely low population size*

The Allee effect is a a basic feature of all of these models, as we showed in Wallace *et al.* 2011[15]. For the model with only one species, the size of the Allee basin (the set of initial conditions that lead to extinction)

decreases as c decreases, making mating more efficient. However, the extinction equilibrium for the single species model is always stable. Near $(x, y, u, v) = (x_{eq}, y_{eq}, 0, 0)$, we have the following inequality due to the Allee effect for (u, v).

$$u' = a * (k - T)uv/(c + v) - bu < a * (k - u - v)uv/(c + v) - bu < 0 \quad (7)$$

A similar statement holds for v. This observation implies that, for the two species model, the two fixed points with exactly one of the species extinct are also stable.

Thus, in the case of two species in competition, we see that the long term behavior of solutions must depend on initial conditions. These models are all density dependent, with the existence of a nontrivial equilibrium (for one or both populations) dependent on having enough population at the start. It is important to keep this phenomenon in mind for the two-species model, as extinction may occur even without competition.

4.2. *The case of one species*

For species in isolation the models predict no difficulty with the persistence of a trait producing a higher death rate for males. A wide and biologically reasonable range of a, b, c, d lead to stable nonzero equilibrium populations.

Equilibrium values are in proportion to death rates. Thus $y* = (b/d)x*$. This model leads to equilibrium values that represent assumption of the heuristic argument that populations with higher death rates for males will tend to have a higher percent of carrying capacity represented by the females. This result justifies the use of this model as a basis for a competitive model to test the heuristic argument given above. Specifically, equilibrium values are given by two equations. Here we set, $k = 1$, $a/b = n$ and $d/b = m$. Both of these ratios are assumed (for biological reasons) to be greater than 1. For the discussion and comparisons that follow we will assume that b, the density independent death rate for females, remains constant. The ratio m will change because the density independent death rate for males, d, changes. We use T_{eq} to denote the equilibrium of the total population.

$$x_{eq} = m[n - 1 + / - \sqrt{(1 - n)^2 - 4n(1 + m)c}]/[2n(1 + m)] \quad (8)$$

$$y_{eq} = [n - 1 + / - \sqrt{(1 - n)^2 - 4n(1 + m)c}]/[2n(1 + m)] \quad (9)$$

$$T_{eq} = [n - 1 + / - \sqrt{(1-n)^2 - 4n(1+m)c}]/[2n] \tag{10}$$

Notice that the total population, T_{eq}, declines as the death rates of males and females diverge. That is, an increase in male death rate causes the overall population to decline, although the population of females will rise.

These expressions give positive real values for $c < (n-1)^2/[4n(1+m)]$. This expression gives a constraint on how efficient the mating strategy must be in order to stabilize the population for the given birth and death rates. Henceforth we will assume that c satisfies this inequality. For convenience we may formalize this constraint.

$$c = (1-n)^2/[4n(1+m)] - \alpha^2 \tag{11}$$

It is worth mentioning that the higher equilibrium is stable in all such cases, whereas the lower one is unstable and marks the boundary for the Allee effect, as in Wallace *et al.*[15]. It is clear from the expression for T_{eq} that increasing either c or m lowers the equilibrium population in these models.

In addition, we can express the density dependent growth rate for the total population at equilibrium as $BR_{eq} = 2bx_{eq}$, giving the following expression. Using equation 10 for c we may express the absolute growth rate at equilibrium.

$$BR_{eq} = bm[n - 1 + \alpha\sqrt{4n(1+m)}]/[n(1+m)] \tag{12}$$

In contrast to the situation for T_{eq}, we see that BR_{eq} rises as α increases. An increase in α corresponds to a decrease in c, which in turn corresponds to more efficient mating habits. The absolute birth rate at equilibrium also rises as m rises, which can be seen with a little algebra that we omit here. A rise in m corresponds to a greater disparity between the (fixed) female death rate and the (larger) male death rate.

In short, this model reproduces, in mathematical form, the heuristic argument given earlier. Two independent runs of the single species model are pictured in Figure 1. One (the middle trajectory), in which both populations remain equal, has identical death rates for male and female. The other run (the top and bottom trajectories), in which death rates differ, has a higher equilibrium population for females than for males, as well as a lower total population at equilibrium.

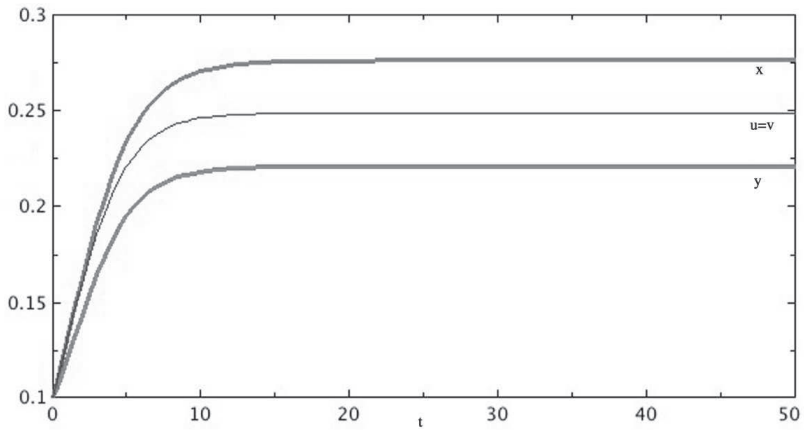

Figure 1. Two independent runs of Equations 1 & 2. For both, $a = 1, b = .5$, $m = 1.25, c = .001, k = 1$. At $t = 0, x, y, u, v = .1$. For the x, y population, $m = 1.25$, while for the u, v population, $m = 1$.

4.3. *Two species in competition*

In the competition model described by Equations 3–6, coexistence is never observed. The outcome of competition is density dependent. Initial conditions determine the successful species. The Allee effect is one reason for density dependent outcomes. But even at higher densities we do not observe coexistence.

An equilibrium exists with all populations extant and can be calculated explicitly, although the eigenvalues of the Jacobian at this location cannot be calculated for the general case. However, all examples for which the eigenvalues of the Jacobian were computed numerically were unstable. In most numerical simulations one species or the other goes extinct. At the boundary between the two extinction basins there appears to be a region of coexistence but we suspect this disappears if the model is run for more iterations. Although any perusal of the literature is far from complete, it seems that nobody reports monochromatic and dichromatic versions of the same species in the same habitat, consistent with the observed numerical results of our model.

We can make the assumption that the total starting populations of the two species, determined by their recent habitat constraints, is random. We can then interpret the likelihood of one species winning this competition

as the proportion of possible initial conditions leading to its survival. This numerical experiment was run on ten by ten a grid of 100 starting populations ranging from 0 to 2. Starting populations were always taken to be with female/male populations in proportion to death rates, as if the populations had reached equilibrium prior to their mutual introduction to each other. Equation 13 describes the competition scenario for the variable quantity x that was used for these experiments. One can easily construct the analogous equations for y, u, v, using the death rate d for y.

$$x = a(2 - x - y - u - v)xy/(c + y) - bx \tag{13}$$

Figures 2 and 3 show a series of experiments using these competition equations. Similar experiments were done across a variety of parameter values, with similar tendencies appearing. Each square grid in these figures represents a pair of starting populations for the males in each of two species. The male starting populations were set to the equilibrium proportions determined by the death rates, as described above. For the species labeled (x, y) therefore we set $y_0 = b/dx_0$. Initial populations range from zero to 2, the carrying capacity. The grid is then color coded to indicate which population eventually dominated. Black squares indicate that the x, y population survived and the u, v population went extinct and white squares indicate the opposite outcome. Light gray squares indicate that both populations were still nontrivial at the end of the run. The dark gray square near the origin represents the extinction of both species.

Figure 2 shows a series of experiments with $a = 1, b = .13, c = .1$ and d varying from .13 to .25. As d increases, the proportion of starting values leading to extinction of x, y decreases. Because initial conditions are chosen by nature, not by the organism, we can interpret this as a probability.

Figure 3 shows a series of experiments with $a = 1, b = .1, d = .19, k = 2$ and c varying from .01 to .19. As c increases, the proportion of starting values leading to extinction of x, y increases.

5. Isolation and Reintroduction of Species

Evolution is not an event. It is a story. One of its main story lines concerns the genetic drift that occurs when two populations are isolated from each other. The single species model in for a species with sexually differentiated death rates and efficient mating developed above supports the hypothesis that a viable population may have higher death rates for males than for females, as long as mating strategies are sufficiently efficient. For this model,

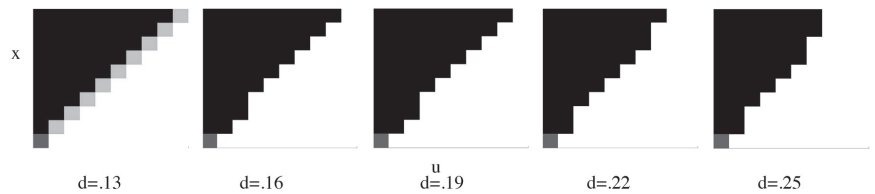

Figure 2. A sample of many runs and who wins: a series of experiments with $a = 1$, $b = .13, c = .1, k = 2$ and d varying from .13 to .25. Black squares indicate that (x, y) wins, white indicates that (u, v) wins. The vertical axis represents the starting population of y and the horizontal axis the starting population of u $(= v)$, both between 0 and 2.

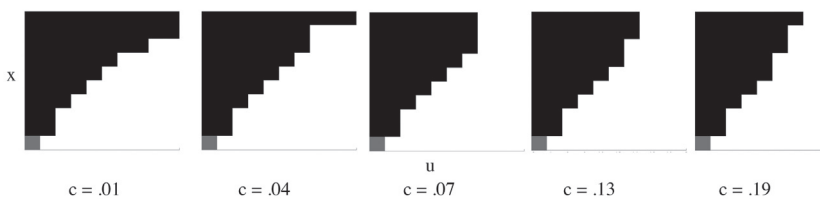

Figure 3. A sample of many runs and who wins: a series of experiments with $a = 1$, $b = .13, d = .19$ and c varying from .01 to .19. Black squares indicate that (x, y) wins, white indicates that (u, v) wins. The vertical axis represents the starting population of y and the horizontal axis the starting population of u $(= v)$, both between 0 and 2.

that criterion is expressed in equation 10 above. From that equation we see that, as m, the ration of male to female death rate, increases, c is forced to decrease to maintain viability. That is, as the death rates increasingly differ, the mating strategy must become more efficient to avoid unconditional extinction of the population. As one example of sexually differentiated death rates we may consider dichromatic bird species. If one accepts the hypothesis that brightly colored birds are more likely targets of predation, then the model for a single species at least partially explains the observation that dichromatism in birds is associated with polygamous and lekking species (Dunn *et al.* 2001[4]).

The second part of the story of species diversification requires that two divergent species meet again. Perhaps a corridor opens between two habitats, or perhaps a flock immigrates to a new area. One would naturally expect two diverging populations to differ in multiple ways. However, for

the sake of argument, we will assume that the only difference between the two populations meeting anew is that one of them has developed sexual dimorphism leading to a higher death rate for males, whereas the other has not. As described above, the outcome is dependent on initial population size.

In Figure 2 we see that the greater the disparity between male and female death rates (other things being equal), the likelier is extinction upon meeting a species with equal male and female death rates. If the starting populations for the two species are unequal, however, there is always some fairly large chance that x, y will win the competition. What this model therefore predicts is that if we look at all competitions between pairs of species identical in every respect except for sexually differentiated death rates, we would expect a nonzero proportion of these competitions to favor the dimorphic species and we would expect that proportion to be less than half. Both of these predictions are sometimes borne out in observations of nature (Sorce *et al.* 1998[13]).

In Figure 3 we see that, as mating becomes less efficient, the dimorphic species becomes less competitive. This experiment confirms the key role that efficient mating strategies play, not only for species growing in isolation, but also for competitive situations.

For the most efficient mating represented in Figure 3 (c=.01), the dimorphic species is less competitive at low population values but more competitive at high population values (of both species). Note that the higher populations correspond to the meeting of more individuals than the habitat can hold, as in the case of a joining of populations with a simultaneous reduction of habitat size. Thus the success of the either species is dependent not only on its intrinsic birth and death rates, but also on the conditions of the habitat into which it is introduced. In this situation the species that has improved its absolute birth rate at the expense of an increase male death rate wins the competition. This observation partially answers the question posed at the start of this paper: When is it advantageous to increase the male death rate?

6. Isolation and Reintroduction with a Twist: The Advantage of Having a Hard Past

Consider two species with efficient mating, identical in every way except for a larger death rate for males in one of them. Suppose that these two species, having grown to equilibrium in isolation, are introduced to each

other in a new, much larger, habitat. From the discussion above we would expect that there is a slightly greater chance that the monomorphic species would prevail. However, new habitats need not be identical to the original ones. In particular, if population densities are low one might expect more cover available to protect against predation, or perhaps fewer predators specific to these species. In this case, the male of the dimorphic species, while still more vulnerable than the female, might enjoy a lower death rate than previously.

In Figure 4 we see the result of such a scenario. Two populations (females x and u respectively) have grown to equilibrium in isolation in identical small habitats ($k = 1$). The male death rate is 1.25 times as great as that of the female ($m = 1.25$) in the first population (x, y), in the second population (u, v), the two rates are equal. Starting with equilibrium values in isolation, we introduce them to each other in a new, much larger habitat ($k = 10$). Both total starting populations are equal, with proportions determined by equilibrium values in isolation. On the left we see the result if the death rate for y remains the same: population (x, y) dies out. But if the death rate for y is mitigated slightly ($m = 1.1$) then the dimorphic population prevails. In this situation the higher female population, x_0 at the start of the competition compensates for the higher death rate ($m = 1.1$) of males. That high initial female population is a feature inherited from growth in isolation with an even higher male death rate.

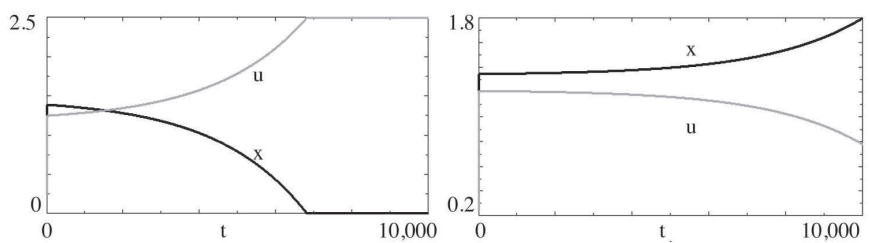

Figure 4. Two examples with $a = 1, b = .5, c = .001, k = 2, x_0 = .276, y_0 = .220, u_0 = v_0 = .248$. On the left, $m = 1.25$. On the right, $m = 1.1$.

7. Extreme Stress Due to Crowding: Some Interesting Dynamics in the Competition Model

For some parameter values and some initial conditions, the model for competing species developed here shows signs of chaotic dynamics. These dynamics usually occur in regions where the population sizes drastically exceeds the carrying capacity of the system. In a few cases where this dynamic appeared, the grid size was refined to 100 by 100, and a fractal pattern began to emerge. Small regions were further refined, and the pattern became more dense. Finally, in a few cases, nearby initial conditions were run individually to verify that they approached different fixed points. Individual runs did not appear chaotic, but there was none the less sensitive dependence on initial conditions in the sense that very close starting values led to very different outcomes, with those favoring extinction of one population interspersed with those favoring extinction of the other.

Figure 5 illustrates what we observed. An apparently anomalous white square sits in the black area of the grid of starting values in Figure 5(A). Upon refining the grid, a fractal pattern appears in Figure 5(B), enlarged for convenience in Figure 5(C). This type of pattern only occurs in regions where the population is very large to start, and is dying off to approach equilibrium. In nature this would correspond to a sudden reduction of habitat, with simultaneous meeting and crowding of formerly separate species. To the extent that our model represents a possible natural situation, it is saying that while growth to equilibrium is orderly, dying off is chaotic, with long term results that are difficult to predict even with nearly perfect information.

It is worth noting here that the Matlab runs in Figure 5 use a version of the Runge-Kutta formula with the Dormand-Prince pair (4,5). This algorithm requires setting a tolerance, in this case of e^{-12}. Changing this tolerance alters the images. Thus it is unclear if the emerging pattern is a result of numerical foibles, a true chaotic system, or a system whose basin boundary has a fractal form.

No matter which is the case, it seems that the species with the higher death rate for males has the advantage in situations of extreme crowding. Such a scenario could result from immediate and severe loss of habitat.

8. Conclusions

To summarize the results of the model and point out some implications, we consider the answers to the questions posed at the start of this paper,

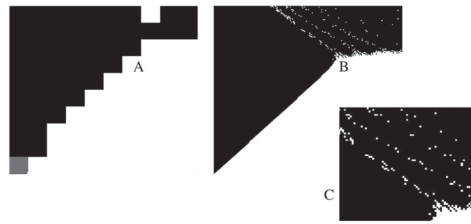

Figure 5. A sample of many runs and who wins: a series of experiments with $a = 1$, $b = .13, c = .01, d = .25, k = 2$. Black squares indicate that (x, y) wins, white indicates that (u, v) wins. The vertical axis represents the starting population of y and the horizontal axis the starting population of u, both between 0 and 2. Inset A shows the result of 100 experiments, whereas B shows a refined grid of 10,000 runs. Inset C is an enlargement (but not a refinement) of the fractal region of B.

describe some results which echo observations of the natural world, and reconsider the null hypothesis in light of our numerical results.

8.1. *Conditions favoring higher male death rates*

The model developed here allows us to give partial answers to the questions posed at the start: When is it acceptable or even advantageous to increase the male death rate in a population? Our answers are partial, because in real populations many factors may be at work besides those considered here. Our results give sufficient conditions, not every possible reason. Even so, we can offer some scenarios under which a high male death rate could be acceptable or even helpful.

It is acceptable to increase the male death rate when a population is growing in isolation, without competition for its niche. Equilibrium values for the population will change, with more females than males, less total population, and a higher absolute birth rate. How far the process of differentiation can go depends on the efficiency of the mating, with more dimorphism possible in species that have found strategies for more efficient mating.

When two similar, relatively small, populations meet in a large habitat, it is acceptable for one to have a higher male death rate provided it has the advantage in numbers at the start. How big an advantage is required depends on how big the male death rate is for the dimorphic population and how efficient the mating strategy is. In such competition, coexistence seems to be unlikely at best, so any advantage (or disadvantage) is absolute, leading to survival (or extinction).

It is advantageous for a population to have an increased male death rate if, when it comes into contact with a similar, monomorphic population, the male death rate improves somewhat. The larger proportion of females in the dimorphic population, combined with a new, somewhat better, death rate for the males, can give the (still) dimorphic population an edge.

Finally, in some situations where two populations come together in very crowded conditions, dying off to equilibrium, the dimorphic population starting with a high percent of females has an advantage. But because the dynamics of such a situation could be chaotic, that advantage is best considered to be a probability.

8.2. *Comparison with observed phenomena*

The standard Lotka-Volterra competition equations allow for the possibility of coexistence of competitors. However, the model developed here does not seem to allow for this eventuality. While species richness based on male dimorphism may exist across niches or habitats, our model predicts that it is unlikely to be found in close company. Of course, an absence of such examples in the literature is not, of itself, evidence of absence of the phenomenon, although it suggests that it is unlikely in the natural world also.

The importance of efficient mating strategies has been remarked upon in various studies. Our models confirm this importance both as an enhancement to the likelihood of survival of dimorphic species and also as an absolute boundary for dimorphism. The analysis of the models suggests that have less efficient mating systems can afford less dramatic dimorphism. While studies of the natural world are complex and confusing on this point, the model does seem to be in line with the general trend of results.

Success of a species upon introduction to a competitor is population dependent in our model. This fits well with some observations, such as Green's study of exotic birds introduced to New Zealand (Green 1997[6]). The population dependent aspect of our models also explains to some extent the complex and seemingly contradictory situations observed in nature. Some collections of species have many dimorphic types and others have few. The existence of a dimorphic species tells us nothing about what competitors it might have had or what the exact circumstances were when they met. If the success of a species when introduced to a competitor depends on its relative population size at the moment of meeting, the relative size of both populations with respect to habitat, and the mating habits of both species

at the time of introduction, then the model tells us to expect a relatively random looking set of outcomes.

Sexual selection has been proposed as a cause of species richness (Panhuis *et al.* 2001[9]). Our model suggests that diversification of niches is required, as coexistence (in the same niche) is never observed. It suggests that divergence of species must include some factor in addition to female preference to explain subsequent coexistence of multiple types, if that is in fact what is observed. Our model does support the possibility of multiple dimorphic species developing in isolation, without of course requiring sexual selection to be the cause.

8.3. *Null hypothesis revisited*

One of the biggest assumptions made about sexual dimorphism is that it is the product of two opposing forces: sexual selection by the female for exaggerated features, and natural selection favoring lower death rates and therefore less visible males. As pointed out earlier, the logic of evolution favoring such fussy females is lacking. Our models show that none of this description need hold. Any amount of genetic drift that produces males with higher death rates can be supported up to a point. Furthermore there are situations in which having vulnerable males in the present or in the past can actually be favored by natural selection alone. A high male death rate is often acceptable and occasionally advantageous.

Although some amount of genetic drift is a required assumption to introduce dimorphic traits, active sexual selection is not. Many studies use dichromatism itself as a basis for assuming sexual selection has occurred, or even as a measure of the intensity of sexual selection (Doherty *et al.* 2003[3]). If nothing else, our results point to the fallacy of such an assumption. Claims of sexual selection, which certainly may occur in some species, need to be based on observation of social behaviors.

The hypothesis that a dimorphic ancestral state is evolving into one where male death rates are being reduced is also an unnecessary assumption. Although the general mechanism of genetic drift would imply that movement from dimorphic to monomorphic can happen, there is no reason to assume that it must happen.

In short, the mathematics of mating, birth, death, and competition are enough to guarantee a wide range of evolutionary patterns favoring sexual dimorphism that increases male death rates, without recourse to auxiliary mechanisms or assumptions.

References

1. Badyaev A. V. and G. E. Hill. 2003. Avian Sexual Dichromatism in Relation to Phylogeny and Ecology Annual Review of Ecology, Evolution, and Systematics 34: 27–49.
2. Darwin C. 1871. The Descent ofMan and Selection in Relation to Sex. John Murray, London, U.K.
3. Doherty P. F. Jr., G. Sorci, J. A. Royle, J. E. Hines, J. D. Nichols and T. Boulinier. 2003. Sexual selection affects local extinction and turnover in bird communities, PNAS 100 10: 5858–5862.
4. (Dunn *et al.* 2001) Dunn P. O., L. A. Whittingham and T. E. Pitcher. 2001. Mating systems, sperm competition and the evolution of sexual dimorphism in birds. Evolution 55: 161–75.
5. Figuerola J. and A. J. GreenA J. 2000. The evolution of sexual dimorphism in relation to mating patterns cavity nesting insularity and sympatry in the *Anseriformes*. Funct. Ecol. 1 4: 701–10.
6. Green R. E. 1997. The Influence of Numbers Released on the Outcome of Attempts to Introduce Exotic Bird Species to New Zealand. Journal of Animal Ecology 66 1: 25–35.
7. Moller A. P. and T. R. Birkhead. 1993. Cuckoldry and sociality: A comparative study of birds. Am. Nat. 142: 118–40.
8. Omland K. E. 1997. Examining two standard assumptions of ancestral reconstructions: Repeated loss of dichromatism in dabblingducks (Anatini). Evolution 51: 1636–46.
9. Panhuis T. M., R. Butlin, M. Zuk and T. Tregenza. 2001. Sexual selection and speciation TRENDS in Ecology & Evolution. 16 7: 364–371
10. Peterson A. T. 1996. Geographic variation in sexual dichromatisimn birds. Bull. Br. Ornithol. Club 116: 156–72.
11. Price T., G. L. Birch. 1996. Repeated evolution of sexual color dimorphism in passerine birds. Auk 113: 842–48.
12. Scott D. K. and T. H. Clutton-Brock. 1989. Mating systems,parasites and plumage dimorphism in waterfowl. Behav. Ecol. Sociobiol. 26: 261–73.
13. Sorci G., A. P. Moller, J. Clobert. 1998. Plumage dichromatism of Birds Predicts Introduction Success in New Zealand. Journal of Animal Ecology. 67 2: 263–269.
14. Verner J. and M. F. Willson. 1969. Mating systems sexual dimorphism and the role of male North American passerine birds in the nesting cycle. Ornithol. Monogr. 9: 1–76.
15. Wallace D. I., R. Agarwal and M. Kobayashi. 2011. Mating Strategies and the Allee Effect: a comparison of mathematical models. BIOMAT 2010, Proceedings of the International Symposium on Mathematical and Computational Biology, Rio de Janeiro, Brazil, World Scientific Press. 192–207.
16. Wiens J . 2001.Widespread loss of sexually selected traits: how the peacock lost its spots. TREE 16: 517–23.

MODELS FOR TWO STRAINS OF THE CAPRINE ARTHRITIS ENCEPHALITIS VIRUS DISEASE

SIMONA COLLINO, EZIO VENTURINO*

Dipartimento di Matematica "Giuseppe Peano",
Università di Torino,
via Carlo Alberto 10, 10123 Torino, Italy
E-mail: simocollino@hotmail.it, ezio.venturino@unito.it

LUCA FERRERI, LUIGI BERTOLOTTI, SERGIO ROSATI
and MARIO GIACOBINI

Department of Veterinary Sciences,
University of Torino
largo Paolo Braccini 2, 10095 Grugliasco (TO) ITALY
E-mail: luca.ferreri@unito.it, luigi.bertolotti@unito.it, sergio.rosati@unito.it,
mario.giacobini@unito.it

We present two models for a farm breeding that is assumed to be infected by just one lentivirus genotype. In the asymptomatic case the disease can be eradicated, while for the more widely spread genotype even the hygienic measures taken by the farmer may be insufficient to contain the epidemics.

1. Introduction

Caprine Arthritis Encephalitis Virus disease (CAEV) is a pathogenic lentivirus in the family Retroviridae that infects both goats and sheep and is closely related to the Maedi-Visna Virus (MVV) of sheep. Examples of known retrovirus are HIV, responsible for the acquired immunodeficiency syndrome in humans, and FIV, responsible for the feline immunodeficiency. CAEV and MVV are classified as Small Ruminant Lentiviruses (SRLV). While SRLVs were once considered to be species-specific, recent studies suggest that they can be transmitted from sheep to goats and vice-versa and can recombine to form new CAEV-MVV strains[3], increasing the risk

*Corresponding author.

that highly pathogenic variants may emerge[5], and thus rendering more complex the animal trade among countries.

Among the five genotypes identified, two affect goats: genotype B has been found worldwide, especially in North America and Europe, while genotype E is geographically localized to limited areas[2,4].

Strain B, which is pathogenic, can be transmitted in a vertical way from mother to offspring through colostrum or milk and this is the major route of SRLV transmission[6]. It can also be conveyed horizontally through blood or saliva.

Strain E, also known as Roccaverano strain, can be transmitted only in a vertical way and is very important because it is not pathogenic. It was indeed first discovered in the Roccaverano goat breed in Piedmont (Italy), as a highly divergent SRLV. It has been hiding from standard serological tests, due to its highly divergent structural proteins, and has also been inadvertently undetected by breeders due to the absence of symptoms[4]. Thus goats infected by genotype E do not cause any problems to the farm.

The first cases of CAEV have been reported in 1974[2]. The disease most frequent symptom is arthritis, but also mastitis which leads to udder deformation, and the more rare pneumonia and encephalitis[3]. CAEV is a pathology characterized by a long period of incubation and then by a progressive chronic course, so initially even though the goats are infected by the virus, clinical signs are not immediately visible, as the symptoms usually appear between the ages of 2 and 5.

For the farmers, the disease represents an economic burden because, after the period of incubation, goats produce less milk, are weaker and can contract other diseases more easily. There is currently no effective treatment for this infection. Due to a high mutation rate of its etiological agent, no vaccine is available for this pathology. So it is necessary to adopt some sanitary measures to control the transmission of the virus in order to avoid its spread. The three most commonly used techniques are "test-and-slaughter", isolating sick goats from the breeding and taking the newborns away from their mothers. "Test-and-slaughter" consists in selecting infected goats and directly slaughter them[2]. In this way the virus is eradicated but this strategy can be used only if the infection prevalence is low. Alternatively, sick goats can be removed from the breeding and kept together with other infected goats of other breeding. Finally, the newborns can be taken away from their mothers and put in a new breeding area where they are raised. After weaning, they will rejoin the original breeding where however they might contract the disease horizontally, from possible

asymptomatic carriers.

In this paper we present two models respectively for the genotypes E and B, in Sections 2 and 3. We assess an important piece of information for the farmer, the so-called replacement rate in presence of these strains, i.e. the number of newborns that must be raised within the breeding to keep it viable in time. We also investigate the possibility and conveniency of adopting a sanitary strategy to control the transmission of the virus. For the strain B, which can be transmitted horizontally, we use a frequency-dependent model to describe the dynamics of the breeding. Our goal for each model is to understand in what way the replacement rate changes and how strict the sanitary measures have to be in order to eradicate the disease and prevent it from becoming endemic.

2. Model for a Genotype E-Affected Goat Breeding

Here we present a model of a breeding in the presence just of genotype E of the CAEV virus, which is asymptomatic. Let the total population be $N(t)$, partitioned among susceptibles $S(t)$ and asymptomatic goats $Y(t)$ infected by the E strain.

Furthermore, we assume that every goat belonging to class $S(t)$ is equally susceptible and the genotype E of the lentivirus is transmitted only in a vertical way. The dynamics of this type of breeding is then:

$$\frac{dS(t)}{dt} = \left[(1-\gamma) + \gamma\left(1 - \theta_E \frac{Y(t)}{N(t)}\right)\right] arN(t) - mS(t), \tag{1}$$

$$\frac{dY(t)}{dt} = \theta_E \frac{Y(t)}{N(t)} \gamma arN(t) - mY(t).$$

The first equation describes the susceptibles dynamics. The number of newborns is given by $arN(t)$. The parameter r represents the goats reproduction rate, m their mortality rate, a is the fraction of newborns that are kept in the farm. Let γ denote the probability of a newborn not to be removed from the breeding. The farmer applies this sanitary strategy to avoid the spread of the disease: the newborns are taken away from their mothers and put in a new breeding area where they are raised. Once weaned, these goats will be placed again in the original breeding. In particular, $\gamma = 0$ means that all newborns are removed straightaway from the breeding, while $\gamma = 1$ indicates that all newborns remain in the breeding with their mothers. Further, θ_E represents the probability of vertical transmission of genotype E, assuming there has been a contact between the newborn and the infected mother. Also, $\theta_E Y(t) N(t)^{-1}$ is the probability of vertical infection, where

$Y(t)N(t)^{-1}$ denotes the probability of a contact with an infected individual. Thus the first term of the first equation states that healthy newborns are obtained either by removing them from their mothers and raised in an isolated breeding, or they do not contract the virus. The last term of the equation represents the natural mortality.

The second equation describes the dynamics of goats infected by genotype E. The first term represents the newborns which have not been removed from the breeding, $\gamma arN(t)$ and that have taken milk from an infected mother, $Y(t)N(t)^{-1}\gamma arN(t)$, and furthermore have been infected, $\theta_E Y(t)N(t)^{-1}\gamma arN(t)$. The last term represents their natural mortality.

We can rewrite the system (1), using as variables the total breeding population $N(t) = S(t) + Y(t)$ and the asymptomatic prevalence, i.e. the fraction which indicates the number of infected goats over the total population: $y(t) = Y(t)N(t)^{-1}$, obtaining

$$\frac{dN(t)}{dt} = (ar - m)N(t), \quad \frac{dy(t)}{dt} = (\gamma\theta_E - 1)ary(t). \tag{2}$$

Because of the limited resources of the farms, the total population is usually kept at a constant value N. Thus, from now on, we set $N(t) = N$.

From the steady state of the first equation of the system (2), instead of finding the equilibria, we can determine the replacement rate a in presence of the genotype E:

$$a = \frac{m}{r} = a_{farm}. \tag{3}$$

Comparing with the results of Ref. 2, the replacement rate is found to be the same as the one of an ideal farm in absence of any kind of disease. This result is due to the non-pathogenecity of the genotype E. The goats do not show any symptom so that they are considered healthy. Substituting a_{farm} into the second equation of (2) we get the reduced system:

$$\frac{dy(t)}{dt} = (\gamma\theta_E - 1)my(t). \tag{4}$$

2.1. *Equilibria and stability*

There is only one equilibrium of the model, for the single equation (4), $y(t) = 0$, because both $0 < \gamma < 1$ and $0 < \theta_E < 1$. Letting $s(t) = S(t)N(t)^{-1}$, we find only one stationary point in the $s - y$ phase space, $(1, 0)$, always feasible. Thus all the goats are susceptible. This equilibrium corresponds to the point $A = (N, 0)$ of the original system (1). It shows

the ideal situation in which the virus is eradicated and the goats are all healthy.

Differentiating equation (4) with respect to $y(t)$ and evaluating the result at equilibrium, we find $(\gamma\theta_E - 1)m < 0$, showing the local asymptotic stability of this point.

Note that the probability of vertical transmission of genotype E θ_E does not affect the stability of the equilibrium. Also the behaviour of the farmer does not modify it: whether newborns are removed from their mothers or not, the system evolves toward a situation where all the goats will be healthy and no longer affected by the virus.

The difference between whether or not to adopt a sanitary strategy to prevent the spread of the disease is the speed with which the equilibrium is reached, as we can see from Figure 1. Since the natural mortality m is the reciprocal of the average reproductive life of a goat, about 10 years, we set $m = 0.1$. In the first frame we take $\gamma = 0.1$, saying that the farmer adopts a removal strategy, while in the second one $\gamma = 0.9$, expressing the fact that no strict sanitary measures are implemented. In the first case the equilibrium is reached faster.

3. Model of a Genotype B-Affected Goat Breeding

We now consider a frequency-dependent model of a breeding only in the presence of the CAEV virus genotype B. Recall that it is pathogenic and characterized by a long period of incubation, followed by a progressive chronic course. We partition the total population of the breeding $N(t)$ into three classes: $S(t)$, as before, the number of susceptible goats, the asymptomatic goats infected by B, $I_a(t)$ and the symptomatic infected goats $I_s(t)$.

We make the following assumptions:

- every goat which belongs to the class $S(t)$ is equally susceptible,
- genotype B of the lentivirus is transmitted both in a horizontal and vertical way,
- there is a period of incubation of the virus whereby some goats are infected but they do not show any symptoms.

Taking into account these assumptions, we can describe the dynamics of a breeding in the presence of genotype B of the virus CAEV using the

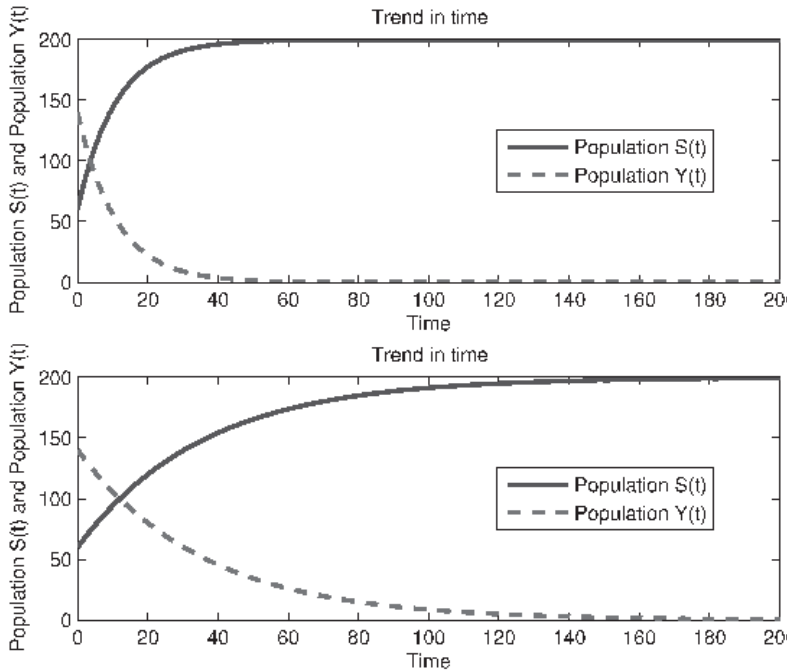

Figure 1. Populations trend $S(t)$ and $Y(t)$ of a breeding which starts with 60 healthy goats, 140 infected by E and values of parameters $a = 0.073$, $r = 1.368$, $m = 0.1$, $\theta_E = 0.8$, $N = 200$. In the first graph $\gamma = 0.1$ while in the second $\gamma = 0.9$.

following frequency-dependent model:

$$\frac{dS(t)}{dt} = \left[(1-\gamma) + \gamma\left(1 - \theta_B \frac{I_a(t)+I_s(t)}{N(t)}\right)\right] arN(t) - mS(t) - \beta S(t)\frac{I_a(t)+I_s(t)}{N(t)}, \tag{5}$$

$$\frac{dI_a(t)}{dt} = \theta_B \frac{I_a(t)+I_s(t)}{N(t)}\gamma arN(t) + \beta S(t)\frac{I_a(t)+I_s(t)}{N(t)} - (\delta+m)I_a(t),$$

$$\frac{dI_s(t)}{dt} = \delta I_a(t) - \mu I_s(t).$$

The first equation represents the dynamics of the susceptible. The newborns come into this class because they are either removed from their mothers and raised in an isolated breeding, or are not immediately removed but they do not contract the virus. The parameter $0 < \theta_B < 1$ as θ_E, represents

the probability of vertical transmission of the genotype B, assuming there has been a contact between the newborn and the infected mother. The last term models the horizontal transmission of the virus, β represents the product of the contact rate between susceptible and infected individuals and the probability of horizontal transmission.

The second equation describes the dynamics of the asymptomatic infected goats. The first term represents the newborns which have not been removed from the breeding, $\gamma arN(t)$, have taken milk from an infected mother, $\frac{I_a(t)+I_s(t)}{N(t)}\gamma arN(t)$, and have been infected, $\theta_B\frac{I_a(t)+I_s(t)}{N(t)}\gamma arN(t)$. The second term accounts for the new infected goats via horizontal transmission; the third term models individuals leaving this class because of either progression to symptomatic disease, at rate δ, or natural mortality.

Finally, the last equation represents the dynamics of the symptomatic infected, the first term accounting the new individuals that enter this class via progression to symptomatic disease, the second one describing natural plus disease-related mortality rate μ.

Simplifying (5) we get

$$\begin{aligned}
\frac{dS(t)}{dt} &= \left(1-\gamma\theta_B\frac{I_a(t)+I_s(t)}{N(t)}\right)arN(t) - mS(t) - \beta S(t)\frac{I_a(t)+I_s(t)}{N(t)},\\
\frac{dI_a(t)}{dt} &= \gamma\theta_B ar(I_a(t)+I_s(t)) + \beta S(t)\frac{I_a(t)+I_s(t)}{N(t)} - (\delta+m)I_a(t),\\
\frac{dI_s(t)}{dt} &= \delta I_a(t) - \mu I_s(t).
\end{aligned}$$

We reformulate the model with the total population $N(t)$. Then, easily:

$$\frac{dN(t)}{dt} = (ar-m)N(t) - (\mu-m)I_s(t). \tag{6}$$

We also consider as new variables the prevalence of the asymptomatic and of the symptomatic individuals $i_a(t) = I_a(t)N(t)^{-1}$ and $i_s(t) = I_s(t)N(t)^{-1}$, to get

$$\begin{aligned}
\frac{d}{dt}i_a(t) = (\gamma\theta_B-1)ari_a(t) + \gamma\theta_B ari_s(t) + (\mu-m)i_a(t)i_s(t) \\
+\beta(i_a(t)+i_s(t))\left[1-(i_a(t)+i_s(t))\right] - \delta i_a(t).
\end{aligned} \tag{7}$$

and

$$\frac{d}{dt}i_s(t) = \delta i_a(t) - (ar+\mu-m)i_s(t) + (\mu-m)i_s(t)^2. \tag{8}$$

The system is made then by equations (6), (7) and (8).

Again, because of the limited resources of the farms, the total population is usually kept at a constant value. From now on we then set $N(t) = N$, the fixed size of the breeding. From the steady state of (6), recalling that $\mu > m$, we determine a,

$$a_{path} = \tfrac{m}{r} + \tfrac{\mu - m}{r} i_s(t) = a_{farm} + \tfrac{\mu - m}{r} i_s(t) > a_{farm}. \tag{9}$$

Thus to keep the total number of goats constant, when a breeding is affected by genotype B, more offsprings must be raised than for a disease-free farm. Also, the replacement rate is directly proportional to the symptomatic infected prevalence: the higher the latter, the more newborns need to be kept in the breeding. We then substitute the replacement rate (9) in (7) and (8) to get the reduced size system:

$$\begin{aligned} \frac{d}{dt} i_a(t) &= (\gamma\theta_B(\mu - m) - \beta) i_s(t)^2 + (\gamma\theta_B(\mu - m) - 2\beta) i_a(t) i_s(t), \\ &\quad + (\gamma\theta_B m - m + \beta - \delta) i_a(t) + (\gamma\theta_B m + \beta) i_s(t) - \beta i_a(t)^2, \\ \frac{d}{dt} i_s(t) &= \delta i_a(t) - \mu i_s(t). \end{aligned} \tag{10}$$

3.1. *Equilibria*

The system's equilibria are the origin $O = (0, 0)$ and the point

$$C = (i_a^C, i_s^C) = \left(\frac{\mu[(\mu + \delta)(\gamma\theta_B m + \beta) - \mu(\delta + m)]}{(\mu + \delta)[\beta(\mu + \delta) - \gamma\delta\theta_B(\mu - m)]}, \frac{\delta}{\mu} i_a^C \right). \tag{11}$$

As $1 = s(t) + i_a(t) + i_s(t)$, the dynamics of (10) evolves entirely in the standard unit simplex $\Sigma = \left\{ (i_a^C, i_s^C) : i_a^C \geq 0, i_s^C \geq 0, i_a^C + i_s^C \leq 1 \right\}$ with vertices given by the origin and the two unit points on the coordinate axes. Hence the equilibrium C is feasible if and only if it lies in Σ, i.e. each component is nonnegative and $i_a^C + i_s^C \leq 1$.

First of all, we study under what conditions i_a^C and i_s^C are nonnegative. Since $i_s^C = \delta\mu^{-1} i_a^C \geq 0$, we need to analyze only i_a^C, studying separately the signs of the numerator and of the denominator.

3.1.1. *Nonnegativity of the numerator of* i_a^C

We begin to study where the numerator of i_a^C is nonnegative rewriting it in terms of the sanitary strategy parameter for the removal of newborns from their mothers $0 < \gamma < 1$:

$$\gamma \geq \frac{\mu(\delta + m) - \beta(\mu + \delta)}{\theta_B m(\mu + \delta)} = \frac{\mu(\delta + m)}{\theta_B m(\mu + \delta)} - \frac{\beta}{\theta_B m} \equiv X_0. \tag{12}$$

First of all, there are two immediate cases: if the right hand side in (12) is nonpositive, the condition is trivially satisfied, while if it is larger than one, (12) is never true. We study then the situations in which (12) is essential. For the right hand side of (12) being positive, we have

$$\beta < \tfrac{\mu(\delta+m)}{\mu+\delta} \equiv X_1, \tag{13}$$

while the right hand side of (12) smaller than one implies

$$\beta \geq \tfrac{\mu(\delta+m)-\theta_B m(\mu+\delta)}{\mu+\delta} = \tfrac{\mu(\delta+m)}{\mu+\delta} - \theta_B m \equiv X_2 \geq 0, \tag{14}$$

where the right hand side is always nonnegative since it reduces to $\mu m(1-\theta_B)+\delta(\mu-\theta_B m) \geq 0$, which is always verified because $0 < \theta_B < 1$ and $\mu > m$. We choose to perform the analysis in terms of the parameter β. Comparing (13) and (14), we immediately observe that $X_2 \leq X_1$, ensuring a nonempty intersection of the solution sets of these inequalities. Therefore, only the three following cases can arise:

- $0 < \beta < X_2$: the condition (12) is impossible by (14), thus the numerator is negative;
- $X_2 \leq \beta < X_1$: the numerator is nonnegative under the condition (12);
- $\beta \geq X_1$: (12) is always true by (13), thus the numerator is always nonnegative.

3.1.2. *Positivity of the denominator of* i_a^C

Now we seek the values of $0 < \gamma < 1$ for which the denominator of i_a^C is positive:

$$\gamma < \tfrac{\beta(\mu+\delta)}{\delta\theta_B(\mu-m)} \equiv X_3, \tag{15}$$

where $\mu - m > 0$. Thus if the right hand side exceeds one, (15) holds unconditionally. This occurs if:

$$\beta > \tfrac{\delta\theta_B(\mu-m)}{\mu+\delta} \equiv X_4. \tag{16}$$

Note that the inequality $X_4 < X_2$ holds because it reduces to $\mu\theta_B(\delta+m) \leq \mu(\delta+m)$ which is always true because $\theta_B < 1$. Thus the solution sets of the inequalities (16) and (14) have a nonempty intersection.

3.1.3. *Non-negative numerators and positive denominators of* i_a^C *and* i_s^C

In summary, i_a^C and i_s^C, both the components of the equilibrium C are nonnegative if:

(i) $X_2 \leq \beta \leq X_1$ whenever (12) holds;
(ii) $\beta \geq X_1$ for any γ.

3.1.4. *Nonpositive numerators and negative denominators of* i_a^C *and* i_s^C

In this situation the opposite conditions as discussed above hold. We find that i_a^C and i_s^C are nonnegative only if $\beta < X_4$, under the following condition:

$$\gamma > X_3. \tag{17}$$

3.1.5. *Non-negativity of the components of the equilibrium*

Summarizing these first results for feasibility of the equilibrium C, we have that the two components of C are nonnegative, $i_a^C \geq 0$ and $i_s^C \geq 0$, in the following cases:

- if $\beta < X_4$, under the condition (17);
- if $X_4 \leq \beta < X_1$ under the condition (12);
- otherwise, for $\beta \geq X_1$ for any value of γ.

3.1.6. *Sum of the components smaller than or equal to one*

To complete the analysis we must ensure that the coexistence equilibrium lies in the unit simplex. Thus we assess for which values of γ we have $i_a^C + i_s^C \leq 1$. Observe that this sum is equivalent to:

$$\frac{(\mu+\delta)(\gamma\theta_B m+\beta)-\mu(\delta+m)}{\beta(\mu+\delta)-\gamma\delta\theta_B(\mu-m)} \leq 1. \tag{18}$$

The denominator is positive if (15) holds, i.e. if (16) holds. In such case (18) reduces to $\mu(m+\delta)(\gamma\theta_B - 1) \leq 0$, which is always true because both $0 < \gamma, \theta_B < 1$.

Assume now that the denominator of (18) is negative. This leads to the opposite inequality $\mu(m+\delta)(\gamma\theta_B - 1) \geq 0$, which is impossible because again $\gamma\theta_B < 1$.

3.1.7. *Feasibility of C*

We can thus conclude that:

- if $X_2 \leq \beta < X_1$ the equilibrium C is feasible if and only if (12) holds.
- if $\beta > X_1$ the equilibrium C is feasible for any value of γ.

3.1.8. *Interpretation*

From this result we gather that for low values of the horizontal transmissibility β the coexistence equilibrium is not feasible. For intermediate values of the contact rate β, namely between X_2 and X_1, the stationary point exists under the condition (12). This implies that not too strict sanitary strategies are used to prevent the spread of the disease. Finally, for values of β larger than X_1, the equilibrium C is always feasible, even if hygienic measures are taken to contain the virus.

We can try and find an estimate for the values of β that characterize the feasibility conditions of the equilibrium C. We know that $m = 0.1$ while we can approximate the mortality μ with 0.8, 0.9 or 1. In fact this parameter is very high because the farmer slaughters immediately an infected symptomatic goat. The latter indeed represents an economic burden for his breeding. Moreover, we assume δ equal to 0.2, 0.3, 0.4 or 0.5, recalling that this parameter indicates the rate at which asymptomatic individuals become symptomatic. We choose this range of values because they describe the period of incubation that varies between 2 and 5 years. Indeed the value of the parameter is the reciprocal of the age of the goats when the symptoms appear for the first time. The graphs in Figure 2 show some possible values for the quantity $\beta = X_2$, with respect to the variations of the probability θ_B of vertical transmission of genotype B, for which we do not know an exact estimate, as well as for θ_E, and for the constant $\beta = X_1$. There is little difference between all the frames. But we report them anyway because we want to show the results for different parameter values. In particular, observe the three areas in different colors. With respect to the variations of the probability θ_B, the white one represents the values of β for which the equilibrium C does not exist, the dark grey one the values of β for which the stationary point is feasible under the condition (12), while the light grey the values of β for which C exists without imposing any other condition on the parameter γ. The first one indicates the range for which the epidemics can be successfully fought. The dark grey area represents the situation in which the farmer's behavior is fundamental on the disease outcome. The last one instead shows the parameter values for which the disease remains endemic in spite of any hygienic measures that can be taken. Observe that the higher the value of δ is, i.e. the earlier the symptoms appear, the greater the white area will be, with the result that for a wider range of values of β the equilibrium C is not feasible. This is good, because as stated above the disease in such cases can be eradicated.

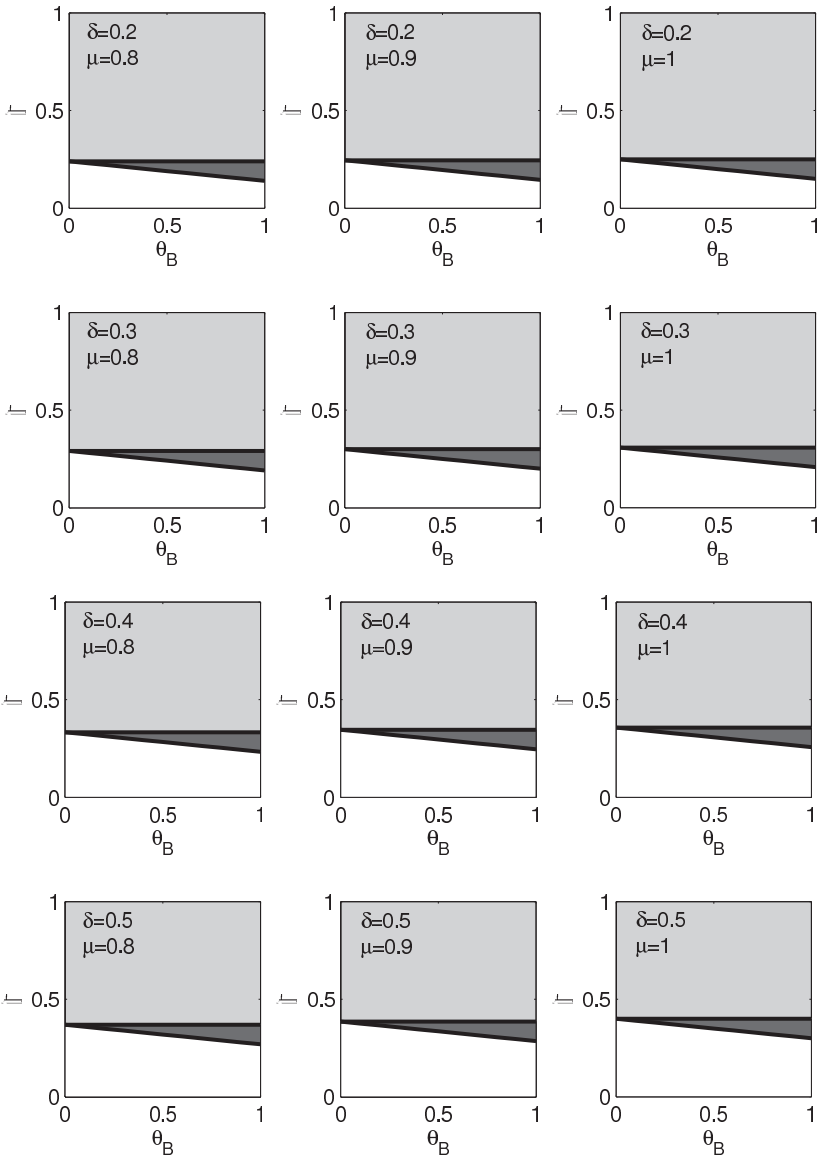

Figure 2. Estimates of the quantities $\beta = \frac{\mu(\delta+m)}{\mu+\delta} - \theta_B m$ and $\beta = \frac{\mu(\delta+m)}{\mu+\delta}$ with respect to the variations of θ_B for different values of δ and μ.

Note also that the dark grey region is small, which implies that instead only for a little range of values of β the farmer can take some measures to contain the disease.

In field situations, many breedings have been discovered to harbor the genotype B, an indication of the fact that β might be large. Figure 2 shows clearly that the parameter region for which the farmer can effectively act taking measures to prevent the disease to spread is very narrow, they light grey area in anyone of these frames. This explains the observation made of the very high occurrence of genotype B in breedings. As a consequence, the strategy of removing newborns from their mothers to fight the disease is clearly insufficient to free the breeding from the virus.

We have shown that if $X_2 < \beta < X_1$ the equilibrium C is feasible if and only if the condition (12) is verified. In this case note that if β coicides with the midpoint of the interval $[X_2, X_1]$, $X_0 = 0.5$. If β is equal to the value corresponding to the point which is located at one fourth of the very same interval, then $X_0 = 0.75$. In general, we have the following result.

Proposition 1. In general, if β is equal to the value corresponding to the point which is at $\frac{1}{k}$ of the interval $[X_2, X_1]$, then $X_0 = \frac{k-1}{k}$.

Proof If we take:

$$\begin{aligned}\beta &= \frac{\mu(\delta+m)}{\mu+\delta} - \theta_B m + \frac{1}{k}\left[\frac{\mu(\delta+m)}{\mu+\delta} - \frac{\mu(\delta+m)}{\mu+\delta} + \theta_B m\right] \\ &= \frac{\mu(\delta+m)}{\mu+\delta} + \left(\frac{1}{k} - 1\right)\theta_B m = \frac{\mu(\delta+m)}{\mu+\delta} + \frac{(1-k)\theta_B m}{k} \\ &= \frac{k\mu(\delta+m) + \theta_B m(\mu+\delta)(1-k)}{k(\mu+\delta)},\end{aligned}$$

then

$$\begin{aligned}X_0 &= [\mu(\delta+m) - \frac{k\mu(\delta+m) + \theta_B m(\mu+\delta)(1-k)}{k(\mu+\delta)}(\mu+\delta)][\theta_B m(\mu+\delta)]^{-1} \\ &= [\mu(\delta+m) - \frac{k\mu(\delta+m)}{k} - \frac{\theta_B m(\mu+\delta)(1-k)}{k}][\theta_B m(\mu+\delta)]^{-1} \\ &= -\frac{\theta_B m(\mu+\delta)(1-k)}{k\theta_B m(\mu+\delta)} = -\frac{1}{k}(1-k) = \frac{k-1}{k}.\end{aligned}$$

So in this situation, the smaller the value of β is, the larger the value of γ will be needed to make the equilibrium feasible. Thus if the farmer adopts a strategy to avoid the spread of the disease, i.e. γ small, the stationary coexistence point will not exist, even if this measure is not too

strict. Viceversa, the larger the value of β is, the smaller the value of X_0. Consequently, the more severe the strategies to preserve the breeding are, the larger is the probability to make the equilibrium not feasible.

3.2. *Stability*

The Jacobian of the system (10) is:

$$J = \begin{pmatrix} J_{11} & J_{12} \\ \delta & -\mu \end{pmatrix},$$

where $J_{11} = -2\beta i_a + (\gamma\theta_B(\mu - m) - 2\beta)i_s + \gamma\theta_B m - m + \beta - \delta$ and $J_{12} = (\gamma\theta_B(\mu - m) - 2\beta)i_a + 2(\gamma\theta_B(\mu - m) - \beta)i_s + \gamma\theta_B m + \beta$.

3.2.1. *Stability of O*

The characteristic equation at the origin is $\lambda^2 - \mathrm{tr}(J_{|O})\lambda + \det(J_{|O}) = 0$. From the Routh Hurwitz criterion, the origin is locally asymptotically stable, if $-\mathrm{tr}(J_{|O}) > 0$ and $\det(J_{|O}) > 0$. For the former we obtain

$$\gamma < \frac{m-\beta+\delta+\mu}{\theta_B m}. \tag{19}$$

We now study the right hand side, recalling that if it is negative (19) is impossible and if it is larger than one (19) becomes trivially true. The condition must instead be satisfied if the right hand side lies between 0 and 1. The former yields

$$\beta < m + \mu + \delta \equiv X_5, \tag{20}$$

while the second case gives

$$\beta > m(1 - \theta_B) + \mu + \delta \equiv X_6. \tag{21}$$

These bounds are consistent, $X_5 < X_6$, giving a nonempty intersection, because $0 < \theta_B < 1$. In summary, for the condition on the trace, we have:

- if $\beta \leq X_6$, then $-\mathrm{tr}(J_{|O}) > 0$ is always verified,
- if $X_6 < \beta < X_5$, then $-\mathrm{tr}(J_{|O}) > 0$ is true under (19),
- if $\beta \geq X_5$, then (19) is impossible so that $-\mathrm{tr}(J_{|O}) \leq 0$ always.

As far as the second condition of the Routh Hurwitz criterion is concerned, we have $\det(J_{|O}) = \mu(m + \delta) - \gamma\theta_B m(\mu + \delta) - \beta(\mu + \delta) > 0$ giving

$$\gamma < X_0. \tag{22}$$

This is the opposite condition (12), hence:

- $0 < \beta \leq X_2$ implies $\det(J_{|O}) > 0$ is always verified;
- if $X_2 < \beta < X_1$ then $\det(J_{|O}) > 0$ is true if (22) holds;
- $\beta > X_1$ implies that (22) is impossible, thus $\det(J_{|O}) \leq 0$ always.

We need now to merge the two Routh Hurwitz conditions. First of all, observe that $X_1 < X_6$, because it reduces to $0 \leq \mu(\mu - \theta_B m) + \delta m(1 - \theta_B) + \delta\mu + \mu^2$, always true in view of $m < \mu$ and $\theta_B < 1$. Thus the origin, which is the disease-free equilibrium, is asymptotically stable if:

- $\beta \leq X_2$ independently of γ;
- $X_2 < \beta < X_1$ if (22) holds.

In these above two situations it is possible to eradicate the disease. In the first one the parameter β is low and this is the reason whereby we can reach a virus-free point. In the second case, for values of $\beta \in [X_2, X_1]$, to obtain stability of the origin we have to impose a condition on the parameter γ, (22), which states that the lower the value of γ is, meaning a better isolation of newborns from their mothers, the larger the probability of the eradication of the disease. In fact γ is the only parameter that we can modify: once the characteristics of the breeding, in particular the natural mortality m, and of the disease are known, namely θ_B, β, δ and μ, a decision can be made on whether a sanitary strategy should be applied to avoid the spread of the virus or conversely if it is not possible to eradicate the disease. Further, in the latter case, the value of X_0 depends on the position of β in the interval $[X_2, X_1]$: the closer the value of β is to the right endpoint of the interval, the more severe the sanitary strategy should be so as to make the origin stable, i.e. to eradicate the disease.

Observe also that if the condition (22), which is always satisfied if the origin is stable, is true, the coexistence equilibrium point C will not be feasible. Conversely, if the latter is feasible, the origin is unstable and the disease cannot be eradicated from a breeding in which the virus is present. Mathematically, this also shows the existence of a transcritical bifurcation between the two equilibria.

3.2.2. *Stability of C*

Also in this case we use the Routh Hurwitz criterion. Consider first $\det(J_{|C}) > 0$; it gives

$$-\mu[-2\beta i_a^C + (\gamma\theta_B(\mu - m) - 2\beta)i_s^C + \gamma\theta_B m - m + \beta - \delta]$$
$$-\delta[(\gamma\theta_B(\mu - m) - 2\beta)i_a^C + 2(\gamma\theta_B(\mu - m) - \beta)i_s^C + \gamma\theta_B m + \beta] > 0.$$

It follows:

$$[\beta(\delta+\mu)-\gamma\delta\theta_B(\mu-m)](i_a^C+i_s^C)+\beta(\delta+\mu)(i_a^C+i_s^C)$$
$$-\gamma\theta_B(\mu-m)(\mu+\delta)i_s^C-\gamma\mu\theta_B m+\mu m-\beta\mu+\delta\mu-\gamma\delta\theta_B m-\beta\delta>0.$$

Using the population values at equilibrium, (11), we obtain

$$\frac{1}{\beta(\mu+\delta)-\gamma\delta\theta_B(\mu-m)}\left\{\beta(\mu+\delta)^2(\gamma\theta_B m+\beta)-\beta\mu(\delta+m)(\mu+\delta)\right.$$
$$\left.+\gamma\delta\mu\theta_B(\mu-m)(\delta+m)-\gamma\delta\theta_B(\mu-m)(\mu+\delta)(\gamma\theta_B m+\beta)\right\}>0,$$

which gives

$$\gamma>X_0, \tag{23}$$

and this coincides with condition (12), which is always satisfied by the feasibility of the point, and it is opposite to the condition (22), which guarantees the stability of the origin as seen in the previous Subsection.

We now analyze the first condition, $-\mathrm{tr}(J_{|C})=-J_{11}^C+\mu>0$ which becomes:

$$\mu-[-2\beta i_a^C+(\gamma\theta_B(\mu-m)-2\beta)i_s^C+\gamma\theta_B m-m+\beta-\delta]>0\ .$$

Again in view of the population values (11) we get

$$\{(\mu+\delta)[\beta(\mu+\delta)-\gamma\delta\theta_B(\mu-m)]\}^{-1}\left\{2\beta(\mu+\delta)^2(\gamma\theta_B m+\beta)\right.$$
$$-2\beta\mu(\mu+\delta)(\delta+m)+[\beta(\mu+\delta)^2-\gamma\delta\theta_B(\mu+\delta)(\mu-m)][m+\mu+\delta$$
$$\left.-\gamma\theta_B m-\beta]-\gamma\theta_B(\mu-m)[\delta(\mu+\delta)(\gamma\theta_B m+\beta)-\delta\mu(\delta+m)]\right\}>0.$$

The denominator of this expression is always positive in view of the feasibility condition (15). We thus study the sign of the numerator:

$$\beta\gamma\theta_B m(\mu+\delta)^2-\gamma\delta\theta_B(\mu-m)[(\mu+\delta)(m+\mu+\delta)-\mu(\delta+m)]$$
$$>2\beta\mu(\mu+\delta)(\delta+m)-\beta^2(\mu+\delta)^2-\beta(\mu+\delta)^2(m+\mu+\delta)$$

which gives

$$\gamma\theta_B[\beta m(\mu+\delta)^2+\delta(m-\mu)(\mu^2+\delta(m+\mu)+\delta^2)]$$
$$>-\beta(\mu+\delta)[\beta(\mu+\delta)+\mu(\mu-m)+\delta(\delta+m)].$$

Now, if

$$\beta>\frac{\delta(\mu-m)[\mu(\mu+\delta)+\delta(m+\delta)]}{m(\mu+\delta)^2}\equiv X_7, \tag{24}$$

then the inequality $-\mathrm{tr}(J_{|C})>0$ will be verified under the condition:

$$\gamma>\frac{-\beta(\mu+\delta)[\beta(\mu+\delta)+\mu(\mu-m)+\delta(\delta+m)]}{\theta_B\left\{\beta m(\mu+\delta)^2+\delta(m-\mu)[\mu(\mu+\delta)+\delta(m+\delta)]\right\}}\equiv\psi, \tag{25}$$

otherwise, if (24) is not true, it will be verified under the condition:

$$\gamma < \psi. \tag{26}$$

We can immediately observe that the condition (25) is always satisfied. In fact recall that $0 < \gamma < 1$; the denominator of the fraction is positive, in view of (24). But the numerator is negative because $\mu > m$, hence the fraction is negative and thus (25) is always satisfied for every value of γ.

We cannot conclude anything about the condition (26). We know that ψ is positive, because both the numerator and the denominator are negative. However, we do not know with certainty if (26) is always satisfied. This can happen if $\psi > 1$.

To conclude the study of the stability of C, it is necessary to compare X_7 in (24), with the quantities X_2 and X_1 that appear in the feasibility conditions of C, see the beginning of Section 3.1.7. There are three possibilities.

(I) The first one is $0 < X_7 < X_2 < X_1$. In this case, β exceeds X_7 in view of the feasibility conditions of the equilibrium C recalled above; if the stationary point C exists, then it will be asymptotically stable, because as we have said before, (25) is always true. So,

- if $\frac{\mu(\delta+m)}{\mu+\delta} - \theta_B m \leq \beta < \frac{\mu(\delta+m)}{\mu+\delta}$, C will be feasible and asymptotically stable under the condition (12,
- if $\beta \geq \frac{\mu(\delta+m)}{\mu+\delta}$, C will be feasible and asymptotically stable for every value of γ.

(II) The second possibility is $0 < X_2 < X_7 < X_1$. In this situation there are also three cases:

- $X_2 \leq \beta < X_7$: the equilibrium C is feasible if the parameter γ satisfies (12) and it will be asymptotically stable if γ satisfies (26). Hence to obtain the stability of the point, it is necessary to have:

  $$X_0 < \gamma < \psi, \tag{27}$$

  therefore the right hand side of the condition (12) must be smaller than the right hand side of the condition (26), but we will see in Lemma 2 below that this is always the case;
- $X_7 < \beta < X_1$: if the condition (12) is verified, the equilibrium will be both feasible and asymptotically stable;
- $\beta \geq X_1$: the equilibrium exists and it is asymptotically stable independently of γ.

(III) The third possibility is $0 < X_2 < X_1 < X_7$. Also in this situation we have three cases:

- $X_2 \leq \beta < X_1$: C is feasible under the condition (12) and it is asymptotically stable if (26) holds, i.e. if and only if γ verifies (27);
- $X_1 \leq \beta < X_7$: the stationary point exists for every value of γ. Hence, if this parameter satisfies (26), C is asymptotically stable;
- $\beta > X_7$: the equilibrium exists and it is asymptotically stable independently of γ.

We need to prove that condition (27) can indeed be obtained.

Lemma 2 The inequality $X_0 < \psi$ holds unconditionally.

Proof Extensively, the claim becomes

$$\frac{\mu(\delta+m)-\beta(\mu+\delta)}{\theta_B m(\mu+\delta)} < \frac{-\beta(\mu+\delta)[\beta(\mu+\delta)+\mu(\mu-m)+\delta(\delta+m)]}{\theta_B\{\beta m(\mu+\delta)^2+\delta(m-\mu)[\mu(\mu+\delta)+\delta(m+\delta)]\}}.$$

Some easy algebraic steps lead to

$$\begin{aligned}\beta(\mu+\delta)(\delta+m)[\mu m(\mu+\delta)+\mu(\mu+\delta)(\mu-m)+\delta^2(\mu-m)\\ +\delta m(\mu+\delta)] > \delta\mu(\mu-m)(\delta+m)[\mu(\mu+\delta)+\delta(m+\delta)]\end{aligned}$$

from which we then have

$$\beta > \frac{\delta(\mu-m)}{\mu+\delta} \equiv X_8.$$

This inequality has to be true in two situations: in the second possibility seen before for $X_2 \leq \beta < X_7$ and in the third possibility, for $X_2 \leq \beta < X_1$. We show now that $X_8 < X_2$. Extensively,

$$\frac{\delta(\mu-m)}{\mu+\delta} < \frac{\mu(\delta+m)-\theta_B m(\mu+\delta)}{\mu+\delta}$$

from which

$$\delta\mu-\delta m < \delta\mu+\mu m-\mu\theta_B m-\delta\theta_B m$$

and finally

$$\mu m(1-\theta_B)+\delta m(1-\theta_B) > 0,$$

which is always true because $0 < \theta_B < 1$. We have thus proved the claim.

3.2.3. *Discussion*

The position of X_7 with respect to X_2 and X_1 controls the stability of the coexistence equilibrium C.

Using the range of values chosen before for μ and δ, the first one ranging between 0.1 and 0.8 while the second one between 0.2 and 0.5, taking $m = 0.1$, we plot the surface $z = X_7 - \mu(\delta + m)(\mu + \delta)^{-1}$ as function of μ and δ in Figure 3. The surface lies always above the plane $z = 0$, so that X_7 is always larger than X_1, showing that we are in the third possibility (III) above, namely $0 < X_2 < X_1 < X_7$.

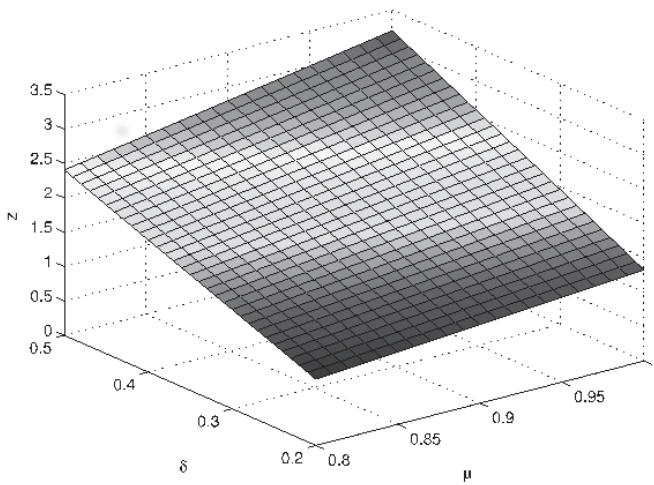

Figure 3. Surface $z = X_7 - \frac{\mu(\delta+m)}{\mu+\delta}$ as function of μ and δ, with $m = 0.1$.

To assess the asymptotic stability of the point C, we need to study if (26) is true. To verify the condition we plot the surface ψ as function of θ_B and β. We consider four situations, where $m = 0.1$, μ is always equal to 0.9 and δ assumes the values 0.2, 0.3, 0.4 and 0.5. From Figure 4 we observe that the surface $\psi(\theta_B, \beta)$ lies always above the plane $\psi = 1$ thereby showing that the condition (26) is always satisfied, which guarantees the stability of the equilibrium. Observe that the range of the parameter β starts from a value larger than zero, because the stationary point C is feasible only if $\beta > X_2$. Thus we are sure to represent the surface from the minimum value that this parameter can assume. Therefore if the equilibrium C exists, it is asymptotically stable.

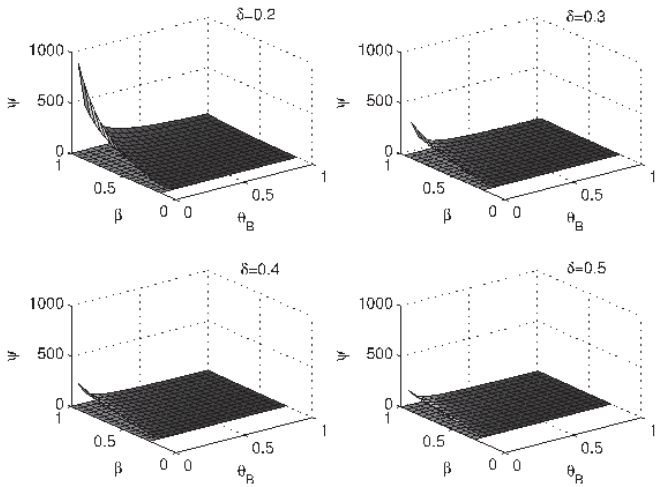

Figure 4. Surface ψ as function of θ_B and β, for $m = 0.1$, $\mu = 0.9$ and different values of δ.

The behaviour of the system is summarized in the following Table 1, that shows the occurrence of the transcritical bifurcation.

Table 1. Equilibria of the system (10) for a breeding affected by genotype B of the virus CAEV.

Condition	O	C	Bifurcation
$\gamma < \frac{\mu(\delta+m)}{\theta_B m(\mu+\delta)} - \frac{\beta}{\theta_B m}$	Stable	Infeasible	
$\gamma = \frac{\mu(\delta+m)}{\theta_B m(\mu+\delta)} - \frac{\beta}{\theta_B m}$			Transcritical
$\gamma > \frac{\mu(\delta+m)}{\theta_B m(\mu+\delta)} - \frac{\beta}{\theta_B m}$	Unstable	Stable	

3.3. *Global stability of the equilibria*

Following the steps outlined in Ref. 2, we can prove the global asymptotic stability of both equilibria, O and C, whenever they are feasible and locally asymptotically stable.

The trajectories are bounded, since they are confined in the unit simplex Σ and its boundaries cannot be crossed in view of the existence and

uniqueness theorem. No cycles can exist either, since by Dulac's theorem, if we consider the following function $B(i_a, i_s) = (i_a i_s)^{-1}$ and evaluating

$$K = \frac{\partial}{\partial i_a}\left[B(i_a, i_s)\frac{di_a}{dt}\right] + \frac{\partial}{\partial i_s}\left[B(i_a, i_s)\frac{di_s}{dt}\right] =$$
$$-\frac{\gamma\theta_B(\mu - m)\, i_s}{i_a^2} - \frac{\gamma\theta_B m}{i_a^2} - \frac{\beta(1 - i_s)}{i_a^2} - \frac{\beta}{i_s} - \frac{\delta}{i_s^2} < 0,$$

in view of the fact that $i_s \leq 1$. When either O or C are stable, since no periodic orbit exists in Σ, the Poincaré-Bendixson theorem guarantees the global asymptotic stability of the equilibrium.

4. Conclusions

We have presented and investigated two models for CAEV-affected goat breedings, assuming that in each one of them only one specific genotype is present. As for genotype B, this is the most common situation found in reality. The far less diffused genotype E is found only in some specific geographic areas, but goats infected by it show no symptoms. In such case sanitary measures are not necessary to render the farm disease-free.

Although in principle it is possible that the genotype B can also be eradicated from a breeding, in practice this is much more difficult, as there are situations in which in spite of the farmer's behavior, the disease will remain endemic. In general, the most likely scenario is that the virus cannot be eradicated. Only for a small parameter range, corresponding to the white areas in the frames of Figure 2, the environment becomes disease-free. The choice of removing newborns from their infected mothers and wean them in a separate environment does therefore appear insufficient as a means to fight the disease.

On the other hand, the situation in which only one genotype is present is likely, but could also not be true in practice. Breedings in which the two genotypes considered here mix together are certainly present in the areas in which the most geographically restricted genotype thrives. The latter could also be spread accidentally or intentionally in confining areas. Therefore the interesting question arises as to how such breedings will evolve in time and what the fate of the disease will be. Such an issue will be addressed in a forthcoming investigation.

Acknowledgments

The project was partially supported by the projects "Metodi numerici in teoria delle popolazioni" and "Metodi numerici nelle scienze applicate" of

the Dipartimento di Matematica “Giuseppe Peano” of the Università di Torino.

References

1. M. J. Keelin, P. Rohani, *Modeling Infectious Disease in humans and animals*, Princeton University Press, (2007).
2. M. Pittavino, L. Ferreri, M. Giacobini, L. Bertolotti, S. Rosati, E. Venturino, *Applied Mathematics and Computation* **227**, 156 (2014).
3. N. Stonos, S. K. Wootton, N. Karrow, *Viruses* **6**(8), 3311 (2014).
4. R. Reina, D. de Andrés and B. Amorena, *Viruses* **5**(8), 1948 (2013).
5. J. C. Minardi da Cruz, D. K. Singh, A. Lamara, Y. Chebloune, *Viruses* **5**(7), 1867 (2013).
6. H. Ramírez, R. Reina, B. Amorena, D. de Andrés, H. A. Martínez, *Viruses* **5**(4), 1175 (2013).
7. Associazione nazionale della pastorizia Roma, *Le razze ovine e caprine in Italia*, Roma, PrimeGraf, 2002.
8. http://www.istitutospallanzani.it/doc/220.eps
9. http://www.capre.it

CONSERVATION OF FORESTRY BIOMASS INTRODUCING VARIABLE TAXATION FOR HARVESTING: A MATHEMATICAL MODEL*

M. CHAUDHARY, J. DHAR

ABV-Indian Institute of Information Science and Technology, Gwalior, 474015, India
E-mail: manisha@iiitm.ac.in, jdhar@iiitm.ac.in

O. P. MISRA

Jiwaji University, Gwalior, 474010, India
E-mail: misra_op58@yahoo.co.in

A conservation model is proposed and analyzed for an age structured forestry biomass exploited by Industrialization. The age structured forestry biomass and Industrialization is considered as dynamic variable. Industries can only harvest the semi-mature and mature trees. Variable taxation works as the control instrument for the excess utilization of forestry biomass by industries. The dynamic behavior of the system is established using the theory of differential equation. Numerical simulation is carried out to support the analytical results. Sensitivity analysis of the parameters is also carried out for all feasible equilibrium points using a normalized forward sensitivity index. A detailed analysis of the proposed model leads to understand how the taxation works toward the conservation of the forestry resource.

1. Introduction

There has been considerable interest in the modeling of harvesting of biological resources such as a fishery in recent decades, where harvest effort is considered to be a dynamic variable, and optimal harvesting policies with taxation are discussed[1,2,3,4,5,6,7,8]. The optimal tax policies for harvesting of the prey predator system is studied in Ref. 9. A proper taxation policy which give best possible benefit through harvesting to community while

*This work is supported by Department of Science and Technology.

preventing the extinction of the predator is discussed in Ref. 10. Understanding and management of renewable natural resources covers various areas such as agriculture, fishery and forestry are a very complex problem as they linked to the sustainability of the underlying natural system. Regulation of renewable resources such as forestry and fishery is an important problem that required serious attention to be paid. Taxation, license fees, lease of property rights, seasonal harvesting, fishing period control, creating reserve zones, etc. can be used as possible control instruments. In fishery resource management, some investigations have been carried out with taxation as a control instrument[6]. Understanding the mechanisms that influence the growth of population and their existence and stability is mathematical modeling of ecosystem. Models come in every size and form, from verbal descriptions and mathematical equations to large scale computer models and the feature that is common to all in the life and social sciences is that they all constitute abstractions and simplifications of the real world. The book mathematical bioeconomics: The mathematics of conservation by Clark[11] is all about the response of individual harvesters to different kinds of harvesting regulations, harvesting efforts, economic incentives, etc., in fishery and forestry.

Both expanding human populations and industrial drivers of deforestation, such as logging and exotic tree plantations, are important drivers of forest loss. Countries with rapid population growth and little surviving forest are also plagued by endemic corruption and low average living standards[12]. Population pressure augmented industrialization deplete forestry resources[13]. In this study it is assumed that even if the population growth (caused by intrinsic growth or migration) is only partially dependent on the resource, the resource biomass are doomed to extinction caused by an increase in population density and population pressure augmented industrialization. The depletion of forest resources caused by population and the corresponding population pressure is studied in Ref. 14, it is assumed that the cumulative density of forest resources and the density of populations follow logistic models with prey-predator type nonlinear interaction terms and it is considered that the carrying capacity of forest resources decreases by population pressure, they also proposed a conservation model to control the population pressure by providing some economic incentives to people. A mathematical model for the conservation of the forestry resource with the growth of alternative (synthetic) industries is studied in Ref. 15 and later, the same study is extended to a delay age structure population model[16]. A multi-criteria framework to address the sustainable

management in industrial forest plantations has been studied in Ref. 17.

Research based on optimal control of renewable resources like fisheries is studied by many researchers, but no one has given attention to the optimal control of forestry resources, from this research we have tried to focus on the optimal control of forestry resources. In the present study an age structured forestry biomass is considered to conserve the forestry biomass together with industrialization as the state variable, responsible for the exploitation of forest biomass, for the same we have taken taxation as the control parameter responsible for over exploitation. Through this paper, we have obtained the criteria for local and global stability of the system. The control problem is formulated and the corresponding optimal equilibrium level of effort I_δ and tax τ_δ is also described.

2. Model Description

We have considered an age structured forestry biomass as pre-mature, semi-mature and mature trees and it is assumed that semi mature and mature forestry trees are harvested by industrialization with the following modeling assumptions:

(1) Age structured forestry biomass, i.e., pre-mature (P), semi-mature (S) and mature trees (M).
(2) Pre-mature trees grow logistically with fixed growth rate and carrying capacity and also there are some government efforts to conserve the same by new plantation.
(3) Semi-mature and mature trees are harvested by the industrialization with different harvesting rates.
(4) Natural wash out rates of semi-mature trees and mature trees are different.
(5) Tax applied on industrialization depends upon the amount of harvesting of semi-mature and mature trees.
(6) Tax to harvest semi-mature trees are higher than that of mature trees.
(7) Level of efforts to harvest semi-mature and mature trees are different.
(8) Increase or decrease in industrialization depends on the harvesting rate of semi-mature and mature trees.
(9) Cost per unit of semi-mature and mature trees are also different.

Schematic diagram for the system is shown in Fig. 1.

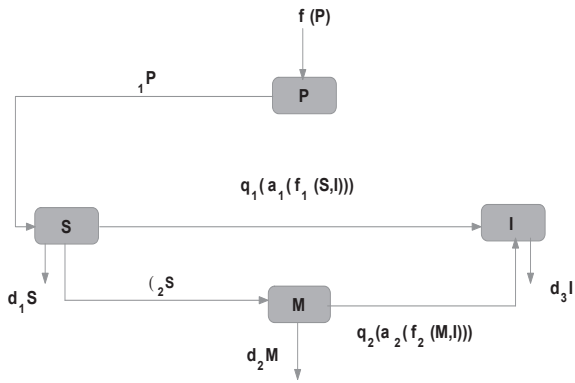

Figure 1. Schematic Diagram.

The conceptual model for the schematic diagram shown in Fig. 1, will be discussed in Section 3 and description of parameters for the system is given in Table 1:

Table 1. Description of parameters.

Parameter	Description
r	intrinsic growth rate of premature trees
k	carrying capacity of forestry biomass
γ	new plantation
β_1	transition rate from pre-mature to semi-mature
β_2	transition rate from semi-mature to mature trees
c_1, c_2	cost per unit of effort expanded to harvest forestry biomass
q_1, q_2	depletion rates of semi-mature and mature trees
p	unit price for harvesting of semi-mature and mature trees
d_1, d_2	natural depletion rates of forestry biomass
d_3	depletion in industrialization by government efforts
a_1, a_2	per unit efforts to harvest trees
τ_1, τ_2, τ_3, τ_4	tax applied for the conservation of forest

3. Conceptual Model: System of Differential Equation

An age-structured, i.e., premature trees (P), semi-mature trees (S), mature trees (M) forestry biomass with Industrialization (I) as a dynamical variables are considered to study the mathematical model. For this, we assumed that Industrialization is wholly depends on semi-mature and mature trees of the forest biomass. In Fig. 1, $f(P)$ is the function of premature

trees and is a combination of its logistic growth and new plantation, defined as $f(P) = rP\left(1-\frac{P}{k}\right)+\gamma P$, similarly $f_1(S,I)$ is the function of semi-mature trees and industrialization, $f_1(S,I) = (a_1(q_1p-\tau(q_1)S)-c_1)$ and $f_2(M,I)$ is function of mature trees and industrial effort, $f_2(M,I) = a_2(M(q_2p-\tau(q_2))I$. According to the schematic flow diagram (see Fig. 1), we formulated the system with the help of following ordinary differential equations:

$$\frac{dP}{dt} = rP\left(1-\frac{P}{k}\right)-\beta_1 P+\gamma P, \tag{1}$$

$$\frac{dS}{dt} = \beta_1 P - q_1 SI - \beta_2 S - d_1 S, \tag{2}$$

$$\frac{dM}{dt} = \beta_2 S - q_2 MI - d_2 M, \tag{3}$$

$$\frac{dI}{dt} = [\{(a_1(q_1p-\tau(q_1)S)-c_1)+a_2(M(q_2p-\tau(q_2))-c_2)\}-d_3]I \tag{4}$$

where $P(0) \geq 0$, $S(0) \geq 0$, $M(0) \geq 0$, $I(0) \geq 0$. Here in this paper we have considered variable taxation which depends on the harvesting of semi-mature and mature forestry populations and defined accordingly, i.e., the taxation to harvest semi-mature trees are higher than that of the mature trees and also taxation is a function of harvesting for both semi-mature and mature trees. For example:

Case 1: When harvesting is below 15% there is no tax for semi-mature and mature trees.

Case 2: When harvesting is between 15% to 40% the tax applied to semi-mature and mature trees are τ_1 and τ_2 respectively.

Case 3: When harvesting is above 40% the tax applied to semi-mature and mature trees are τ_3 and τ_4 respectively. In the next section, we will check the dynamic behavior of the system.

4. Dynamical Behavior of the System

4.1. *System boundedness*

System (1)–(4) is bounded with region of attraction

$$\Omega = \{(P,S,M,I)\epsilon R_+^4 : 0 \leq P+S+M \leq \frac{m}{\theta}, 0 \leq I \leq \frac{\rho}{\xi}\},$$

attract all solutions initiating in the interior of positive orthant. For first three age structured forestry biomass equations (1)–(3), let us consider a time dependent function $W = P + S + M$. Clearly,

$$\frac{dW}{dt} = \frac{dP}{dt} + \frac{dS}{dt} + \frac{dM}{dt}. \tag{5}$$

Using equations (1)–(3) in the above expression (5) with a little algebra, we obtain

$$\frac{dW}{dt} \leq rP\left(1 - \frac{P}{k}\right) + cP + \gamma P - \theta(P + S + M),$$

where θ is chosen as the minimum of $\{c, d_1, d_2\}$.

$$\frac{dW}{dt} + \theta W(t) \leq \frac{(r + c + \gamma)^2 k}{4r} = m(say).$$

As $t \to \infty, 0 \leq W(t) \leq \frac{m}{\theta}$, later using above result in (4), we have

$$\frac{dI}{dt} \leq (a_1 q_1 + a_2 q_2) p \frac{m}{\theta} - a_1 c_1 I - a_2 c_2 I - d_3 I,$$

substituting $\xi = a_1 c_1 I - a_2 c_2 I - d_3$ and $\rho = (a_1 q_1 + a_2 q_2) p \frac{m}{\theta}$, we get

$$\frac{dI}{dt} + \xi I \leq \rho,$$

as $t \to \infty, 0 \leq I(t) \leq \frac{\rho}{\xi}$. Hence the system (1)–(4) is bounded.

4.2. *Equilibrium analysis*

The proposed system has three biological feasible equilibria, equilibria for all the three cases are defined below

4.2.1. *Equilibrium analysis (Case 1)*

(1) The trivial case, i.e., E_0=(0, 0, 0, 0), existence of trivial case is obvious and hence omitted.

(2) Non-trivial case $\bar{E} = (\bar{P}, \bar{S}, \bar{M}, 0)$ when forestry biomass exist and industrialization does not exist, here $\bar{P} = \frac{k(r+\gamma-\beta_1)}{r}$; $\bar{S}$=$\frac{k\beta_1(r+\gamma-\beta_1)}{r(d_1+\beta_2)}$; $\bar{M}$= $\frac{k\beta_1\beta_2(r+\gamma-\beta_1)}{rd_2(d_1+\beta_2)}$ and the non-trivial case exists when $r + \gamma > \beta_1$.

(3) Interior equilibrium E^*=(P^*, S^*, M^*, I^*) all the state variable co-exist, where $P^* = \frac{k(r+\gamma-\beta_1)}{r}$; $S^* = \frac{z_1}{(q_1 I^* + \beta_2 + d_1)}$;

$M^* = \frac{\beta_2 z_1}{(q_1 I^* + \beta_2 + d_1)(q_2 I^* + d_2)}$ and I^* is given by the root of the quadratic equation

$$Z_1 I^{*2} + Z_2 I^* + Z_3 = 0,$$

where z_1, z_2, Z_1, Z_2, Z_3 is given as:

$z_1 = \frac{\beta_1 k(r-\beta_1+\gamma)}{r}, \quad z_2 = (a_1 c_1 + a_2 c_2), \quad Z_1 = z_2 q_1 q_2,$
$Z_2 = z_2\beta_2 q_2 + z_2 q_1 d_2 + d_1 q_2 z_2 - a_1 q_1 z_1 q_2,$
$Z_3 = z_2\beta_2 d_2 + d_1 d_2 z_2 - a_1 q_1 p z_1 d_1 - a_2 q_2 p z_1 \beta_2.$

Existence of S^* and M^* depends on I^*, when I^* is positive real i.e., $Z_3 < 0$ which implies $z_2(\beta_2 d_2 + d_1 d_2) < z_1(a_1 q_1 p d_2 + a_2 q_2 p \beta_2)$. Hence, the interior equilibrium $E^*=(P^*, S^*, M^*, I^*)$ exists only when $r + \gamma > \beta_1$ and $Z_3 < 0$.

4.2.2. *Equilibrium analysis (Case 2)*

(1) The trivial case, i.e., $E_0=(0, 0, 0, 0)$, existence of trivial case is obvious and hence omitted.
(2) Non-trivial case $\bar{E} = (\bar{P}, \bar{S}, \bar{M}, 0)$ when forestry biomass exist and industrialization does not exist, here $\bar{P} = \frac{k(r+\gamma-\beta_1)}{r}$; $\bar{S}=\frac{k\beta_1(r+\gamma-\beta_1)}{r(d_1+\beta_2)}$; $\bar{M}= \frac{k\beta_1\beta_2(r+\gamma-\beta_1)}{rd_2(d_1+\beta_2)}$ and the non-trivial case exists when $r + \gamma > \beta_1$.
(3) Interior equilibrium $E^*=(P^*, S^*, M^*, I^*)$ all the state variable co-exist, where $P^* = \frac{k(r+\gamma-\beta_1)}{r}$; $S^* = \frac{z_1}{(q_1 I^* + \beta_2 + d_1)}$; $M^* = \frac{\beta_2 z_1}{(q_1 I^* + \beta_2 + d_1)(q_2 I^* + d_2)}$ and I^* is given by the root of the quadratic equation

$$Z_1 I^{*2} + Z_2 I^* + Z_3 = 0,$$

where z_1, z_2, Z_1, Z_2, Z_3 is given as:

$z_1 = \frac{\beta_1 k(r-\beta_1+\gamma)}{r}, \quad z_2 = (a_1 c_1 + a_2 c_2), \quad Z_1 = z_2 q_1 q_2,$
$Z_2 = z_2\beta_2 q_2 + z_2 q_1 d_2 + d_1 q_2 z_2 - a_1 q_1 z_1 q_2 (p - \tau_1),$
$Z_3 = z_2\beta_2 d_2 + d_1 d_2 z_2 - a_1 q_1 (p - \tau_1) z_1 d_1 - a_2 q_2 (p - \tau_2) z_1 \beta_2.$

Now, S^* and M^* exists when I^* is positive real i.e., $Z_3 < 0$ which implies $z_2(\beta_2 d_2 + d_1 d_2) < z_1(a_1 q_1 (p-\tau_1) d_2 + a_2 (p-\tau_2) q_2 \beta_2)$. Hence, the interior equilibrium $E^*=(P^*, S^*, M^*, I^*)$ exists only when $r + \gamma > \beta_1$ and $Z_3 < 0$.

Equilibriums for case 3 is similar as in the case 2 (replace τ_1 by τ_3 and τ_2 by τ_4).

Next we find local and global stability of the interior equilibrium points in case 1, case 2 and case 3.

4.3. *Local stability*

To find the local stability of the system we first find the Jacobian corresponds to the system (1)–(4)

$$J = \begin{bmatrix} a_{11} & 0 & 0 & 0 \\ a_{21} & a_{22} & 0 & a_{24} \\ 0 & a_{32} & a_{33} & a_{34} \\ 0 & a_{42} & a_{43} & a_{44} \end{bmatrix},$$

where $a_{11}=-r+\gamma-\beta_1-\frac{2P^*r}{k}$, $a_{21}=\beta_1$, $b_{22}=-d_1-I^*q_1-\beta_2$, $b_{24}=-S^*q_1$, $a_{32}=\beta_2$, $a_{33}=-d_2-I^*q_2$, $a_{24}=-M^*q_2$, $a_{42}=I^*pa_1q_1$, $a_{43}=I^*pq_2a_2$, $a_{44}=-d_3+a_1(-c_1+S^*pq_1+a_2(-c_2+M^*pq_2)$ for case 1.

4.3.1. *Case 1:*

The characteristic equation corresponding to the Jacobian for case 1 is defined as

$$\lambda^4 + A_{11}\lambda^3 + A_{12}\lambda^2 + A_{13}\lambda + A_{14} = 0.$$

Here, $A_{11}=\frac{rP^*}{k}+d_1+d_2+q_1I^*+q_2I^*+\beta_2$, $A_{12}=\frac{rd_1P^*}{k}+\frac{rd_2P^*}{k}+d_1d_2+\frac{rq_1P^*I^*}{k}+q_1d_2I^*+pa_1q_1^2S^*I^*+\frac{rq_2P^*I^*}{k}+d_1q_2I^*+q_1q_2I^{*2}+pa_2q_2^2M^*I^*+\frac{r\beta_2P^*}{k}+d_2\beta_2+q_2\beta_2I^*$, $A_{13}=\frac{P^*rd_1d_2}{k}+\frac{P^*I^*rd_2q_1}{k}+\frac{I^*pP^*rS^*a_1q_1^2}{k}+I^*pS^*a_1d_2q_1^2+\frac{I^*P^*rd_1q_2}{k}+\frac{I^{*2}P^*q_1q_2}{k}+I^{*2}pq_1^2q_2S^*+\frac{I^*MjpP^*ra_2q_2^2}{k}+I^*M^*pa_2d_1q_2^2+I^2M^*pa_2q_1q_2^2+\frac{P^*rd_2\beta_2}{k}+\frac{I^*P^*ra_2\beta_2}{k}+I^*pS^*a_2q_1q_2\beta_2+I^*M^*pa_2q_2^2\beta_2$ and $A_{14}=\frac{I^*}{k}(pra_1d_2q_1^2P^*S^*+ra_1q_1^2q_2P^*S^*+ra_2pd_1q_2^2P^*M^*+ra_2q_1q_2^2P^*M^*I^*+pra_2q_1q_2\beta_2P^*S^*+ra_2q_2^2\beta_2pP^*M^*$.

Applying Routh-Hurwitz criteria, the system is locally asymptotically stable as all the co-efficient of the characteristic equation are positive. Since price is always greater than the tax, $A_{11}>0$, $A_{12}>0$, $A_{13}>0$ and $A_{14}>0$, also

$$A_{11}A_{12}A_{13} - A_{13}^2 - A_{11}^2A_{14} > 0.$$

Thus we can say that interior equilibrium is locally asymptotically stable for case 1.

4.3.2. *Case 2:*

In case 2 the characteristic equation is

$$\lambda^4 + B_{11}\lambda^3 + B_{12}\lambda^2 + B_{13}\lambda + B_{14} = 0.$$

Here, $B_{11}=\frac{rP^*}{k}+\frac{\beta_1P^*}{S^*}+\frac{S^*\beta_2}{M^*}$, $B_{12}=I^*(p-\tau_1)a_1q_1^2S^*+I^*M^*(p-\tau_2)a_2q_2^2+\frac{P^{*2}r\beta_1}{kM^*}+\frac{P^*\beta_1\beta_2}{M^*}$, $B_{13}=\frac{I^*(p-\tau_1)P^*rS^*a_1q_1^2}{k}+\frac{I^*M^*(p-\tau_2)P^*ra_2q_2^2}{k}+$

$\frac{I^*M^*(p-\tau_2)P^*a_2q_2^2\beta_1}{S^*} + \frac{I^*(p-\tau_1)S^{*2}a_1q_1^2\beta_2}{M^*} + I^*(p-\tau_2)S^*a_2q_1q_2\beta_2 + \frac{P^{*2}r\beta_1\beta_2}{kM^*}$ and $B_{14} = \frac{I^*}{k}(\frac{(p-\tau_2)I^*M^*P^{*2}ra_2q_2^2\beta_1}{S^*} + \frac{(p-\tau_1)P^*rS^{*2}a_1q_1^2\beta_2}{M^*} + (p-\tau_2)P^*rS^*a_2q_1q_2\beta_2$.

Again applying Routh-Hurwitz criteria, the system is locally asymptotically stable as all the co-efficient of the characteristic equation are positive. As we have assumed price is always greater than the tax, $B_{11} > 0$, $B_{12} > 0$, $B_{13} > 0$ and $B_{14} > 0$, also

$$B_{11}B_{12}B_{13} - B_{13}^2 - B_{11}^2B_{14} > 0.$$

Remark: Analysis for the local stability of the system in case 3 is same as in the case 2.

4.4. *Global stability*

To prove the global stability of the system in case 1 first we consider a positive definite Lyapunov function

$$V = \left(P - P^* - P^* \ln \frac{P}{P^*}\right) + \frac{m_1}{2}(S-S^*)^2 + \frac{m_2}{2}(M-M^*)^2 + \left(I - I^* - I^* \ln \frac{I}{I^*}\right).$$

Differentiating above equation, doing some mathematical manipulation and choosing, $m_1 = \frac{a_1p}{S^*}$, $m_2 = \frac{q_2p}{M^*}$, we have

$$\begin{aligned}\frac{dV}{dt} \leq & -\frac{r}{k}(P-P^*)^2 + \left(\frac{a_1p}{S^*}\right)\beta_1(P-P^*)(S-S^*) \\ & - \left(\frac{a_1p}{S^*}\right)(\beta_2+d_1)(S-S^*)^2 - \left(\frac{q_2p}{M^*}\right)d_2(M-M^*)^2 \\ & + \left(\frac{q_2p}{M^*}\right)\beta_2(S-S^*)(M-M^*). \end{aligned} \tag{6}$$

Conditions for $\frac{dV}{dt}$ to be negative definite are:

$$(i) \quad 2r(\beta_2+d_1) > m_1\beta_1^2k \quad \text{and}$$

$$(ii) \quad 2m_1(\beta_2+d_1) > m_2\beta_2^2.$$

Interior equilibrium is globally stable under the above two conditions for case 1.

In case 2 we choose the same positive definite function and doing the same calculation as for case 1. In case 2 choosing $m_1 = \frac{a_1(p-\tau_1)}{S^*}$ and $m_2 = \frac{a_2(p-\tau_2)}{M^*}$ we will get the following two conditions for the global stability of case 2.

$$(i) \quad 2r(\beta_2+d_1) > m_1\beta_1^2k \quad \text{and}$$

$$(ii) \quad 2m_1(\beta_2+d_1) > m_2\beta_2^2.$$

Hence the interior equilibrium is globally stable under the above two conditions for case 2.

Remark: Similarly for case 3 choosing $m_1=\frac{a_1(p-\tau_3)}{S^*}$ and $m_2=\frac{a_2(p-\tau_4)}{M^*}$ We can say that the interior equilibrium is globally stable for case 3.

5. Optimal Harvesting Policy

For optimal harvesting, we have used the Pontryagin's maximum principle. Q is the continuous time stream of revenues and is defined by

$$Q = \int_0^\infty e^{-\delta t}\pi(P, S, M, I, \tau, t)dt, \tag{7}$$

where δ as the instantaneous rate of annual discount. Thus, our objective is to maximize Q subject to the equations (1)–(4) and the control constraints

$$0 \le \tau \le \tau_{1max} \text{ and } 0 \le \tau \le \tau_{2max}. \tag{8}$$

Hamiltonian for the control problem is defined as:

$$\begin{aligned} H = {} & e^{-\delta t}[pq_1a_1S + pq_2a_2M - c_1a_1 - c_2a_2]I + \lambda_1(t)[rP\left(1-\frac{P}{k}\right) - \beta_1P + \gamma P] \\ & + \lambda_2(t)[\beta_1P - q_1SI - b_2S - d_1S] + \lambda_3(t)[\beta_2S - q_2MI - d_2M] \\ & + \lambda_4(t)[[\{(a_1(q_1S(p-\tau_1) - c_1) + a_2(q_2M(p-\tau_2) - c2)\} - d_3]I]. \end{aligned} \tag{9}$$

The analysis for the optimal control is same as in Refs. 3 and 6 hence omitted. The values of λ_3, λ_2 and λ_1 are

$$\lambda_3 = \frac{b_{11}}{(a_{11}+\delta)}e^{-\delta t}, \quad \lambda_2 = \frac{b_{22}}{(a_{22}+\delta)}e^{-\delta t} \text{ and } \lambda_1 = \frac{b_{33}}{(a_{33}+\delta)}e^{-\delta t}, \tag{10}$$

where $a_{11} = \frac{\beta_2 S}{M}$, $b_{11} = pq_2a_2I$, $a_{22} = \frac{\beta_1 P}{S}$, $b_{22} = (\frac{b_{11}}{a_{11}+\delta}\beta_2 - pq_2a_2I)$, $a_{33} = \frac{rP\lambda_1}{k}$ and $b_{33} = (\frac{b_{22}}{a_{22}+\delta} + \frac{\beta_2 S}{M})$.

Singular path equation for the optimal control is defined as

$$-[pq_1a_1S+pq_2a_2M-c_1a_1-c_2a_2]e^{-\delta t}+q_1S\frac{b_{22}}{(a_{22}+\delta)}e^{-\delta t}+q_2M\frac{b_{11}}{(a_{11}+\delta)}e^{-\delta t} = 0. \tag{11}$$

Let $S^* = S_\delta$ and $M^* = M_\delta$ are the optimal equilibrium population. Optimal equilibrium level of industrial effort and tax are given respectively by

$$I_\delta = \frac{1}{q_2M_\delta}\left(\beta_2S_\delta - d_2M_\delta\right),$$

and

$$\tau_{1\delta} = \frac{pa_1q_1S_\delta + pa_2q_2M_\delta - a_1c_1 - a_2c_2 - a_2q_2\tau_2M_\delta - d_3}{(a_1q_1S_\delta)}.$$

We have found that $\lambda_1(t)e^{\delta t}$ and $\lambda_2(t)e^{\delta t}$ is independent of time in an optimum equilibrium. Hence, both $\lambda_2(t)$ and $\lambda_3(t)$ remains bounded as $t \to \infty$. From the analysis, it is clear that net economic revenue for the system is zero, i.e.,

$$\pi\left(S_\infty, M_\infty, I, \tau\right) = 0, \text{ when } \delta \to \infty.$$

In case of infinite discount rate, the economic rent is zero and hence both semi-mature and mature trees of forestry biomass remain unexploited. Over exploitation of forestry biomass, government may increase the tax and or discount rate to slow down or stop harvesting semi-mature and mature forestry trees.

Remark: Analysis of optimal control for case 3 is similar as in case 2.

6. Numerical Simulation

Source of parameter values used for numerical simulation is described in Table 2. Parameter values β is taken as β_1 and ϕ is taken here as d_3 for the system (1)–(4).

Table 2. Source of parameters.

Parameter	Case 1	Case 2	Case 3	Source
r	1.5	1.5	1.5	[15]
k	100	100	100	[6]
β_1	0.7	0.7	0.7	[15]
γ	0.03	0.03	0.03	assumed
q_1	0.15	0.4	0.5	assumed
β_2	0.3	0.3	0.3	assumed
d_1	0.25	0.25	0.25	assumed
q_2	0.15	0.4	0.5	assumed
d_2	0.1	0.1	0.1	assumed
a_1	0.01	0.01	0.01	assumed
p	0.5	0.5	0.5	[6]
$\tau(q_1)$	0	τ_1= 0.2	τ_3=0.3	assumed
$\tau(q_2)$	0	τ_2=0.15	τ_4=0.4	assumed
c_1	0.002	0.002	0.002	assumed
a_2	0.02	0.02	0.02	assumed
c_2	0.002	0.002	0.002	assumed
d_3	0.01	0.01	0.01	[14]

For the set of parameters described in Table 2, conditions for the existence of equilibrium are satisfied for case 1, 2 and 3. Graphical representation for different values of τ (depends upon the harvesting rate) are shown in Figs. 2, 3 and 4.

Using the same set of parameter as before in Table 2, just by imposing a tax (depends on the harvesting rate), we can see as the harvesting of the forestry resource increases the amount of tax increase and is shown in

Figs. 2, 3 and 4. We have also shown by Fig. 5 when the condition for the existence of interior equilibrium violate, no of the population can exist.

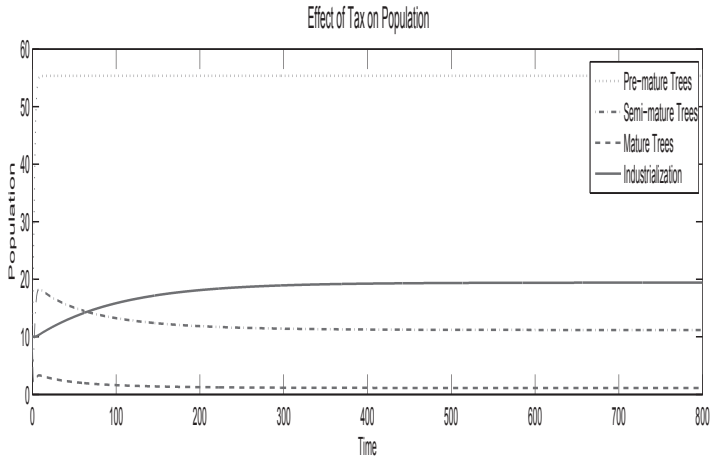

Figure 2. Population distributions with respect to the time when harvesting is below 15%.

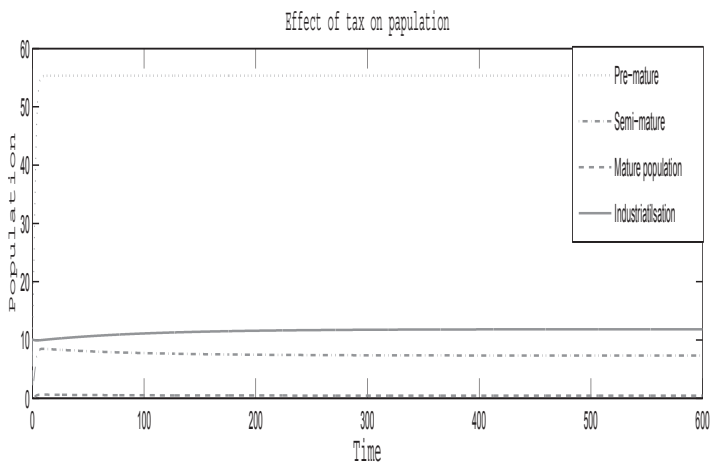

Figure 3. Population distributions with respect to the time when harvesting is between 15% to 40%.

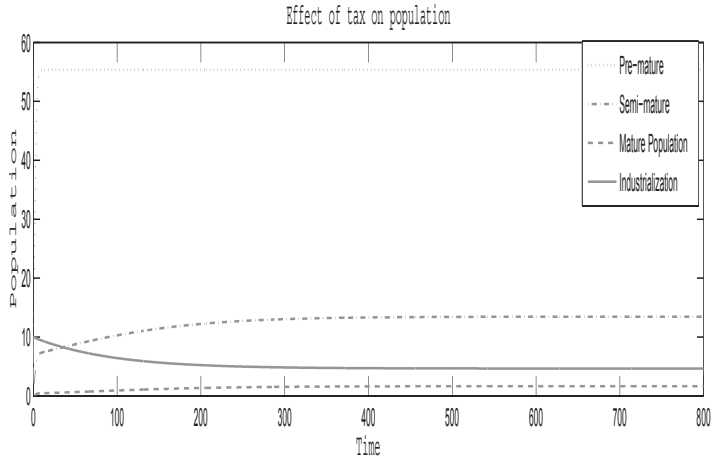

Figure 4. Population distributions with respect to the time when harvesting is above 40%.

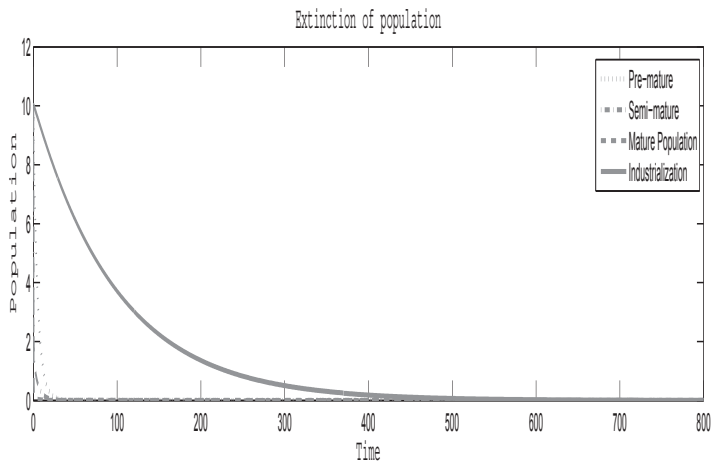

Figure 5. Extinction of population.

7. Sensitivity Analysis

We have used normalized forward sensitivity index to show the sensitivity of the interior equilibrium. For a detailed understanding of sensitivity analysis see Ref. 18.

Table 3. Sensitivity of Parameters.

Parameter (y_j)	$\gamma_{y_j}^{P^*}$	$\gamma_{y_j}^{S^*}$	$\gamma_{y_j}^{M^*}$	$\gamma_{y_j}^{I^*}$
r	0.807229	0.0979747	-0.677241	0.791575
k	1	0.121372	-0.83897	0.980607
β_1	-0.843373	0.01901	-0.131405	0.153589
γ	0.0361446	0.00438693	-0.0303242	0.0354436
q_1	0	-0.876333	-0.854833	-0.021954
β_2	0	-0.117929	0.815174	0.0683081
d_1	0	-0.00573733	0.0396587	-0.046354
q_2	0	-0.00229493	-0.984137	0.00256129
d_2	0	0.00229493	-0.0158635	-0.00256129
a_1	0	-0.765837	-1.6029	0.854725
p	0	-1.43794	-3.00961	1.60484
τ_1	0	0.511723	1.07104	-0.571116
τ_2	0	0.0475905	0.0996069	-0.0531141
c_1	0	0.00174678	0.003656	-0.00194952
a_2	0	-0.107551	-0.225104	0.120034
c_2	0	0.00349355	0.00731201	-0.00389903
d_3	0	0.873388	1.828	-0.974759

Sensitivity of interior equilibrium for case 2 is described in Table 3, from the analysis we have observed that:

(1) P^* is sensitive to parameters r and β_1.
(2) S^* is sensitive to β_2, d_3, q_1, τ_1, a_1 and a_2 and highly sensitive to p.
(3) M^* is sensitive to r, β_1, β_2, q_1, q_2, a_2, k and highly sensitive to p, d_3, a_1 and τ_1.
(4) I^* is sensitive to r, β_1, d_3, a_1, a_2, τ_1 and τ_2 and highly sensitive to p.

Similarly, we can find the sensitivity of parameter for case 1 and case 3.

8. Conclusions

The present paper is parted up in three cases. Initially we have considered an age structured forestry biomass (pre-mature, semi-mature, mature trees) with industrialization and we have considered that the taxation is wholly depends on the level of harvesting of semi-mature and mature forestry trees. **Case 1** when harvesting is below 15%, **Case 2** when harvesting is in between 15% to 40% and **Case 3** when harvesting is above 50%. Forestry resources are exploited by industries and conserve by applying taxation. We have discussed all the three cases, the stability of the system is established using the theory of differential equation. We have also obtained the singular path, optimal equilibrium levels of effort I_δ and tax τ_δ for optimal control. Figs. 2, 3 and 4 show the existence of interior equilibrium for all the three cases, extinction of all populations is also shown in 5 as the equilibrium condition violated.

Acknowledgment

The authors are thankful to Department of Science and Technology for their financial support File No. SR/WOS-A/MS-21/2013.

References

1. K. Chaudhuri, *Ecological Modelling.* **41, 1**, 17–25(1988).
2. T. Pradhan and K. S. Chaudhuri, *Ecological Modelling.* **121, 1**, 1–16 (1999).
3. B. Dubey, P. Sinha and P. Chandra, *Journal of Biological Systems.* **11, 1**, 27–41 (1995).
4. K. Chakraborty, M. Chakraborty and T. K. Kar, *Applied Mathematics and Computation.* **217, 21**, 287 (2011).
5. B. Dubey, A. Patra and S. K. Sahani, *Applications & Applied Mathematics.* **9, 2**, 4492 (2014).
6. B. Dubey and A. Patra, *Nonlinear Anal.* **18**, 37–52 (2013).
7. B. Dubey, A. Patra and R. K. Upadhayay, *Applications & Applied Mathematics.* **9, 1**, 217–245 (2014).
8. M. Chaudhary, J. Dhar and O. P. Misra, *Modeling Earth Systems & Environment.* **1, 4**, 1–10 (2015).
9. C. Lio, Q. Zhang and J. Li, *Abstract and Applied Analysis.* **2013**, (2013).
10. T. K. Kar, *Communications in Nonlinear Science and Numerical Simulation.* **10, 2**, 121–131 (2005).
11. C. W. Clark, *John Wiley & Sons.* **91**, (2010).
12. F. W. Laurance, *Current Science.* **93**, 1544–1550 (2007).
13. B. Dubey, S. Sharma, P. Sinha and J. B. Shukla, *Applied Mathematical Modelling.* **33, 7**, 3002–3014 (2007).
14. A. K. Misra and K. Lata, *Chaos, Solitons & Fractals.* **46**, 1–11 (2013).
15. M. Chaudhary, J. Dhar and G. P. Sahu, *International Journal of Biological Sciences.* **4**, 798–802 (2013).
16. M. Chaudhary and J. Dhar, *Engineering (NUiCONE), 2013 Nirma University International Conference on Engineering.* **86**, 1–5 (2013).
17. J. C. Gimenez, M. Bertomeu, B. Diaz and R. Luis,*Forest Ecology and Management.* **291**, 367–376 (2013).
18. N. Chitnis, J. M. Hyman and J. M. Cushing, *Bulletin of mathematical biology.* **70, 5**, 1272–1296 (2008).

STABILITY ANALYSIS OF A TWO SPECIES COMPETITION MODEL WITH FUZZY INITIAL CONDITIONS: FUZZY DIFFERENTIAL EQUATION APPROACH ENVIRONMENT

S. PAUL,* P. BHATTACHARYA
National Institute of Technology, Agartala,
Jiraniya- 799046,
Tripura, India
E-mail: paul.susmita14@gmail.com, pbhattacharya2001@yahoo.co.in

K. S. CHAUDHURI
Jadavpur University,
Kolkata- 700032,
West Bengal, India
E-mail: chaudhuriks@gmail.com

Having attracted much attention in the past few years, predator-prey system provides a good mathematical model to present the association among predators and preys. The novel concept of this paper is that the prey predator model is developed in fuzzy environment by considering the imprecise nature of the biological parameters. This paper explores stability analysis of this competition model with fuzzy initial conditions. Here we have used fuzzy generalized differentiable approach. We derived the model formulation of our stated model and discussed about Equilibrium points and their feasibility. The fuzzy solution and stability concepts are developed by prior numerical simulations.

1. Introduction

In the area of theoretical ecology the research was started by Lotka and Volterra. Though the first theoretical management of population dynamics was presented by Malthus and Verhulst formed a mathematical model based on logistic equation. The Lotka-Volterra model is an intervention competition model: two species are assumed to diminish each others per capita

*Work partially supported by grant 2-4570.5 of the Swiss National Science Foundation.

growth rate by direct intervention. The Lotka-Volterra model of intraspecific competition has been a useful starting point for biologists thinking about the outcomes of competitive interactions between species. The assumptions of the model (e.g., there can be no migration and the carrying capacities and competition coefficients for both species are constants) may not be very realistic, but are necessary simplifications. A variety of factors not included in the model can affect the outcome of competitive interactions by affecting the dynamics of one or both populations. Environmental change, disease, and chance are just a few of these factors.
Mathematical models of population growth have been formed [9] to provide an impalpable of some significant aspect of true ecological situation. The meaning of each parameter in the models has been defined biologically. Verhust first proposed three-parameter model for the growth of single-species populations that shows a logistic sigmoid growth curve for time. Pearl and reed independently expressed the same model, which cover mathematically an upper asymptote and a rate constant. The former and latter have been illustrated biologically as the carrying capacity of the environment and the intrinsic rate of natural increase in the population, respectively. The increasing study of realistic and effictively useful mathematical models in population biology, whether we are dealing with a human population with or without its age distribution, population of an endangered species, bacterial or viral growth and so on,is a reflection of their use in helping to understand the dynamic process involved and in making practical prediction.

In theoretical ecology the majority of the researchers have developed their models based on the assumption that the biological parameters are precisely known. But the scenario in reality is different. The values of all parameters cannot be always known precisely for the various reasons like - lack of data, lack of information, mistakes in the measurement process and determining the initial conditions. So, from this we may come to the conclusion that, to overcome the limitations of these models with imprecise parameters are more realistic and helpful.

Fuzzy set theory [11] is a powerful tool to overcome these problems. Initially, the derivative for fuzzy valued mappings was developed by [14], and generalized and extended the concept of Hukuhara differentiability for set-valued mappings to the class of fuzzy mappings. Subsequently, using the Hukuhara derivative, by [3, 5] started to develop a theory for FDE. But it soon appeared that the Hukuhara derivative has a shortcoming which fuzzifies the solution as time goes on. To overcome this situation in [1, 2]

the concept of strongly generalized derivative was introduced and in [7, 10, 13] this concept studied for higher order fuzzy differential equations. This concept, allows us to overcome the above mentioned shortcoming.

In this paper, we have considered a Triangular fuzzy prey-predator model (TFPPM). Here we have considered imprecise biological parameters for making the model more realistic and after Hukuhara differentiable we analysis the stability [8] of this model and obtain graphical solutions for the problem under consideration.

2. Model Formulations

Here we consider the following prey-predator model,

$$\begin{aligned} \frac{dx(t)}{dt} &= x(t)[r_1 - \tfrac{b_{11}}{k_1}x(t) - b_{12}y(t)] - q_1Ex(t) \\ \frac{dy(t)}{dt} &= y(t)[r_2 - \tfrac{b_{22}}{k_2}y(t) + b_{21}x(t)] - q_2Ey(t) \end{aligned} \tag{1}$$

Here $x(t)$ and $y(t)$ denote the population density of the rst species and the second species, respectively. Here r_i, k_i, b_{ij}, q_i $(i, j = 1, 2)$ are all positive constants and r_i are the intrinsic growth rate of prey and predator species respectively, k_i are the carrying capacity of prey and predator species respectively, $b_{ij}(i = j)$ are the coefficients of intraspecic competition of prey and predator species respectively, $b_ij(i \neq j)$ measure the degree to which the presence of species j affects the growth of species i. Then we fuzzify the linear part of [15] the system (1) by [4, 6] symmetric triangular fuzzy number and let $x(t)$, $y(t)$ are non negative fuzzy functions.
Therefore (1) becomes;

$$\begin{aligned} \frac{\widetilde{dx}(t)}{\widetilde{dt}} &= x(t)[\tilde{r}_1 - \tfrac{\tilde{b}_{11}}{\tilde{k}_1}x(t) - \tilde{b}_{12}y(t)] - q_1Ex(t) \\ \frac{\widetilde{dy}(t)}{\widetilde{dt}} &= y(t)[\tilde{r}_2 - \tfrac{\tilde{b}_{22}}{\tilde{k}_2}y(t) + \tilde{b}_{21}x(t)] - q_2Ey(t) \end{aligned} \tag{2}$$

with initial condition $\tilde{x}(t_0) = \tilde{x}_0, \tilde{y}(t_0) = \tilde{y}_0$.
The above fuzzy prey-predator model with combined harvesting can be represented using the concept of Hukuhara derivative by the following fuzzy differential equations

$$\begin{aligned}
\frac{dx_l(t,\alpha)}{dt} &= x_l(t,\alpha)[r_{1l} - \frac{b_{11r}}{k_1 r}x_r(t,\alpha) - b_{12r}y_r(t,\alpha) - q_1E] \\
\frac{dx_r(t,\alpha)}{dt} &= x_r(t,\alpha)[r_{1r} - \frac{b_{11l}}{k_1 l}x_l(t,\alpha) - b_{12l}y_l(t,\alpha) - q_1E] \\
\frac{dy_l(t,\alpha)}{dt} &= y_l(t,\alpha)[r_{2l} - \frac{b_{22r}}{k_2 r}y_r(t,\alpha) + b_{21l}x_l(t,\alpha) - q_2E] \\
\frac{dy_r(t,\alpha)}{dt} &= y_r(t,\alpha)[r_{2r} - \frac{b_{22l}}{k_2 l}y_l(t,\alpha) + b_{21r}x_r(t,\alpha) - q_2E]
\end{aligned} \tag{3}$$

with $(x(t_0))_\alpha = [x_{0l}(\alpha), x_{0r}(\alpha)], (y(t_0))_\alpha = [y_{0l}(\alpha), y_{0r}(\alpha)]$.

3. Equilibrium Points and Their Feasibility

3.1. *Trivial equilibrium*

Total extinction of all x_l, x_r, y_l, and y_r, i.e. $e_0(x_{l0}, x_{r0}, y_{l0}, y_{r0})$ where $x_{l0} = 0, x_{r0} = 0, y_{l0} = 0, y_{r0} = 0$ and it always feasible.

3.2. *Axial equilibrium*

System (3) gives an axial equilibrium point is $e_1(x_{l1}, x_{r1}, y_{l1}, y_{r1})$, where, $x_{l1} = \frac{k_{1l}(r_{1r} - Eq_1)}{b_{11l}}, x_{r1} = \frac{k_{1r}(r_{1l} - Eq_1)}{b_{11r}}, y_{l1} = 0, y_{r1} = 0$.
Here the axial equilibrium point $e_1(x_{l1}, x_{r1}, y_{l1}, y_{r1})$ is feasible if, $E < \frac{r_{1r}}{q_1}$ and $E < \frac{r_{1l}}{q_1}$. i.e. $E < min(\frac{r_{1r}}{q_1}, \frac{r_{1l}}{q_1})$.

3.3. *Coexistence equilibrium*

System (3) gives a coexistence equilibrium point $e^*({x_l}^*, {x_r}^*, {y_l}^*, {y_r}^*)$, where,
${x_l}^* = \frac{k_{1l}(b_{22l}r_{1r} - b_{12l}k_{2l}r_{2r} - Eb_{22l}q_1 + Eb_{12l}k_{2l}q_2)}{b_{11l}b_{22l} + b_{12l}b_{21l}k_{1l}k_{2l}}$,
${x_r}^* = \frac{k_{1r}(b_{22r}r_{1l} - b_{12r}k_{2r}r_{2l} - Eb_{22r}q_1 + Eb_{12r}k_{2r}q_2)}{b_{11r}b_{22r} + b_{12r}b_{21r}k_{1r}k_{2r}}$,
${y_l}^* = \frac{k_{2l}(b_{11l}r_{2r} + b_{21l}k_{1l}r_{1r} - Eb_{11l}q_2 - Eb_{21l}k_{1l}q_1)}{b_{11l}b_{22l} + b_{12l}b_{21l}k_{2l}k_{1l}}$,
${y_r}^* = \frac{k_{2r}(b_{11r}r_{2l} + b_{21r}k_{1r}r_{1l} - Eb_{11r}q_2 - Eb_{21r}k_{1r}q_1)}{b_{11r}b_{22r} + b_{12r}b_{21r}k_{2r}k_{1r}}$.
Now the coexistence equilibrium point $e^*({x_l}^*, {x_r}^*, {y_l}^*, {y_r}^*)$ is feasible, if

$$max(\frac{b_{12l}k_{2l}r_{2r} - b_{22l}r_{1r}}{b_{12l}k_{2l}q_2 - b_{22l}q_1}, \frac{b_{12r}k_{2r}r_{2l} - b_{22r}r_{1l}}{b_{12r}k_{2r}q_2 - b_{22r}q_1}) < E <$$

$$min(\frac{b_{21l}k_{1l}r_{1r} + b_{11l}r_{2r}}{b_{21l}k_{1l}q_1 + b_{11l}q_2}, \frac{b_{21r}k_{1r}r_{1l} + b_{11r}r_{2l}}{b_{21r}k_{1r}q_1 + b_{11r}q_2}).$$

4. Stability Analysis of TFPPM

In this section we discuss the Equilibrium points and their feasibility and at these Equilibrium points the local stabilities of the stated TFPPM.

We study local stability of the each equilibrium points of the TFPPM by calculating the variational matrix at the corresponding equilibrium points. The variational matrix of the system (3) is given by,

$$V = \begin{pmatrix} r_{1l}-Eq_1-B_r & \frac{-b_{11r}x_l}{k_{1r}} & 0 & -b_{12r}x_l \\ \frac{-b_{11l}x_r}{k_{1l}} & r_{1r}-Eq_1-B_l & -b_{12l}x_r & 0 \\ 0 & b_{21r}y_l & r_{2l}-Eq_2+C_r & -\frac{b_{22r}y_l}{k_{2r}} \\ b_{21l}y_r & 0 & -\frac{b_{22l}y_r}{k_{2l}} & r_{2r}-Eq_2+C_l \end{pmatrix}$$

where:

$B_r = b_{12r}y_r + \frac{b_{11r}x_r}{k_{1r}}$, $B_l = b_{12l}y_l + \frac{b_{11l}x_l}{k_{1l}}$

$C_r = b_{21r}x_r - \frac{b_{22r}y_r}{k_{2r}}$, $C_l = b_{21l}x_l - \frac{b_{22l}y_l}{k_{2l}}$

4.1.

Now, the variational matrix of system (3) at $e_0(x_{l0}, x_{r0}, y_{l0}, y_{r0})$ is given by

$$V(e_0) = \begin{pmatrix} r_{1l} - Eq_1 & 0 & 0 & 0 \\ 0 & r_{1r} - Eq_1 & 0 & 0 \\ 0 & 0 & r_{2l} - Eq_2 & 0 \\ 0 & 0 & 0 & r_{2r} - Eq_2 \end{pmatrix}$$

Therefore the eigen values of the characteristic equation of $V(e_0)$ are $\lambda_1 = r_{1l} - Eq_1, \lambda_2 = r_{1r} - Eq_1, \lambda_3 = r_{2l} - Eq_2, \lambda_4 = r_{2r} - Eq_2$. Now, e_0 become stable if $\lambda_1 < 0, \lambda_2 < 0, \lambda_3 < 0, \lambda_4 <$ 0.i.e. $r_{1l} - Eq_1 < 0, r_{1r} - Eq_1 < 0, r_{2l} - Eq_2 < 0, r_{2r} - Eq_2 < 0$. Which implies that $\frac{r_{1l}}{q_1} < E, \frac{r_{1r}}{q_1} < E, \frac{r_{2l}}{q_2} < E$ and $\frac{r_{2r}}{q_2} < E$. So we come to the following theorem,

Theorem 4.1: The trivial equilibrium $e_0(0, 0, 0, 0)$ of the system (3) is locally asymptotically stable if $E > max(\frac{r_{1l}}{q_1}, \frac{r_{1r}}{q_1}, \frac{r_{2l}}{q_2}, \frac{r_{2r}}{q_2})$.

4.2.

Now, the variational matrix of system (3) at $e_1(x_{l1}, x_{r1}, y_{l1}, y_{r1})$, is given by

$$V(e_1) = \begin{pmatrix} r_{1l}-Eq_1-\frac{b_{11r}x_{r1}}{k_{1r}} & \frac{-b_{11r}x_l 1}{k_{1r}} & 0 & -b_{12r}x_{l1} \\ \frac{-b_{11l}x_{r1}}{k_{1l}} & r_{1r}-Eq_1-b_{12l}y_l-\frac{b_{11l}x_{l1}}{k_{1l}} & -b_{12l}x_{r1} & 0 \\ 0 & 0 & r_{2l}-Eq_2+b_{21r}x_{r1} & 0 \\ 0 & 0 & 0 & r_{2r}-Eq_2+b_{21l}x_{l1} \end{pmatrix}$$

Therefore the eigen values of the characteristic equation of $V(e_1)$ are

$\lambda_1 = -\sqrt{(r_{1l} - Eq_1)(r_{1r} - Eq_1)}, \lambda_2 = \frac{b_{11r}r_{2l} - Eb_{11r}q_2 + b_{21r}k_{1r}r_{1l} - Eb_{21r}k_{1r}q_1}{b_{11r}}$,

$\lambda_3 = \sqrt{(r_{1l} - Eq_1)(r_{1r} - Eq_1)}, \lambda_4 = \frac{b_{11l}r_{2r} - Eb_{11l}q_2 + b_{21l}k_{1l}r_{1r} - Eb_{21l}k_{1l}q_1}{b_{11l}}$.

Here the eigen values λ_1 and λ_3 of $V(e_1)$ are pure complex conjugate root if either $(r_{1l} - Eq_1) < 0$ or $(r_{1r} - Eq_1) < 0$. So e_1 become stable if $\lambda_2 < 0$ and $\lambda_4 < 0$. i.e. $E > \frac{b_{11r}r_{2l}+b_{21r}k_{1r}r_{1l}}{b_{11r}q_2+b_{21r}k_{1r}q_1}, E > \frac{b_{11l}r_{2r}+b_{21l}k_{1l}r_{1r}}{b_{11l}q_2+b_{21l}k_{1l}q_1}$. So we come to the following theorem,

Theorem 4.2: The axial equilibrium $e_1(x_{l1}, x_{r1}, 0, 0)$ of the system (3) is locally asymptotically stable if either

(i) $\frac{r_{1l}}{q_1} < E$, (ii) $E > max(\frac{b_{11r}r_{2l}+b_{21r}k_{1r}r_{1l}}{b_{11r}q_2+b_{21r}k_{1r}q_1}, \frac{b_{11l}r_{2r}+b_{21l}k_{1l}r_{1r}}{b_{11l}q_2+b_{21l}k_{1l}q_1})$.

Or,

(iii) $\frac{r_{1r}}{q_1} > E$, (iv) $E < max(\frac{b_{11r}r_{2l}+b_{21r}k_{1r}r_{1l}}{b_{11r}q_2+b_{21r}k_{1r}q_1}, \frac{b_{11l}r_{2r}+b_{21l}k_{1l}r_{1r}}{b_{11l}q_2+b_{21l}k_{1l}q_1})$.

4.3.

Now, the variational matrix of system (3) at $e^*({x_l}^*, {x_r}^*, {y_l}^*, {y_r}^*)$, is given by

$$V(e^*) = \begin{pmatrix} 0 & \frac{-b_{11r}{x_l}^*}{k_{1r}} & 0 & -b_{12r}{x_l}^* \\ \frac{-b_{11l}{x_r}^*}{k_{1l}} & 0 & -b_{12l}{x_r}^* & 0 \\ 0 & b_{21r}{y_l}^* & 0 & \frac{-b_{22r}{y_l}^*}{k_{2r}} \\ b_{21l}{y_r}^* & 0 & \frac{-b_{22l}{y_r}^*}{k_{2l}} & 0 \end{pmatrix}$$

Therefore, the characteristic equation of $V(e^*)$ is given by $\lambda^4 + a_2\lambda^2 + a_4 = 0$ where, $a_1 = 0, a_3 = 0$,
$a_2 = -(\frac{b_{11l}b_{11r}{x_l}^*{x_r}^*}{k_{1l}k_{1r}} - b_{21r}b_{12l}{x_r}^*{y_l}^* + \frac{b_{22r}b_{22l}{y_r}^*{y_l}^*}{k_{2r}k_{2l}} - b_{12r}b_{21l}{y_r}^*{x_l}^*)$,
$a_4 = {x_l}^*{x_r}^*{y_l}^*{y_r}^*(\frac{b_{11r}b_{22r}}{k_{2r}} + b_{12r}b_{21r})(\frac{b_{22l}b_{11l}}{k_{1l}k_{1r}} + b_{12l}b_{21l})$.

Now, by Routh-Hurwitz condition, if $a_1 > 0, a_3 > 0, a_4 > 0$ and $a_1a_2a_3 > {a_3}^2 + {a_1}^2a_4$ then the system is stable. It is clear that $a_1 = 0, a_3 = 0$. So, e^* is unstable.

5. Numerical Simulations

We first consider the imprecise biological parameter values are, $r_1 = (0.4, 0.6, 0.7), r_2 = (0.09, 0.1, 0.5), b_{11} = (0.2, 0.4, 0.6), b_{12} = (0.4, 0.42, 0.44), b_{21} = (0.4, 0.42, 0.44), b_{22} = (0.09, 0.1, 0.3), k_1 = (23, 35, 39), k_2 = (44, 50, 55)$.

Now we consider the condition of trivial equilibrium, when $q_1 = 0.3, q_2 = 0.4, E = 7$ and the initial conditions $x(t_0) = \tilde{x}_0 = (0.5, 0.7, 0.8), y(t_0) =$

$\tilde{y}_0 = (0.5, 0.7, 0.9)$.
i.e. $(x(t_0))_\alpha = [0.5 + 0.2\alpha, 0.8 - 0.1\alpha], (y(t_0))_\alpha = [0.5 + 0.2\alpha, 0.9 - 0.2\alpha]$.

Then the condition of Theorem 4.1 is satisfied. And the trivial equilibrium point $e_0(0, 0, 0, 0)$ is locally asymptotically stable. Using these values of parameter and the initial condition the dynamics of system (3) is graphically presented in Fig. 1. This figure shows that the rate of population $(x(t), y(t))$ decline to zero i.e. approaches the trivial equilibrium e_0, which supports our calculated result in Theorem 4.1.

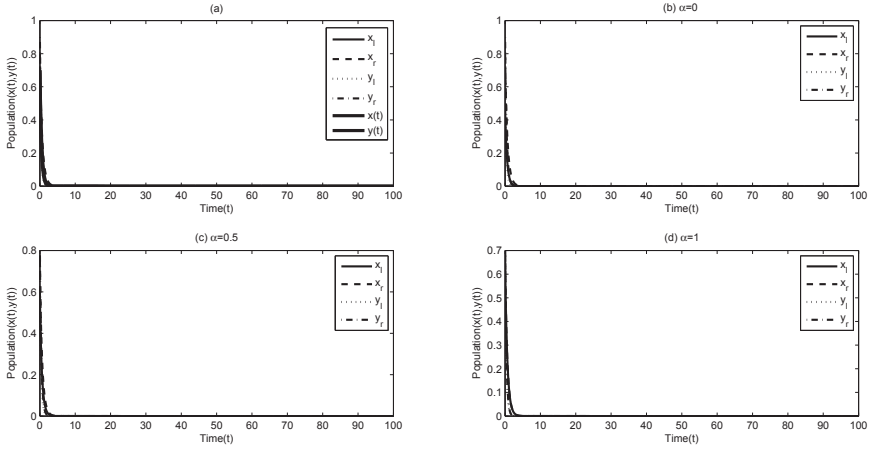

Figure 1.

Fig. 1(a) Crisp solution and fuzzy solution for $\alpha = 0$ and here we see that the crisp solution lies between the fuzzy solutions. So application of fuzziness of trivial equilibrium in system (3) is justified and hence it is acceptable. Fuzzy solution of system of equation (3) for $(b)\alpha = 0, (c)\alpha = 0.5, (d)\alpha = 1$. Here we observe that $x_l(t, \alpha), y_l(t, \alpha)$ are increases and $x_r(t, \alpha), y_r(t, \alpha)$ are decreases with increasing , hence the solution is a strong solution. When α increases the difference between x_l, x_r and y_l, y_r are decreases and at $\alpha = 1$ they become crisp solution. So we say that the graphical solution of trivial equilibrium of system (3) is biologically meaningful, furthermore the graphical solution is coherent with the crisp solution.

Now we consider the axial equilibrium condition when $q_1 = 0.1, q_2 = 0.5, E = 5$ with the imprecise biological parameter values given in above example and the initial conditions $x(t_0) = \tilde{x}_0 = (0.5, 0.7, 0.8), y(t_0) = \tilde{y}_0 = (0.5, 0.7, 0.9)$. Then the condition stated in Theorem 4.2 is satisfied, which

implies that the axial equilibrium $e_1(x_{l1}, x_{r1}, 0, 0)$ is stable. The dynamics of system (3) according to this condition is graphically presented in Fig. 2, which shows that the first species (x_{l1}, x_{r1}) exist and the second species goes to extinct with increasing α, i.e. the graphical result approaches the axial equilibrium e_1. This result supports our analytical result given in Theorem 4.2.

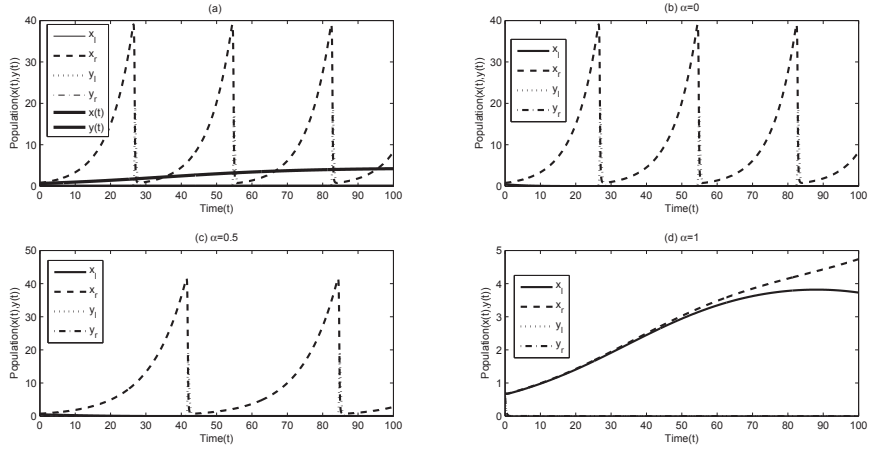

Figure 2.

Fig. 2(a) Crisp solution and fuzzy solution for $\alpha = 0$ and in this figure we see that the crisp solution lies between the fuzzy solutions. So application of fuzziness of axial equilibrium in system (3) is justified and hence it is acceptable. Fuzzy solution of system of equation (3) for $(b)\alpha = 0, (c)\alpha = 0.5, (d)\alpha = 1$. Here we observe that $x_l(t, \alpha), y_r(t, \alpha)$ are increases and $x_r(t, \alpha), y_l(t, \alpha)$ are decreases with increasing α, hence the solution is a strong solution. When α increases the difference between x_l, x_r and y_l, y_r are decreases and at $\alpha = 1$ they become crisp solution. So we say that the graphical solution of axial equilibrium of system (3) is biologically meaningful, i.e. the figure (a), (b), (c) shows that there exist a interaction between prey-predator species and figure (d) shows that the condition of axial equilibrium.

Next we consider the coexistence equilibrium condition when $q_1 = 0.01, q_2 = 0.2, E = 3.3$ with the imprecise biological parameter values given in above example and the initial conditions $x(t_0) = \tilde{x}_0 =$

$(0.5, 0.7, 0.8), y(t_0) = \tilde{y}_0 = (0.5, 0.7, 0.9)$. Here the coexistence equilibrium $e^*({x_l}^*, {x_r}^*, {y_l}^*, {y_r}^*)$ is unstable. The dynamics of system (3) according to this condition is graphically presented in Fig. 3, which shows that all the species $({x_l}^*, {x_r}^*, {y_l}^*, {y_r}^*)$ exist i.e. the graphical result approaches the co-existence equilibrium e^*. This result supports our analytical result given in section 4.3 and except for $\alpha = 1$. Here only Fig. 3(d) shows that the system (3) becomes stable and the others show that the system is unstable.

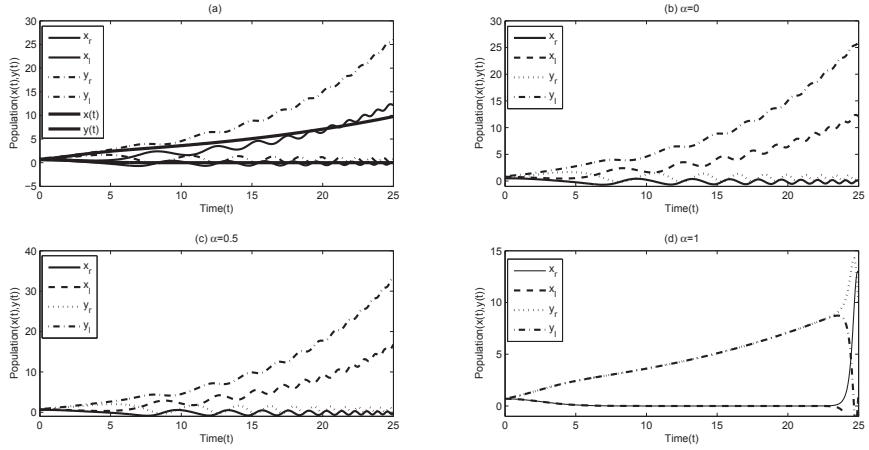

Figure 3.

Fig. 3(a) Crisp solution and fuzzy solution for $\alpha = 0$ and this figure shows that the crisp solution lies between the fuzzy solutions. So application of fuzziness of coexistence equilibrium in system (3) is also acceptable. Fuzzy solution of system of equation (3) for $(b)\alpha = 0, (c)\alpha = 0.5, (d)\alpha = 1$. Here we observe that $x_l(t, \alpha), , y_r(t, \alpha)$ are increases and $x_r(t, \alpha), y_l(t, \alpha)$ are decreases with increasing α , hence the solution is a strong solution. When α increases the difference between x_l, x_r and y_l, y_r are decreases and at $\alpha = 1$ they become crisp solution. So we say that the graphical solution of coexistence equilibrium of system (3) is biologically meaningful, i.e. all the figure (a), (b), (c), (d) shows that the condition of coexistence equilibrium.

6. Conclusions

Fuzzy differential equations arise naturally, when imprecision occurs in problems which are analyzed and using fuzzy differential equations is unavoidable, because expressing imprecision with fuzzy sets compare to classical is a more realistic approach.

In this paper we propose Stability analysis of a two species competition model with fuzzy initial conditions by using fuzzy differential equation approach.We propose stability of Trivial Equilibrium, Axial Equilibrium and Coexistence equilibrium of the Triangular fuzzy prey-predator model (TFPPM) by calculating the variational matrix at the corresponding equilibrium points and discussed their feasibility. Fuzzy solutions of different problems are discussed under various g-H differentiable cases. We provide an example to demonstrate the results and discuss the graphical representation of corresponding example in different cases. The simulation results and figures show that the proposed model and the method of discussing this model were effective.

Acknowledgments

Author Susmita Paul is thankful to National Institute of Technology, Agartala, India for providing financial support for her research work.

References

1. Bede, B. and Gal, S. G., Generalizations of the differentiability of fuzzy number valued functions with applications to fuzzy differential equation, *Fuzzy Sets and Systems*, **151**, 581–599 (2005).
2. Bede, B., Rudas, I. J. and Bencsik, A. L., First order linear fuzzy differential equations under generalized differentiability, *Inform. Sci.*, **177**, 1648–1662 (2007).
3. Chalco-Cano, Y. and Roman-Flores, H., On the new solution of fuzzy differential equations, *Chaos Solitons Fractals*, **38**, 112–119 (2006).
4. Gal, S. G., Approximation theory in fuzzy setting, in: G. A. Anastassiou (Ed.), Handbook of Analytic-Computational Methods in Applied Mathematics (Chapman and Hall/CRC Press, Boca Raton, FL), 617–666 (2000).
5. Kaleva, O., Fuzzy differential equations, *Fuzzy Sets and System*, **24**, 301–317 (1987).
6. Kandel, A., Fuzzy Mathematical Techniques with Applications, Addison-Wesley (1986).
7. Khastan, A., Bahrami, F. and Ivaz, K., New results on multiple solutions for nth-order fuzzy differential equations under generalized differentiability, boundary value problems 2009, Article ID 395–714 (2009).

8. Krivan, V. and G. Colombo, A non-stochastic approach for modeling uncertainty in population dynamics, *Bull. Math. Biol.*, **60** (1998).
9. Murray, J. D., Mathematical Biology, *Berlin: Springer* (1990).
10. Ortega, N., L. C. Barros and E. Massad, Fuzzy gradual rules in epidemiology, *Kybernetes. Int. J. Syst. Cybernetics*, **32**, 460–477 (2003).
11. Pedrycz, W. and F. Gomide, An Introduction to Fuzzy Sets: Analysis and Design, Massachusetts Institute of Technology (1998).
12. Puri, M. and Ralescu, D., Differential and fuzzy functions, *J. Math. Anal. Appl.*, **91**, 552–558.
13. Sugeno M., Theory of Fuzzy integrals and its applications, PhD thesis, Tokyo Institute of Technology, Japan (1974).
14. Wu, C. and Gong, Z., On Henstock integral of fuzzy-number-valued functions I, *Fuzzy Sets and Systems*, **120**, 523–532 (2001).
15. Zadeh, L. A., Fuzzy sets. Inf. Control, **8**, 338–353 (1965).

MAGNETIC RESONANCE GUIDED HIGH INTENSITY FOCUSED ULTRASOUND – MATHEMATICAL MODELING OF AN INNOVATIVE, STATE OF THE ART TECHNOLOGY FOR CANCER THERAPY*

J. MURLEY

University of Waterloo,
200 University Avenue West,
Waterloo, ON N2L 3G1, Canada
E-mail: jmurley@uwaterloo.ca

J. THANGARAJ, J. DRAKE† and A. WASPE†

University of Toronto,
563 Spadina Crescent,
Toronto, ON M5S 2J7 Canada,
E-mail: jeyan.thangaraj@mail.utoronto.ca, james.drake@sickkids.ca,

S. SIVALOGANATHAN

Centre for Math Medicine, The Fields Institute,
222 College Street,
Toronto, ON M5T 3J1, Canada
E-mail: ssivaloganathan@uwaterloo.ca

Traditionally chemotherapy, radiotherapy, and surgery have been the primary therapeutic interventions used to treat cancers. Over the last decade, High Intensity Focused Ultrasound (HIFU) has emerged as a potentially powerful additional primary therapeutic modality for certain cancers. In addition to avoiding side effects associated, for example, with chemotherapy and radiotherapy, it also presents a non-invasive alternative to surgery which still has the potential to completely eradicate solid tumours. In this paper, we briefly present a possible classical set-up to administer HIFU and discuss the mathematical modeling of HIFU in the context of bone sarcomas. Finally, we briefly discuss several possible alternative applications of HIFU ranging from clot lysis to a potential method for relaxing the Blood Brain Barrier in order to permit the delivery of chemotherapeutic agents (in the context of brain tumours). These lead to many interesting questions that should be amenable to mathematical modeling.

*This work is supported by NSERC.

†Hospital for Sick Children, 555 University Avenue, Toronto, ON M5G 1X8 Canada.

1. Introduction

The struggle of humankind with cancer has been documented throughout recorded history. Thus, it is no surprise that the earliest evidence of cancer has been found in the fossilized bone tumours of mummies of ancient Egypt and in ancient.[8] Cancer is a general term used to describe many different diseases that are caused by the uncontrolled division and accumulation of mutated cells in an organism. These resulting malignant cells form tumours that can affect a single organ or can spread to other organs through the process of metastasis.[5] A 2013 survey carried out by the American Medical Association showed that cancer is poised to overtake cardiovascular diseases as the leading cause of mortality in industrialized countries. Over the course of the year, 14.9 million new people were diagnosed with cancer, and another 8.2 million people lost their lives to cancer. Cancer continues to pose a major threat to public health worldwide, and the rates of cancer incidences have increased in most countries since 1990. Breast cancer is most prevalent amongst women and lung cancer is most prevalent amongst men, although rates of prostate cancer amongst men are increasing faster than any other types of cancer. Progress has been made in cancer prevention and treatment, but due to an aging global population and increased rates of smoking and obesity, cancer is still proving to be a major risk factor.[13] As research continues to reveal more about the complex multi-scale nature of cancer, new treatments, like High Intensity Focused Ultrasound (HIFU), are emerging in an attempt to develop non-invasive therapies that have minimal side effects.[2]

HIFU as a cancer therapy is a relatively new development which has yet to gain widespread acceptance in a clinical setting. While HIFU was conceptually developed in the mid-1950s and was used to some success in treating some neurological conditions, its uses remained few and far between and two or three decades of technological advances were necessary before the technology became suitable for clinical applications.[15] In recent years due to significant technological advances, HIFU has gained traction as a therapeutic modality and is now used in a number of applications, ranging from painless removal of uterine fibroids[15] to non-invasive destruction of solid tumours.[2]

In this paper, we focus on the use of HIFU to treat bone sarcomas. In the first section, a contextual setting for cancer therapy is briefly developed before examining the specific case of HIFU therapy. In the subsequent three sections, the standard methods of mathematical modeling for HIFU

are presented. In the second section, a model of ultrasound propagation is given in the form of the acoustic wave equations. In the third section, the effect of ultrasound on tissue temperature is considered and modeled. In the fourth section, the resulting effect on the ablation of tissue at the HIFU focal point is presented based on the previous mathematical models. In the fifth section, we present preliminary numerical results for the solution of this mathematical model for a simplified initial boundary value problem. In the sixth and final section, we discuss possible future research directions for this work.

2. Carcinogenesis and Modern Therapies

Before focussing on possible therapeutic interventions for cancer, it seems prudent to gain a deeper understanding of the mechanisms underlying carcinogenesis. Cancer is fundamentally a genetic disease since it is initiated through the mutation of genes that code for the synthesis of proteins regulating cell differentiation and growth (proto-oncogenes). These mutated genes (known as oncogenes) do not lead to the synthesis of proteins that regulate mitosis and the cells begin to divide in an uncontrolled fashion. Cancer cells have evaded the normal control checkpoints that regulate growth and proliferation, growing and proliferating in an uncontrolled fashion. Furthermore, as the cancer progresses, cancer cells use the circulatory system to start new colonies of cancer cells throughout the body (metastases).[5]

In the 20th and 21st centuries, multiple therapeutic modalities have emerged, including chemotherapy, radiotherapy, surgery, hormone therapy, immunotherapy, stem cell therapy, and gene therapy, yet no definitive cure for cancer exists. The various treatments can be administered separately or in combination for greater efficacy. For example, radiotherapy is often administered with chemotherapy to improve the effects of radiation. All of these treatments have shown some effectiveness in treating particular cancers, but also have shown some crucial limitations that need to be overcome.[5]

For example, radiation therapy is a cancer treatment where cancerous cells are killed by ionizing radiation and different types of radiation therapies have been developed to administer the radiation to different regions of the body. These include Three-Dimensional Conformal Radiotherapy, conformal proton beam radiation therapy, Intensity Modulated Radiotherapy, and Image Guided Radiotherapy, amongst others.[5] The challenge in radiation therapy is to ensure that radiation is administered in such a manner

that the cell kill is maximized for cancer cells and minimized for normal cells. Another difficulty is that different tumours show different radio sensitivities; that is, the effectiveness of radiation therapy varies from case to case making it difficult for doctors to predict whether the treatment will be effective for particular cases. In addition, radiation therapy results in several adverse side effects, ranging from skin reactions, mouth dryness, hair loss, nausea, vomiting, fatigue, to loss of appetite.[5]

Chemotherapy is another therapeutic modality often used to shrink the size of a tumour, increase the effectiveness of radiotherapy, and treat cancers like leukemia and lymphoma. Despite the breadth of its uses, chemotherapy often compromises the immune systems of patients, leaving them vulnerable to opportunistic diseases and infections. Side effects include fatigue, shortness of breath, dizziness, easy bruising, bleeding of the gums, hair loss, dryness of hair and skin, nausea, loss of appetite, constipation, and diarrhea. Also, certain alkylating agents, inhibitors, and antimetabolites can result in neurotoxic effects on the central nervous system.[5]

High Intensity Focused Ultrasound (HIFU) is a novel emerging technology used in the non-invasive treatment of benign and malignant tumours. HIFU has been found to have a lot of potential within the field of oncology either being used by itself or in combination with other forms of treatment due to its precision and non-invasiveness, leaving patients with fewer side effects than radiotherapy, chemotherapy, or surgery.[24] The overall principle of HIFU is to focus multiple ultrasound transducers so that ultrasound waves propagate and focus on a cancerous tumour in the body (see Figure 1). This results in intense heating which either leads to hyperthermia or thermal ablation. The effect is similar to that of focussing light through a magnifying glass to ignite a piece of paper, however, ultrasound waves (mechanical sound waves with frequencies greater than $20kHz$) are being focused instead of light waves. HIFU can be used in clinical hyperthermia to increase the effectiveness of other treatments like chemotherapy, but more often it is used in thermal ablation to completely kill cancerous tumours. In order to provide doctors with real-time temperature data of their patients, HIFU is often used in combination with Magnetic Resonance (MR) thermometry.[30] The goal with HIFU is to minimize heating in healthy tissue, and maximize heating in cancerous tumours to the point of thermal ablation. HIFU has already been shown to be effective in treating prostate, bone, brain, and liver cancer.[24] However, in order to continue to improve its efficacy, effective models of heat transfer, acoustic wave propagation, and thermal dosage must be developed and further refined.[30]

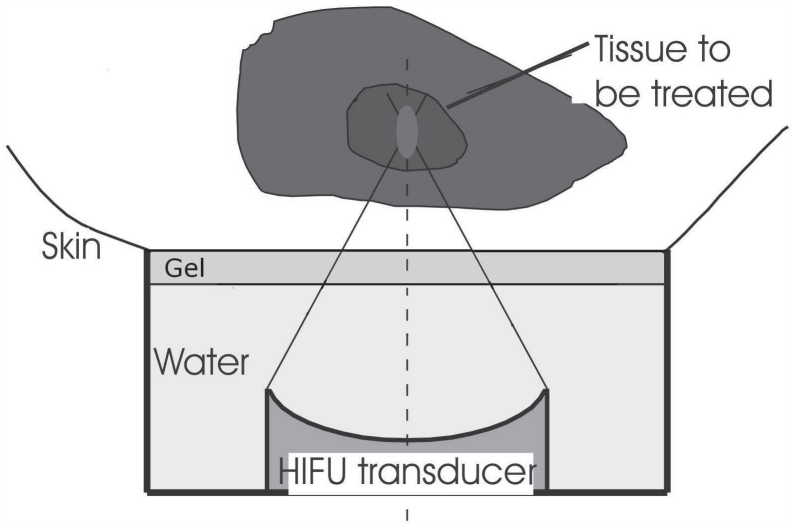

Figure 1. Diagram of clinical set-up.

2.1. *HIFU clinical procedure*

High-intensity focused ultrasound refers to a subset of therapeutic ultrasound practices, with applications including improving immune response to cancer cells (immunotherapy) and stopping internal bleeding (hemostasis).[2] In this paper we focus on HIFU surgical methods for removing tumour tissue (tumour necrosis), although the general methodology is similar to the other HIFU cases.[2]

The ultrasound in this method is produced by a transducer, typically operating in a frequency range of 1–10 MHz — most commonly in the range of 2–4 MHz, although certain applications may require 20 MHz ultrasound. The transducer is typically curved and is arranged so that the acoustic waves produced by it converge to a point within approximately 15 cm of the transducer.[2] The ultrasound field is set so that, near the transducer, the acoustic intensity is insufficient to have any significant effect on the adjacent tissue. However, near the focal point, the intensity of energy deposition is much higher.[15] In the case of tumour necrosis, this heating can cause thermal denaturation of proteins, destroying tumour tissue.[2]

In order to avoid unnecessary reflection and refraction of the ultrasound wave, the transducer is placed in a water bath and a gel pad is placed between the water bath and the skin of the patient, as the high water

content in soft tissues gives it similar acoustic properties to water and the gel.[12,16,18]

3. Acoustics

The classic model for acoustic waves, ignoring nonlinear effects, is the Helmholtz equation, which is developed using Euler's equations of fluid dynamics, assuming only small variations in wave velocity, pressure, and fluid density.[21]

$$\frac{\partial^2 \phi}{\partial^2 t} - c^2 \Delta \phi = 0 \tag{2.1}$$

where ϕ is the velocity potential, for wave velocity $v = \nabla\phi$; $c = \sqrt{\frac{\partial p_0}{\partial \rho_0}}$ is a constant parameter; p_0 is the equilibrium pressure; and ρ_0 is the equilibrium density. While this equation is derived for fluids, it is used for soft tissues as well. Due to the high water content of soft tissues, it is typical to treat them as fluids for acoustic modeling.[2,10]

One particular solution of the Helmholtz equation that is commonly used in HIFU modeling is the Rayleigh-Sommerfeld integral.[7,27] The derivation assumes that the transducer rests in an infinite plane that is otherwise rigid and that the acoustic waves from the transducer propagate in one direction into an infinite homogeneous fluid medium.[27] In actual practice, the region is neither infinite nor homogeneous,[11] but making these assumptions, the Rayleigh integral is[16]

$$\phi_n(r,t) = \frac{1}{2\pi} \int\int u \frac{e^{ikR}}{R} dS_0 \tag{2.2}$$

where r is the location of a point in the fluid medium, t is time, ϕ_n is the velocity potential at position r, u is the velocity of the transducer movement normal to the surface, S_0 is the surface of the transducer, R is the distance between the point on the transducer and the point at r, and c_0 is the speed of sound in the medium.

In the case of a slightly curved transducer where the normal velocity u along the radius of curvature of the transducer is time harmonic, the solution to the Rayleigh-Sommerfeld integral may be approximated in the form of a series by considering the transducer as a set of N point sources. In a homogeneous region, the solution may be written as

$$\phi = \frac{1}{2\pi} \sum_{i=1}^{N} u_i \frac{e^{-\imath k r_i}}{r_i} S_i \tag{2.3}$$

where the subscript i represents the value for the ith point source. In the case where there are multiple homogeneous layers, the solution may be written in the form

$$v = -\frac{\partial \phi}{\partial r} = \frac{\imath k}{2\pi} \sum_{i=1}^{N} u_i \frac{e^{-\imath k r_i}}{r_i} \Big(1 - \frac{\imath}{k r_i}\Big) S_i T cos(\theta_2) \tag{2.4}$$

where T is the transmission coefficient and θ_2 is the angle the transmitted wave makes with the boundary. This velocity potential is converted into pressure for use in the ultrasound heating term as

$$p = \imath \omega \rho \phi \tag{2.5}$$

In more recent mathematical literature on the subject, the Khokholov-Zabolotskaya-Kuznetsov (or KZK) nonlinear wave equation has been used to model the propagation of ultrasound through soft tissue.[10] The derivation of the KZK equation is largely similar to the Helmholtz equation, making similar assumptions, but using nonlinear continuity equations in order to include nonlinear effects.[20,21,37] This results in an equation of the form[2]

$$\frac{\partial p}{\partial z} - \frac{\beta}{{c_0}^3 \rho_0} p \frac{\partial p}{\partial \tau} - \frac{b}{2{c_0}^3 \rho_0} - \frac{b}{2{c_0}^3 \rho_0} \frac{\partial^2 p}{\partial \tau^2} = \frac{c_0}{2} \int_{-\infty}^{\tau} \Delta_{\perp} p(\tau') d\tau' \tag{2.6}$$

where z is the coordinate along the direction of the sound wave propagation and τ is a delayed time variable for sound wave propagation along the axis of motion such that $\tau = t - \frac{z}{c_0}$. This form of the KZK equation has four terms, which are, in order: the change in pressure along the direction of the main sound wave movement; a nonlinear term, where β is a nonlinear coefficient; a term for attenuation (the loss of intensity as the wave passes through the medium), where b is a dissipative coefficient; and a term for diffraction (the bending of sound waves due to obstacles), where $\Delta_{\perp}$ is a Laplacian operator only for coordinates perpendicular to z.

This equation can more accurately describe the propagation of the ultrasound waves than the Rayleigh-Sommerfeld integral,[2] but the numerical solution of the Rayleigh-Sommerfeld integral requires simpler numerical methods and is less computationally demanding.[2,16] For this reason, the most appropriate model will depend on the particular application. In some cases, the nonlinear aspects of the KZK equation can be significant enough to justify the increased computational load, but in other cases, the difference between the two models is negligible and the Rayleigh-Sommerfeld integral considerably simplifies the numerical computation.[2]

4. Temperature Distribution

In certain applications of focused ultrasound treatments, such as lithotripsy, the acoustic pressure is the main source of the therapeutic effect, but in the case of HIFU, the effect of acoustic pressure is secondary to the effect of the elevated temperature from this effect.[2] This makes it necessary to model the temperature distribution in the tissue.

Typically, the model used for this purpose is the Pennes bioheat equation.[2] This model was developed based on measurements taken in 1948 of the forearm temperature at rest and takes the form of a standard heat equation[26]

$$\rho c_p \frac{\partial T}{\partial t} = \nabla \cdot (k \nabla T) + \omega_b c_{p,b} (T_a - T) + q_m \tag{3.1}$$

where T represents the tissue temperature and t represents the time. The first two terms in this equation take the form of the standard heat equation, where ρ represents the tissue density, c_p represents the tissue specific heat, and k is the heat conductivity. The third term accounts for heat being conducted by blood of a different temperature flowing through the tissue in the form of Fick's Law, where ω_b represents the blood volumetric perfusion rate, $c_{p,b}$ is the blood specific heat, and T_a is the arterial blood temperature. The final term, q_m, is the metabolic heat source term arising from surrounding tissue.[26]

This equation was derived for the case of tissue at room temperature, but it has since become the standard model for temperature propagation through tissue[19] by replacing the metabolic heat source term by a outside heat source - in this case, the heat from the HIFU therapy.[2] This heat term may be derived from the acoustic pressure p as

$$q_m = \frac{\alpha < p^2 >}{\rho c_0} \tag{3.2}$$

where α is the absorption coefficient, ρ is the tissue density, and c_0 is the speed of sound in the tissue.[16]

A number of attempts have been made to develop an improved model for the propagation of heat in biological tissues.[19,33] Variations on the current model most often reference the blood perfusion heat term. While the first two terms are in the form of the standard heat equation, the blood perfusion term is less well-defined.[19] In particular, the blood perfusion parameter ω_b is not derived from measured properties in the tissue, but is found by fitting the Pennes bioheat equation to temperature profiles in tissue and so may be more of a fitting parameter to the heat equation rather than a physical

quantity.[33] Alternate derivations have included altering the form of the term to include a spatial derivative term in temperature,[33] including stochastic effects,[3] and treating the blood and tissue temperatures separately using porous medium theories,[19,35] amongst others.[1] However, results from these new derivations have all been found to be relatively close to the results from the Pennes bioheat equation and are generally more computationally intensive. For this reason, no alternate derivation has gained widespread acceptance as a replacement for the standard bioheat equation.[19]

5. Thermal Dose

In order to measure the therapeutic effect that is clinically relevant, it is insufficient to only consider the distribution of the ultrasound or of the heat produced when that energy is absorbed. The clinically relevant factor is the effect that this heat and ultrasound have on the tissue. While tissue damage can result from other effects of focused ultrasound, such as from pressure waves as is the case in lithotripsy or from cavitation bubbles, current models of tissue damage for this application of HIFU consider thermal effects to be sufficiently dominant that other forms of tissue damage are insignificant.[2]

The main process resulting in this tissue damage is the denaturation of proteins.[38] Protein denaturation originally was defined as a process wherein the protein is irreversibly changed from a soluble form to an insoluble form, usually, but not exclusively, due to the application of heat. This definition has since expanded to include a wider variety of reactions that convert proteins from their natural state which are sometimes reversible.[17]

As this reaction is temperature dependent - and, in current models, is considered to be solely temperature-dependent - the classic model for this type of reaction is the Arrhenius equation, which measures the change in the rate of chemical reactions due to temperature, and may be written as[17]

$$k_{T_1} = k_{T_0} e^{\mu(T_1 - T_0)/(2T_0T_1)} \tag{4.1}$$

where T_0, T_1 represent two temperatures in Kelvin; k_{T_0}, k_{T_1} represent the reaction rate at these two temperatures; and μ is a constant which is referred to by several names, such as the "temperature characteristic" and the "apparent activation energy."[17] The Arrhenius equation can also be derived in the form of the observed velocity of the reaction, v, such that[17]

$$v(T) = Ae^{-E/RT} = Ae^{-\Delta H/2T} \tag{4.2}$$

where T is the absolute temperature in Kelvin, R is the universal gas constant, and $\Delta H = \frac{2E}{R}$ is the energy of activation.[9] In this application, the

parameter A is approximately equal to[9,17]

$$A(T) = 2.05(10^{10})e^{\Delta s/2}T \tag{4.3}$$

However, A is usually treated as a constant, as variation in A has minimal impact on $v(T)$, for the typical parameter values associated with our particular application.[9]

The most well-known[16] model for the macroscale effect of heat on tissue is the thermal dose model.[29] Defining $\frac{1}{\tilde{D}_0} = v(T)$ as exponential slope of the heat inactivation survival curve, the change in the slope per degree change in the temperature, R, is[9]

$$R = \frac{\tilde{D}_0 \ at \ T+1}{\tilde{D}_0 \ at \ T} = e^{-\Delta H/2T(T+1)} \tag{4.4}$$

In a similar form to the relation between reaction rates in (4.1), the time required to have the same effect at different constant temperatures can be related by

$$t_1 = t_2 R^{T_1 - T_2} \tag{4.5}$$

for constant temperatures T_1, T_2 and elapsed times t_1, t_2.[29] A variable temperature may be written as an integral by approximating it as a Riemann sum and taking the limit as $\Delta t \to 0$. Using $43°C$ as a reference temperature, the thermal dose at $43°C$

$$TD_{43°} = \int_0^t R^{43°C - T(t')} dt' \tag{4.6}$$

where the thermal dose $TD_{43°C}$ is the time taken to cause an equivalent reaction in the tissue at $43°C$ to the temperature profile T over time t.[29] Irreversible thermal damage to the tissue is considered to have taken place at 240 equivalent minutes at $43°C$.[2]

The parameters for the Arrhenius equation are determined by taking the natural log of $v(T)$ and linearly fitting $\ln v(T)$ to $\frac{1}{T}$.[9] However, the Arrhenius equation only provides a good fit as long as the range of temperatures is not too large.[17] In the case of the thermal dose model, this is demonstrated by taking two sets of parameter values: one below $43°C$ and one above it.[9] For these parameter values, the value of R does not change significantly and so may be approximated by[29]

$$R = \begin{cases} 0.25 : T(t) < 43° \\ 0.5 \ \ : T(t) \geq 43° \end{cases} \tag{4.7}$$

These parameters fit the survival curves of the studied Chinese hamster ovary cells, but they consider only the range of temperatures between $37^{\text{deg}}C$ and $46^{\text{deg}}C$,[9] although a similar study on baby hamster kidney cells discovered a similar relation up to $57°C$.[4] The values are considered reasonable even in the higher temperature ranges used in HIFU, which can exceed $70^{\text{deg}}C$,[2] but some studies in pig skin burn models suggest that the Arrhenius equation parameters may change at higher temperatures under a different thermal damage model.[34]

This thermal damage model also uses the Arrhenius equation as its basis for derivation, but instead of considering equivalent time, a damage variable $\Omega(t)$ is defined as the log of the fraction of denatured protein[38] and can be shown to be

$$\Omega(t) = A \int_0^t e^{E/RT(t')} dt' \tag{4.8}$$

Coagulation is considered to have occurred when $\Omega \geq 1$.[38] When used in skin burn studies, other critical values can be used for different degrees of burn; the critical value for coagulation in this context is equivalent to that of a second-degree burn.[31] Zhou *et al.*[38] and other works in therapeutic thermal coagulation[32,23] give one value for the parameters in the thermal damage equation, but studies in pig skin burns[34] suggest that these parameter values are only valid in a certain temperature range.

6. Preliminary Numerical Results

6.1. *3-D problem*

We consider the Pennes Bioheat Equation (3.1) in a simplified model consisting of three regions: the soft tissue on the outside, the bone marrow in the middle, and the cortical bone between the two. We remove the metabolic heat source term from the Pennes bioheat equation as noted in Section 3. We assume that the bone and soft tissue are homogeneousand isotropic. Also, we assume that at the focal point of the ultrasoun, the tissue is at a prescribed temperature.

We use Dirichlet conditions on the boundaries and on the focal point of the ultrasound. Also, at the interfaces between the flesh and bone, we equate the heat flux from both sides:

$$k_{x,L} \frac{\partial T_L}{\partial x} = k_{x,R} \frac{\partial T_R}{\partial x} \tag{1}$$

where the subscript L denotes the limit from one side of the interface, and the subscript R denotes the limit from the other side of the interface. The

above equations need to be augmented with an initial condition:

$$T(x, y, z, t = 0) = T_o(x, y, z) \tag{2}$$

where (x,y,z) is defined on the domain $D = \{(x, y, z) \in R^2 | x_a < x < x_b, y_c < y < y_d, z_e < z < z_f\}$

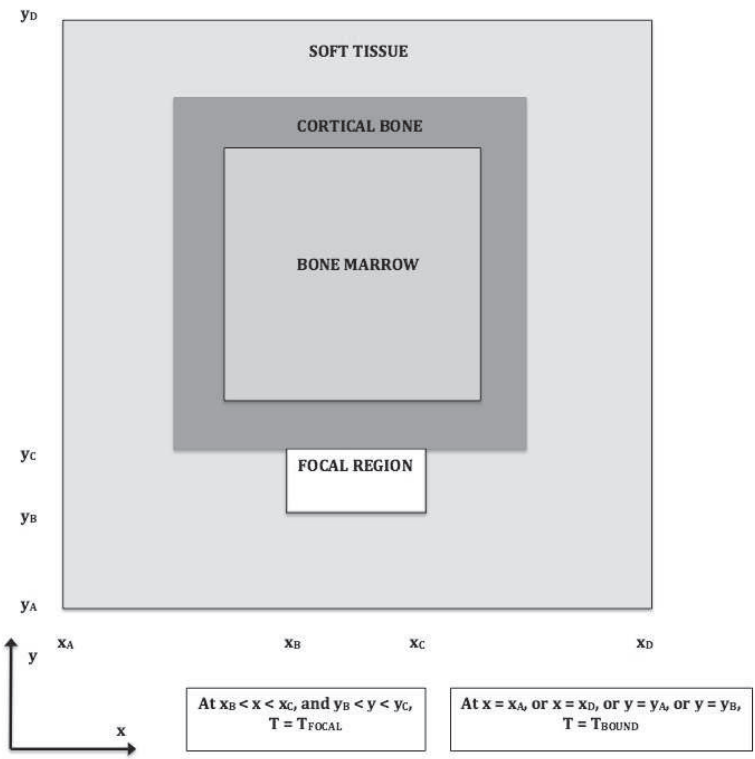

Figure 2. A cross-section of the three-dimensional model.

6.2. *Method of solution*

Due to the interior conditions from the focal point of the ultrasound, and the interface conditions, an analytical solution for this problem is not possible, so we solve it numerically. The method we use is the fully implicit finite difference method.

In order to use the fully implicit method, we discretize the problem. We discretize the time derivative as:

$$\frac{\partial T}{\partial t}(x_i, y_j, z_k, t_l) = \frac{T_{i,j,k,l} - T_{i,j,k,l-1}}{\Delta t} \tag{3}$$

where the subscripts i, j, k, and l represent the indices for the x, y, z, and t axes, respectively, $T_{i,j,k,l} = T(x_i, y_j, z_k, t_l)$, and Δt represents the increment in the t direction. Next, we discretize the second derivatives using the unequal finite difference method. By not forcing the spatial steps on both sides to be equal, it gives us more freedom when solving this problem, and potentially more accuracy:

$$\frac{\partial^2 T}{\partial x^2}(x_i, y_j, z_k, t_l) = \frac{T_{i+1,j,k,l} - T_{i,j,k,l}}{(x_{i+1} - x_{i-1})(x_{i+1} - x_i)} - \frac{T_{i,j,k,l} - T_{i-1,j,k,l}}{(x_{i+1} - x_{i-1})(x_i - x_{i-1})} \tag{4}$$

Similarly, we do this for the second derivatives with respect to y and z. At the interfaces, we discretize the interface conditions:

$$k_{x,L}\frac{\partial T_L}{\partial x} = k_{x,L}\frac{T_{i+1} - T_i}{x_{i+1} - x_i} = k_{x,R}\frac{T_i - T_{i-1}}{x_i - x_{i-1}} = k_{x,R}\frac{\partial T_R}{\partial x} \tag{5}$$

6.3. *Parameters*

The parameters for the thermal conductivity, density, heat capacity, and blood perfusion rate of flesh and bone are given in Table 1, obtained from Francis Duck, *Physical Properties of Tissue*[11]

Table 1. Tissue parameters.

	Flesh	Bone	Blood	Marrow
$\rho[\frac{kg}{m^3}]$	1100	1990	1052	1027
$c_p[\frac{J}{kgK}]$	3430	1300	3840	2750
ω_b	0.000200	0	N/A	0.000046
$k_x[\frac{W}{mK}]$	0.293	0.496	0.530	0.220

We assume 0 blood perfusion inside of the cortical bone and bone marrow for the sake of simplicity. For the boundary conditions we set the exterior boundaries to be $33°C$ to represent skin temperature, and the boundaries in the x-direction to be a quadratic fit where at the ends they are $33°C$ and in the middle it is $38°C$, representing the maximum internal body temperature that we assume to occur in the middle of the body.

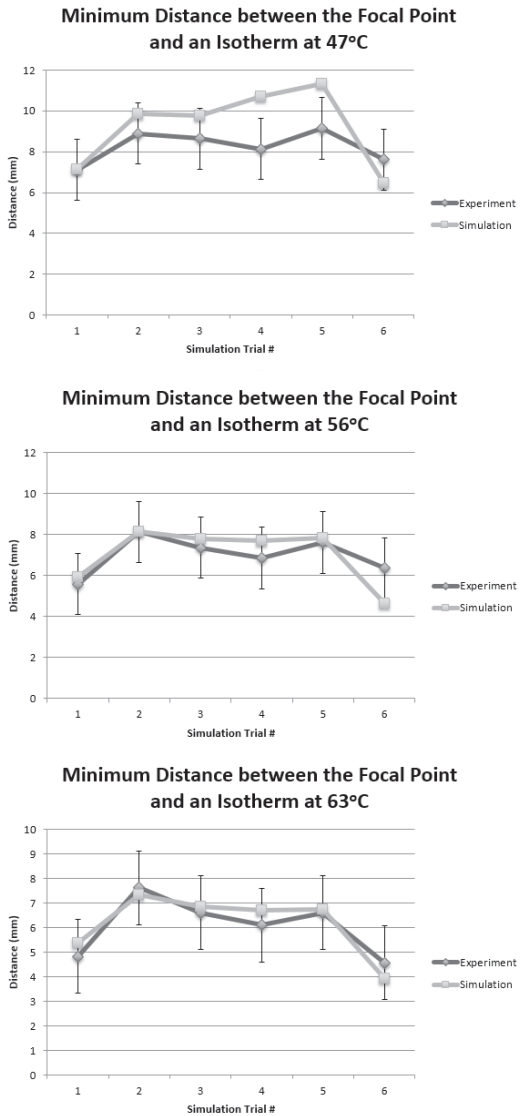

Figure 3. A comparison of the size of heated region between simulation and experimental results. The plots demonstrate the distance from the focal point to the contour at temperature a. $47°C$, b. $56°C$, and c. $63°C$. Average error in this distance was $-0.4 \pm 0.9mm$.

6.4. *Preliminary results*

The simulation was run under the same conditions as used in the experimental set-up shown in Table 2 and the results were compared with the experimental results in Figure 3. The simulation matches closely with the experiment for higher temperatures. In regions at lower temperatures, the smaller increase in temperature due to the ultrasound away from the focal point has a more significant effect.

Table 2. Schedule of experiment.

	Max Temperature ($^\circ C$)	Time (s)
Sonication Trial 1	77	20
Rest		210
Sonication Trial 2	74	20
Rest		165
Sonication Trial 3	82	20
Rest		120
Sonication Trial 4	83	20
Rest		120
Sonication Trial 5	82	20
Rest		510
Sonication Trial 6	72	20

7. Future Directions

While clinical applications of HIFU have greatly increased in the past decade,[15] modeling and treatment planning for HIFU lags behind that of similar, more established treatment modalities, such as radiation.[2] Radiation therapy modeling is a well-studied problem and clinical applications are guided by well-developed computer programs powered by mathematical models, although work remains to be done in these areas as well.[28] However, work towards developing such mathematically guided programs and software for HIFU has begun, such as through the work of researchers at the Hospital for Sick Children,[16] although much work still remains to be carried out.

Currently, while there is no unanimity as to which models should be used, the use of the models is unidirectional in the sense that a model of acoustic propagation is used to derive the acoustic pressure; this pressure term is used to calculate the ultrasound heat source for the model for tissue temperature distribution; and finally, this tissue temperature is used to calculate the thermal damage. This view of the relation between the models

is a simplification of the actual variation in tissue properties. It is known that the tissue parameters for both the acoustic and heat equations change in damaged tissue[6,14,36] and, similarly, these tissue parameters' values will change under high pressures and temperatures.[14,20,21] It is uncertain at this time how significant these dependencies are, as parameter values for biological tissues under even typical conditions can be difficult to obtain. A recent paper[14] reports that thermal parameters in pig livers changed by approximately 20% after being thermally damaged, even upon being cooled, suggesting that at least the relation between thermal damage and temperature models is significant. This paper does not provide a great deal of evidence on how these parameters change over time when being damaged, but it does provide at least endpoints for the change. Even should a suitable model for the change in these parameters be found, though, it may require further adjustments to the equations chosen, as many were derived under the assumption of constant or nearly constant parameters. In particular, all of the mentioned acoustic equations were derived under the assumption of constant parameters.[21,20,26,37]

There are also some questions concerning the accuracy of the thermal dose and thermal damage models. The thermal dose model in particular was derived for temperatures between 38 and $46°C$,[9] but in HIFU treatments, the temperatures often rise as high as $70°C$.[2] It is generally considered that the thermal dose model remains accurate in this wider range,[2] but the Arrhenius model that underlies the derivation of both the thermal dose and thermal damage models is known to only be accurate in small temperature ranges for biological processes,[17] which is the reason the value of R changes at $43°C$.[9] No evidence has been provided that the parameters of the Arrhenius model does not change at higher temperatures[9,4] and a change in the parameters for the thermal damage model above $50-55°C$ in skin burn models compared to the parameter values around $40°C$[34] suggest that this change should happen. Either R in the thermal dose equation may have more than two values to be accurate in the range of temperatures for HIFU or a new equation may be derived for a model like the Arrhenius model that is accurate in a wider range of temperatures.

In addition, while heat is the dominant effect on tissue in HIFU treatments, acoustic pressure still has an effect on tissue, which is relevant in some applications. For example, certain frequencies and intensities of HIFU results in the formation of bubbles in bodily fluids like blood (cavitation), which have a variety of effects on both the body and the propagation of the ultrasound itself. Some of these effects are desirable for certain applications

and some can cause issues with other applications.[2] However, modeling of these effects is not well defined and in some cases are too imprecise to give the necessary information, such as when attempting to temporarily open the blood-brain barrier in drug delivery.[22]

While there remain numerous unsolved problems in HIFU modeling and it has not reached the point of predictive modeling and treatment planning seen in radiation therapy, these solutions are not out of reach. Mathematical models can provide a better understanding of the potential applications of HIFU and a better preparation for the differences in individual patients. It is possible and desirable to reach the point of treatment planning of HIFU as achieved by radiation therapy in the present day.

Acknowledgements

The authors are grateful for financial support through an NSERC CGS-D to JM and NSERC Discovery and CHRP Grants to JD, SS, and AW.

References

1. H. Arikin, L. X. Xu and K. R. Holmes, *IEEE Trans. Biomed. Eng.* **41**, 97 (1994).
2. M. R. Bailey *et al.*, *Acoust. Phys.* **49**, 369 (2003).
3. J. W. Baish, *J. Biomech. Eng.* **116**, 521 (1994).
4. K. D. Bauer and K. J. Henle, *Radiat. Res.* **78**, 251 (1979).
5. O. Baykara, *Horizons in Cancer Research* **57**, 105 (2015).
6. N. L. Bush, I. Rivens, R. ter Haar and J. C. Bamber, *Ultrasound Med. Biol.* **19**, 789 (1993).
7. D. Cathignol, O. A. Sapozhnikov and Y. Theillere, *J. Acoust. Soc. Am.* **105**, 2612 (1999).
8. A. R. David and M. R. Zimmerman, *Nat. Rev. Cancer* **10**, 728 (2010).
9. W. C. Dewey *et al.*, *Radiology* **123**, 463 (1977).
10. Dontsov, E. V. and Guzina, B. B. (2013). "On the KZK-type equation for modulated ultrasound fields." *Wave Motion* **50**(4): 763–775.
11. F. A. Duck, *Physical properties of tissues*, Academic press (2013).
12. J. K. Enholm *et al.*, *IEEE Trans. Biomed. Eng.* **57**, 103 (2010).
13. C. Fitzmaurice *et al.*, *JAMA Oncol.* **1**, 505 (2015).
14. S. R. Guntur, K. I. Lee, D.-G. Paeng, A. J. Coleman and M. J. Choi, *Ultrasound Med. Biol.* **39**, 1771 (2013).
15. J. Hindley *et al.*, *Am. J. Roentgenol.* **183**, 1713 (2004).
16. J. T. Hudson, *Simulating Thermal Effects of MR-guided Focused Ultrasound (MRgFUS) in Cortical Bone and its Surrounding Tissue*, PhD diss. (2014).
17. F. H. Johnson, H. Eyring and M. J. Polissar, *The Kinetic Basis of Molecular Biology*, John Wiley & Sons, Inc., New York (1954).
18. F. Kallel *et al.*, *Ultrasound Med. Biol.* **25**, 641 (1999).

19. A. R. Khaled and K. Vafai, *Int. J. Heat Mass Transfer* **46**, 4989 (2003).
20. V. P. Kuznetsov, *J. Sov. Phys. Acoust.* **16**, 467 (1971).
21. L. D. Landau and E. M. Lifshitz, *Fluid Mechanics: Second Edition*, Pergamon Press (1987).
22. N. McDonnald, N. Vykhodtseva and K. Hynynen, *Phys. Med. Biol.* **51**, 793 (2006).
23. A. L. McKenzie, *Phys. Med. Biol.* **35**, 1175 (1990).
24. H. Odéen *et al.*, *J. Ther. Ultrasound* **2**, 19 (2014).
25. H. T. O'Neil, *J. Acoust. Soc. Am.* **21**, 516 (1949).
26. H. H. Pennes, *J. Appl. Physiol.* **1**, 93 (1948).
27. A. D. Pierce, *Acoustics*, Acoustical Society of America, New York (1989).
28. E. B. Podgorsak, *Radiation Oncology Physics*, International Atomic Energy Agency, Vienna (2005).
29. S. A. Sapareto and W. C. Dewey, *Int. J. Radiat. Oncol.* **10**, 787 (1984).
30. D. Schlesinger *et al.*, *Med. Phys.* **40**, 080901 (2013).
31. D. A. Torvi and J. D. Dale, *J. Biomech. Eng.* **116**, 250 (1994).
32. A. J. Welch, *IEEE J. Quantum Electron.* **20**, 1471 (1984).
33. W. Wulff, *IEEE Trans. Biomed. Eng.* **6**, 494 (1974).
34. F. Xu, P. F. Wang, M. Lin, T. J. Lu and E. Y. K. Ng, *J. Mech. Med. Biol.* **10**, 373 (2010).
35. Y. Xuan and W. Roetzel, *Chem. Eng. Technol.* **20**, 268 (1997).
36. L. Yin *et al.*, *Ultrasound Med. Biol.* **39**, 1760 (2013).
37. E. A. Zabolotskaya and R. V. Khokhlov *J. Sov. Phys. Acoust.* **15**, 35 (1969).
38. J. Zhou, J. K. Chen and Y. Zhang, *Comput. Biol. Med.* **39**, 286 (2009).

THE EFFECTS OF FIBROBLASTS ON WAVE DYNAMICS IN A MATHEMATICAL MODEL FOR HUMAN VENTRICULAR TISSUE

ALOK RANJAN NAYAK

Robert Bosch Centre for Cyber Physical Systems,
Indian Institute of Science,
Bangalore 560012, India
E-mail: alokiisc05@gmail.com

RAHUL PANDIT

Department of Physics,
Indian Institute of Science,
Bangalore 560012, India
E-mail: rahul@physics.iisc.ernet.in

We present systematic numerical studies of electrical-wave propagation in two-dimensional (2D) and three-dimensional (3D) mathematical models, for human, ventricular tissue with myocyte cells that are attached (a) regularly and (b) randomly to distributed fibroblasts. In both these cases we show that there is a parameter regime in which single rotating spiral- and scroll-wave states (RS) retain their integrity and do not evolve to a state ST that displays spatiotemporal chaos and turbulence. However, in another range of parameters, we observe a transition from ST to RS states in both 2D or 3D domains and for both cases (a) and (b). Our studies show that the ST-RS transition and rotation period of a spiral or scroll wave in the RS state depends on (i) the coupling strength between myocytes and fibroblasts and (ii) the number of fibroblasts attached to myocytes. We conclude that myocyte-fibroblast coupling strength and the number of fibroblasts are more important for the ST-RS transition than the precise way in which fibroblasts are distributed over myocyte tissue.

1. Introduction

Approximately 16% of all deaths in the industrialized world are caused by cardiac arrhythmias like ventricular tachycardia (VT) and ventricular fibrillation (VF)[1,2]. There is a broad consensus that the analogs of VT and VF in mathematical models for cardiac tissue are, respectively, (a) a single rotating spiral or scroll wave of electrical activation and (b) spiral-

wave or scroll-wave turbulence, which displays broken electrical waves and spatiotemporal chaos[3,4,5,6]. Thus, it is very important of study such spiral and scroll waves to develop an understanding of life-threatening cardiac arrhythmias. Such studies are truly interdisciplinary because they require inputs from biology, bio-medical engineering, cardiology, on the one hand, and physics, nonlinear dynamics, and numerical methods, on the other. We use methods from these areas to solve the nonlinear, partial-differential equations for state-of-the-art mathematical models for cardiac tissue with myocytes and fibroblasts. We build on our earlier studies of this problem[7,8] to elucidate the role of two different forms of myocyte-fibroblast couplings on spiral- and scroll-wave dynamics in such models by using theoretical ideas from spatiotemporal chaos.

It is useful to begin with an overview of experimental and computational studies of cardiac myocytes and fibroblasts. Cardiac fibroblasts, which are inexcitable cells, often multiply and connect with cardiac myocytes during *fibrosis*[9,10,11], a process of cardiac-tissue healing after a myocardial infarction. Fibroblasts in cell culture and in intact tissue can couple with myocytes by expressing either the connexins-43 (Cx43) or Cx45[12,13,14,15,16]. Zlochiver, *et al.*[15] have shown the expression of Cx43 between fibroblasts and myocytes in a monolayer of myocytes and fibroblasts of neonatal rats; Miragoli, *et al.*[16] have reported that Cx43 and Cx45 are expressed among fibroblasts and between fibroblasts and myocytes in cultured fibroblasts coated over rat-ventricular-myocyte strands. Both experimental and computational studies have shown that such coupling between myocytes and fibroblasts enhances electrical-signal propagation in cardiac tissue[15,17,16,18,7]; this enhancement increases with N_f, the number of fibroblasts that are attached to a myocyte. In cell-culture experiments, Miragoli, *et al.*[16] have found that the conduction velocity (CV) decreases with an increase in the density of fibroblasts in cultured strands of neonatal-rat myocytes coated by fibroblasts; studies by McSpadden, *et al.*[17] have found that CV decreases as the fibroblast number increases on the top of a myocyte layer in a monolayer of neonatal-rat cardiac myocytes, which are electrotonically loaded with a layer of cardiac fibroblasts. Zlochiver, *et al.*[15] have shown that CV decreases as (i) the gap-junctional conductance increases or (ii) the fibroblasts density increases in their experiments with fibroblasts of neonatal rats; they have also obtained similar result in their computational studies in a two-dimensional (2D) sheet of myocyte tissue in the dynamic Luo-Rudy (LRd) model[19,20] by inserting fibroblasts. Computational studies by Xie, *et al.*,[18] have shown that CV decreases as they increase the gap-junctional

coupling or the fibroblasts density in a 2D LR1 myocyte model[21], with either randomly attached or randomly inserted fibroblasts. In simulations with the 2D TNNP04 model (due to ten Tusscher, *et al.*[22]), Nayak, *et al.*[7] have found that CV either decreases or increases, with attached fibroblasts, as they increase the gap-junctional coupling. The experimental and computational investigations mentioned above show that both the gap-junctional coupling and N_f enhance CV and, therefore, they can play a crucial role in spiral- and scroll-wave dynamics in mathematical models for cardiac tissue.

We develop and investigate two models with different arrangements of fibroblasts that are attached to myocytes. In the first arrangement there is a regular, spatially periodic attachment of fibroblast, whereas, in the second arrangement, fibroblasts are attached randomly to myocytes. Our study has been designed to understand the effects of fibroblast organization, fibroblast density, and the myocyte-fibroblast coupling on spiral- and scroll-wave dynamics. We use two parameter sets for myocytes. The first set leads to a stable rotating spiral or scroll (RS) wave; the second leads to spiral- or scroll-wave-turbulence (ST) states in an isolated myocyte domain. By investigating an ST state in the presence of fibroblasts, we observe that both models, with regularly and randomly attached fibroblasts, show transitions from an ST to an RS state, depending on the myocyte-fibroblast coupling G_j and the maximum number N_f of fibroblasts attached to a myocyte in our simulation domain. We find that, once ST is converted to RS, the spiral or scroll rotation period increases as we increase G_j and N_f. Our study with an RS state and fibroblasts shows that an RS remains unchanged in both models with regularly and randomly attached fibroblast; and the rotation period increases as we increase G_j and N_f.

The remainder of this paper is organized as follows. Section 2 is devoted to a description of our model and the numerical methods we use. Section 3 is devoted to our results. Section 4 contains a discussion of the significance of our results.

2. Model and Methods

In this Section, we describe the details of our myocyte-fibroblast models for two-dimensional (2D) and three-dimensional (3D) tissue. We also explain the numerical-simulation techniques that we use to solve the partial differential equations (PDEs) that comprise our mathematical models. We also discuss the methods that we use to analyze the data from our numerical simulations.

2.1. *Model*

The 2D and 3D myocyte domains, with attached fibroblasts, can be modeled by the following PDEs and ordinary-differential-equations (ODEs)[23,24]:

$$\frac{\partial V_m}{\partial t} = \frac{-I_m + N_f(\mathbf{x})I_j}{C_m} + D\nabla^2 V_m, \tag{1}$$

$$\frac{\partial V_f}{\partial t} = \frac{-I_f - I_j}{C_f}, \tag{2}$$

where

$$I_j = G_j(V_f - V_m); \tag{3}$$

here C_m is the total cellular capacitance of a myocyte, V_m is the myocyte transmembrane potential, i.e., the voltage difference between intra- and extra-cellular spaces, and I_m is the sum of all the ionic currents that cross the myocyte cell membrane; C_f, V_f, and I_f are, respectively, the total cellular capacitance, the transmembrane potential, and the sum of all ionic currents for the fibroblast; $N_f(\mathbf{x})$ is the number of identical fibroblasts attached to a myocyte in our simulation domain at the point $\mathbf{x}$; and I_j, G_j, and D are, respectively, the gap-junctional current, the myocyte-fibroblasts gap-junctional conductance, and the diffusion coefficient that is related to the gap-junctional conductance between myocytes.

For myocytes, we use the state-of-the-art mathematical model for human ventricular tissue developed by ten Tusscher and Panfilov (the TP06 model)[25]. In the TP06 model the total ionic current is

$$I_m = I_{Na} + I_{CaL} + I_{to} + I_{Ks} + I_{Kr} + I_{K1} \tag{4}$$

$$+I_{NaCa} + I_{NaK} + I_{pCa} + I_{pK} + I_{bNa} + I_{bCa},$$

where I_{Na} is the fast, inward Na^+ current, I_{CaL} the L-type, slow, inward Ca^{2+} current, I_{to} the transient, outward current, I_{Ks} the slow, delayed, rectifier current, I_{Kr} the rapid, delayed, rectifier current, I_{K1} the inward, rectifier K^+ current, I_{NaCa} the Na^+/Ca^{2+} exchanger current, I_{NaK} the Na^+/K^+ pump current, I_{pCa} and I_{pK} the plateau Ca^{2+} and K^+ currents, and I_{bNa} and I_{bCa} the background Na^+ and Ca^{2+} currents, respectively. The full sets of equations for this model, including the ODEs for the ion-channel gating variables and the ion dynamics, are given in Refs. 7 and 26.

We follow MacCannell, *et al.*[27] to model the fibroblasts as passive elements. The fibroblast ionic current I_f is

$$I_f = G_f(V_f - E_f), \tag{5}$$

where G_f and E_f are, respectively, the conductance and the resting membrane potential for the fibroblast.

Physical units in our model are as follows: time t is in milliseconds (ms), V_m and V_f are in millivolts (mV), C_m and C_f are in picofarads (pF), I_m and I_f are in picoamperes (pA), G_f is in nanoSiemens (nS), E_f is in mV, G_j is in nS, and D is in $\mathrm{cm}^2/\mathrm{ms}$.

We study models with (a) regularly attached fibroblasts and (b) randomly attached fibroblasts. In case (a), $N_f(\mathbf{x}) = N_f$ for all site $\mathbf{x}$ in our simulation domain. In case (b) we choose $N_f(\mathbf{x})$ randomly at each site $\mathbf{x}$; $N_f(\mathbf{x})$ can be any integer from 0 to N_f, with equal probability for any one of these values.

2.2. *Methods*

Our 2D and 3D simulation domains are, respectively, squares (1024×1024 grid points) and rectangular parallelepipeds ($1024 \times 1024 \times 8$ grid points). We use 5-point and 7-point stencils for the Laplacian in 2D and 3D, respectively, and a finite-difference scheme with step sizes $\delta x = \delta y = 0.25$ mm in 2D, and $\delta x = \delta y = \delta z = 0.25$ mm in 3D, i.e., our simulation domains are $256 \times 256\ \mathrm{mm}^3$ (in 2D) and $256 \times 256 \times 2\ \mathrm{mm}^2$ (in 3D). For time marching we use a forward-Euler scheme with $\delta t = 0.02$ ms. We use Neumann (no-flux) conditions at the boundaries of our simulation domain.

For numerical efficiency, we have carried out our simulations on parallel computers, with an MPI code that we have developed for the TP06 model. Our code divides the 2D (or 3D) simulation domain into n columns (or slabs) along the x-direction of the domain, i.e., each processor carries out the computations for $(1024/n) \times 1024$ and $(1024/n) \times 1024 \times 16$ grid points, respectively, for 2D and 3D domains. To compute the Laplacian at the interface of processor boundaries, we use two extra grid lines (or surfaces), which can send and receive the data from left- and right-neighbor processors. The Neumann boundary condition is taken care of by adding an extra layer of grid points on the boundaries of the simulation domain of each processor.

Reference 28 suggests that we must have $D\delta t/(\delta x^2) < 1/2d$ for numerical stability, where d is the dimension of the simulation domain. For the TP06

model, with diffusion coefficients $D = 0.00154$ cm^2/ms,[25] time step $\delta t = 0.02$ ms, and space step $\delta x = 0.25$ mm, the value of $D\delta t/(\delta x)^2$ is $\simeq 0.05$; for the TP06 model, the quantity $1/2d = 0.25$ and $\simeq 0.17$, for the 2D and 3D domains, respectively, i.e., we have numerical stability because $D\delta t/(\delta x)^2 < 1/2d$.

We check the accuracy of our numerical scheme, as in Ref. 28, by varying both δt and δx in a cable-type domain of myocytes[26,7] and by measuring CV of a plane wave, which is injected into the domain by stimulating its left boundary for 3 ms with a stimulus of strength 150 pA. With $\delta x = 0.25$ mm, CV increases by 1.1% when we change δt from 0.02 to 0.01 ms; if we decrease δx from 0.25 to 0.15 mm, with $\delta t = 0.02$ ms, then CV increases by 3.1%; these changes are similar to those found in other studies[22,28,29,26].

Although the numerical method we use satisfies both numerical-stability and accuracy conditions, an inappropriately large δx can give irregular wavefront-curvature, as a consequence of numerical artifacts[28,7,26]; this leads to unphysical wave dynamics. We check that our results are free from such numerical artifacts by investigating the spatiotemporal evolution of an expanding wave front that emerges from a point stimulus. We find that fronts of the expanding wave do not deviate substantially from circles, when we apply a point stimulus of strength 450 pA for 3 ms at the center of the domain.

We use two parameter sets P1 and P2 for myocytes to obtain, respectively, a stable rotating spiral (RS) and a spiral-turbulence (ST) states in our 2D simulation domain, and a stable rotating scroll or scroll-wave turbulence in our 3D domain. The parameter set P1 is the original one used in the TP06 model[25,7,26]. In the P2 parameter set, we use the following parameters, with all other parameters the same as in the original TP06 model: (a) G_{Kr}, the I_{Kr} conductance, is 0.172 nS/pF; (b) G_{Ks}, the I_{Ks} conductance, is 0.441 nS/pF; (c) G_{pCa}, the I_{pCa} conductance, is 0.8666 nS/pF; (d) G_{pK}, the I_{pK} conductance, is 0.00219 nS/pF; and (e) τ_f, the time constant of the f gating variable that is associated with the I_{CaL} current, is increased 2 times compared to its value in the TP06 model[25,7,26]. Our fibroblasts parameters are as follows: $C_f = 6.3$ pF, $G_f = 4$ nS, $E_f = -49.0$ mV, and G_j in the range $0 \le G_j \le 6$ nS.[7,30]

To obtain spiral and scroll waves we use the S1-S2 cross-field protocol[31,32,26]. We apply a stimulus (S1) of strength 150 pA for 3 ms to the left boundaries of our simulation domains, to form a plane wave. We then apply the second (S2) stimulus, with the same strength and duration as the S1 stimulus, from the bottom boundary and with 0 mm $\le y \le$ 125 mm

in 2D, and 0 mm $\leq y \leq$ 125 mm and 0 mm $\leq z \leq$ 2 mm in 3D. This protocol leads to the formation of spiral and scroll waves, respectively, in our 2D and 3D domains.

To examine the spatiotemporal evolution of our system, we obtain pseudocolor or isosurface plots of V_m, time series of V_m, from representative points (x = 125 mm, y = 125 mm for 2D, and x = 125 mm, y = 125 mm, z = 1.25 mm for 3D), which we mark with an asterisk ($*$) in all pseudocolor plots of V_m. We examine the inter-beat interval (IBI), by using this time series with 4.4×10^5 data points; the IBI is the interval between two successive spikes in this time series. We obtain the power spectra $E(\omega)$, of the time series of V_m, by using 2×10^5 data points; to eliminate transients we remove the initial 2.4×10^5 data points. To obtain the rotation period T of a spiral, in an RS state, we average over the last 5 rotations of that RS.

3. Results

In subsection 3.1, we begin by studying spiral-wave dynamics in a 2D domain of myocytes without fibroblasts; we then introduce fibroblasts, either regularly or randomly, and examine the effects they have on spiral-wave dynamics. Subsection 3.2 contains the results of our studies of scroll-wave dynamics in our 3D simulation domain.

3.1. *Spiral-wave dynamics in our 2D model*

In Fig. 1(A), we show a pseudocolor plot of V_m, at time t = 8.8 s, for the parameter set P1, in our 2D simulation domain without fibroblasts; the initial condition evolves to a state with a single rotating spiral (RS). The local time series of $V_m(x, y, t)$, from the representative point shown by the asterisk in Fig. 1(A), is given in Fig. 1(B) for 0 s $\leq t \leq$ 8.8 s; a plot of the IBI versus the beat number is given in Fig. 1(C), which shows that, after initial transients, the spiral wave rotates periodically with an average rotation period $T \simeq 212$ ms. The power spectrum $E(\omega)$ in Fig. 1(D) has discrete peaks at the fundamental frequency $\omega_f \simeq 4.75$ Hz and its harmonics. The periodic time series of V_m, the flattening of the IBI, and the discrete peaks in $E(\omega)$ demonstrate that the time evolution of the spiral wave, with the P1 parameter set, is periodic. In Figs. 1(E)–(H), we show the exact analogs of Figs. 1(A)–(B) for the P2 parameter set. The non-periodic local time series in Fig. 1(F), the fluctuating IBI in Fig. 1(G), and the broad-band nature of $E(\omega)$ in Fig. 1(H) are characteristic of the ST state. The pseudocolor plot in Fig. 1(E), at time t = 8.8 s, shows such an ST state, which arises

from the steep slope of the action-potential-duration-restitution (APDR) plot[25,8]. In summary, then, in the absence of fibroblasts, the parameter sets P1 and P2 lead, respectively, to (a) an RS state and (b) an ST state in our 2D simulation domain.

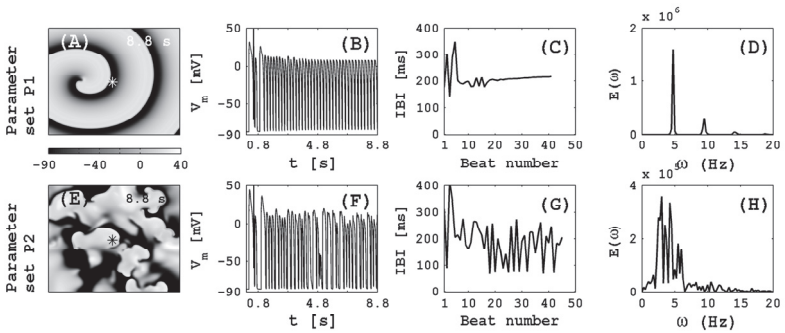

Figure 1. The rotating-spiral (RS) and spiral-turbulence (ST) states in a 2D domain in the absence of fibroblasts. For the parameter set P1, the pseudocolor plot of V_m in (A), the periodic nature of the local time series for V_m from the representative point (marked by an asterisk $*$ in (A) in (B), the flattening IBI with an average rotation period $T \simeq 212$ ms in (C), and the discrete peaks in the power spectrum with the fundamental frequency $\omega_f = 4.75$ Hz and its harmonics in (D) characterize the RS state. The exact analogs of plots (A)–(D) are shown, respectively, in (E)–(H) for the P2 parameter set; the irregular local time series, the fluctuating behavior of the IBI and the broad-band nature of the power spectrum characterize the ST state.

We now examine the effects of fibroblasts on spiral-wave dynamics in both RS and ST states. We begin our investigation with the P1 parameter set and with the regularly attached fibroblast model with $1 \leq N_f \leq 6$ and 1 nS $\leq G_j \leq 8$ nS; the remaining parameters for fibroblasts are as in subsection 2.2.

In Figs. 2(A1)–(A4) we show pseudocolor plots of V_m, at time $t = 8.8$ s, with the P1 parameter set for regularly attached fibroblast model with $G_j = 4$ nS and different values of N_f. The analogs of Figs. 2(A1)–(A4) are shown in Figs. 2(B1)–(B4) for the P2 parameter set. The plots in the first row of Fig. 2 show that the RS state, which we obtain in the absence of fibroblasts, does not evolve into an ST state; however, the spiral-arm width W_d decreases as we increase N_f, for a fixed value of G_j (first row of Fig. 2). We define W_d to be the difference of the radial distance between the wave front and the wave back of a spiral arm, whose center is located at the spiral core. Such a decrease of W_d is related to the shortening of the action-

potential-duration (APD) of a myocyte-fibroblast composite that has been discussed in Refs. 8 and 7.

For the P2 parameter set, we observe a transition from an ST to an RS state as we increase N_f for a fixed value of G_j (second row of Fig. 2). Such an ST-RS transition is the consequence of the suppression of the steep APDR slope of a myocyte-fibroblast composite at the cellular level[8,33]. Once the ST state is suppressed, a single spiral in an RS state rotates periodically as shown Figs. 2(B2)–(B4). In Figs. 2(C) and (D), we plot, respectively, the rotation period T of a spiral wave in an RS state versus N_f, for different values of G_j, for the P1 and P2 parameter sets. We find that T increases as (i) N_f increases, with a fixed value of G_j, and (ii) G_j increases, with a fixed value of N_f. This increase of T is a consequence of the decrease of CV that is associated with a decrease of the upstroke velocity of a myocyte-fibroblast composite AP in its depolarization phase, as shown in Refs. 7, 8 and 18. Furthermore, we observe that the minimum

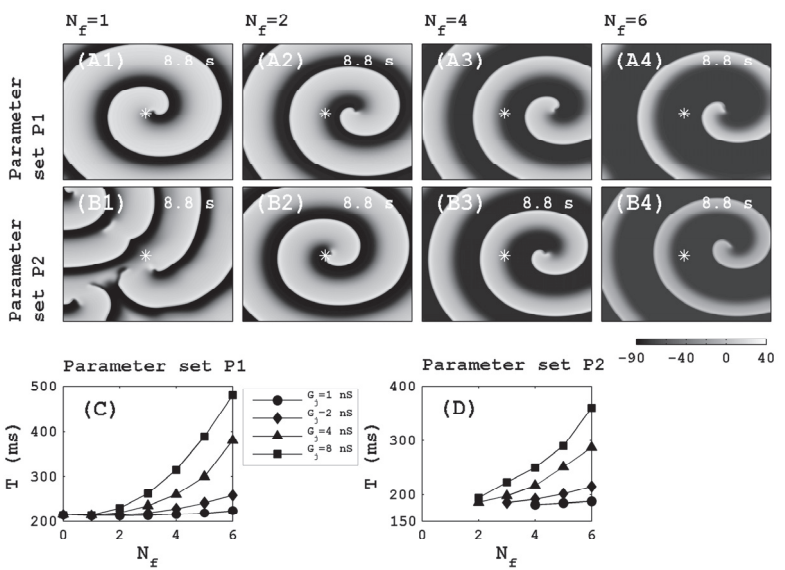

Figure 2. Various RS and ST states in our 2D domain for the regularly attached fibroblast model. (A1)–(B4) Pseudocolor plots of V_m, with G_j = 4 nS for N_f = 1, 2, 4, and 6, illustrate that the RS state (parameter set P1) remains in an RS state as N_f increases (first row). However, an ST state (parameter set P2) shows a transition to an RS state as N_f increases (second row). (C)–(D) The rotation period T of RS increases as N_f increases, for a fixed value of G_j, and vice-versa, for both the P1 and P2 parameter sets.

value of N_f, required for the ST-RS transition, decreases as G_j increases, for the P2 parameter set.

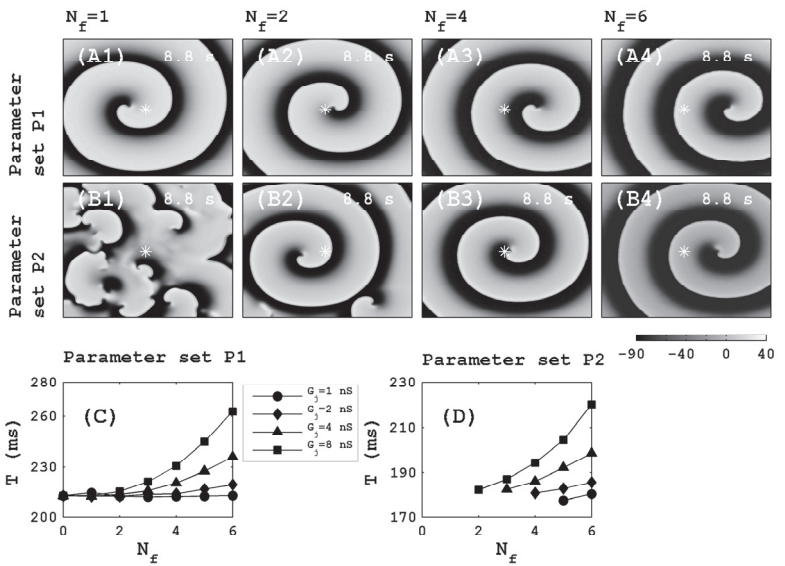

Figure 3. Various RS and ST states in our 2D domain for the randomly attached fibroblast model (this figure is the analog of Fig. 2). The results are qualitatively similar to those in Fig. 2 for the regularly attached fibroblast case. Note that the minimum value of N_f, for a fixed value of G_j, for the ST-RS transition, is higher compared to that in Fig. 2(D).

We focus next on spiral-wave dynamics, with P1 and P2 parameter sets, in our randomly attached fibroblast model. In Fig. 3, we show the exact analogs of Fig. 2, but now for the randomly attached fibroblast model. The pseudocolor plots in Figs. 3(A1)–(A4) show that the randomness in attaching fibroblasts does not lead to an RS-ST transition for the P1 parameter set. However, inspite of the randomness in the arrangement of fibroblasts, we observe an ST-RS transition for the P2 parameter set (see Figs. 3(B1)–(B4)), which is qualitatively similar to the ST-RS transition in the P1 case (compare the second rows of Figs. 2 and 3). However, the minimum value of N_f, required for an ST-RS transition, is higher for the randomly attached fibroblast model than in the regularly attached case (compare Figs. 2(D) and 3(D)).

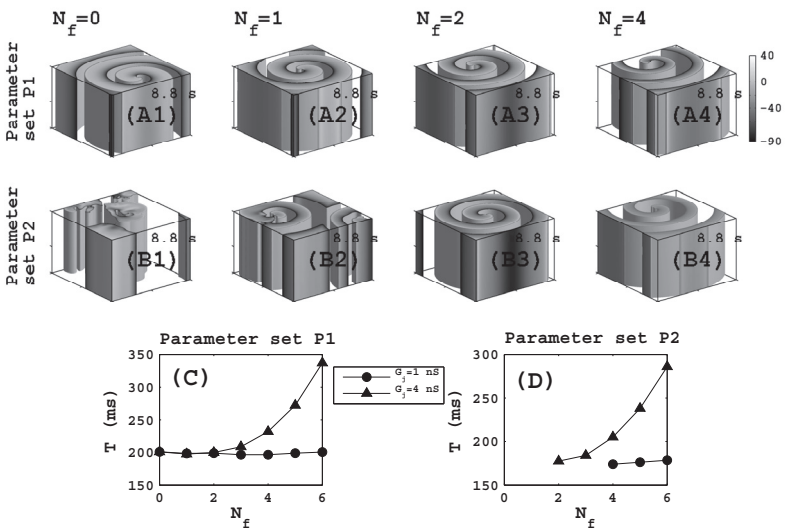

Figure 4. The rotating-scroll and scroll-wave-turbulence states, in our 3D simulation domain of size $256 \times 256 \times 2$ mm^3, for the regularly attached fibroblast model, are shown in (A1)–(B4) via isosurface plots of V_m. The myocyte-fibroblast coupling strength G_j = 4 nS. The scroll-arm width of a rotating scroll, with the P1 parameter set, decreases as N_f increases (first row). The scroll-wave turbulence, associated with the P2 parameter set, is converted to a rotating scroll as N_f increases (second row). (C)–(D) Plots of the rotation period T of a scroll wave in a rotating-scroll state, for the P1 and P2 parameter sets; for both parameter sets T increases as G_j increases; note that, for the ST-RS transition, the minimum value of N_f decreases as G_j increases.

3.2. *Scroll-wave dynamics in our 3D model*

We turn now to a systematic study of scroll-wave dynamics in our 3D simulation domain. For both the P1 and P2 parameter sets and both regularly and randomly attached fibroblast models, we carry out simulations to study the dependence of scroll-wave dynamics on N_f and G_j. We present our numerical results below.

In Figs. 4(A1), (A2), (A3) and (A4), we show, respectively, isosurface plots of V_m, at time t = 8.8 ms, for the P1 parameter set in our regularly attached fibroblast model with G_j = 4 nS and N_f = 0 (i.e., isolated myocytes), N_f = 1, N_f = 2, and N_f = 4. In the absence of fibroblasts, i.e., N_f = 0, the P1 parameter set displays a rotating scroll wave with fundamental frequency $\omega_f \simeq 5$ Hz and rotation period T $\simeq$ 201 ms; this is consistent, because $\omega_f \simeq 1/\mathrm{T}$. In Fig. 4(C), we plot T versus N_f for G_j = 1 nS (•) and 4 nS (▲). We find that T increases as we increase (i) N_f, for a fixed value

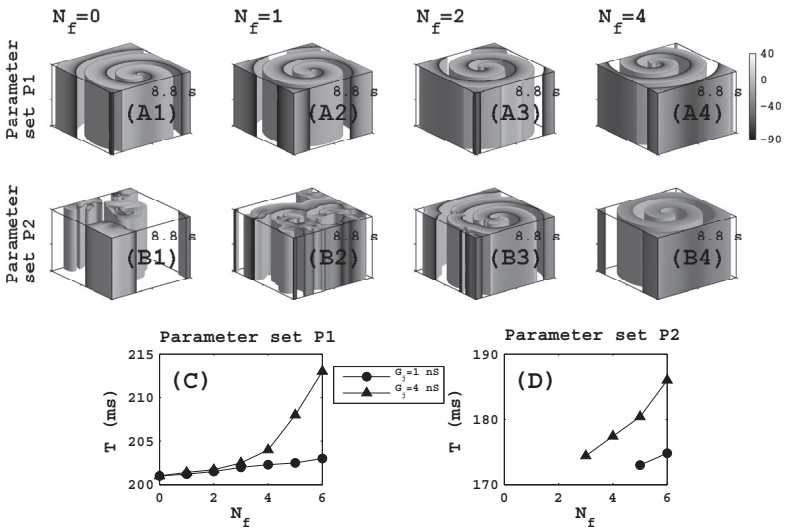

Figure 5. The rotating-scroll and scroll-wave-turbulence states, in our 3D simulation domain for the randomly attached fibroblast model; the exact analog of Fig. 4. The results are qualitatively similar to those for the regularly attached fibroblast case. Note that the ST-RS transition N_f value, for a fixed value of G_j, is higher than its counterpart in Fig. 4(D).

of G_j, or (ii) G_j, for a fixed value of N_f. In Figs. 4(B1)–(B4) and (D), we show, respectively, the exact analogs of Figs. 4(A1)–(A4) and (C), for the P2 parameter set. In the absence of fibroblasts and for the P2 parameter set, we obtain a scroll-wave-turbulence state (Fig. 4(B1)); this scroll-wave turbulence is converted to a rotating scroll if we have $N_f > 2$ (second row of Fig. 4). Once the scroll-wave turbulence state is suppressed, a rotating scoll rotates with a period T, which increases as we increase N_f for a fixed value of G_j, and vice-versa (Fig. 4(D)). Furthermore, from Fig. 4(D), we find that the minimum value of N_f, required for the ST-RS transition, is 4 and 2, respectively, for G_j = 1 nS (•) and 4 nS (▲). The isosurface plots in Fig. 4 show that the width W_d of a scroll-wave arm in the rotating-scroll state decreases as we increase N_f for both the P1 and P2 parameter sets. The mechanisms of the ST-RS transition, and increase of T and a decrease of W_d, as we increase N_f and G_j, are the same as those we have found in our 2D studies.

In Fig. 5 we show the exact analog of Fig. 4 for the randomly attached fibroblast model, with both the P1 and P2 parameter sets. Our scroll-

wave results here are similar to those for the case of regularly attached fibroblast model. From Fig. 5(D), we find that the minimum value of N_f, for the ST-RS transition, is 5 and 3, respectively, for G_j = 1 nS (•) and 4 nS (▲). Note that this minimum value of N_f is higher for the randomly attached fibroblast model than it is for the regularly attached fibroblast model (compare Figs. 4(D) and 5(D)).

4. Conclusions

We have presented the most extensive numerical study carried out so far of the effects of fibroblasts on spiral- and scroll-wave dynamics in a mathematical model for human ventricular tissue with fibroblasts, attached regularly or randomly to myocytes. Our numerical study has been designed to uncover the role of (i) the organization of fibroblasts in ventricular tissue (i.e., to compare regular and random arrangements), (ii) myocyte-fibroblast coupling G_j, and (iii) the density of fibroblasts, i.e., the maximum number of fibroblasts N_f attached to a myocyte. One of the principal results of our studies is that spiral- and scroll-wave dynamics depend only slightly on the details of the organization of fibroblasts in ventricular tissue. However, the ST-RS transition, the stability of spiral- and scroll-wave turbulence, the rotation period of a rotating spiral and scroll, and the width of a rotating spiral and scroll arms, depend sensitively on N_f and G_j.

Earlier studies have investigated the effects of fibroblasts on spiral-wave dynamics by introducing randomly diffuse fibroblasts in a myocyte domain[15,34]. Such randomly diffuse fibroblasts in a myocyte domain inhibit electrical-wave propagation, and initiate spiral-wave turbulence state. Studies by Xie, *et al.*[18] have found that spiral-wave breakup occurs, in an LR1 model, because of randomly diffuse fibroblasts in a localized area of a simulation domain; Zlochiver, *et al.*[15] have shown from their experiments and simulations that a rotating spiral becomes unstable and, finally, spiral breakup occurs, as they increase the percentage of diffuse fibroblasts. Majumder, *et al.*[34] have shown from their numerical experiments that a transition from an RS to various ST states occurs depending on the percentage of fibroblasts in their simulation domain. In our attached-fibroblast model studies, fibroblasts do not inhibit wave propagation[7]; however, fibroblasts attached to a myocyte can lower the steepness of the APDR curve, depending on the values of G_j and N_f.[8,33] Such a lowering of the steep slope of the APDR eliminates spiral- and scroll-wave turbulence in our 2D and 3D simulation domains[35,36,37,38]. Therefore, we observe an ST-RS transition.

Earlier studies in Ref. 33 have observed ST-RS spiral-wave transitions because of a suppression of the steep portion of the APDR slope in a 3D model consisting of myocytes, fibroblasts, and extracellular space by using the LR1 model[21]. However, those studies have not investigated the spiral- and scroll-wave transition as a function of N_f and G_j. Our study shows that both N_f and G_j are important factors during the fibrosis process[39,10].

We suggest that our results from *in silico* studies can be verified in *in vitro* experiments. Furthermore, by using advanced cell-culture techniques[40,41,42], our 2D and 3D numerical results can be tested easily in *cell-culture* experiments.

Acknowledgments

We thank the Department of Science and Technology (DST), India, the University Grants Commission (UGC), India and the Robert Bosch Centre for Cyber Physical Systems (RBCCPS), IISc, for support.

References

1. A. S. Go, D. Mozaffarian, V. L. Roger, E. J. Benjamin, J. D. Berry, M. J. Blaha, S. Dai, E. S. Ford, C. S. Fox, S. Franco, *et al.*, *Circulation* **129**, e28 (2014).
2. D. P. Zipes and H. J. Wellens, *Circulation* **98**, 2334 (1998).
3. J. M. Davidenko, A. V. Pertsov, R. Salomonsz, W. Baxter and J. Jalife. (1992).
4. A. M. Pertsov, J. M. Davidenko, R. Salomonsz, W. T. Baxter and J. Jalife, *Circulation research* **72**, 631 (1993).
5. R. A. Gray, A. M. Pertsov and J. Jalife, *Nature* **392**, 75 (1998).
6. J. Jalife, R. A. Gray, G. E. Morley and J. M. Davidenko, *Chaos: An Interdisciplinary Journal of Nonlinear Science* **8**, 79 (1998).
7. A. R. Nayak, T. Shajahan, A. Panfilov and R. Pandit, *PLoS One* **8**, e72950 (2013).
8. A. R. Nayak and R. Pandit, *unpublished manuscript*.
9. G. Krenning, E. M. Zeisberg and R. Kalluri, *Journal of cellular physiology* **225**, 631 (2010).
10. A. Biernacka and N. G. Frangogiannis, *Aging and disease* **2**, 158 (2011).
11. C. A. Souders, S. L. Bowers and T. A. Baudino, *Circulation research* **105**, 1164 (2009).
12. M. Rook, A. Van Ginneken, B. e. de Jonge, A. El Aoumari, D. Gros and H. Jongsma, *American Journal of Physiology-Cell Physiology* **263**, C959 (1992).
13. P. Camelliti, G. P. Devlin, K. G. Matthews, P. Kohl and C. R. Green, *Cardiovascular research* **62**, 415 (2004).

14. L. Chilton, W. R. Giles and G. L. Smith, *The Journal of physiology* **583**, 225 (2007).
15. S. Zlochiver, V. Munoz, K. L. Vikstrom, S. M. Taffet, O. Berenfeld and J. Jalife, *Biophysical journal* **95**, 4469 (2008).
16. M. Miragoli, G. Gaudesius and S. Rohr, *Circulation research* **98**, 801 (2006).
17. L. C. McSpadden, R. D. Kirkton and N. Bursac, *American Journal of Physiology-Cell Physiology* **297**, C339 (2009).
18. Y. Xie, A. Garfinkel, P. Camelliti, P. Kohl, J. N. Weiss and Z. Qu, *Heart Rhythm* **6**, 1641 (2009).
19. C.-H. Luo and Y. Rudy, *Circulation research* **74**, 1071 (1994).
20. C.-H. Luo and Y. Rudy, *Circulation Research* **74**, 1097 (1994).
21. C.-H. Luo and Y. Rudy, *Circulation research* **68**, 1501 (1991).
22. K. Ten Tusscher, D. Noble, P. Noble and A. Panfilov, *American Journal of Physiology-Heart and Circulatory Physiology* **286**, H1573 (2004).
23. J. Keener and J. Sneyd, *Mathematical physiology*, interdisciplinary applied mathematics 8 (1998).
24. A. V. Panfilov, A. V. Holden, *et al.*, *Computational biology of the heart*, Wiley, 1997).
25. K. Ten Tusscher and A. Panfilov, *Am J Physiol Heart Circ Physiol* **291**, H1088 (2006).
26. A. R. Nayak, *PhD thesis*, Indian Institute of Science (2013).
27. K. A. MacCannell, H. Bazzazi, L. Chilton, Y. Shibukawa, R. B. Clark and W. R. Giles, *Biophysical journal* **92**, 4121 (2007).
28. R. Clayton and A. Panfilov, *Progress in biophysics and molecular biology* **96**, 19 (2008).
29. T. Shajahan, A. R. Nayak and R. Pandit, *PLoS One* **4**, e4738 (2009).
30. Y. Xie, A. Garfinkel, J. N. Weiss and Z. Qu, *American Journal of Physiology-Heart and Circulatory Physiology* **297**, H775 (2009).
31. A. R. Nayak and R. Pandit, *Frontiers in physiology* **5**, 207 (2014).
32. R. Majumder, A. R. Nayak and R. Pandit, *Heart Rate and Rhythm* **269**, Springer (2011).
33. V. S. Petrov, G. V. Osipov and J. Kurths, *Chaos: An Interdisciplinary Journal of Nonlinear Science* **20**, 045103 (2010).
34. R. Majumder, A. R. Nayak and R. Pandit, *PloS one* **7**, e45040 (2012).
35. Z. Qu, J. N. Weiss and A. Garfinkel, *Physical Review E* **61**, 727 (2000).
36. Z. Qu, F. Xie, A. Garfinkel and J. N. Weiss, *Annals of biomedical engineering* **28**, 755 (2000).
37. J. N. Weiss, P.-S. Chen, Z. Qu, H. S. Karagueuzian and A. Garfinkel, *Circulation Research* **87**, 1103 (2000).
38. A. Garfinkel, Y.-H. Kim, O. Voroshilovsky, Z. Qu, J. R. Kil, M.-H. Lee, H. S. Karagueuzian, J. N. Weiss and P.-S. Chen, *Proceedings of the National Academy of Sciences* **97**, 6061 (2000).
39. T. P. Nguyen, Z. Qu and J. N. Weiss, *Journal of molecular and cellular cardiology* **70**, 83 (2014).
40. Y. Haraguchi, T. Shimizu, T. Sasagawa, H. Sekine, K. Sakaguchi, T. Kikuchi, W. Sekine, S. Sekiya, M. Yamato, M. Umezu, *et al.*, *Nature protocols* **7**, 850

(2012).
41. T. Shimizu, M. Yamato, Y. Isoi, T. Akutsu, T. Setomaru, K. Abe, A. Kikuchi, M. Umezu and T. Okano, *Circulation research* **90**, e40 (2002).
42. T. A. Baudino, A. McFadden, C. Fix, J. Hastings, R. Price and T. K. Borg, *Microscopy and microanalysis* **14**, 117 (2008).

A SIMPLE LOGISTIC SIGMOIDAL MODEL PREDICTS OXIDATIVE STRESS THRESHOLDS IN NEWLY DIAGNOSED DIABETICS ON GLUCOSE CONTROL THERAPY

RASHMI KULKARNI*

Department of Biology
Indian Institute of Science Education and Research
Dr Homi Bhabha Road,
Pashan, Pune 411008, INDIA
E-mail: rashmi.k@students.iiserpune.ac.in

Oxidative stress (OS) is a central causal locus through which hyperglycemia leads to post-diabetic complications. Using a mechanistically derived minimal mathematical model, we showed that steady state OS and glycemic state (GS) in newly diagnosed type 2 diabetics can be fitted well using a Goldbeter-Koshland function (GK) [Kulkarni R *et al.*, PLoS ONE 9(6): e100897, 2014]. In clinical usage, however, it would be attractive to use a simpler model to describe changes in OS as GS is controlled. Here we use a logistic sigmoidal function (LS) and compare the two models. Both the models capture a quantal dose-response relationship between plasma glutathione (an oxidative stress marker) and glucose for each diabetic individual (n=48, for both the models). Individual diabetic curves show variation in response to the glycemic treatment which can be captured in terms of parameters of the model, namely, GSH_{max}: maximal glutathione level attained by diabetic patient, v: glucose concentration when plasma glutathione is half maximal and k: slope of the curve. Parameter distributions of v and GSH_{max} predicted by both the models are comparable, but distributions of k show considerable variation. Further, the measures of model selection, namely, mean sum of squared errors and Akaike's information criterion (AIC) suggest that LS model fits better compared to the GK model. Overall, our analysis shows that the LS model is a simple and statistically better alternative to the GK model to establish a quantitative relationship between OS and GS. We hope that OS threshold predictions by the LS model would help in the clinical investigations of hyperglycemia mediated OS responses.

*RK was funded by Council for Scientific and Industrial Research, Government of India.

1. Introduction

Recent studies in cell lines, animal models and human trials establish that oxidative stress (OS) is causally associated with the development of insulin resistance and post-diabetic complications[1,2,3,4]. OS is the central causal locus through which hyperglycemia leads to post-diabetic complications[5,6,7]. Therefore, controlling OS internally can potentially reduce the rate of development of diabetes complications. However, anti-oxidant interventional studies in humans to control OS have either failed or have not been conclusive in controlling diabetes[8,9]. A quantitative understanding of how much and how long OS needs to be controlled with respect to the glycemic state (GS) is key in utilising OS control as a diabetes treatment. Therefore, there is a need to establish a quantitative relationship between the OS-GS state of an individual.

In order to gain a quantitative understanding of OS-GS relationship we used data from a longitudianal study performed on newly-diagnosed diabetics kept on the glycemic treatment[10] (for more information see Materials and Methods section 2.1). Various OS markers were measured at 0, 4 and 8 weeks of the intervention. Our primary analysis suggested that among the various OS markers measured, plasma glutathione improves rapidly over the 8 weeks period of the glycemic treatment. Henceforth, for the sake of simplicity, plasma glutathione pool will be referred to as GSH_t. GSH_t is comprised of reduced (GSH) and oxidised (GSSG) forms, of which GSH is the major anti-oxidant buffer of the cell[11]. GSH scavenges reactive oxygen species produced due to metabolic processes and gets oxidised into GSSG. Together, GSH-GSSG redox couple maintains the optimal redox environment in the cell. Also, it has been shown that $\frac{GSH}{GSSG}$ ratio and plasma glutathione can be used as measures of the plasma OS state[12,13,14,15]. GSH infusions in diabetic subjetcs is known to improve insulin sensitivity[17]. Therefore, GSH_t is a promising OS state marker to monitor the diabetes progression.

In Kulkarni *et al.*, we performed a heirarchical cluster analysis on GSH_t values pooled from 0 and 8 weeks diabetics and non-diabetics[16]. Three distinct GSH_t ranges emerge from the cluster analysis: before therpay diabetic, after therapy diabetic (recovery period) and non-diabetic. GSH_t also showed an inverse relation with the GS in terms of the HbA_{1c} (glycated heamoglobin, a marker of the glycemic state). Based upon the results we proposed that OS-GS dose-response would have a *nonlinear graded* relationship. Further, a mechanistic minimal model was used to capture

this trend, which gives the Goldbeter-Koshland like functional form at the steady-state[16] (for more information see Appendix section 5.2). Individual diabetic fits showed considerable variation in response to the glucose treatment. Based upon our results we proposed a "tailor-made" glucose control therapy target for each diabetic patient[16].

In our earlier study, for mathematical modeling purpose, we assumed that the GSH_t will be conserved over the two months study period. Mechanistically, before treatment GSSG pools would be higher and eventually get converted into GSH as glycemic stress is reduced due to diabetes treatment. This interconversion gives rise to the GK functional form at the steady state[16]. It is interesting to ask how this assumption ought to be relaxed for improving the model. For instance, there might be other complex mechanisms such as changes in transport rates of GSH and GSSG contribute to the observed pattern[18,20]. Besides, the complex GK functional form may not be feasible to use in the clinical settings. Nevertheless, the steady-state dose-responses can be fitted using simple functional form, which retains the predictive power. Therefore, we used the logistic sigmoidal (LS) model to fit the data. Its simple functional form is probably more suitable for practical purpose in the clinical setting to define the glucose targets for diabetics. Our model selction analysis shows that the LS model is statistically better alternative to the GK model. We propose that the simple LS model can be used over the GK model to (a) monitor progress of glucose therapy in terms of OS (b) define glucose targets in terms of the OS state attained by the diabetic patient.

2. Materials and Methods

2.1. *Subjects information*

We reused the dataset on newly-diagnosed type 2 diabetic patients (n = 54) attending the Diabetes Unit, KEM Hospital and healthy non-diabetic subjects (n = 50) to compare the two models[10,16]. Newly-diagnosed diabetic patients were defined as individuals who had blood glucose levels >6.9 mmol/L and HbA_{1c} values >6.5% (47.5 mmol/mol), and had no diabetes associated secondary complications. No anti-diabetic medication was given before the diagnosis. Non-diabetic subjects were volunteers from the academic institutions in Pune. Additional details about the anthropomorphic characteristics, gender, age, BMI, and drug treatments for diabetic patients are provided in the Appendix section 5.1. Fasting blood samples were collected at the interval of 0, 4 and 8 weeks from the diabetic patients and

non-diabetic subjects. Plasma glucose, insulin and various oxidative stress markers including GSH_t were measured using biochemical assays[10]. Diabetic patients were advised on physical activity and diet and were put on anti-diabetic drugs to control hyperglycemia as prescribed. Patients were advised not to take any oral antioxidant and multivitamin supplements as a part of the diet. Pregnant women, chronic smokers and those receiving antioxidants, individuals with excessive alcohol intake, individuals with inflammatory or malignant diseases and those with clinical infection, were excluded from the analysis. Subjects with a recent cardiovascular event and symptomatic heart disease were also excluded. Purpose and nature of the study was explained to all the study subjects and their written informed consent was obtained. The study protocol was approved by the Institutional Ethical Committee, KEM Hospital and Research Centre, Pune[10].

2.2. *Statistical analysis*

Student's t-test for comparison of means was used for comparison of the best fit parameters obtained by the GK and LS models at 95% confidence interval. Also, Akaike's Information Criterion (AIC) along with sum of squared errors, were used as model selection criteria for comparison of two models.

2.3. *Mathematical models and data fitting*

In earlier study, we proposed a mechanistic model to account for the steady state GSH_t-glucose dose-response in newly-diagnosed diabetics[16]. The steady-state functional form of the GK model is provided in the Appendix section 5.2. However, the complex nature of the GK model may not be suitable for the practical purpose in clinical intervention. Therefore, we propose a simpler statistical function to capture the graded dose-response between GSH_t and glucose. A monotonically decreasing functional form of logistic sigmoidal function is used for fitting the data, which is given by:

$$GSH_t(glucose) = GSH_{min} + \frac{GSH_{diff}}{1 + e^{k(glucose-v)}} \tag{1}$$

More information on the mathematical properties of the LS model is provided in the Appendix section 5.3. The LS Model has an extra parameter GSH_{min}, the baseline GSH_t before therapy, which is fixed by the GSH_t value at the 0-week. It is important to note that in the LS model, $GSH_{diff} = GSH_{max} - GSH_{min}$. Therefore, both the models are characterised by

GSH_{max}: the maximal GSH_t pool attained by the diabetic patient at low glucose, k: the slope of the dose-response and v: the glucose concentration at which GSH_t is half-maximal. The parameters are obtained by fitting four GSH_t-glucose data points for each diabetic patient namely, 0, 4 and 8 weeks GSH_t-glucose pairs and maximal non-diabetic GSH_t defined by the age of a diabetic individual, given by the equation $GSH_t = 1354.5 - 14.3 \times Age$ (for more information see Appendix section 5.4). The average non-diabetic glucose value is paired with the asymptotic GSH_t non-diabetic value obtained using above equation.

The optim() function in R was used to optimize the function and obtain the best fit parameters for each diabetic case. Internally, Nelder-Mead algoritham was used for the optimization. The lower bound for v was set at 5mM, which means that if the trend in the glycemic control did not work properly or if the algorithm could not fit the function, a standard glucose control regime would be applied. The GK model fits were also obtained using the same methodology and compared with the LS model fits.

3. Results

3.1. *The LS model is parametrically comparable with the GK model*

We fitted GSH_t and glucose data to the LS and GK models for each diabetic patient (for more information see Materials and Methods section 2.3). It was observed that GSH_t shows age-dependence in non-diabetics and therefore asymptotic GSH_t value for each diabetic would vary depending upon age. The age-dependence of GSH_t was implicitly accounted for in the fitting process, so that we could fit patients across age distribution (for more information see Appendix section 5.4). In 48 out of 49 patients meaningful fits could be obtained for both the models (Figure 1). The GSH_t shows nonlinear graded response to glucose, switching at a critical glucose threshold, v. Each fit is therefore characterized by three parameters, namely, GSH_{max}: the maximal GSH_t corresponding to very low glucose, v: the threshold point, i.e. the glucose concentration for which the GSH_{max} is half-maximal and k: a slope factor that determines the steepness of the GSH_t-glucose response curve. Figure 2 shows corresponding parameter distributions for the GK and LS models. Parameters v and GSH_{max} have physiological relevance originating from the functional form of the models, however, parameter k is not readily comparable. Therefore, we compared v and GSH_{max} parameter distributions of the two models.

Parametrically the two models give comparable fits and distributions of the parameters v and GSH_{max} do not differ significantly (Figure 2).

Figures 1(a) and 1(b), show individual diabetic fits obtained by the GK and LS models, respectively. The grey lines depict individual dose-response curves with considerable variation. A dotted bold curve indicates "population-averaged curve" (PAC) for a given model with averaged values of v, k and GSH_{max} over the individual curves. We note that the PAC for the LS model (characterised by v=6.6, k=4.4, GSH_{diff}=712, GSH_{max}=846) is steeper compared to the GK model (characterised by v=6.9, k=82.2, GSH_{max}=905). The solid black dot is an inflection point for the PAC. The bold solid middle portion is the sensitive part of the PAC. This portion is defined as $(v/4)$ on both sides of the inflection point as the inflection region. The PACs show biphasic responses in the inflection region around the inflection point: lower GSH_t in the hyperglycemic range and switches to the asymptotic higher GSH_t range associated with lower or non-diabetic glucose range. It is intersting to observe that the upper portion of the inflection region falls into the "impaired fasting glucose" (IFG) ranges defined by ADA nad WHO (5.5-6.9mM). A diabetic person in this zone is prone to develop diabetes at a faster rate. The lower part of the solid black portion is the recovery phase of the diabetics after 8 weeks of glucose control therapy. The individual diabetic curves obtained by the LS model can be used to define "tailor-made" glucose control therapies based upon OS state achieved in comparison to GS state. We used model selection criteria to compare the model performances, which is described in the next session.

3.2. *Model selection criteria suggest that the LS model fits are statistically better to the GK model*

We used measures of model selection to compare the fits obtained by the two models. Figure 3 shows histograms of log-transformed SSE for the GK and LS models, respectively. The mean sum of squared errors were found to be considerably lower for the LS model ($MSSE_{LS} = 6.48$ versus $MSSE_{GK} = 8.40$, p-value <0.05). Also, we used Akaike's information criterion (AIC scores) to compare the performances of the two models. Lower the AIC score, better the fitting procedure. The mean AIC score was found to be significantly lower for the LS model (mean $AIC_{LS} = 27.2$ versus mean $AIC_{GK} = 34.0$, p-value <0.05). Therefore, though the parameter distributions obtained by the two models do not differ significantly, model selection

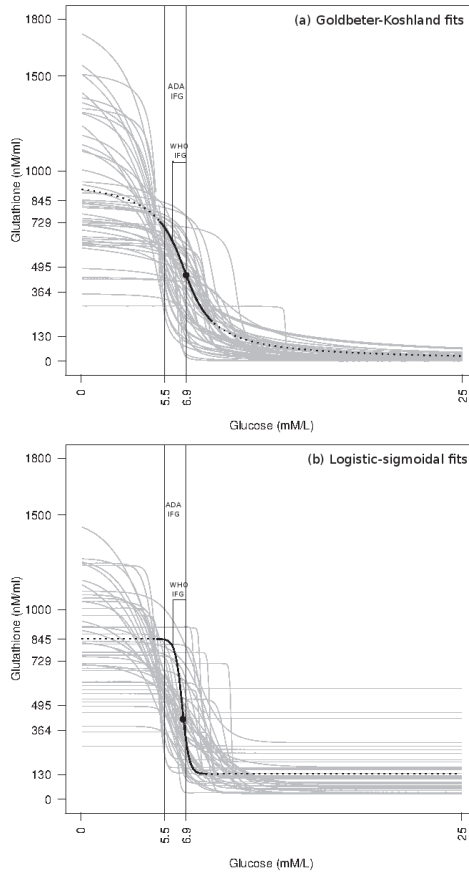

Figure 1. GSH_t-glucose dose-response curves obtained by fitting the GK and LS models to individual diabetic data points. In 48 out of 49 individuals meaningful fits were obtained by each model. Grey lines indicate individual diabetic fits which show considerable variation to glycemic control. The dotted bold black curve is the "population-averaged curve" (PAC). The solid black curve is the sensitive portion of the PAC and the black dot represents inflection point (v) of the curve. Figures 1(a) and 1(b) show individual dose-responses obtained by the GK model and the LS model, respectively. The PAC for the LS model (parameterised by v=6.6, k=4.4, GSH_{diff}=712 and GSH_{max}=846) is steeper compared with PAC for the GK model (parameterised by v=6.9, k=82.2 and GSH_{max}=905). The upper portion of the solid black curve falls into the sensitive regime of "impaired fasting glucose" (5.5-6.9mM) as suggested by the ADA and WHO guidelines. The diabetic patient in this zone will rapidly lead into fully blown diabetic status. The threshold for this is given by v. It is interesting to note that the inflection point for the LS and GK model fall near to upper bound of the IFG regime (6.9mM). Also, lower portion of the solid black curve represents recovery phase from the glycemic treatment where, 80% of the 8-weeks GSH_t values lie.

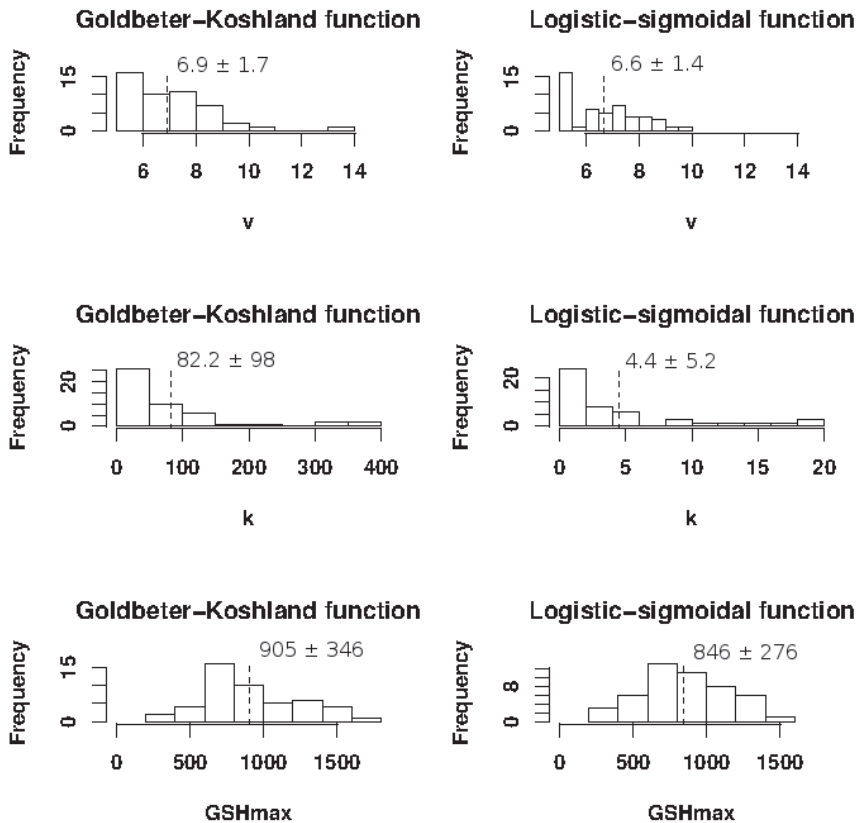

Figure 2. Parameter histogram comparison obtained by fitting Goldbeter-Koshland function (GK) and Logistic sigmoidal function (LS) to individual diabetic patients (n=48). Vertical black dotted lines indicate corresponding $mean \pm sd$ values for the population-averaged parameter values. The population-averaged values of the parameters v and GSH_{max} obtained by the GK and LS models do not differ signaificantly (p-values: 0.44 and 0.36 at 95% confidence interval, respectively). However, the distributions of the third parameter k differ by the order of magnitude.

analysis demonstrates that the simple LS model performs statistically better in comparison to the GK model.

4. Discussion

Our results suggest that the simple LS model can be used for constructing GSH_t-glucose dose-response in newly-diagnosed diabetics over the GK model. The physiologically relevant parameters, v and GSH_{max}, remain

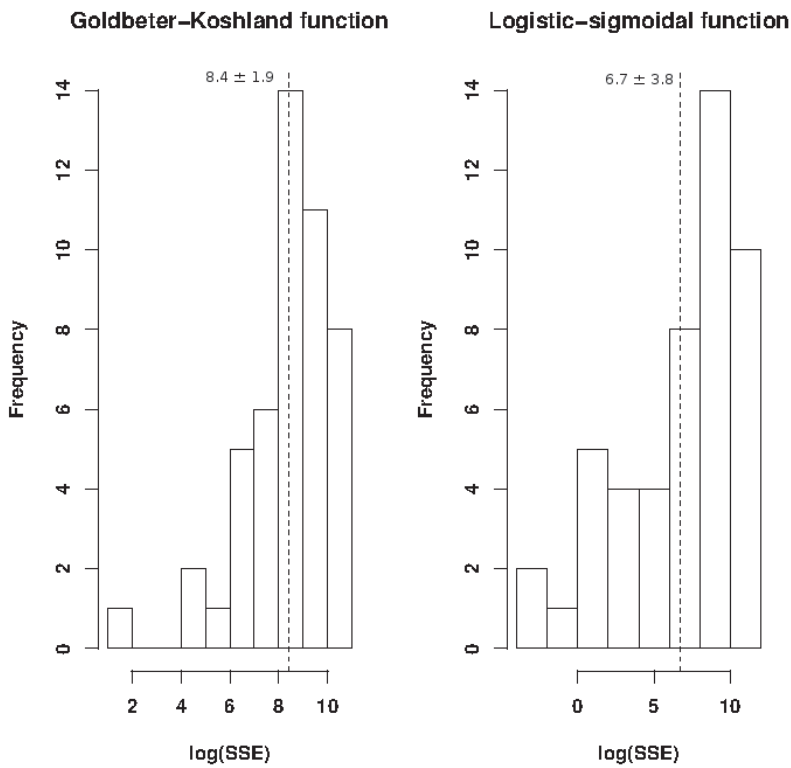

Figure 3. **Comparison of sum of squared erros (SSE) obtained by GK and LS fits (n=48)**. Vertical black dotted lines indicate corresponding $mean \pm sd$ values for the population-averaged SSE. The population-averaged SSE obtained by two models differ significantly and found to be lower for LS model (p-value <0.05).

comparable with the GK model. However, distributions of the third parameter k, which defines the slope of the curve, differ by an order of magnitude. The exact origin of this difference is not clear. In the GK model the slope factor k, is defined as a rate constant, which has a complex non-linear functional origin. This complexity of the slope factor is not present in the LS model. Further mathematical properties of the LS model suggests that the v is not perfectly half maximal but slightly greater than $GSH_{max}/2$ (for more information see Appendix 5.3). However, the slight increase in v is within the standard deviation of the v of the PAC for the LS model, hence may not affect the predictive power.

In a few cases, where the glucose therapy may not have worked properly,

we observed that the GSH_t did not increase concomitantly with the glucose therapy. In such cases curve fitting predicted unphysiological v values, especially below 5mM glucose. To avoid this unphysiological prediction, in the curve fitting procedure we set lower bound of v to 5mM, the standard diabetic treatment regime. We also observed that in couple of cases GSH_t was decreased along with glucose control instead of increasing. In such cases the GSH_{min} need not be the 0-week GSH_t value. Hence in the algorithm we choose the minimum value of GSH_t from the three visits to set as GSH_{min} value. Interestingly, both the models could capture nonlinear OS-GS trajectory in such cases and retains the predictive power. Another technical problem that could arise in curve fitting procedure is that curve starts with the lowest GSH_t level provided, and below which no association between OS-GS exists. In principle, OS-GS relation can exist beyond the lowest GSH_t level provided. However, this discrepancy can be overcome by considering the "solid black portion" of the PAC (Figure 1). Notice that the predictive power of the glucose control lies in the upper portion of the solid black curve which coincides with the IFG band after crossing the threshold value v. The lower portion of the solid black line lies below the inflection point and therefore the changes in the lower portion may not affect predictions of the glucose control targets significantly.

There is a daily variation in the plasma glucose and GSH_t levels. To account for the daily variation in the plasma glucose we used HbA_{1c} converted glucose values (for more information see Appendix section 5.5). Fluctuations in the average plasma glucose over the period of three months is reflected in the HbA_{1c} value. Therefore, HbA_{1c} is considered as a stable marker of glycemic load and accepted standard for the glycemic state. The daily variation in GSH_t is around 15–30%[19]. To account for this variation in the fitting procedure, we randmly varied GSH_t pools by 15–30% (for more information see Appendix section 5.6). We noticed an intersting feature in the curves which have v closer to 5mM. These cases show bifurcation in the curve fitting procedure and show two distinct curve fittings with bimodality in the parameter values. However, for patient cases with higher values of v (beyond 5.8mM), no such phenomenon is observed and fits are robust. We speculate that steeper dose-response curves are fragile and need to be evaluated with more number of data points, accounting for the daily variation in the GSH_t levels.

We propose that the nature of OS-GS trajectory in the initial stages of diabetes is atleast *partially reversible* and shows *non-linear graded* response. This leads to few open questions: what would be the nature of OS-GS curve

as diabetes progresses? Would it retain reversible graded dose-response as observed in newly-diagnosed diabetics? The proposals made in our study, albeit simple and speculative, indicate the need for larger epidemiological longitudinal human trials to answer these questions. Also, there are multiple complex underlying mechanisms which can contribute to systemic OS-GS changes[20]. And in principle, the simple physiological GK model[16] or phenomenological LS model can be improved to incarporate complex mechanisms in future.

Overall our studies suggest that the LS model can be used to capture the GSH_t-glucose dose-response in newly-diagnosed diabetics. Its simple functional form is suitable in the clinical practice for designing glucose control targets. We propose that this curve fitting procedure with multiple time points can turned out to be useful for the OS based diabetes treatment.

5. Appendix

5.1. *Anthropomorphic characteristics of non-diabetic and diabetic subjects and anti-diabetic treatment details*

Table 1 shows anthropomorphic characteristics of non-diabetic and diabetic subjects. In the non-diabetic group, two subjects were removed: Case 16 was removed due to missing data and case 14 developed diabetes during the study period. In the diabetic group, five patients were removed due to missing data points either in BMI (Cases 42,48) glucose or in 8-weeks GSH_t (Cases 5,8,53). Therefore, anthropomorphic characteristics of 48 non-diabetics and 49 diabetics are listed below.

Table 1. Summary of the anthropomorphic characteristics: Gender, age and BMI of non-diabetics (n=48) and diabetics (n=49) used in the data analysis [Adapted from Kulkarni *et al.*, PLoS One, 2014].

Characteristic		**Non-diabetic**	**Diabetic**
Gender	Female/Male	23/25	22/27
Age	Mean ± Std. Dev.	32.8 ± 11.78	47.8 ± 10.5
	Range	22-64	29-76
BMI	Mean ± Std. Dev.	23.75 ± 3.2	26.0 ± 3.6
	Range	16.8-33.3	20.3-41.6

Table 2 gives details about anti-diabetic medication given to diabetic subjects for two months. Among 48 diabetics, 21% received combination of biguanides and sulphonamides drug treatment, 21% received biguanide drug treatment and remaining and 58% received DPP-4 inhibitor or gliptin treatment.

Table 2. Summary of anti-diabetic drug treatment given to 48 diabetic subjects over the period of 8 weeks. [Adapted from Kulkarni *et al.*, PLoS One, 2014].

Drug treatment	Number of diabetics
DPP-4 inhibitor	28
Biguanide	10
Combination of drugs (Biguanide and sulphonamides)	10

5.2. *The Goldbeter-Koshland functional form*

The steady-state GSH_t-glucose response was captured by Goldbeter-Koshland functional form (GK), derived from a minimal mathematical model. It has a monotonically decreasing sigmoidal functional form, which is given by:

$$GSH_t(glucose) = \frac{-(v \cdot GSH_{max} - v \cdot k - Glu \cdot k - GSH_{max} \cdot Glu) - \sqrt{\begin{array}{c} v^2 \cdot {GSH_{max}}^2 + \\ v^2 \cdot k^2 + k^2 \cdot {glucose}^2 \\ + {glucose}^2 \cdot {GSH_{max}}^2 + \\ 2 \cdot {glucose}^2 \cdot k \cdot GSH_{max} \\ -2 \cdot {GSH_{max}}^2 \cdot glucose \cdot v + \\ 2 \cdot k^2 \cdot v \cdot glucose \\ +2 \cdot v^2 \cdot k \cdot GSH_{max} - \\ 4 \cdot glucose \cdot GSH_{max} \cdot v \cdot k \end{array}}}{2 \cdot (glucose - v)} \tag{2}$$

For more information on the mathematical derivation and properties of the GK model refer to supplementary information Kulkarni R., *et al.*, PLoS One, 2014.[16]

5.3. *Physiological interpretation of the parameters of the LS model*

The LS model is characterised by three parameters, v, k and GSH_{max}. GSH_{diff} is the difference between $GSH_{max} - GSH_{min}$. The physiological interpretation can be obtained as follows:

(1) By putting Glu = 0, in the Equ.[1], we obtain, $GSH_t(glucose) = GSH_{min} + GSH_{diff} = G_{max}$. Therefore, at the low glucose GSH_{max} is reached.
(2) By putting Glu = v, in the Equ.[1], we obtain, $GSH_t(glucose) = GSH_{min} + \frac{GSH_{diff}}{2} = \frac{GSH_{max} + GSH_{min}}{2}$ Therefore, v is the threshold of glucose where GSH_t is half-maximal.

5.4. *GSH_t dependence on age in non-diabetics*

We found that GSH_t is negatively correlated with the non-diabetic age. This negative relation was used in the asymptotic GSH_t determination in diabetics for curve fitting procedure. Figure 4 shows the results of the regression analysis.

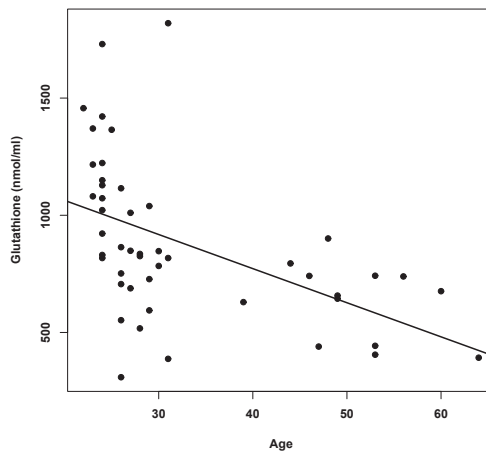

Figure 4. Linear regression of GSH_t against age in non-diabetics (n=48). GSH_t levels are affected due to aging in non-diabetics. The equation for this regression line is GSH_t = 1354.5 - 14.3 ×age, where p-values for the intercept and slope being <0.05 and 0.0002, respectively, at a 95% confidence interval. BMI doesn't contribute to GSH_t levels significantly (Data not shown, p-value for the slope of -5.24 being 0.73 at a 95% confidence interval) [Adapted from Kulkarni R., *et al.*, PLoS One, 2014].

5.5. *Accounting for the daily variation in glucose and GSH_t levels in an individual*

Glycated hemoglobin, HbA_{1c}, is a marker of average blood sugar level over approximately 3 months, and heavily weighted over the last 45–60 days. In contrast to the blood sugar levels glycated hemoglobin level is therefore stabler to fluctuations. In order to reduce variation in the fits we chose to model GSH_t against HbA_{1c}, not fasting glucose. A robust linear regression was used to obtain the relationship between GSH_t against HbA_{1c} as shown in the (Figure 5).

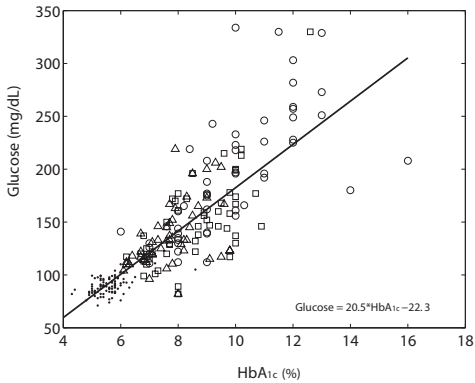

Figure 5. Linear regression between fasting glucose and HbA_{1c}. Fasting glucose and Hb1Ac values were taken from • : Non-diabetic; ○: diabetic 0 week; □ : diabetic 4 weeks; △ : diabetic 8 weeks. This equation is used to convert HbA_{1c} into a glucose value for model fitting. R-squared for the robust linear regression fit is 0.99. [Adapted from Kulkarni R., *et al.*, PLoS One, 2014].

The relationship between fasting glucose and HbA_{1c} is given by,

$$Glu = 20.5 \times HbA_{1c} - 22.3. \tag{3}$$

HbA_{1c} levels of diabetics were converted into equivalent glucose levels using Eq. (3) and used in the fitting procedure. We think therefore that the estimates are reliable with respect to glucose measurements.

5.6. *Accounting for the daily variation in the GSH_t levels and robustness of the fits*

To account for the daily variation in GSH_t levels, we assumed that there is approaximately 15% daily variation in the GSH_t levels.[19] A random number generator was used to vary the GSH_t levels within $GSH_t \pm 15\% GSH_t$ range. This is added to $GSH_t - 15\% GSH_t$. The GSH_t levels simulated for each 0, 4 and 8 weeks were used to fit the curve. This procedure was repeated to obtain 1000 simulated datasets for each case study. All the analysis was performed using statistical package R. We observed that for values v closer to 5mM-5.5mM, curve fitting procedure is fragile and shows two distinct curve fittings. However, this feature disappears as value of v increases beyond 5.5mM of v.

Acknowledgements

I would like to thank Prof. Saroj Ghaskadbi and Dr. Jhankar Acharya from Department of Zoology, Savitribai Phule Pune University, Pune for sharing the diabetic patient data. I would like to thank Dr. Pranay Goel, Assistant Professor, Indian Institute of Science Education and Research, Pune for valuable suggestions on the data analysis and manuscript writing.

References

1. Hoehn, K. L., *et al.*, *Insulin resistance is a cellular defense mechanism*, Proc Natl Acad Sci USA 106(42): 17787–92 (2009).
2. Houstis, N., Rosen, E. D. and Lander, E. S. *Reactive oxygen species have a causal role in multiple forms of insulin resistance*, Nature 440: 944–48 (2006).
3. Anderson, E. J., *et al.*, *Mitochondrial H2O2 emission and cellular redox state link excess fat intake to insulin resistance in both rodents and humans*, J. Clin. Invest. 119, 573–581 (2009).
4. Evans, J. L., *et al.*, *The molecular basis for oxidative stress induced insulin resistances*, Antioxid. Redox Signal. 7, 1040–1052 (2005).
5. Brownlee, M. *Biochemistry and molecular cell biology of diabetic complications*, Nature 414(6865): 813–820 (2001).
6. Meigs, J. B., *et al.*, *Association of oxidative stress, insulin resistance, and Diabetic risk phenotypes The Framingham offspring study*, Diabetes care 30(10): 2529–35 (2007).
7. Evans, J. L., Goldfine, I. D., Maddux, B. A. and Grodsky, G. M., *Oxidative stress and stress-sactivated signaling pathways: a unifying hypothesis of type 2 diabetes* Endocr Rev 23(5): 599–622 (2002).
8. Bjelakovic, G., Nikolova, D., Gluud, L. L., Simonetti, R. G. and Gluud, C. *Mortality in randomized trials of antioxidant supplements for primary and secondary prevention: systematic review and meta-analysis*, JAMA 297(8): 842–857 (2007).
9. Miller, E. R., Pastor-Barriuso, R., Dalal, D., Riemersma, R. A., Appel, L. J. and Guallar, E. *Meta-analysis: high-dosage vitamin E supplementation may increase all-cause mortality*, Ann. Intern. Med. 142(1): 37–46 (2005).
10. Acharya, J. D., Pande, A. J., Joshi, S. M., Yajnik, C. S., Ghaskadbi, S. S. *Treatment of hyperglycaemia in newly diagnosed diabetic patients is associated with a reduction in oxidative stress and improvement in -cell function*, Diabetes Metab Res Rev. 30(7): 590 (2014).
11. Meister, A. *Glutathione metabolism*, Meth Enzymol 251: 3–7 (1995).
12. Jones, D. P., *et al.*, *Redox state of glutathione in human plasma*, Free Radic Biol Med 28(4): 625–35 (2000).
13. Schafer, F. Q. and Buettner, G. R. *Redox environment of the cell as viewed through the redox state of the glutathione disulfide/glutathione couple*, Free Radic Biol Med 30(11): 1191–212 (2001).
14. Paolisso, G., *et al.*, *Plasma GSH/GSSG affects glucose homeostasis in healthy*

subjects and non-insulin-dependent diabetics, Amer Physiol Soc 263: E435–40 (1992).
15. Jimnez-Osorio, A. S., *et al.*, *Nrf2 and Redox Status in Prediabetic and Diabetic Patients*, Int. J. Mol. Sci., 15(11): 20290–20305 (2014).
16. Kulkarni, R., Acharya, J., Ghaskadbi, S. and Goel, P. *Thresholds of oxidative stress in newly diagnosed diabetic patients on intensive glucose-control therapy*, PLoS One 9(6): e100897 (2014).
17. Paolisso, G., *et al.*, *Glutathione infusion potentiates glucose-induced insulin secretion in aged patients with impaired glucose tolerance*, Diabetes Care 15(1): 1–6 (1992).
18. Raftos, J. E., Whillier, S. and Kuchel, P. W. *Glutathione Synthesis and Turnover in the Human Erythrocyte Alignment of a model based on detailed enzyme kinetics with experimental data*, J. Biol. Chem. 285(31): 23557–23567 (2010).
19. Blanco, R. A., *et al.*, *Diurnal variation in GSH and cysteine redox states in human plasma*, Am. J. Clin. Nutr., 86(4), 2007.
20. Reed, M. C., *et al.*, *A mathematical model of GSH metabolism*, Theor Biol Med, 5, 2008.

INDEX